Lecture Notes in Mathematics 2167
CIME Foundation Subseries

Pasquale Ciarletta · Thomas Hillen
Hans Othmer · Luigi Preziosi
Dumitru Trucu

Mathematical Models and Methods for Living Systems

Levico Terme, Italy 2014

Luigi Preziosi · Mark Chaplain
Andrea Pugliese *Editors*

Springer

Lecture Notes in Mathematics 2167

More information about this series at http://www.springer.com/series/#304

Fondazione C.I.M.E., Firenze

C.I.M.E. stands for *Centro Internazionale Matematico Estivo*, that is, International Mathematical Summer Centre. Conceived in the early fifties, it was born in 1954 in Florence, Italy, and welcomed by the world mathematical community: it continues successfully, year for year, to this day.

Many mathematicians from all over the world have been involved in a way or another in C.I.M.E.'s activities over the years. The main purpose and mode of functioning of the Centre may be summarised as follows: every year, during the summer, sessions on different themes from pure and applied mathematics are offered by application to mathematicians from all countries. A Session is generally based on three or four main courses given by specialists of international renown, plus a certain number of seminars, and is held in an attractive rural location in Italy.

The aim of a C.I.M.E. session is to bring to the attention of younger researchers the origins, development, and perspectives of some very active branch of mathematical research. The topics of the courses are generally of international resonance. The full immersion atmosphere of the courses and the daily exchange among participants are thus an initiation to international collaboration in mathematical research.

C.I.M.E. Director (2002 – 2014)
Pietro Zecca
Dipartimento di Energetica "S. Stecco"
Università di Firenze
Via S. Marta, 3
50139 Florence
Italy
e-mail: zecca@unifi.it

C.I.M.E. Director (2015 –)
Elvira Mascolo
Dipartimento di Matematica "U. Dini"
Università di Firenze
viale G.B. Morgagni 67/A
50134 Florence
Italy
e-mail: mascolo@math.unifi.it

C.I.M.E. Secretary
Paolo Salani
Dipartimento di Matematica "U. Dini"
Università di Firenze
viale G.B. Morgagni 67/A
50134 Florence
Italy
e-mail: salani@math.unifi.it

CIME activity is carried out with
the collaboration and financial support
of INdAM (Istituto Nazionale di Alta
Matematica)
For more information see CIME's homepage:
http://www.cime.unifi.it

Pasquale Ciarletta • Thomas Hillen • Hans Othmer •
Luigi Preziosi • Dumitru Trucu

Mathematical Models and Methods for Living Systems

Levico Terme, Italy 2014

Luigi Preziosi • Mark Chaplain • Andrea Pugliese
Editors

In collaboration with

CIRM
CENTRO INTERNAZIONALE
PER LA RICERCA MATEMATICA

Springer

FONDAZIONE CIME
ROBERTO CONTI
CENTRO INTERNAZIONALE MATEMATICO ESTIVO
INTERNATIONAL MATHEMATICAL SUMMER CENTER

Authors
Pasquale Ciarletta
Politecnico di Milano
Dip. Matematica
Milano, Italy

Thomas Hillen
Mathematical & Statistical Sciences
University of Alberta
Edmonton
Alberta, Canada

Hans Othmer
School of Mathematics
University of Minnesota
Minneapolis
Minnesota, USA

Luigi Preziosi
Mathematical Sciences
Politecnico di Torino
Torino, Italy

Dumitru Trucu
Dept. of Mathematics
University of Dundee
Dundee, United Kingdom

Editors
Luigi Preziosi
Mathematical Sciences
Politecnico di Torino
Torino, Italy

Mark Chaplain
School of Mathematics and Statistics
University of St. Andrews
St. Andrews, United Kingdom

Andrea Pugliese
Department of Mathematics
Università di Trento
Povo, Italy

ISSN 0075-8434 ISSN 1617-9692 (electronic)
Lecture Notes in Mathematics
ISBN 978-3-319-42678-5 ISBN 978-3-319-42679-2 (eBook)
DOI 10.1007/978-3-319-42679-2

Library of Congress Control Number: 2016950724

Mathematics Subject Classification (2010): 92Cxx

Printed on acid-free paper

This Springer imprint is published by Springer Nature
The registered company is Springer International Publishing AG Switzerland

Preface

Understanding the mechanisms used by cells to move, to self-organise and to develop in tissues is not only fundamental in embryogenesis but is also relevant in tissue engineering and in other environmental and industrial processes involving the growth and homeostasis of biological systems, e.g. biofilm growth. Growth and organisation processes are also important in many diseases and tissue degeneration and regeneration processes, such as tumour growth, tissue vascularization, heart and muscle functionality and cardiovascular diseases.

In the last decade there has been a burst in the development of mathematical models aimed at studying the behaviour of such biological systems. In doing that, the most difficult point to be taken care of is that by definition biological systems are alive which means that, for instance, they do not respond in a passive way to external chemical and mechanical stimuli, but react actively. They are also able to modify their internal state according to the surrounding environment. Modelling this aspect requires to deeply question and re-analyse whether the classical tools used to model inert matter are proper enough to describe active behaviours. For instance, in continuum mechanics, the concept of evolving natural configurations was proposed to describe the active behaviour of cells, cell ensembles and entire tissues, e.g. muscle and heart (see, for instance, Chap. 4).

In some cases, it is necessary to link mathematical techniques that appear very different. For instance, the study of networks describing chemical reactions occurring inside the cells is interlinking more and more with kinetic theories and continuum mechanics. In fact, more in general what happens at a certain spatial scale, i.e. subcellular, cellular or tissue scale, is logically and functionally linked with what happens at other scales (see, for instance, Chap. 5). For instance, the behaviour of a cell depends on the one hand on the interaction it has with the surrounding environment (see, for instance, Chap. 3) and on the other hand on the chemical reactions occurring inside it (see, for instance, Chap. 1). The two aspects are then related through feedback loops, so that describing a phenomenon without considering what happens at a smaller or at a larger scale results in a strong oversimplification. From the mathematical point of view, this leads to the need of

using multiscale methods and upscaling techniques to connect phenomena occurring at different scales, like the diffusive limits described in Chap. 2.

Keeping this in mind, the aim of the C.I.M.E.-C.I.R.M. summer school on Mathematical Models and Methods for Living Systems was to give an introduction to several mathematical models and methods used to describe the behaviour of living systems. In more detail, then

- Chapter 1, authored by Hans Othmer, deals with models of cell motion starting from the reaction networks occurring at the cytoskeleton level to end with the motion of cell aggregates. In particular, the chapter gives an overview of how chemical and mechanical signals are integrated, how spatial differences in signals are produced and how propulsive and adhesive forces are controlled.
- Chapter 2, authored by Thomas Hillen and Amanda Swan, having in mind the modelling of cell motion, deals with transport models and their relations with individual-based random walk models and reaction-diffusion equations. The model is then applied to bacterial movement, amoeboid movement of cells and the spread of metastasis in anisotropic tissues like the growth of glioblastoma in the brain.
- Chapter 3, authored by Luigi Preziosi and Marco Scianna, focuses on the interaction of cells with the surrounding environment, taking into account several phenomena occurring at the cellular level, such as the role of the nucleus stiffness and the adhesion mechanisms between cells and the fibre network forming the extracellular matrix. With this aim in mind, several mathematical models are introduced, e.g. age-structured models, cellular Potts models and continuum mechanics models.
- Chapter 4, authored by Pasquale Ciarletta and Valentina Balbi, deals with a continuous chemomechanical approach to morphogenesis. The basic evolution laws for both volumetric and interfacial processes are derived and then applied to the study of pattern formation in biological systems treated either as fluids or as solids.
- Chapter 5, authored by Dumitru Trucu, Pia Domschke, Alf Gerisch, and Mark A.J. Chaplain, deals with a multiscale model of cancer invasion. The main focus of the modelling is how the molecular processes occurring at the level of individual cells (micro-scale) and the processes occurring at the tissue level (cell population or macro-scale) are connected and affect each other. Initially a single tissue scale model of cancer invasion is presented based around a system of non-local partial differential equations where the specific roles of cell-cell adhesion and cell-matrix adhesion are explored. This leads naturally to the development of a general spatio-temporal-structured cell population modelling framework which considers the role of cell-receptor dynamics in cancer invasion. Finally, a multiscale moving boundary modelling framework for cancer invasion is developed. In each case, computational simulations are presented which all aim to predict how far cancer cells can invade into healthy normal tissue.

As a concluding remark, we express our deepest gratitude to all the people that have contributed to the success of this C.I.M.E.-C.I.R.M. summer school: the

lecturers, the authors that have contributed to this volume, the participants and all the persons in charge of the organisation. We thank both C.I.M.E. and C.I.R.M. for their financial support, without which the school and therefore this lecture note would have never been possible.

St. Andrews, UK — Mark Chaplain
Torino, Italy — Luigi Preziosi
Povo, Italy — Andrea Pugliese

Acknowledgements

CIME activity is carried out with the collaboration and financial support of INdAM (Istituto Nazionale di Alta Matematica) and MIUR (Ministero dell'Istruzione, dell'Università e della Ricerca).

Contents

Chapter 1
Cell-Based, Continuum and Hybrid Models of Tissue Dynamics

Hans G. Othmer

Abstract Movement of amoeboid cells is involved in embryonic development, wound repair, the immune response to bacterial invasion, and tumor formation and metastasis. Individual cells detect extracellular chemical and mechanical signals via membrane receptors, and this initiates signal transduction cascades that produce intracellular signals. These signals control the motile machinery of the cell and thereby determine the spatial localization of contact sites with the substrate and the sites of force-generation needed to produce directed motion. The coordination and control of this complex process of direction sensing, amplification of spatial differences in the signal, assembly of the motile machinery, and control of the attachment to the substratum involves numerous molecules whose spatial distribution serves to distinguish the front from the rear of the cell, and whose temporal expression is tightly controlled. How chemical and mechanical signals are integrated, how spatial differences in signals are produced, and how propulsive and adhesive forces are controlled are issues that are amenable to mathematical modeling. An overview of some approaches to these complex problems is the subject of this chapter.

1.1 Introduction

Cell and tissue movement is an integral part of many biological processes, such as large-scale tissue rearrangements or translocations that occur during embryogenesis, wound healing, angiogenesis, the immune response, and axon growth and migration. Individual cells such as bacteria migrate toward better environments by a combination of taxis and kinesis, and macrophages and neutrophils use these same processes to find bacteria and cellular debris as part of the immune response. Our understanding of signal transduction and motor control in flagellated bacteria such as *E. coli* that move by swimming and bias their movement by control of their run lengths is quite advanced [2, 93, 108] compared with our understanding of how amoeboid cells such as macrophages crawl through tissues. Some basic issues in the

Supported in part by NSF Grants DMS-0817529 & -1311974 and by NIH Grant GM 29123.

H.G. Othmer (✉)
School of Mathematics, University of Minnesota, Minneapolis, MN 55455, USA
e-mail: othmer@math.umn.edu

L. Preziosi et al. (eds.), *Mathematical Models and Methods for Living Systems*,
Lecture Notes in Mathematics 2167, DOI 10.1007/978-3-319-42679-2_1

latter context include how directional information is extracted from the extracellular signals, how cells develop and maintain polarity, how cells exert traction on their environment, and how adhesion to substrates or other cells is controlled.

Many eukaryotic cells can detect both the magnitude and direction of extracellular signals using receptors embedded in the cell membrane. When the signal is spatially nonuniform they may respond by directed migration either up or down the gradient of the signal, a process called taxis. When the extracellular signal is a diffusible molecule the response is chemotactic, and when it is an adhesion factor attached to the substrate or extracellular matrix (ECM) the process is called haptotaxis [1]. Cells frequently must integrate several signals downstream of the respective receptors, but the mechanisms for doing this are not well understood [45]. Chemotaxis controls the migration of single-celled organisms such as the slime mold *Dictyostelium discoideum* (Dd hereafter), toward a source of cyclic AMP (cAMP), and the movement of leukocytes toward attractants released by bacteria in a tissue. Movement toward a chemoattractant involves directional sensing and orientation, assembly of the motile machinery, polarization of the cell, and control of the attachment to the substratum or ECM. Many eukaryotic cells share common mechanisms, to be described shortly, for sensing and responding to chemoattractant gradients via G-protein-coupled receptors (GPCRs), and to adhesion gradients via integrins or their homologs.

At sufficiently high densities a cell's movement is strongly influenced by that of its neighbors. In some cases cells repeatedly form contacts with neighbors to gain traction, and then break them, only to re-attach to other nearby cells. Examples occur in the streaming and slug stages of the slime mold Dd, to be described later. In other cases cells remain attached to one another, and movement involves massive, coordinated rearrangements of entire tissues, such as folding of the neural plate to form a tube [26, 103]. Movement in both cases involves the same processes as for individual cells, with the addition of more-or-less tight coupling between the movement of neighboring cells, and we refer to both cases as tissue movement.

The classical description of amoeboid cell movement—which roughly speaking is 'crawling' movement that involves cell deformation and protrusions of various types—involves at least four different stages: protrusion, attachment to the substrate, translocation of the cell body, and detachment of the rear (Fig. 1.1) [71, 88]. (1) Cells first extend directed protrusions (lamellipodia, filopodia, or pseudopodia) at the leading edge. The force for this results from localized actin polymerization (discussed later) into cross-linked networks of filaments in lamellipodia or bundles of filaments in filopdia or pseudopodia. Behind the protrusion there is a region of actin disassembly, where filaments are disassembled, crosslinks broken and actin monomers recycled to the site of active polymerization [1]. (2) To persist, protrusions must anchor to the substrate, the extracellular matrix (ECM), or another cell via adhesive complexes, which serve as sites for molecular signaling and force transmission [91, 92]. In mesenchymal motion such as in fibroblasts, the adhesive complexes at the leading edge grow into larger focal adhesions that serve as traction 'pads' over which the cell body moves [33, 90]. (3) Next, depending on the cell type, actomyosin filaments contract at the front, in the perinuclear region, or at the

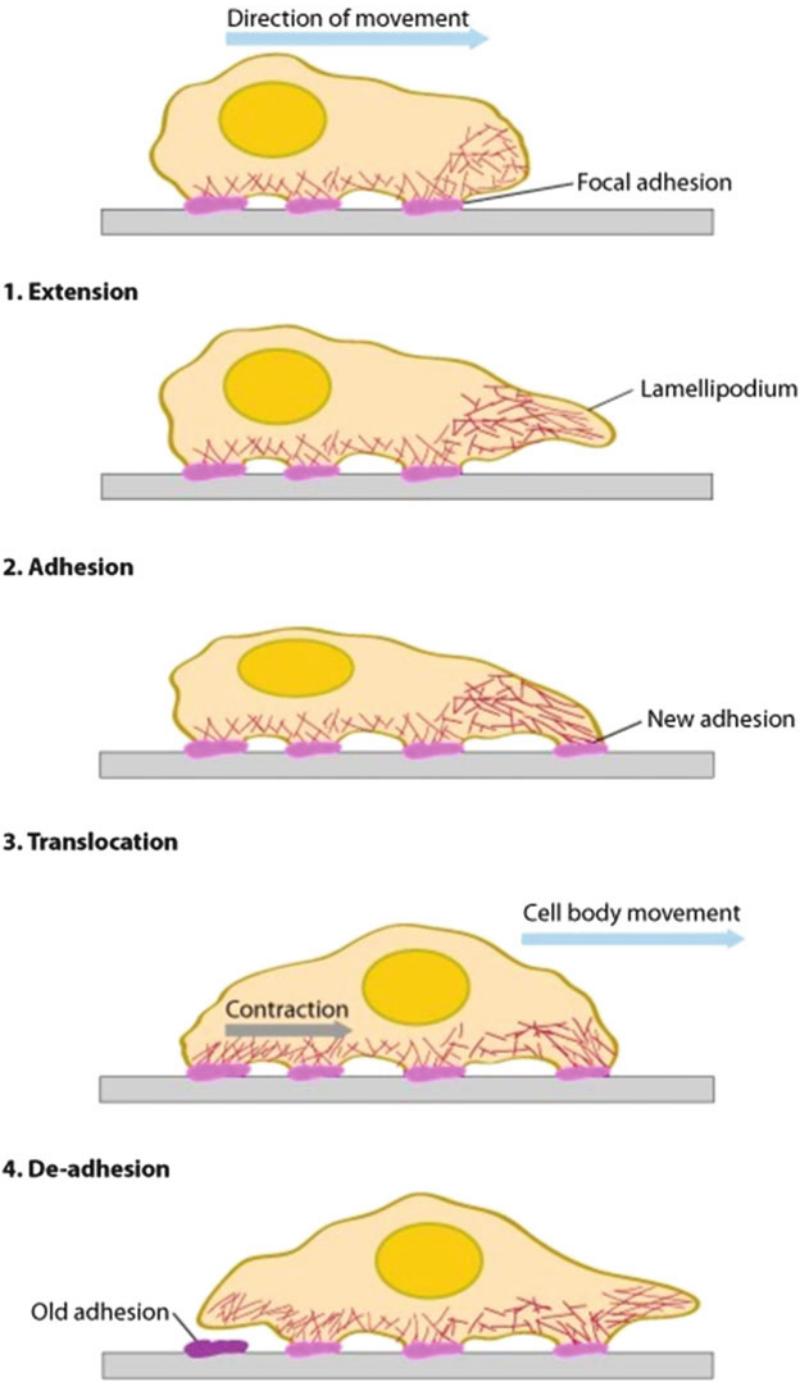

Fig. 1.1 The four stages of eukaryotic cell motion. From [3]

rear, to move the cell body forward. (4) Finally, cells release attachments at the rear [80]. In Dd or keratocytes the adhesion is weak and cells move rapidly, whereas in fibroblasts it is strong and cells move slowly.

The cytoplasm in many amoeboid cells has been characterized as a viscoelastic material whose properties are dominated by actin filaments, intermediate filaments and microtubules, collectively termed the cytoskeleton [54]. The controlled deformation and remodeling of the cytoskeleton that are involved in the shape deformations and protrusions are essential for movement. Its stress/strain response can be varied from that of a solid to that of a liquid by controlled assembly, cross-linking, and disassembly of its components. Thus the cytoskeleton is a dynamically-reorganizable nanomachine. The biochemical control processes, the microstructure of the cytoskeleton, and the formation and dissolution of adhesion sites are coordinated at the whole-cell level to produce the forces needed for movement [5, 8, 61]. Much is known about the biochemical details of the constituent steps in signaling and force generation, and the focus is now shifting to understanding whole-cell movement. For this one needs a mathematical model that links molecular-level behavior with macroscopic observations on forces exerted, cell shape, and cell speed because the large-scale mechanical effects cannot be predicted from the molecular biology of individual steps alone. However, how to formulate a multiscale model that integrates the microscopic steps into a macroscopic model is poorly understood in this context. What is needed are successively more complex model systems that will enable one to test the major modules in an integrated model sequentially. Some of these components are discussed later, and in the following section we begin with actin dynamics. However we first introduce a model system that is widely-used for both experimental and theoretical studies.

1.1.1 Dictyostelium Discoideum as a Model System

The cellular slime mold *Dictyostelium discoideum* is an important system for the study of many developmental processes, including intercellular communication, chemotaxis and differentiation. In a favorable environment the free-ranging individual amoeba feed on bacteria and divide by binary fission, but if the food supply is exhausted an elaborate developmental program is initiated (Fig. 1.2). After a period of starvation the cells attain relay competence and can respond to an external cyclic AMP signal by synthesizing and releasing cyclic AMP. This is called the relay response. The fraction of relay competent cells in a population increases with time after starvation, and at 10 h post-starvation almost all cells are relay competent [43]. At about 8 h post-starvation the cells begin aggregating in response to periodic waves of cyclic AMP initiated by randomly-located pacemaker cells. The proportion of autonomously-signaling cells in an aggregation field rises from zero at about 7 h post starvation and saturates at a small fraction of the total population within 21 h [82]. At the end of aggregation the cells form a cylindrical slug or grex which may migrate on the substrate for some time. Following migration the slug forms a fruiting

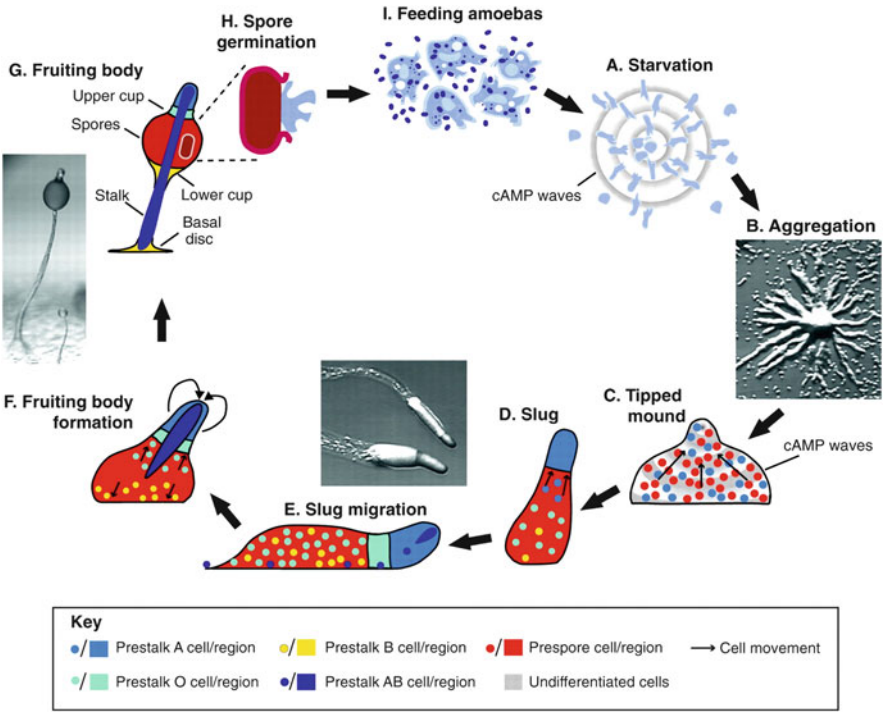

Fig. 1.2 (**a**)–(**i**) The life cycle of Dictyostelium. From [86] with permission

body, which consists of an erect stalk that supports a spherical cap containing spores. Under favorable conditions of temperature and humidity the spores are released and can germinate, and the cycle begins anew [6].

Many biological networks that occur in higher organisms first appeared in lower organisms such as Dd, and thus Dd has been widely-used for studying signal transduction, chemotaxis, and cell motility. Dd uses adenosine 3',5'-monophosphate (cAMP) as a messenger for signaling by randomly-located pacemaker cells that emit cAMP periodically in time to control cell movement in various stages of development [74]. The production by pacemakers and relay of cAMP pulses by cells that are excitable but not oscillatory, leads to cAMP waves that propagate outward from a pacemaker, and this coupled with chemotactic movement toward the source of cAMP, facilitates the recruitment of widely-dispersed cells (Fig. 1.3). In early aggregation the cells move autonomously, but in late aggregation and in the slug stage they interact strongly and the collective motion is tissue-like [74]. In the absence of cAMP stimuli Dd cells extend protrusions called pseudopods in random directions. Aggregation-competent cells respond to cAMP stimuli by suppressing existing pseudopods and rounding up (the 'cringe response'), which occurs within about 20 s after the initial stimulus and lasts about 30 s [20]. Under uniform elevation of the ambient cAMP this is followed by extension of pseudopods in various directions, and an increase in the motility [44, 101, 105]. A localized

Fig. 1.3 Spiral cell density waves observed in aggregation. From [89] with permission

application of cAMP elicits the cringe response followed by a localized extension of a pseudopod near the point of application of the stimulus [95]. How the cell determines the direction in which the signal is largest, and how it organizes the motile machinery to polarize and move in that direction, are major questions from both the experimental and theoretical viewpoint. Since cAMP receptors remain uniformly distributed around the cell membrane during a tactic response, receptor localization or aggregation is not part of the response [55]. Well-polarized cells are able to detect and respond to chemoattractant gradients with a 2 % concentration difference between the anterior and posterior of the cell [76]. Directional changes of a shallow gradient induce polarized cells to turn, whereas large changes lead to large-scale disassembly of motile components and creation of a new 'leading edge' directed toward the stimulus [37].

The first step in developing models for the movement of individuals and population-level aggregation patterns is to identify the distinct processes involved in

producing the different types of response. What a cell must do can be summarized as follows.

- Some cells (or small groups of cells) must become pacemakers. It is known from theoretical studies that a single cell suffices to create an aggregation wave [29], but this has not been demonstrated experimentally.
- A cell must detect the external cAMP and transduce it into an internal signal. A model of this process is discussed later.
- It must choose a direction in which to move and rebuild the cytoskeleton if needed to exert the necessary forces for movement.
- Cells must amplify and relay the signal, and adapt to the ambient signal.
- They must respond to an oncoming wave but not to a receding wave (this is the 'back-of-the-wave' problem), and they must move for an appropriate length of time.
- Eventually a cell interacts with its neighbors and moves collectively, first in pairs, then in streams, then in the slug and finally in the erection of the fruiting body.
- Slightly later it has to 'decide' what type of cell to become in the final fruiting body. This is a collective decision reached by the community (absent cheaters!).
- The entire aggregate has to stop migrating and erect the fruiting body.

The central theme in this chapter can be summarized in the question 'how do we model and analyze these behaviors, and what do we learn from that process?' Since there are many processes involved we approach these steps individually, and for the description of single cell behavior we modularize it as shown in Fig. 1.4.

1.2 Actin Dynamics

1.2.1 The Basic Biochemistry

Actin is a cellular protein that exists either in the globular, monomeric form, called G-actin, or in the polymeric two-stranded filament form, called F-actin. In solution G-actin can self-assemble into long filaments, into bundles, and into higher-dimensional structures. The filaments are long and flexible in vitro, and buckle easily, but in vivo cells create a dense dendritic network of short, branched filaments by tightly coupling nucleation, branching, and cross-linking of filaments in the lamellipodium, a thin (0.1–0.2 μm), sheet-like protrusion at the leading edge of a moving cell [21, 94]. Figure 1.4 shows the processes and some of the auxiliary molecules involved in vivo, and suggests the complexity of models to describe this. Table 1.1—revised from [80]—gives representative concentrations of G- and F-actin, and various auxiliary molecules.

The stiffness of the network enables new filaments to exert force on the membrane and provides the structural basis for polymerization-driven protrusion. The type of structure formed is tightly controlled by extracellular mechanical

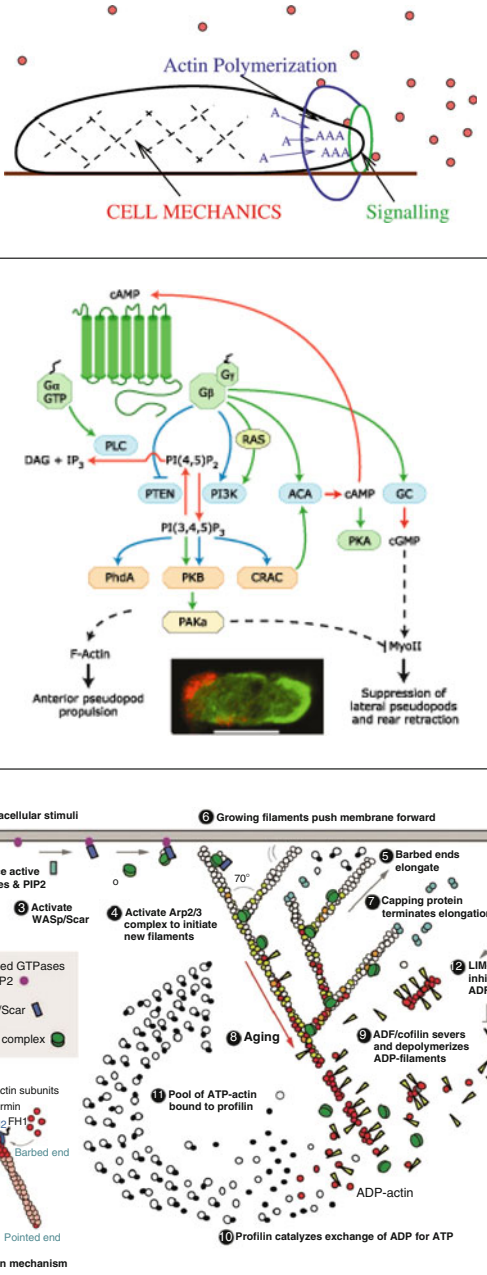

Fig. 1.4 *Top*: A schematic of the modularization of the processes involved in movement at the cell level. *Center*: A schematic of the signal transduction network that activates intracellular processes involved in movement (From [59] with permission). *Green arrows*, enzyme activation; *blue arrows*, membrane localization; *red arrows*, production and signalling; *dashed arrow*, complex regulations that have yet to be fully established. (Image) Myosin heavy chain (MHC) and actin filament distribution in polarized cells. *Lower*: The dendritic actin network, showing some of the major components involved (From [79], with permission)

Table 1.1 Concentrations in μM of actin and auxiliary molecules in various systems

Protein	Acanthamoeba	Dictyostelium	Neutrophil	Xenopus egg
Polymerized actin	100	90	100	4
Unpolymerized actin	100	160	300	12
Profilin	100			5
ADF/cofilin	20	<100		3
Arp2/3 Complex	2-4	present	1–2	

and chemical signals and by intracellular regulatory molecules. Depending on the context and the signal, a variety of motility structures can be formed, ranging from microspikes and filopdia, to larger pseudopodia and broad lamellipodia. In lamellipodia the structure of the dendritic network represents a balance between the formation of actin polymers at the leading edge, most of which occurs at the membrane, and the depolymerization of actin from the meshwork in the interior of the cell. The half-life of actin filaments in the lamellipodium ranges from around 20 s–2 min [98] and is correlated with cell speed: turnover is more rapid in rapidly-moving cells than in slower ones [66]. In any case the turnover of filaments is more than two orders of magnitude faster than the turnover of pure actin filaments in solution [111], and the in vivo system is far from thermodynamic equilibrium and under tight control. This should be contrasted with man-made polymers, which typically are static and designed for long-term stability. Additional discussion of the processes involved is given in [11].

Pollard et al. [80] provide an excellent overview of the basic issues by the series of questions around which they organize their review of the biochemistry. These serve here to provide an overview of areas in which mathematical modeling may be productive.

1. *How do cells maintain a pool of unpolymerized actin subunits?*
2. *How are signals directed to the Arp2/3 complex?*
3. *How do cells create actin filaments with free barbed ends?*
4. *How do new filaments elongate?*
5. *How do growing filaments push the membrane forward?*
6. *What limits the growth of filaments?*
7. *How are filaments marked for depolymerization?*
8. *How do filaments depolymerize?*
9. *How do stable filaments survive in the cytoplasm?*
10. *How are subunits recycled to the ATP-actin-profilin pool?*

We will not address all of these, but to these we add the question 'how do these processes balance to control the length distribution and the dynamic response?', as shown in Fig. 1.5.[1]

[1] Phalloidin functions by binding and stabilizing F-actin and thus this may not represent the true in vitro distribution, but later we obtain very similar distributions.

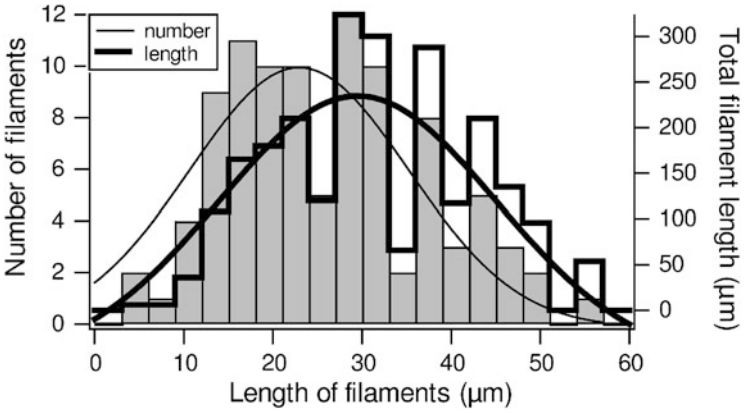

Fig. 1.5 The size distribution of actin filaments determined by fluorescence of phalloidin-rhodamine tagged actin (From [63])

In solution and in vivo G-actin can bind to either ATP (the high-energy triphosphate form) or ADP (the diphosphate form), and the phosphate group in G-ATP is slowly hydrolyzed to ADP. Thus there are three monomer types, G-ATP, G-ADP-P_i, and G-ADP, that can bind to a filament, and each filament is asymmetric in that the rate of monomer addition is higher at the plus (barbed) end than at the minus (pointed) end for all monomer types (see Fig. 1.6). The asymmetry of the filament stems in part from the fact that monomeric units are asymmetric themselves, having a plus and minus end.

Because nucleation of a new filament is energetically less favorable (it requires formation of a trimer, as seen later) than addition to an existing one, the tendency in an in vitro solution is to produce longer rather than more filaments. Thus some insight into the dynamics of a solution can be gotten from a simple model in which the monomers are not distinguished and only addition and release at the plus and minus ends are taken into account. At each end of a filament the reaction

$$A_m + c_m \underset{k^-}{\overset{k^+}{\rightleftarrows}} A_{m+1} \tag{1.1}$$

occurs, where A_m is the filament and c_m is the G-actin monomer concentration. If we neglect all processes but addition or release at the ends, the evolution at each end is governed by the equation

$$\frac{dA_m}{dt} = -k^+ c_m \cdot A_m + k^- A_{m+1}, \tag{1.2}$$

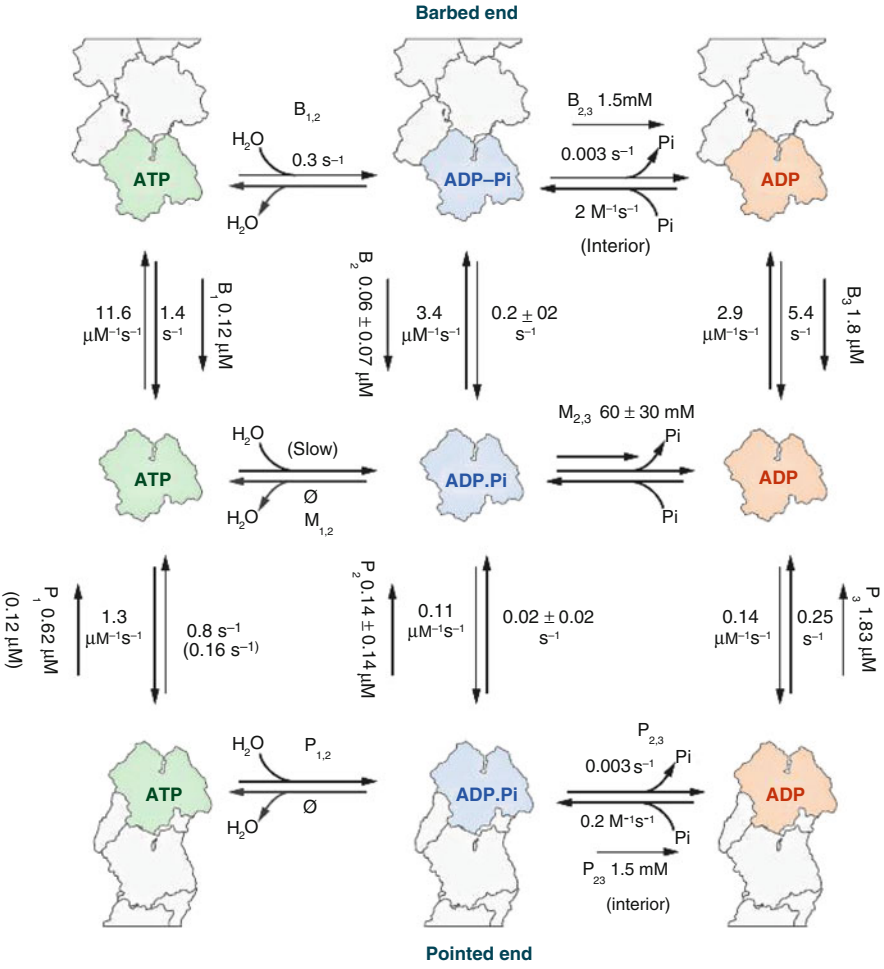

Fig. 1.6 The full set of binding rates. From [79], with permission

and therefore at equilibrium

$$K_d \equiv \frac{k^-}{k^+} = \frac{c_m \cdot A_m}{A_{m+1}} \qquad \text{or} \qquad c_m = \frac{K_d \cdot A_{m+1}}{A_m}.$$

Consequently for each given form of the monomer there is a critical concentration $c_\pm \sim K_d$ for each end of a filament at which the on- and off-rates exactly balance. Above this the filament grows at that end, while below it the end shrinks. G-ATP has a much higher on-rate at the plus end than at the minus end (cf. Fig. 1.6), and therefore the critical concentration c_+ is lower than the critical concentration c_- for the minus end. Now consider what happens as the G-actin concentration is changed.

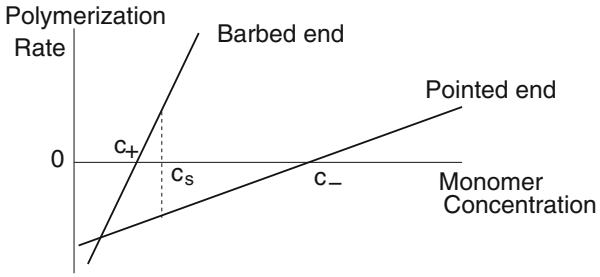

Fig. 1.7 The growth rates of plus and minus ends for G-ATP as a function of the monomer concentration

Since $c_+ < c_-$, the crossover for net growth at the plus end is reached at a lower concentration than at the minus end. For any $c < c_+$ a filament shrinks, and for any concentration $c > c_-$ the filament grows. Thus there is a unique $c_+ < c_s < c_-$ at which net growth at the plus end is balanced by net decay at the minus end, and the length remains constant (cf. Fig. 1.7). For this reason the process is called treadmilling at $c = c_s$. Note that the center of mass of the filament does not remain fixed in space during treadmilling.

In reality, the cycle consists of addition of a G-ATP at the plus end, hydrolysis of the ATP to ADP as the monomer traverses the filament, and loss of a G-ADP at the minus end. Obviously this is a highly-simplified picture, since there is a non-zero rate of addition of G-ADP at the plus end and hydrolysis is probably not obligatory. There is also a more serious problem—at physiological conditions there is about 100 μM unpolymerized actin (Table 1.1), and most of this is in the G-ATP form [84]. However, if one computes the K_d from Fig. 1.6 one sees that the K_d at both ends is much less than this, so according to Fig. 1.7, both ends grow and all actin should be polymerized. Thus there must be other factors involved, some of which are discussed next in the context of binding proteins.

1.2.2 Regulation of Polymerization, Filament Severing and Branching

Motility in amoeboid cells requires localized remodeling of actin networks at the leading edge, or formation of actin bundles in precise locations such as filopodia, and this usually involves additional proteins that regulate actin filament assembly and disassembly locally. Proteins involved in actin-filament turnover are usually localized at the leading edge and are spatially-regulated. The barbed ends of the filaments face towards the leading edge where actin assembly predominates, which leads to cycles of assembly at the front and disassembly in the rear of a lamellipodium. Electron-microscopic images of the lamellipodia of keratocytes

and fibroblasts show an extensively-branched array of actin filaments [called the dendritic brush—cf. Fig. 1.4 (lower)] at the leading edge [94].

The proteins involved in local control of filament and network formation can be grouped according to their function as follows.

- Sequestering proteins: these sequester actin monomers to prevent spontaneous nucleation of filaments ($\beta-$thymosins) or interact with actin monomers to enhance nucleotide exchange (profilin).
- Crosslinking proteins: these cross-link the actin filaments and can induce a sol-to-gel transition. Examples are α-actinin. Others such as vinculin, talin, and zyxin link the actin network beneath the membrane, which is called the cortex, to the plasma membrane.
- Severing proteins: these sever F-actin to generate more filament ends for assembly or disassembly (the ADF family (actin depolymerization factor/cofilin; ADC) of proteins, gelsolin).
- Other proteins function to cap filament ends to regulate addition or loss of actin subunits (capping protein, gelsolin, the Arp2/3 complex), to nucleate filament growth (the Arp2/3 complex), or to enhance subunit dissociation by cofilin.

A schematic of how the different types of proteins affect the filaments and network structure is shown in Fig. 1.8. Their role is also illustrated in Fig. 1.4 (lower).

Despite the high concentrations of G-actin in many cells, filaments rarely nucleate spontaneously in vivo in the presence of the monomer-binding proteins profilin and thymosin-4 [80]. These sequestering proteins maintain a pool of actin ready to polymerize upon the creation of barbed ends [80], although as is seen in Table 1.1, cells such as Dd lack both, so the story may be more complex. Gelsolin

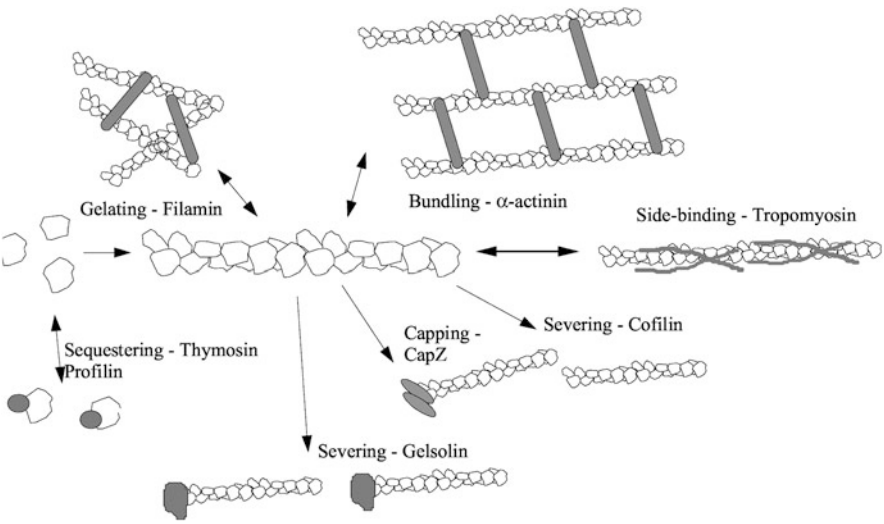

Fig. 1.8 A schematic of the effects of the various types of proteins

and other capping proteins also serve to prevent filament growth by capping the ends, as will be discussed later.

The interplay between all the factors involved produces a size distribution of actin filament lengths. One example is shown in Fig. 1.5, which is for a relatively simple situation, wherein either there is only actin monomer initially (albeit there is a protein phallodin that localizes the fluorescent label and stabilizes long filaments). Others also find an exponential length distribution under normal conditions [87], and we will see later how these can be reconciled.

1.3 A Mathematical Model for In Vitro Filament Dynamics

To gain some understanding of the evolution of the filament length distribution, we consider a closed system containing N monomers of a single type, we incorporate nucleation of filaments, and we analyze the temporal evolution of the distribution. The development here follows that in Hu et al. [47]. Let M_i denote a filament of length i and let C_i be the corresponding concentration. Of course this implicitly assumes that it makes sense to speak of concentrations, since initially there are no filaments present, but we defer until later a discussion of stochastic effects. Thus we consider the sequence

$$\underbrace{\mathcal{M}_1 + \mathcal{M}_1 \underset{k_1^-}{\overset{k_1^+}{\rightleftarrows}} \mathcal{M}_2 \underset{k_2^-}{\overset{k_2^+ \mathcal{M}_1}{\rightleftarrows}} \mathcal{M}_3}_{\textit{Nucleation}} \quad \underbrace{\underset{k_3^-}{\overset{k_3^+ \mathcal{M}_1}{\rightleftarrows}} \mathcal{M}_4 \quad \cdots \mathcal{M}_n \underset{k_n^-}{\overset{k_n^+ \mathcal{M}_1}{\rightleftarrows}} \mathcal{M}_{n+1} \cdots}_{\textit{Propagation}}$$

Define the flux from a filament of length n-1 into a filament of length n as

$$j_n \equiv k_{n-1}^+ C_1 C_{n-1} - k_{n-1}^- C_n.$$

Then the evolution equations can be written

$$\begin{aligned}
\frac{dC_1}{dt} &= -2(k_1^+ C_1^2 - k_1^- C_2) - \textstyle\sum_{n=2}^{N}(k_n^+ C_1 C_n - k_n^- C_{n+1}) = -2j_2 - \textstyle\sum_{n=3}^{N} j_n \\
&\vdots \\
\frac{dC_n}{dt} &= (k_{n-1}^+ C_1 C_{n-1} - k_{n-1}^- C_n) - (k_n^+ C_1 C_n - k_n^- C_{n+1}) = j_n - j_{n+1} \\
\frac{dC_N}{dt} &= (k_{N-1}^+ C_1 C_{N-1} - k_{N-1}^- C_N) = j_N.
\end{aligned}$$

Since the system is closed the evolution is subject to the conservation condition $\sum_{n=1}^{N} nC_n = C_0$, and this implies that solutions exist globally in time for any finite N.

The steady state can be found as follows. Define $K_n \equiv k_n^+/k_n^-$; then the steady state relations $j_i = 0$ lead to

$$C_n = K_{n-1}C_1C_{n-1} = K_{n-1}K_{n-2}C_1^2C_{n-2} = \cdots = \left(\prod_{i=1}^{n-1} K_i\right) C_1^n \equiv \Lambda_n C_1^n$$

and the conservation condition becomes

$$\sum_{n=1}^{N} nC_n = \sum_{n=1}^{N} n\Lambda_n C_1^n = C_0.$$

The left-hand side in the last equality is monotone increasing in C_1 and vanishes at zero, and therefore the steady-state is unique. One can also prove [47] that

- The Gibb's free energy $G = \sum_{n=1}^{N} x_n\mu_n$ is a Lyapunov function. Here the chemical potentials are defined as

$$\mu_n = \mu_n^0(T,P) + RT\ln\frac{C_n}{C_T} = \mu_n^0(T,P) + RT\ln x_n.$$

  Further, x_n is the mole fraction of species n and C_T is the total concentration, including water. Since actin solutions are typically in the 10–100 μM range [80], we can ignore the small changes in total concentration that accompany polymerization and thus assume that C_T is constant at constant temperature and pressure. Thus the solution always converges to the steady state.
- For any fixed N >3, there exists a critical concentration C_0^* such that the profile is monotone increasing for $C_0 > C_0^*$ and $n \geq 4$, and monotone decreasing for $C_0 < C_0^*$. The critical C_0^* gives $C_1 = K^{-1}$, where $K = K_j$ for $j \geq 3$.
- For any fixed $C_0 > 0$ there exists an $N > 3$ such that the profile is monotone decreasing.

1.3.1 The Initial Evolution of the Distribution

The next objective is to understand the evolution of the length distribution in vitro. To fix the context, we stipulate that the initial condition is a pure monomer pool in a volume of 2000 μm^3, which is a typical cell size. We always the state initial conditions as concentrations, but we display the results in terms of the numbers of the different types of species. To convert between them use the fact that 1 μM corresponds to 600 molecules/μm^3; thus the total number of monomers in the standard volume used is 1.2×10^6. We know from the preceding that the final distribution is monotonic, and for these initial conditions it is monotone increasing, but the computational result in Fig. 1.10 shows that the evolution is complex. In that

figure and hereafter we use rate constants from [87] given as follows.

$$k_n^+ = 10 \quad \text{for all n} \quad k_1^- = 10^6 \quad k_2^- = 10^3 \quad k_n^- = 1 \quad n \geq 3$$

Here first-order rate constants have units s^{-1} and second-order constants have units $\mu M^{-1} \cdot s^{-1}$. For these rate constants the critical concentration is 0.1 μM—above this the filaments grow and below this they shrink. Since the trimer → dimer and the dimer→ monomer steps are 3 and 6 orders of magnitude faster, resp., than other first-order steps, it is difficult to nucleate filaments in solution unless the monomer pool, and hence the forward rate k^+C_1, is sufficiently large.

To understand the evolution shown in Fig. 1.10, we lump the species into four pools, comprising monomers, dimers, trimers, and filaments of length four and longer, respectively. From this diagram one can see that different processes may balance at different stages of the evolution, as seen in Fig. 1.10. There are three distinct regimes in Fig. 1.10: the first one characterized by formation of the maximum peak height in the distribution, the second is a polymerization-driven advective phase in which the mean length increases in a wave-like movement along the length axis, and the third is a diffusive stage in which monomers are redistributed among filaments and the length distribution evolves to the steady-state distribution. The long final phase in which the profile converges to the steady state distribution is not shown in the figure.

The disparity between the off-rates for filaments of length greater than three monomers and those for dimers and trimers leads to four well-defined time scales in the early dynamics that arise from different balances in Fig. 1.9. In increasing order in the evolution they are (1) equilibration of monomers and dimers ($T_1 \sim (k_1^- + 4k^+C_1(0))^{-1} \sim \mathcal{O}(10^{-6})$ s), (2) the time at which the trimers reach their maximum ($T_2 \sim (k_2^- + 9 \cdot k_2^+ K_1 C_1(0)^2)^{-1} \sim \mathcal{O}(10^{-3})$ s), (3) establishment of the total number of filaments (T_3: $\sim$ 30 s), and (4) equilibration of the monomer pool with the filaments (T_4: to be estimated later). T_1 only plays a role in a perturbation analysis done later.

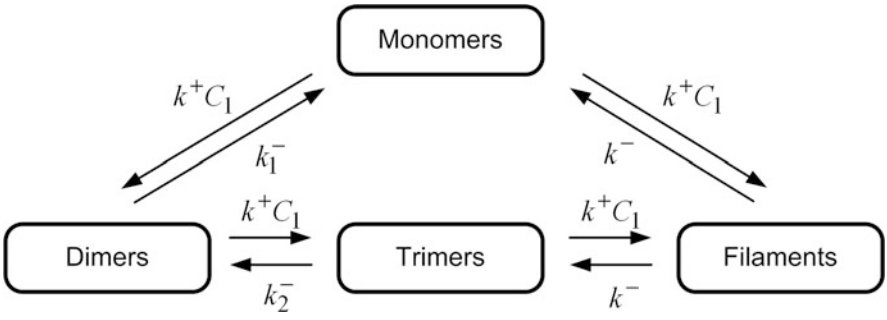

Fig. 1.9 A schematic of the network for nucleation and filament growth

On the time scale T_2 the trimer population peaks, and then dimers and trimers equilibrate with the monomer pool, whereas the slower formation of filaments can be neglected on this scale. As is shown in [47], one can truncate the steady-state equations at trimers and estimate the number of them quite accurately on this time scale. Following this, filaments are formed from the trimers, and the monomer pool decreases due to both filament formation and monomer addition to the growing filaments. In this phase the trimer concentration or number decreases monotonically, and when it reaches a level at which there is only one trimer, the total number of filaments essentially stops increasing. Of course at this point stochastic effects will play a significant role.

Once most of the trimers have been converted into filaments the total number of filaments of length at least four is fixed, and the system enters a hyperbolic phase in which the mean length of the filaments increases. This phase corresponds to the wave-like movement of the peak in the distribution (Fig. 1.10), which ends at around 30 s. This is followed by the penultimate phase in which the monomer concentration is approximately at the critical level and the number of filaments is approximately constant. In this phase there is a slow redistribution of monomers among the filaments.

To understand the hyperbolic, diffusive and terminal regimes mathematically, begin with the evolution of the filaments for $n = 4, 5, \ldots, N-1$ written as follows.

$$\begin{aligned}\frac{dC_n}{dt} &= (k_n^+ C_1 C_{n-1} - k_n^- C_n) - (k_{n+1}^+ C_1 C_n - k_{n+1}^- C_{n+1}) \\ &= -(k^+ C_1 - k^-)(C_n - C_{n-1}) + \frac{k^+ C_1 + k^-}{2}(C_{n+1} - 2C_n + C_{n-1}).\end{aligned}$$

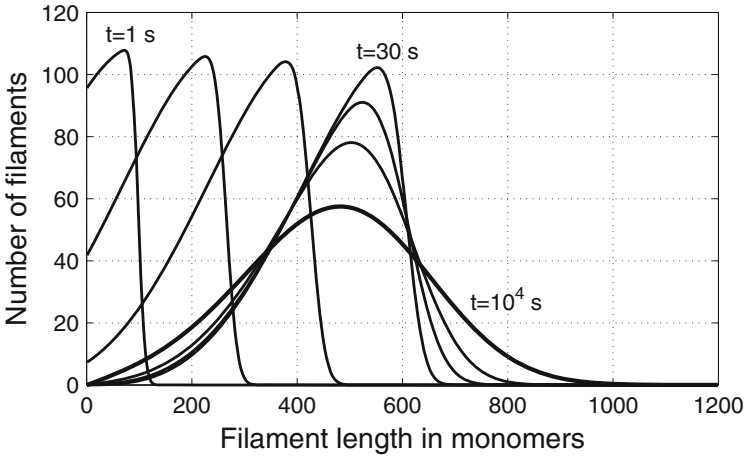

Fig. 1.10 The time evolution of the filament length distribution, starting from a G-actin concentration of 10 μM. The profiles correspond to 1, 3, 6, 30, 10^3, 3×10^3, and 10^4 s, respectively. From [47], with permission

If us denote by $C(x)$ the concentration of filaments of length $x = n\delta$ (where δ is the half length of a monomer), then we have the continuous approximation as

$$\begin{aligned}\frac{\partial C(x)}{\partial t} &= k^+C_1(C(x-\delta) - C(x)) - k^-(C(x) - C(x+\delta)) \\ &\approx -(k^+C_1 - k^-)\delta\frac{\partial C}{\partial x} + \frac{k^+C_1 + k^-}{2}\delta^2\frac{\partial^2 C}{\partial x^2}\end{aligned}$$

and from this we see that the convective velocity is $(k^+C_1 - k^-)$ in monomer/s, which vanishes at the critical concentration, and that the diffusion coefficient is $(k^+C_1 + k^-)/2$ monomer^2/s. When the monomer concentration C_1 is above the critical concentration the filaments polymerize as they diffuse, at the rate $k^+C_1 - k^-$ monomer/s, but when the monomer concentration drops to the critical value the polymerization essentially stops and diffusion dominates. Before establishment of the monomer-polymer equilibrium, convection dominates diffusion, and one observes in the computational results that the maximum of the length distribution increases at a predictable speed [47].

1.3.2 The Long-Time Evolution of the Distribution

In the final stage of the evolution the unimodal distribution evolves, albeit very slowly, into an exponential steady-state distribution. If one assumes that the monomer pool is approximately constant at the critical concentration in this phase, one has the linear system

$$\frac{dC}{dt} = \left[\begin{array}{c|c} K_1 & K_2 \\ \hline K_3 & K_4 \end{array}\right] C + \Gamma \equiv KC + \Gamma, \tag{1.3}$$

where

$$C = (C_2, C_3, \cdots,)^T \qquad \Gamma = \left(k_1^+C_1^2, 0, \cdots 0\right)^T$$

and the $(N-1) \times (N-1)$ matrix K is given by

$$K = \left[\begin{array}{cc|ccc} -(k^+C_1 + k_1^-) & k_2^- & 0 & 0 & \cdots \\ k^+C_1 & -(k^+C_1 + k_2^-) & k^- & 0 & \cdots \\ \hline 0 & k^+C_1 & -(k^+C_1 + k^-) & k^- & \cdots \\ \vdots & & k^+C_1 & -(k^+C_1 + k^-) & k^- \\ \vdots & & & k^+C_1 & -(k^+C_1 + k^-) \\ \vdots & & & 0 & \vdots \end{array}\right]$$

The following properties are established in [47].

- The matrix K has two large negative eigenvalues given approximately by $-k_1^-$ and $-k_2^-$, corresponding to the relaxation rate of monomers $\leftrightarrow$ dimers and dimers $\leftrightarrow$ trimers, respectively.
- The remaining eigenvalues are those of K_4 to lowest order. K_4 is a perturbation of a tridiagonal matrix of the form

$$K_4 = (k^+C_1)\mathbf{J} - (k^+C_1 + k^-)\mathbf{I} + k^-\mathbf{J}^T$$

where $\mathbf{J}$ is the lower diagonal shift.
- The eigenvalues of this are

$$\lambda_p = -(k^+C_1 + k^-) + 2\sqrt{k^-k^+C_1}\cos\theta_p \qquad \theta_p \equiv \frac{p\pi}{N+1}$$

- Since $k^+ = 10$, $k^- = 1$, the critical concentration is $C_{1,crit} = 0.1$, it follows that

$$\lambda_p \to 0 \quad \text{as} \quad N \to \infty.$$

This shows that the slowly-evolving quasi-attractor in the diffusive stage is *not* an artifact of the assumption that the maximum filament length is finite. A more detailed spectral analysis of K shows that the slowest mode relaxes on a time scale of order of N^2, which for $N = 2000$ is of order 10^6 s [47]. This exceptionally slow relaxation provides a possible explanation for why different experiments lead to different conclusions concerning the steady-state distribution.

1.4 Stochastic Analysis of Actin Dynamics

Thus far we have modeled actin dynamics from a continuum, deterministic viewpoint, and the analysis of the resulting models gives significant insights into the evolution of filaments in solution. However, as we noted at several points, when there are only a few copies present of a particular species the deterministic model probably breaks down, and a stochastic description should be used. As we also noted previously, G-actin is present in three different forms, but to simplify the analysis we considered only one heretofore. In particular, ATP has not been singled out for any role beyond supplying the necessary energy, which is stored in some unspecified way in the filament lattice and dissipated by hydrolysis as a monomer moves from the plus to the minus end of a filament. Thus a more precise description of filament dynamics would include adding G-ATP at the plus end, hydrolysis, release of the inorganic phosphate P_i as ATP is hydrolyzed, and dissociation of G-ADP at the minus end. We deal with these issues in this section.

Actin rapidly hydrolyzes ATP upon polymerization [4] and releases bound phosphate several 100 s later [70]. ATP hydrolysis and phosphate dissociation do not cause immediate filament disassembly, but enable interaction with depolymerizing factors such as cofilin. ATP hydrolysis by actin thereby determines the overall rate of filament turnover, and some suggest that the nucleotide bound to actin filaments serves as a timer to control actin filament turnover [4].

In addition, actin filaments can be stiffened by actin-binding molecules such as the toxin phalloidin, which has been shown to delay the release of inorganic phosphate after ATP hydrolysis, i.e., the lifetime of the intermediate F-actin-ADP-Pi is significantly increased by phalloidin [25]. Thus it seems reasonable to conclude that the portion of the filament with P_i bound will be stiffer than the part following release, and this suggests that one should perhaps take position along the filament into account when considering either or both branching and severing. A summary of how some of the sequestering and severing proteins contribute to maintaining the filament length is shown in Fig. 1.11. Obviously unpolymerized actin can be sequestered in a variety of states so as to maintain a pool for rapid polymerization.

In addition to simple breakup of filaments, they can also exhibit large length fluctuations, due to the stochastic exchange of monomers between the filament and the monomer pool. Early theoretical studies on a single-monomer-type model like that used in the previous section predicted that at the steady 'treadmilling' state, the filament length distribution undergoes a diffusion process at the rate k^-, the off rate of monomer at filament ends [72]. However, as we showed in the previous section, the instantaneous diffusion rate constant is the mean of the polymerization and depolymerization rates. In these models both the elongation rate and diffusion constant are linear functions of monomer concentration over the entire concentration range. However, Carlier et al. showed that the growth rate of filaments can be described to first order by two distinct linear functions applicable in different regimes of monomer concentration [14]. Filaments depolymerize below

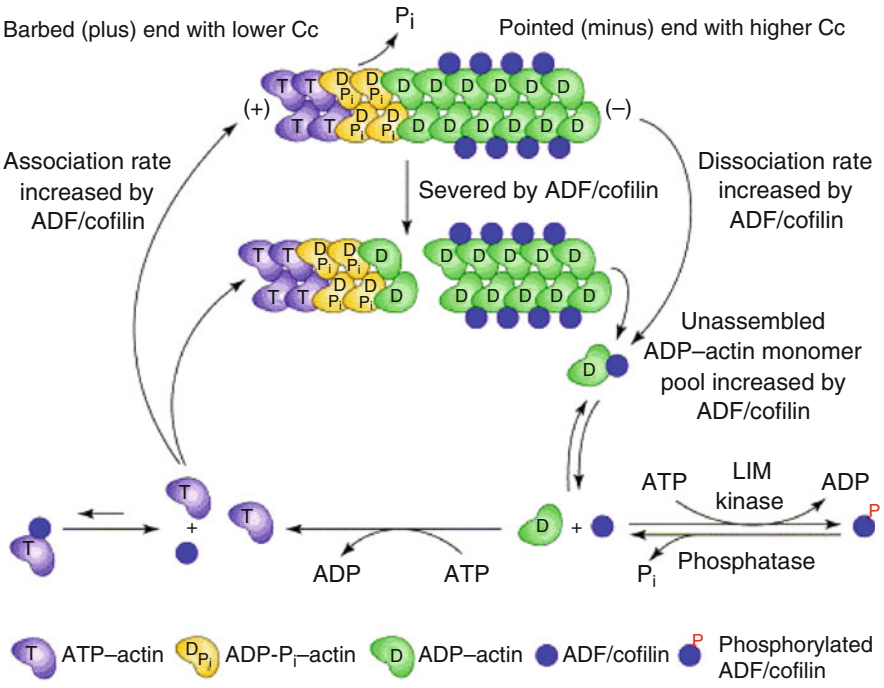

Fig. 1.11 A schematic of the effects of ADF/cofilin and profilin on filament length (From [17])

a critical concentration, whereas above it filaments grow at a constant rate and the slope of the elongation rate below the critical concentration is higher than that above it. At the critical concentration the growth rate vanishes, and filaments treadmill. In a seminal experiment, Fujiwara et al. observed that individual filaments show surprisingly large length fluctuations in the treadmilling phase [34], and other experiments confirmed this high diffusion rate [60]. A stochastic simulation that illustrates the large length fluctuations at the barbed end is shown in Fig. 1.12.

One sees there that the pointed end shrinks continuously, with relatively small fluctuations in the mean position of the end. However, there are large fluctuations at the barbed (upper) end of the filament. One sees in (b) that when the filament has an ATP cap (red) it grows, and that it decreases rapidly when the end monomer contains ADP (see inset to (b) at ~ 232 s). Furthermore, a significant number of ADP-Pi monomers, in which both ADP and phosphate are still bound to the protein, survive to the pointed end in this realization.

This example raises several questions, namely (1) how does one do stochastic simulations of polymer networks, and (2) what are interesting questions and what can be learned from them. Some answers to the second one are as follows.

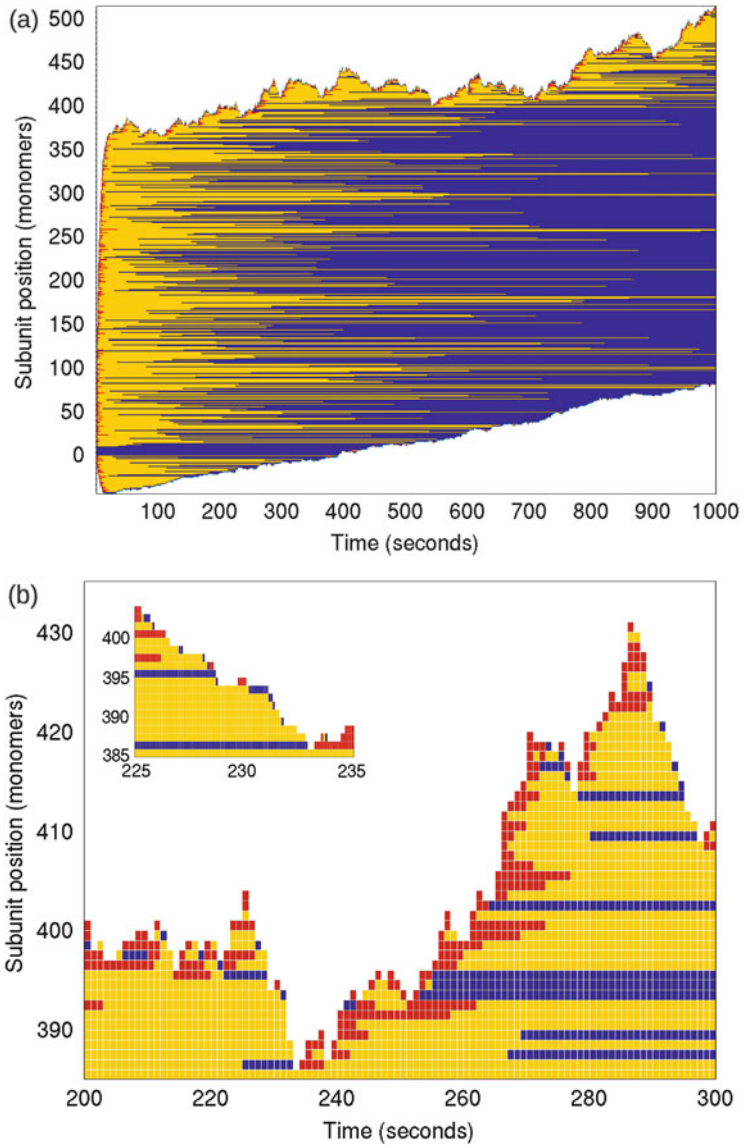

Fig. 1.12 (**a**) and (**b**) The length and nucleotide profile of a single filament during the polymerizing and treadmilling phase. Here the barbed end is at the *top* and the pointed end at the *bottom*—the former growing and the latter shrinking. *Red* represents an ATP-containing monomer, *yellow* ADP-Pi, and *blue* ADP-actin-containing monomers. Time in (**a**) and (**b**) is divided into 1-s steps, whereas in the inset to (*b*) it is divided into 0.1-s blocks. From [46] with permission

- What is the average nucleotide profile of an actin filament?
- How do different biochemical factors such as ADF/cofilin alter the average nucleotide profile and conversely, how does the nucleotide profile affect the action of these factors?
- What is the dynamic response of the distribution of length and nucleotide profiles to an "external" signal that produces an increased amount of globular actin?
- Can the types of catastrophes described above that occur near the critical concentration be explained?
- In what regimes are both the continuous and the stochastic models valid, and when must one use a stochastic model?

1.4.1 The Mathematical Description of Reaction Networks

Suppose we have a set $\mathcal{M}$ of s chemical species $\mathcal{M}_i$ that participate in a total of r reactions. We write the reactions as

$$\sum_i^{reac.} \nu_{ij}^{reac} \mathcal{M}_i \to \sum_i^{prod} \nu_{ij}^{prod} \mathcal{M}_i \qquad j = 1, \ldots r,$$

where ν_{ij} is the stoichiometric coefficient of the ith species in the jth reaction. The set of reactions gives rise to a directed graph $\mathcal{G}$ as follows. Each linear combination of reactants or products is called a complex, and each complex is identified with a vertex V_k in $\mathcal{G}$ and a directed edge E_ℓ is introduced into $\mathcal{G}$ for each reaction. The topology of $\mathcal{G}$ is encoded in its vertex-edge *incidence matrix* $\mathcal{E}$, which is defined as follows.

$$\mathcal{E}_{i\ell} = \begin{cases} +1 & \text{if } E_\ell \text{ is incident at } V_i \text{ and is directed toward it} \\ -1 & \text{if } E_\ell \text{ is incident at } V_i \text{ and is directed away from it} \\ 0 & \text{otherwise} \end{cases}$$

Suppose there p complexes—then $\mathcal{E}$ has p rows and r columns, and every column has exactly one $+1$ and one -1. Each edge carries a nonnegative weight $R_\ell(c)$ given by the intrinsic rate of the corresponding reaction. For example, the simple reaction $\mathcal{M}_1 + \mathcal{M}_2 \rightleftharpoons \mathcal{M}_3$ is written as the two steps $C(1) \to C(2)$ and $C(2) \to C(1)$, where $C(1) \equiv \mathcal{M}_1 + \mathcal{M}_2$ and $C(2) \equiv \mathcal{M}_3$. This network gives rise to the following graph and incidence matrix.

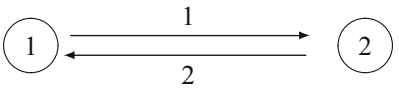

$$\mathcal{E} = \begin{bmatrix} -1 & 1 \\ 1 & -1 \end{bmatrix}$$

The evolution equation for the concentrations $(c_1, c_2)^T$ of $\mathcal{M}_1$ and $\mathcal{M}_2$ now has the factored form

$$\frac{dc}{dt} = \nu \mathcal{E} R(c), \;\; c(0) = c_0 \qquad \nu \equiv \begin{bmatrix} 1 & 0 \\ 1 & 0 \\ 0 & 1 \end{bmatrix}$$

The weight functions R_j define a flow on the graph, and one says that the flow is balanced if $\mathcal{E}R(c) = 0$ [73]. In this case the fluxes entering and leaving each vertex are balanced and the solution can be represented in terms of cycles in the graph. Similar statements apply in general. For a network governed by ideal mass-action kinetics the composition $(c_1, c_2, \cdots, c_s)^T$ satisfies the evolution equations

$$\frac{dc}{dt} = \nu \mathcal{E} R(c), \;\; c(0) = c_0 \tag{1.4}$$

where

$$R_\ell(c) = k_\ell P_j(c) = k_\ell \prod_{i=1}^{s} c_i^{\nu_{ij}}$$

This class of kinetics is called vertex-controlled, because the flows on an edge are controlled by the composition of the complex at the source vertex

One can also describe the evolution of a reacting system in terms of the number of molecules present for each species. Let $n = (n_1, n_2, \ldots, n_s)$ denote the discrete composition vector whose ith component n_i is the number of molecules of species $\mathcal{M}_i$ present in the volume V. This is related to the composition vector c by $n = \mathcal{N}_A V c$, where $\mathcal{N}_A$ is Avagadro's number, and although the n_i take discrete values, they are regarded as continuous when large numbers are present. Thus the deterministic evolution for n is

$$\frac{dn}{dt} = \nu \mathcal{E} \tilde{\mathcal{R}}(n) \tag{1.5}$$

where $\tilde{\mathcal{R}}(n) \equiv \mathcal{N}_A V R(n/\mathcal{N}_A V)$. In particular, for ideal mass-action kinetics

$$\tilde{\mathcal{R}}_\ell(n) = \mathcal{N}_A V k_\ell P_j(n/\mathcal{N}_A V) \tag{1.6}$$

$$= \mathcal{N}_A V k_\ell \prod_{i=1}^{s} \left(\frac{n_i}{\mathcal{N}_A V} \right)^{\nu_{ij}} = \frac{k_\ell}{(\mathcal{N}_A V)^{\sum_i \nu_{ij} - 1}} \prod_{i=1}^{s} (n_i)^{\nu_{ij}} \tag{1.7}$$

$$= = \hat{k}_\ell \prod_{i=1}^{s} (n_i)^{\nu_{ij}}. \tag{1.8}$$

This is still a deterministic description, and in a stochastic description the numbers of the individual components are followed in time and the reactions are modeled as a continuous-time Markov jump process. Let $N_i(t)$ be a random variable that represents the number of molecules of species $\mathcal{M}_i$ at time t, and let N denote the vector of N_is. Let $P(n,t)$ be the joint probability that $N(t) = n$, i.e., $N_1 = n_1, N_2 = n_2, \ldots, N_s = n_s$. Clearly the state of the system at any time is now a point in $\mathcal{Z}_0^s$, where $\mathcal{Z}_0$ is the set of nonnegative integers. Formally the master equation that governs the evolution of P is

$$\frac{d}{dt}P(n,t) = \sum_{m\in\mathcal{S}(n)} \mathcal{R}(m,n)\cdot P(m,t) - \sum_{m\in\mathcal{T}(n)} R(n,m)\cdot P(n,t) \tag{1.9}$$

where $\mathcal{R}(m,n)$ is the probability per unit time of a transition from state m to state n, $\mathcal{R}(n,m)$ is the probability per unit time of a transition from state n to state m, $\mathcal{S}(n)$ is the set of all states that can terminate at n after one reaction step, and $\mathcal{T}(n)$ is the set all states reachable from n in one step of the feasible reactions. The notation is meant to suggest the 'source' and 'target' states at n; one could also call $\mathcal{S}(n)$ the predecessors of state n and $\mathcal{T}(n)$ the successors of state n. The predecessor states must be positive for conversion, degradation and catalytic reactions. Similar bounds on the target states are naturally enforced by zero rates of reaction when the reactants are absent.

The sets $\mathcal{S}(n)$ and $\mathcal{T}(n)$ are easily determined using the underlying graph structure. It follows from the definition of ν and $\mathcal{E}$ that the ℓth reaction $C(j) \to C(k)$ induces a change $\Delta n^{(\ell)} = \nu\mathcal{E}_{(\ell)}$ in the number of molecules of all species after one step of the reaction, where subscript ℓ denotes the ℓth column. Therefore the state $m = n - \nu\mathcal{E}_{(\ell)}$ is a source or predecessor to n under one step of the ℓth reaction. Similarly, states of the form $m = n + \nu\mathcal{E}_{(\ell)}$ are reachable from n in one step of the ℓth reaction. Once the graph of the network and the stoichiometry are fixed, we can sum over reactions rather than sources and targets, and consequently the master equation takes the form

$$\frac{d}{dt}P(n,t) = \sum_{\ell} \mathcal{R}_\ell(n - \nu\mathcal{E}_{(\ell)})\cdot P(n - \nu\mathcal{E}_{(\ell)}, t) - \sum_{\ell} \mathcal{R}_\ell(n)\cdot P(n,t) \tag{1.10}$$

However, the transition probabilities $\mathcal{R}_\ell(n)$ are not simply the macroscopic rates $\tilde{\mathcal{R}}_\ell(n)$ if the reactions are second-order (or higher), because as Gillespie [41] and others have noted, combinatorial effects may play a significant role when the number of molecules is small. Hereafter we restrict attention to mass-action kinetics, and we suppose that the ℓth reaction involves conversion of the jth to the kth complex: $C(j) \to C(k)$. Then using Gillespie's notation, we can write,

$$\mathcal{R}_\ell = c_\ell h_{j(\ell)}(n) \tag{1.11}$$

where c_ℓ is the probability per unit time that the molecular species in the jth complex react, $j(\ell)$ denotes the reactant complex for the ℓth reaction, and $h_{j(\ell)}(n)$ is the number of independent combinations of the molecular components in this complex. Thus

$$c_\ell = \frac{k_\ell}{(\mathcal{N}_A V)^{\sum_i \nu_{ij(\ell)}-1}} = \hat{k}_\ell \tag{1.12}$$

and

$$h_{j(\ell)} = \prod_i \binom{n_i}{\nu_{ij(\ell)}}. \tag{1.13}$$

In the definition of h we use the standard convention that $\binom{n}{0} = 1$.

The master equation (1.10) is not solvable in general, and it is generally even difficult to obtain a closed set of equations for the moments of the distribution $P(n,t)$ when the network involves bimolecular reactions, since the evolution equation for a kth-order moment typically involves higher-order moments [36]. However, for linear reaction systems one can solve for first and second moments explicitly (modulo solving a spectral problem) and one can do this in a distributed system governed by a reaction-diffusion equation that is discretized in space [35, 56].

Remark 1 In the deterministic description of a reacting system the existence of a compact invariant set implies that solutions are bounded and exist globally in time, but the deterministic invariant set may have no significance in the stochastic description. However, the probabilities of very large numbers of species can be very small.

Consider the simple process $\phi \xrightarrow{k_1} A \xrightarrow{k_2} \phi$, and let $p_n(t)$ be the probability of having n molecules of A in the system at time t. Let $\Omega = exp(-k_2 t)$; then

$$p_n(t) = \frac{1}{k_2 n!}\left(\frac{k_1}{k_2}\right)^{n-1}(1-\Omega)^{n-1}\left(k_1(1-\Omega)^2 + k_2 n\Omega\right)\cdot exp\left(-\frac{k_1}{k_2}(1-\Omega)\right)$$

Therefore the stationary distribution is a Poisson distribution given by

$$\lim_{t\to\infty} p_n(t) = \frac{1}{n!}\left(\frac{k_1}{k_2}\right)^n exp\left(-\frac{k_1}{k_2}\right),$$

Thus $p_n(t)$ is non-zero for arbitrarily large n in both the transient and stationary distributions, but it decays rapidly with n. For example, if $k_1/k_2 \sim \mathcal{O}(1)$ and $n = 25$, $p_n \sim \mathcal{O}(10^{-25})$ in the stationary distribution. Even if the stationary mean $k_1/k_2 \sim \mathcal{O}(10)$, $p_n \leq 10^{-10}$ for $n \geq\sim 50$ (one must always choose n greater than the mean in order that $p_k < p_n$ for $k > n$).

1.4.2 The Stochastic Simulation Algorithm

Since it is generally impossible to solve the master equation analytically in interesting cases, numerical simulation methods have to be used. Numerous stochastic simulation algorithms (SSAs) have been proposed since the original exact algorithms, called the first reaction method and the direct method, were formulated by Gillespie [42]. Suppose that the system volume V is well-mixed and that there are r reactions amongst s species, as before. In Gillespie's notation, the probability density for reaction type ℓ is

$$p_\ell(\tau) = h_\ell c_\ell e^{-\sum_{i=1}^{r} h_i c_i \tau} = a_\ell e^{-a_0 \tau} \tag{1.14}$$

where

$$a_\ell = c_\ell h_\ell, \quad a_0 = \sum_{i=1}^{r} a_i.$$

In the Monte Carlo simulation algorithm of the direct method, a basic reaction cycle comprises three steps: first, determine the waiting time for the next reaction; second, determine which reaction will occur; and lastly, update the system state to reflect changes in the species involved as reactants or products in the reaction that has occurred. Accordingly, during each cycle two random numbers $r_1, r_2 \in \text{URN}[0,1]$ are generated, one of which is used to calculate the waiting time according to

$$\tau = -\frac{\ln(r_1)}{a_0} \tag{1.15}$$

and the other of which is used to determine the next reaction type ℓ according to

$$\sum_{i=1}^{j-1} a_i < r_2 \cdot a_0 \leq \sum_{i=1}^{\ell} a_i. \tag{1.16}$$

The detailed algorithm is as follows.

Gillespie's Direct Method

1. Initialization (set the initial numbers of molecules, and set $t = 0$).
2. Calculate the reaction rate functions $R_i (i = 1, \ldots, r)$.
3. Generate two random numbers r_1 and r_2 from a uniform distribution on $(0, 1)$.
4. Calculate τ as follows:

$$R_0(n) = \sum R_j(n), \qquad \tau = \frac{1}{R_0(n)} ln \frac{1}{r_1}$$

5. Determine the smallest integer n_0 that satisfies

$$\sum_{i=1}^{n_0} R_i(n) > r_2 R_0(n)$$

6. Update the states of the species to account for changes due to reaction n_0 and set $t = t + \tau$.
7. Go to 2.

For large systems the algorithm is computationally costly, especially if there is a wide disparity in the reaction rates, and many ways of optimizing the original direct method algorithm by reducing the cost of specific steps have been proposed. These include pre-ordering the reactions according to their firing frequency and recomputing only the propensities of reactions which are affected by the current reaction [13], by an optimal binning algorithm [85], or by an extended enhanced direct method used for polymer dynamics to be described next [65].

A deficiency in using the direct method or most modifications of it in simulating polymer systems is that we have to account for the fact that new 'species' are created continuously, and thus the underlying state space can change as the simulation proceeds. These new species arise from polymerization/depolymerization, fragmentation of filaments, annealing of filaments, and the hydrolysis of ATP and the release of phosphate. This has led to a new algorithm described in [65], called the MO algorithm, that is significantly faster than the direct method. A comparison of the times for the two methods is shown in Fig. 1.13. A major factor that leads to the large reduction in computational time as compared with the direct method is the use of equivalence classes of species, as described in [65].

An example of the results when the method is applied to actin filament dynamics is shown if Fig. 1.14. In that figure the simulation involves a volume of $1000\,\mu m^3$ initially containing 150 filaments, each $4\,\mu m$ long. The initial actin concentration is $0.7\,\mu M$ and the actin filaments are initially composed of ADP-actin monomers only, while the initial G-actin pool consists of ATP actin only. Each filament is characterized by its length and nucleotide sequence, and the state of the system is characterized by the numbers of filaments of various lengths and nucleotide sequences.The reaction channels incorporated are those mentioned above, namely, polymerization/depolymerization, fragmentation of filaments, annealing of filaments, and the hydrolysis of ATP and the release of phosphate. With respect to fragmentation, it was assumed that at each time there is an equal probability of breakage, modelled as a Poisson process, at every possible position on the filament. Larger filaments are more prone to fragmentation due to the fact they contain more locations at which fragmentation can occur.

There are many other outstanding questions to be addressed in the context of filament dynamics, and next we turn to in vivo experiments and modeling that deal with the rebuilding of the cytoskeleton following treatment that depolymerizes the actin network.

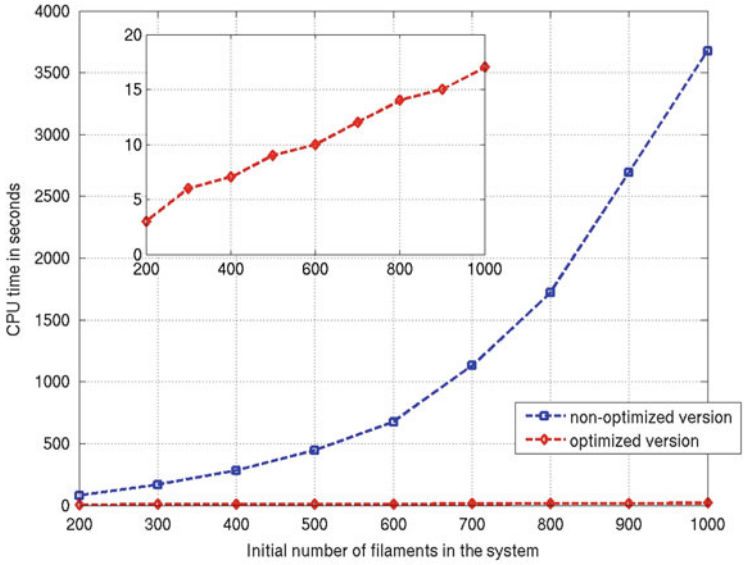

Fig. 1.13 A comparison of the computational times for the direct and modified methods. From [65] with permission

1.4.3 Actin Wave Dynamics in Dictyostelium Discoideum

A central question in cell motility is how a cell generates the forces necessary to produce movement by controlled remodeling of the cytoskeleton. In the absence of directional signals Dd cells explore their environment randomly, and thus the intracellular biochemical networks that control the mechanics must be tuned to produce signals that generate this random movement. Thus far there is little understanding about how the dynamic rebuilding is controlled, but some insights have been gained by observing the rebuilding of the actin network following treatment with latrunculin A (latA). LatA sequesters monomers with high affinity and leads to depolymerization of the network, and following washout of it, the rebuilding of the actin network can be observed using total internal reflection microscopy (TIRF) and confocal microscopy. TIRF targets labeled species within a thin region near the cell-substrate interface (usually less than 200 nm) and thus allows visualization of components near the surface. An example of the evolution in time of the reconstruction of the network is shown in Fig. 1.15. The waves shown in this figure only arise at those parts of the cell membrane in contact with a substrate, and thus membrane-surface interaction is essential. Actin structures in the shape of spots initially form on the ventral membrane of the substrate-attached (SA) cell, and then propagate radially in roughly circular shape with a prominent wave front and a decaying wave back [40], as seen in Fig. 1.16. TIRF imaging shows that the wave propagates not via direct transport of existing filaments, but rather, through *de*

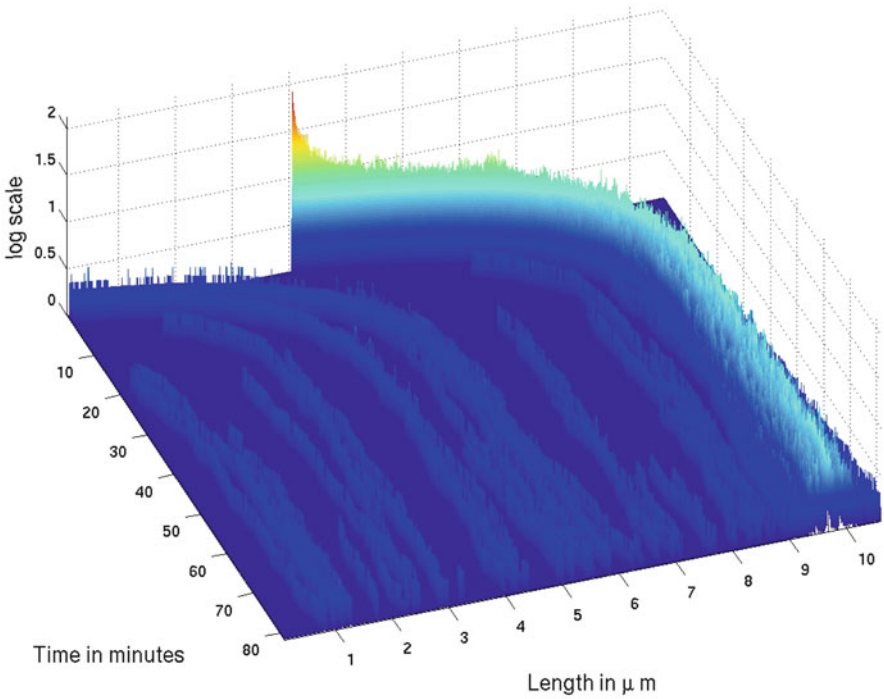

Fig. 1.14 The results of a typical simulation that includes fragmentation

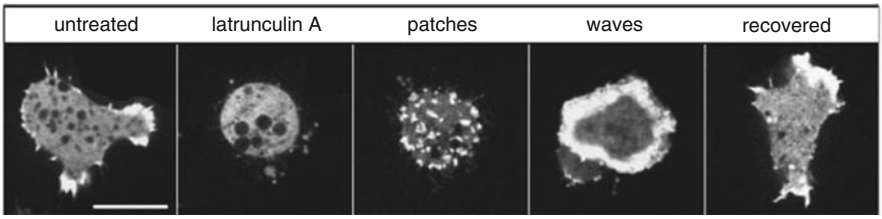

Fig. 1.15 The spatial patterns of actin network re-organization after treatment with latA and washout of the drug. The images shown, from *left to right*, are cells moving on a glass surface before the treatment with latA; cells after 16–20 min of incubation with 5 mM latA; patches that appear after the wash-out of latA; waves appear at a later stage of reorganization before normal cell shape is recovered. Patches are formed within the first 15 min after the removal of latA, waves are most abundant after 20–30 min, and recovered cells are observed after 40 min or longer. From [40] with permission

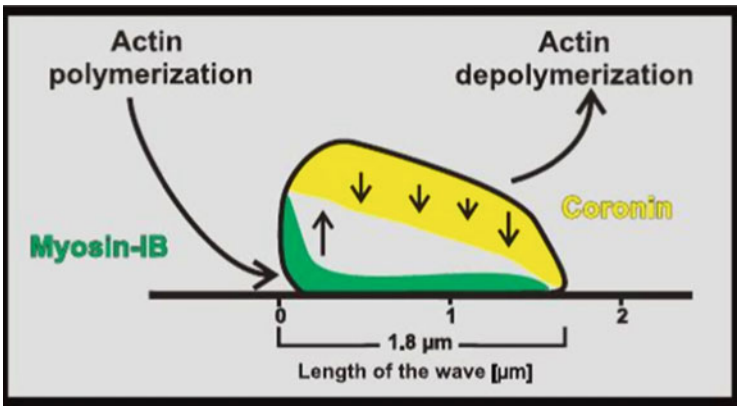

Fig. 1.16 A cross-sectional view of the actin network within a wave, showing net polymerization at the *front* and net depolymerization at the *top* and rear (From [9], with permission)

novo polymerization at the leading edge of the wave and *in situ* depolymerization at the trailing edge [40]. Imaging of the three-dimensional actin waves shows that continual growth of the actin network at the membrane pushes the network upward into the cytoplasm as shown in the schematic in Fig. 1.16.

Imaging of labeled components has identified the critical actin-binding proteins (ABP's) involved in network re-construction [9]. The actin network in the wave is believed to be dendritic, similar to that in the lamellipodium, due to the high concentration of Arp2/3 complexes measured. The Arp2/3 complex is composed of seven subunits, and can be activated by binding to nucleation-promoting factors (NPF's), G-actin and existing filaments. This interaction can lead to the formation of new filaments, in which the Arp2/3 complex caps the pointed end and attaches it to the primary filament. In latA-treated Dd cells, myosin-IB (MyoB), a single-headed motor molecule that binds to the membrane and to actin filaments in the cortex, is localized at the wave front, close to the membrane. The scaffolding protein CARMIL is probably recruited to the wave front by MyoB, and acts as an NPF for the Arp2/3 complex. In addition to CARMIL, other NPF's, such as WASP and SCAR [81], may activate Arp2/3. However, NPF's must first be activated on the membrane by binding to phospholipids. It is also observed that coronin, which is bound to filaments at the top and the back of the wave (cf. Fig. 1.16), probably destabilizes the network by removing Arp2/3 from a branch junction, thus exposing the pointed end to depolymerization [12]. A suggested schematic of these interactions is shown in Fig. 1.17 [9].

The signaling cascades that initiate and sustain the actin waves are not well-defined as yet, but a skeleton of the network has been established, and there are several distinct phases involved. The fact that waves are only initiated on membrane that is attached to a surface means that there is an unknown dependence on substrate adhesion. However, the relationship is complex, because it has been shown that a wave of activated integrin receptor follows F-actin both temporally and spatially

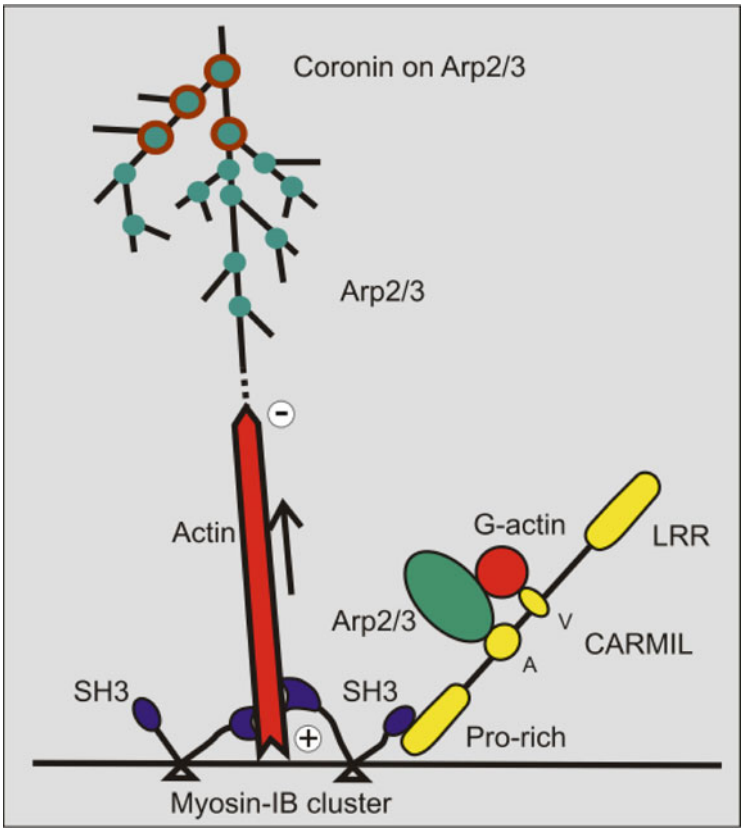

Fig. 1.17 A schematic of a suggested model for actin wave formation. The tail of Myo-IB (*blue*) binds to the plasma membrane while the motor attempts to move toward the plus end of an actin filament, which maintains attachment of the growing filament to the membrane. The head may also attach to the scaffold protein CARMIL (*yellow*), which links it to the Arp2/3 complex, where new branches are formed via Arp2/3 binding (*green*). The activity of the Arp2/3 complex is inhibited by coronin (*brown circles*). (From [9] with permission)

[15]. Thus one must construct a model that contains the essential processes, and a schematic of the model developed in [58] is shown in Fig. 1.18. That model is a continuum model and was shown to capture the essential features of the waves. However, it is too detailed for our purposes here, and we adopt a simpler scheme to describe the role of the actin network in the propagating waves. A schematic of the simplified network is shown in Fig. 1.19.

The following major assumptions have been made in the simplified model (J. Hu, V. Khamviwath, H.G. Othmer, A stochastic model for actin waves in eukaryotic cells, 2012. Unpublished manuscript).

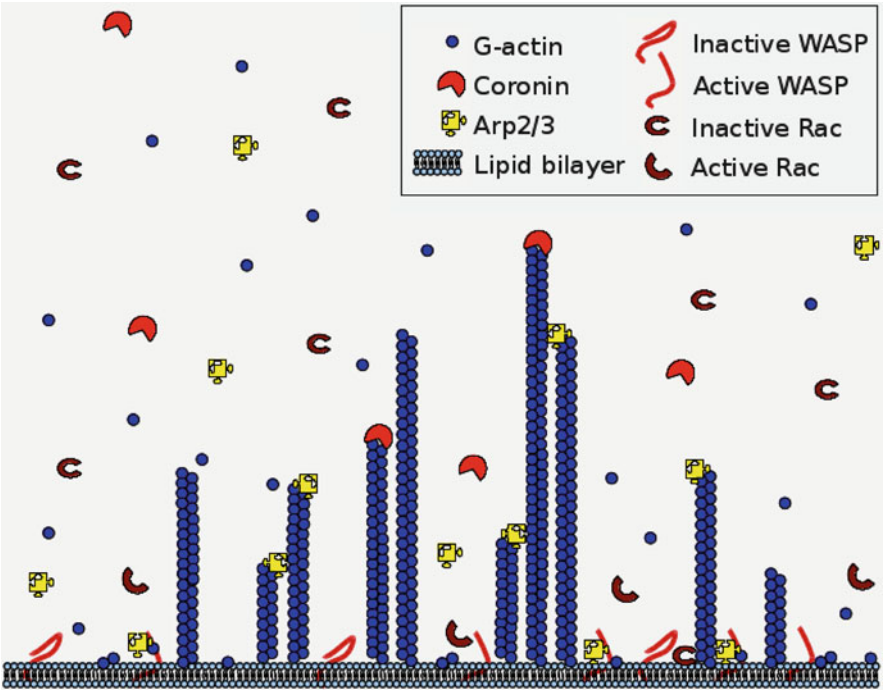

Fig. 1.18 A schematic of the stochastic model for actin waves. From [58], with permission

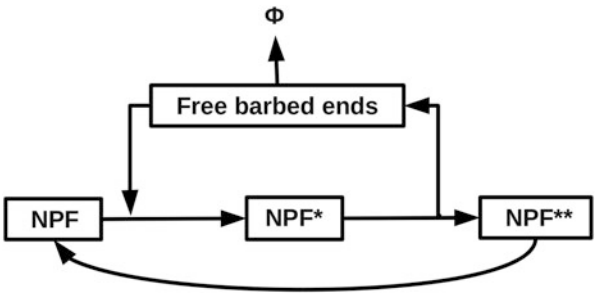

Fig. 1.19 The interconversion of the three states in the simplified model. From J. Hu, V. Khamviwath, H.G. Othmer (A stochastic model for actin waves in eukaryotic cells, 2012. Unpublished manuscript)

1. We assumed that a single molecule, NPF, in its three states is responsible for the signaling. This retains the main features of the signaling network, such as the positive feedback loop between signaling and actin dynamics.
2. The existence of an inactive state of NPF, namely NPF**, and its slow recovery to NPF controls the collapse of actin wave at the rear.

3. We assume that backbone filament nucleation sites exist on the membrane. They can generate backbone filaments, which provides a basal level of actin network on the membrane. We also assume that filament branching always requires a docking site for Arp2/3 on other filaments, either a backbone or a previously-formed branched filament.
4. NPF is activated only by free barbed ends that are in close proximity to the membrane. In other words, only active filament ends in the proximity of the membrane participate in the positive feedback.

The Mathematical Model The system domain is the rectangular solid $\Omega^{3d} = [0, L_x] \times [0, L_y] \times [0, L_z]$, where L_x, L_y, L_z are the lengths in the three axial directions. The interior of Ω^{3d} represents the cytosol, and the membrane is represented by the plane $\Omega^{2d} = [0, L_x] \times [0, L_y] \times [z = 0]$. The state variables are divided into three groups: the diffusible species in the cytosol, membrane-bound species and filament-associated species. We suppress the presence of time and space variables in equations for the evolution of the state variables unless they are needed for clarity. The definitions and values of the parameters used in the equations are defined in the next section.

The evolution of the mobile cytosolic species—G-actin (g), Arp2/3 (arp), coronin (cor) and capping proteins (cp)—are governed by

$$\begin{aligned}
\frac{\partial [g]}{\partial t} &= D_g \nabla^2 [g] + \mathcal{R}_g \\
\frac{\partial [arp]}{\partial t} &= D_{arp} \nabla^2 [arp] + \mathcal{R}_{p1} \\
\frac{\partial [cp]}{\partial t} &= D_{cp} \nabla^2 [cp] + \mathcal{R}_{cp} \\
\frac{\partial [cor]}{\partial t} &= D_{cor} \nabla^2 [cor] - \mathcal{R}_{p2} + \mathcal{R}_{p1}
\end{aligned}$$

with homogeneous Neumann boundary conditions on the surface $\partial\Omega^{3d}$ except on the membrane Ω^{2d}. On that surface the fluxes are given by

$$\begin{aligned}
-D_g \frac{\partial}{\partial z}[g]|_{z=0} &= -k^+_{bk}[g]|_{z=0} \cdot F_{bkfree} \\
&\quad -k^+_{gan}[g]|_{z=0} \cdot [npf^*_arp] + k^-_{gan}[npf^*_arp_g] \\
-D_{arp} \frac{\partial}{\partial z}[arp]|_{z=0} &= -k^+_{an}[arp]|_{z=0} \cdot [npf^*] + k^-_{an}[npf^*_arp] \\
-D_{cp} \frac{\partial}{\partial z}[cp]|_{z=0} &= -k^+_{cap}[cp]|_{z=0} \cdot F_{bkfree} \\
-D_{cor} \frac{\partial}{\partial z}[cor]|_{z=0} &= 0
\end{aligned}$$

where $\mathcal{R}$'s represent various reactions at filament ends, and F_{bkfree} the concentration of backbone filaments (J. Hu, V. Khamviwath, H.G. Othmer, A stochastic model for actin waves in eukaryotic cells, 2012. Unpublished manuscript).

The proteins that reside on the membrane are the various states of NPF's and their association with Arp2/3 and G-actin. We allow 2D diffusion for free (non-complexed) states of NPF's, but not for complexes. The dynamics of these state variables satisfy

$$\begin{aligned}
\frac{\partial[npf]}{\partial t} &= D_{npf}\nabla^2[npf] - k_{actv}F_{brfree}\cdot[npf] + k_{deg}[npf^*] + k_{recov}[npf^{**}] \\
\frac{\partial[npf^*]}{\partial t} &= D_{npf^*}\nabla^2[npf^*] + k_{actv}F_{brfree}\cdot[npf] \\
&\quad -k_{deg}[npf^*] - k_{an}^+[arp]|_{z=0}\cdot[npf^*] + k_{an}^-[npf^*_arp] \\
\frac{\partial[npf^*_arp]}{\partial t} &= k_{an}^+[arp]|_{z=0}\cdot[npf^*] - k_{an}^-[npf^*_arp] \\
&\quad -k_{gan}^+[g]|_{z=0}\cdot[npf^*_arp] + k_{gan}^-[npf^*_arp_g] \\
\frac{\partial[npf^*_arp_g]}{\partial t} &= k_{gan}^+[g]|_{z=0}\cdot[npf^*_arp] - k_{gan}^-[npf^*_arp_g] \\
&\quad -k_{nucl}[npf^*_arp_g]\cdot F_{btot} \\
\frac{\partial[npf^{**}]}{\partial t} &= D_{npf^{**}}\nabla^2[npf^{**}] + k_{nucl}[npf^*_arp_g]\cdot F_{btot} - k_{recov}[npf^{**}]
\end{aligned}$$

on the domain Ω^{2d}, with zero Neumann boundary conditions at $\partial\Omega^{2d}$. The averaged concentrations of free barbed ends and total barbed ends of branched filaments within the nucleation zone adjacent to the membrane are

$$\begin{aligned}
F_{brfree} &= \frac{1}{L_{nucl_zone}} \sum_{n\le\frac{2L_{nucl_zone}}{\delta}} \left\{ \sum_{n_L,p_{tag}} f_r(n,n_L,0,p_{tag}) \right\} \\
F_{btot} &= \frac{1}{L_{nucl_zone}} \left\{ \sum_{n_L} f_k(n_L) + \sum_{n\le\frac{2L_{nucl_zone}}{\delta}} \left(\sum_{n_L,b_{tag},p_{tag}} f_r(n,n_L,b_{tag},p_{tag}) \right) \right\}.
\end{aligned}$$

Backbone filaments are generated on nucleation sites and remain attached to the sites until they are capped and thus considered as a member of the connected branched filaments. We assume that the latter is a rigid filament cluster, which is able to move vertically due to the polymerization at the membrane-adjacent barbed end of any member filament. The nucleation site is occupied by attached backbone filament and cannot nucleate new backbone filament until the occupied one is capped. Let S_f denote the concentration of free nucleation sites for backbone

filament. These species satisfy the following equations.

$$\begin{aligned}
\frac{\partial S_f}{\partial t} &= -k^+_{nuk}[g]|_{z=0}S_f + k^+_{cap}[cp]|_{z=0}\sum_{n\geq 2} f_k(n) + k^-_{nuk}f_k(1)\\
\frac{\partial f_k(1)}{\partial t} &= k^+_{nuk}[g]|_{z=0}S_f - k^-_{nuk}f_k(1) + k^-_{pk}f_k(2) - k^+_{bk}[g]|_{z=0}f_k(1)\\
\frac{\partial f_k(n)}{\partial t} &= k^+_{bk}[g]|_{z=0}f_k(n-1) + k^-_{pk}f_k(n+1)\\
&\quad - (k^+_{bk}[g]|_{z=0} + k^-_{pk})f_k(n) - k^+_{cap}[cp]|_{z=0}f_k(n), \quad (n \geq 2)
\end{aligned}$$

The dynamics of the branched filament is dictated by the filament-end reactions, which include the Arp2/3 removal facilitated by coronin binding and subsequent depolymerization at the pointed end, and polymerization and capping at the barbed end. The details are given in J. Hu, V. Khamviwath, H.G. Othmer (A stochastic model for actin waves in eukaryotic cells, 2012. Unpublished manuscript).

As written these equations appear to describe a continuum description, and as noted earlier, a related continuum description is analyzed in [58]. However there are generally few nucleation sites and other species may be present in low copy numbers, which suggests that a stochastic description is more appropriate. We saw earlier how this is done for a well-mixed system, and to develop an algorithm here we have to extend this to incorporate diffusion. This leads to several questions, which include (1) how does one discretize the domain correctly, and (2) how does one develop an efficient computational algorithm. The first question is answered in [57], and the second is addressed is a somewhat simpler context in [48]. A brief summary of the algorithm is as follows.

The membrane domain is partitioned into square compartments of size $l_x \times l_y$, and the cytoplasmic space into cubic compartments of size $l_x \times l_y \times l_z$, where the side lengths are all $0.1\,\mu$m. This is small enough that each compartment can be considered well-mixed. The Monte Carlo method is used to generate realizations of the stochastic model, and specifically, we implement the numerical algorithm using a modified Gillespie direct method described earlier and in [65]. In the original Gillespie direct method, two random numbers are generated for advancing the model system in each time step: one random number is used to determine the waiting time for the next reaction, and the other is used to determine which reaction type occurs [41]. In this method the reactions are distinguished by the reactants involved, and therefore, for instance, the reaction of monomer depolymerization from the pointed end of a filament of length n is considered different from that of size $n+1$. In the MO method, the state of the systems consists of equivalence classes of filaments characterized firstly by their length, and then subdivided into classes of the same nucleotide profile. In the model developed here the nucleotide profiles play no role. Then monomer depolymerization from filaments of any size is considered as one reaction type in an equivalence class of reactants. Another reaction type consists of all the reactions involving monomer addition at a barbed

end, irrespective of how long the elongating filament is, which is legitimate since the on-rate for monomer addition is independent of the filament length. Thus a third random number is needed after the reaction type that occurs is determined in order to decide which reaction within the equivalence class occurs. This treatment reduces the computational cost by 2-3 orders of magnitude by making an optimal use of the structure of the underlying reaction network (cf. [65] and Fig. 1.13).

The detailed algorithm is as follows. Suppose that the system has N_{rct_type} equivalent reaction classes and that the rate constant of the jth reaction type is r_j. Assume that there are N_{cmprt} computational compartments, in the ith of which there are RA_i^j possible reactions for reaction type j. Therefore, for the jth reaction class of the domain, the total number of this reaction in the entire domain is $RA_{tot}^j = \sum_{i=1}^{N_{cmprt}} RA_i^j$. In addition, suppose $\widehat{RA}_k^j$ denotes the total number of reactions of type j in the k-th subset in the totality of N_{sub} subsets. After setting the above system configuration, the state of the system is advanced as follows. At time t_i, the steps proceed as follows.

1. Generate a random number to determine the waiting time Δt_i for the next reaction by the reaction propensities derived from $RAtot^j$ and r_j according to the Gillespie direct method.
2. Generate a second random number, and decide which reaction type the next reaction will be from $RAtot^j$ and r_j according to the Gillespie direct method.
3. Generate a third random number and decide in which compartment the reaction type determined in Step 2 is located. In this step, instead of checking the N_{cmprt} compartment one by one, we first subdivide the compartments into subsets, determine in which subset the reacting compartment falls, and then within that subset determine the appropriate reaction compartment. In essence this is done as in step one, except that we compute total propensities within subsets and use these to determine the subset, in effect treating subsets as individual steps. (An optimization of the choice of the number of subsets is shown in Fig. 1.20.)
4. In the chosen compartment, we proceed as follows.
   - if the reactants for the chosen reaction are identical molecular species, pick any reactants to react. For example, for molecular diffusion, which molecule of the same type diffuses out of the current compartment makes no difference, since the combinatorial coefficient used in computing propensities reflects the identity of the species.
   - if the reactants are not identical molecular species, then generate another random number to decide which reactant or reactant pair to react. For example, if the pointed-end depolymerization is to occur in the reacting compartment, the filaments whose pointed end lies in the compartment may be of different lengths, and thus we must randomly choose one of these filaments.
5. Update the system configuration, and advance the time to $t_{i+1} = t_i + \Delta t_i$ where Δt_i is the random time determined in step 1. Repeat Steps 1–4 until the targeted time is reached.

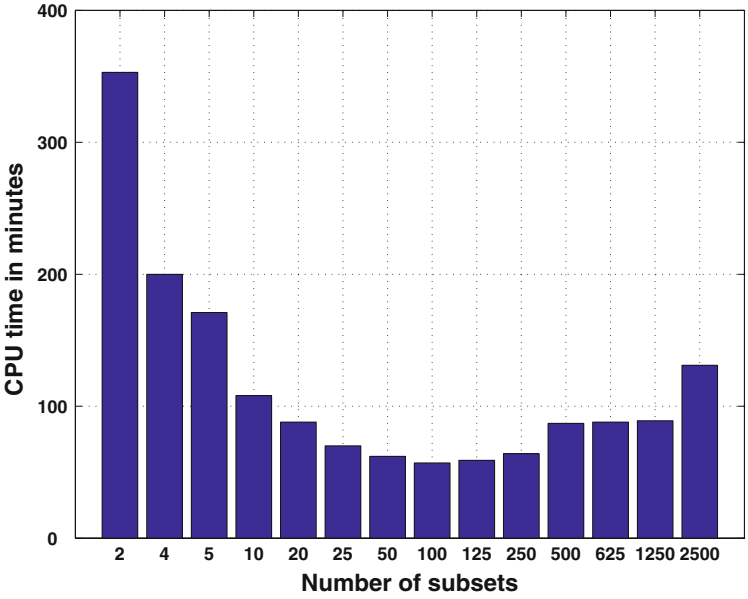

Fig. 1.20 The CPU time for a computation as a function of the number of sub-domains in the domain

The effect of subdividing of the total number of compartments in Step 3 on the computational time is shown in a simulation trial which produces the results shown in Fig. 1.20.

The stochastic model of actin assembly at the membrane, one realization of which is shown in Fig. 1.21, predicts the emergence and propagation of actin waves. In this simulation, the membrane-bound NPF partially activated at the lower left corner triggers downstream actin assembly that propagates outward as shown in the snapshot at 5.0 s in Fig. 1.21. Subsequently, the wave expands radially until it hits a boundary, where it dies. Occasionally new waves emerge spontaneously in the wake of the primary wave, as is observed experimentally. If waves are initiated at several points in the domain the waves annihilate when they meet. Thus the system has the standard characteristics of an excitable system.

One can analyze the dynamics along a line in the direction of propagation and one finds that the wave travels at about 0.1 μm/s, comparable to what is observed experimentally. Moreover, the increase in actin density at the wave front is steep, compared with the decay at the back of the wave. The F-actin level in the area well behind the wave is stabilized at about 20–25 % of that at the wave peak, consistent with the qualitative description of experimental results shown in Fig. 1.16.

While much remains to be done, some of the essential processes are embedded in the model, and some of the experimental observations can be replicated.

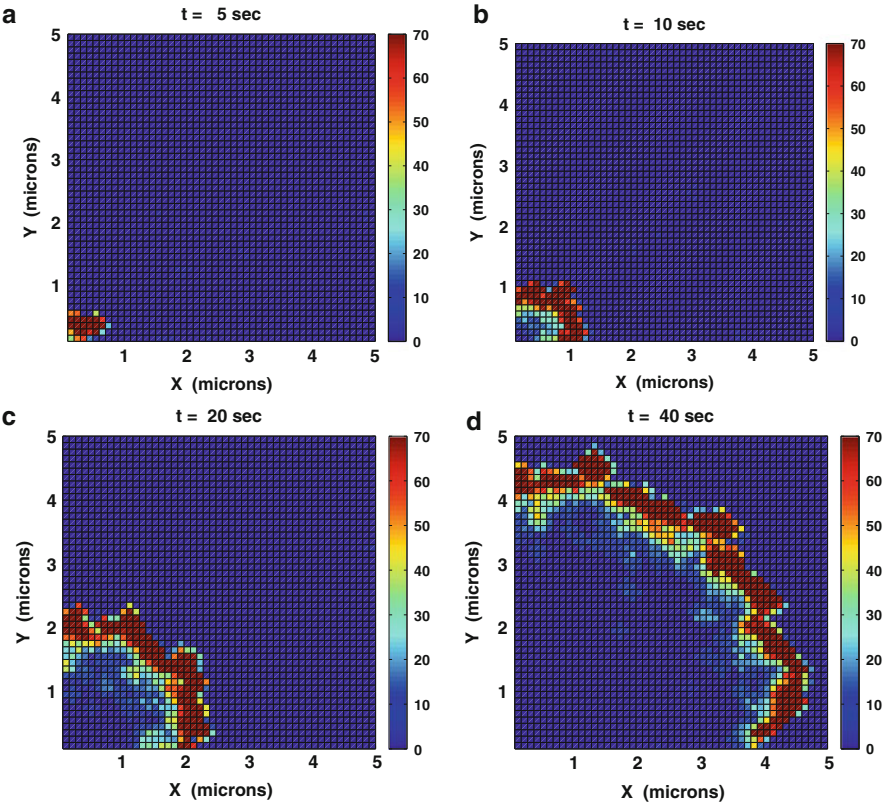

Fig. 1.21 A computational TIRF sequence for the formation and propagation of an F-actin wave. The initial G-actin concentration is 10 μM, and half of the NPF is activated at the *lower left corner*. The color index indicates the total F-actin within 100 nm of the membrane projected to each membrane compartment. The maximal density in the *color representation* is set to be 70 monomers per compartment, and thus densities larger than 70 are not distinguishable. [From J. Hu, V. Khamviwath, H.G. Othmer (A stochastic model for actin waves in eukaryotic cells, 2012. Unpublished manuscript)]

1.5 Signal Transduction, Direction Sensing and Relay

In Sect. 1.1.1 we listed the steps that a single cell must execute to successfully aggregate. These include signal detection, signal transduction, direction sensing, signal relay and movement. The mechanics of movement have not been 'solved' in previous sections, but some of the issues involved in modeling actin dynamics have been addressed. In this section we focus on the signaling aspects of the cellular response, which as was discussed earlier, centers on cAMP. Figure 1.22 shows the primary steps involved in detection, transduction, relay and the connection with the actin network. There are two main pathways in this diagram, one that leads to

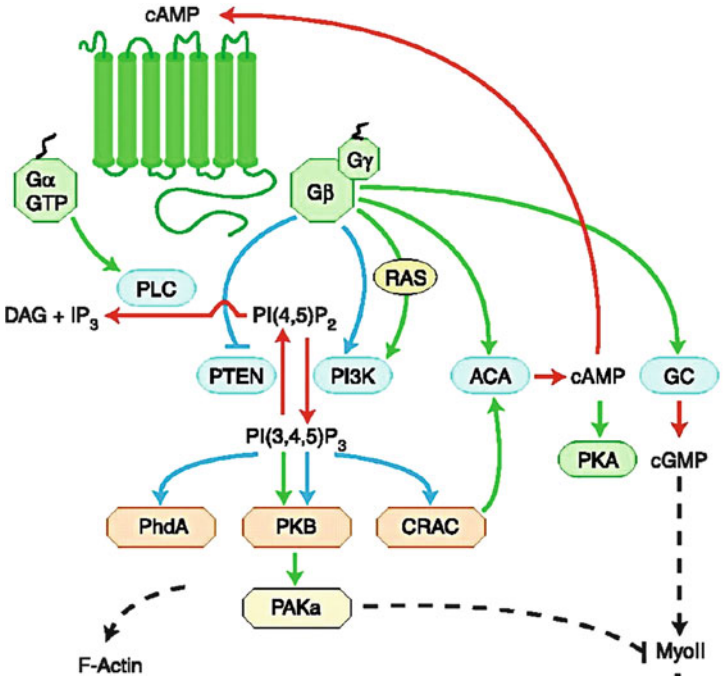

Fig. 1.22 Signal transduction in *Dictyostelium discoideum*. Modified from [59]

production of cAMP via $G_{\beta\gamma}$ and adenylyl cyclase (ACA) and secretion of cAMP—the relay response, and one that leads to modification of the cytoskeleton via $G_{\beta\gamma}$ PI3K, etc. Despite the number of components shown, the diagram only contains some of the principal actors, and we will not discuss all the components in that diagram in detail, but only those directly involved in steps considered later.

The first intracellular response to a change in extracellular cAMP is an increase in activated G proteins, catalyzed by the increase in cAMP-occupied receptors (GPCRs). G-proteins consist of an α subunit, G_α that contains a GTP/GDP binding domain as well as intrinsic GTPase activity, and a complex of a G_β and a G_γ subunit. The α and $\beta\gamma$ subunits dissociate after activation, and each can regulate the activity of different targets, including adenylyl cyclase, the enzyme that catalyzes cAMP production. A subsequent step is the generation of pleckstrin homology (PH) binding sites by the phosphorylation of the membrane lipid PtdIns(4,5)P_2 (PIP_2) by phosphoinositide 3-kinases (PI3Ks) to produce PtdIns(3,4,5)P_3 (PIP_3), which in turn is dephosphorylated to produce PtdIns(3,4)P_2 ($PI34P_2$). In Dd PIP_3 is produced by a class IA type kinase (PI3K1 and PI3K2) and a class IB type, kinase designated $PI3K_\gamma$ [19]. The former are activated via cytosolic tyrosine kinases, whereas the latter consists of a catalytic unit and a regulatory unit that is activated by $G_{\beta\gamma}$. Both PIP_3 and $PI34P_2$ provide binding sites for various cytosolic proteins containing PH domains (PHds) and recruitment is rapid: localization of PHds at the

membrane peaks 5–6 s after global stimulation with cAMP [19, 49]. Both green-fluorescent-protein (GFP)-tagged CRAC (cytosolic regulator of adenylyl cyclase) and a PH_{CRAC}-GFP construct accumulate at the membrane following stimulation [32, 55]. PI3K is constitutively expressed, but both PIP_3 and $PI34P_2$ are tightly regulated by the phosphatases PTEN and SHIP, and within 10–15 s following uniform cAMP changes the PHds return to the cytoplasm, probably because the PH binding sites have been destroyed [19, 76]. This burst of PIP_3 at the membrane couples the extracellular signal to actin polymerization [52]. The level of activated G-proteins in continuously-stimulated cells reaches a stimulus-dependent level, while membrane-associated CRAC first increases, but then returns to its basal level. Therefore adaptation of the PIP_3 and cAMP responses is downstream of $G_{\beta\gamma}$ [53], and a recently-developed model shows that this occurs at the level of Ras [18], which is activated by $G_{\beta\gamma}$ (see Fig. 1.22). As is shown in Fig. 1.15, the increase in PIP_3 trails the actin increase in the developing waves, which suggests that there is a feedback from actin to the earlier steps in signal transduction shown in Fig. 1.22. Theoretical predictions as to how PI3Ks, PTEN and SHIP are spatially-regulated help in understanding how cells respond to changes in the signal [18, 58] .

Chemotactic signals also produce a rapid, transient, PI3K-dependent activation of Akt/PKB, a protein kinase that is essential for polarization and chemotaxis: mutants lacking Akt/PKB cells cannot polarize properly when placed in a chemotactic gradient and the cells move slowly [68]. Akt/PKB is activated upon recruitment to the membrane, and in Dd it activates the kinase PAKa, which regulates myosin II assembly, cortical tension, and retraction of the uropod (the tail) of the cell [19] (see Fig. 1.22). PIP_2 provides another link between signal transduction and mechanical events in that it acts as a second messenger that regulates the adhesion of the plasma membrane to the underlying cytoskeleton [67, 83].

There are a number of models for how cells extract directional information from the cAMP field. It was shown in [23], using what is in essence a model for the $G_{\beta\gamma}$-AC-cAMP part of the network in Fig. 1.22, that a cell experiences a significant difference in the front-to-back ratio of cAMP when a neighboring cell begins to signal. This shows that it is certainly possible that PI3K components in the signal-transduction pathway may also show significant front-to-back differences. Meinhardt [69] postulated an activator-inhibitor model with a third species that serves as a local inhibitor. Amplification of small external differences involves a Turing instability in the activator-inhibitor system, coupled to a slower inactivator that suppresses the primary activation. While this model produces qualitatively correct results, there is no biochemical basis for it; it is purely hypothetical and omits some of the major known processes, such as recruitment of molecules to the cell membrane from the cytosol. Several methods for achieving perfect adaptation to any extracellular signal are discussed, some of which are closely related to a simplified model of adaptation proposed earlier [74].

More recently, a model that takes into account some of the known biochemical steps, such as activation of $PI3K_\gamma$ and subsequent activation of other enzymes

involved in the phosphorylation and de-phosphorylation of membrane lipids, has been proposed [62]. The positive feedback in this scheme arises from activation of PIP_2 production, but this model also ignores recruitment of most PHds to the cell membrane. A recent model based on detailed descriptions of the underlying biochemistry can replicate a variety of experimental observations that are not addressed by other models [18]. In particular, it shows that front-to-back symmetry breaking can occur at the level of Ras, and it provides a solution to the 'back-of -the-wave' problem.

The other main pathway concerns the production and secretion of cAMP, and we turn to this next. Several methods for achieving perfect adaptation to any extracellular signal are discussed in [74], and we discuss one of these in detail.

1.5.1 The Model for Signal Transduction and Relay

There are three main configurations that shed light on different aspects of a cell's response to cAMP. In the first the cells are perfused with a cAMP stream of known concentration, and the downstream level of labeled carbon is measured to determine the cell's response. These perfusion experiments, done primarily by Devreotes [27, 28], were the first to characterize the input-output response of cells. In this configuration the cAMP secreted by cells in response to the stimulus is quickly washed away, thereby precluding self-stimulation. The second configuration applies when cells are suspended in a well-mixed solution and feedback via self-stimulation occurs. Experiments of this type were done before the perfusion experiments and showed that under certain conditions the extracellular cAMP in the solution could oscillate periodically in time [39, 107]. The third configuration obtains in aggregation fields, where cells are simply plated out and allowed to develop. As shown in Fig. 1.3, complex patterns of cAMP and cell density can emerge. We shall begin with a model for the first two configurations, and then apply it to the third one.

The network for the main steps in the transduction scheme used in the model developed in [96] is shown in Fig. 1.23 and the detailed biochemical reactions are given below it.

There are three major pathways in the transduction of and adaptation to an extracellular perfusing cAMP signal ($cAMP_0$: H for short) in perfusion experiments. In the stimulus pathway H binds to GPCRs R_s, and the complex HR_s catalyzes the activation of the stimulatory G protein G'_s. This in turn binds with the inactive form of adenylate cyclase (UC) and produces the activated form of adenylate cyclase (G'_sAC). A GTPase activity intrinsic to the α subunit of the G protein terminates the activation. In the inhibitory pathway, an inhibitory G protein G'_i is produced by analogous steps. However, the symmetry between the pathways is broken at this point, because G'_i binds with HR_s, and in this bound form HR_s cannot activate G_s. Finally in the pathway for the production and secretion of cAMP, the activated

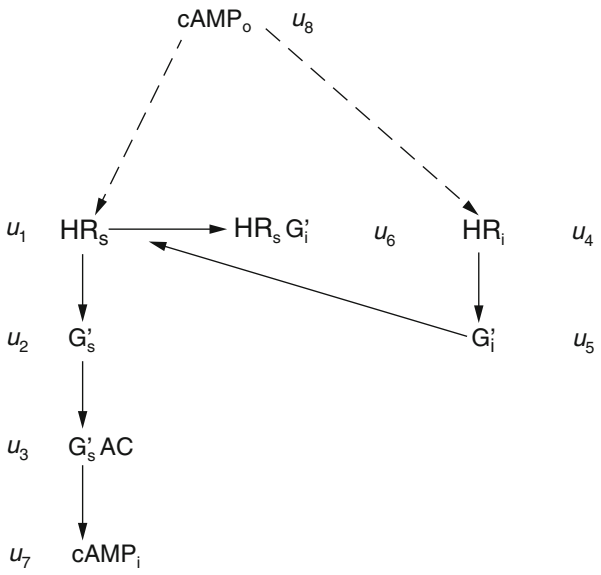

Fig. 1.23 A schematic of the interactions in the model. An extracellular cAMP stimulus serves both as the stimulus and the inhibitory signal. Adaptation arises from the action of G_i' on the cAMP-receptor complex. *Legend*: $cAMP_o$; extracellular cAMP, R_s; receptor for the stimulatory pathway, HR_s; $cAMP_o$-receptor complex, G_s'; activated stimulatory G protein, $G_s'AC$; activated form of adenylate cyclase, $cAMP_i$; intracellular cAMP, R_i; cAMP receptor in the inhibitory pathway, HR_i; cAMP-receptor complex in the inhibitory pathway, G_i'; activated form of the inhibitory G protein, HR_sG_s'; complex between HR_s and G_s'. The *symbols* u_j indicate the dimensionless concentration of that species

adenylate cyclase ($G_s'AC$) catalyzes the turnover of ATP to intracellular cAMP ($cAMP_i$). $cAMP_i$ in turn is hydrolyzed by intracellular phosphodiesterase ($iPDE$) or is secreted into the extracellular medium ($cAMP_o^*$). Here the '*' on $cAMP_o^*$ is to distinguish the secreted cAMP from the stimulatory cAMP in the perfusion solution, which is denoted by H. Further details about this model as well as kinetic parameters involved can be found in the original papers [96, 97]. The reader should note that we use G_i' to activate adenylyl cyclase, which does not agree with Fig. 1.22, where $G_{\beta\gamma}$ is used. The latter is probably correct, although at the time the model was formulated this was not known. The model could easily be re-formulated to use $G_{\beta\gamma}$ as the effector in the stimulatory pathway, but this has not been done. On the inhibitory side of the pathway the best evidence is that a different G_α is used for inhibition [10], as in the model, but the details of how this is done are not known.

The steps in cAMP production and release

(I) The stimulus pathway

$$
\begin{aligned}
H + R_s &\underset{k_{-1}}{\overset{k_1}{\rightleftarrows}} HR_s \\
HR_s + G_s &\underset{k_{-2}}{\overset{k_2}{\rightleftarrows}} HR_sG_s \\
HR_sG_s + GTP &\xrightarrow{\hat{k}_3} HR_s + G'_s \\
&\quad +GDP + \beta\gamma \\
G'_s + UC &\underset{k_{-4}}{\overset{k_4}{\rightleftarrows}} G'_sAC \\
G'_s &\xrightarrow{k_5} sGDP + P_i \\
G'_sAC &\xrightarrow{k_5} \alpha_sGDP + UC \\
&\quad +P_i \\
\alpha_sGDP + \beta\gamma &\xrightarrow{k_6} G_s
\end{aligned}
$$

(II) The inhibitory pathway

$$
\begin{aligned}
H + R_i &\underset{h_{-1}}{\overset{h_1}{\rightleftarrows}} HR_i \\
HR_i + G_i &\underset{h_{-2}}{\overset{h_2}{\rightleftarrows}} HR_iG_i \\
HR_iG_i + GTP &\xrightarrow{\hat{h}_3} HR_i + G'_i \\
&\quad +GDP + \beta\gamma \\
G'_i + HR_s &\underset{h_{-4}}{\overset{h_4}{\rightleftarrows}} HR_sG'_i \\
G'_i &\xrightarrow{h_5} \alpha_iGDP + P_i \\
HR_sG'_i &\xrightarrow{h_6} H + R_s + G'_i \\
HR_sG'_i &\xrightarrow{h_5} HR_s + \alpha_iGDP \\
&\quad +P_i \\
\alpha_iGDP + \beta\gamma &\xrightarrow{h_7} G_i
\end{aligned}
$$

(III) The production and secretion of intracellular cAMP

$$
\begin{aligned}
G'_{\alpha_s}AC + ATP &\underset{l_{-1}}{\overset{\hat{l}_1}{\rightleftarrows}} G'_{\alpha_s}AC - ATP \\
G'_{\alpha_s}AC - ATP &\xrightarrow{l_2} cAMP_i + G'_{\alpha_s}AC \\
cAMP_i + iPDE &\underset{l_{-3}}{\overset{l_3}{\rightleftarrows}} cAMP_i - iPDE \\
cAMP_i - iPDE &\xrightarrow{l_4} AMP + iPDE \\
cAMP_i &\xrightarrow{l_5} cAMP^*_o
\end{aligned}
$$

This system of reactions involves fourteen species and six combinations of conserved species, and is thus described by eight independent differential equations. As we showed in [96], this model can describe the input-output behavior in the perfusion experiments very well. However, in order to better describe certain aspects of the oscillation experiments and the wave propagation studied in [97], we introduced a basal activity for the un-activated adenylate cyclase, which produces the basal cAMP concentration in the cytoplasm in the absence of an extracellular signal. The additional reaction steps introduced by the basal activity are

$$
\begin{aligned}
UC + ATP &\underset{l_{-5}}{\overset{l_5}{\rightleftarrows}} UC - ATP \\
UC - ATP &\xrightarrow{l^*_5} cAMP_i + UC.
\end{aligned}
\tag{1.17}
$$

A second modification was to introduce a modified secretion function

$$dsr(cAMP_i) = \begin{cases} dsr_1 * cAMP_i & \text{if cAMP}_i \ < dsw \\ dsr_2 * (cAMP_i - dsw) + dsr_1 * dsw & \text{if cAMP}_i \ > dsw \end{cases} \tag{1.18}$$

and the secretion step

$$cAMP_i \xrightarrow{dsr} cAMP_o^*. \tag{1.19}$$

where dsr_1 is the basal secretion rate, dsr_2 is the active secretion rate, and dsw is the threshold concentration. The corresponding dimensionless parameters will be denoted as sr_1, sr_2, sw, and sr. The piecewise linear character of the function $dsr(\cdot)$ can introduce difficulties for certain numerical schemes that require more smoothness than C^0, and incomputations we use a smoothed version of $dsr(\cdot)$. In dimensionless form the governing equations are as follows [97].

$$\begin{aligned}
\frac{du_1}{d\tau} &= \alpha_H(\tau) - (\alpha_H(\tau) + \alpha_1)u_1 + (\beta_5 - \alpha_H(\tau))u_6 - \beta_4 u_1 u_5 \\
\frac{du_2}{d\tau} &= \alpha_2\alpha_3 c_1 u_1 - (1 + \alpha_4)u_2 - \alpha_2\alpha_3 c_1 u_1(u_2 + u_3) + \alpha_4 u_2 u_3 \\
\frac{du_3}{d\tau} &= \alpha_4 u_2 - u_3 - \alpha_4 u_2 u_3 \\
\frac{du_4}{d\tau} &= \beta_H(\tau) - (\beta_H(\tau) + \beta_1)u_4 \\
\frac{du_5}{d\tau} &= \beta_2\beta_3 c_2 u_4 - \beta_5 u_5 + \beta_6 c_3 u_6 - c_3\beta_4 u_1 u_5 - \beta_2\beta_3 c_2 u_4(u_5 + c_3 u_6) \\
\frac{du_6}{d\tau} &= -(\beta_5 + \beta_6)u_6 + \beta_4 u_1 u_5 \\
\frac{du_7}{d\tau} &= \gamma_1\gamma_2 u_3 - sr(u_7) - \gamma_4\frac{u_7}{u_7 + \gamma_3} + \gamma_5(1 - \Gamma_7 u_3) \\
\frac{du_8^*}{d\tau} &= sr(u_7)
\end{aligned} \tag{1.20}$$

To describe the dynamics of suspensions, we only have to append reactions for the extracellular dynamics and equations for the evolution of extracellular cAMP, and this leads to the additional differential equations

$$\begin{aligned}
V_o\frac{dy_{14}}{dt} &= NV_c dsr(y_{12}) + NA_c l_{-6} y_{15} + V_o l_{-8} y_{16} - NA_c l_6 y_{14} z_8 - NV_c l_8 y_{14} z_9 \\
\frac{dy_{15}}{dt} &= -(l_{-6} + l_7)y_{15} + l_6 y_{14} z_8 \\
V_o\frac{dy_{16}}{dt} &= -V_o(l_{-8} + l_9)y_{16} + NV_c l_8 y_{14} z_9.
\end{aligned} \tag{1.21}$$

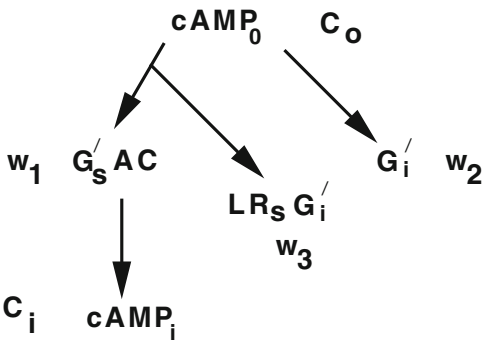

Fig. 1.24 The reduced network for the five primary variables in the reduced model. The symbols C_i, C_o and w_i i = 1,2,3 beside a species corresponds to the *symbol* used in the equations at (1.23)

Here y_{14} stands for $[cAMP_o]$, y_{15} for $[mPDE - cAMP_o]$, y_{16} for $[ePDE - cAMP_o]$, z_8 for free $[mPDE]$, z_9 for the free $[ePDE]$, V_o for the volume of the extracellular medium, V_c for the volume of a cell, A_c for the surface area of a cell, and N for the total number of cells. In addition to the differential equations, there are two other conservation equations, namely,

$$\begin{aligned} y_{15} + z_8 &= [mPDE]_T \\ y_{16} + \tfrac{NV_c}{V_o} z_9 &= \tfrac{NV_c}{V_o} [ePDE]_T \end{aligned} \tag{1.22}$$

It is clear that the newly introduced variables y_{15}, y_{16} are both positive and bounded. In fact, we have

$$0 \le y_{15} \le [mPDE]_T \quad 0 \le y_{16} \le \frac{nV_c}{V_o} [ePDE]_T.$$

It follows from this that y_{14} is also bounded.

The resulting eight-dimensional system can be further reduced by carefully analyzing the relative time variation of different components. Then, by applying a singular perturbation reduction,[2] the system can be reduced to a five-dimensional system for the variables shown in Fig. 1.24. To avoid confusion, we use the symbols w_i, C_i and C_o to denote the remaining variables, and then have the final form of the reduced system for perfusion experiments and well-mixed suspensions. In the following equations Greek letters and lower case c's represent constants. The definitions of the following parameters differ from those used earlier [97]: $L_5 = (l_{-5} + l_5^*)/(l_5[ATP])$, $\Gamma_5 = \gamma_5/(1 + L_5) = 2.4$, $L_7 = l_1/(l_{-1} + l_2)$ and $\Gamma_7 = 1 + L_7 = 1.091$; the remaining parameter values are the same as those in [97]. Many of the parameters in this model can be obtained from the literature, but the

[2] A brief introduction to this technique is given in Appendix.

remainder must be estimated.

$$\begin{aligned}
\frac{dw_1}{d\tau} &= \alpha_4 u_2(1-w_1) - w_1 \\
\frac{dw_2}{d\tau} &= \beta_2\beta_3 c_2 u_4(1-w_2-c_3w_3) - \beta_5 w_2 + \beta_6 c_3 w_3 - c_3\beta_4 u_1 w_2 \\
\frac{dw_3}{d\tau} &= -(\beta_5+\beta_6)w_3 + \beta_4 u_1 w_2 \\
\frac{dC_i}{d\tau} &= \gamma_1\gamma_2 w_1 + \Gamma_5(1-\Gamma_7 w_1) - \gamma_4\frac{C_i}{C_i+\gamma_3} - sr(C_i) \\
\frac{dC_o}{d\tau} &= \frac{\rho}{1-\rho}\left(sr(C_i) - \gamma_7\frac{C_o}{C_o+\gamma_6} - \gamma_9\frac{C_o}{C_o+\gamma_8}\right).
\end{aligned} \tag{1.23}$$

To illustrate the interpretation of terms in these equations, consider the fourth equation, that for the change in cAMP_i. The first term represents the production of cAMP_i via the activated cyclase, the second term represents the basal production of cAMP_i, the third term represents the rate at which cAMP_i is degraded by PDE, and the last term represents the rate at which it is secreted. As a result of applying the singular perturbation, some rapidly-varying variables are related to others via algebraic equations. Most are eliminated completely, but it is convenient to retain some of these quantities for the purpose of explaining how the system functions. They are the fraction of R_s bound, the amount of activated G_s, and the fraction of R_i bound, which in dimensionless form are given by

$$u_1 = \frac{\alpha_0 C_o + (\beta_5 - \alpha_0 C_o)w_3}{\alpha_1 + \alpha_0 C_o + \beta_4 w_2} \quad u_2 = \frac{\alpha_2\alpha_3 c_1 u_1(1-w_1)}{1+\alpha_4+\alpha_2\alpha_3 c_1 u_1 - \alpha_4 w_1}$$

$$u_4 = \frac{\beta_0 C_o}{\beta_1 + \beta_0 C_o}.$$

1.5.2 The Dynamics Under Imposed and Self-Generated Stimuli

A qualitative description of how this system responds to stimuli is as follows. Suppose first that cAMP_o is clamped, and that the system is adapted to a given level of cAMP_o. A change in cAMP_o is reflected in the stimulatory (inhibitory) pathway via a change in the term $\alpha_o C_o$ ($\beta_o C_o$) that appears in the fraction u_1 (u_4) of stimulatory (inhibitory) receptors bound with ligand. On the stimulatory side, this input is immediately reflected in a change in u_2 (G_s') because the activation is fast. This increases the amount of activated cyclase (w_1), and this in turn produces more $cAMP_i$ and the relay response. Simultaneously, but on a slightly slower time scale, the inhibitory pathway activates the inhibitory G-protein G_i, which competitively

interferes with the production of G_s', and hence the activation of the cyclase. This interference then leads to adaptation in the model, and the combination of relay and adaptation qualitatively explains the response in the context of perfusion experiments. When $cAMP_o$ is not clamped a positive feedback loop is created via the secretion of $cAMP_i$. Depending on how it is tuned, this feedback system leads either to amplification of a pulse of $cAMP_o$ or to sustained oscillations. Using experimentally-determined parameters where possible, and estimates for the remaining parameters, this system predicts a time course of cAMP levels and secretion rates that agrees both qualitatively and quantitatively with experimentally-observed results in perfusion and suspension experiments.

In Fig. 1.25 we show the response to a single step change and to a four-step increase in $cAMP_o$ in a simulated perfusion experiment, using the model above developed in [97]. The response shown there is based on experimental parameters where they are known, and one sees that the system does not adapt fully at large stimuli. However this can be corrected by a simple modification of the dynamics [74]. At all stimulus levels the cAMP and secretion responses peak at about 1 min after stimulation, which is as observed experimentally [16].

In Fig. 1.26 we show the intracellular and extracellular cAMP oscillations in a suspension of cells. The amplitudes of the intracellular cAMP oscillations matches well with the experimental observations shown in the right-hand panel, but the extracellular concentration is lower. This depends on the secretion rate, the amount of the extracellular phosphodiesterase that degrades the CAMP, and other factors. Suffice it to say that the model captures the essential aspects of the cellular response, both to imposed stimuli and in suspensions, and therefore can be used to study aggregation of spatially-distributed populations.

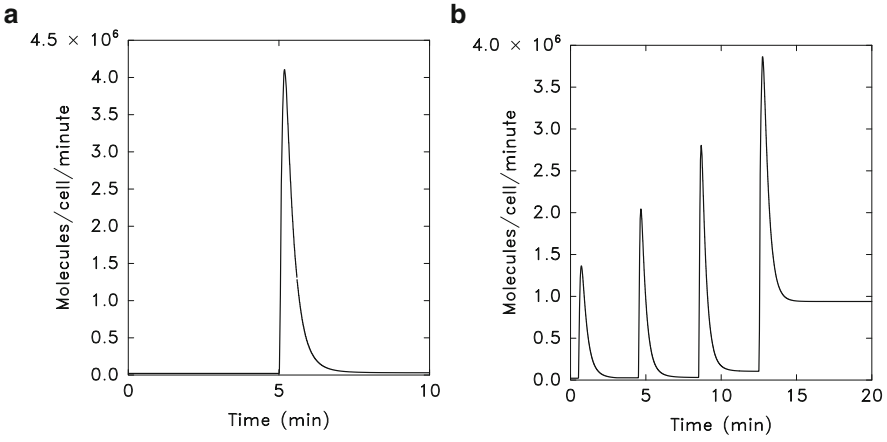

Fig. 1.25 The predicted secretion rate in response to imposed stimuli. *Left*: The response to a step from 0 to 1 μM in extracellular cAMP. *Right*: The response to a sequence of three tenfold steps from 0 to 1 μM in extracellular cAMP

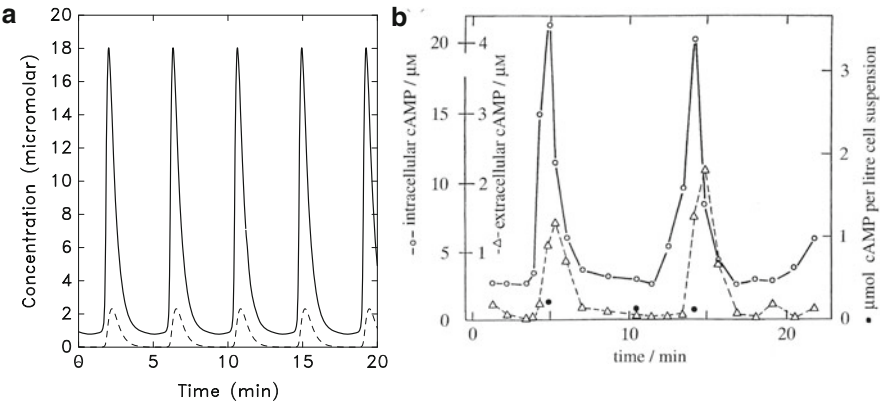

Fig. 1.26 *Left*: Periodic oscillations in a numerical simulation of suspension experiments for $\gamma_2 = 0.4$. *Solid line*: intracellular cAMP; *dashed line*: extracellular cAMP. *Right*: Experimental measurements of intracellular (*open circle*) and extracellular (*triangle*) cAMP concentration. Redrawn from Fig. 2 of Gerish and Wick [38]

1.5.3 The Reaction-Diffusion Equations for Early Aggregation

In aggregation fields the concentrations vary in space as well as time, and this leads to new phenomena. At the very least this requires a different equation for the extracellular cAMP, which can diffuse throughout space. Here one also has to decide whether to introduce a continuum density for the cells, or retain a hybrid description in which $cAMP_o$ satisfies a reaction-diffusion equation and the cells are treated as point particles. We adopt the latter description here, and this leads to the following equations. In these equations the superscript ^{i} denotes the ith cell, $\mathbf{x}_i$ denotes the spatial position of the ith cell, and the dependence of w_j^i and C_i^i on $\mathbf{x}_i$ is implicit in the equations.

$$\frac{dw_1^i}{d\tau} = \alpha_4 u_2^i - w_1^i - \alpha_4 u_2^i w_1^i$$

$$\frac{dw_2^i}{d\tau} = \beta_2\beta_3 c_2 u_4^i - \beta_5 w_2^i + \beta_6 c_3 w_3^i - c_3\beta_4 u_1^i w_2^i - \beta_2\beta_3 c_2 u_4^i (w_2^i + c_3 w_3^i)$$

$$\frac{dw_3^i}{d\tau} = -(\beta_5 + \beta_6) w_3^i + \beta_4 u_1^i w_2^i$$

$$\frac{dC_i^i}{d\tau} = \gamma_1\gamma_2 w_1^i + \Gamma_5(1 - \Gamma_7 w_1^i) - \gamma_4 \frac{C_i^i}{C_i^i + \gamma_3} - sr(C_i^i)$$

$$\frac{\partial C_o}{\partial \tau} = \Delta_1 \nabla^2 C_o(\mathbf{x}) - \hat{\gamma}_9 \frac{C_o(\mathbf{x})}{C_o(\mathbf{x}) + \gamma_8} + \sum_{i=1}^{N} \frac{V_c}{V_o} \delta(\mathbf{x} - \mathbf{x}_i) \left(sr(C_i^i) - \gamma_7 \frac{C_o(\mathbf{x})}{C_o(\mathbf{x}) + \gamma_6} \right)$$

$$u_1^i = \frac{\alpha_0 C_o(\mathbf{x}_i) + (\beta_5 - \alpha_0 C_o(\mathbf{x}_i))w_3^i}{\alpha_1 + \alpha_0 C_o(\mathbf{x}_i) + \beta_4 w_2^i} \qquad u_2^i = \frac{\alpha_2\alpha_3 c_1 u_1^i (1 - w_1^i)}{1 + \alpha_4 + \alpha_2\alpha_3 c_1 u_1^i - \alpha_4 w_1^i}$$

$$u_4^i = \frac{\beta_0 C_o(\mathbf{x}_i)}{\beta_1 + \beta_0 C_o(\mathbf{x}_i)}$$

The next question is how to solve these equations. The geometry of a two-dimensional domain is as shown in Fig. 1.27, wherein the size of the cells is exaggerated.

The computational algorithm can be summarized as follows—for details see [22].

1. Solve the extracellular equation on a regular grid, using an Alternating-Direction Implicit (ADI) method for the partial differential equation, lagging the secretion term.
2. Interpolate cAMP from the grid to the cell positions and update the intracellular variables and the secretion by an implicit scheme.
3. Update cell movement. If a cell is not moving, should it begin to move? If so, compute the direction and start movement. If it is moving, should it continue?
4. Transfer the secreted cAMP to the grid and repeat the cycle.

Two examples of the wave patterns in aggregation predicted by the model are shown in Fig. 1.28. These are certainly qualitatively consistent with the experimentally-observed waves in Fig. 1.3.

What do the analysis and computations of the continuum and cell-based models explain and predict? Some of these are discussed here—for others see the original literature cited above.

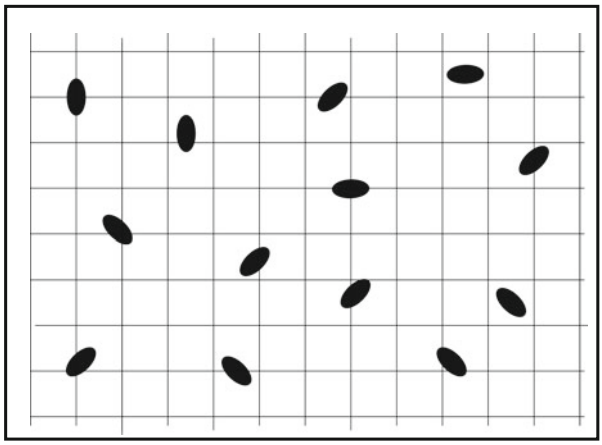

Fig. 1.27 The computational grid for the aggregation problem. The *black ellipses* represent the cells, but not to scale

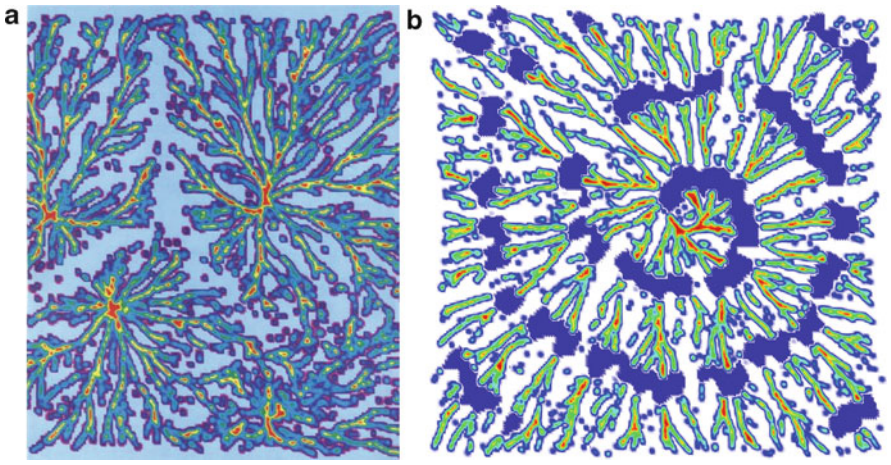

Fig. 1.28 Aggregation waves. On the *left* is shown a large field in which several pacemakers organize local aggregation patterns. On the *right* is the spiral cAMP wave (*dark blue*) superimposed on the cell streams. Note that in both images some cells are *left* behind. The time evolution of these patterns shows that cells always move toward the highest local concentration of cAMP, which leads to the observed streams

- A single cell can be a pacemaker. This is not addressed herein, but is done in [29].
- The continuum model predicts the effect of density and cell excitability on the frequency of oscillation, the wave speed, and the size of the central core.
- The cell-based model provides an explanation for the origin of streaming and the origin of spiral waves: computations show that cell movement and random variations in cell density are necessary for streaming and facilitate the generation of spirals.
- The model predicts that cells must choose a direction within 10–15 s in order to orient to the local gradient.
- Computations show that aggregation is very robust with respect to the choice of direction of movement.

Of course the model for cAMP production is not correct in detail—experiments since its formulation have contributed greatly to our understanding of the signal transduction network leading to cAMP production, but the input-output behavior is quantitatively correct, and thus all questions that depend only on this can be addressed. As we show here and in the original papers, the exterior problem dealing with aggregation can be addressed and the predictions are quite accurate. One major factor that is missing is the cell-cell interaction that occurs when cells make contact. This is addressed in the following section.

1.6 Multicellular Problems

Collective cell motion occurs in the streaming, mound and slug stages of Dd [74], as well as in vertebrate embryos [106]. In Dd streams this involves small numbers of cells, but the slug is composed of about 10^5–10^6 cells (cf. Fig. 1.29). Weijer et al. [31] have developed techniques to visualize the effects of signal-transduction

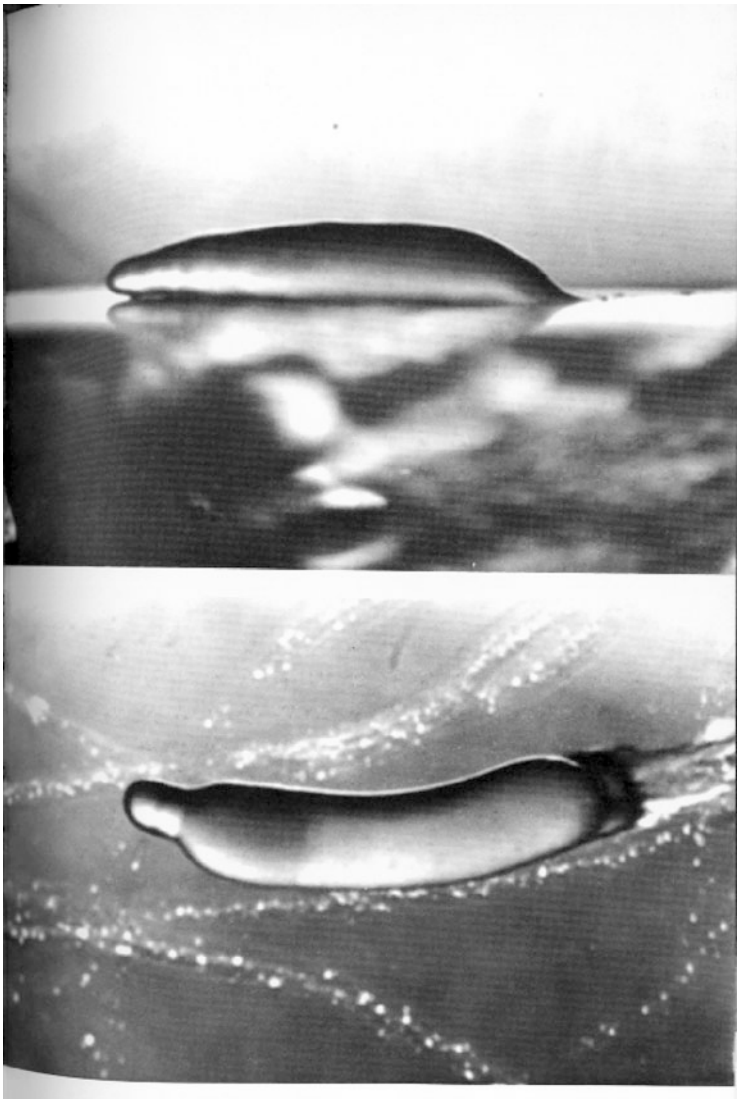

Fig. 1.29 A side and top view of a Dd slug gliding on a substrate

at the single cell level, by imaging the fluorescence from GFP-tagged PHds in response to cAMP signals. They record the movement of individual cells in three dimensions, and find that when wild-type cells are imaged in aggregation streams, their movement is very much like that of cells moving as individuals, despite the fact that new adhesion systems are expressed at this stage. The cells in the center of the stream tend to move slightly faster than those at the edge.

Mixing mutants lacking myosin II with wild type cells has shed light on the role of myosin II in multicellular motility. Mutants lacking myosin II accumulate at the edges of aggregation streams and the back of the slug, and become distorted by their adhesive interaction with wild-type cells [109]. There are two adhesion systems, characterized as A and B, expressed during the aggregation stage, and either or both may be responsible for excluding the myosin II null cells. Xu et al. postulate that mhcA$^-$ cells cannot generate sufficient protrusive force to disrupt contacts between adherent cells in streams, but can enter streams where the cells are weakly adherent [109].

The motion of Dd slugs is mechanically very similar to the motion of single cells. Vardy et al. [100] show that the slug leaves behind cell prints in the slime sheath as it migrates. The cell prints are either parabolic or elliptic in shape. Because the cell prints are sharp, i.e. exhibit no smearing near their boundary, they speculate that the cells that make up the prints are temporarily stationary and secrete a "traction protein" that allows the slug to adhere to the substratum. It is not known whether these traction proteins are related to integrins or contact proteins, but the underlying mechanics of the motion of a slug is conceptually similar to single cell motion. As will be clear later, similar computational techniques will apply in the two cases. We begin with a description of a single cell.

1.6.1 The Mechanics of a Single Cell

As will be clear from the previous sections, the movement of an individual cell involves the integration of numerous processes, and to incorporate all of these into a realistic model of a deformable cell is overly ambitious at this point. In particular, the details of how actin networks are reorganized under the membrane in response to extracellular signals is a complex process that is only partially understood, and it is not feasible to incorporate the level of detail required to describe this in a multicellular model at present. However, it may be possible to understand aspects of tissue motion, in particular that of the Dd slug, with a relatively simple mechanical model of a cell. This has been done in [24, 75], and a schematic of the cell model is shown in Fig. 1.30. In the approach taken in previous work, the opposite extreme in descriptions is adopted; cells are treated as incompressible viscoelastic solids and their stress-strain response characteristics are lumped into three elements that coincide with the three major axes. Along each axis the stress-strain behavior is described by a nonlinear version of a standard Kelvin element, as shown in Fig. 1.30. Since there is an elastic element in each branch the immediate response to a step

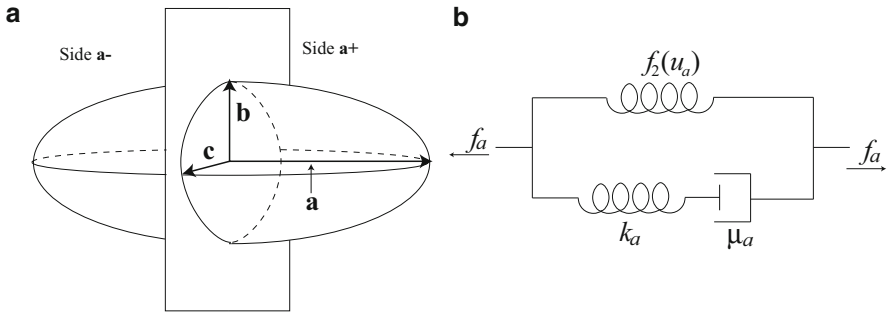

Fig. 1.30 A schematic of the model cell and the element of a standard *solid*, or Kelvin element along each axis of the ellipsoid. It consists of a nonlinear spring in parallel with a Maxwell element, which comprises a linear spring in series with a dashpot

change in the applied force is a step change in displacement in the elastic elements, followed by slower flow in the viscous element. Release of the external forces leads to a return to the rest length of the element, and since we assume that the elements are identical along the three axes, the equilibrium shape is spherical.

This is a reasonable first description, since the cytoplasm in many amoeboid cells has been characterized as a viscoelastic material whose properties are dominated by actin filaments and microtubules. However, the elastic modulus of actin solutions is concentration dependent [64], and they exhibit strain hardening [110], a property that may be important in slug movement.

When the cell deforms due to interactions with other cells or an obstacle, the three deformations are not arbitrary, because we stipulate that the total volume of the cell must be conserved.[3] In [75] the constant volume constraint was satisfied by first computing the deformation and then correcting the change in all radii so as to correct the volume.

In the computational algorithm we can decompose the total stress on an ellipsoid into the shear along the axes of the ellipsoid and an additional 'isotropic' part reflected in a pressure that constrains the overall deformation so as to satisfy the constraint that the volume remains constant. In a continuum description of an incompressible material this pressure serves as a Lagrange multiplier that forces satisfaction of the incompressibility condition. In [24] and what follows here the pressure is the deviation from a rest state and therefore may have either sign: a negative pressure causes the cell to compress and a positive pressure causes the cell to expand.

[3]This may not be true in reality, and we could allow small changes without changing the results. Osmotic fluxes may well change the total volume during deformations, but this has not been characterized experimentally, and incorporating it would add a great deal of complexity for an as yet unquantifiable increase in accuracy.

The equation governing the length of an axis of a cell is

$$u_a' = \left(\frac{k_a}{\mu_a}[f_a(t) + \bar{p} - f_2(u_a)] + f_a'(t)\right)\left(\frac{df_2(u_a)}{du_a} + k_a\right)^{-1}, \tag{1.24}$$

where u_a is the change in the length of the **a** axis, f_2 is the force from the spring in parallel, μ_a is the viscous coefficient of the dashpot, k_a is the spring constant for the spring in the Maxwell element, f_a is the magnitude of the force applied at each end in opposite directions, and $\bar{p}$ is the force due to pressure. There are three such equations one for each axis and one equation due to the volume constraint given by

$$0 = u_a'(u_b + b_0)(u_c + c_0) + (u_a + a_0)u_b'(u_c + c_0) + (u_a + a_0)(u_b + b_0)u_c', \tag{1.25}$$

where a_0, b_0, and c_0 are the initial lengths of the cell axes. This system of ordinary differential equations determines the shape of a cell and is solved numerically.

1.6.2 The Multicell Problem

Suppose there are N cells in an aggregate, sufficiently close so that at least some cells may be in contact. The forces that a cell may be subject to are classified as follows [24].

- Active forces $\mathbf{T}_{i,j}$ a cell exerts on neighboring cells or the substrate: the reaction force to this is denoted $\mathbf{M}_{j,i}$.
- The reaction to forces exerted by other cells on it.
- Dynamic drag forces that arise as a moving cell forms and breaks adhesive bonds with neighboring cells.
- Static frictional forces that exist when cells are rigidly attached to each other or to the substrate.

We let $\mathcal{N}_i^a$ denote the neighbors, including the substrate, of i upon which a cell can exert traction. The 'neighbor' relation is symmetric for all cells; if cell i can exert traction on cell j, then cell j can exert traction on cell i, but not true for the substrate, which is passive in that it does not generate stress. The motive force that i generates is

$$\mathbf{M}_i = \sum_{j \in \mathcal{N}_i^a} \mathbf{M}_{j,i},$$

and the total traction force which other cells exert on it is

$$\mathbf{T}_i = \sum_{j \in \mathcal{N}_i^a} \mathbf{T}_{j,i}.$$

The *dynamic friction force* on cell i due to interaction with j is defined as

$$\mathbf{D}_{j,i} = \mu_{ij}(v_j - \mathbf{v}_i),$$

where μ_{ij} is the friction coefficient, which is symmetric. Thus, the total dynamic friction force on cell i, due to the set $\mathcal{N}_i^d$ of cells that interact with i via a frictional force, is

$$\mathbf{D}_i = \sum_{j\in\mathcal{N}_i^d} \mathbf{D}_{j,i} = \sum_{j\in\mathcal{N}_i^d} \mu_{ij}(\mathbf{v}_j - \mathbf{v}_i).$$

By definition, statically-bound cells function as one rigid object, so that if i is bound to j and j is bound to k, then i is bound to k. In particular, if i is statically bound to the substrate either directly or indirectly then it can transmit forces applied to it to the substrate. These are the only type of chains that can transmit stress from the interior; a chain of say four cells statically bound to each other but not bound to the substrate simply functions as a larger unit. If S_{ji} denotes the static binding force on the ith cell when bound to the jth, then $S_{ji} = -S_{ij}$ and the cell-cell forces cancel on all but those cells attached to the substrate. Let $\mathcal{N}_i^s$ denote the set of cells that statically bind to cell i; then the total force on the ith cell is the sum of all the foregoing, viz.,

$$\begin{aligned}\mathbf{F}_i &= \mathbf{M}_i + \mathbf{T}_i + \mathbf{D}_i + \sum_{j\in\mathcal{N}_i^s} \mathbf{S}_{ji} \qquad (1.26)\\ &= \sum_{j\in\mathcal{N}_i^a} \mathbf{M}_{j,i} + \sum_{j\in\mathcal{N}_i^a} \mathbf{T}_{j,i} + \sum_{j\in\mathcal{N}_i^d} \mu_{ij}(\mathbf{v}_j - \mathbf{v}_i) + \sum_{j\in\mathcal{N}_i^s} \mathbf{S}_{ji}.\end{aligned}$$

If we sum these over all cells we see that the sum of the tractions and motive forces, as well as sum of the dynamic friction force, vanish for all cell-cell interactions in the interior of the slug. The surviving terms are those due to direct interaction of a cell with the substrate, or the indirect interaction via a chain of statically-connected cells that is connected to the substrate. The latter takes the form of a force on an interior cell equal and opposite to the traction force it exerts on a statically-connected chain of cells. Thus in the absence of static binding there is no mechanism by which an interior cell can transmit stress to the boundary, and accordingly, there can be no volumetric forces on the slug in a continuum description in the absence of other mechanisms.

In any case, one has to define precisely how cells exert forces on one another, how to model the active forces, the drag forces, etc. This is a rather involved process, the details of which are given in [24], and will not be repeated here. The computational algorithm defined in [24, 75] proceeds as follows.

Step 1. Locate all cells that are within a given distance from cell i.

Step 2. Search the cell's neighborhood to determine if the cAMP levels are above threshold, and if so find the direction of the highest cAMP concentration.

Step 3. If necessary, orient the cell towards the direction of the highest cAMP concentration.

Step 4. Find all the forces that act on the cell, $\mathbf{F}^{net}$ from each of the neighbor cells found in Step 1, deform the three axes of the ellipsoid, and move the cell according to (2).

Figure 1.31 shows one example of the aggregation patterns that results from the application of this algorithm. This simulation is done with 2500 cells, but the cAMP output of each computational cell is equivalent to that of 16 real cells (see [75] for details). Similar results are obtained with 10K cells and a fourfold reduction of their cAMP output. In these simulations, it was assumed that the cAMP distribution is uniform in the z direction, which is sufficiently accurate during early aggregation, because the cell distribution is essentially 2D, but for mound formation

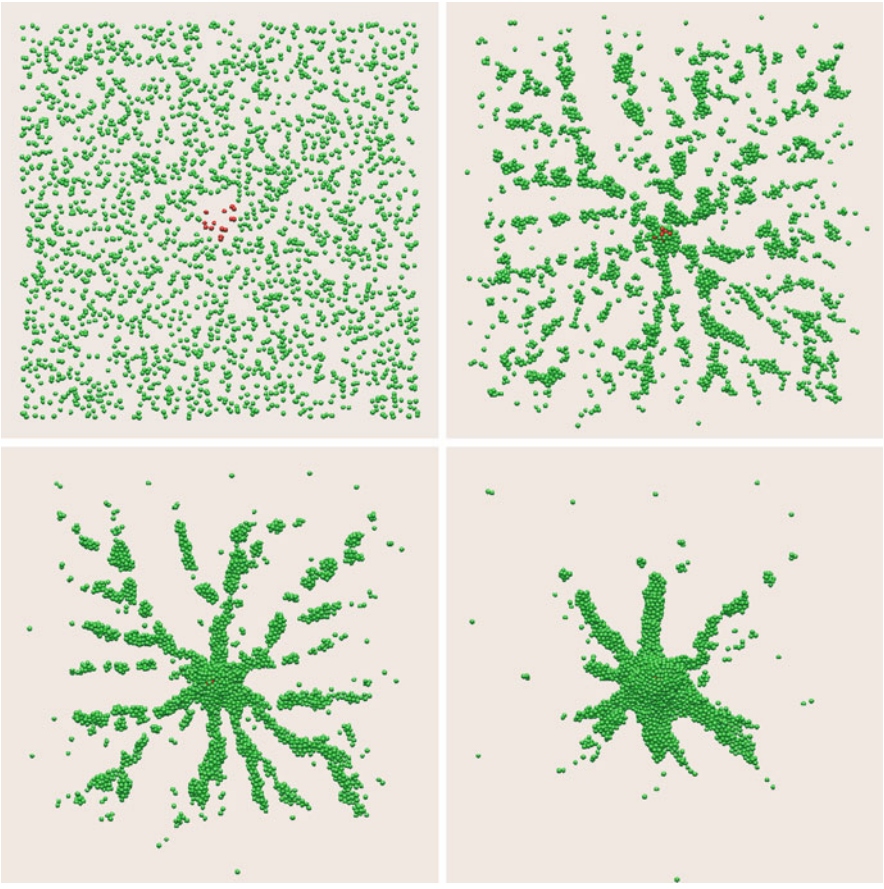

Fig. 1.31 The early aggregation pattern, driven by pacemakers (*red*) in the center of a field of cells. The times beginning at the *upper left*, are 0, 80, 160, and 320 min. From [75], with permission

and movement of the slug a 3D computation is needed. However, Fig. 1.32 shows that the initial stages of mound formation results when cells at the center are pushed upward by the inward movement of the outer cells.

The similarity with the patterns that emerge when the cells are treated as particles and their movement governed by formal rules, as in Fig. 1.28 (left), is evident. However the more detailed treatment of the mechanics allows for more realistic comparisons between the theoretical predictions and the experimental results.

For example, Bonner [7] discovered how to produce two-dimensional slugs that are only one cell layer thick and migrate between a glass slide and a drop of mineral oil. In Fig. 1.33 we show the computational equivalent of this experiment with a 2D slug whose movement is driven by pacemaker cells at the front. In the upper left panel another group of pacemaker cells is introduced at the side, and subsequent frames show how this pacemaker organizes a secondary slug which then breaks away. This also occurs in Bonner's 2D slugs, although there the new pacemaker arises spontaneously, presumably due to variations in properties of the cells, whereas in the computational experiment the second pacemaker is imposed. Aside from this, the results are quite similar.

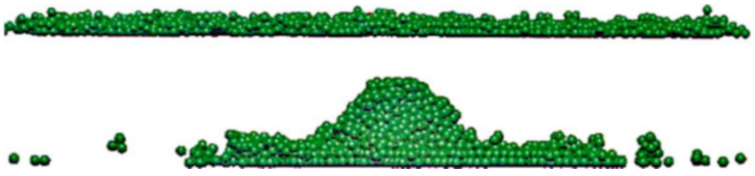

Fig. 1.32 A cross-sectional view of the aggregation field at 80 (*top*) and 320 (*bottom*) min. From [75], with permission

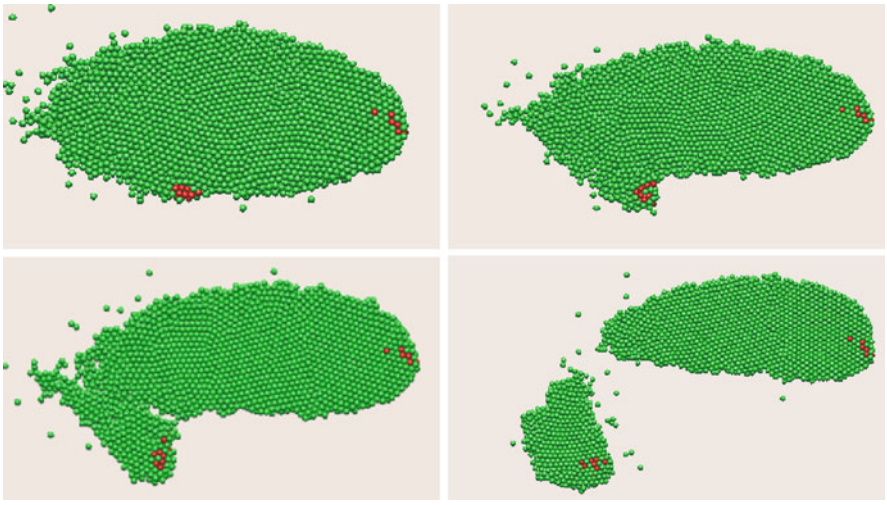

Fig. 1.33 A migrating 2D slug with an auxiliary pacemaker. From [75], with permission

Detailed modeling of the later stages of slug movement is very complicated because a slug can frequently elevate the leading one third of the slug as if to sample the environment, and then touch down again, thus moving in a pulsatile motion. During migration, cAMP waves propagate down the length of the slug [30] and cells begin to differentiate into pre-stalk and pre-spore cells that eventually become the stalk and spore cells in the next stage of the life cycle, the fruiting body. How the proportions of cell types are determined is a long-standing question [77], and some of the complexities of slug stage movement and patterning are discussed in the work of Weijer and collaborators [78, 102, 104]. We shall not pursue this further, but for one final question.

1.6.3 Who Does the Work in the Slug?

According to our earlier discussion of the mechanics, if our description of cell interactions properly accounts for cell-cell and cell-substrate interactions, then cells in the interior of the slug can only contribute to movement of the slug if there is a chain of rigidly-connected cells that attaches to the substrate. In [24] this is called the bedspring model, since the rigid cells form a network that transmits stress to the boundary and allows other cells to crawl through it. This is similar to what occurs when a single cell migrates through a tissue, but in order for this mechanism to work in the Dd slug, the network must be dynamic and cells must be able to "freeze" when stress is applied, but also to move. Beautiful experiments in which the total force exerted by a slug was measured on a rotating table seemed to indicate that the motive force scales with the number of cells in the slug, rather than the number in contact with the substrate [50, 51]. These experiments motivated a computational study of which cells provide the motive force in the slug. Using an extension of the cell-based model described in the previous section, a large number of simulations were done using different aspect ratios of the slugs [24]. The initial configurations ranged through 250 cases having from 1 to 5 cells in the width and height, and from 1 to 10 cells in the length of the slug. In all cases the cells were stimulated to move in a fixed direction by a traveling wave. The results are shown in Fig. 1.34. It is clear from the left panel that the force scales with the number of cells in contact with the surface, but the right panel suggests how one could conclude that it scales with the volume of the slug. There the force generated by slugs having the same ratio of volume to area in contact with the surface fall on a straight line, but the slope varies with that ratio. Thus if this ratio was approximately constant in the experiments one could conclude that the force scale with the volume.

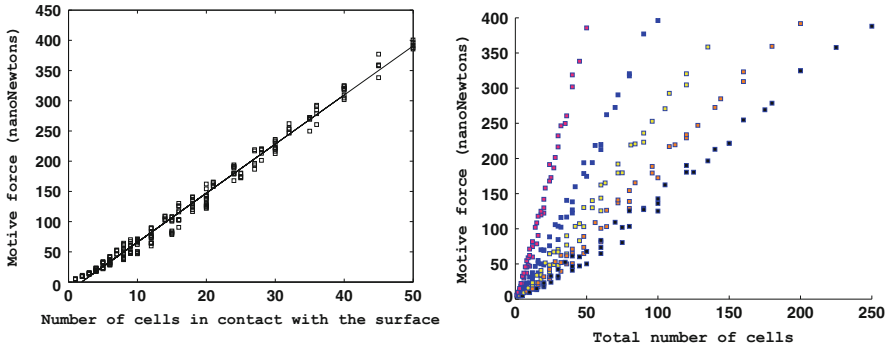

Fig. 1.34 Data from 250 different simulations for the translational force of the slug in nanoNewtons (*vertical axis*) and the number of cells in contact with the surface (*left*), or the total number of cells in the slug (*right*) (*horizontal axis*). Five lines are clear in the *right panel*—these correspond to subsets of the data in which the initial height of the slug is held constant, which implies that the volume of the slug and the surface area in contact with the substrate are proportional. From [24] with permission

1.7 Conclusion

In these notes we have attempted to describe a number of interesting problems connected with cell motility and to indicate some aspects on which progress toward understanding them has been made. Hopefully the reader will have gained some insight into the role of mathematical modeling and analysis in the resolutions of these problems, but will also recognize that much is yet to be done. We are in fact a long way from a complete understanding of cell motility, either from the experimental side, where experiments can shed light on specific processes, or from the mathematical side, where the interactions of the underlying processes can only be understood through mathematical modeling and computational analysis.

Appendix: Singular Perturbation Reduction

We know how to express reaction dynamics as the evolution equation

$$\frac{dx}{dt} = f(x,p) \tag{1.27}$$

where $x \in M \subseteq R^n$ and $p \in R^p$. Suppose there is a separation of variables into those that vary rapidly and those that change slowly on the chosen time scale. This leads

to a system of equations of the form

$$\begin{aligned} \frac{dx}{dt} &= f(x, y, \epsilon, p) \\ \epsilon \frac{dy}{dt} &= g(x, y, \epsilon, p) \end{aligned} \tag{1.28}$$

wherein ϵ is a small parameter and x (resp., y) is a slow (resp., fast) variable on the t time scale.

- What are the implications of this separation for understanding the dynamics?
- More precisely, can we use the separation of time scales to reduce the dimensionality of the problem we have to analyze?

The following simple example will illustrate some of the underlying ideas. Consider the reaction

$$A \xrightarrow{k_1} B \xrightarrow{k_2} C, \tag{1.29}$$

where A, B, and C are generic chemical species. We assume mass action kinetics and first-order reactions and therefore can write the governing equations as

$$\begin{aligned} \dot{x} &= k_1 x \\ \dot{y} &= k_1 x - k_2 y \\ \dot{z} &= k_2 y. \end{aligned} \tag{1.30}$$

where x, y, and z stand for the concentration of A, B, and C, resp. In addition we have the conservation condition

$$(x + y + z)(t) = (x + y + z)(0). \tag{1.31}$$

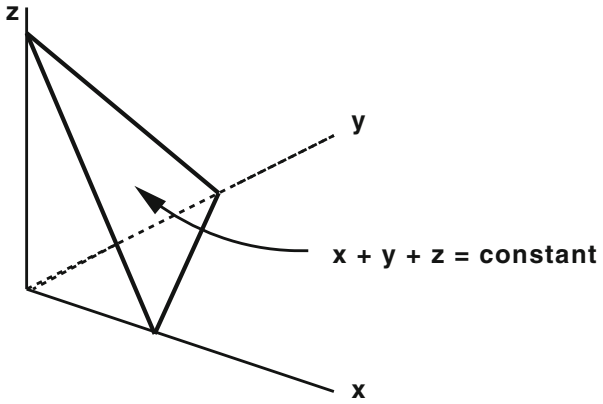

Clearly A and B will disappear completely in the steady state, and the exact solution for the transient problem for A and B is

$$x = x_0 e^{-k_1 t}$$
$$y = y_0 e^{-k_2 t} + \frac{k_1 x_0}{k_2 - k_1}[e^{-k_1 t} - e^{-k_2 t}].$$

If $k_2 \gg k_1$, then after a time $t \sim \mathcal{O}(1/k_2)$ we have

$$y(t) \sim \frac{k_1 x_0 e^{-k_1 t}}{k_2} = \frac{k_1}{k_2} x(t).$$

But this is what we would get directly if we set $\dot{y} = k_1 x - k_2 y = 0$ since then

$$y = \frac{k_1 x}{k_2}.$$

This is what we call the 'pseudo-steady-state' or PSS value of y , (or alternatively, the 'quasi-steady-state' QSS value of y), and the hypothesis that we can do this is called the 'pseudo-(or quasi) steady-state hypothesis'—the PSSH or QSSA. Can we justify setting $\dot{y} = 0$ analytically, and how do we understand it geometrically?

To formalize this reduction, consider the system

$$\frac{dx}{d\tau} = f(x, y) \tag{1.32}$$

$$\epsilon \frac{dy}{d\tau} = g(x, y),$$

where $x \in R^n$, $y \in R^m$, and $\epsilon > 0$ is a small parameter.

Let $y = \phi(x)$ be one of the solutions of the system

$$g(x, y) = 0 \tag{1.33}$$

defined on a closed bounded domain $D \subset R^n$. The *degenerate or slow system* associated with (1.33) and the solution $y = \phi(x)$ is the system

$$\frac{dx}{d\tau} = f(x, \phi(x)). \tag{1.34}$$

The solution $y = \phi(x)$ is said to be *isolated* on D if there exists an $\eta > 0$ such that (1.33) has no solution other than ϕ with the property that

$$\|y - \phi(x)\| < \eta.$$

The associated *adjoined (or fast) system* is

$$\frac{dy}{ds} = g(x^*, y), \tag{1.35}$$

where x^* is regarded as a parameter.

- The isolated solution $y = \phi(x)$ is said to be *positively stable* in D if for all x^* in D the points $y = \phi(x^*)$ are asymptotically stable stationary points, in the sense of Lyapunov, of the adjoined system.
- The *domain of influence* of an isolated, positively stable $y = \phi(x)$is the set of points (x^*, y^*) such that the solution of the adjoined system with the initial conditions $y(0) = y^*$ tends to $\phi(x^*)$ as $s \to \infty$.

One of the earliest formal statements of what is now know as a singular perturbation reduction is given by *Tikhonov's theorem* [99].

Theorem 2 *If some root $y = \phi(x)$ of $g = 0$ is an isolated, positively stable root in some bounded closed domain D, if the initial point $(x(0), y(0))$ belongs to the domain of influence of this root, and if the solution of the degenerate system belongs to D for $0 \le t \le T$, then the solution $(x(t, \epsilon), y(t, \epsilon))$ of the original system tends to the solution $(\bar{x}(t), \bar{y}(t))$ of the degenerate or slow system , as ϵ approaches 0, the passage to the limit*

$$\lim_{\epsilon \to 0} y(t, \epsilon) = \tilde{y}(t) = \phi(\bar{x}, t)$$

holding for $0 < t \le T^0 < T$, and the passage to the limit

$$\lim_{\epsilon \to 0} x(t, \epsilon) = \bar{x}(t)$$

holding for $0 \le t \le T^0 < T$.

The geometry behind the theorem is qualitatively as shown in the following sketch.

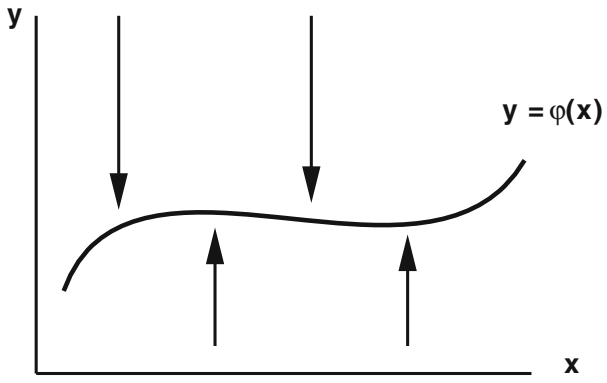

Remarks

(1) This can be generalized to allow ϵ and t dependence in the right-hand side of the DE.
(2) If y is sufficiently close to $\phi(x)$ then on the fast time scale this analysis can be viewed in the framework of center manifold theory.
(3) There are many variations on the theme and many expositions of it.

1.8 Glossary

Actin is one of the most abundant proteins found in eukaryotic cells and is highly conserved throughout evolution. Actin monomers polymerize in an ATP-dependent process to form polarized actin filaments. The helical actin filament has a barbed end and a pointed end. In non-muscle cells, the dynamic organization of filamentous actin gives rise to various cell structures, such as filopodia, lamellipodia, and stress fibers.

AKT/PKB Cellular homologue of AKT retroviral oncogene protein Ser/Thr kinase. Also called Protein Kinase B because of homology with Protein Kinase A and Protein Kinase C family members. AKT has an amino-terminal pleckstrin homology (PH) domain that binds to the lipid products of phosphoinositide 3-kinase, phosphatidylinositol-3,4-bisphosphate and phosphatidylinositol-3,4,5-trisphosphate. This binding locates it at the plasma membrane where it becomes phosphorylated on Thr-308 (human AKT1) in the activation loop of the catalytic domain by phosphoinositide-dependent kinase 1 (PDK1). This phosphorylation leads to activation. Full activation requires phosphorylation at a second site (Ser-473 of human AKT). Mammals have at least three distinct genes for AKT family members (AKT1, AKT2 and AKT3) and they appear to at least partially redundant in function.

Alpha-actinin is an actin cross-linking protein that belongs to the spectrin superfamily. It forms antiparallel homodimers in a rod-like structure with one actin-binding domain on each side of the rod. It can, therefore, cross-link two filaments of actin.

Arp2/3 (Actin-related protein complex) Extracellular and intracellular signals that initiate actin cytoskeletal rearrangements flow through the Arp2/3 complex. The Arp2/3 complex is composed of seven subunits, two unconventional actin proteins, Arp2 and Arp3, and five additional proteins. One copy of each subunit is present in the complex. In addition to contributing to the nucleation of actin filaments, the Arp2/3 complex caps the slow-growing pointed ends of actin filaments and promotes the elongation of the actin filament at the fast-growing barbed end. Arp2/3 complexes are localized at the branch point of two different filaments, binding to both the side of the mother filament and the pointed end of the daughter filament. These interactions create an approximate 70° angle with the actin barbed end oriented towards the plasma membrane. These observations serve as the basis

for the "dendritic nucleation" model in which Arp2/3, through its interaction with F-actin, is a key regulator of the unique meshwork of F-actin in the lamellipodial structure. The Arp2/3 complex influences the strictly regulated reorganization of the actin cytoskeleton in response to various signaling pathways.

B-Raf is a serine/threonine protein kinase that is a member of the Raf family of protein kinases. Raf-B can be activated by the small GTPase Ras as well as Rap1. cAMP activates MAP-Kinase through B-Raf.

Cdc42 is a Rho-family GTPase that was first identified as a regulator of cell polarity and budding in yeast. In mammalian cells, Cdc42 is activated in response to integrins and bradykinin. Activated Cdc42 induces formation of actin-rich structures known as filopodia. Cdc42 affects actin directly by binding to its effector WASP, an activator of Arp2/3 and actin polymerization. During cell migration, Cdc42 is also responsible for polarization of the cell.

Chemotaxis the directed movement of a microorganism or cell in response to a chemical stimulus.

G-proteins G-proteins are heterotrimeric proteins comprising alpha, beta and gamma subunits. When bound to guanine nucleotide diphosphate (GDP), G-proteins are inactive, and are activated when bound to guanine nucleotide triphosphate (GTP). When activated, they split into alpha-GTP and beta-gamma subunits that are separately used for control of downstream processes. The alpha subunit has intrinsic hydrolysis activity that removes a phosphate group, whereupon the alpha-GDP subunit recombines with a beta-gamma subunit.

G-protein coupled receptors (GPCRs) G-protein-coupled receptors are integral membrane proteins with seven membrane-spanning helices. G-protein is bound to the receptor in its inactive state, and when a ligand is bound, the receptor may undergo a conformational change that facilitates the GDP-GTP exchange on a G protein, which then detaches from the receptor. GPCRs can desensitize when exposed to ligand for a sufficient length of time as a result of phosphorylation of a cytoplasmic receptor domain by protein kinases.

In vitro the recreation of biological processes in an artificial laboratory environment.

In vivo biological processes that take place within a living organism or cell.

Kinase an enzyme that catalyzes addition of a phosphoryl group to proteins.

MLCK (Myosin Light Chain kinase) is a serine/threonine kinase that phosphorylates the regulatory light chain (RLC) of the molecular motor myosin, resulting in increased contraction. In nonmuscle cells MLCK is involved in the regulation of cell motility.

MLCP (Myosin Light Chain phosphatase) dephosphorylates the regulatory light chain of molecular motor myosin, thus inactivating it. MLCP is involved in the regulation of the actin cytoskeleton and cell spreading.

PAK (p21-activated kinase) is a serine/threonine kinase that binds to and is activated by Rho family GTPases. The PAK family of kinases is highly conserved among species. PAK family members have an N-terminal kinase domain and a C-terminal p21 Rac and Cdc-42-binding domain. The binding of Rho family GTPases to the C-terminus of PAK causes a conformational change resulting in

autophosphorylation and activation of the kinase. PAK family members have been shown to play a role in actin polymerization and cytoskeletal dynamics.

PI3K Phosphoinositide 3-kinase catalyzes the phosphoryation of phosphatidylinositol-4,5-bisphosphate to produce phosphatidylinositol-3,4, 5-trisphosphate. The enzyme is cytosolic and become localized to the plasma membrane, which activates the catalytic subunit. Binding of the catalytic subunit to activated Ras appears to enhance the membrane association and activation.

Phosphatase an enzyme that removes the phosphoryl group from proteins.

Protease (proteinase, proteolytic enzyme) an enzyme that degrades proteins, such as collagen, laminin, and fibrin.

PTEN is a phosphatase that can dephosphorylate the lipid products or phosphoinositide 3-kinase, especially phosphatidylinositol-3,4,5-trisphosphate. By dephosphorylating these lipids, PTEN attenuates signaling via the phosphoinositide 3-kinase pathway.

Rac is a small GTP-binding protein which belongs to the Ras superfamily. Rac activity depends on the ratio of GTP/GDP bound forms. GEFs (guanine nucleotide exchange factors), GAPs (GTPase activating proteins) and GDIs (guanine nucleotide dissociation inhibitors) thus determine its activity by regulating of the GTP/GDP bound form. The downstream effectors of Rac are involved in regulation of the cytoskeleton.

Ras is a small protein that is activated by exchange proteins of the SOS (Son of Sevenless) or Ras-GRF (Ras GDP Releasing Factor) family. The release of GDP and binding of GTP 'activates' Ras, allowing it to bind to downstream effectors, including phosphoinositide 3-kinase (PI3K). Ras is anchored at the plasma membrane via a carboxy-terminal farnesyl group. One function of Ras is to facilitate localization of its cytosolic effectors at the plasma membrane. Mutant forms of Ras that stabilize the GTP bound state contribute to tumor formation.

Rho GTPase is a member of Rho family of small GTP binding proteins, which include Rho A, B, G. It is active in the GTP-bound state and inactive when bound to GDP. Activation of Rho results in its association with a wide variety of effector molecules and leads to activation of downstream signaling cascades. Rho proteins exhibit intrinsic GTPase activity Rho that is significantly stimulated by GTPase activating proteins (GAPs). Conversely, GTP exchange factors (GEFs) promote exchange of GDP for GTP, thus activating Rho. Rho GTPase regulates actin cytoskeleton organization and assembly, in particular actin stress fibers and focal adhesion formation. It is involved in cellular processes that depend on actin cytoskeleton such as cell spreading and migration.

RLC (Regulatory Light Chain of myosin) binds to the neck region of Heavy Chain (HC) of myosin and regulates its motor activity. When RLC is phosphorylated by myosin light chain kinase on Ser19 it causes conformational changes in myosin and activates its motor function. Dephosphorylation of RLC by myosin light chain phosphatase negatively regulates myosin activity. Phosphorylation of RLC in smooth muscle cells leads to initiation of contraction, whereas in striated muscles it increases speed and force of contractions. There is also evidence that in nonmuscle

cells myosins are participating in cell motility, spreading, cytokinesis and vesicle transport.

ROCK Rho kinase/ROKalpha/ROCK-II and a related protein p160ROCK/ROCK-I are serine/threonine kinases. Integrin-dependent activation of Rho family small GTPases induces Rho-Rho kinase interaction and facilitates translocation of Rho kinase to the cell membrane. Rho kinase facilitates formation of focal adhesions and actin stress fiber assembly. It cooperates with other Rho effectors to regulate the formation of actin structures. Rho kinase associates with and phosphrylates myosin phosphatase. Phosphorylation leads to the inhibition of phosphatase activity and thereby enhances myosin-mediated contractility. Rho kinase has been shown to facilitate tumor cell invasion due to its role in cytoskeletal reorganization. In addition, Rho kinase promotes cytokinesis by phosphorylation of myosin light chain at the cleavage furrow.

Small G proteins A class of monomeric, low molecular weight (20–25 kDa) GTP-binding proteins that regulate a variety of intracellular processes. The GTP bound form of the protein is active and is inactivated by an intrinsic GTPase activity, which is controlled by GTPase activators (GAPs), GDP dissociation inhibitors (GDIs), and guanine nucleotide exchange factors (GEFs).

SOS (Son of Sevenless) is an exchange factor that stimulates GDP release from Ras to allow GTP binding and formation of the active state. SOS has a pleckstrin homology (PH) domain that mediates binding to the membrane.

WASP (The Wiskott-Aldrich Syndrome protein) mediates a variety of signals from kinases, receptors, and small G proteins to the Arp2/3 complex and the actin cytoskeleton. Homologs in the WASP family include SCAR and WAVE. The family members share two similar domains: one that mediates interactions of WASP with adaptor proteins such as profilin, and another involved in interaction with Arp2/3 complex and G-actin. GTP-Cdc42 binding to WASP stimulates the Arp2/3 complex resulting in actin polymerization.

References

1. B. Alberts, A. Johnson, J. Lewis, M. Raff, K. Roberts, P. Walter, *Molecular Biology of the Cell*, 4th edn. (Garland Science, New York, London, 2002)
2. U. Alon, M.G. Surette, N. Barkai, S. Leibler, Robustness in bacterial chemotaxis. Nature **15**, 168–171 (1999)
3. R. Ananthakrishnan, A. Ehrlicher, The forces behind cell movement. Int. J. Biol. Sci. **3**(5), 303–17 (2007)
4. L. Blanchoin, T.D. Pollard, Hydrolysis of ATP by polymerized actin depends on the bound divalent cation but not profilin. Biochemistry **41**(2), 597–602 (2002)
5. D. Boal, *Mechanics of the Cell* (Cambridge University Press, Cambridge, 2002)
6. J.T. Bonner, *The Cellular Slime Molds* (Princeton University Press, Princeton, NJ, 1967)
7. J.T. Bonner, A way of following individual cells in the migrating slugs of Dictyostelium discoideum. Proc. Natl. Acad. Sci. **95**(16), 9355–9359 (1998)
8. D. Bray, *Cell Movements: From Molecules to Motility* (Garland Publishing, New York, 2001)

9. T. Bretschneider, K. Anderson, M. Ecke, A. Müller-Taubenberger, B. Schroth-Diez, H.C. Ishikawa-Ankerhold, G. Gerisch, The three-dimensional dynamics of actin waves, a model of cytoskeletal self-organization. Biophys. J. **96**(7), 2888–2900 (2009)
10. J.A. Brzostowski, C.A. Parent, A.R. Kimmel, A Gα-dependent pathway that antagonizes multiple chemoattractant responses that regulate directional cell movement. Genes Dev. **18**, 805–15 (2004)
11. B. Bugyi, M.F. Carlier, Control of actin filament treadmilling in cell motility. Annu. Rev. Biophys. **39**, 449–470 (2010)
12. L. Cai, A.M. Makhov, D.A. Schafer, J.E. Bear, Coronin 1B antagonizes cortactin and remodels arp2/3-containing actin branches in lamellipodia. Cell **134**(5), 828–842 (2008)
13. Y. Cao, H. Li, L. Petzold, Efficient formulation of the stochastic simulation algorithm for chemically reacting systems. J. Chem. Phys. **121**(9), 4059–67 (2004)
14. M. Carlier, D. Pantaloni, E. Korn, The effects of Mg2+ at the high-affinity and low-affinity sites on the polymerization of actin and associated ATP hydrolysis. J. Biol. Chem. **261**, 10785–10792 (1986)
15. L.B. Case, C.M. Waterman, Adhesive F-actin waves: a novel integrin-mediated adhesion complex coupled to ventral actin polymerization. PLoS One **6**(11), e26631 (2011)
16. M.Y. Chen, R.H. Insall, P.N. Devreotes, Signaling through chemoattracnt receptors in *Dictyostelium*. Trends Genet. **12**(2), 52–57 (1996)
17. H. Chen, B.W. Bernstein, J.R. Bamburg, Regulating actin-filament dynamics in vivo. Trends Biochem. Sci. **25**(1), 19–23 (2000). Review
18. Y. Cheng, H.G. Othmer, A model for direction sensing in *dictyostelium discoideum*: Ras activity and symmetry breaking driven by a $g_{\beta\gamma}$- mediated, $g_{\alpha 2}$-ric8 – dependent signal transduction network. PLoS Comput. Biol. **12**, e1004900 (2016)
19. C.Y. Chung, S. Funamoto, R.A. Firtel, Signaling pathways controlling cell polarity and chemotaxis. Trends Biochem. Sci. **26**(9), 557–566 (2001). Review
20. J. Condeelis, A. Bresnick, M. Demma, S. Dharmawardhane, R. Eddy, A.L. Hall, R. Sauterer, V. Warren, Mechanisms of amoeboid chemotaxis: an evaluation of the cortical expansion model. Dev. Genet. **11**(5–6), 333–340 (1990)
21. L.P. Cramer, M. Siebert, T.J. Mitchison, Identification of novel graded polarity actin filament bundles in locomoting heart fibroblasts: implications for the generation of motile force. J. Cell Biol. **136**(6), 1287–1305 (1997)
22. J.C. Dallon, H.G. Othmer, A discrete cell model with adaptive signalling for aggregation of dictyostelium discoideum. Philos. Trans. R. Soc. Lond. B Biol. Sci. **352**(1351), 391–417 (1997)
23. J.C. Dallon, H.G. Othmer, A continuum analysis of the chemotactic signal seen by *dictyostelium discoideum*. J. Theor. Biol. **194**(4), 461–483 (1998)
24. J.C. Dallon, H.G. Othmer, How cellular movement determines the collective force generated by the dictyostelium discoideum slug. J. Theor. Biol. **231**, 203–222 (2004)
25. P. Dancker, L. Hess, Phalloidin reduces the release of inorganic phosphate during actin polymerization. Biochim. Biophys. Acta **1035**(2), 197–200 (1990)
26. L.A. Davidson, R.E. Keller, Neural tube closure in xenopus laevis involves medial migration, directed protrusive activity, cell intercalation and convergent extension. Development **126**(20), 4547–4556 (1999)
27. P.N. Devreotes, T.L. Steck, Cyclic $3', 5'$ AMP relay in *Dictyostelium discoideum* II. Requirements for the initiation and termination of the response. J. Cell Biol. **80**, 300–309 (1979)
28. P.N. Devreotes, P.L. Derstine, T.L. Steck, Cyclic $3', 5'$ AMP relay in *Dictyostelium discoideum* I. A technique to monitor responses to controlled stimuli. J. Cell Biol. **80**, 291–299 (1979)
29. G. DeYoung, P.B. Monk, H.G. Othmer, Pacemakers in aggregation fields of *Dictyostelium disc oideum*. Does a single cell suffice? J. Math. Biol. **26**, 486–517 (1988)
30. D. Dormann, C.J. Weijer, Propagating chemoattractant waves coordinate periodic cell movement in dictyostelium slugs. Development **128**(22), 4535–4543 (2001)

31. D. Dormann, G. Weijer, C.A. Parent, P.N. Devreotes, C.J. Weijer, Visualizing PI3 kinase-mediated cell-cell signaling during dictyostelium development. Curr. Biol. **12**(14), 1178–1188 (2002)
32. R.A. Firtel, R. Meili, Dictyostelium: a model for regulated cell movement during morphogenesis. Curr. Opin. Genet. Dev. **10**(4), 421–427 (2000). Review
33. P. Friedl, K. Wolf, Tumour-cell invasion and migration: diversity and escape mechanisms. Nat. Rev. Cancer **3**(5), 362–74 (2003)
34. I. Fujiwara, S. Takahashi, H. Tadakuma, S. Ishiwata, Microscopic analysis of polymerization dynamics with individual actin filaments. Nat. Cell. Biol. **4**(9), 666–673 (2002)
35. C. Gadgil, C.H. Lee, H.G. Othmer, A stochastic analysis of first-order reaction networks. Bull. Math. Biol. **67**, 901–946 (2005)
36. C.W. Gardiner, *Handbook of Stochastic Methods* (Springer, Berlin, Heildeberg, 1983)
37. G. Gerisch, Chemotaxis in dictyostelium. Annu. Rev. Physiol. **44**(1), 535–552 (1982)
38. G. Gerisch, U. Wick, Intracellular oscillations and release of cyclic AMP from *Dictyostelium* cells. Biochem. Biophys. Res. Commun. **65**, 364–370 (1975)
39. G. Gerisch, D. Hulser, D. Malchow, U. Wick, Cell communication by periodic cyclic amp pulses. Philos. Trans. R. Soc. Lond. **272**, 181–192 (1975)
40. G. Gerisch, T. Bretschneider, A. Muler-Taubenberger, E. Simmeth, M. Ecke, S. Diez, K. Anderson, Mobile actin clusters and traveling waves in cells recovering from actin depolymerization. Biophys. J. **87**(5), 3493–3503 (2004)
41. D.T. Gillespie, A general method for numerically simulating the stochastic time evolution of coupled chemical reactions. J. Comput. Phys. **22**, 403–434 (1976)
42. D.T. Gillespie, Exact stochastic simulation of coupled chemical reactions. J. Phys. Chem. **81**(25), 2340–2361 (1977)
43. A.R. Gingle, Critical density for relaying in *Dictyostelium discoideum* and its relation to phosphodiesterase secretion into the extracellular medium. J. Cell Sci. **20**, 1–20 (1976)
44. A.L. Hall, A. Schlein, J. Condeelis, Relationship of pseudopod extension to chemotactic hormone-induced actin polymerization in amoeboid cells. J. Cell Biol. **37**(3), 285–299 (1988)
45. B. Heit, S. Tavener, E. Raharjo, P. Kubes, An intracellular signaling hierarchy determines direction of migration in opposing chemotactic gradients. J. Cell Biol. **159**(1), 91–102 (2002)
46. J. Hu, H.G. Othmer, A theoretical analysis of filament length fluctuations in actin and other polymers. J. Math. Biol. **63**(6), 1001–1049 (2011)
47. J. Hu, A. Matzavinos, H.G. Othmer, A theoretical approach to actin filament dynamics. J. Stat. Phys. **128**(1–2), 111–138 (2007)
48. J. Hu, H.W. Kang, H.G. Othmer, Stochastic analysis of reaction–diffusion processes. Bull. Math. Biol. **76**, 854–894 (2014)
49. M. Iijima, Y.E. Huang, P. Devreotes, Temporal and spatial regulation of chemotaxis. Dev. Cell **3**(4), 469–478 (2002). Review
50. K. Inouye, Measurement of the motive force of the migrating slug of dictyostelium discoideum by a centrifuge method. Protoplasma **121**, 171–177 (1984)
51. K. Inouye, I. Takeuchi, Analytical studies on migrating movement of the pseudoplasmodium of *Dictyostelium Discoideum*. Protoplasma **99**, 289–304 (1979)
52. R.H. Insall, O.D. Weiner, PIP3, PIP2, and cell movement–similar messages, different meanings? Dev. Cell. **1**(6), 743–747 (2001)
53. C. Janetopoulos, T. Jin, P. Devreotes, Receptor-mediated activation of heterotrimeric G-proteins in living cells. Science **291**(5512), 2408–2411 (2001)
54. P.A. Janmey, Mechanical properties of cytoskeletal polymers. Curr. Opin. Cell Biol. **2**, 4–11 (1991)
55. T. Jin, N. Zhang, Y. Long, C.A. Parent, P.N. Devreotes, Localization of the G protein $\beta\gamma$ complex in living cells during chemotaxis. Science **287**(5455), 1034–1036 (2000)
56. H.W. Kang, L. Zheng, H.G. Othmer, A new method for choosing the computational cell in stochastic reaction–diffusion systems. J. Math. Biol. **60**, 1017–1099 (2012)
57. H.W. Kang, L. Zheng, H.G. Othmer, A new method for choosing the computational cell in stochastic reaction-diffusion systems. J. Math. Biol. **60**, 1017–1099 (2012)

58. V. Khamviwath, J. Hu, H.G. Othmer, A continuum model of actin waves in dictyostelium discoideum. PloS One **8**(5), e64272 (2013)
59. A.R. Kimmel, C.A. Parent, The signal to move: D. discoideum go orienteering. Science **300**(5625), 1525–1527 (2003)
60. J.R. Kuhn, T.D. Pollard, Real-time measurements of actin filament polymerization by total internal reflection fluorescence microscopy. Biophys. J. **88**(2), 1387–1402 (2005)
61. D.A. Lauffenburger, A.F. Horwitz, Cell migration: a physically integrated molecular process. Cell **84**, 359–369 (1996)
62. A. Levchenko, P.A. Iglesias, Models of eukaryotic gradient sensing: application to chemotaxis of amoebae and neutrophils. Biophys. J. **82**(1 Pt 1), 50–63 (2002)
63. L. Limozin, M. Barmann, E. Sackmann, On the organization of self-assembled actin networks in giant vesicles. Eur. Phys. J E **10**(4), 319–330 (2003)
64. F.C. MacKintosh, Theoretical models of viscoelasticity of actin solutions and the actin cortex. Biol. Bull. **194**(3), 351–353 (1998). No abstract available
65. A. Matzavinos, H.G. Othmer, A stochastic analysis of actin polymerization in the presence of twinfilin and gelsolin. J. Theor. Biol. **249**(4), 723–736 (2007)
66. J.L. McGrath, E.A. Osborn, Y.S. Tardy, C.F. Dewey Jr, J.H. Hartwig, Regulation of the actin cycle in vivo by actin filament severing. Proc. Natl. Acad. Sci. USA **97**(12), 6532–7 (2000)
67. S. McLaughlin, J. Wang, A. Gambhir, D. Murray, PIP_2 and proteins: interactions, organization and information flow. Annu. Rev. Biophys. Biomol. Struct. **31**, 151–175 (2002). Review
68. R. Meili, C. Ellsworth, S. Lee, T.B. Reddy, H. Ma, R.A. Firtel, Chemoattractant-mediated transient activation and membrane localization of akt/PKB is required for efficient chemotaxis to cAMP in dictyostelium. EMBO J. **18**(8), 2092–2105 (1999)
69. H. Meinhardt, Orientation of chemotactic cells and growth cones: models and mechanisms. J. Cell Sci. **17**(17), 2867–2874 (1999)
70. R. Melki, S. Fievez, M.F. Carlier, Continuous monitoring of pi release following nucleotide hydrolysis in actin or tubulin assembly using 2-amino-6-mercapto-7-methylpurine ribonucleoside and purine-nucleoside phosphorylase as an enzyme-linked assay. Biochemistry **35**(37), 12038–45 (1996)
71. T.J. Mitchison, L.P. Cramer, Actin-based cell motility and cell locomotion. Cell **3**, 371–379 (1996). Review. No abstract available
72. F. Oosawa, S. Asakura, *Thermodynamics of the Polymerization of Protein* (Academic, New York, 1975)
73. H.G. Othmer, A graph-theoretic analysis of chemical reaction networks (1979). Lecture Notes, Rutgers University. Available at www.math.umn.edu/~othmer/graphrt.pdf
74. H.G. Othmer, P. Schaap, Oscillatory cAMP signaling in the development of dictyostelium discoideum. Comments Theor. Biol. **5**, 175–282 (1998)
75. E. Palsson, H.G. Othmer, A model for individual and collective cell movement in *dictyostelium discoideum*. Proc. Natl. Acad. Sci. **97**, 11448–11453 (2000)
76. C.A. Parent, P.N. Devreotes, A cell's sense of direction. Science **284**(5415), 765–770 (1999). Review
77. E. Pate, H.G. Othmer, Differentiation, cell sorting and proportion regulation in the slug stage of *Dictyostelium discoideum*. J. Theor. Biol. **118**, 301–319 (1986)
78. M. Pineda, C. Weijer, R. Eftimie, Modelling cell movement, cell differentiation, cell sorting and proportion regulation in dictyostelium discoideum aggregations. J. Theor. Biol. **370**, 135–150 (2015)
79. T.D. Pollard, Regulation of actin filament assembly by arp2/3 complex and formins. Annu. Rev. Biophys. Biomol. Struct. **36**, 451–477 (2007)
80. T.D. Pollard, L. Blanchoin, R.D. Mullins, Molecular mechanisms controlling actin filament dynamics in nonmuscle cells. Annu. Rev. Biophys. Biomol. Struct. **29**(1), 545–76 (2000)
81. A.Y. Pollitt, R.H. Insall, WASP and SCAR/WAVE proteins: the drivers of actin assembly. J. Cell Sci. **122**(Pt 15), 2575–2578 (2009). doi:10.1242/jcs.023879

82. R.K. Raman, Y. Hashimoto, M.H. Cohen, A. Robertson, Differentiation for aggregation in the cellular slime molds: the emergence of autonomously signalling cells in *Dictyostelium discoideum*. J. Cell. Sci. **21**, 243–259 (1976)
83. D. Raucher, T. Stauffer, W. Chen, K. Shen, S. Guo, J.D. York, M.P. Sheetz, T. Meyer, Phosphatidylinositol 4,5-bisphosphate functions as a second messenger that regulates cytoskeleton-plasma membrane adhesion. Cell **100**(2), 221–228 (2000)
84. J. Rosenblatt, P. Peluso, T.J. Mitchison, The bulk of unpolymerized actin in xenopus egg extracts is ATP-bound. Mol. Biol. Cell **6**(2), 227–36 (1995)
85. K.R. Sanft, H.G. Othmer, Constant-complexity stochastic simulation algorithm with optimal binning. J. Chem. Phys. **143**(8), 074108 (2015)
86. P. Schaap, Evolutionary crossroads in developmental biology: dictyostelium discoideum. Development **138**(3), 387–396 (2011)
87. D. Sept, J. Xu, T.D. Pollard, J.A. McCammon, Annealing accounts for the length of actin filaments formed by spontaneous polymerization. Biophys. J. **77**(6), 2911–2919 (1999)
88. M.P. Sheetz, D. Felsenfeld, C.G. Galbraith, D. Choquet, Cell migration as a five-step cycle. Biochem. Soc. Symp. **65**, 233–43 (1999)
89. F. Siegert, C.J. Weijer, Analysis of optical density wave propagation and cell movement in the cellular slime mould *Dictyostelium discoideum* **49**, 224–232 (1991)
90. J.V. Small, Microfilament-based motility in non-muscle cells. Curr. Opin. Cell Biol. **1**, 75–79 (1989)
91. J.V. Small, T. Stradal, E. Vignal, K. Rottner, The lamellipodium: where motility begins. Trends Cell Biol. **12**(3), 112–120 (2002). Review
92. D.R. Soll, The use of computers in understanding how animal cells crawl, in *International Review of Cytology*, vol. 163, ed. by K.W. Jeon, J. Jarvik (Academic, New York, 1995), pp. 43–104
93. P.A. Spiro, J.S. Parkinson, H.G. Othmer, A model of excitation and adaptation in bacterial chemotaxis. Proc. Natl. Acad. Sci. **94**(14), 7263–7268 (1997)
94. T.M. Svitkina, G.G. Borisy, Arp2/3 complex and actin depolymerizing factor/cofilin in dendritic organization and treadmilling of actin filament array in lamellipodia. J. Cell Sci. **145(5)**, 1009–26 (1999)
95. J. Swanson, D.L. Taylor, Local and spatially coordinated movements in *D*ictyostelium discoideum amoedae during chemotaxis. Cell **28**, 225–232 (1982)
96. Y. Tang, H.G. Othmer, A G protein-based model of adaptation in *Dictyostelium discoideum*. Math. Biosci. **120**(1), 25–76 (1994)
97. Y. Tang, H.G. Othmer, Excitation, oscillations and wave propagation in a G-protein-based model of signal transduction in Dictyostelium discoideum. Philos. Trans. R. Soc. Lond. B Biol. Sci. **349**(1328), 179–95 (1995)
98. J.A. Theriot, T.J. Mitchison, Actin microfilament dynamics in locomoting cells. Nature **352**(6331), 126–131 (1991)
99. A. Tikhonov, Systems of differential equations containing small parameters multiplying derivatives. Math. Sb. **31**, 575–586 (1952)
100. P.H. Vardy, L.R. Fisher, E. Smith, K.L. Williams, Traction proteins in the extracellular matrix of *Dictyostelium discoideum* slugs. Nature **320**(6062), 526–529 (1986)
101. B. Varnum, K.B. Edwards, D.R. Soll, *Dictyostelium* amebae alter motility differently in response to increasing versus decreasing temporal gradients of cAMP. J Cell Biol. **101**, 1–5 (1985)
102. B. Vasiev, C.J. Weijer, Modelling of dictyostelium discoideum slug migration. J. Theor. Biol. **223**, 347–59 (2003)
103. J.B. Wallingford, L.A. Niswander, G.M. Shaw, R.H. Finnell, The continuing challenge of understanding, preventing, and treating neural tube defects. Science **339**(6123), 1222002 (2013)
104. C.J. Weijer, Signalling during dictyostelium development, in *Dictyostelids* (Springer, Berlin, 2013), pp. 49–70

105. D. Wessels, J. Murray, D.R. Soll, Behavior of *Dictyostelium* amoebae is regulated primarily by the temporal dynamic of the natural cAMP wave. Cell Motil. Cytoskeleton **23**(2), 145–156 (1992)
106. L. Wolpert, R. Beddington, T. Jessel, P. Lawrence, E. Meyerowitz, J. Smith, *Principles of Development* (Oxford University Press, Oxford, 2002)
107. B. Wurster, K. Schubiger, U. Wick, G. Gerisch, Cyclic GMP in *Dictyostelium discoideum*: oscillations and pulses in response to folic acid and cyclic AMP signals. FEBS Lett. **76**, 141–144 (1977)
108. X. Xin, H.G. Othmer, A trimer of dimers- based model for the chemotactic signal transduction network in bacterial chemotaxis. Bull. Math. Biol. **74**, 2339–2382 (2012)
109. X.S. Xu, A. Kuspa, D. Fuller, W.F. Loomis, D.A. Knecht, Cell-cell adhesion prevents mutant cells lacking myosin II from penetrating aggregation streams of dictyostelium. Dev. Biol. **175**(2), 218–226 (1996)
110. J. Xu, Y. Tseng, D. Wirtz, Strain hardening of actin filament networks. regulation by the dynamic cross-linking protein alpha-actinin. J. Biol. Chem. **275**(46), 35886–35892 (2000)
111. S.H. Zigmond, Recent quantitative studies of actin filament turnover during locomotion. Cell Motil. Cytoskeleton **25**, 309–316 (1993)

Chapter 2
The Diffusion Limit of Transport Equations in Biology

Thomas Hillen and Amanda Swan

"A smart model is a good model." -Tyra Banks

Abstract Transport equations add a whole new level of modelling to our menu of mathematical models for spatial spread of populations. They are situated between individual based models, which act on the microscopic scale and reaction diffusion equations, which rank on the macro-scale. Transport equations are thus often associated with a *meso* scale. These equations use movement characteristics of individual particles (velocity, turning rate etc.), but they describe a population by a continuous density.

T. Hillen (✉) • A. Swan
Centre for Mathematical Biology, University of Alberta, Edmonton, AB, Canada T6G 2R3
e-mail: thillen@ualberta.ca; acswan@ualberta.ca

L. Preziosi et al. (eds.), *Mathematical Models and Methods for Living Systems*,
Lecture Notes in Mathematics 2167, DOI 10.1007/978-3-319-42679-2_2

In this chapter we introduce transport equations as a modelling tool for biological populations, where we outline the relations to biological measurements. The link to individual based random walk models and the relation to diffusion equations are discussed. In particular, the diffusion limit (or parabolic limit) forms the main part of this chapter. We present the detailed mathematical framework and we discuss isotropic versus non-isotropic diffusion. Throughout the manuscript we investigate a large variety of applications including bacterial movement, amoeboid movement, movement of myxobacteria, and pattern formation through chemotaxis, swarming or alignment.
We hope to convince the reader that transport equations form a useful alternative to other models in certain situations. Their full strength arises in situations where directionality of movement plays an important role.

2.1 Introduction to Movement Models

Many biological problems lend themselves well to mathematical models. Often we use these models to predict the behaviour of a population. We can attempt to predict only population size using ordinary differential equation models of the population dynamics, or attempt to predict spatial characteristics of the population through the use of partial differential equation models. In either case, certain simplifications are necessary. A key question, which must be addressed when dealing with population models, is how to obtain a model for the macroscopic behaviour of a population based on information about individuals in the population.

2.1.1 Measurements

As a first example, we consider the case of randomly moving individuals, and discuss how we may use information about these individuals to derive a model for the population. First, consider a random variable X_t that represents the location of an individual at time t. On the population level we consider two statistical measures as illustrated in Fig. 2.1a:

(A) **Population measurements:**
(A.1) Mean location: $\bar{X}_t = E(X_t)$, and
(A.2) Mean quadratic variation: $(\sum_{i=1}^{n}(X_{ti} - \bar{X}_t)^2)/(n-1) = V(X_t)$

These two measures represent characteristic values of the population based on averages of movement of their individuals. In many cases we can also consider characteristics of the individual particles themselves:

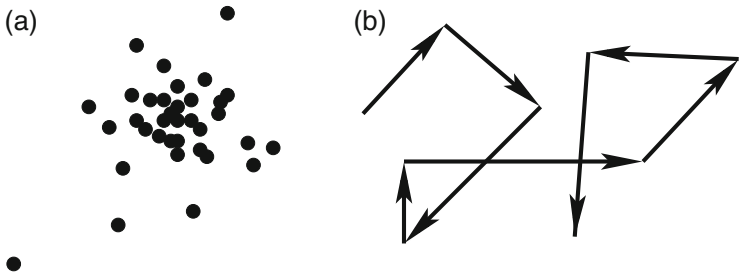

Fig. 2.1 (**a**): schematic of individuals undergoing a random walk; the locations can be used to estimate a mean location and a mean squared displacement. (**b**): measurement of individual movement path for speed, turning rate and turning angle distribution

(B) **Individual measurements:**
(B.1) The mean speed, γ
(B.2) The mean turning rate, μ, and
(B.3) The distribution of newly chosen directions, $T(v, v')$, where v and v' are the new and previous velocities, respectively.

These measures correspond to the situation seen in Fig. 2.1b. The measure $T(v, v')$ is often referred to as a kernel, and can be described as the probability density of turning into velocity v given previous velocity v'. For a homogeneous environment, this will typically be a uniform distribution, but for directed environments, the distribution may not be uniform. For example, for a cancer cell moving within a brain, it will be more likely to turn into alignment with the fibrous brain structures than to travel orthogonally. This means that the turning kernel will have a higher probability in the direction of this fibre.

The aim of this manuscript is to develop mathematical models which are based on the above observations. In particular, we are interested in the following questions:

Q1: How can we make a mathematical model for these types of measurements?
Q2: How are these models related?

2.1.2 Random Walk on a Grid

To derive a first and simple model on the population level, we first consider a random walker on a one dimensional grid [45, 60]. In this situation, consider an individual starting at point 0, and having some probability $0 < q < 1$ of moving to the right, and some probability $1 - q$ of moving to the left. In this example, we assume that there is 0 probability of the random walker staying where it is. We let δ be the spatial step and τ be the time step. This situation is illustrated in Fig. 2.2a.

We now consider X_n to be a random variable representing the position of a random walker that started at 0 after n discrete steps. After one step the expected

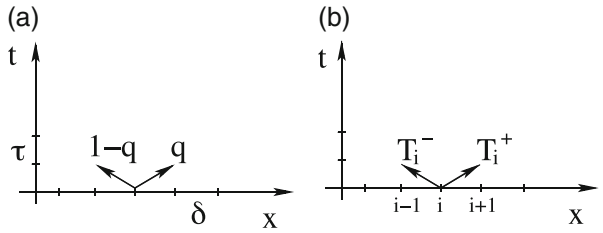

Fig. 2.2 (**a**): simple random walk with constant jump probabilities q and $1-q$. (**b**): random walk with variable jump probabilities $T_i^{\pm}$

value of X_1 is

$$E(X_1) = \sum_y xp(x=y) = \delta q + (-\delta)(1-q) = \delta(2q-1), \tag{2.1}$$

where we are summing over the whole domain. Now if we want to compute $E(X_2)$, we simply take

$$E(X_2) = E(X_1) + \sum_y xp(x=y) = \delta(2q-1) + \delta q + (-\delta)(1-q) = 2\delta(2q-1).$$

We can recursively define the expectation after n steps $E(X_n)$ to be

$$E(X_n) = \delta(2q-1) + E(x_{n-1}) = n\delta(2q-1). \tag{2.2}$$

We now notice that if $q = \frac{1}{2}$ in Eq. (2.2), we have that $E(X_n) = 0$. This makes sense, as we would expect to find no net displacement when the probabilities for moving left and right are equal. If however $q > \frac{1}{2}$, then we have a higher probability of moving to the right, thus we would expect the net movement to be to the right. We see that in this case $E(X_n) > 0$, as expected. Conversely, when $q < \frac{1}{2}$, we have $E(X_n) < 0$, and see net movement to the left.

We can also consider the variance of our random variable. This is computed using the following formula:

$$V(X_1) = E(X_1^2) - E(X_1)^2. \tag{2.3}$$

We have $E(X_1)$ as computed in (2.1), so we easily find that $E(X_1)^2 = \delta^2(2q-1)^2$. We next compute

$$E(X_1^2) = \sum_y x^2 p(x=y) = \delta^2 q + (-\delta)^2(1-q) = \delta^2.$$

Therefore,

$$V(X_1) = \delta^2 - \delta^2(2q-1)^2 = 4\delta^2 q(1-q),$$

and by the same argument as for the expectation,

$$V(X_n) = 4n\delta^2 q(1-q).$$

These measurements are for the discrete time situation, where an individual performs n jumps, $n \in \mathbb{N}$. How do these compare to the continuous time situation? If we consider a time step to have length τ, then $t = n\tau$ and $n = \frac{t}{\tau}$. We then define a mean velocity c and a diffusion coefficient D as:

$$c = \frac{E(X_t)}{t} = \frac{\delta}{\tau}(2q-1), \qquad D = \frac{1}{2}\frac{V(X_t)}{t} = \frac{2\delta^2}{\tau}q(1-q). \tag{2.4}$$

2.1.3 A Continuous Random Walk

To derive a mathematical description of the random walk from above, we introduce $p(x,t)$ as probability density for the location of the random walker. We begin with a description of the discrete case discussed above. If we want to define an equation for $p(x, t+\tau)$, we are looking for the probability that an individual will be found at x at time $t+\tau$. We note that the only way for an individual to arrive at position x at time $t+\tau$, is to come from the grid point to the left, or to the right from time t. We use the **Master equation** approach

$$p(x, t+\tau) = qp(x-\delta, t) + (1-q)p(x+\delta, t), \tag{2.5}$$

where $q, 1-q$ are the probabilities for a jump to the right/left per unit of time τ, respectively. In order to determine the continuous limit of this discrete equation, we assume that τ and δ are small parameters. Then a formal Taylor expansion becomes

$$p + \tau p_t + \frac{\tau^2}{2}p_{tt} + h.o.t. = q\left(p - \delta p_x + \frac{\delta^2}{2}p_{xx} - h.o.t.\right) + (1-q)\left(p + \delta p_x + \frac{\delta^2}{2}p_{xx} + h.o.t.\right).$$

Simplifying, we obtain

$$p_t(x,t) = \frac{\delta}{\tau}(1-2q)p_x(x,t) + \frac{\delta^2}{2\tau}p_{xx}(x,t) + h.o.t.. \tag{2.6}$$

We see that the dominating terms in Eq. (2.6) are the standard advection-diffusion equation

$$p_t(x,t) + cp_x(x,t) = Dp_{xx}(x,t)$$

with

$$c = \frac{\delta}{\tau}(1-2q) \quad \text{and} \quad D = \frac{\delta^2}{2\tau}.$$

At this stage we can study different possible limit scenarios for $\delta, \tau \to 0$ and $q \to 1/2$. We can do this in a number of ways, and we present three choices below. Of course, there are many more choices of these scalings, but most of them will not lead to a useful limit equation. In other words, if δ, τ, q do not scale as indicated below, then this method is not appropriate.

(a) $\frac{\delta}{\tau} \to \alpha$=constant. Then $\frac{\delta^2}{\tau} = \delta\frac{\delta}{\tau} \to 0$, which causes the diffusive term to vanish, and we are left with a simple **transport equation**

$$p_t + cp_x = 0.$$

(b) $\frac{\delta^2}{\tau} \to 2D$ =constant, then we can consider two cases:

(b.1) if $q = \frac{1}{2}$, then $c = 0$, and we obtain a pure **diffusion equation**

$$p_t = Dp_{xx}.$$

(b.2) If $q \to \frac{1}{2}$ in such a way that $\frac{\delta}{\tau}(1-2q) \to c$, and $\frac{\delta^2}{2\tau} = \frac{D}{4q(1-q)} \to D$, then the scaling results in the **advection-diffusion equation**

$$p_t + cp_x = Dp_{xx}, \tag{2.7}$$

where c and D are given by the measurements (2.4)

$$c \approx \frac{E(X_t)}{t}, D \approx \frac{1}{2}\frac{V(X_t)}{t}.$$

Summary

- When δ and τ scale in the same way, then we obtain a transport equation. This case is called **drift dominated**.
- When $\delta^2 \sim \tau$, we have the **diffusion dominated** case.
- Only in the case where $q - \frac{1}{2} \sim \tau$ do we get both terms, an advection and a diffusion term (**mixed case**).

2.1.4 Outline of This Manuscript

We have seen that population measurements lead us in a very natural way to drift-diffusion models of the type (2.7). If individual measurements are available, then the framework of transport equations becomes available, which we develop in the next sections. Of course there is a close relation between individual behaviour and population behaviour. This is reflected in our theory through the *parabolic limit* or *drift-diffusion limit*.

Above, we related population measurements to population drift and diffusion terms. Using the parabolic limit, we will be able to relate individual measurements to population drift and diffusion.

In Sect. 2.2 we consider the one-dimensional version of the transport equations. Individuals can only move up or down a linear feature, so that the movement is essentially one dimensional. The one-dimensional formulation has the advantage that most computations can be carried out and even explicit solutions can be found. We summarize results on invasions and pattern formation as well as applications to growing and interacting populations, chemotaxis, swarming and alignment.

In Sect. 2.3 we formally define transport equations and then define the mathematical setup. We introduce the basic assumptions (T1)–(T4) and we immediately explore the spectral properties of the *turning operator*.

Section 2.4 is devoted to the diffusion limit. Based on biological observations, we introduce a time and space scaling which, in the limit of macroscopic time and spaces scales, leads to a diffusion equation. Important is the structure of the resulting *diffusion tensor D*, which can be *isotropic* ($D = \alpha\mathbb{I}$), or anisotropic. We find easy-to-check conditions for the isotropy of the diffusion tensor. In Sect. 2.4 we also consider examples of bacterial movement, amoeboid movement, myxobacteria and chemotaxis. Finally, we introduce an important biological concept of *persistence*, which leads us back to biological measurements. The persistence, also called *mean cosine*, can easily be measured in many situations.

There are interesting further developments for individual movement in oriented habitats. Unfortunately, we are not able to include all these models and applications here, hence we chose to give a detailed list of references for further reading in Sect. 2.5.

2.2 Correlated Random Walk in One Dimension

The one dimensional correlated random walk is an extension of the diffusion random walks studied earlier, as it allows for correlation of movement from one time step to the next; in particular correlation in velocity. These models are easy to understand and they form a basis for the understanding of higher dimensional transport equations. In fact, many of the abstract methods, which we introduce later for transport equations, are simply illustrated in the one-dimensional context.

However, the 1-D model is not only a motivating example, it is a valid model for random walk on its own and it has been applied to many interesting biological problems. See for example the review article of Eftimie [10] on animal swarming models.

In the following sections we will introduce the model and various equivalent variations, we will discuss suitable boundary conditions, and we will write the model in an abstract framework, which will become important later.

2.2.1 The Goldstein-Kac Model in 1-D

Taylor [56] and Fuerth [15] developed the one dimensional correlated random walk model in the same year. Goldstein [18] and Kac [39] formulated it as a partial differential equation, and this is where we start. Let $u^{\pm}(x,t)$ denote the densities of right/left moving particles. The *Goldstein-Kac model* for correlated random walk is

$$\begin{aligned} u_t^+ + \gamma u_x^+ &= -\tfrac{\mu}{2}u^+ + \tfrac{\mu}{2}u^- \\ u_t^- - \gamma u_x^- &= \tfrac{\mu}{2}u^+ - \tfrac{\mu}{2}u^-, \end{aligned} \tag{2.8}$$

where γ denotes the (constant) particle speed and $\mu/2 > 0$ is the rate of switching directions from plus to minus or *vice versa*. We can also consider an equivalent formulation as a *one-dimensional transport equation*

$$\begin{aligned} u_t^+ + \gamma u_x^+ &= -\mu u^+ + \tfrac{\mu}{2}(u^+ + u^-) \\ u_t^- - \gamma u_x^- &= -\mu u^- + \tfrac{\mu}{2}(u^+ + u^-), \end{aligned} \tag{2.9}$$

where now $\mu > 0$ is the rate of directional changes; new directions are chosen as plus or minus with equal probability $1/2$. The systems (2.8) and (2.9) are equivalent, however the second formulation allows us to consider the system in the transport equation framework, as well as prepare it for extension to higher dimensions.

Another equivalent formulation arises if we look at the total population $u = u^+ + u^-$ and the population flux $v = \gamma(u^+ - u^-)$:

$$\begin{aligned} u_t + v_x &= 0 \\ v_t + \gamma^2 u_x &= -\mu v, \end{aligned} \tag{2.10}$$

which is also known as *Cattaneo system* [38]. This formulation will be more natural for scientists with experience in continuum mechanics, as the first equation is a conservation of mass equation, while the second equation can be seen as a momentum equation, where the flux adapts to the negative population gradient with a time factor or $e^{-\mu t}$. See Joseph and Preziosi [38] for a detailed connection to continuum mechanics and to media with memory. Here, we stay with the interpretation of population models.

If we assume the solutions are twice continuously differentiable, we get yet another closely related equation. Indeed, differentiating the first equation of (2.10) by t and the second by x we get

$$\begin{aligned} u_{tt} + v_{xt} &= 0 \\ v_{xt} + \gamma^2 u_{xx} &= -\mu v_x, \end{aligned} \tag{2.11}$$

which can be rearranged into an equation for u alone, making use of (2.10) in order to substitute $v_x = -u_t$:

$$\frac{1}{\mu} u_{tt} + u_t = \frac{\gamma^2}{\mu} u_{xx}, \tag{2.12}$$

which is the *telegraph equation*. This equation can be derived for the electrical potential along a transatlantic telegraph cable; a quite astonishing relation for our original random walk model. In this equation we then clearly see the relation to a diffusion equation. Just imagine that $\mu \to \infty$ and we loose the second time derivative term. At the same time we let $\gamma \to \infty$ such that

$$0 < \lim_{\gamma \to \infty, \mu \to \infty} \frac{\gamma^2}{\mu} =: D < \infty.$$

Then D becomes the diffusion coefficient and the parabolic limit equation reads

$$u_t = D u_{xx}. \tag{2.13}$$

We see that the one-dimensional model for correlated random walk is in fact closely related to transport in media with memory as well as to transatlantic cables. This reinforces the universality of mathematical theories, and the fact that often unexpected relations can be found.

2.2.2 Boundary Conditions

It is an interesting exercise to find appropriate boundary conditions for these models. Let us focus on the correlated random walk model (2.8). Since the model equations are hyperbolic, we need to look at the characteristics. For the first equation, the characteristics are $x(t) = x + \gamma t$ and for the second equation they are $x(t) = x - \gamma t$. Hence the variable u^+ needs boundary conditions on the left boundary, while no boundary condition on the right boundary. In Fig. 2.3 we indicate the characteristics with arrows. Formally, we define the domain boundary of $\Omega = [0, l] \times [0, t)$ as *hyperbolic boundary*

$$\partial\Omega = \delta\Omega^+ \cup \delta\Omega^-$$

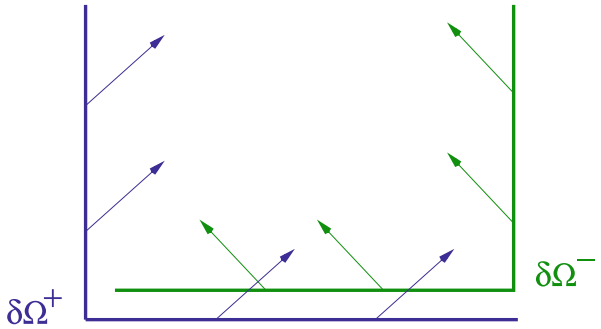

Fig. 2.3 Illustration of the two parts of the hyperbolic boundary of Ω. *Arrows* indicate the directions of the characteristics

with

$$\delta\Omega^+ := \{0\} \times [0,t) \cup [0,l] \times \{0\}, \qquad \delta\Omega^- := [0,l] \times \{0\} \cup \{l\} \times [0,t).$$

Then u^+ needs boundary conditions at $\partial\Omega^+$ and u^- needs boundary conditions at $\partial\Omega^-$ (see Fig. 2.3).

Both quantities require initial conditions at time $t = 0$:

$$u^+(x,0) = u_0^+(x), \qquad u^-(x,0) = u_0^-(x).$$

On the sides of the domain we can mimic the classical Dirichlet, Neumann and periodic boundary conditions.

- Dirichlet boundary conditions describe a given concentration at the boundaries. In the hyperbolic case this means a given *incoming* concentration

$$u^+(0,t) = \alpha_1(t), \qquad u^-(l,t) = \alpha_2(t).$$

  In the case of $\alpha_1 = \alpha_2 = 0$ we call these the homogeneous Dirichlet boundary conditions.
- Neumann boundary conditions describe the flux at the boundary. Hence in our case

$$\gamma(u^+(0,t) - u^-(0,t)) = \beta_1(t), \qquad \gamma(u^+(l,t) - u^-(l,t)) = \beta_2(t).$$

  In the no-flux case they become homogeneous Neumann boundary conditions

$$u^+(0,t) = u^-(0,t), \qquad u^-(l,t) = u^+(l,t).$$

- Periodic boundary conditions are as expected

$$u^+(0,t) = u^+(l,t), \qquad u^-(l,t) = u^-(0,t).$$

The corresponding initial-boundary value problems for the correlated random walk as well as for the Cataneo equations and for the telegraph equation have been studied in great detail in [28], including results on existence, uniqueness, and positivity. One curious result is the fact that the Dirichlet problem regularizes, while the Neumann and periodic problems do not regularize. In the Dirichlet problem singularities or jumps are washed out at the boundary, while the Neumann case they are reflected and in the periodic case they are transported around the domain.

2.2.3 Abstract Formulation

The main part of this manuscript provides analysis of a generalization of the one-dimensional correlated random walk to higher dimensions. We will construct an abstract framework of function spaces and turning operators, and the one dimensional model will arise as a special case. To prepare this relation, we now formulate Eq. (2.8) as a differential equation in a Banach space. In fact, we use the (equivalent) system (2.9) and introduce an *integral operator* $\mathscr{T}$ for the last term on the right hand sides:

$$\mathscr{T} : \mathbb{R}^2 \to \mathbb{R}; \qquad \begin{pmatrix} u^+ \\ u^- \end{pmatrix} \mapsto \frac{1}{2}(u^+ + u^-).$$

Here it does not look like an integral operator, but the higher dimensional version will include an integration. In fact here the integration is over the discrete space $V = \{+\gamma, -\gamma\}$. The operator norm of this linear operator can be easily computed to be

$$\|\mathscr{T}\|_1 = \frac{1}{2},$$

where the operator norm is defined as

$$\|\mathscr{T}\|_1 = \sup_{\|\phi\|_1 = 1} \|\mathscr{T}\phi\|_1.$$

It will be important later that this norm is less than or equal to 1. The whole right hand side of the system (2.9) defines another operator, which we call the *turning operator* $\mathscr{L}$:

$$\mathscr{L} : \mathbb{R}^2 \to \mathbb{R}^2; \qquad \begin{pmatrix} u^+ \\ u^- \end{pmatrix} \mapsto \begin{pmatrix} -\mu u^+ + \mathscr{T}(u^+, u^-) \\ -\mu u^- + \mathscr{T}(u^+, u^-) \end{pmatrix}.$$

If we write $\mathscr{L}$ as a matrix, we get

$$\mathscr{L} = \frac{\mu}{2}\begin{pmatrix} -1 & 1 \\ 1 & -1 \end{pmatrix}$$

we obtain eigenvalues of $\lambda_1 = 0$ and $\lambda_2 = -\mu$. The zero eigenvalue corresponds to the fact that the total population size is conserved for Eq. (2.9). The corresponding eigenspace is spanned by the vector $(1,1)^T$. Hence the kernel of $\mathscr{L}$ is given as

$$\ker\mathscr{L} = \langle\begin{pmatrix} 1 \\ 1 \end{pmatrix}\rangle.$$

The abstract formulation appears a bit staged, but this will form the framework for the multi dimensional situation.

2.2.4 Explicit Solution Using Bessel Functions

There exists an explicit solution of the correlated random walk model (2.8) using Bessel functions. Based on Poincare's [54] Bessel function solutions for the one-dimensional telegraph equation (2.12) on $\mathbb{R}$, Hadeler [21] modified these solutions to find explicit solutions to the correlated random walk system (2.8) on $\mathbb{R}$.

Let us recall some basic facts about the modified Bessel functions. For $k \in \mathbb{N}$ we denote by J_k the Bessel functions of first kind, and by $I_k(x) := e^{k\pi i}J_k(ix)$ the modified Bessel functions with purely imaginary argument. For $k = 0$ and $k = 1$ we have the relations

$$I_0(x) = J_0(ix) = \sum_{k=0}^{\infty} \frac{1}{(k!)^2}\left(\frac{x}{2}\right)^{2k} \quad \text{and} \quad I_1(x) = \frac{d}{dx}I_0(x).$$

The functions $I_0(x)$, $I_1(x)$ and $I_1(x)/x$ are real analytic and positive for $x > 0$. For an initial condition $u_0 \in L^p$ the solution of $u(t,x) = (u^+(t,x), u^-(t,x))$ of (2.8) on $\mathbb{R}$ can then be written as

$$\begin{aligned} u^+(t,x) &= u_0^+(x-\gamma t)e^{-\mu t/2} + \int_{x-\gamma t}^{x+\gamma t} K(t,x,y)u_0^-(y)dy \\ &\quad + \int_{x-\gamma t}^{x+\gamma t} K_+(t,x,y)u_0^+(y)dy \\ u^-(t,x) &= u_0^-(x+\gamma t)e^{-\mu t/2} + \int_{x-\gamma t}^{x+\gamma t} K(t,x,y)u_0^+(y)dy \\ &\quad + \int_{x-\gamma t}^{x+\gamma t} K_-(t,x,y)u_0^-(y)dy \end{aligned}$$

with integral kernels

$$K(t,x,y) := \frac{\mu e^{-\mu t/2}}{4\gamma} I_0\left(\frac{\mu}{2\gamma}\sqrt{\gamma^2 t^2 - (y-x)^2}\right)$$

$$K_\pm(t,x,y) := \frac{\mu e^{-\mu t/2}}{4\gamma} \frac{I_1\left(\frac{\mu}{2\gamma}\sqrt{\gamma^2 t^2 - (y-x)^2}\right)}{\sqrt{\gamma^2 t^2 - (y-x)^2}} (\gamma t \mp (y-x)).$$

For further reading on where these solutions come from, see [28]. From this representation we see that solutions are in $L^\infty([0,\infty)\times\mathbb{R})$ for initial conditions in L^∞. The integrals are absolutely continuous such that possible discontinuities can only travel along the characteristics $x-\gamma t = c$ and $x+\gamma t = c$.

Additionally, if u_0 is k–times differentiable then u is also. In general we conclude:

$$u_0 \in L^\infty(\mathbb{R}) \Longrightarrow u \in L^\infty([0,\infty)\times\mathbb{R})$$
$$u_0 \in C^k(\mathbb{R}) \Longrightarrow u \in C^k([0,\infty)\times\mathbb{R}).$$

2.2.5 *Correlated Random Walk Models for Chemotaxis*

Chemotaxis describes the active orientation of individuals, such as cells or bacteria, on gradients of a chemical signal, which is produced by the cells themselves. In many examples, such as *Dictyostelium discoideum* (*DD*) or *Escherichia coli*, this process leads to macroscopic cell aggregations. Chemotaxis is a prototype of self organization, where the resulting pattern is more than the sum of its parts. Keller and Segel [40] started a systematic modelling in the 1970s and since then a large amount of literature has been published on chemotaxis. The models have been developed to accurately describe biological experiments and the models have inspired a generation of mathematicians working on finite time blow up as well as spatial pattern formation. For further details we recommend the two review articles by Horstmann [37] and by Hillen and Painter [30].

We can model chemotactic behaviour via a correlated random walk model. The action of the chemical signal on the movement mechanics of cells is very different in eukaryotic cells versus amoeboid cells. In *E. coli*, for example, the chemical sensing receptors are internally coupled to the rotation mechanisms of the flagella. If the cell encounters an increasing signal concentration, it prolongs straight movement and reduces reorientations. This in effect leads to oriented movement up a signal gradient [14, 48]. In our context this corresponds to a change in turning rate μ depending on the signal strength and its gradient. Amoeboid cells, however, are moving through tread milling of an internal actin-myosin filament mechanism. Amoeboid cells are able to detect directions of increased chemical signal and they can actively choose directions and adapt their speed. In this particular case, the turning rate as well as the speed are affected by the signal S [6]. In one dimension,

the corresponding hyperbolic chemotaxis model reads

$$\begin{aligned} u_t^+ + (\gamma(S)u^+)_x &= -\mu^+(S,S_x)u^+ + \mu^-(S,S_x)u^- \\ u_t^- - (\gamma(S)u^-)_x &= \mu^+(S,S_x)u^+ - \mu^-(S,S_x)u^- \\ \tau S_t &= D_S S_{xx} + \alpha(u^+ + u^-) - \beta S, \end{aligned} \tag{2.14}$$

where $u^{\pm}(x,t)$ are as before, the densities of right and left moving particles respectively. The density of the chemical signal is given by $S(x,t)$, and $\gamma(S)$ and $\mu(S,S_x)$ are the density dependent speed and turning rate. Notice that here μ is used without a factor of $1/2$, so it is a turning rate (and not a rate of change of direction). The last equation in (2.14) describes diffusion, production and decay of the chemotactic signal $S(x,t)$, where $D_S > 0$ is the diffusion coefficient of the signal, $\alpha > 0$ is the production rate as produced from the total cell population $u^+ + u^-$ and $\beta > 0$ is a constant decay rate. The parameter $\tau > 0$ is used to indicate that signal diffusion might happen on a faster (or slower) time scale than cell movement.

As in our derivation from (2.12) to (2.13) we can use scaling arguments to compute a parabolic limit (see [32, 33] for details):

$$u_t = \left(A(S,S_x)u_x - \chi(S,S_x)uS_x\right)_x . \tag{2.15}$$

It is interesting to see how the diffusivity A and the chemotactic sensitivity χ depend on speed γ and turning rate μ. The diffusivity is

$$A(S,S_x) = \frac{\gamma^2(S)}{\mu^+(S,S_x) + \mu^-(S,S_x)} \tag{2.16}$$

while the chemotactic flux is

$$\chi(S,S_x)S_x = -\frac{\gamma(S)}{\mu^+(S,S_x) + \mu^-(S,S_x)} \left(\gamma'(S)S_x + (\mu^+(S,S_x) - \mu^-(S,S_x))\right). \tag{2.17}$$

When $\chi > 0$, we have *positive taxis*, which supports aggregation. Here we have two effects which can cause positive chemotactic flow:

1. If $\gamma = \gamma(S)$ and $\gamma'(S) < 0$, then particles slow down at high concentrations of S which leads to aggregation at high concentrations of S. Or, alternatively,
2. If $\mu^+ < \mu^-$ for $S_x > 0$, then the turning rate is reduced when moving up the gradient of S, which also leads to aggregation.

Specifically, we study two examples.

Example 1 (And Homework) Assume $\gamma =$const and

$$\mu^{\pm}(S,S_x) = \frac{\gamma}{2A}\left(\gamma \mp \varphi(S)S_x\right)^+ .$$

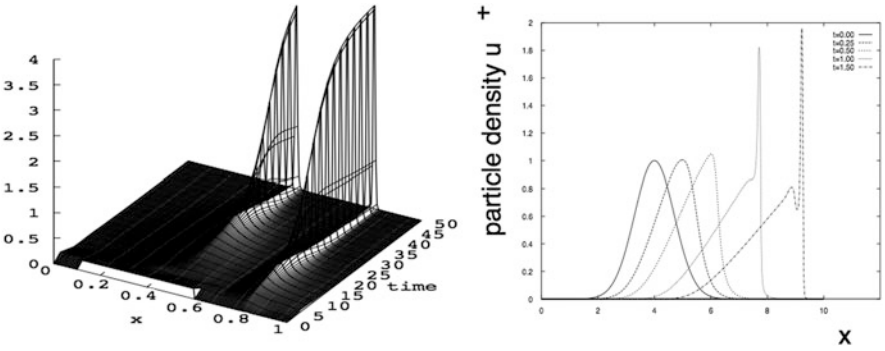

Fig. 2.4 *Left*: two aggregations evolve from a compactly supported initial condition for a case corresponding to Example 1. *Right*: occurrence of a sharp gradient due to Burger's equation terms as in Example 2. In both simulations the initial signal concentration is linearly increasing from *left to right* (not shown)

1. Describe a biological situation for the above choice of μ and γ. Does this choice correspond to the bacterial or amoeboid case? Explain.
2. Compute the diffusivity A and the chemotactic flux χS_x.

Example 2 For the second example, we consider the case where $\tau = D = 0$, and $\gamma(S) = S$. Then the last equation of (2.14) can be solved as $S = \frac{\alpha}{\beta}(u^+ + u^-)$ and we therefore have that the left hand side of the first equation of (2.14) becomes

$$\begin{aligned} u_t^+ + (\gamma(S)u^+)_x &= u_t^+ + \left(\tfrac{\alpha}{\beta}(u^+ + u^-)u^+\right)_x \\ &= u_t^+ + \tfrac{\alpha}{\beta}\left(u^{+2}\right)_x + \tfrac{\alpha}{\beta}\left(u^+u^-\right)_x . \end{aligned} \tag{2.18}$$

We see that the first two terms on the right hand side come from Burger's equation. The standard form of Burger's equation is $u_t + (u^2)_x = 0$, and it is well known that Burger's equation has shock solutions [2]. Hence in this case we might expect shock solutions for the chemotaxis model. In [33] we use the method of viscosity solutions to further analyse the appearance of sharp gradients in chemotaxis invasion waves [see Fig. 2.4 (right)].

2.2.6 *Reaction Random Walk Systems*

The above random walk models have been considered under (local) preservation of particles. However, these models can also be used to describe growing, shrinking and interacting populations through *reaction random walk systems* [22]. If using

diffusion equations, then the most often used assumption is an independence between species movement and species growth and death, leading to a typical reaction diffusion equation $u_t = Du_{xx} + f(u)$. In the correlated random walk (2.8) the population has been split into right and left moving populations, hence the inclusion of reaction terms must be done carefully. We follow Hadeler [19–21] and present three ideas from the literature:

(i) A straight forward analog of the reaction diffusion modelling was introduced in [36] leading to the reaction random walk system

$$u_t^+ + \gamma u_x^+ = \frac{\mu}{2}(u^- - u^+) + \frac{1}{2}f(u^+ + u^-)$$
$$u_t^- - \gamma u_x^- = \frac{\mu}{2}(u^+ - u^-) + \frac{1}{2}f(u^+ + u^-).$$

The reaction acts symmetrically between the two classes and newborn particles choose either direction with the same probability. Holmes [36] showed the existence of travelling waves for this model, while in [24] and [25] we developed Turing instabilities and Lyapunov functions, respectively.

(ii) If the reaction is split into growth and death terms, like $f(u) = u\,m(u) - u\,g(u)$, where $m(u)$ denotes a birth rate and $g(u)$ a death rate, then the above splitting is inappropriate, as death of a right moving particle leads to reduction of left moving particles. Individuals can only be discounted from their own class. Hence the reaction random walk model needs to be modified in the form

$$u_t^+ + \gamma u_x^+ = \mu(u^- - u^+) + \frac{1}{2}(u^+ + u^-)\,m(u^+ + u^-) - u^+\,g(u^+ + u^-)$$
$$u_t^- - \gamma u_x^- = \mu(u^+ - u^-) + \frac{1}{2}(u^+ + u^-)\,m(u^+ + u^-) - u^-\,g(u^+ + u^-).$$

(iii) Here we consider the same reaction terms as in (ii) but we additionally assume that the movement direction of newborn particles correlates to the direction of their mother by a parameter $\tau \in [0, 1]$. The corresponding model equations are

$$u_t^+ + \gamma u_x^+ = \mu(u^- - u^+) + (\tau u^+ + (1-\tau)u^-)\,m(u^+ + u^-) - u^+\,g(u^+ + u^-)$$
$$u_t^- - \gamma u_x^- = \mu(u^+ - u^-) + ((1-\tau)u^+ + \tau u^-)\,m(u^+ + u^-) - u^-\,g(u^+ + u^-).$$

If $\tau = 1/2$ we have case (ii). For $\tau > 1/2$ the daughter particles tend to prefer the same direction as the mother and for $\tau < 1/2$ they prefer the opposite.

Earlier we derived a Cattaneo system and a telegraph equation (2.12) from a correlated random walk (2.8). We can do the same transformation for a reaction random walk model. The corresponding *reaction Cattaneo model* for the total

population $u = u^+ + u^-$ and flux $v = \gamma(u^+ - u^-)$ then becomes

$$\begin{aligned} u_t + \gamma v_x &= f(u) \\ v_t + \gamma u_x &= -h(u)\, v, \end{aligned}$$

with

$$f(u) = \begin{cases} f(u) & \text{in case (i)} \\ u\, m(u) - u\, g(u) & \text{in case (ii) and (iii)}, \end{cases}$$

$$h(u) = \begin{cases} \mu & \text{in case (i)} \\ \mu + g(u) & \text{in case (ii)} \\ \mu + (1 - 2\tau)m(u) + g(u) & \text{in case (iii)}. \end{cases}$$

The boundary conditions transform as

- homogeneous Dirichlet

$$u(t, 0) = -v(t, 0), \qquad u(t, l) = v(t, l).$$

- homogeneous Neumann

$$v(t, 0) = 0, \qquad v(t, l) = 0.$$

- Periodic

$$u(t, 0) = u(t, l), \qquad v(t, 0) = v(t, l).$$

To further investigate the relation to a telegraph equation, we focus on the case (i). The reaction Cattaneo system in this case is

$$\begin{aligned} u_t + \gamma v_x &= f(u) \\ v_t + \gamma u_x &= -\mu\, v. \end{aligned}$$

We assume that solutions are twice continuously differentiable and we differentiate the first equation with respect to t and the second with respect to x and we eliminate v to obtain the *reaction telegraph equation*

$$u_{tt} + (\mu - f'(u))u_t = \gamma^2 u_{xx} + \mu f(u).$$

The above transformation applied to cases (ii) and (iii) would not lead to a single telegraph equation, unless $\tau = 1/2$ and $g = 0$, which is case (i) (see also [21, 22]).

2.2.7 *Correlated Random Walk Models for Swarming*

The correlated random walk models have also been used to describe animal alignment and swarming. Pfistner [53] and Lutscher and Stevens [42] developed and analysed a non-local correlated random walk model for alignment and rippling of myxobacteria. Myxobacteria are rod shaped bacteria that are known to form tightly aligned swarms which sometimes show spatial rippling. The following model of Pfisnter [53] and Lutscher and Stevens [42] was able to explain these patterns:

$$u_t^+ + \gamma u_x^+ = -\mu^+ u^+ + \mu^- u^-$$
$$u_t^- - \gamma u_x^- = \mu^+ u^+ - \mu^- u^-$$

with turning rates

$$\mu^\pm = F\left(\int_{-R}^{R} \alpha(r) u^\pm(t, x \pm r) + \beta(r) u^\mp(t, x \pm r) dr\right). \tag{2.19}$$

The turning rates depend non-locally on the surrounding population up to a sampling radius $R > 0$. The kernel $\alpha(r)$ describes the influence of individuals that move away from x, while the β-term describes the contribution of particles that move towards x. A careful choice of $\alpha(r)$ and $\beta(r)$ enabled them to model alignment and rippling.

Eftimie et al. [10, 11] generalized this approach and separated the three major interaction modes of local repulsion, intermediate alignment and long range attraction. A schematic is shown in Fig. 2.5. They assume that the turning rate $\mu^\pm(y_r^\pm, y_{al}^\pm, y_a^\pm)$ is a function of a repulsive signal $y_r^\pm$, an alignment signal $y_{al}^\pm$ and an attractive signal $y_a^\pm$. Each of these signals has a non-local form as in (2.19), where the corresponding weights $\alpha_r, \alpha_{al}, \alpha_a$ and $\beta_r, \beta_{al}, \beta_a$ concentrate their weight in the corresponding spatial distances around x, as illustrated in Fig. 2.5. There are many possible choices of these weight functions, and Eftimie [10] presents a detailed review of relevant possibilities. Depending on the choice of these weight functions, the model is able to describe travelling pulses, travelling trains, static pulses, breathers, feathers, ripples and many more. The non local model for correlated random walk is a rich source of interesting patterns and interesting mathematics

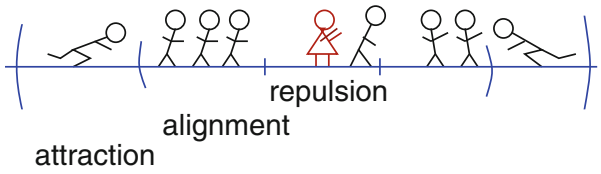

Fig. 2.5 Illustration of the non-local swarming model of Eftimie. The closest area is repulsive, the intermediate region supports alignment and the far region is attractive

and a full mathematical analysis is just beginning. For more details see the excellent review of Eftimie [10].

2.3 Transport Equations

We can extend the ideas introduced in Sect. 2.2 to higher dimensions in the form of the transport equation. Transport equations are a powerful tool to derive mesoscopic models for the spatial spread of populations. With *mesoscopic* we denote an intermediate scale, where properties of individual cells are used in the modelling, however, cells are not represented as individual entities, like in individual based modelling, rather, they are presented as macroscopic densities. Transport equations are particularly useful if the movement velocity (= speed · direction) of the individuals is of importance. The theory of kinetic transport equations developed from the Boltzmann equation and the thermodynamics of diluted gases (see e.g. [3]) and has since been developed for biological populations as well [46, 52]. One major difference between physical and biological applications is the number of conserved quantities. While in ideal gas theory five quantities are conserved (mass, three momentum components, energy), in biological populations, we often only conserve mass. Mathematically the conserved quantities are reflected as linearly independent functions in the kernel of a so called *turning operator*. The kernel of the turning operator in gas theory is five dimensional, while in our applications it is one dimensional. The kernel of the turning operator sets the stage for the mathematical details later. Hence this difference in size of the kernel is, in a nutshell, the main difference between physical and biological applications. The rest is details, which we will present as fully as possible in this manuscript.

We need to distinguish two important cases. Case 1: the kernel of the turning operator contains only constant functions and case 2: the kernel is spanned by a function that depends on the velocity. Such a function is called *Maxwellian* in a physical context [52]. The first case allows for a quite general theory as was developed in Othmer and Hillen in [29, 47], while the second case is more complicated. We use the remainder of this manuscript to study case 1,where we explain the mathematical setup, derive the parabolic limit, and apply the method to chemotaxis. Case 2 is covered in the literature [4, 8, 27, 31, 52] and we plan a summary of that case in a forthcoming textbook [35].

2.3.1 The Mathematical Set-Up

We begin by parameterizing a population density $p(x, v, t)$ by space x, velocity v and time t. This allows us to incorporate individual cell movement into the model, an important feature which distinguishes transport models from macroscopic models. As we are typically dealing with biological phenomena, we take $t \geq 0$ and $x \in \mathbb{R}^n$,

with $n = 2, 3$. The case of $n = 1$ corresponds to the one-dimensional correlated random walk, which we discussed already in Sect. 2.2. The velocities v are taken from V, where $V \subset \mathbb{R}^n$ and $V = [s_1, s_2] \times \mathbb{S}^{n-1}$ or $V = s\mathbb{S}^{n-1}$. The general transport equation for a population density $p(x, v, t)$ is thus

$$p_t + v \cdot \nabla p = -\mu p + \mu \int_V T(v, v')p(x, v', t)dv', \tag{2.20}$$

where we omitted the arguments, except in the integral. The terms on the left hand side describe the particles' movement in space, while the terms on the right hand side describe how the particles change direction. The parameter μ is the *turning rate*, which describes how often the particles change direction. As such, $\frac{1}{\mu}$ describes the mean run length. In other words, $\frac{1}{\mu}$ represents how long a particle travels on average in a straight line before it changes direction. The distribution $T(v, v')$ inside the integral is called the *turning kernel*, or *turning distribution*, and describes the probability that a cell traveling in the direction of v' will turn into the direction of v. As such, the first term on the right hand side describes cells turning out of velocity v, while the integral term describes cells turning into velocity v from all other directions $v' \in V$. Together, these two terms are called the *turning operator*. Here we follow the theory as developed by Stroock [55], Othmer et al. [46] and Hillen and Othmer [29, 47].

Given the compact set V of possible velocities, we work in the function space $L^2(V)$ and we denote by $\mathscr{K} \subset L^2(V)$ the cone of non-negative functions. Given by the right hand side of Eq. (2.20) we define an integral operator on $L^2(V)$; $\mathscr{T} : L^2(V) \to L^2(V)$ as

$$\mathscr{T}\phi(v) = \int_V T(v, v')\phi(v')dv'$$

with adjoint

$$\mathscr{T}^*\phi(v') = \int_V T(v', v)\phi(v')dv'.$$

The integral kernel T and the integral operator $\mathscr{T}$ set the stage for the theory. In the context of biological applications, we make the following general assumptions. We will now list these general assumptions, with a detailed explanation of each assumption following.

Basic Assumptions

(T1) $T(v, v') \geq 0$, $\int_V T(v, v')dv = 1$, and $\int_V \int_V T^2(v, v')dv'dv < \infty$.

(T2) There is a function $u_0 \in \mathscr{K}\backslash\{0\}$, a $\rho > 0$ and an $N > 0$ such that for all $(v, v') \in V \times V$, either

(a) $u_0(v) \leq T^N(v', v) \leq \rho u_0(v)$, or
(b) $u_0(v) \leq T^N(v, v') \leq \rho u_0(v)$,

where the N-th iterate of T is

$$T^N(v', v) = \int_V \dots \int_V T(v', w) \dots T(w_{N-1}, v) dw_1 \dots dw_{N-1}.$$

(T3) $\|\mathscr{T}\|_{\langle 1\rangle^\perp} < 1$, where $L^2(V) = \langle 1\rangle \oplus \langle 1\rangle^\perp$.
(T4) $\int_V T(v, v')dv' = 1$.

Assumption (T1) Assumption (T1) implies that $T(\cdot, v')$ is a non-negative probability density on V. The fact that $T \in L^2(V \times V)$ implies that $\mathscr{T}$ and $\mathscr{T}^*$ are Hilbert-Schmidt operators, defined as follows [23]:

Definition 1 An integral operator $\mathscr{T}f(v) = \int T(v, v')f(v')dv'$ with $T \in L^2(V \times V)$ is called a *Hilbert-Schmidt operator*.

Hilbert-Schmidt operators have some compactness properties:

Theorem 1 ([23]) *Hilbert-Schmidt operators are bounded and compact.*

Furthermore, (T1) implies that $\mathscr{T}$ and $\mathscr{T}^*$ are positive operators.

Assumption (T2) We will show that assumption (T2a) ensures that $\mathscr{T}^*$ is u_0-positive in the sense of Krasnosleskii [41], while (T2b) ensures that $\mathscr{T}$ is u_0-positive. One of these is sufficient. Krasnoselskii defines u_0-positivity as follows.

Definition 2 Let X be a Banach space, $\mathscr{K}$ the non-negative cone and $L : X \to X$ linear. Then

(a) L is positive if $L : \mathscr{K} \to \mathscr{K}$.
(b) Let L be positive. L is u_0-bounded from below if there is a fixed $u_0 \in \mathscr{K}\backslash\{0\}$ such that $\forall \phi \in \mathscr{K}\backslash\{0\}\ \exists N > 0, \alpha > 0$ with

$$\alpha u_0 \le L^N \phi.$$

(c) Let L be positive. L is u_0-bounded from above if there is a fixed $u_0 \in \mathscr{K}\backslash\{0\}$ such that $\forall \psi \in \mathscr{K}\backslash\{0\}\ \exists N > 0, \beta > 0$ with

$$L^N \psi \le \beta u_0.$$

(d) L is u_0-positive if conditions (b) and (c) are both satisfied.
(e) $\mathscr{K}$ is reproducing if for all $\phi \in X$ there exist $\phi^+, \phi^- \in \mathscr{K}$ such that $\phi = \phi^+ - \phi^-$.

Using this definition, we can prove the following Lemma:

Lemma 1 *Assumption (T2a) implies that $\mathscr{T}^*$ is u_0-positive, while (T2b) implies that $\mathscr{T}$ is u_0 positive.*

Proof Consider $\phi \in \mathscr{K}$. We compute the iterate

$$\begin{aligned} T^{*N}\phi &= \int_V T(v', w_1)\cdots T(w_{N_1}, v)\phi(v')dw_1 \ldots dw_{N+1}dv' \\ &= \int_V T^N(v', v)\phi(v')dv' \\ &\geq \int_V u_0(v)\phi(v')dv' = u_0(v)\int_V \phi(v')dv' = \alpha u_0(v). \end{aligned}$$

The last inequality is a direct consequence of (T2a). Similarly, we have

$$T^{*N}\phi \leq \int_V \rho u_0(v)\phi(v')dv' = \rho\int_V \phi(v)dv u_0(v) = \beta u_0(v).$$

The second statement has a very similar proof. □

Condition (T2) has an interesting biological meaning. It is not assumed that the kernel T is positive. In fact, it is allowed for T to have support that is smaller than V, but some iterate of T must cover V. For example if individuals are able to turn for up to 45 degrees per turn, then they are able to reach any direction after 4 turns. In that case T^4 would be u_0 positive. See Fig. 2.6 for an illustrative explanation. Using (T2) we are more general than most of the publications on transport equations in biology. It is almost always assumed that $T > 0$, but here we can relax that assumption.

The u_0 positivity is already sufficient to have a Krein-Rutman property:

Theorem 2 (Krasnoselskii, [41], Theorems 2.10, 2.11) *Let K be a reproducing non-negative cone in X. Let L be u_0-positive. Let $\varphi_0 \in \mathscr{K}$ be an eigenfunction of L. Then*

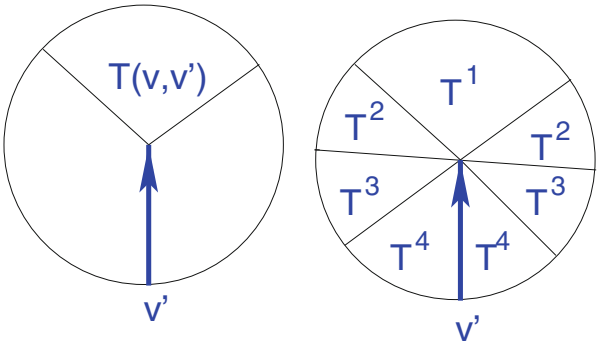

Fig. 2.6 Illustration of the iterates of a turning operator. On the *left* we indicate the support of a turning kernel that allows directional changes of up to 45°. On the *right* we indicate the range of the iterates T^1, T^2, T^3, T^4. After four turns, all directions are possible

(i) $L\varphi_0 = \lambda_0\varphi_0$ *and* λ_0 *is a simple, leading eigenvalue,*
(ii) φ_0 *is unique in* $\mathscr{K}$ *up to scalar multiples, and*
(iii) $|\lambda_0| > |\lambda|$ *for all other eigenvalues* λ.

In our case we have

$$\mathscr{T}^* 1 = \int_V T(v', v) 1 dv' = 1$$

by (T1). Hence $\varphi_0 = 1 \in \mathscr{K}$ is the leading non-negative eigenfunction of $\mathscr{T}^*$ with eigenvalue $\lambda_0 = 1$. All of the other eigenvalues are such that $|\lambda| < 1$. We also have

$$\mathscr{T} 1 = \int_V T(v, v') dv' = 1$$

by (T4).This means that we also have that $\varphi_0 = 1$ is the leading non-negative eigenfunction of $\mathscr{T}$.

Assumption (T3) Note that in Krasnoselskii's theorem above it is assumed that there exists an eigenfunction in $\mathscr{K}$. This is not always the case, and assumption (T3) ensures the existence of a spectral gap between the leading eigenvector $\varphi_0 = 1$ and the remainder of the spectrum. We will show later that if $\mathscr{T}$ is a normal operator (or if $\mathscr{T}^*$ is normal), then (T2) implies (T3).

Assumption (T4) Condition (T4) looks as natural as the second condition in (T1). It has, however a very different meaning. The meaning of (T4) is that the eigenvalue equation

$$\int_V T(v, v')\phi(v') dv' = \lambda\phi(v)$$

has a constant solution $\phi(v) = 1$ with eigenvalue $\lambda = 1$. This is a very special case that allows us to develop a full theory and to do the macroscopic scalings done later in this chapter. If the leading eigenfunction $\varphi_0(v)$ is not constant the methods will change slightly, and particular care must be given to the resulting non-isotropic diffusion equations, which is discussed elsewhere [31, 35]. Both cases are equally important in terms of applications.

2.3.2 The Turning Operator

The *turning operator* describes the whole right hand side of (2.20) and is given by $\mathscr{L} : L^2(V) \to L^2(V)$:

$$\mathscr{L}p(v) = -\mu p(v) + \mu\mathscr{T}p(v)$$

with adjoint

$$\mathscr{L}^* p(v) = -\mu p(v) + \mu \mathscr{T}^* p(v).$$

We can now write down a result about the spectrum of the turning operator.

Lemma 2 *Assume (T1)–(T4). Then 0 is a simple eigenvalue of $\mathscr{L}^*$ and $\mathscr{L}$ with leading eigenfunction $\varphi_0 = 1$. All other eigenvalues λ satisfy $-2\mu < Re\lambda < 0$. All other eigenfunctions have integral zero.*

Proof Both $\mathscr{T}$ and $\mathscr{T}^*$ have a spectral radius of 1, which implies that $\mu\mathscr{T}$ has a spectral radius of μ. We therefore have

$$-2\mu < \mathrm{Re}\lambda < 0.$$

If $\varphi \neq \varphi_0$ is another eigenfunction, then $\varphi \in \langle 1 \rangle^\perp$ which implies

$$0 = \int_V \varphi(v) 1 dv = \int_V \varphi(v) dv.$$

□

Condition (T3) allows us to introduce another constant, called μ_2, which will give us information about the dissipativity of the turning operator. Consider $\psi \in \langle 1 \rangle^\perp$ then

$$\begin{aligned}\int_V \psi \mathscr{L} \psi dv &= -\mu \int_V \psi^2 dv + \mu \int_V \psi \mathscr{T} \psi dv \\ &\leq -\mu(1 - \|\mathscr{T}\|_{\langle 1 \rangle^\perp}) \int_V \psi^2 dv \\ &= -\mu_2 \|\psi\|_2^2\end{aligned}$$

with $\mu_2 = \mu(1 - \|\mathscr{T}\|_{\langle 1 \rangle^\perp})$ and $\|\mathscr{T}\|_{\langle 1 \rangle^\perp} < 1$.

2.3.3 Normal Operators

In this section we discuss what it means for an operator to be normal, and explore some of the consequences of this characteristic.

Definition 3 An operator A is defined to be normal if $AA^* = A^*A$.

Theorem 3 ([5], p. 55, et. seq.) *If A is normal, then there exists a complete orthogonal set of eigenfunctions. A has a spectral representation $A = \sum \lambda_j P_j$ where λ_j are the eigenvalues and P_j the spectral projections.*

If $\mathscr{T}$ is normal, then we can choose an orthonormal basis ϕ_n with $\|\phi_n\| = 1$.

Lemma 3 *If $\mathscr{T}$ is normal, then (T3) follows from (T1) and (T2).*

Proof Consider the operator norm of $\mathscr{T}$ on $\langle 1\rangle^{\perp}$:

$$\begin{aligned}
\|\mathscr{T}\|_{\langle 1\rangle^{\perp}} &= \sup_{\substack{\phi\in\langle 1\rangle^{\perp}\\ \|\phi\|_2=1}} \|\mathscr{T}\phi\|_2 \\
&= \sup_{\phi} \|\mathscr{T}\sum_{n=1}^{\infty}\alpha_n\phi_n\|_2 \\
&= \sup_{\phi} \|\sum_{n=2}^{\infty}\alpha_n\lambda_n\phi_n\|_2 \\
&= \sup_{\phi} \left(\sum_{n=2}^{\infty}|\alpha_n\lambda_n|^2\right)^{\frac{1}{2}} \\
&< \sup_{\phi} \left(\sum_{n=2}^{\infty}|\alpha_n|^2\right)^{\frac{1}{2}} = \|\phi\|_2 = 1.
\end{aligned}$$

□

In our case we need to check if $\mathscr{T}$ is normal:

$$\begin{aligned}
\mathscr{T}\mathscr{T}^*\phi &= \mathscr{T}\left(\int_V T(v,v')\phi(v')dv'\right) \\
&= \int_V\int_V T(v,v'')T(v',v'')\phi(v')dv'dv'' \\
\mathscr{T}^*\mathscr{T}\phi &= \int_V\int_V T(v'',v)T(v'',v')\phi(v')dv'dv''.
\end{aligned}$$

In order for our operator to be normal, we thus obtain the necessary symmetry condition

$$\int_V T(v,v'')T(v',v'')dv'' = \int_V T(v'',v)T(v'',v')dv''.$$

This is satisfied, for example, when T is a symmetric kernel of the form $T(v,v') = T(v',v), \forall(v,v') \in V^2$.

2.3.4 Important Examples

We now consider two important examples, and investigate how the theory discussed so far applies.

2.3.4.1 Example 1: Pearson Walk

For the first example, we will choose our space of directions to be a sphere of constant radius, i.e. $V = s\mathbb{S}^{n-1}$. This means that our particles can choose any direction, and will travel with constant speed. We will choose the simplest turning kernel, which is constant and normalized: $T(v, v') = \frac{1}{|V|}$.

We will now check (using ✓) if our four basic assumptions are satisfied for this simple choice of V and T.

(T1) $T \geq 0$ ✓, $\int_V T dv = 1$ ✓, $\int_V \int_V T^2 dv dv' = 1$ ✓, and so the conditions of assumption (T1) are met.

(T2) Not only do we have that $T \geq 0$, but we actually have the stronger condition $T > 0$. This implies that $\mathscr{T}$ is u_0-positive. ✓

(T3) We have

$$\mathscr{T}^*\phi = \int_V \frac{1}{|V|}\phi(v')dv' = \mathscr{T}\phi = \int_V \frac{1}{|V|}\phi(v)dv.$$

We can thus conclude that $\mathscr{T}$ is self adjoint and henceforth it is normal. Then by Lemma 3, we can conclude that (T3) is satisfied. ✓

(T4) $\int_V T dv' = 1$. ✓

The Pearson walk satisfies all assumptions (T1)–(T4), and it will form our prototype for the theory and scaling developed later.

2.3.4.2 Example 2: Movement on Fibre Networks

There are many examples that arise naturally in biology where the particles in question, whether they be animals or cells, make their turning decisions based on their environment. For example, glioma cells diffusing in the brain will use the white matter tracts as highways for their movement [9, 16, 17, 59]. We also see this phenomenon in ecology, where wolves will use paths that are cut in the forest for oil exploration to hunt more efficiently [43, 44]. We thus consider in this example these types of situations, where the turning kernel is given by an underlying anisotropy of the environment. We use unit vectors $\theta \in \mathbb{S}^{n-1}$ to describe the anisotropies of the

environment through a directional distribution $q(x, \theta)$ with

$$\int_{\mathbb{S}^{n-1}} q(x, \theta) d\theta = 1 \quad \text{and} \quad q(x, \theta) \geq 0.$$

In the context of glioma growth, $q(x, \theta)$ denotes the distribution of nerve fibre directions in each location x [50]. In the example of wolf movement the function q would provide information of preferred movement directions due to roads or seismic lines [31]. We assume that individuals favour directions that are given by the environment, and, for simplicity, we consider unit speed $|v| = 1, V = \mathbb{S}^{n-1}$. We also make the simplifying assumption that it does not matter which direction an individual was previously travelling, essentially neglecting inertia. Then $T(v, v', x) = q(x, v)$. The assumption (T1)–(T4) relate to the v dependence only, hence in the following we ignore the x dependence in q, noting, however, that q, in general, would depend on x.

(T1) $q \geq 0$ ✓, $\int_V T(v, v')dv = \int_V q(v)dv = 1$, ✓and $\int_V \int_V q^2(v)dvdv' = |V| \cdot \int_V q^2(v)dv < \infty$, henceforth $q \in L^2(\mathbb{S}^{n-1})$. ✓

(T2) We first compute the iterates:

$$\begin{aligned} T^N(v', v) &= \int_V \cdots \int_V T(v', w_1) \cdots T(w_{N-1} v) dw_1 \cdots dw_{N-1} \\ &= \int_V \cdots \int_V q(v') q(w_1) \cdots q(w_{N-1}) dw_1 \cdots dw_{N-1} \\ &= q(v'). \end{aligned}$$

Condition (T2a) therefore becomes:

$$u_0(v) \leq q(v') \leq \rho u_0(v),$$

which is satisfied only if $q > 0$.
The condition (T2b) becomes:

$$u_0(v) \leq q(v) \leq \rho u_0(v),$$

and so we have a weaker condition, only requiring that q be u_0 positive.

(T3) Is $\mathscr{T}$ normal? $\mathscr{T}$ would be normal if

$$\int_V q(v) q(v') dv'' = \int_V q(v'') q(v'') dv''$$

which is equivalent to the condition

$$|V| q(v) q(v') = \|q\|_2^2.$$

We see that this is true if q =const., bringing us back to the Pearson case. In general then, $T(v,v') = q(v)$ is not normal. We must therefore do some more work in order to verify (T3). We can compute $\|\mathscr{T}\|_{\langle 1\rangle^\perp}$ directly:

$$\begin{aligned}\|\mathscr{T}\|_{\langle 1\rangle^\perp} &= \sup_{\substack{\phi\in\langle 1\rangle^\perp \\ \|\phi\|=1}} \left\| \int_V q(v)\phi(v')dv' \right\| \\ &= \sup \left\| q(v) \int_V \phi(v')dv' \right\| \\ &= 0.\end{aligned}$$

Therefore on $\langle 1\rangle^\perp$ the operator $\mathscr{T}$ is the zero operator. This satisfies assumption (T3), but it also shows that the splitting of $L^2(V) = \langle 1\rangle \oplus \langle 1\rangle^\perp$ is not a good choice here. Indeed, we will later see that we should choose $L^2(V) = \langle q\rangle \oplus \langle q\rangle^\perp$.
Finally, we check condition (T4).

$$\int_V T(v,v')dv' = q(v)|V| = 1,$$

which is only true for $q(v)$ =const.

So for this example, if $T(v,v') = q(v)$ is not constant, then it fails (T4) and (T3) which is problematic.

2.3.4.3 Example 3 (Homework) Symmetric Kernels

Check if symmetric kernels of the form a), b) or c) satisfy the assumptions (T1)–(T4):

$$\begin{aligned} a) &\qquad T(v,v') = t(|v-v'|) \\ b) &\qquad T(v,v') = t(v-v') \\ c) &\qquad T(v,v') = t(v'). \end{aligned}$$

2.3.5 Main Spectral Result

In this section, we summarize the results thus far into one main theorem and provide a proof of the missing pieces.

Theorem 4 ([29]) *Assume (T1)–(T4). Then*

1) 0 is a simple leading eigenvalue of $\mathscr{L}$ with unique eigenfunction $\varphi_0 = 1$,
2) All other eigenvalues λ are such that $-2\mu < \mathrm{Re}\lambda \leq -\mu_2 < 0$ and all other eigenfunctions have zero mass.
3) $L^2(V) = \langle 1\rangle \oplus \langle 1\rangle^\perp$ and for all $\psi \in \langle 1\rangle^\perp$:

$$\int_V \psi \mathscr{L}\psi dv \leq -\mu_2 \|\psi\|_2^2, \quad \text{where} \quad \mu_2 = \mu\Big(1 - \|\mathscr{T}\|_{\langle 1\rangle^\perp}\Big),$$

4) $\|\mathscr{L}\|$ has a lower and upper estimate

$$\mu_2 \leq \|\mathscr{L}\|_{\mathscr{L}(L^2(V),L^2(V))} \leq 2\mu,$$

5) $\mathscr{L}_{\langle 1\rangle^\perp}$ has a linear inverse $\mathscr{F}$ (pseudo-inverse) with

$$\frac{1}{2\mu} \leq \|\mathscr{F}\|_{\langle 1\rangle^\perp} \leq \frac{1}{\mu_2}.$$

Proof We have already verified parts 1)–3) earlier in this section, thus we now prove 4) and 5). To verify 4):

$$\begin{aligned}
\|\mathscr{L}\|_{\mathscr{L}(L^2(V),L^2(V))} &= \sup_{\substack{\phi\in L^2(V)\\ \|\phi\|=1}} \|\mathscr{L}\phi\|_2 \\
&\leq \sup_{\phi=\alpha+\phi^\perp} \left(\underbrace{\|\mathscr{L}\alpha\|_2}_{=0} + \|\mathscr{L}\phi^\perp\|_2 \right) \\
&= \sup_{\phi^\perp\in\langle 1\rangle^\perp} \|\mathscr{L}\phi^\perp\|_2 \\
&= \sup_{\phi^\perp\in\langle 1\rangle^\perp} \|-\mu\phi^\perp + \mu\mathscr{T}\phi^\perp\|_2 \\
&\leq \sup_{\phi\in\langle 1\rangle^\perp} \mu\|\phi^\perp\|_2 + \mu\|\mathscr{T}\phi^\perp\|_2 \\
&\leq \sup_{\phi^\perp\in\langle 1\rangle^\perp} 2\mu\|\phi^\perp\|_2
\end{aligned}$$

and $\forall\phi \in \langle 1\rangle^\perp$, $\|\phi\|_2 = 1$ we have

$$\mu_2\|\phi\|_2^2 \leq -\int \phi\mathscr{L}\phi dv \underset{\text{Hölder}}{\leq} \|\phi\|_2 \cdot \|\mathscr{L}\phi\|_2 \leq \|\mathscr{L}\|_{\mathscr{L}(L^2(V),L^2(V))},$$

which implies $\mu_2 \leq \|\mathscr{L}\| \leq 2\mu$.

Part 5) follows directly from $\mathscr{F} = \left(\mathscr{L}|_{\langle 1\rangle^\perp}\right)^{-1}$. For example, if $\mathscr{F}\phi = z$ and $\phi, z \in \langle 1\rangle^\perp$, then $\mathscr{L}z = \phi$ and

$$\|\phi\| = \|\mathscr{L}z\|$$

$$\begin{aligned}
&\Rightarrow \mu_2\|z\| \le \|\phi\| \le 2\mu\|z\| \\
&\Rightarrow \frac{1}{2\mu}\|\phi\| \le \|z\| \le \frac{1}{\mu_2}\|\phi\| \\
&\Rightarrow \frac{1}{2\mu}\|\phi\| \le \|\mathscr{F}\phi\| \le \frac{1}{\mu_2}\|\phi\|.
\end{aligned}$$

□

2.3.6 *Existence and Uniqueness*

Since the transport equation as formulated in (2.20) is linear, we immediately get existence and uniqueness of solutions as follows. We denote the shift operator $A := -(v \cdot \nabla)$ with domain of definition

$$D(A) = \{\phi \in L^2(\mathbb{R}^n \times V) : \phi(., v) \in H^1(\mathbb{R}^n)\}.$$

The shift operator is skew-adjoint and, according to Stone's theorem [7, 51] it generates a strongly continuous unitary group on $L^2(\mathbb{R}^n \times V)$. The right hand side of (2.20) is given by the bounded operator $\mathscr{L}$, hence it is a bounded perturbation of the shift group. Consequently, (2.20) also generates a strongly continuous solution group on $L^2(\mathbb{R}^n \times V)$. Moreover. given initial conditions $u_0 \in D(A)$, then a unique global solution exists in

$$C^1([0,\infty), L^2(\mathbb{R}^n \times V)) \cap C([0,\infty), D(A)).$$

2.4 The Formal Diffusion Limit

The computation of the diffusion limit, as presented here, is one of the standard methods for the analysis of transport equations. The equation type of a transport equation is hyperbolic, as it is based on pieces of ballistic motion, interspersed with directional changes. As the frequency of these changes becomes large, and the speed is large, then the movement looks, on a macroscopic scale, like diffusion (see Fig. 2.7). Mathematically, this macroscopic limit can be obtained via a formal asymptotic expansion with a small parameter ε. This parameter ε relates the ratio

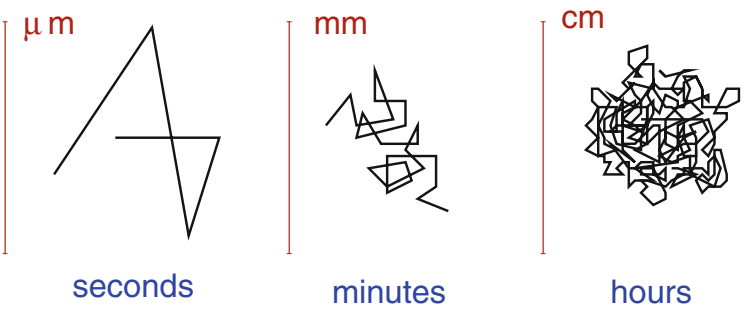

Fig. 2.7 Illustration of the relevant scalings for *E. coli* movement. While the time scales vary from seconds to minutes to hours, the spatial scale changes of the order of μm to mm to cm

of the microscopic spatial scale to a macroscopic spatial scale. We will see that the above assumptions (T1)–(T4) allow us to obtain a well defined and uniformly parabolic limit equation, where the diffusivity is given by the turning kernel T. Before we present the scaling method in Sect. 2.4.2, we discuss realistic scaling arguments for *E. coli* bacteria in Sect. 2.4.1

2.4.1 Scalings

We now consider the movement of *E. coli* bacteria as an example of different time and spatial scales [1, 14] . *E. coli* move by rotating their flagella, which are attached to the outside membrane of the bacterium. If most flagella rotate counterclockwise, they tend to align and propel the bacterium forward in a straight line. If many flagella rotate clockwise, then the alignment of the flagella is lost, they point in very different directions, which leads to a rotation of the cell. The clockwise - counterclockwise rotation of the flagella is controlled by an internal chemical signalling pathway, which is influenced by external signals [14]. As seen through a microscope, the bacteria fulfill a typical *run and tumble* movement, where longer periods of straight movement are interspersed by short moments of reorientations. On an individual scale, *E. coli* turn about once per second. Hence a mean turning rate μ satisfies $\frac{1}{\mu} \sim \frac{1}{s}$. From the point of view of the cell, we call this the timescale of turning $\tau_{\text{turn}} = \mathcal{O}(1)$. If observed over 50–100 turns, the trajectories appear directed, and a net displacement can easily be measured. We call this the intermediate drift time scale $\tau_{\text{drift}} \sim \mathcal{O}\left(\frac{1}{\varepsilon}\right)$, and $\varepsilon \sim 10^{-2}$. If we allow for 2500–10,000 turns, then the trajectories look like diffusion and random movement. Hence we introduce a third time scale of $\tau_{\text{diff}} \sim \mathcal{O}\left(\frac{1}{\varepsilon^2}\right)$. Just by the scale of observation, we identify three time scales, a time scale of turning τ_{turn}, a drift time scale τ_{drift} and a diffusion time scale τ_{diff}.

Mathematically, we identify the three scales through nondimensionalization. This serves to remove dimension from the problem, thus simplifying the model. In many situations, this will also reduce the number of parameters which we are dealing with, and it often allows us to identify large and small parameter combinations. In the case of transport equations, as introduced in the previous section, we introduce

$\tilde{v} = \frac{v}{s}$: where s is the characteristic speed. In case of *E. coli* it is about 10–20 $\mu\mathrm{m\,s}^{-1}$,

$\tilde{x} = \frac{x}{L}$: where L is the characteristic length scale. For *E. coli* bacterial colonies are of the order of 1 mm–1 cm, and

$\tilde{t} = \frac{t}{\sigma}$: where σ is the macroscopic time scale of observation. In the bacterial case it is about 1–10 h.

If we apply these scalings, then the transport equation becomes

$$\frac{1}{\sigma}\frac{\partial p}{\partial \tilde{t}} + \frac{s}{L}\tilde{v}\cdot\nabla_{\tilde{x}} p = -\mu p + \mu\int_V T p dv'.$$

Using the values which we identified for *E. coli*, we find

$$\sigma \approx 1 - 10\,\mathrm{h} = 3600 - 36{,}000\,\mathrm{s} \sim 10^4\,\mathrm{s},$$

and

$$\frac{s}{L} \approx \frac{10\mu\mathrm{ms}^{-1}}{10^{-3}\mathrm{m}} = \frac{10\cdot 10^{-6}\,\mathrm{ms}^{-1}}{10^{-3}\mathrm{m}} = 10^{-2}\mathrm{s}^{-1}.$$

When $\varepsilon = 10^{-2}$, we then have $\frac{1}{\sigma} \sim \varepsilon^2$ and $\frac{s}{L} \sim \varepsilon$. If we remove the $\sim$, then we obtain the resulting scaled transport equation:

$$\varepsilon^2 p_t + \varepsilon v\cdot\nabla p = \mathscr{L} p. \tag{2.21}$$

2.4.2 The Formal Diffusion Limit

To compute the formal diffusion limit, we will begin by studying a regular perturbation, or Hilbert expansion of p with respect to ε. This gives us

$$p(x,v,t) = p_0(x,v,t) + \varepsilon p_1(x,v,t) + \varepsilon^2 p_2(x,v,t) + h.o.t. \tag{2.22}$$

We will begin by substituting this expansion into Eq. (2.21) and match orders of ε.

Order ε^0

$$\mathscr{L}p_0 = 0,$$

which implies that p_0 is in the kernel of $\mathscr{L}$, hence

$$p_0(t, x, v) = \bar{p}(x, t),$$

which is independent of v. We get this from the first result of Theorem 4.

Order ε^1

$$v \cdot \nabla p_0 = \mathscr{L}p_1. \tag{2.23}$$

This equation can be solved for p_1 if $v \cdot \nabla p_0 \in \langle 1 \rangle^{\perp}$, so we need to check if this solvability condition is satisfied. Computing the following inner product of $v \cdot \nabla p_0$ and 1 we find:

$$\int_V v \cdot \nabla p_0 dv = \nabla \left(\underbrace{\int_V v dv}_{\substack{=0 \text{ due to} \\ \text{symmetry of } V}} \bar{p} \right) = 0.$$

Hence Eq. (2.23) can be solved as $p_1 = \mathscr{F}(v \cdot \nabla p_0) = \mathscr{F}(v \cdot \nabla \bar{p})$,

Order ε^2

$$p_{0_t} + v \cdot \nabla p_1 = \mathscr{L}p_2. \tag{2.24}$$

This case is a bit more complicated to solve than the first two cases. Here we have two options for how to proceed; a) integrate, or b) use the solvability condition. In the case studied here, a) and b) are equivalent, however, in other more general cases we would choose option a) and integrate (see Sect. 2.4.6) .

If we integrate Eq. (2.24), we obtain

$$\int_V p_{0_t} + v \cdot \nabla p_1 dv = 0,$$

since the right hand side integrates to 0. Plugging in the results from the order 0 and order 1 matching, this becomes

$$\int_V \bar{p}_t(x, t) dv + \int_V v \cdot \nabla \mathscr{F}(v \cdot \nabla \bar{p}(x, t)) dv = 0.$$

Since $\bar{p}_t$ does not depend on v, we can simplify the first term. Also, since ∇ is a spatial derivative, and the integral is over the velocity space, we can take the derivative out of the integral in the second term. This equation thus becomes

$$|V|\bar{p}_t(x,t) + \nabla \cdot \int_V v\mathscr{F}vdv \cdot \nabla\bar{p}(x,t).$$

We can simplify this to

$$\bar{p}_t = \nabla \cdot D\nabla\bar{p} \tag{2.25}$$

where the diffusion tensor D is defined to be

$$D = -\frac{1}{|V|}\int_V v\mathscr{F}v^{\perp}dv = -\frac{1}{|V|}\int_V v \otimes \mathscr{F}vdv.$$

Where we use two equivalent forms to denote an exterior product. We can write this in index notation as well

$$\nabla \cdot D\nabla = \sum_{i,j=1}^{n} \partial_i D^{ij}\partial_j, \quad \text{with} \quad D^{ij} = -\frac{1}{|V|}\int_V v^i \mathscr{F}v^j dv.$$

The components in the diffusion tensor D give the relative rates of diffusion in different directions. This process thus allows for the directional rate of spread to vary. If D is a constant multiple of the identity matrix of appropriate dimension, then the resulting diffusion is called *isotropic*. Alternatively, if the rates of spread do in fact vary with direction, we have *anisotropic* diffusion.

2.4.2.1 Example: Pearson Walk

We can once again consider the Pearson walk as an example. Recall from before that for this example we choose $V = s\mathbb{S}^{n-1}$ and $T(v,v') = \frac{1}{|V|}$. We first must compute the inverse operator $\mathscr{F}$. Given $\phi \in \langle 1\rangle^{\perp}$, we wish to find $z \in \langle 1\rangle^{\perp}$ such that $\mathscr{L}z = \phi$. We will use the fact that $z \in \langle 1\rangle^{\perp}$ implies $\int_V z(v)dv = 0$.

Now if we apply the operator $\mathscr{L}$, we have that $\mathscr{L}z = \phi$ is equivalent with

$$-\mu z(v) + \mu \underbrace{\int_V \frac{1}{|V|}z(v')dv'}_{=0} = \phi(v),$$

and so $z(v) = -\frac{1}{\mu}\phi(v)$. Hence

$$\mathscr{F} = -\frac{1}{\mu} \quad \text{as multiplication operator.}$$

Then for this example, we find that the diffusion tensor is

$$D = \frac{1}{\mu|V|}\int_V vv^{\mathrm{T}}dv.$$

In order to have an explicit form for D, we must then compute

$$\int_V vv^{\mathrm{T}}dv, \quad \text{with} \quad V = s\mathbb{S}^{n-1}.$$

For example, in 2-dimensions: $V = s\mathbb{S}^1$, and $v = s\begin{pmatrix}\cos\phi\\ \sin\phi\end{pmatrix}$. We can then explicitly compute

$$vv^{\mathrm{T}} = s^2\begin{pmatrix}\cos^2\phi & \cos\phi\sin\phi\\ \cos\phi\sin\phi & \sin^2\phi\end{pmatrix},$$

and so

$$D = \frac{s^2}{|V|}\int_0^{2\pi}\begin{pmatrix}\cos^2\phi & \cos\phi\sin\phi\\ \cos\phi\sin\phi & \sin^2\phi\end{pmatrix}sd\phi.$$

We can then solve by integrating component wise. If we consider this tensor in 3 dimensions, then we have double integrals of trigonometric functions to solve. This is still possible, but tedious. In higher dimensions the integral becomes more and more cumbersome. In the proof of the next Lemma we propose a clever use of the divergence theorem to compute the above integral in any dimension. As shown by Hillen in [26], this method can be generalized to higher dimensions and higher velocity moments.

Lemma 4 *Let $V = s\mathbb{S}^{n-1}, \omega_0 = |\mathbb{S}^{n-1}|$, then $|V| = s^{n-1}\omega_0$ and*

$$\int_V vv^{\mathrm{T}}dv = \frac{\omega_0 s^{n+1}}{n}\mathbb{I},$$

where $\mathbb{I}$ is the n-dimensional identity matrix.

Proof Since $\int_V vv^{\mathrm{T}}dv$ is a tensor, we use two test vectors $a, b \in \mathbb{R}^n$ and use tensor notation, i.e. summation over repeated indices

$$a_i b_i = \sum_{i=1}^{n} a_i b_i$$

then

$$\begin{aligned} a^T \int_V vv^{\mathrm{T}} dv\ b &= \int_V a_i v_i v_j b_j dv \\ &= s \int_V \frac{v_i}{|v|}(a_i v_j b_j) dv \\ &\underbrace{=}_{\substack{\text{divergence} \\ \text{theorem}}} s \int_{B_s(0)} \mathrm{div}_{v_i}(a_i v_j b_j) dv \\ &= s \int_{B_s(0)} a_i b_i dv \\ &= s|B_s(0)| a_i b_i \end{aligned}$$

We can compute $|B_s(0)|$ as follows

$$|B_s(0)| = s^n |B_1(0)| = s^n \int_{B_1(0)} dv = \frac{s^n}{n} \int_{B_1(0)} \mathrm{div}_v v dv.$$

If we apply the divergence theorem again this becomes

$$\frac{s^n}{n} \int_{\mathbb{S}^{n-1}} \sigma \cdot \sigma d\sigma = \frac{s^n}{n} |\mathbb{S}^{n-1}| = \frac{s^n}{n} \omega_0,$$

where $\omega_0 \equiv |\mathbb{S}^{n-1}|$. Then

$$a^{\mathrm{T}} \int_V vv^{\mathrm{T}} dv\ b = a^T \frac{s^n}{n} |\mathbb{S}^{n-1}| b = \frac{s^{n+1}}{n} \omega_0 a^{\mathrm{T}} b$$

for all vectors $a, b \in \mathbb{R}^n$. We therefore obtain

$$\int_V vv^{\mathrm{T}} dv = \frac{\omega_0 s^{n+1}}{n} \mathbb{I}.$$

□

Remarks

1. For general symmetric V, there exists $\kappa > 0$ such that $\int_V vv^{\mathrm{T}} dv = \kappa \mathbb{I}$.
2. In [26] explicit formulas for all higher velocity moments $\int_V v_i v_j \cdots v_k dv$ were computed.

Now returning to our discussion of the Pearson walk example. We can explicitly compute the diffusion tensor using the above discussion, i.e.

$$D = \frac{1}{\mu|V|}\int_V vv^{\mathrm{T}}dv = \frac{1}{\mu|V|}\frac{\omega_0 s^{n+1}}{n}\mathbb{I},$$

and since $|V| = s^{n-1}\omega_0$, this simplifies to

$$D = \frac{s^2}{\mu n}\mathbb{I}.$$

This diffusion tensor corresponds to isotropic diffusion, and so the use of the tensor is not necessary, and we can simply use a diffusion coefficient. This gives the isotropic diffusion equation

$$\bar{p}_t = \frac{s^2}{\mu n}\Delta\bar{p}.$$

2.4.3 Ellipticity of the Diffusion Tensor

The above limit construction leads to a diffusion-like equation (2.25) and the first question is under which condition is the operator $\nabla \cdot D\nabla$ uniformly parabolic. We will see that here the condition (T3) and the corresponding constant μ_2 are important.

Lemma 5 *Assume (T1)–(T4). The diffusion tensor D is uniformly elliptic, i.e.*

$$\exists \kappa > 0 \text{ such that} \varphi \cdot D\varphi \geq \kappa|\varphi|^2.$$

Proof Let $\varphi \in \mathbb{R}^n$ and compute

$$\varphi \cdot D\varphi = -\frac{1}{|V|}\int_V (\varphi \cdot v)\mathscr{F}(\varphi \cdot v)dv.$$

Since $\varphi \cdot v \in \langle 1\rangle^{\perp}$, we can apply $\mathscr{F}$ i.e. there exists $z = \mathscr{F}(\varphi \cdot v)$ and $\mathscr{L}z = \varphi \cdot v$. Then

$$\begin{aligned}\varphi \cdot D\varphi &= -\frac{1}{|V|}\int_V \mathscr{L}z(v)z(v)dv \\ &\geq \frac{\mu_2}{|V|}\|z(v)\|_2^2 \quad \text{from our spectral result}\end{aligned}$$

$$= \frac{\mu_2}{|V|}\int_V \left|\mathscr{F}\left(\frac{\varphi}{|\varphi|}\cdot v\right)\right|^2 dv|\varphi|^2$$
$$\geq c_0\frac{\mu_2}{|V|}|\varphi|^2$$

with

$$c_0 = \min_{|\varphi|=1}\int_V |\mathscr{F}(\varphi\cdot v)|^2 dv > 0.$$

Note that indeed $c_0 > 0$ since $\|\mathscr{F}\|_{\langle 1\rangle^\perp} > \frac{1}{2\mu}$. The integral $\int_V |\mathscr{F}(\varphi\cdot v)|^2 dv$ does not depend on the choice of φ, since V is symmetric. □

Theorem 5 ([12, 51]) *Assume (T1)–(T4). The differential operator $\nabla\cdot D\nabla$ generates an analytic semigroup on $L^2(\mathbb{R}^n)$. For $p(0,.,v) \in L^2(\mathbb{R}^n)$ and $\bar{p}_0(x) = \int p(0,x,v)dv$ there exists a unique global solution $\bar{p}(x,t)$ of*

$$\bar{p}_t = \nabla\cdot D\nabla\bar{p}$$

with the following properties:

$$(i) \qquad \bar{p}\in C([0,\infty), L^2(\mathbb{R}^n))$$
$$(ii) \qquad \frac{\partial\bar{p}}{\partial t}\in C^\infty((0,\infty)\times\mathbb{R}^n)$$
$$(iii) \qquad \|\bar{p}(.,t)\|_\infty \text{ is a decreasing function of } t.$$

Corollary 1 (Regularity, [57]) *For each $m\in\mathbb{N}$ and each $0<\vartheta<\infty$ there exists a constant $C_0 = C_0(m,\vartheta,\|\bar{p}_0(.,t)\|_2)$such that*

$$\|\bar{p}\|_{C^m((\vartheta,\infty)\times\mathbb{R}^n)} \leq C_0.$$

2.4.4 Graphical Representations of the Diffusion Tensor

There are two intuitive ways to graphically represent a diffusion tensor: ellipsoids and peanuts. Let D denote a three dimensional diffusion tensor.

1. The fundamental solution of the standard diffusion equation in $\mathbb{R}^n$, i.e.

$$u_t = \nabla\cdot D\nabla u$$

is the multidimensional Gaussian distribution, of the form

$$G(x,\tilde{x}) = C\exp\Big(-(x-\tilde{x})^T D^{-1}(x-\tilde{x})\Big).$$

with an appropriate normalization constant C. This function describes the probability density of finding a random walker at a distance $w = x - \tilde{x}$ from a starting point $\tilde{x}$. Hence the level sets of $w^T D^{-1} w$ describe locations of equal probability, which is the *diffusion ellipsoid*:

$$\mathscr{E}_c := \{w \in \mathbb{R}^n : w^T D^{-1} w = c\}$$

If the value of the constant is changed, we will obtain different ellipsoids, though all will be similar in the geometric sense. As such, the constant is often chosen to be equal to 1.

2. The function from $S^{n-1} \to \mathbb{R}$ defined as $\theta \mapsto \theta^T D\theta$ gives the *apparent diffusion coefficient in direction* θ, and also the *mean squared displacement in that direction* and it is called the *peanut*.

These objects are, in fact not the same. While the probability level sets are ellipsoids, the apparent diffusion coefficient is typically peanut shaped, as can be seen for our examples in Fig. 2.8.

We chose examples of diffusion tensors in diagonal form. If they are not in diagonal form, then the ellipsoids or peanuts are rotated relative to the coordinate axis. The diffusion ellipsoid for a diagonal diffusion matrix $D = \mathrm{diag}(\lambda_1, \lambda_2, \lambda_3)$ is

$$\mathscr{E}_1 = \left\{ w \in \mathbb{R}^n : \left(\frac{w_1}{\sqrt{\lambda_1}}\right)^2 + \left(\frac{w_2}{\sqrt{\lambda_2}}\right)^2 + \left(\frac{w_3}{\sqrt{\lambda_3}}\right)^2 = 1 \right\},$$

which is clearly an ellipsoid. The peanut in this case is the map

$$\theta \mapsto \lambda_1 \theta_1^2 + \lambda_2 \theta_2^2 + \lambda_3 \theta_3^2.$$

In Fig. 2.8 we consider

$$D_1 := \begin{pmatrix} 5 & 0 & 0 \\ 0 & 3 & 0 \\ 0 & 0 & 1 \end{pmatrix}, \qquad D_2 = \begin{pmatrix} 8 & 0 & 0 \\ 0 & 1 & 0 \\ 0 & 0 & 0.2 \end{pmatrix}.$$

Having peanuts and ellipsoids, there is a nice way to visualize the condition of ellipticity of D.

Definition 4 D is uniformly elliptic, if there exists a constant $\kappa > 0$ such that

$$\theta^T \cdot D\theta > \kappa |\theta|^2, \tag{2.26}$$

for all vectors $\theta \in \mathbb{R}^n$.

Lemma 6 *1. The diffusion tensor D is uniformly elliptic, iff the peanut of D contains a ball centered at the origin.*

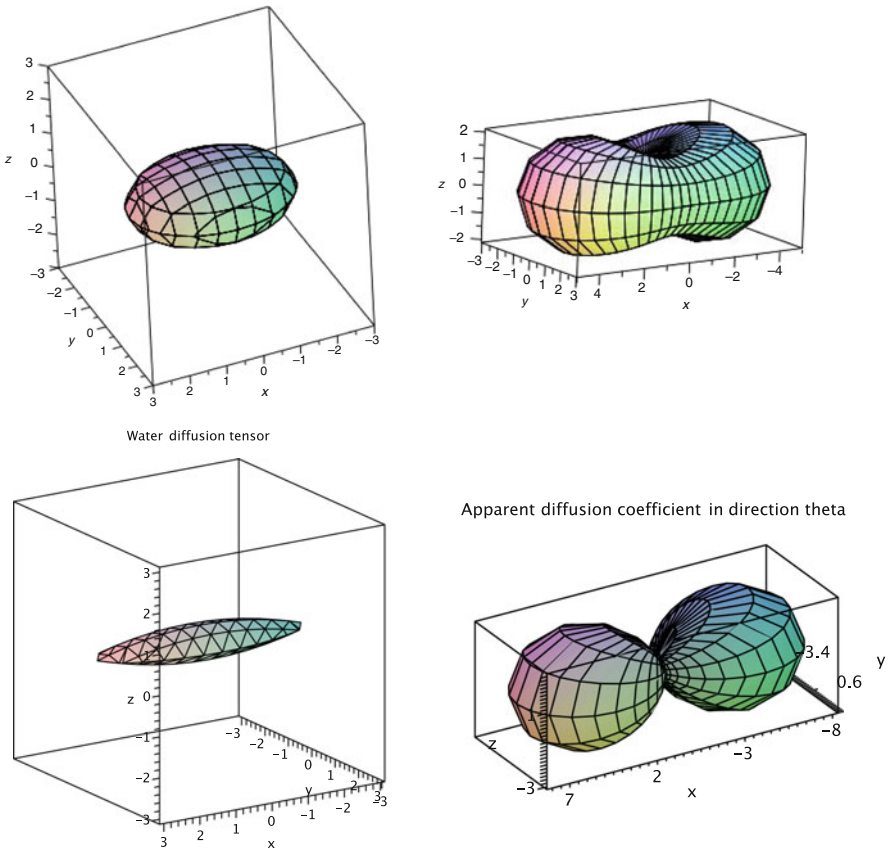

Fig. 2.8 *Left*: diffusion ellipsoid. *right*: the corresponding peanut for the apparent diffusion in direction θ. *Top row*: example D_1, *bottom row*, example D_2

2. *The diffusion tensor D is uniformly elliptic, iff the ellipsoid of D contains a ball centered at the origin.*

Proof Let us consider the peanut case first. The map $\theta \to \kappa|\theta|^2$ can be written as $\theta \to \kappa\theta^T\mathbb{I}\theta$ with the identity matrix $\mathbb{I}$. Hence it is also a peanut. A very special peanut, in fact, since it is a ball of radius κ. Then condition (2.26) says that the peanut of D contains the peanut of $\kappa\mathbb{I}$.

Related to the diffusion ellipsoid, we need to work a little more.

"$\Longrightarrow$" Assume D is uniformly elliptic, and consider v with $v^TD^{-1}v = 1$. Without restriction, we can study the level set of level 1. We claim:

Claim 1: $|v| > \sqrt{\kappa}$.

To prove Claim 1. we need to show two more statements:

Claim 2: $\inf_{|\phi|=1} \|D\phi\| \geq \kappa$**.**

Assume Claim 2 is not true. Then there exists ϕ_0 with $|\phi_0| = 1$ such that $\|D\phi_0\| < \kappa$. However,

$$\kappa = \kappa|\phi_0|^2 \leq \phi_0 D\phi_0 \leq |\phi_0|\|D\phi_0\| < \kappa,$$

which is a contradiction. Hence Claim 2 is true.
Claim 3: $\|D^{-1}\|_{op} \leq \frac{1}{\kappa}$.
Claim 2 implies that $\kappa\|\phi\| \leq \|D\phi\|$, for all $\phi \in \mathbb{R}^n$. Let $z := D\phi$, such that $\phi = D^{-1}z$. Then

$$\kappa\|D^{-1}z\| \leq \|z\| \quad \Longrightarrow \quad \frac{\|D^{-1}z\|}{|z|} \leq \frac{1}{\kappa}.$$

Hence Claim 3 is true.
Finally, to prove Claim 1 we estimate:

$$1 = v^T D^{-1} v \leq \|D^{-1}\|_{op}\|v\|^2 \leq \frac{1}{\kappa}|v|^2$$

Hence $|v| \geq \sqrt{\kappa}$ and the ellipsoid $\mathscr{E}_1$ contains a ball of radius $\sqrt{\kappa}$.
"$\Longleftarrow$" If the ellipsoid contains a ball of radius r, then it is non degenerate and it has n main axis e_i, with lengths α_i, $i = 1, \ldots, n$. These can be arranged such that $0 < r \leq \alpha_1 \leq \alpha_2 \leq \cdots \leq \alpha_n$. The main axis vectors are eigenvectors or generalized eigenvectors of D^{-1} with eigenvalues α_i^2, $i = 1, \ldots, n$. Then D has the same eigenvectors and generalized eigenvectors with eigenvalues $\lambda_i = \alpha_i^{-2}$, $i = 1, \ldots, n$. Then $\theta^T D\theta \geq \kappa|\theta|^2$ for

$$\kappa := \min\left\{\frac{1}{\alpha_i^2}, \imath = 1, \ldots, n\right\} = \frac{1}{\alpha_n^2}.$$

□

We show an illustration for the case of example D_1 in Fig. 2.9.

2.4.4.1 An Anisotropic Random Walk

In order to get an approximation of the overall behaviour of a population in an anisotropic random walk, we consider an individual based model in which each individual performs a random walk. We then show a frequency plot of where each individual ends up. We show that the frequency plot closely matches the solution of the corresponding diffusion model.

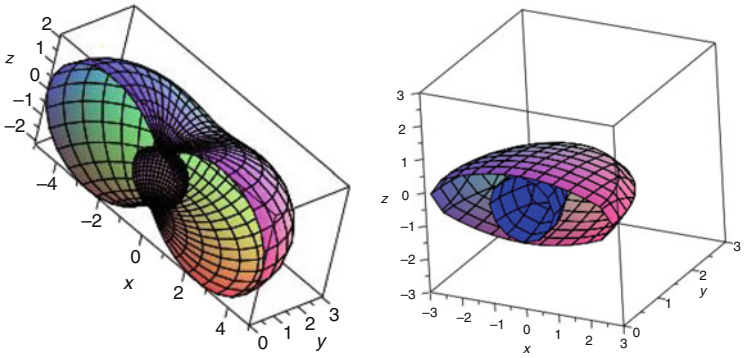

Fig. 2.9 *Left*: the peanut of D_1 contains a ball. *Right*: the ellipsoid of case 1 contains a ball of radius 1

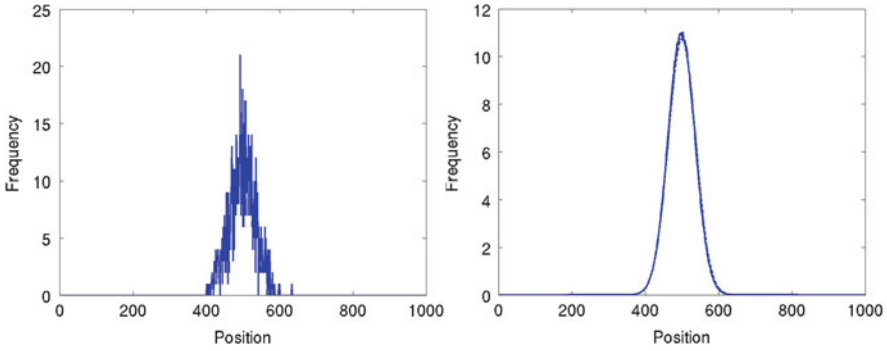

Fig. 2.10 (**a**): frequency plot of the population after 2000 iterations of a random walk. Notice that the highest number of individuals are found near the starting point ($x = 0$). (**b**): plot showing the average frequency plot over 1000 runs of a population after 2000 iterations (*solid line*), and the corresponding Gaussian curve (*dotted line*)

1-Dimensional Simulations

As a first simulation, we can perform a random walk in one-dimension. It is important to note that in one dimension, there is no such thing as anisotropy since there is only one direction along which particles can diffuse. Additionally, the one dimensional diffusion equation does not permit a diffusion tensor, and instead can only have a diffusion coefficient. For the one dimensional random walk, we begin with 1000 particles at the origin. At each time step, a random decision is made with equal probability of moving to the left, moving to the right, or staying where it is. Figure 2.10a shows the results of such a simulation after 2000 time steps. There is a higher concentration of individuals near the starting point ($x = 0$), however for a single simulation, the results are very noisy. As such, it is better to consider an average frequency plot over many runs. Figure 2.10b shows the frequency plot that

results when the average frequency over 1000 runs is computed. This is the solid line in the plot. We then use the variance of the points in this distribution to plot the corresponding Gaussian curve. This curve is the dotted line. It is clear from this that the distribution of particles after a one-dimensional random walk very closely approximates a Gaussian distribution.

2-Dimensional Simulations

As discussed above, when we are in higher dimensions, we can replace our diffusion coefficient with a matrix. When this matrix is a constant multiple of the identity, particles are spreading out with equal rates in all directions, corresponding to isotropic diffusion. When this matrix is not a constant multiple of the identity, particles spread at different rates in different directions. This is anisotropic diffusion. To get a better idea about what anisotropic diffusion looks like, we can compare the results of an isotropic random walk to those of an anisotropic random walk, both in two dimensions.

For an isotropic random walk in two dimensions, we started 1000 individuals at the origin and again let them spread out following some given set of rules. To determine each individual's next step, a random angle was generated and a constant step size was assigned. The distribution of these individuals after 100 time steps is shown in the left column of the top row of Fig. 2.11. We see that the distribution looks approximately circular with the highest concentration found where the particles began [at $(0, 0)$]. A frequency plot of this data would be noisy, just as in one dimension, so for the frequency plot we considered the average over 150 runs. The result is shown in the right hand column of the top row of Fig. 2.11. This frequency plot shows a roughly Gaussian distribution, as was seen in one dimension.

Simulation of an anisotropic random walk in two dimensions followed a similar procedure with one notable difference. Instead of choosing a fixed step size, individuals could move further in certain directions. We began with 1000 individuals at the origin, just as we did in the isotropic case, and once again allowed 100 iterations. A random angle was generated for each individual, however the step size depended on this angle. A dominant direction was chosen along which individuals could move further, corresponding to the dominant eigenvector of the diffusion tensor. The step size was then determined by the diffusion ellipsoid. In this case, the dominant direction was chosen to be the positive and negative y-axis. Not surprisingly then, the resulting distribution showed an ellipsoidal shape with the highest concentration found at the origin. More spread occurred in the chosen dominant direction. Such a distribution can be seen in the first column of the second row of Fig. 2.11. The frequency plot for the average distribution over 150 runs is shown in the right hand column of the second row of Fig. 2.11.

An exercise such as this allows us to visualize anisotropic diffusion. When these individuals have a preference for diffusing in a given direction, we see that we end up with a distribution that is "stretched" in that direction. For biological situations,

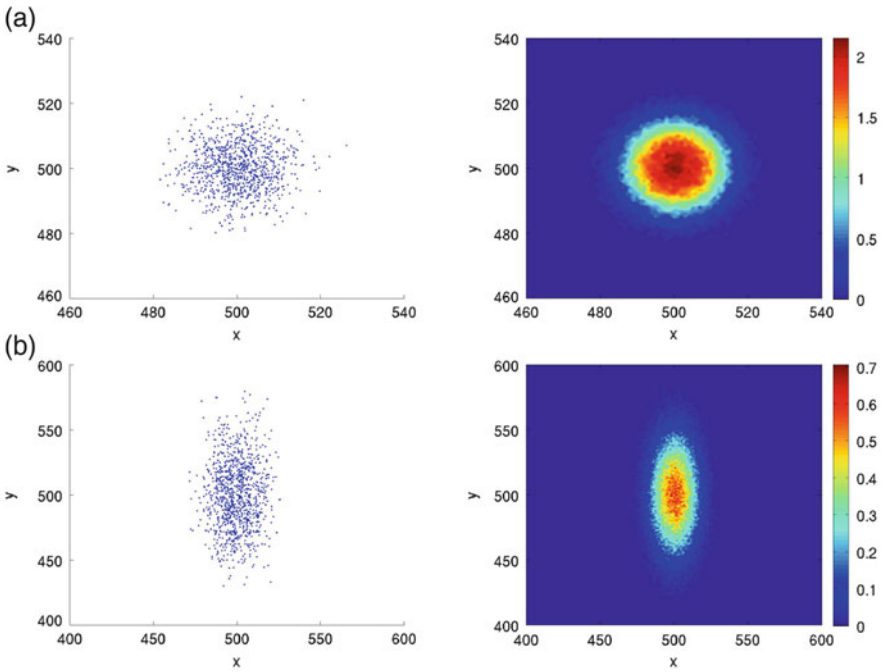

Fig. 2.11 *Top row*: (**a**). Plot showing the distribution of 1000 particles after 100 iterations of an isotropic random walk. (**b**). Frequency plot showing the average frequency over 150 runs of an the isotropic random walk as described in part (**a**). *Bottom row*: (**a**). Plot showing the distribution of 1000 particles after 100 iterations of an anisotropic random walk. (**b**). Frequency plot showing the average frequency over 150 runs of an the anisotropic random walk as described in part (**a**)

such as cancer cells travelling on white matter tracts in the brain, this means we would expect to see the cells travel more along this particular direction than in perpendicular directions. This results in irregular shapes of spread as is commonly seen in cancer models. As such, anisotropy of diffusion tensors provide us a valuable tool for making more accurate and useful models.

2.4.5 Anisotropic vs. Isotropic Diffusion

Now, depending on the form of the diffusion tensor D, we can obtain either *anisotropic* or *isotropic* diffusion. As mentioned before, We call the diffusion isotropic if $D = \alpha\mathbb{I}$ for some $\alpha > 0$; otherwise diffusion is called anisotropic. For isotropic diffusion the rate of spread is equivalent in all directions. The resulting distributions are spherical in nature. Anisotropic diffusion, however, occurs when the rate of diffusion varies in different directions. This can arise from many biological problems where animals have certain preferred directions of motion.

The rates of spread in these directions are effectively higher, and the resulting distributions are ellipsoidal in nature, aligned with the dominant direction of spread.

In this section we will derive criteria on the turning kernel T and on the turning operator $\mathscr{L}$ that ensure that the corresponding parabolic limit is isotropic. For this we introduce the *expected velocity*

$$\bar{v}(v) := \int_V T(v, v')v'dv' \tag{2.27}$$

For the Pearson walk, with $V = s\mathbb{S}^{n-1}$, and $T(v, v') = \frac{1}{|V|}$we find an expected velocity of

$$\bar{v}(v) = \int_V \frac{1}{|V|} v'dv' = 0.$$

More generally, if T has the form $T(v)$, then $\bar{v}(v) = 0$ as well.

Also, if we integrate the expected velocity, then we get zero by condition (T1):

$$\int_V \bar{v}(v)dv = \int_V \int_V T(v, v')v'dv'dv = 0.$$

To decide if the diffusion limit is isotropic or anisotropic we compare three statements:

(St1) There exists an orthonormal basis $\{e_1, \ldots, e_n\} \subset \mathbb{R}^n$ such that the coordinate mappings $\phi_i : V \to \mathbb{R}, \phi_i(v) = v_i$ are eigenfunctions of $\mathscr{L}$ with common eigenvalue $\lambda \in (-2\mu, 0)$, for all $i = 1, \ldots, n$.

(St2) The expected velocity is parallel to v, i.e.

$$\bar{v}(v) \parallel v \quad \text{and} \quad \gamma := \frac{\bar{v}(v) \cdot v}{v^2}$$

is the *adjoint persistence* with $\gamma \in (-1, 1)$.

(St3) There exists a diffusion coefficient $d > 0$ such that $D = d\mathbb{I}$ (isotropic).

Theorem 6 *Assume (T1)–(T4) and that V is symmetric w.r.t. SO(n), where SO(n) is the special orthogonal group of size n. Then we have the inclusions*

$$(St1) \quad \Leftrightarrow \quad (St2) \quad \Rightarrow (St3).$$

The constants λ, γ, d are related as

$$\gamma = \frac{\lambda + \mu}{\mu}, \quad d = -\frac{K_V}{|V|\lambda} = \frac{K_V}{|V|\mu(1-\gamma)},$$

where K_V is given by

$$\int v v^T dv = K_V \mathbb{I}.$$

Moreover, if there is a matrix M such that $\bar{v}(v) = Mv$ for all $v \in V$ then all three statements are equivalent.

Proof (St1) $\Leftrightarrow$ (St2):

$$\begin{aligned}
(\text{St1}) &\Leftrightarrow \mathscr{L} v_i = \lambda v_i, \qquad \forall i \\
&\Leftrightarrow -\mu v_i + \mu(\bar{v}(v))_i = \lambda v_i \\
&\Leftrightarrow (\bar{v}(v))_i = \gamma v_i, \qquad \gamma = \frac{\lambda + \mu}{\mu} \\
&\Leftrightarrow (\text{St2})
\end{aligned}$$

(St1) $\Rightarrow$ (St3): The coordinate mappings ϕ_i are eigenfunctions of $\mathscr{L}$ and $\phi_i \in \langle 1 \rangle^{\perp}$. Hence ϕ_i are also eigenfunctions for $\mathscr{F}$ with eigenvalue λ^{-1} for each $i = 1, \ldots, n$. Then

$$\begin{aligned}
e_k D e_j &= -\frac{1}{|V|} \int_V v_k \mathscr{F} v_j dv \\
&= -\frac{1}{|V|} \frac{1}{\lambda} \int_V v_k v_j dv \\
&= -\frac{K_V}{|V|\lambda} \delta_{kj}
\end{aligned}$$

(St3) $\Rightarrow$ (St1) see Hillen and Othmer [29] □

2.4.5.1 Examples

Example 1, Pearson Walk As seen earlier, for the Pearson walk we have $\bar{v}(v) = 0$ and consequently also $\gamma = 0$. Still, statement (St2) is true and we find isotropic diffusion with diffusion coefficient

$$d = \frac{K_V}{|V|\mu} = \frac{s^2}{n\mu}.$$

Example 2, Symmetric T Now we again assume $V = s\mathbb{S}^{n-1}$ but now T is symmetric of the form $T(v, v') = t(|v - v'|)$. The expected velocity

$$\bar{v}(v) = \int_V T(v, v') v' dv' = \int_V t(|v - v'|) v' dv',$$

which is not entirely trivial to compute. To do this, we consider a given $v \in V$. Since $V = s\mathbb{S}^{n-1}$ is a ball of radius s, the level sets

$$\Gamma_a := \{v' \in V : |v - v'| = a\}$$

are circles on $\mathbb{S}^{n-1}$ surrounding v, for $a \in (-1, 1)$. Then on Γ_a we have $t(|v-v'|) = t(a)$. Then we can split our integral

$$\begin{aligned}\int_V t(|v - v'|)v'dv' &= \int_{-1}^{1}\int_{\Gamma_a} t(|v - v'|)v'dv'da \\ &= \int_{-1}^{1} t(a)\int_{\Gamma_a} v'dv'da \\ &= \int_{-1}^{1} t(a)da\ c_1\ v \\ &= c_2\ v\end{aligned}$$

where we use the fact that the symmetric integral $\int_{\Gamma_a} v'dv'$ is in direction v and c_1, c_2 are appropriate constants (note c_1 can be negative). Hence $\bar{v}(v)$ is parallel to v, and statement (St2) holds. Hence the diffusion limit is isotropic.

Example 3, Nonisotropic For this example, we will consider a constant kernel T, perturbed by a second order correction term

$$T(v, v') = \frac{1}{|V|} + v^{\mathrm{T}}\mathscr{M}v, \text{with}\mathscr{M} \in \mathbb{R}^{n\times n}\text{and}V = s\mathbb{S}^{n-1}.$$

Then we have

$$D = \frac{s^2}{n\mu}\left(\mathbb{I} + \frac{|V|s^2}{n}\mathscr{M}\left(\mathbb{I} - \frac{|V|s^2}{n}\mathscr{M}\right)^{-1}\right),$$

which is non- isotropic (see details in [29]).

Example 4, Chemotaxis For our last example, we will define T to be

$$T(v, v') = \frac{1}{|V|} + \varepsilon Q(v, v', S)\nabla S$$

which, as we will derive in the next section, gives a chemotaxis model with

$$D = \frac{s^2}{n\mu}\text{and}\chi(S) = \frac{1}{|V|}\int_V\int_V vQ(v, v', S)dv'dv.$$

For many more examples, see [47].

2.4.6 Chemotaxis

In the case of chemotaxis, the turning rate and the turning kernel might depend on the signal $S(x,t)$. We study these as perturbations (see [47]). Note that we cannot use v for the signal concentration, since it is used for the velocities. Hence here we use S.

$$T(v,v',S(\cdot)) = T_0(v,v') + \varepsilon^k T_1(v,v',S(\cdot)),$$

$$\mu(v,S(\cdot)) = \mu_0 + \varepsilon^\ell \mu_1(v,S(\cdot)),$$

and study the four pairwise combinations when $k,\ell = 0,1$. We assume that T_0 satisfies (T1)–(T4), and that for T_1 we have

$$T_1 \in L^2, \qquad \int_V T_1(v,v',S(\cdot))dv = 0,$$

$$|T_1(v,v',S)| \le T_0(v,v',S).$$

Consider then the example generated when

$$T(v,v',S(\cdot)) = T_0(v,v') + \varepsilon\alpha(S)(v\cdot\nabla S)$$

which says it is more likely to choose a new direction in the direction of ∇S. Then

$$\begin{aligned}\mathscr{L}\varphi(v) &= -\mu\varphi(v) + \mu\int_V T(v,v')\varphi(v')dv' + \varepsilon\mu\alpha(S)\int_V (v\cdot\nabla S)\varphi(v')dv'\\ &= \mathscr{L}_0\varphi(v) + \varepsilon\mu\alpha(S)(v\cdot\nabla S)\bar{\varphi}(x,t),\\ &= \mathscr{L}_0\varphi + \varepsilon\mathscr{L}_1\varphi\end{aligned}$$

where $\bar{\varphi} = \int_V \varphi dv$, and $\mathscr{L}_1\varphi = \mu\alpha(S)(v\cdot\nabla S)\bar{\varphi}(x,t)$. Because of the perturbed structure of the right hand side, we cannot directly apply the theory from above. Instead, we again compare orders of ε. The scaled transport equation is now

$$\varepsilon^2 p_t + \varepsilon v\cdot\nabla p = \mathscr{L}_0 p + \varepsilon\mathscr{L}_1 p$$

$\boldsymbol{\varepsilon^0}$

$$0 = \mathscr{L}_0 p_0 \Rightarrow p_0 = p_0(x,t)$$

$\boldsymbol{\varepsilon^1}$

$$v \cdot \nabla p_0 = \mathscr{L}_0 p_1 + \mathscr{L}_1 p_0$$

which is equivalent with

$$v \cdot \nabla p_0(x,t) - \mu\alpha(S)(v \cdot \nabla S)\bar{p}_0 = \mathscr{L}_0 p_1.$$

Since $\bar{p}_0 = \int_V p_0(x,t)dv = |V|p_0$ we can write this as

$$v \cdot \nabla p_0 - \mu\alpha(S)(v \cdot \nabla S)|V|p_0 = \mathscr{L}_0 p_1.$$

To solve for p_1, we need to check that the left hand side is in the correct space so that we may invert our operator. We thus check the solvability condition

$$\int_V v dv \cdot \nabla p_0 - \mu\alpha(S)|V| \int_V v dv \cdot \nabla S p_0 = 0,$$

which is true due to the symmetry of V. Then

$$p_1 = \mathscr{F}_0\Big(v \cdot \nabla p_0 - \mu|V|\alpha(S)(v \cdot \nabla S)p_0\Big),$$

where $\mathscr{F}_0$ is the pseudo inverse of the unperturbed part $\mathscr{L}_0$.

$\boldsymbol{\varepsilon^2}$

$$p_{0_t} + v \cdot \nabla p_1 = \mathscr{L}_0 p_2 + \mu\alpha(S)(v \cdot \nabla S)\bar{p}_1$$

We integrate this last equation to obtain

$$\begin{aligned} &|V|p_{0_t} + \int_V v \cdot \nabla \mathscr{F}_0 \left(v \cdot \nabla p_0 - \mu|V|\alpha(S)(v \cdot \nabla S)p_0\right) dv \\ &= 0 + \mu\alpha(S) \underbrace{\int_V v \cdot \nabla S dv}_{=0} \bar{p}_1. \end{aligned}$$

Hence

$$|V|p_{0_t} + \nabla \cdot \int_V v \mathscr{F}_0 v dv \cdot \nabla p_0 - \mu|V| \nabla \cdot \int_V v \mathscr{F}_0 v dv \cdot \alpha(S) \nabla S p_0 = 0.$$

We arrive at a (possibly anisotropic) chemotaxis equation

$$p_{0_t} = \nabla \left(D \nabla p_0 - \mu|V|\alpha(S)p_0 D \nabla S\right)$$

where

$$D = -\frac{1}{|V|}\int_V v\mathscr{F}_0 v dv.$$

Notice that the diffusion tensor D appears in both terms, this means that the chemotaxis term carries the same anisotropy as the diffusion term, as it should, since the cells move in a given (possibly anisotropic) environment and both movement terms should be affected by anisotropy.

Finally, if we consider the Pearson walk with $T_0(v, v') = \frac{1}{|V|}$ and $D = \frac{s^2}{n\mu}\mathbb{I}$, then we obtain the classical (isotropic) chemotaxis model

$$p_{0t} = \nabla(d\nabla p_0 - \chi(S)p_0\nabla S)$$

with $d = \frac{s^2}{n\mu}$ and $\chi(S) = \frac{|V|\alpha(S)s^2}{n}$.

2.4.6.1 Other Cases

We considered an order ε perturbation of T in detail in the previous section. We can also consider order one perturbations, and perturbations of μ. Doing this we get into technical challenges that we skip in this manuscript. For details we refer to [47]. Here we simply list the corresponding examples.

Examples

1. In case of bacterial movement, bacteria tend to turn more often if they move down a gradient and less often if they move up a gradient. This can be expressed through a perturbed turning rate

$$\mu(S) = \mu_0(1 - \varepsilon b(S)(v \cdot \nabla S)). \tag{2.28}$$

   If we combine this with the Pearson walk for $T = 1/|V|$, then we obtain a chemotaxis model

$$p_{0,t} = \nabla(d\nabla p_0 - \chi(S)p_0\nabla S),$$

   with

$$\chi(S) = \frac{s^2}{n}b(S).$$

   The function $b(S)$ describes the signal sensing mechanism of the cells. Here we see how this term enters the chemotaxis model.
2. Amoeba are able to modify their turning rate as well as actively choose a favourable direction. This can be modelled by using a perturbed turning rate as

above (2.28) as well as a perturbed turning kernel as we did above. In a special case we consider

$$T(v, v', S) = \frac{1}{|V|}\Big(1 + \varepsilon a(S)(v \cdot S)\Big).$$

Then we obtain a chemotaxis model with chemotactic sensitivity

$$\chi(S) = \frac{s^2}{n}(a(S) + b(S)),$$

hence both effects combine in a linear way.

3. If myxobacteria encounter a stream of myxobacteria moving in a given direction b, then they also turn into that direction. This can be expressed through a special kernel of

$$T(v, v') = \kappa(v \cdot b)(v' \cdot b).$$

In addition we consider the perturbed turning rate (2.28). The parabolic limit is of chemotaxis form

$$p_{0,t} = \nabla(D\nabla p_0 - V(p_0, S)\nabla S)$$

with nonisotropic diffusion

$$D = \frac{s^2}{\mu_0 n}\left(\mathbb{I} + \frac{|V|s^2}{n}\kappa bb^T\left(\mathbb{I} - \frac{|V|s^2}{n}\kappa bb^T\right)^{-1}\right).$$

Unfortunately, we have not been able to give a biological interpretation of this diffusion tensor.

4. It is also possible to include volume constraints into the transport equation framework. For example choosing

$$\mu(S) = \mu_0\Big(1 - \varepsilon b(S)(v \cdot \nabla S)\beta(\int p dv)\Big),$$

where β is a decreasing function. Then

$$p_{0,t} = \nabla(d\nabla p_0 - p_0\beta(p_0)\chi(S)\nabla S),$$

which is the volume filling chemotaxis model as introduced by Hillen and Painter [28].

2.4.7 Persistence

An important biological quantity is the *persistence*. It is an indicator for the particles to keep their heading when doing a turn. A particle which never changes direction, i.e. performs a ballistic motion, would have persistence 1, while a Brownian particle has persistence 0. The persistence in the context of transport models is easily defined. Consider a given incoming velocity v'. Then the expected outgoing velocity is

$$\hat{v}(v') := \int_V T(v, v')v dv$$

and the average outgoing speed is

$$\hat{s} := \int_V T(v, v')\|v\| dv.$$

The *index of persistence* ψ_α is defined as

$$\psi_\alpha(v') = \frac{\hat{v} \cdot v'}{\hat{s}s'} \text{where } s' = \|v'\|.$$

Hence the parameter γ, which we introduced in Theorem 6 is the persistence of the adjoint turning operator, or the adjoint persistence.

Exercise It is an interesting exercise to find out under which conditions is $\gamma = \psi_\alpha$. This is certainly true for a symmetric kernel, but is it also true for normal kernels?

2.4.7.1 Example

Assume that turning depends only on the relative angle

$$\theta := \arccos\left(\frac{v \cdot v'}{\|v\|\|v'\|}\right).$$

Then $T(v, v') = h(\theta(v, v')) = h(\theta - \theta'), h(-\theta) = h(\theta)$. For example, in 2-dimensions, with $s = 1$, we have $v = \begin{pmatrix} \cos\theta \\ \sin\theta \end{pmatrix}$ and for normalization we need

$$\int_V T(v, v')dv = \int_0^{2\pi} h(\theta - \theta')d\theta = 1.$$

This is equivalent to

$$\int_{-\theta'}^{2\pi-\theta'} h(\alpha)d\alpha = 2\int_0^{\pi} h(\alpha)d\alpha = 1.$$

The expected outgoing velocity is

$$\begin{aligned}
\hat{v}(\theta') &= \int h(\theta-\theta')\begin{pmatrix}\cos\theta\\ \sin\theta\end{pmatrix}d\theta, \text{ and with } \alpha := \theta-\theta' \\
&= \int h(\alpha)\begin{pmatrix}\cos(\alpha+\theta')\\ \sin(\alpha+\theta')\end{pmatrix}d\alpha \\
&= \int h(\alpha)\begin{pmatrix}\cos\alpha\cos\theta'-\sin\alpha\sin\theta'\\ \sin\alpha\cos\theta'+\cos\alpha\sin\theta'\end{pmatrix}d\alpha \\
&= \begin{pmatrix}\cos\theta'\int h(\alpha)\cos\alpha d\alpha-\sin\theta'\int \underbrace{h(\alpha)\sin\alpha}_{=0}\,d\alpha \\ \cos\alpha'\int \underbrace{h(\alpha)\sin\alpha}_{=0}\,d\alpha+\sin\theta'\int h(\alpha)\cos\alpha d\alpha\end{pmatrix} \\
&= \int h(\alpha)\cos\alpha d\alpha\begin{pmatrix}\cos\theta'\\ \sin\theta'\end{pmatrix}.
\end{aligned}$$

Then the persistence is given as

$$\begin{aligned}
\psi_\alpha &= \hat{v}(\theta')\cdot v' = \int h(\alpha)\cos\alpha d\alpha(\cos\theta'\cdot\sin\theta')\begin{pmatrix}\cos\theta'\\ \sin\theta'\end{pmatrix} \\
&= \int h(\alpha)\cos\alpha d\alpha,
\end{aligned}$$

where we can see why the persistence is sometimes called the *mean cosine*.

It is similar in 3-dimensions, where we normalize as:

$$2\pi\int_0^\pi h(\theta)\sin\theta d\theta = 1$$

and the persistence turns out to be (we skip the details):

$$\psi_\alpha = 2\pi\int_0^\pi h(\theta)\cos\theta\sin\theta d\theta$$

Again this is a mean cosine using the correct θ component of the 2-dimensional surface element in 3-D: $sin\theta d\theta$.

Persistence indices are easy to measure based on the above formulas, i.e. one follows individual particle tracks and computes the mean cosine for all the turns. It has been found that slime mold *Dictyostelium discoideum* have a persistence of about $\psi_\alpha = 0.7$, whereas the persistence of *E. coli* bacteria is about $\psi_\alpha = 0.33$.

2.4.8 *Summary and Conclusions*

In this section we considered the parabolic limit of transport equations in the case of constant equilibrium distribution. The general conditions (T1)–(T4) allowed us to develop a full theory including classifications into isotropic and anisotropic diffusion and including standard chemotaxis models. However, some important examples such as $T(v, v') = q(v)$ are not included, and the question of what to do with these cases remains. We recommend the following original publications for extended theory and applications to glioma growth and wolf movement.

2.5 Further Reading for Transport Equations in Oriented Habitats

Transport equations for movement in oriented habitats falls outside the theory developed here. In fact, as we have seen in example Sect. 2.3.4.2, these models do not satisfy condition (T4), and also condition (T3) is problematic. Hence the mathematical framework needs to be changed accordingly. The key is a split of the $L^2(V)$ space into the kernel of L and it's orthogonal complement. We are unable to develop this theory here, hence we just refer to the pertinent literature for further reading on theory and applications. While these applications were not discussed here, the material of this chapter should provide the reader with the tools that they need to understand the further readings.

- In [27, 49] we introduced a transport equation model for the migrative movement of mesenchymal cells in collagen tissues. Careful modelling and simulations revealed effects to network formations and finger-like invasions of cancer metastasis.
- In [31] the theory is formally extended to the case of oriented habitats. We not only consider the parabolic scaling, but we also discuss alternative scaling methods such as the hyperbolic scaling and the moment closure method, and we discuss their relations. One example in [31] is an application to wolf movement along seismic lines.
- In [13, 50] the transport equation framework is developed for application to brain tumor spread (glioma, glioblastoma multiform). We make extensive use of a new MRI imaging technique called diffusion tensor imaging (DTI). The nonisotropic diffusion limit of a transport model allows us to include DTI imaging into a glioma spread model. The above manuscripts contain the modelling details and we are currently working on model validation with clinical data.
- In [34] we develop a fully measure-valued solution theory for the transport equations. Measure valued solutions arise naturally in highly aligned tissues and the classical L^1 or L^2 theories for transport equations are no longer sufficient. We

were able to use this framework to identify non classical *pointwise steady states*, which explain observed network structures.
- in [58] we give a full analysis of the one-dimensional transport model for movement in oriented habitats.

Acknowledgements We are grateful for CIME to support this interesting summer school and who invited us to contribute this book chapter. We also thank Dr. K. Painter for continued collaboration and his support of these lecture notes. The work of TH and AS is supported by NSERC grants.

K.P. Hadeler [22] has published a book chapter entitled *Reaction Random Walk Systems* where the results of our Sect. 2.2.6 are discussed in great detail. Hadeler's book chapter arose as one of the CIME lecture notes from a workshop in 1997. We are honoured to be able to continue Hadeler's work through these CIME notes on transport equations.

References

1. H.C. Berg, D.A. Brown, Chemotaxis in Escherichia coli. Analysis by three-dimensional tracking. Nature **239**, 500–504 (1972)
2. A. Bressan, *Hyperbolic Systems of Conservation Laws* (Oxford University Press, Oxford, 2000)
3. C. Cercignani, R. Illner, M. Pulvirenti, *The Mathematical Theory of Diluted Gases* (Springer, New York, 1994)
4. F.A.C.C. Chalub, P.A. Markovich, B. Perthame, C. Schmeiser, Kinetic models for chemotaxis and their drift-diffusion limits. Monatsh. Math. **142**, 123–141 (2004)
5. J.B. Conway, *A Course in Functional Analysis* (Springer, New York, 1985)
6. J.C. Dallon, H.G. Othmer, A discrete cell model with adaptive signalling for aggregation of Dictyostelium discoideum. Philos. Trans. R. Soc. Lond. B **352**, 391–417 (1997)
7. R. Dautray, J.-L. Lions, *Mathematical Analysis and Numerical Methods for Science and Technology* (Springer, Heidelberg, 2000)
8. Y. Dolak, C. Schmeiser, Kinetic models for chemotaxis: hydrodynamic limits and spatio-temporal mechanics. J. Math. Biol. **51**, 595–615 (2005)
9. G.A. Dunn, J.P. Heath, A new hypothesis of contact guidance in tissue cells. Exp. Cell Res. **101**(1), 1–14 (1976)
10. R. Eftimie, Hyperbolic and kinetic models for self-organized biological aggregations and movement: a brief review. J. Math. Biol. **65**(1), 35–75 (2012)
11. R. Eftimie, G. de Vries, M.A. Lewis, Complex spatial group patterns result from different animal communication mechanisms. Proc. Natl. Acad. Sci. **104**, 6974–6979 (2007)
12. K.J. Engel, R. Nagel, *One-Parameter Semigroups for Linear Evolution Equations* (Springer, New York, 2000)
13. C. Engwer, T. Hillen, M. Knappitsch, C. Surulescu, A DTI-based multiscale model for glioma growth including cell-ECM interactions. J. Math. Biol. **71**(3), 551–582 (2015)
14. R. Erban, H. Othmer, From signal transduction to spatial pattern formation in E. coli: a paradigm for multiscale modeling in biology. Multiscale Model. Simul. **3**(2), 362–394 (2005)
15. R. Fürth, Die Brownsche bewegung bei berücksichtigung einer Persistenz der Bewegungsrichtung. Z. Phys. **2**, 244–256 (1920)
16. A. Giese, R. Bjerkvig, M.E. Berens, M. Westphal, Cost of migration: invasion of malignant gliomas and implications for treatment. J. Clin. Oncol. **21**(8), 1624–1636 (2003)
17. A. Giese, L. Kluwe, B. Laube, H. Meissner, M.E. Berens, M. Westphal, Migration of human glioma cells on myelin. Neurosurgery **38**(4), 755–764 (1996)
18. S. Goldstein, On diffusion by discontinuous movements and the telegraph equation. Q. J. Mech. Appl. Math. **4**, 129–156 (1951)

19. K.P. Hadeler, Travelling fronts for correlated random walks. Can. Appl. Math. Q. **2**, 27–43 (1994)
20. K.P. Hadeler, Travelling fronts in random walk systems. FORMA Jpn. **10**, 223–233 (1995)
21. K.P. Hadeler, Reaction telegraph equations and random walk systems, in *Stochastic and Spatial Structures of Dynamical Systems*, ed. by S.J. van Strien, S.M. Verduyn Lunel (Royal Academy of the Netherlands, Amsterdam, 1996), pp. 133–161
22. K.P. Hadeler, Reaction transport systems, in *Mathematics Inspired by Biology*, ed. by V. Capasso, O. Diekmann. Lecture Notes in Mathematics, vol. 1714, CIME Letures 1997, Florence (Springer, New York, 1999), pp. 95–150
23. P.R. Halmos, V.S. Sunder, *Bounded Integral Operators on L2 Spaces* (Springer, Heidelberg, 1978)
24. T. Hillen, A Turing model with correlated random walk. J. Math. Biol. **35**, 49–72 (1996)
25. T. Hillen, Qualitative analysis of semilinear Cattaneo systems. Math. Models Methods Appl. Sci. **8**(3), 507–519 (1998)
26. T. Hillen, On the L^2-closure of transport equations: the general case. Discrete Contin. Dyn. Syst. Ser. B **5**(2), 299–318 (2005)
27. T. Hillen, M^5 mesoscopic and macroscopic models for mesenchymal motion. J. Math. Biol. **53**(4), 585–616 (2006)
28. T. Hillen, Existence theory for correlated random walks on bounded domains. Canad. Appl. Math. Q. **18**(1), 1–40 (2010)
29. T. Hillen, H.G. Othmer, The diffusion limit of transport equations derived from velocity jump processes. SIAM J. Appl. Math. **61**(3), 751–775 (2000)
30. T. Hillen, K.J. Painter, A user's guide to PDE models for chemotaxis. J. Math. Biol. **58**, 183–217 (2009)
31. T. Hillen, K.J. Painter, Transport and anisotropic diffusion models for movement in oriented habitats. in *Dispersal, Individual Movement and Spatial Ecology: A Mathematical Perspective*, ed. by M. Lewis, P. Maini, S. Petrovskii (Springer, Heidelberg, 2013), p. 46
32. T. Hillen, A. Stevens, Hyperbolic models for chemotaxis in 1-d. Nonlinear Anal. Real World Appl. **1**(1), 409–433 (2001)
33. T. Hillen, C. Rohde, F. Lutscher, Existence of weak solutions for a hyperbolic model for chemosensitive movement. J. Math. Anal. Appl. **260**, 173–199 (2001)
34. T. Hillen, P. Hinow, Z.A. Wang, Mathematical analysis of a kinetic model for cell movement in network tissues. Discrete Contin. Dyn. Syst. B **14**(3), 1055–1080 (2010)
35. T. Hillen, K. Painter, A. Swan, *Modelling with Transport Equations in Biology* Springer (in preparation)
36. E.E. Holmes, Are diffusion models too simple ? a comparison with telegraph models of invasion. Am. Nat. **142**, 779–795 (1993)
37. D. Horstmann, From 1970 until present: the Keller-Segel model in chemotaxis and its consequences I. Jahresberichte der DMV **105**(3), 103–165 (2003)
38. D.D. Joseph, L. Preziosi, Heat waves. Rev. Mod. Phys. **61**, 41–73 (1988)
39. M. Kac, A stochastic model related to the telegrapher's equation. Rocky Mt. J. Math. **4**, 497–509 (1956)
40. E.F. Keller, L.A. Segel, Initiation of slime mold aggregation viewed as an instability. J. Theor. Biol. **26**, 399–415 (1970)
41. M.A. Krasnoselskii, *Positive Solutions of Operator Equations* (P. Noordhoff, Groningen, 1964). English translation of Russian original
42. F. Lutscher, A. Stevens, Emerging patterns in a hyperbolic model for locally interacting cell systems. J. Nonlinear Sci. **12**, 619–640 (2002)
43. H.W. McKenzie, Linear features impact predator-prey encounters: analysis and first passage time, 2006. M.Sc. thesis, University of Alberta
44. H.W. McKenzie, E.H. Merrill, R.J. Spiteri, M.A. Lewis. How linear features alter predator movement and the functional response. R. Soc. Interface Focus **2**(2), 205–216 (2012)
45. A. Okubo, S.A. Levin, *Diffusion and Ecological Problems: Modern Perspectives* (Springer, New York, 2002)

46. H.G. Othmer, S.R. Dunbar, W. Alt, Models of dispersal in biological systems. J. Math. Biol. **26**, 263–298 (1988)
47. H.G. Othmer, T. Hillen, The diffusion limit of transport equations II: chemotaxis equations. SIAM J. Appl. Math. **62**(4), 1122–1250 (2002)
48. H.G. Othmer, C. Xue, Multiscale models of taxis-driven patterning in bacterial populations. SIAM Appl. Math. **70**(1), 133–167 (2009)
49. K.J. Painter, Modelling migration strategies in the extracellular matrix. J. Math. Biol. **58**, 511–543 (2009)
50. K.J. Painter, T. Hillen, Mathematical modelling of glioma growth: the use of diffusion tensor imaging DTI data to predict the anisotropic pathways of cancer invasion. J. Theor. Biol. **323**, 25–39 (2013)
51. A. Pazy, *Semigroups of Linear Operators and Applications to Partial Differential Equations* (Springer, New York, 1983)
52. B. Perthame, *Transport Equations in Biology* (Birkhäuser, Boston, 2007)
53. B. Pfistner, A one dimensional model for the swarming behavior of myxobacteria, in *Biological Motion*, ed. by W. Alt, G. Hoffmann. Lecture Notes on Biomathematics, vol. 89 (Springer, New York, 1990)
54. H. Poincaré, Sur la propagation de l'électricité. Compt. Rend. Ac. Sci. **117**, 1027–1032 (1893)
55. D.W. Stroock, Some stochastic processes which arise from a model of the motion of a bacterium. Probab. Theory Relat. Fields **28**, 305–315 (1974)
56. G.I. Taylor, Diffusion by discontinuous movements. Proc. Lond. Math. Soc. **20**(1), 196–212 (1920)
57. M.E. Taylor, *Partial Differential Equations III* (Springer, New York, 1996)
58. Z.A. Wang, T. Hillen, M. Li, Mesenchymal motion models in one dimension. SIAM J. Appl. Math. **69**(2), 375–397 (2008)
59. M.L. Ware, M.S. Berger, D.K. Binder, Molecular biology of glioma tumorgenesis. Histol. Histopathol. **18**, 207–216 (2003)
60. E. Zauderer, *Partial Differential Equations*, 3rd edn. (Wiley, Hoboken, 2006)

Chapter 3
Mathematical Models of the Interaction of Cells and Cell Aggregates with the Extracellular Matrix

L. Preziosi and M. Scianna

Abstract It is nowadays understood that the interactions cells have with the fibrous environment they live in determine their behaviour. In fact, for instance, they play a fundamental role in cell motion, in tumour invasion and metastatization, in stem cell differentiation, and in tissue development.

In this chapter, we will describe several models that deal with different aspects characterizing these interactions. In particular, from the tutorial point of view, the topic will be used as a playground to briefly present several modelling frameworks, e.g., age-structured models, individual cell-based models, continuum mechanics, and mixture theory.

The models presented will be usually characterised by multiscale aspects because, for instance, the physical parameters determining cell motion and duplication are affected by the expression of proteins inside the cell and of receptors at its membrane. In turn, the behaviour of cellular aggregates and of tissues depends on the behaviour of single cells. For this reason, some upscaling tool will also be described.

3.1 Biological Relevance of Cell-ECM Interaction

Soft tissues are made of many cell types that live in a fibrous and aqueous environment. The fibrous infrastructure, that is generally called extracellular matrix and shortened as ECM, is a collection of filamentary molecules secreted by specific cell types, mainly fibroblasts. The ECM provides structural and biochemical support to the ensemble of cells. Its composition can considerably change, as it is made of several insoluble constituents like collagen, elastin, proteoglycan, fibronectin, all interlinked to form a structured network. The ECM is either found in the interstitial space between cells (in this case it is also called *interstitial matrix*) or arranged in thin sheets of fibers called *basement membranes*, that separate the epithelium

L. Preziosi (✉) • M. Scianna
Dipartimento di Scienze Matematiche, Politecnico di Torino, Torino, Italy
e-mail: luigi.preziosi@polito.it; marcosci1@alice.it

L. Preziosi et al. (eds.), *Mathematical Models and Methods for Living Systems*,
Lecture Notes in Mathematics 2167, DOI 10.1007/978-3-319-42679-2_3

from the connective tissue. In the following, for sake of simplicity we will often consider blood and lymphatic vessels as part of the ECM: in fact they are strongly cross-linked with matrix fibers, though the relative characteristic cross section is considerably different (collagen-like bundles are at least one order of magnitude less than a μm in diameter, white blood and lymphatic vessels are at least one order of magnitude larger than a μm in size) (Fig. 3.1). In this respect, the ensemble of ECM fibers and vessels will be hereafter denoted as extracellular network and shortened as ECN.

Cell behavior is significantly regulated by specific interactions between cells and their surrounding environment, in particular with the ECM. These signal exchanges, largely mediated by transmembrane adhesion molecules, among which integrins are the most important ones, give also rise to feedback mechanisms on the environment itself, as cells has the ability to modify it.

Specifically, cell-ECM interactions are fundamental in determining both migration-related phenomena, such as wound healing and spread of metastasis, and proliferation-related phenomena, such as tumor growth, tissue development, and homeostasis.

It is known that, in addition to the well known phenomenon of *chemotaxis*, i.e., the motion toward higher concentration of a soluble chemical factor called chemoattractant, there are several cell migratory modes affected by cell-matrix interactions:

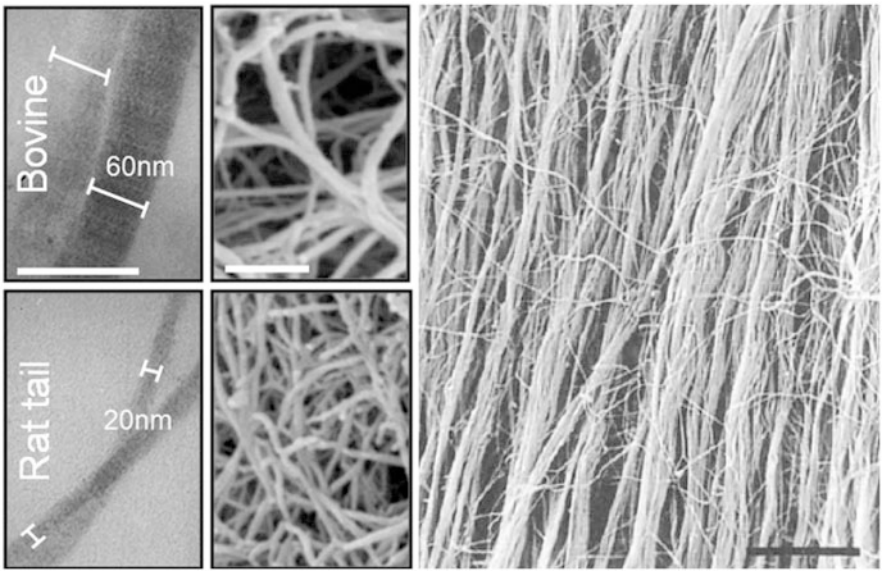

Fig. 3.1 Morphological characteristics of bovine (*top*) and rat tail (*bottom*) collagen fibrils (*left*) and network (*right*). Images partially modified from [84]. On the *right*, arrangement of collagen fibrils in thicker fibers of the lamina radialis of an aortic valve leaflet (scale bar, 8 μm)

- *haptotaxis*, i.e., cell preferential movement towards regions with higher concentrations of cellular adhesion sites or substrate-bound chemoattractants [10];
- *durotaxis*, i.e., cell migration towards regions of the matrix with a higher rigidity [43]. In more details, when the substratum is heterogeneous from a mechanical point of view, cells lying in a softer region tend to move away if they encounter along their way a stiffer region. *Viceversa*, cells lying in a stiffer region tend to stay away from softer regions they encounter along their way;
- cell crawling towards stretching forces and away from compressive forces, in the sense that if a substratum is stretched (e.g., with a pipette tip) in a point say leftward, then a cell on the immediate right will move left (toward the micropipette) and a cell on the immediate left will move left (away from the micropipette);
- cell directional locomotion along the fibers of a strongly anisotropic substratum [14].

In addition, it is widely know from experimental data that composition, mechanical properties, and microstructure of matrix environments can influence cell migration as well. In this respect, as we shall discuss in more details in the last section, two important processes are involved in cell response to mechanical cues coming from the ECM environment, thereby gaining an increasing attention from biologists and biomedical engineers: *Mechanosensing* and *Mechanotransduction*. The former defines how cells sense the mechanical forces around them, i.e., either through membrane-bound ion channels, that open or close up under stress or shear to modulate the influx/outflux of ions, or through a direct transmission of stress and shear from the ECM to the actin cytoskeleton (via adhesion complexes and transmembrane adhesion protein, e.g., of the integrin family). The latter has to do with the effective cell response to mechanical cues. This can be done either directly, i.e., by the expression of genes in the nucleus when it is pulled by the actin cytoskeleton, or through the activation of several chemical pathways. As an example, a stretch acting on an adhesion molecule called Talin causes the unfolding of the molecule with the consequent exposure of some binding sites that might trigger selected downstream protein cascades [25, 70] (see Fig. 3.2).

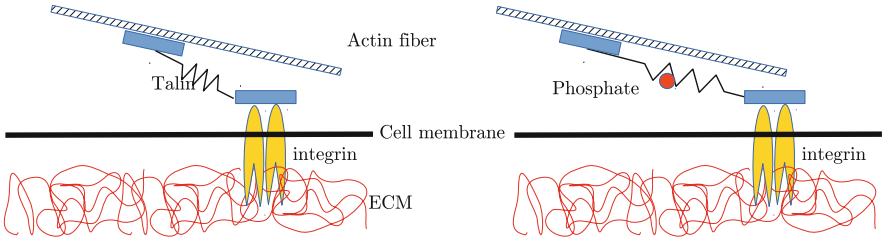

Fig. 3.2 Mechanotransduction by the mechanically induced unfolding of Talin

Of course, cell behavior and homeostasis, as well as growth, survival, and death, strongly depend on many chemical factors, that are dissolved in the extracellular liquid and are uptaken or produced by the cells themselves.

From a mathematical viewpoint, a proper description of such a complex system can be very hard and strongly depends on the scale of interest. It is clear that what occurs at the cellular and subcellular level (i.e., the so-called *microscopic scale*) has a very relevant role but, in order to describe the behavior of soft tissues, in most cases it is preferable to work at the super-cellular level (i.e., the so-called *macroscopic scale*). The number of cells involved in tissue dynamics is in fact excessive to be dealt with by single cell-based approaches.

In order to understand the basic difficulties we refer to, it is useful to imagine the following ideal experiment. Consider a soft tissue (for instance, a liver or a small tumor mass) or an artificial scaffold: they both look homogeneous. Then cut from them several smaller specimens: also these specimens may look identical from a macroscopic point of view. However, their microscopic configuration is completely different, as each specimen is characterized by an own distribution of cells, vessels, collagen fibres, matrix pores. This implies that the deformation under stress of single cells and/or of extra-cellular matrix components, the motion of the interstitial fluid in the intracellular space, the flow in blood and lymphatic vessels, or the pathways of diffusing chemicals in the extra-cellular space will be dramatically different, at the microscopic level, from specimen to specimen. One could even say that the experiment is not microscopically repeatable, since it is not possible for other researchers to exactly cut the same specimen. Also the same researcher would have a very hard time in obtaining the same microscopic measurements, although he could use the same specimen, since the slightest change in initial or boundary condition would result in considerable differences in the microscopic evolution of the system. For this reason, many experiments need be done and some averaging over the experiments is needed in order to take care of the variability of the geometric characteristics of the specimen.

In addition, it is technically almost impossible to give an exact description of the microscopic evolution the system from both the theoretical and the experimental point of view. Luckily, the interest in achieving such a level of details is very little. The interest in fact generally lies in obtaining a description of some "gross features" of the behavior of the tissue, such as the mechanical behavior of the tissue, the uptake of drug, the growth of the mass, the oxygenation of the tissue, and so on. These macroscopic features, which might probably be obtained through some averaging, need to be predictable, repeatable, insensible to small changes in initial and boundary conditions. Clearly, measuring average concentrations and velocities gives little information about the microscopic behavior, for instance, of the living cells of the tissue, but the information is probably quite appropriate for the biomedical purposes under consideration.

However, understanding the microscopic behavior of cells and their interactions with the other constituents, and in particular with the ECM, is fundamental to deduce constitutive modelling that properly reflect the microscopic phenomena.

In this chapter we will describe several models dealing with different aspects of cell-ECM interaction. In particular, Sect. 3.2 will describe a mathematical model of cell-ECM adhesion that takes into account of bond rupture and renewal to get to the type of macroscopic relationship to be expected as a function of the microscopic phenomena.

Section 3.3 will describe a continuum mechanics model able to analyze the role of cell nucleus in cell motion. The nucleus in fact the most voluminous and rigid subcellular organelle and therefore constitutes a steric hindrance for cell migration in tight and dense ECM networks.

Section 3.4 will introduce an individual cell-based model called cellular Potts model that, in this specific case, is able to mimic the dynamics of single cells moving in microchannels and in fibrous networks. This model points out that the cell migratory behavior is mainly dependent on the relation between the nucleus dimensions and the characteristic size of the surrounding matrix environment. In this respect, optimal cell movement is observed in matrix structures larger than the nucleus diameter but smaller than the diameter of the overall cell [62, 65]. These results are also confirmed by a wide range of experimental data, as for instance in [13, 52].

Section 3.5 will then give the basic knowledge of mixture theory that is applied in Sect. 3.6 to deduce a macroscopic model of cell aggregates and tumor masses. As a relevant feature, such an approach accounts the results obtained by the model described in the previous sections.

Finally, Sect. 3.7 will briefly compare passive and active motion of cell aggregates in an ECN. In particular, chemotaxis will be modelled either as an external force or as an internal active reaction of the cell, which is able to pull on the ECM to move towards the source of the chemical factor. Some perspectives on modelling mechanosensing and mechanotransduction is given in the last section as well.

3.2 A Model of Cell-ECM Adhesion

The modelling of cell movement in physiological environments has to account a common bias. Even in the "easiest situation" cells do not swim in a liquid, but rather they struggle to find their way in an extremely thick gel. The reason relies in the order of magnitude of the Reynolds number that they experience during motion. The Reynolds number is given by $Re = UL/\nu$, where U is the characteristic velocity of the body, L its characteristic size, and ν is the kinematic viscosity of the fluid. All self-propelling bodies that are familiar to us, from fishes to ourselves, from ships to airplanes, move in situations characterized by high Reynolds numbers. For instance, being the kinematic viscosity of water about $10^{-6}\,\mathrm{m}^2/\mathrm{s}$ the order of magnitude of the Reynolds number of swimmers in a swimming pool may range between 10^5 and 10^6 according to whether they are practitioners or athletes. Fishes can be faster, but are usually smaller: so, in this case, the order of magnitude of the Reynolds number is closer to $10^3 - 10^4$. Cells are much smaller (i.e., $L_{cell} \approx 10\,\mu\mathrm{m}$) and move much

slower. For instance, a fish keratocyte, one of the fastest cell types, crawls on gel substrata at a speed of 15 μm/min, while spermatozoa swim at a speed of 50 μm/s. Indeed, the resulting Reynolds number is of the order of 10^{-6} for the former and of the order of 10^{-4} for the latter. Life at this low Reynolds number is completely different [59]. As a comparison, a person swimming even in peanut butter (or better Nutella chocolate cream) at a speed of 1 m/min would only experience a Reynolds number of the order 0.1. In order to go down to the values experienced by cells, one should move in asphalt or in just molten glass at 500 °C at a speed of 1 m/s. This is probably very hard, because it needs a huge strength. More realistically, fixing the force that a swimmer can apply to move in a fluid, using Stokes drag law it can be observed that its velocity will be nearly inversely proportional to the kinematic viscosity of the fluid he/she is swimming in. This means that in a chocolate cream the swimmer will move slowlier and the relative Reynolds number will be of the order of 10^{-4}. However, this motion rather than swimming would be more similar to grabbing on the "extremely viscous fluid" to make a hole in it and have a stroke to move forward. In this respect, the motion of a spermatozoum is much closer to that of a corkscrew penetrating a cork than that of a helix of a boat rotating in the sea.

Similarly, when cells are moving in the ECM, they are grabbing to the fibers, exerting forces through the adhesion bonds, and advancing in the tissue by detaching bonds in their rear part and making new ones at their front edge. In this process, the life-cycle of each single cell-ECM adhesion bond consists of three phases:

1. formation in a relaxed configuration;
2. stretching while the cell is moving with respect to the ECM;
3. disruption.

3.2.1 Evolution of the Distribution of Adhesion Bonds

In this section we want to present a model describing the attachment-detachment process of cell-ECM adhesive bonds. In order to do that we consider the ensemble of cells and the surrounding ECM as two constituents of a mixture, i.e., in any physical point of the domain both cells and ECM can coexist. Referring to Sect. 3.6 where the details of mixture theory will be introduced, here it is enough to consider the motion of cells and ECM as given by two maps $\chi_c(\mathbf{X}_c, t)$ and $\chi_m(\mathbf{X}_m, t)$, respectively. Referring to Fig. 3.3, an adhesive bond between cells and ECM is activated if the two constituents locally superpose at a given time (i.e., if a material cell point and a material ECM point superpose at a given time). In this respect, if a cell-ECM bond has an age a and is formed in the point $\mathbf{x}_b$, then

$$\chi_m(\mathbf{X}_m, t-a) = \chi_c(\mathbf{X}_c, t-a) = \mathbf{x}_b.$$

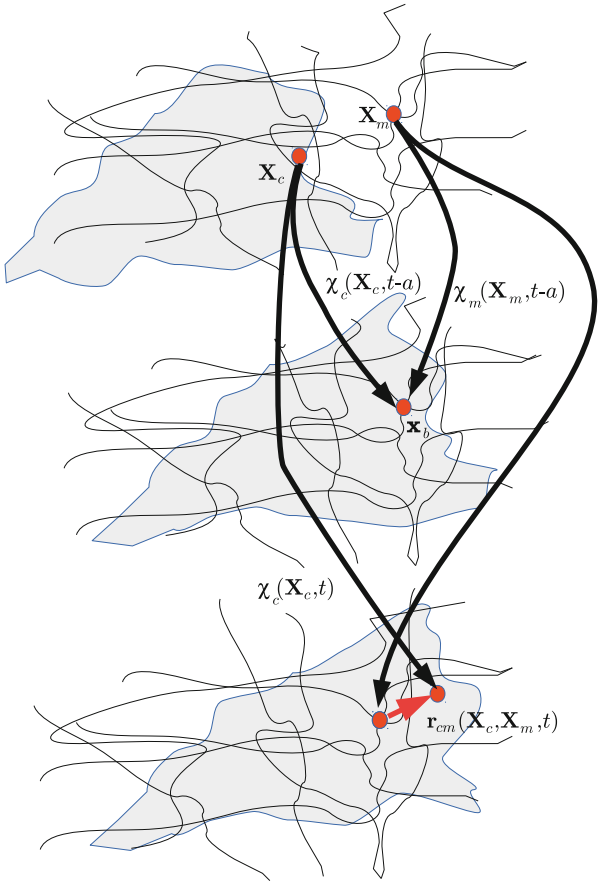

Fig. 3.3 Superposition of material points of cells and ECM. We advice the reader that in spite of the fact that for descriptive purposes the two components are represented as a fiber network and a cell, a material point has to be considered much bigger than the one drawn, i.e., it contains many focal adhesion points and many cells

Following [57], the present stretching of the bond (and its possible rupture) can be assumed to depend on the present relative distance between the cell and the ECM points that had come in contact at time $t - a$, i.e.,

$$\mathbf{r}_{cm}(\mathbf{X}_c, \mathbf{X}_m, t) = \chi_c(\mathbf{X}_c, t) - \chi_m(\mathbf{X}_m, t)\,. \tag{3.1}$$

Referring to again the diagram in Fig. 3.3 and recalling that the body points $\mathbf{X}_c$ and $\mathbf{X}_m$ were superposed at time $t - a$, we remark that

$$\mathbf{X}_m = \chi_m^{-1}(\mathbf{x}_b, t-a) = \chi_m^{-1}(\chi_c(\mathbf{X}_c, t-a), t-a)\,. \tag{3.2}$$

The vector field $\mathbf{r}_{cm}$ can then be written as a function of $(\mathbf{X}_c, a, t)$ as

$$\mathbf{r}_{cm}(\mathbf{X}_c, a, t) = \chi_c(\mathbf{X}_c, t) - \chi_m(\chi_m^{-1}(\chi_c(\mathbf{X}_c, t-a), t-a), t)\,. \tag{3.3}$$

The *microscopic force* $\widehat{\mathbf{F}}_{cm}^{mic}(\mathbf{X}_c, \mathbf{X}_m, t)$ acting on $\mathbf{X}_c$ because of the adhesive interaction with $\mathbf{X}_m \in \mathcal{B}_m^*$ can be assumed to depend on position, age of the bonds and time through $\mathbf{r}_{cm}$, i.e.,

$$\widehat{\mathbf{F}}_{cm}^{mic}(\mathbf{X}_c, \mathbf{X}_m, t) = \mathbf{F}_{cm}^{mic}(\mathbf{r}_{cm}(\mathbf{X}_c, a, t))\,. \tag{3.4}$$

In [57], it was proved that if the renewal time of a bond is much shorter than the characteristic time needed by a cell to move across a cell length or, equivalently, if the stretch of the bond is much smaller than the cell size, then Eq. (3.3) can be simplified by a Taylor expansion to

$$\mathbf{r}_{cm} \simeq a\ (\mathbf{v}_c(\mathbf{x}, t) - \mathbf{v}_m(\mathbf{x}, t))\ , \tag{3.5}$$

where $\mathbf{x} = \chi_c(\mathbf{X}_c, t)$ in order to simplify the notation. Equation (3.5) simply states that, as a first approximation, the stretching of the bond is proportional to its age and to the relative velocity of the points of the cell and of the ECM that were connected by the adhesion bond at time $t - a$. In other words, (3.5) means that

$$\frac{\partial \mathbf{r}_{cm}}{\partial a} = \mathbf{v}_c(\mathbf{x}, t) - \mathbf{v}_m(\mathbf{x}, t)\,. \tag{3.6}$$

The continuum assumption requires that in a material point of the domain there are many focal adhesion points that for instance had formed in several instants in the past. From the modelling point of view, this means that the ensemble of bonds has to be described through a distribution function over the age. In this respect, the total interaction force exchanged in $\mathbf{X}_c$ at any given time t, which results from all the active cell-ECM bonds, can be written as

$$\mathbf{m}_{cm}^{ad}(\mathbf{X}_c, t) = \int_0^{+\infty} \mathbf{F}_{cm}^{mic}(\mathbf{r}_{cm}(\mathbf{X}_c, a, t))\mu(da)\,, \tag{3.7}$$

where the measure $\mu(da)$ is related to the density of bonds with age in the interval $[a, a + da]$ and is given by

$$\mu(da) = f_{cm}(\mathbf{X}_c, a, t)\, da\,,$$

$f_{cm}(\mathbf{X}_c, a, t)$ being the distribution function of bonds linking $\mathbf{X}_c$ to the other point $\mathbf{X}_m$ that was superimposed to $\mathbf{X}_c$ at time $t - a$.

Therefore, the number density of bonds formed at time t is

$$N_{cm}(\mathbf{X}_c, t) = \int_0^{+\infty} f_{cm}(\mathbf{X}_c, a, t)\, da\,, \tag{3.8}$$

and

$$A = \frac{1}{N} \int_0^{+\infty} a f_{cm}(\mathbf{X}_c, a, t)\, da\,,$$

is the bonds mean age.

Recalling classical methods used in structured population dynamics or in kinetic theories, the distribution function evolves according to

$$\dot{f}_{cm} := \frac{\partial f_{cm}}{\partial t} + \frac{\partial f_{cm}}{\partial a} = -\eta_{cm}, \tag{3.9}$$

where η_{cm} describes detachment processes while the bond is aging and possibly stretching.

Focusing on the dependence of the detachment rate η_{cm} on the microscopic force $\mathbf{F}_{mic}$, we can assume that a bond breaks up at a rate that depends both on the magnitude of the microscopic force exerted on it and on its age, that is,

$$\eta_{cm}(\mathbf{X}_c, a, t) = \zeta_{cm}(F_{cm}^{mic}(\mathbf{r}_{cm}(\mathbf{X}_c, a, t)), a) f_{cm}(\mathbf{X}_c, a, t)\,, \tag{3.10}$$

where $F_{cm}^{mic} = |\mathbf{F}_{cm}^{mic}|$.

In the next section we will explain how to deduce ζ_{cm} either from some experimental data or from proper assumptions on its dependence from the microscopic force.

3.2.2 The Quasi-Stationary Limit

The aim of this section is to relate the microscopic measurement with the macroscopic constitutive laws defining the interaction force $\mathbf{m}_{cm}^{ad}$. A way to upscale the information obtained at the subcellular level is suggested by Ölz and Schmeiser, who solved in [51] a similar problem when dealing with actin cytoskeleton dynamics.

To do that, we first need to join Eq. (3.9) with a proper boundary condition. We could take the rate of bond formation to be constant but, as will soon be evident, this would lead to a paradox. In fact, if the cell barely moves, bonds always form but hardly break. So, in the limit, an infinite number of bonds forms, resulting therefore in an infinite adhesion force. To address this issue, it is useful to observe that a cell can locally expose on its membrane only a maximum amount of integrins. Indeed, the number density N_{max} of active bonds per unit volume is, in a first approximation,

proportional to the volume ratio occupied by the cells, or better to the ratio of cell-ECM contact area per unit volume. In this respect, we can assume that the formation of new bonds is proportional to the bonds that can still be formed, i.e., recalling (3.8),

$$f_{cm}(\mathbf{X}_c, a=0, t) = \beta\,(N_{max} - N_{cm}(\mathbf{X}_c, t))$$

$$= \beta\left(N_{max} - \int_0^{+\infty} f_{cm}(\mathbf{X}_c, a, t)\,da\right). \tag{3.11}$$

Using again the assumption that the bond breaking length is much smaller than cell diameter, it is possible to work in the quasi-stationary limit

$$\begin{cases} \dfrac{\partial f_{cm}}{\partial a}(\mathbf{X}_c, a) = -\zeta_{cm}(F_{cm}^{mic}(\mathbf{r}_{cm}(\mathbf{X}_c, a)), a) f_{cm}(\mathbf{X}_c, a)\,, \\ f_{cm}(\mathbf{X}_c, a=0) = \beta\left(N_{max} - \displaystyle\int_0^{+\infty} f_{cm}(\mathbf{X}_c, a)\,da\right). \end{cases} \tag{3.12}$$

This limit is studied from the analytic point of view in [49].

Denoting by

$$Z_{cm}(\mathbf{X}_c, a) = \int_0^a \zeta_{cm}(F_{cm}^{mic}(\mathbf{r}_{cm}(\mathbf{X}_c, \alpha)), \alpha)\,d\alpha\,,$$

for any ζ_{cm}, the boundary value problem in (3.12) can be solved explicitly to get

$$f(\mathbf{X}_c, a) = \frac{\beta N_{max} \exp\left[-Z_{cm}(\mathbf{X}_c, a)\right]}{1 + \beta \displaystyle\int_0^{+\infty} \exp\left[-Z_{cm}(\mathbf{X}_c, a)\right]\,da}\,, \tag{3.13}$$

and, from (3.7),

$$\mathbf{m}_{cm}^{ad} = \frac{\beta N_{max} \displaystyle\int_0^{+\infty} F_{cm}^{mic}(\mathbf{r}_{cm}(\mathbf{X}_c, a)) \exp\left[-Z_{cm}(\mathbf{X}_c, a)\right]\,da}{1 + \beta \displaystyle\int_0^{+\infty} \exp\left[-Z_{cm}(\mathbf{X}_c, a)\right]\,da}\,. \tag{3.14}$$

Taking

$$\mathbf{F}_{cm}^{mic}(\mathbf{r}_{cm}(\mathbf{X}_c, a)) = -k_{cm}^{mic}\mathbf{r}_{cm}(\mathbf{X}_c, a)\,, \tag{3.15}$$

where k_{cm}^{mic} is the elastic constant of a microscopic bond, and recalling (3.5), we have that

$$\mathbf{F}_{cm}^{mic} = -k_{cm}^{mic} a(\mathbf{v}_c - \mathbf{v}_m)\,. \tag{3.16}$$

and therefore

$$\mathbf{m}_{cm}^{ad} = \frac{-k_{cm}^{mic}\beta N_{max}\displaystyle\int_0^{+\infty} a \exp\left[-\int_0^a \zeta_{cm}(k_{cm}^{mic} v_{rel}\alpha)d\alpha\right] da}{1+\beta\displaystyle\int_0^{+\infty} \exp\left[-\int_0^a \zeta_{cm}(k_{cm}^{mic} v_{rel}\alpha)d\alpha\right] da}(\mathbf{v}_c - \mathbf{v}_m)\,,$$

with $v_{rel} = |\mathbf{v}_c - \mathbf{v}_m|$.

In the following, it will be useful to rewrite the integrals in (3.14) in terms of the microscopic force rather than of the age of the bond, i.e.,

$$|\mathbf{m}_{cm}^{ad}| = \frac{N_{max}\displaystyle\int_0^{+\infty} Fe(F)\,dF}{W + \displaystyle\int_0^{+\infty} e(F)\,dF}\,, \tag{3.17}$$

where $W = k_{cm}^{mic} v_{rel}/\beta$ and

$$e(F) = \exp\left[-\frac{1}{k_{cm}^{mic} v_{rel}}\int_0^F \zeta(\phi)\,d\phi\right]. \tag{3.18}$$

Equations (3.2.2) or (3.17) state the dependence of the cell-ECM macroscopic interaction force from the microscopic characteristics of the cell-ECM adhesion bonds. In particular, cell-ECM macroscopic adhesiveness relies on the density of bonds exposed along the cell membrane, the contact area between cells and ECM per unit volume, the rate of bond formation, the bond rigidity, and the detachment rate. In this respect, it can be regarded as a *multiscale* link between models operating at different scales.

3.2.3 Examples of Interaction Forces

Given a proper law of bond detachment ζ_{cm}, Eq. (3.14) is able to determine the corresponding interaction force $\mathbf{m}_{cm}$. For instance, assuming a constant renewal of bonds

$$\zeta_{cm} = \zeta_0\,,$$

that is independent from the force acting on them. Then from (3.14) one obtains

$$\frac{\mathbf{m}_{cm}^{ad}}{N_{max}} = -\frac{k_{cm}^{mic}}{\zeta_0}\frac{\gamma}{1+\gamma}(\mathbf{v}_c - \mathbf{v}_m)\,, \tag{3.19}$$

where $\gamma = \beta/\zeta_0$. Equation (3.19) is a Darcy's-like relationship, i.e., a classical drag law that asserts the proportionality between the adhesive interaction force and the relative velocity.

In three-dimensional settings, the cell-ECM interaction force, in addition to the above-mentioned adhesive part, is determined by a further contribution, which is due to the tortuosity of the extracellular matrix and therefore to the fact that cells have to move in an intricate network of fibres. In this respect, when a cell moves from a point to another point of the network (see Fig. 3.4a), even in absence of adhesive interactions, it crawls in a sort of porous medium. The corresponding contribution

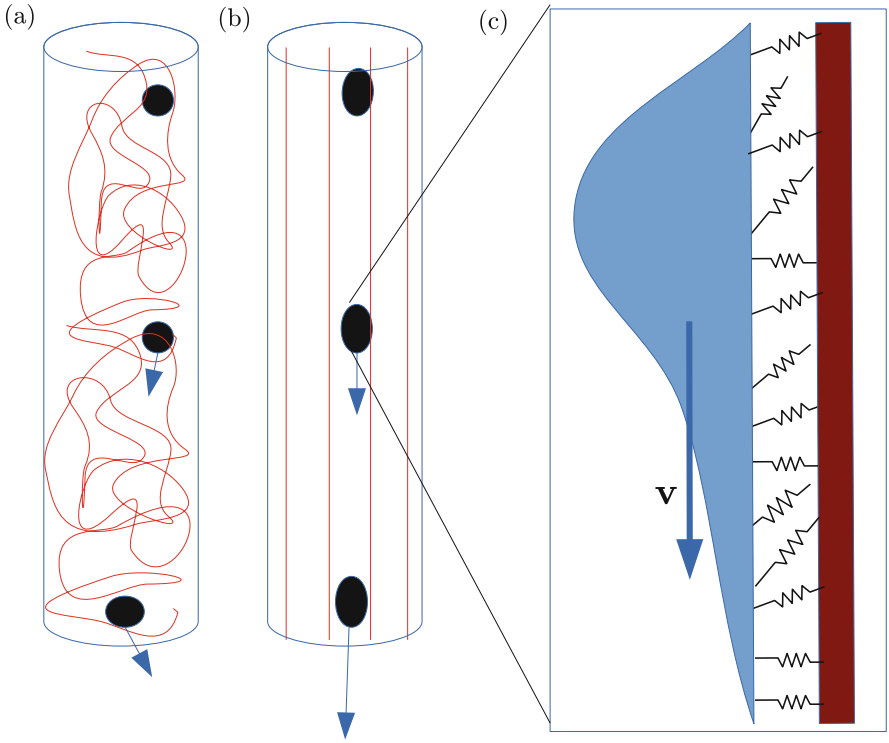

Fig. 3.4 Schematic representation of possible cell-ECM interactions. (**a**) Effect of fiber tortuosity. (**b**)–(**c**) Effect of cell-ECM adhesiveness

of the interaction force can be modelled again by a Darcy's-like law:

$$\mathbf{m}_{cm}^{D}(\mathbf{x},t) = -\frac{1}{M_D(\mathbf{x},t)}(\mathbf{v}_c(\mathbf{x},t) - \mathbf{v}_m(\mathbf{x},t))\,. \tag{3.20}$$

where M_D is a motility coefficient through the porous ECM in absence of adhesiveness.

It is useful to remark that the adhesive interaction term (3.19) has a different origin and therefore it is present even if cells move in an ideal straight channel in the ECM with the force aligned to it. In this case cells would in fact experience a traction force $\mathbf{m}_{cm}^{ad}$, resulting from the adhesive interaction with the ECM (see Fig. 3.4b).

However, it is true that, in the case of a constant renewal of bonds (i.e., independent from the force acting on them), the two contributions are similar and therefore can be merged, obtaining a general linear relationship of the following type

$$\mathbf{m}_{cm}(\mathbf{x},t) = -\frac{1}{M(\mathbf{x},t)}(\mathbf{v}_c(\mathbf{x},t) - \mathbf{v}_m(\mathbf{x},t))\,, \tag{3.21}$$

where M can be interpreted as a *motility coefficient*. In fact, for a given interaction, force small values of M result in small relative velocities. In anisotropic situations the motility coefficient should be replaced by a *motility tensor* able to describe those cases in which the motility depends on the direction of motion, e.g., it is easier to move along ECM fibers than across them. So, Eq. (3.21) rewrites as

$$\mathbf{m}_{cm}(\mathbf{x},t) = -\mathbf{M}^{-1}(\mathbf{x},t)(\mathbf{v}_c(\mathbf{x},t) - \mathbf{v}_m(\mathbf{x},t))\,. \tag{3.22}$$

Conversely, from the above discussion it appears evident that when in mathematical models one assumes that the interaction force is proportional to the relative velocity, it is implicitly assumed that bonds renewal at the membrane is independent from the force acting on them.

This assumption is sufficiently consistent when dealing with developmental issues and embryonic tissues as, in those cases, adhesive links are weak and cells are very motile. However, in the case of mature tissues, different hypotheses need be done. For example, one can introduce the possibility that bonds constantly renew only after a threshold microscopic force F_0, that is

$$\zeta_{cm}(F_{cm}^{mic}) = \zeta_0 H(F_{cm}^{mic} - F_0)\,, \tag{3.23}$$

where H is the Heavyside function. In this case,

$$\frac{|\mathbf{m}_{cm}^{ad}|}{N_{max}} = F_0 \frac{\frac{1}{2} + \gamma\omega + \gamma^2\omega^2}{1 + (1+\gamma)\omega}\,, \tag{3.24}$$

where $\omega = \dfrac{k_{cm}^{mic} v_{rel}}{\beta F_0}$.

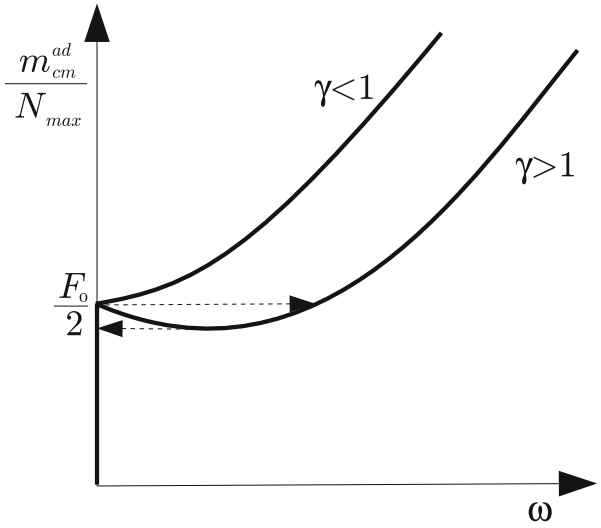

Fig. 3.5 Macroscopic adhesion laws when $\zeta_{cm}(F^{mic}) = \zeta_0 H(F^{mic} - F_0)$

Then, for small relative velocities, $|\mathbf{m}_{cm}^{ad}|$ behaves like $F_0 N_{max}[1 + (\gamma - 1)\omega]/2$ while for large relative velocities it goes to the oblique asymptote

$$|\mathbf{m}_{cm}^{ad}| = F_0 N_{max}\left[\frac{\gamma}{(1+\gamma)^2} + \frac{\gamma}{(1+\gamma)}\omega\right].$$

This behavior, shown in Fig. 3.5, is compatible with the one proposed in [56] based on the assumption that if cells are not pulled strong enough, they move together with the ECM. If the force overcomes the threshold $F_0 N_{max}/2$, cells instead detach from the ECM. If, then, the rate of formation of new bonds is faster than the rate of detachment, i.e., $\gamma > 1$, then the relative velocity increases with the force. Otherwise, if the rate of formation of new bonds is slower than the rate of detachment, i.e., $\gamma < 1$, then the force-relative velocity relation decreases to increase back again at higher values of relative velocity. This means that when the interaction force increases over the threshold, the velocity jumps to the branch on the right of the graph in Fig. 3.5 following the rightward arrow. If then the force is lowered again, then upon reaching the minimum the relative velocity jumps back to zero (following the leftward arrow in Fig. 3.5), giving rise to a sort of mesenchymal-epithelial transition. Adding Darcy's contribution (3.20) substantially does not modify the above discussion but for the identification of the presence of a minimum or not, now identifiable by the value of γ.

In spite of the simplicity of (3.19) and (3.24), however, it is more proper to obtain ζ_{cm} from assumptions or experimental data focused on the bond-breaking distribution $b(F_{cm}^{mic})$ (e.g., those in Fig. 3.6). The distribution $b(F_{cm}^{mic})$ has a compact

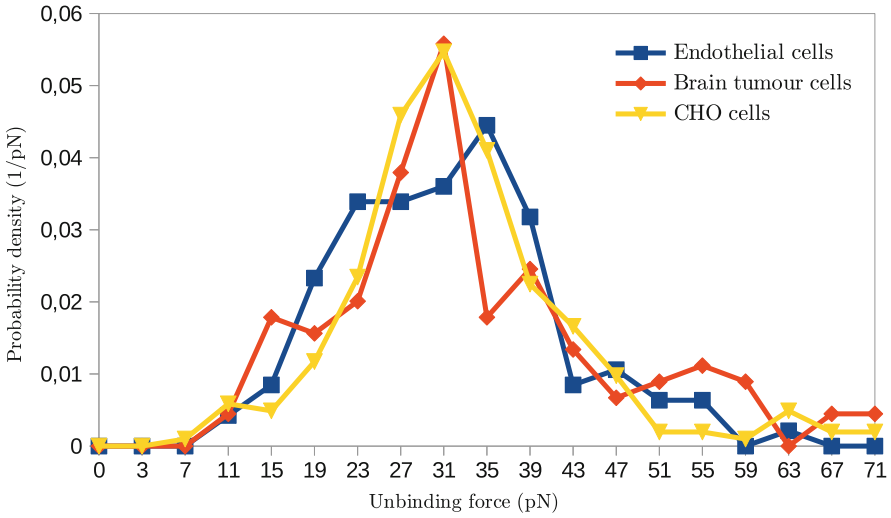

Fig. 3.6 Distribution function of the force of unbinding events (data from [71])

support, namely it vanishes for $F_{cm}^{mic} > F_M$ as a result of the fact that after a maximal sustainable force all bonds will break.

In this respect, one has that

$$\zeta_{cm}(F_{cm}^{mic}) = \frac{b(F_{cm}^{mic})}{B(F_{cm}^{mic})} = -\frac{1}{B(F_{cm}^{mic})}\frac{dB}{da}(F_{cm}^{mic}), \tag{3.25}$$

where, because of Eq. (3.16),

$$\zeta_{cm}(F_{cm}^{mic}) = -\frac{k^{mic}v_{rel}}{B(F_{cm}^{mic})}\frac{dB}{dF_{cm}^{mic}}(F_{cm}^{mic}), \qquad \text{for} \quad F_{cm}^{mic} < F_M, \tag{3.26}$$

where F_M is the sup of the support of b and

$$B(F_{cm}^{mic}) = \int_{F_{cm}^{mic}}^{F_M} b(\phi)\, d\phi \tag{3.27}$$

is the survival function. If, as discussed before, there is a minimal force F_0 needed to break adhesion bonds, then $b = 0$ for $F_{cm}^{mic} < F_0$, and therefore from(3.25) $\zeta_{cm}(F_{cm}^{mic}) = 0$. For a similar reason $\zeta_{cm}F_{cm}^{mic} = 0$ also for $F_{cm}^{mic} > F_M$.

Integration by parts gives that the mean value of $b(F)$ is

$$m_b = F_0 + \int_{F_m}^{F_M} \frac{B(F)}{B(F_0)}\, dF, \tag{3.28}$$

where F_0 is the inf of the support of b, while the standard deviation σ is given by

$$\sigma^2 = F_0^2 + 2\int_{F_m}^{F_M} F\frac{B(F)}{B(F_0)}\,dF - m_b^2\,. \tag{3.29}$$

Of course, different breaking distributions would give rise to different macroscopic forces. However, it can be observed that $e(F)$ in (3.18) is given by

$$e(F) = \frac{B(F)}{B(F_0)}\,. \tag{3.30}$$

Obviously, $e(F) = 1$ for $F < F_0$, and $e(F_M) = 0$. We can then extend $e(F)$ and $B(F)$ assuming that they vanish for $F > F_M$. Hence, from (3.17), (3.28), and (3.29), we obtain

$$\frac{|\mathbf{m}_{cm}^{ad}|}{N_{max}} = \frac{\dfrac{F_0}{2} + \displaystyle\int_{F_0}^{F_M} \frac{FB(F)}{F_0B(F_0)}\,dF}{1+\omega+\displaystyle\int_{F_0}^{F_M}\frac{B(F)}{B(F_0)}\,dF} = \frac{\sigma^2+m_b^2}{2(\omega F_0+m_b)}\,, \tag{3.31}$$

that decreases from $b_0 = (1+\frac{\sigma^2}{m_b^2})\frac{m_b}{2}$ to zero as the relative velocity increases. This is due to the fact that at high relative velocities, bonds brokage is more frequent than bonds formation, whose characteristic rate is given by β. Also in this case there is a threshold stress determining cell detachment. We remark that m_b and σ are properties of the bond-breaking distribution function that can be experimentally measured. For instance, in [71] $m_b \approx 28, 29, 29$ pN and $\sigma \approx 10, 9, 10$ pN, respectively for Chinese hamster ovary cells, malignant human brain tumor cells, and human endothelial cells, respectively. Higher values can be deduced from the data in [2], that gives $m_b \approx 73$ pN and $\sigma \approx 38$ pN in the case of VE-cadherin-Fc fusion protein.

Referring to Fig. 3.7, it should be noticed that, when $\mathbf{m}_{cm}^{ad}$ and $\mathbf{m}_{cm}^{D}$ are summed, we have

$$\mathbf{m}_{cm} = -N_{max}\frac{\sigma^2+m_b^2}{2(\omega F_0+m_b)}\frac{\mathbf{v}^c-\mathbf{v}^m}{v_{rel}} - M(\mathbf{v}_c-\mathbf{v}_m)\,, \tag{3.32}$$

so that $|\mathbf{m}_{cm}|$ might have a minimum for

$$v_{rel} = \sqrt{\frac{(\sigma^2+m_b^2)\beta}{2k^{mic}M}} - \frac{\beta m_b}{k^{mic}}\,, \qquad \text{if} \quad \frac{2\beta M}{k^{mic}N_{max}} < 1+\frac{\sigma^2}{m_b^2}\,.$$

$|\mathbf{m}_{cm}|$ then grows to infinity because $|\mathbf{m}_{cm}^{D}|$ becomes dominant. The behavior is then similar to the one shown in Fig. 3.5.

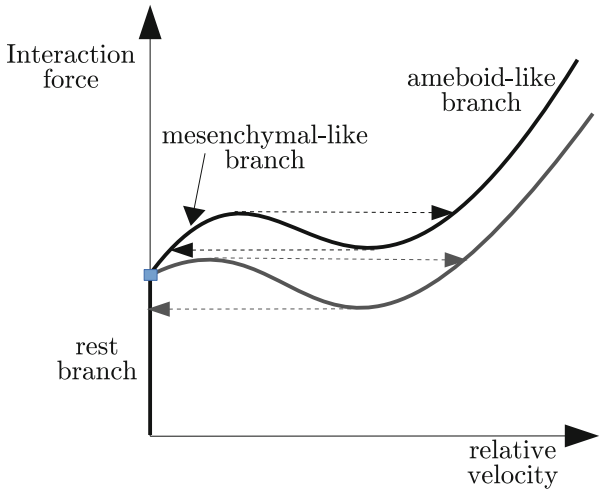

Fig. 3.7 Sketch of the interaction forces. The *right-pointed arrows* indicate a transition that resembles the one between mesenchymal and ameboid motion. The *left-pointed arrows* indicate either the reverse transition (*upper*) or a transition to rest (*lower*). The *little square* indicates a transition from rest to a mesenchymal-type motion

Without entering in the details of the computation (we refer to [57] for that), if we consider in addition to a force-driven detachment, as the one just described, a continuous renewal of the bonds (as the one giving rise to (3.21)) or a continuous renewal after a minimal force (as the one giving rise to (3.24)) then one has a total interaction force characterized by a cubic-like curve, as the one shown in Fig. 3.7. The branch on the left, that starts from the origin if $F_0 = 0$ and away from it if $F_0 \neq 0$, can be denoted as *mesenchymal-like* branch, whereas the one on the right can be referred as the *ameboid-like* branch. The former is in fact characterized by smaller velocities and is adhesion-dominated, while the latter is characterized by larger velocities and is more related to cell difficulties in moving within the network of fibres.

So, if the stress acting on cells is too high they might jump to the ameboid-like or Darcy branch. Otherwise, when the stress decreases below the minimum, they will jump to the adhesion-dominated or mesenchymal-like branch. Such a behavior resembles an ameboid-to-mesenchymal transition (black arrows), or possibly an ameboid-to-epithelial transition (gray arrows). It is however necessary to advise the reader that the above description is a strong simplification of reality: we in fact neglect selected chemical mechanisms and cascades involved in the overall process.

An interesting dynamics can be described by the following reasoning: Referring to Fig. 3.8, assume that the interaction force is fixed (the dashed line in the figure) and to have different clones characterized by different relationships between interaction force and relative velocity, and specifically different intersections with the interaction force axis. The clone corresponding to the top figure will stay at

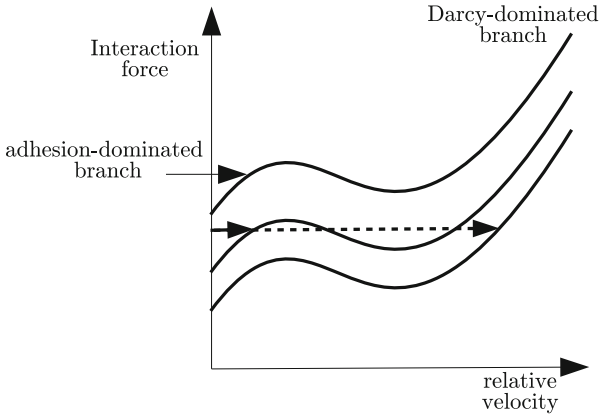

Fig. 3.8 Behavior of a cell experiencing a given interaction force depending on the relationship between interaction force and relative velocity. In the case of the *upper curve*, the cell will stay at rest. In the case of the *middle curve* it will slowly move (*full arrow*). In the case of the *lower curve* it will move much faster (*dotted arrow*)

rest, while the one corresponding to the curve in the middle will slowly move (thicker arrow). For the clone corresponding to the bottom curve the cell can move even faster (thinner arrow) going directly to what we called ameboid-like branch or Darcy-dominated branch.

Summarizing, in our opinion, the key features characterizing the relationship between the microscopic properties of the cell-ECM detachment rate and the properties of the macroscopic interaction force are the following:

- the absence of a minimal force needed to trigger detachment, i.e., $F_0 = 0$, leads to an interaction force initially proportional to the relative velocity between cells and ECM;
- on the opposite, the presence of a minimal force needed to start breaking the adhesion bonds, i.e., $F_0 \neq 0$, leads to a threshold behavior also for the interaction force, in the sense that below a given value there is no relative motion between cells and ECM;
- finally, the existence of a maximal force sustained by cell-ECM bonds leads to a regime that is dominated by Darcy's contribution.

3.3 Modelling the Influence of the Nucleus

The discussion done in the previous section has not taken into account of the presence of the nucleus, which is the stiffest subcellular organelle. This might be a plausible hypothesis when dealing with two-dimensional motions of cells over substrates. In fact, in these cases cell-ECM interactions occur below the cell and

therefore the nucleus can freely move in the physiological liquid above the ECM. In three-dimensional set-ups, things are very different. In fact, when passing through dense and rigid ECMs the nucleus needs to considerably deform and squeeze in the narrow gaps present in the network. In this respect, the migration capabilities of the cell mainly relies both on the microstructure of the ECM and on the deformability of the nucleus because of the high compliance of the cytosol.

In this section, we will briefly describe a continuous model (developed in [21]), able to describe the effect of nucleus remodelling on a cell trying to penetrate a narrow 3D structure. Although *in vivo* fibre structures and bundles are arranged into really complex networks (i.e., characterized by strongly varying local densities that create pores and gaps of different dimensions), the problem is here simplified by considering the ECM as a parallel cylindrical channel, composed of fibres and bundles that provide directional guidance cues to cells. This is of course a strong assumption. However, it can represent a good approximation of more regular scaffolds used in tissue engineering. Moreover, it can help to make a first step towards the description of the *in vivo* phenomenon.

3.3.1 Modelling the Deformation of the Elastic Nucleus

In order to penetrate into pores smaller than the its dimension, the nucleus has to deform. The amount of energy required depends on the mechanical characteristics both of the nucleus and of its membrane, as well as on the shape adapt to squeeze within the ECM structure. For sake of simplicity, in [21], the matrix-like environment is assumed to be organized as a microchannel of radius R_p. Although in that work different conditions have been analyzed, we here will only present the case in which the nucleus is assumed to be elastic, with a negligible contribution from the membrane, and will eventually deform into an ellipsoid, as represented in Fig. 3.9 (bottom) while the overall cells is assumed to achieve a cigar-like shape.

This is consistent with experimental observations [36, 80], which have provided that if matrix pores have a cylindrical shape, as in an artificial regular microchannel, the nucleus acquires an elongated morphology, with the longer axis aligned with the axis of the microchannel. Cell elongation is also associated with the formation of actin bundles on either sides of the nucleus, that are responsible of the nuclear deformation and help maintaining the deformed configuration by generating compressive forces [80]. The shape of the deformed nucleus can therefore be approximated by a prolate ellipsoid [80, 82], with smaller axis R_p and the larger axis equal to R_n^3/R_p^2 where R_n is the initial stress-free radius of the nucleus, so that the deformation preserves the volume of the nucleus. As found in [21] and shown in next Fig. 3.10, the case in which the cell nucleus is deformed in a cigar-like shape leads to the same behavior not only from the qualitative but also from the quantitative viewpoint.

Let us assume that all the energy required by the cell to completely penetrate into the microchannel is spent to deform its internal solid nucleus, which is treated as an elastic material. We recall once again that in fact the cytoplasm can easily invade

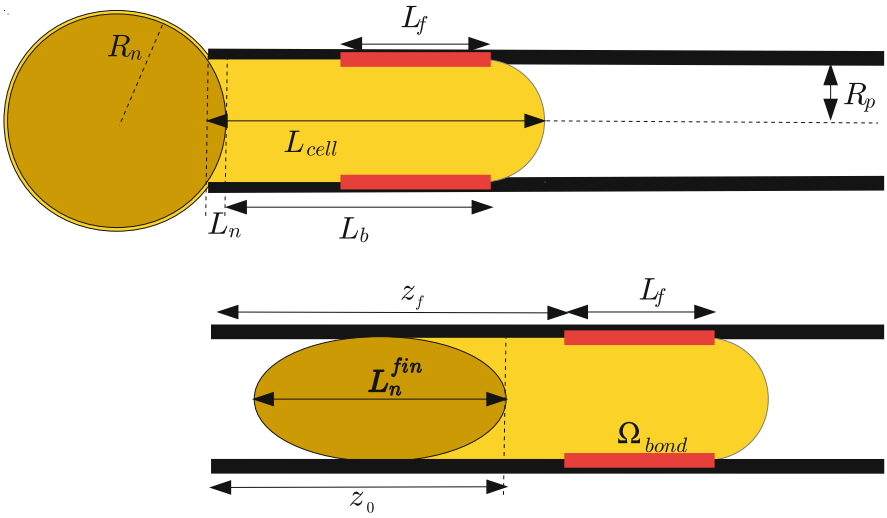

Fig. 3.9 Schematic representation of cell displacement and nucleus deformation

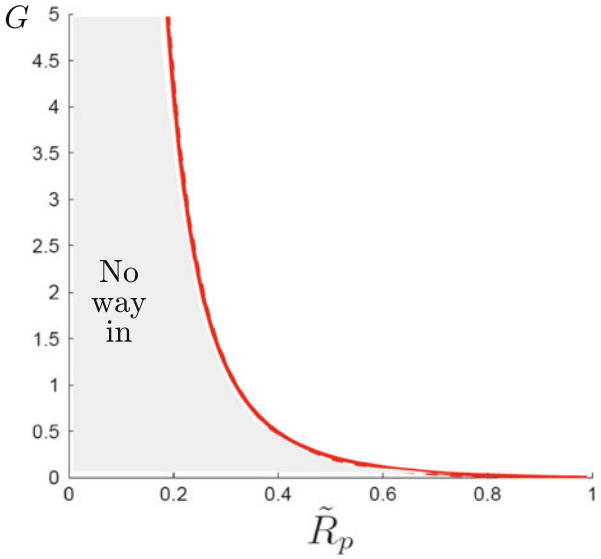

Fig. 3.10 Entry criterium for cell nucleus deforming on an ellipsoid to penetrate a microchannel. The result for a cigar-like shape is also show by a *dashed line*, but it is nearly undistinguishable

the channel due to its high deformability. The energy required to deform the initially spherical shape of the nucleus to the shape it takes to get in the microchannel can then be compared with the work that can be done by the adhesion traction forces the cell can exert in order to advance in the microchannel.

To compute the energy required to deform the nucleus, we have to set a proper constitutive equation, that represents the response of the material to deformations, and then to calculate the deformation gradient $\mathbf{F}$. For sake of simplicity, we assume that the nucleus behaves like an incompressible neo-Hookean material, so that the elastic stored energy per unit volume is given by

$$\mathcal{W} = \frac{\mu}{2}[\mathrm{tr}\,\mathbf{C} - 3]\,, \tag{3.33}$$

where $\mathbf{C} = J^{2/3}\mathbf{F}^T\mathbf{F}$, $J = \det\mathbf{F}$, and μ is the shear modulus of the nucleus.

The deformation of a sphere in a prolate ellipsoid with the same volume is simply given by a uniaxial deformation

$$\mathbf{F} = \mathrm{diag}\left\{\frac{R_p}{R_n}, \frac{R_p}{R_n}, \frac{R_n^2}{R_p^2}\right\}\,,$$

where R_n is the radius of the spherical nucleus. Therefore, Eq. (3.33) yields to

$$\mathcal{W} = \frac{\mu}{2}\left(2\frac{R_p^2}{R_n^2} + \frac{R_n^4}{R_p^4} - 3\right)\,,$$

which, integrated over the total volume V of the initial sphere, gives the total energy required to pass from the initial to the final configuration, namely

$$\mathcal{W}_{tot} = \int_V \mathcal{W}\,dV = \frac{2}{3}\pi\mu R_n^3\left(2\frac{R_p^2}{R_n^2} + \frac{R_n^4}{R_p^4} - 3\right)\,. \tag{3.34}$$

The above Eq. (3.34) links the elastic energy of deformation to the mechanical properties of the nucleus (μ) and to the radii both of the nucleus itself (R_n) and of the pore (R_p).

3.3.2 Modelling the Cell Traction Force

To describe cell entry into ECM channels, a fundamental step is the definition of the adhesive forces that are necessary for cell deformation and subsequent migration. Such an adhesive force can be thought as the resultant of all forces generated by single cell-ECM bonds on the surface of contact through the contraction of cytoskeletal elements. In this respect, adhesion can be modulated by the density of expressed and activated integrins on the membrane, i.e., $\rho_b = N_{integrin}/S_{cell-ECM}$ (where $N_{integrin}$ is the number of integrins over the surface of contact between the cell and the ECM, which is identified by $S_{cell-ECM}$), and by the density of

substratum ligands (ECM adhesive sites) covering the surface of the microchannel, here represented by the ECM surface ratio, $\alpha_{ECM} = S_{ECM}/S_{channel}$.

As previously commented, we assume that the cytoplasm can easily penetrate inside the channel without any effort (see Fig. 3.9), so that the action of adhesive bonds has the effect of:

- translating the cytosolic region, that keeps the same shape with a tip that is modelled as a spherical cap;
- leading to the advancement of the nucleus that, being at the entrance of the microchannel, needs also to deform to penetrate into the structure.

We can say that the length of the region of the cytoplasm in front of the nucleus and in contact with the channel wall is approximately constant. We can further assume that on such a cylindrical surface, defined as Ω_{bond} in Fig. 3.9, adhesive bonds form and traction forces are exerted. The region Ω_{bond} can extend over to the entire cylindrical portion of the membrane of length L_b, especially when the size of the microchannel is not too small and therefore the cytoplasm does not protrude much within the microchannel. However, when the pore dimension is much smaller than the cell dimension, the cytoplasm will elongate considerably within the microchannel. In this case, it can be assumed that traction forces are exerted only in the portion of its membrane closer to the tip. In both cases, when the cytoplasm is completely inside the microchannel, it can be observed that the dimension of the domain Ω_{bond} is nearly constant throughout the penetration of the nucleus.

Accepting that the density of bonds on cell surface, ρ_b, and the portion of the channel wall composed of ECM adhesive sites, α_{ECM}, do not depend on time, the total adhesion force is

$$F_{ad} = \int_{\Omega_{bond}} \rho_b(\mathbf{x})\alpha_{ECM}(\mathbf{x})F_{bond}(\mathbf{x})\, d\Sigma\,,$$

where F_{bond} is the z-component of the force generated through cytoskeleton contraction, as a consequence of bond formation.

Although ρ_b and α_{ECM} may be generally functions of the space, in the homogeneous case, the equation above simplifies into

$$F_{ad} = \rho_b\alpha_{ECM}\int_{\Omega_{bond}} F_{bond}(\mathbf{x})\, d\Sigma = 2\pi R_p\rho_b\alpha_{ECM}\int_0^{L_b} F_{bond}(x, y, z_0 + \zeta)\, d\zeta\,.$$

The total adhesive force pulling the cell is therefore a function of the radius R_p of the microchannel, the density of bonds ρ_b, the surface fraction of the channel composed of extracellular matrix, α_{ECM}, and the integral of the single bond forces over the length of contact.

In particular, under the assumption that the length of the cylindrical section for which bonds are formed is given by the portion of the cell in front of the nucleus in

contact with the channel (see Fig. 3.9), we have that

$$L_b = L_{cell} - R_p - L_n \,,$$

where L_{cell} is the initial length of the cell inside the channel (which corresponds to the length of the deformed cytoplasm) and L_n is the portion of the nucleus that can enter the channel without any deformation. An easy geometrical reasoning, based on volume conservation both of the cytoplasm and of the nucleus, gives

$$\begin{aligned} L_{cell} &= R_p \left[\frac{4}{3} \frac{R_c^3 - R_n^3}{R_p^3} + \frac{1}{3} + \frac{L_n^2}{R_p^3} \left(R_n - \frac{L_n}{3} \right) \right] , \\ L_n &= R_n - \sqrt{R_n^2 - R_p^2} \,, \end{aligned} \tag{3.35}$$

where R_n the radius of the nucleus and R_c the radius of the cell. Once that a proper function representing bonds forces is provided the process of adhesive force description is accomplished.

We consider the case in which cells are able to form bonds only over a certain area of the contact region, e.g., the apical portion of the deformed cell with length L_f, i.e., $\Omega_{bond} = \{\mathbf{x} : \ r = R_p, \theta \in [0, 2\pi), z \in [z_f, z_f + L_f]\}$. Therefore, assuming a constant force F_b in the domain we can take

$$F_{bond}(z_0 + \zeta) = F_b H(\zeta - (L_b - L_f)) \,, \qquad \text{for} \quad 0 < \zeta < L_b \,,$$

where H is the Heaviside function, which means that if $L_b < L_f$ traction forces acts over the entire cylindrical portion of the domain ahead of the nucleus. Otherwise, if $L_b > L_f$ they act only on an apical portion having length L_f. Therefore, the total adhesive force is represented by the following relation

$$F_{ad} = 2\pi R_p \rho_b \alpha_{ECM} F_b \min\{L_b, L_f\} \,. \tag{3.36}$$

A similar relation would be achieved if the adhesive force do not act on a single interval but on a set of disconnected intervals, whose sum however is the same. It is in fact the sum of the sizes of the intervals that matters and not the specific localization and distribution of the "adhesive sites". Analogously, it would be possible to use a linear dependence of the force on the distance from the nucleus: in this case the result would be equal to the case in which the mean force is constantly exerted in the entire interval.

3.3.3 A Penetration Criterium from an Energy Balance

In order to penetrate into a microchannel, the total traction that the cell is able to exert must be larger than the deformation-related force exerted by the nucleus in the rear of the cell. In order to get an approximated criterium able to state if the cell is allowed to invade the subnuclear structure, in [21] the work that can be done by the traction force is compared with the elastic energy necessary to deform the nucleus.

In particular, the work required to have the cell completely inside the channel should be provided by adhesive forces which, using (3.36), can be written as

$$W_{ad} = F_{ad}L = 2\pi R_p \rho_b \alpha_{ECM} F_b \min\{L_b, L_f\} L\,,$$

where L is the total displacement of the cell nucleus after its penetration inside the channel, that is given by $L = L_n^{fin} - L_n$, where L_n^{fin} is the final length of the nucleus when it is totally inside the channel and L_n is the length of the nucleus that can freely enter the channel without any deformation (given by Eq. (3.35)). Then, for the ellipsoidal shape we have that

$$L = \frac{R_n^3}{R_p^2} - R_n + \sqrt{R_n^2 - R_p^2}\,.$$

The criterium relies on the observation that, in order to penetrate into the microchannel, the work done by the adhesion forces must be larger than the energy required to deform the nucleus, i.e.,

$$\mathcal{W}_{ad} \geq \mathcal{W}_{tot} = \frac{2}{3}\pi\mu R_n^3 \left(2\frac{R_p^2}{R_n^2} + \frac{R_n^4}{R_p^4} - 3\right)\,. \tag{3.37}$$

By scaling all distances with R_n and writing all material parameters on the right-hand-side, it is possible to identify a crucial dimensionless number

$$G = \frac{\rho_b \alpha_{ECM} F_b^M}{\mu}\,, \tag{3.38}$$

representing the ratio between adhesive bond properties and nuclear mechanical parameters. This number is characterized by the fact that at the numerator there are all the quantities related to the traction forces (adhesion bond densities, surface ratio of ECM, force exerted by bonds) whereas at the denominator we have the parameter describing the mechanical properties of the cell nucleus, namely its shear modulus.

From (3.37) we then have the criterium

$$G \geq \frac{2}{3} \frac{2\tilde{R}_p^2 + \dfrac{1}{\tilde{R}_p^4} - 3}{\left(\dfrac{2}{\tilde{R}_p^2} - 1 + \sqrt{1 - \tilde{R}_p^2} \right) \min\{\tilde{L}_b, \tilde{L}_f\}}, \tag{3.39}$$

drawn in Fig. 3.10, where $\tilde{R}_p = R_p/R_n$, $\tilde{L}_b = L_b/R_n$, and $\tilde{L}_f = L_f/R_n$.

The curve starts from 0 when the radius of the nucleus is equal to that of the microchannel, corresponding to the fact that in this case no work is necessary to penetrate the structure. On the other hand, it goes to infinity like $1/\tilde{R}_p^3$, when $\tilde{R}_p \to 0$.

It can be noticed that, for every $\tilde{R}_p$, it is possible to uniquely identify a minimum value of G above which the nucleus can be pulled inside the channel. Conversely, knowing nuclear mechanical and adhesive properties, it is possible to identify the minimum value of R_p that allows a nucleus of radius R_n to enter the channel.

Being G the ratio between adhesive and mechanical properties, Eq. (3.39) shows that cells with a more rigid nucleus (i.e., characterized by higher values of μ), should either increase the number of adhesive bonds (ρ_b), or the number of focal points in contact with ECM (α_{ECM}), or even bond strength (F_b).

This finding is in qualitative agreement with a number of experimental works, such as [3, 61, 84], where cell migratory capability is associated with nuclear deformations and the existence of critical channel radii above which cell can enter. Moreover, it is comparable with the results that will be described in the following section, confirming that mechanical properties of the nucleus can affect the cell entry into channels. Equation (3.39) can be of great value, for instance, in scaffold design. In fact, if cell mechanical properties and their capabilities to express bonds are known, it is then possible to evaluate the pore size that allows the cells to penetrate the rigid network.

3.4 Cell Migration by Cellular Potts Models

The model described in the previous section gives a criterium determining whether a cell is able or not to enter a microchannel or a ECM network, but it compares configurations without giving a dynamic idea on the phenomenon. In this respect, in order to describe the motion of single cells or of small aggregates, it is more convenient to use individual cell-based approaches. One of them is the cellular Potts model (CPM), i.e., a grid-based stochastic method able to mimic the behavior of cells using an energetic approach. In fact, the model relies on the assumption that cell behavior and interactions with the local microenvironment can be described by a generalized energy (or *hamiltonian*). In this respect, it is useful to clarify in advance that in reality cells use energy supplies to perform many tasks and actions (e.g., to

move, proliferate, perform task, do their job, even die). When using a CPM, the underlying hypothesis is that during their random migratory behavior, deformations of cells that require more energy are more unlike to happen.

3.4.1 Compartmentalized Cellular Potts Models

CPM simulation domains are d-dimensional regular lattices $\Omega \subset \mathbb{R}^d$, where $d = 2, 3$ (we will specify the spatial dimensions according to the specific application described in the following). Each lattice site $\mathbf{x} \in \Omega \subset \mathbb{R}^d$ is labeled by an integer number, $\sigma(\mathbf{x}) \in \mathbb{N}$, which can be interpreted as a degenerate *spin* originally coming from statistical physics [31, 54]. As classically adopted in CPM applications,

- the border of a lattice site $\mathbf{x}$ is identified by $\partial\mathbf{x}$;
- one of its neighbors by $\mathbf{x}'$;
- its overall neighborhood by $\Omega'_{\mathbf{x}}$, i.e.,

$$\Omega'_{\mathbf{x}} = \{\mathbf{x}' \in \Omega : \mathbf{x}' \text{ is a neighbor of } \mathbf{x}\} .$$

Subdomains of contiguous sites with identical spins form discrete objects $\Sigma_{\overline{\sigma}}$, i.e.,

$$\Sigma_{\overline{\sigma}} = \{\mathbf{x} \in \Omega : \sigma(\mathbf{x}) = \overline{\sigma}\} ,$$

which are characterized by an object type, $\tau(\Sigma_{\overline{\sigma}})$.

In all the cell-matrix systems of our interest, following the compartmentalized approach described in [63], each virtual cell, denoted by η, is defined as a compartmentalized element, composed of two subregions which, in turn, are classical CPM objects Σ_σ (see Fig. 3.11):

- The nucleus, a central cluster of type $\tau = N$;
- The surrounding cytosol, of type $\tau = C$.

Each cell compartment is obviously characterized, as an additional attribute, by the cluster id $\eta(\Sigma_\sigma)$ to identify the individual it belongs to.

The extracellular environment is differentiated in the interstitial fluid and a polymeric-like state, as typically employed for *in vitro* assays. The former is assumed to be reproduced by a single element of type $\tau = M$, that is isotropically distributed throughout the simulation domain. The latter represents either an ECM fiber network, or a bioengineered scaffold or microchannel structure. Referring to Fig. 3.11, it is treated as standard, non-compartmentalized CPM objects of type $\tau = P$.

Cell movement results from an iterative and stochastic reduction of a free energy of the overall system, defined by the *hamiltonian* H, whose expression will be clarified below. The core algorithm of CPMs is a modified Metropolis method for Monte Carlo-Boltzmann dynamics [22, 23, 48]. Procedurally, at each time step t,

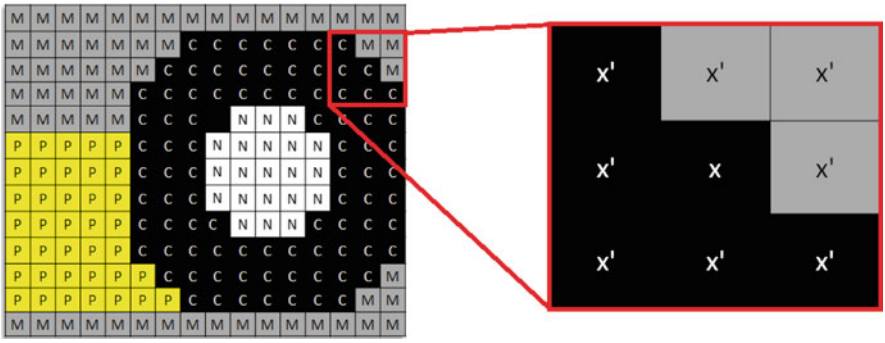

Fig. 3.11 A typical CPM grid and representation of a compartmentalized cell and of its extracellular environment. The cell is composed of the nucleus, a central cluster of type $\tau = N$, and of the surrounding cytosol of type $\tau = C$. The extracellular space is instead differentiated in a medium-like state ($\tau = M$) and a polymeric-like state ($\tau = P$). On the *right*, the eight lattice site surrounding $\mathbf{x}$ represent the neighborhood of $\mathbf{x}$ denoted by $\Omega'_{\mathbf{x}}$

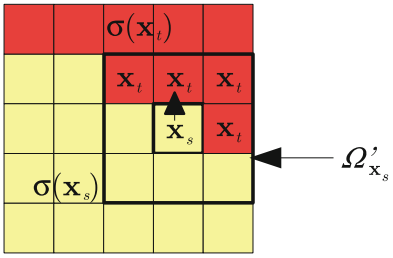

Fig. 3.12 Possible choices $\mathbf{x}_t$ for $\mathbf{x}_s$ to copy its spin and the actually randomly chosen attempt. *Red squares* and *yellow squares* belong to different object types. The neighborhood of $\mathbf{x}_s$ is represented by $\Omega'_{\mathbf{x}_s}$

called Monte Carlo Step (MCS), a lattice site $\mathbf{x}_s$ (s for *source*) belonging to a cell compartment $\Sigma_{\sigma(\mathbf{x}_s)}$ is selected at random and attempts to copy its spin, $\sigma(\mathbf{x}_s)$, into one of its unlike neighbors, $\mathbf{x}_t \in \Omega'_{\mathbf{x}_s} : \mathbf{x}_t \notin \Sigma_{\sigma(\mathbf{x}_s)}$ (t for *target*), also randomly selected (see Fig. 3.12). Such a trial spin update is accepted with a Boltzmann-like probability function $P(\sigma(\mathbf{x}_s) \to \sigma(\mathbf{x}_t))$, which reads as

$$P(\sigma(\mathbf{x}_s) \to \sigma(\mathbf{x}_t))(t) = \tanh(T_{\Sigma_{\sigma(\mathbf{x}_s)}}(t)) \min\left\{1\ ,\ \exp\left(\frac{-\Delta H}{T_{\Sigma_{\sigma(\mathbf{x}_s)}}(t)}\right)\right\}. \tag{3.40}$$

ΔH is the net difference of the system energy, which is defined by the *hamiltonian* H, due to the proposed change of domain configuration. $T_{\Sigma_{\sigma(\mathbf{x}_s)}}(t) > 0$ is a Boltzmann temperature, that measures the agitation rate of the moving object $\Sigma_{\sigma(\mathbf{x}_s)}$. Indeed, for $\tau(\Sigma_{\sigma(\mathbf{x}_s)}) = N$, $T_{\Sigma_{\sigma(\mathbf{x}_s)}} = T_N$ gives the agitation rate of cell nucleus, while, for $\tau(\Sigma_{\sigma(\mathbf{x}_s)}) = C$, $T_{\Sigma_{\sigma(\mathbf{x}_s)}} = T_C$ is a measure of the intrinsic motility

of the overall cell, as it gives the frequency of the ruffles of its cytosol (which, on a molecular level, are determined by polarization/depolarization processes of the actin cytoskeleton). T_N is a low value, resulting in the passive motion of the nucleus, which, unable to have an autonomous movement, is dragged by the surrounding cytosol, characterized instead by a higher T_C (see [63] for a more detailed mechanical explanation). The ECM polymeric components are instead assumed fixed and immutable, only representing a restriction for cell movement.

The first factor in (3.40) takes into account of the fact that the effective motion of a cell is strongly dependent on subcellular dynamics governing its possibility to move. For example, a "frozen" cell (i.e., with negligible intrinsic motility) does not extend its pseudopods toward a chemical source even if it senses a high chemotactic gradient (which, in the absence of other external forces, results in $\Delta H \ll 0$). This may occur for example because a cell

- does not have enough chemicals to trigger its motility programme, e.g., ATP or calcium;
- has been pretreated with motion-inhibiting proteins, such as cytochalasin B, that prevents the formation of the actin network;
- is simply frozen at a temperature of 4 °C.

In the cases of our interest, for any given time t, the system *hamiltonian*, whose minimization drives the evolution of the system, is composed of at least two terms

$$H(t) = H_{shape}(t) + H_{adhesion}(t). \tag{3.41}$$

H_{shape} models the geometrical attributes of simulated objects (both subcellular compartments and matrix components), which are written as non-dimensional relative deformations in the following quadratic form

$$\begin{aligned} H_{shape}(t) &= H_{volume}(t) + H_{surface}(t) \\ &= \sum_{\Sigma_\sigma} \left[\kappa_{\Sigma_\sigma}(t) \left(\frac{v_{\Sigma_\sigma}(t) - V_{\tau(\Sigma_\sigma)}}{v_{\Sigma_\sigma}(t)} \right)^2 + \nu_{\Sigma_\sigma}(t) \left(\frac{s_{\Sigma_\sigma}(t) - S_{\tau(\Sigma_\sigma)}}{s_{\Sigma_\sigma}(t)} \right)^2 \right], \end{aligned} \tag{3.42}$$

depending on the actual volume and surface of the object, $v_{\Sigma_\sigma}(t)$ and $s_{\Sigma_\sigma}(t)$ (which reduce, respectively, to its surface and perimeter in two dimensions), as well as on the same quantities in the relaxed state, $V_{\tau(\Sigma_\sigma)}$ and $S_{\tau(\Sigma_\sigma)}$, corresponding to its initial measures. The formulation of (3.42), which is different from standard CPMs, allows to have finite energetic contributions, as well as a blow up in the case of $v_{\Sigma_\sigma}(t), s_{\Sigma_\sigma}(t) \to 0$ (i.e., CPM objects can not artificially disappear, as it might happen in some cases for the classical CPMs, see again [63] for a detailed explanation). The coefficients $\kappa_{\Sigma_\sigma}(t) > 0$ and $\nu_{\Sigma_\sigma}(t) > 0$ play the role of mechanical moduli in units of energy. In particular, $\kappa_{\Sigma_\sigma}(t)$ refer to volume changes and therefore to the compressibility of Σ_σ, while $\nu_{\Sigma_\sigma}(t)$ relates to the degree of deformability/elasticity of the related object, i.e., the ease with which it is able to remodel. Indeed, assuming that a cell does not significantly grow during

migration, the fluctuations of its volume are kept negligible with high constant values $\kappa_{\Sigma_\sigma} = \kappa \gg 1$, for $\tau(\Sigma_\sigma) \in \{N, C\}$. Moreover, cells moving in matrix environments are typically deformable, but their nuclei show a higher rigidity w.r.t. the cytoplasm region. Indeed, in general, it is consistent to assume

$$\nu_{\Sigma_\sigma:\tau(\Sigma_\sigma)=C} = \nu_C < \nu_{\Sigma_\sigma:\tau(\Sigma_\sigma)=N} = \nu_N \,.$$

However, we will discuss the specific values (and/or constitutive laws) of these model parameters in the following, analyzing, in particular, their effect on cell migratory dynamics. The extracellular environment is instead assumed to have homogeneous mechanical and microstructural properties: in particular the polymeric matrix component are assumed to be rigid by setting $\kappa_P = \nu_P \gg 1$.

$H_{adhesion}$ is the general extension of Steinberg's Differential Adhesion Hypothesis (DAH) [23, 67, 68]. In particular, it is differentiated in the contributions due either to the generalized contact tension between the nucleus and the cytoplasm within the same cell, or to the effective adhesion between a cell and an extracellular component

$$\begin{aligned} H_{adhesion}(t) &= H^{int}_{adhesion}(t) + H^{ext}_{adhesion}(t) \\ &= \sum_{\substack{(\partial\mathbf{x}\in\partial\Sigma_\sigma)\cap(\partial\mathbf{x}'\in\partial\Sigma_{\sigma'}) \\ \eta(\Sigma_{\sigma(\mathbf{x})})=\eta(\Sigma_{\sigma(\mathbf{x}')})}} J^{int}_{\tau(\Sigma_{\sigma(\mathbf{x})}),\tau(\Sigma_{\sigma(\mathbf{x}')})} \\ &\quad + \sum_{\substack{(\partial\mathbf{x}\in\partial\Sigma_\sigma)\cap(\partial\mathbf{x}'\in\partial\Sigma_{\sigma'}) \\ \eta(\Sigma_{\sigma(\mathbf{x})})\neq\eta(\Sigma_{\sigma(\mathbf{x}')})}} J^{ext}_{\tau(\Sigma_{\sigma(\mathbf{x})}),\tau(\Sigma_{\sigma(\mathbf{x}')})}, \end{aligned} \tag{3.43}$$

where $\mathbf{x}$ and $\mathbf{x}'$ are two neighboring sites (i.e., $\mathbf{x}' \in \Omega'_{\mathbf{x}}$) and $\Sigma_{\sigma(\mathbf{x})}$ and $\Sigma_{\sigma(\mathbf{x}')}$ two neighboring objects. The coefficients $J_{\tau(\Sigma_{\sigma(\mathbf{x})}),\tau(\Sigma_{\sigma(\mathbf{x}')})} \in \mathbb{R}$ are binding forces per unit area, and are obviously symmetric with respect to the indices. In particular,

- $J^{int}_{N,C}$ implicitly models the forces exerted by intermediate actin filaments and microtubules to anchor the nucleus to the cell cytoskeleton, preventing cell fragmentation;
- $J^{ext}_{C,C}$ represents the local adhesive strength between neighbouring cells, a measure of the local quantity of active and exposed cadherin molecules;
- $J^{ext}_{C,P}$ and $J^{ext}_{C,M}$ evaluate the heterophilic contact interactions between a cell and an extracellular component. On the one hand, $J^{ext}_{C,P}$ measures the affinity between integrins complexes on the cell surface and the insoluble matrix components. On the other hand, $J^{ext}_{C,M}$ possibly accounts for the adhesiveness between the cell membrane and specific soluble ligands present in the medium.

Specifically, assumed $J^{int}_{N,C} \ll 0$ to prevent cell splitting, we give null contribution to the adhesive interactions between a moving cell and an extracellular component (i.e., $J^{ext}_{C,M} = J^{ext}_{C,P} = 0$). This choice, successfully used in another similar model of *in vitro* cell migration [65], is done to analyze the direct influence of cell deformability on its motile behavior, and is consistent with the experimental literature, which

widely demonstrates that most cell lines display sustained ameboid motility in confined environments in a poorly adhesive mode [39, 61]. $J^{ext}_{C,C}$ is finally kept high to avoid cell-cell adhesive interactions that may affect cell movement. By setting constant and homogeneous values for the bond energies Js, we here assume a uniform distribution of adhesion molecules both on cell surfaces and in the external environment, without any change during the observation time.

In the following set of simulations, we will add (and explain) other contributions in the *hamiltonian* functional that will be needed to model specific cell behaviors.

3.4.2 Cell Migration in a 3D Microchannel Device

As a first application in the present section we analyze cell migration in three-dimensional fixed microchannel architectures. Following [62] the simulation domain $\Omega \subset \mathbb{R}^3$ indeed reproduces a bioengineered device with channel structures of various widths and a planar surface just outside their entrances, as shown in Fig. 3.13. This experimental architecture is typically used in literature to analyze cell migration both on open spaces and through precisely confined environments (see [61] and references therein).

The *hamiltonian* is given by the contributions introduced in Eq. (3.41), as well as by a further term describing cell persistent migration, which is determined by the ability of moving individuals to polarize, i.e., to differentiate in a leading and a trailing surface. For each individual η, this inertial, shape-dependent motion is modeled with a further energy term, which is coherently a running mean over the

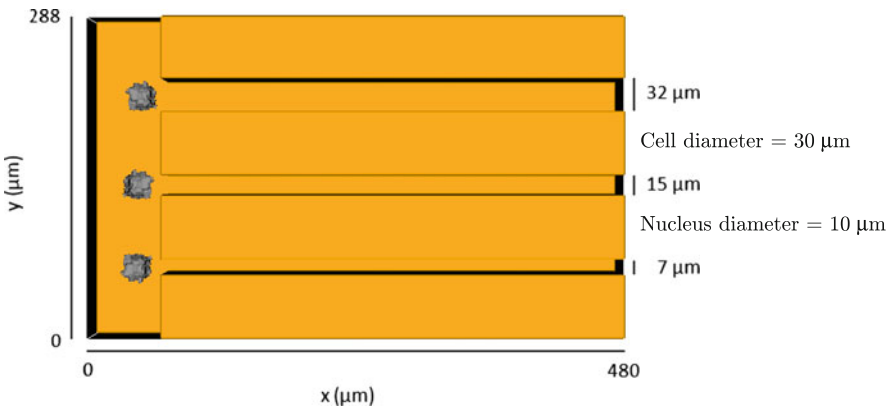

Fig. 3.13 The simulation domain Ω reproduces a micro-fabricated device with channels of various width and a planar surface just outside their entrance. In particular, the *top channel* is larger than the overall cell diameter, while the *bottom channel* is smaller than nuclear dimensions. Initially, the cells are seeded on the flat substrate near the channel walls

cell past movements [1, 64]

$$H_{persistence} = \mu^{\eta}_{pers}(t)||\mathbf{v}_{\eta}(t) - \mathbf{v}_{\eta}(t - \Delta t)||^2, \tag{3.44}$$

where $\mathbf{v}_{\eta}(t)$ is the instantaneous velocity of the cell center of mass. The parameter μ^{η}_{pers} controls the persistence time of cell η and is

$$\mu^{\eta}_{pers}(t) = \mu_{pers,0}\left[\frac{L_{\eta}(t)}{L_0} - 1\right], \tag{3.45}$$

where L_0 is the initial cell diameter and L_{η} is the current length of the longer axis of the cell, which is approximated with an ellipsoid [46]. Obviously $L_{\eta} \geq L_0$, since we have assumed that the cell deforms but does not grow during migration. Equation (3.45) is based on the experimental evidence provided in [28], where in similar conditions elongated vascular cells have seen to have a longer persistence time than more rounded cells. This is explained with the observation that cell polarization is a cytoskeleton-driven process: the more a cell is polarized (i.e., the longer its main axis is), the more its actin filaments are oriented in such a direction, thereby requiring a longer time to reorient into a new direction and to establish a new direction of motion. Coherently, from (3.45), if $\mu^{\eta}_{pers} = 0$ the cell η undergoes an uncorrelated Brownian motion. Otherwise, if μ^{η}_{pers} is very large, its motion is almost ballistic.

Referring to Fig. 3.13, in all simulations, the cells are initially seeded on the planar substrate in the close proximity to the channel entrances displaying an unpolarized morphology. Indeed, they are hemispheres with a radius of 15 μm, while the nucleus is a central sphere with a diameter of 10 μm.

The elasticity of the cell cytosolic region is modelled by a low value of $\nu_C < 1$, whereas the nuclear cluster is made stiffer by setting a higher value of $\nu_N \gg 1$.

As reproduced in Fig. 3.14, all individuals initially show a random migration on the flat surface (i.e., until nearly 2 h). Then, when approaching the channel walls, they start walking along them. At this regard, it is useful to underline that this preferred cell movement is completely autonomous, as we do not include in the model any chemical gradient or bias, or any a priori direction for moving individuals. In the case of the channel with the largest cross-section, the cell is able to quickly enter and migrate within the structure, but not to reach the opposite border within the final time of the simulation, as shown in Fig. 3.14. This individual in fact fluctuates and "rebounds" between the internal walls of the channel, whose width does not represent a significant geometrical *contact guidance*, thereby remaining almost in the middle of the structure.

At the intermediate channel width (i.e., smaller than cellular dimensions and bigger than nuclear dimensions), the cell is able to squeeze into and move within the microstructure, as shown in Fig. 3.14. In particular, it remodels towards an elongated shape and migrates to the other end of the device. The transition from a stationary cell morphology to a polarized shape, which is completely self generating and due to the geometry of the matrix environment, is fundamental in determining

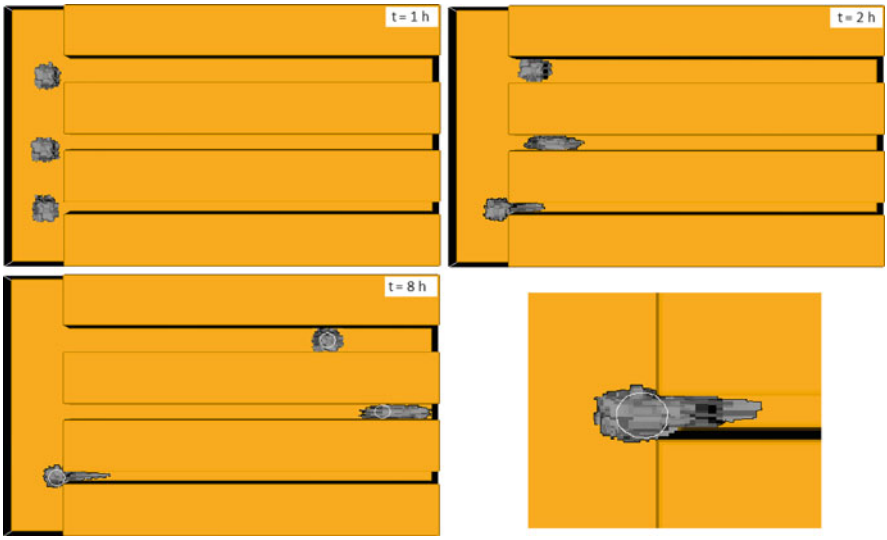

Fig. 3.14 Migratory behavior within the microchannel structure of cells with an elastic cytosol and a rigid nucleus (i.e., $\nu_C < 1 \ll \nu_N$). Images of a time-lapse simulation taken at t = 1, 2, and 8 h. By remodelling their cytoskeleton, the cells are able to enter both the largest and the intermediate channel. However, due to the presence of a stiff nucleus, cell migration into the smallest structure is prohibited. Magnification of moving cell in the close proximity of the smallest channel entrance. It is straightforward to see how the stiff voluminous nucleus is not able to pass through the confined space, allowing only the penetration of part of the cytosol. For better visualization, cell nuclei are manually *encircled*

the persistent component in cell movement. From a modelling viewpoint, cell elongation in fact increases the relative magnitude of the persistence term (3.44) in the overall *hamiltonian*, given by coefficient μ^{η}_{pers}. Therefore, once the cell has established the direction of movement within the channel, it is energetically disadvantageous to change direction and is forced to maintain the direction of locomotion.

Finally, the corresponding cell is not able to enter the smallest channel. If the front of its cytoplasm quickly extends into the structure, the voluminous nuclear region can not deform and pass through such a highly constrained space, therefore inhibiting the individual from pulling inside its entire body, as clearly reproduced in Fig. 3.14.

We next address the question to what extent a variation in cell nucleus elasticity enables cell invasion and movement into highly confined spaces. With a biological viewpoint, the decrement of ν_N corresponds to a modification of the chromatin structure, a remodelling of lamin filaments or an experimental treatment with micromolar concentrations of bioactive lipids (such as sphingosylphosphorylcholine, shortened as SPC), whose activity leads to a substantial translocation of the keratin network towards a perinuclear rearrangement [4]. More specifically, we set $\nu_C < \nu_N < 1$, as

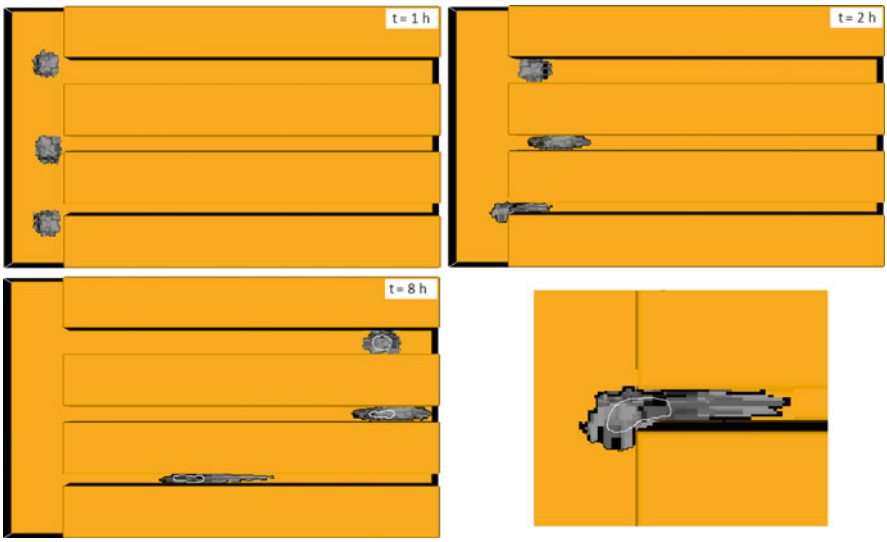

Fig. 3.15 Migratory behavior within the microchannel structure of cells with an elastic cytosol and a deformable nucleus (i.e., $\nu_C < \nu_N < 1$). Images of a time-lapse simulation taken at t = 1, 2, and 8 h. The enhancement in nucleus elasticity enables cells to enter also in the smallest channel. Magnification of moving cell in the close proximity of the smaller channel entrance. It is straightforward to see how the nucleus can now squeeze to pass within the channel entrance, allowing the entire individual to invade the structure. For better visualization cell nuclei are manually *encircled*

the cell cytoplasmic region is still softer than the nuclear cluster which is, however, more deformable w.r.t. the previous simulation setting.

The analysis of the model outcomes, summarized in Fig. 3.15, reveals that, in the case of the largest channel, the deformability of the nucleus does not appreciably affect cell migratory behavior. When the channel dimension decreases to the intermediate range, though the cell morphology looks almost similar to the previous case, the nuclear elasticity provides a further facilitation for the movement of the entire individual. This is due both to the fact that the cell can now more easily and more quickly pass through the channel entrance and to the fact that it can more efficiently migrate within its walls, as also its voluminous nuclear region is able to assume a more elongated and "mobile" configuration, allowing a more efficient deformation of the entire cell body. Finally, the enhancement of the nucleus elasticity results in a significant change in the migratory phenotype of the cell approaching the smallest channel, as it is now able to invade the structure. Such a change in the motile behavior is the obvious consequence of the fact that it now compresses and pulls its nuclear region within the confined environment, as represented in Fig. 3.15.

In order to summarize and to analyze from another viewpoint the results presented so far, in Fig. 3.16, we plot the average velocity of cells, defined as the average velocity of their center of mass [47, 53, 65], both on the flat surface

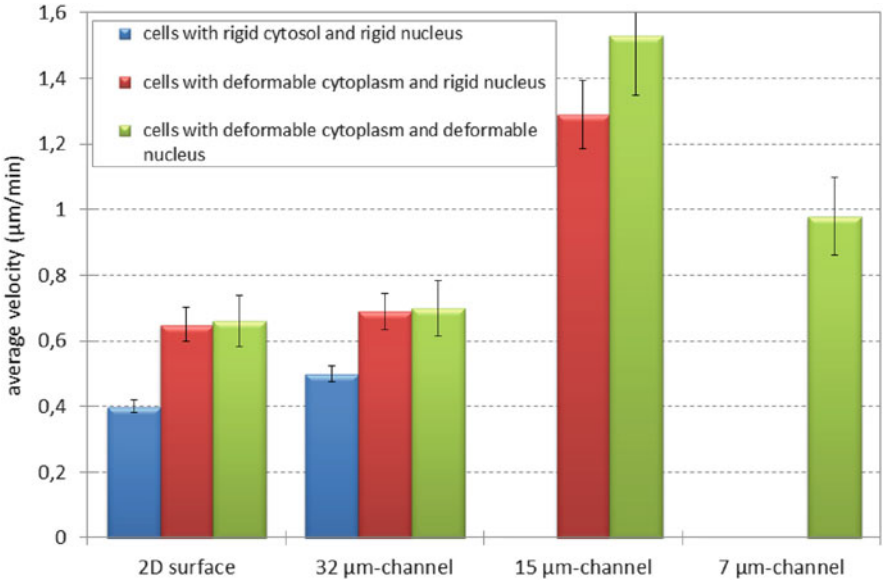

Fig. 3.16 Comparison of the average migration speed of cells moving either on the flat surface or within the different microchannels. Cell velocity on both the bidimensional substrate and in the larger channel is substantially low, and does not significantly depend on cytosol and nucleus rigidities. On the contrary, cell speed within more confined structures is generally two-fold higher and is further enhanced by the possibility of nucleus deformability

and within the different channel structures. This comparison allows to elucidate and to further quantify the differences between cell migratory phenotypes in specific geometric conditions. The random movement of rigid cells on the planar substrate is characterized by a low 0.4 μm/min-speed, which slightly increases for individuals with a deformable cytoplasm, reaching almost 0.6 μm/min. There is no further variation upon the enhancement of the nuclear compressibility. An analogous behavior, with almost similar values, is observed for cell migration in the largest channel, confirming that extracellular environments whose dimensions are greater than cellular measures do not represent guidance cues, but rather behave as open spaces. In the case of the intermediate channel, cells with an elastic cytosol display instead an approximately two-fold increment in cell migration speed ($\approx$ 1.1 μm/min), which is significantly enhanced when allowing nuclear deformability ($\approx$ 1.5 μm/min). Finally, in the case of the smallest channel, the cell average velocity (obviously evaluated only for cells with an elastic nucleus) slightly decreases again to less than 1 μm/min. The explanation resides in the fact that although the nucleus is deformable, it is however stiffer (and less motile) than the surrounding cytoplasm and therefore takes more time to remodel and move, slowering the overall individual.

These results first reveal two distinct migratory phenotypes, that are proposed to occur for cells placed either in open structures (i.e., 2D surfaces or large channels)

or in confined architectures (i.e., channels smaller than cellular dimensions). In the first case, the movement of cells is widely independent from their elastic properties, whereas it is widely known to strongly rely on their adhesive strengths [39]. On the contrary, the efficacy of cell migration in 3D constrained environments is mainly determined by the deformation ability of the moving individuals (in particular, of their voluminous nucleus), which adapt to the geometrical characteristic of the environment. At this regard, it is indeed possible to identify an optimal dimension of an extracellular structure which results in a sustained cell locomotion: Smaller than the cellular measures but higher than the nuclear diameter.

3.4.3 Cell Migration in Two-Dimensional Matrix Microtracks

In this second part of the section, we present a CPM specifically designed to analyze MMP-dependent and MMP-independent cell migration in two-dimensional matrix microtracks. Accordingly, the simulation domain $\Omega \subset \mathbb{R}^2$ reproduces an *in vitro* dense collagenous matrix characterized by well-defined microtracks, which can be experimentally generated by laser ablation (see for instance [29] and references therein). In particular, the scaffold pattern consists of two perpendicular channels, which are equal in length (270 μm) and width. In order to exploit different geometries, the diameter of the microtracks varies in the different sets of simulations similarly to the case of the microchannel structure proposed in the first part of the section (bottom panels of Fig. 3.17).

In this second CPM application, the *hamiltonian* functional used is exactly the same as the one defined in Eq. (3.41). However, the persistent cell movement is no longer implemented by a further energetic term but by asymmetric biases added in the Boltzmann probability function, which now reads as

$$P(\sigma(\mathbf{x}_s) \to \sigma(\mathbf{x}_t))(t) = \tanh(T_{\Sigma_{\sigma(\mathbf{x}_s)}}(t)) \min\left\{1\ ,\ \exp\left(\frac{-\Delta H + w_1 + w_2}{T_{\Sigma_{\sigma(\mathbf{x}_s)}}(t)}\right)\right\}. \tag{3.46}$$

More specifically, following [72–76], w_1 models the inertial shape-dependent self-propulsion of a cell by altering the probability assigned to each spin update as

$$w_1(\sigma(\mathbf{x}_s) \to \sigma(\mathbf{x}_t)) = P_{pers}\frac{\mathbf{p}_\eta}{|\mathbf{p}_\eta|} \cdot (\mathbf{x}_t - \mathbf{x}_s), \tag{3.47}$$

where P_{pers} sets the magnitude of the cell autonomous motility and $\mathbf{p}_\eta$ is the polarity vector of η (top-left panel of Fig. 3.17), which, on a molecular level, may represent spatial differences in its biochemical state. The coefficient P_{pers} is here set constant in time: However, it may vary with the specific length of an individual (see for instance Eq. (3.45)) or with the intracellular level of motile proteins. The cell polarity vector is then updated by considering a spontaneous decay and a

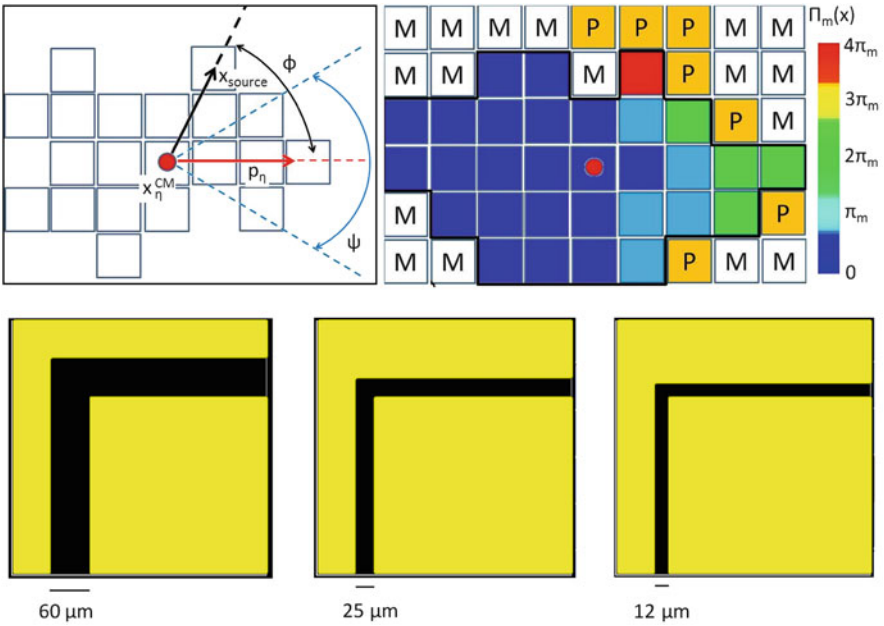

Fig. 3.17 *Top-Left panel*: Geometrical characteristics of the moving cell. $\mathbf{x}^{CM}_{\eta(\Sigma_{\sigma(\mathbf{x}_s)})}$ indicates the center of mass of cell η, whose site $\mathbf{x}_s$ is attempting to move. The *red vector* $\mathbf{p}_\eta$ represents the cell polarity vector, which forms the angle ϕ with the direction of the vector $(\mathbf{x}_s - \mathbf{x}^{CM}_\eta)$. The width of the leading edge is instead defined by the angle ψ, which is formed by the segments connecting $\mathbf{x}^{CM}_\eta$ with extreme sites of the frontal part of the cell membrane, see also [72]. *Top-right panel*: MMP-production mechanism. Only a cell site located in the frontal part of the border of a cell can secrete proteolytic enzymes. In particular, the quantity of produced proteases is proportional to the quantity of ECM insoluble components in its first neighborhood. The *bold black border* indicates the membrane of the cell, the *red dot* its center of mass. *Bottom panels*: The simulation domain Ω reproduces a bidimensional dense collagenous lattice with microtracks of well-defined dimensions. In particular, we will analyze cell migration within channels (1) larger than the overall cell diameter, which is 30 μm; (2) smaller than the overall cell diameter but larger than the nuclear diameter, which is 16 μm; and (3) smaller than the nucleus size

reinforcement from cell displacements as, for each MCS,

$$\Delta\mathbf{p}_\eta = -\frac{1}{t_\mathbf{p}}\mathbf{p}_\eta + \Delta\mathbf{x}^{CM}_\eta, \tag{3.48}$$

where $t_\mathbf{p}$ is a characteristic memory length of the polarization vector, which can be also defined as the inverse of a rate of spontaneous decay, and $\Delta\mathbf{x}^{CM}_\eta$ is the net displacement of the cell center of mass during the actual MCS. The term w_1 establishes therefore a direct positive feedback loop involving cell movement and polarity [75], which corresponds to the molecular feedback regulation between the

activation of rho GTPases and the processes involved in cellular motility such as expansion of the cytosol and polymerization of cytoskeletal elements.

The term w_2 instead models the fact that membrane dynamics (i.e., extensions/retractions of filopods and pseudopods) are more pronounced at the leading edge of a polarized cell, while they are almost poor at the sides and the trailing edge. Indeed, defining as ψ_η the width of the leading edge of cell η, we set

$$w_2(\sigma(\mathbf{x}_s) \to \sigma(\mathbf{x}_t)) = P_{dyn} S\left(\frac{\psi_\eta}{2} - \phi(\mathbf{p}_\eta\ ,\ \mathbf{x}_s - \mathbf{x}_\eta^{CM})\right), \tag{3.49}$$

where $S(\cdot)$ is the sign function, P_{dyn} sets the magnitude of this effect, and $\phi(\cdot, \cdot)$ denotes the absolute value of the angle between vectors $\mathbf{p}_\eta$ and $(\mathbf{x}_s - \mathbf{x}_\eta^{CM})$, see again the top-left panel of Fig. 3.17. It is useful to emphasize that the asymmetric corrections w_1 and w_2 replace and are preferable to the standard $H_{persistence}$ contribution to the *hamiltonian* introduced in Eq. (3.44), which only implicitly defines the polarization process of the moving cell as its ability to maintain the direction of the velocity characterizing its recent past movements. More in details, $H_{persistence}$ forces the moving individual to choose configurations that do not change its velocity, as it is a sort of "passive" term. In other words, a cell taking a direction of movement for a specific reason (i.e., due to chemical or geometrical stimuli) keeps such a path because it is energetically convenient. On the contrary, the biases w_1 and w_2 implement an "active" self-propulsion, since at each time step the cell reinforces its polarization with localized membrane fluctuations.

In all simulations, the cell is initially seeded just near the entrance of the vertical channel and it is characterized by a polarity vector $\mathbf{p}_\eta$ directed towards the vertical direction. This translates the assumption that the individual has already penetrated the microtrack and, chosen the direction of movement, it has organized its shape accordingly. Finally, ten annealed MCS are run before each simulation in order to let the cell realistically arranges its body within the structure. We recall that the cell has an overall target area of $\approx 800\,\mu\text{m}^2$, which would correspond to a diameter of $30\,\mu\text{m}$ in a resting, un-polarized, morphology. The nucleus is instead a central and round cluster of $8\,\mu\text{m}$ of radius.

3.4.3.1 MMP-Independent Cell Migration

In this first simulation setting we analyze the role in cell migration of cell elasticity. In this respect, cells are allowed to remodel both the cytoplasmic region and the nucleus, as we set $\nu_C < \nu_N < 1$.

In the case of the microtrack with the largest cross-section, the cell quickly looses its initial polarization and turns back to a roundish shape. Then, in the absence of chemotactic (or other) cues, it starts to fluctuate and "rebound" between the channel walls, without displaying a significant penetration within the structure. As already commented in Sect. 3.4.2, the largest microtrack does not in fact represent a

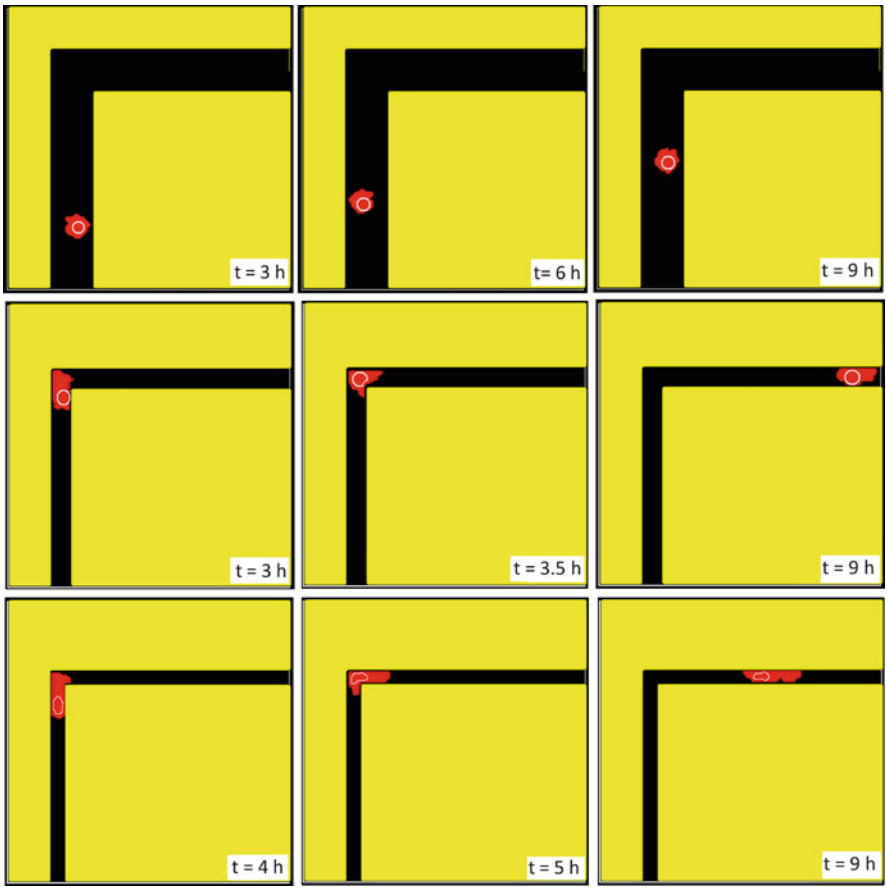

Fig. 3.18 MMP-independent cell migration. Representative images from the simulations showing cell locomotion within the different matrix microtracks. In all panels, the nucleus is manually *encircled* for the reader's convenience

significant geometrical *contact guidance* for the moving cell, which remains almost in the middle of the pattern in a resting, non-motile morphology, see Fig. 3.18.

At the intermediate channel width (i.e., smaller than cellular dimensions but larger than nuclear dimensions), the cell is able to maintain the polarized morphology and to undergo a persistent movement within the vertical microtrack. Such an inertial shape-dependent migration is actively reinforced at each MCS by the asymmetric biases added to the Boltzmann probability function. At the end of the vertical channel, the individual spontaneously reorganizes and then turns the direction of motion, thereby invading the horizontal structure. From a modelling viewpoint, the shape transition is driven by the evolution of the cell polarity vector: referring to Eq. (3.48), the cell center of mass in fact slowly displaces towards the open space on the right, as the cell can not overcome the vertical barrier. Once

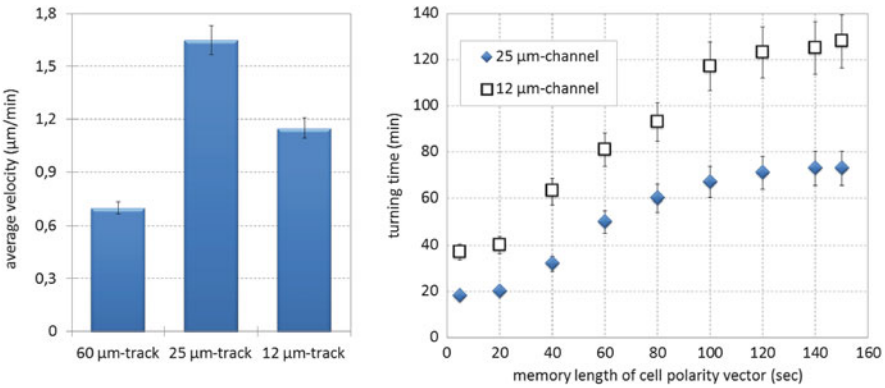

Fig. 3.19 *Left plot*: Bimodal behavior of the average cell migration velocity within the different microtracks. *Right graph*: Turning time vs. memory length of the cell polarity vector, $t_{\mathbf{p}}$. All the values in the plots are represented as means $\pm$ s.d. over 50 realizations

the cell has repolarized, the new direction of movement is finally established and maintained by the terms w_1 and w_2. In this case, the elasticity of the nucleus is not fundamental for the overall cell movement, since the track is large enough. However, it allows a more efficient deformation of the entire cell body in the angle between the channels (see indeed Fig. 3.18).

Finally, in the smallest track, both the cell and its nucleus adopt a cigar-like shape to invade the structure. Without a proteolytic activity, the only way for the cell to move within such a confined space is in fact an ameboid motion, which requires the substantial deformation and squeezing also of its more voluminous compartment. In particular, the individual is again able to turn morphology and direction of movement, but it takes a longer time. At the end of the observation time, the cell still localizes in the central part of the channel, as it does not reach the opposite border of the scaffold. This is indicative of a slower velocity of migration.

In this respect, Fig. 3.19 (left panel) shows a bimodal behavior of speeds, that allows to identify an optimal channel dimension for cell migration: Smaller than the cellular diameter but larger than the nuclear diameter. In particular, the use of subcellular structures as a contact guidance resulting in a sustained cell locomotion relies upon the deformation ability of the moving individual and, mainly, of its voluminous nucleus, which needs to adapt to the geometrical characteristic of the tracks. In particular, the cell velocities measured in the presented CPM are surprisingly similar to those evaluated in the model proposed in the previous subsection, even if the persistent cell-dependent motion is, as already underlined, modeled with different approaches. This is indicative of the fact that both assumptions provide, although with different viewpoints, a realistic description of the directional locomotion of polarized cells.

Focusing on the relation between the *turning time* of the cell, i.e., the time needed to remodel and establish the new direction of movement, and the value given to the

memory length of the polarity vector, $t_{\mathbf{p}}$, in Fig. 3.19 (right) we observe that for both the intermediate and the smallest channel increments in $t_{\mathbf{p}}$ correspond to increments in the cell *turning time*, until a saturation value. This is biologically realistic, as $t_{\mathbf{p}}$ models the time needed to the intracellular machinery to resynchronize the polarity in the new direction of movement, i.e., to activate molecular pathways able to reinforce cytoskeletal actin polymerization towards the open space. The same graph also gives a further proof of the fact that a subnuclear structure represents a steric hindrance for cell movement, partially inhibiting its locomotion. In fact, though the cell is able to compress and pull its nuclear region within the smallest tracks, it takes a significantly longer time to remodel and turn direction of motion.

3.4.3.2 MMP-Dependent Cell Migration

To overcome situations in which limited space inhibits migration, rigid cells are able to activate a proteolytic mechanism consisting in the expression of matrix degrading enzymes, named metalloproteinases (MMP) [82]. As a result, barrier-free matrix spaces may be created and microtracks can be enlarged enhancing migration and invasion.

To analyze this phenomenon, in the following sets of simulations, the assumption of constant nucleus elasticity is dropped and replaced by a dependence from MMP-dependent cascades. In more details, nucleus elasticity is enhanced when all the MMP activity is inhibited, as widely demonstrated in the recent experimental literature for different tumor cell lines [16, 17, 83]. Following these considerations, we set

$$\nu_N = \nu_0 \left(\frac{1 + a\ \pi_m}{1 + b\ \pi_m} \right) , \tag{3.50}$$

where $a = 2$, $b = 1$, $\nu_0 < 1$ and π_m is the MMP production rate, that will be defined in Eq. (3.53). However, even if π_m=0, we opt to maintain $\nu_N > \nu_C$, since the cytoplasmic region of the cell remains typically softer than the nuclear cluster, as previously commented.

The matrix metalloproteinases secreted by cells are denoted by $m(\mathbf{x}, t)$ and evolve following a standard reaction-diffusion equation

$$\frac{\partial m}{\partial t}(\mathbf{x}, t) = \underbrace{P(\mathbf{x}, t)}_{production} + \underbrace{D_m \nabla^2 m(\mathbf{x}, t)}_{diffusion} - \underbrace{\lambda_m m(\mathbf{x}, t) \delta(\tau(\Sigma_{\sigma(\mathbf{x})}), M)}_{decay} , \tag{3.51}$$

where $\delta(\tau(\Sigma_{\sigma(\mathbf{x})}), M) = 1$ in the interstitial medium M and 0 elsewhere. λ_m and D_m are, respectively, the decay rate and the effective diffusion coefficient of proteolytic enzymes, constant and homogeneous in the whole extracellular environment. A low value of D_m is set to model a proteolytic mechanism strongly localized in the regions close to cell membranes, in agreement with experimental evidence [84]. The term

$P(\mathbf{x}, t)$ models the local production of proteases from the cell surface that occurs, as widely demonstrated in literature both in general [35] and in particular for vascular [66] and metastatic cells [77], at the leading edge and at the neighboring parts of the lateral edges of the cell membrane. So,

$$P(\mathbf{x}, t) = \begin{cases} \sum_{\partial \Sigma_{MMP}} \pi_m(\partial \mathbf{x}, t) & \text{if} \quad \phi(\mathbf{p}_\eta \, , \, \mathbf{x} - \mathbf{x}_\eta^{CM}) \in (0, \frac{\pi}{2}); \\ 0 & \text{else}, \end{cases} \tag{3.52}$$

where

$$\partial \Sigma_{MMP} = \partial \mathbf{x} \in \partial \Sigma_\sigma : \tau(\Sigma_\sigma = C) \wedge \tau(\Sigma_{\sigma(\mathbf{x}' \in \Omega'_\mathbf{x})}) = P \, , \tag{3.53}$$

that is, referring to the top-right panel of Fig. 3.17, MMP production only occurs where it is really needed, i.e., only where the cell senses a matrix component in its close neighborhood, which indeed represents an obstacle for its movement.

Finally, to reproduce matrix degradation, a lattice grid site $\mathbf{x}$ belonging to the polymeric part of the ECM becomes a generalized medium (fluid) site when the local level of MMPs is sufficiently high. This change is implemented by switching its type τ from P to M.

Given that the largest track does not represent a significative obstacle for cell migration, therefore not requiring MMP-activity, we first focus on the intermediate channel. As reproduced in Fig. 3.20a, the cell maintains the polarity and easily invades the vertical track. In particular, the extracellular scaffold is not significantly altered by the proteolytic machinery, as the ECM structure does not represent a steric obstacle for cell persistent migration along the channel walls. The directional movement is then maintained despite the horizontal wall of the channel: the fully activated MMP activity is in fact able to generate a *de novo* vertical track, allowing the cell to maintain the polarity and the relative direction of motion.

Interestingly, as shown in Fig. 3.20b, *as soon as* the MMP secretion rate slightly decreases, a well-defined *de novo* part of the vertical track is no longer generated. Consequently, the cell loses its polarity, reverts back to a roundish morphology and starts wandering in the close proximity, while slowly degrading the surrounding matrix in a random-isotropic way. This behavior is somewhat consistent for a large region of values assumed by π_m, see again Fig. 3.20b. An almost complete inhibition of the proteolytic machinery (i.e., $\pi_m = 10^{-5}$ s^{-1}) eventually results again in an ameboid movement of the cell.

These results are biologically relevant, as they clearly demonstrate that the most efficient cell migration within a confined subcellular structure can be achieved

1. with the maximal activity of cell matrix-degrading enzymes, which for instance allow the migrating individual to maintain the predefined direction of movement (i.e., mesenchymal locomotion);
2. with an ameboid sustained locomotion, which allows the migrating individual to use the surrounding environment as a geometric guidance.

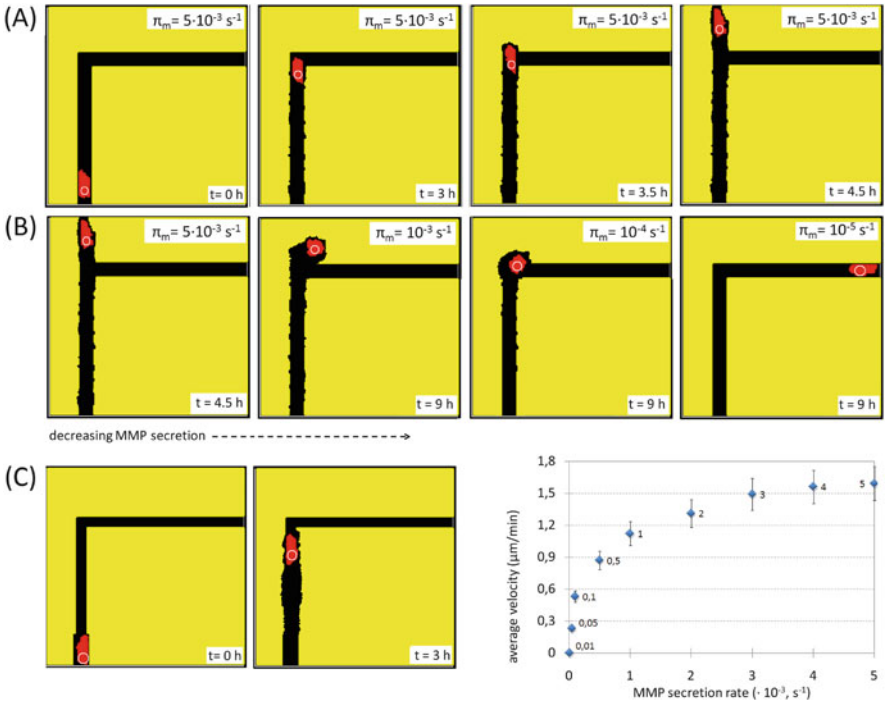

Fig. 3.20 (**a**)–(**b**) MMP-dependent cell migration in the intermediate track for different values of MMP secretion rate. (**c**) MMP-dependent cell migration in the subnuclear track. *Left panels*: The proteolytic machinery generates a lateral widening of the microchannel, allowing the cell to pull into its voluminous and rigid nucleus. *Right graph*: The velocity of migration increases with the value of the MMP secretion rate, π_m, until a threshold limit. In particular, the speed of the cell with fully activated MMPs nearly matches the one observed for the MMP-deprived cell moving within the intermediate channel, see Fig. 3.19 (*left panel*). The numerical labels within the graph indicate the exact values assumed by π_m. In each case, we represent mean $\pm$ s.d. over 50 realizations. In all representative simulation images, the nucleus is manually *encircled* for the reader's convenience

Analogous outcomes would be obtained by keeping fixed π_m, while increasing the value of the amount of MMPs needed to degrade a matrix component.

We then pass to analyze cell migration in the smallest microtrack. In particular, the initial part of the channel is widened to allow the entrance of the cell nucleus, which is now characterized by a high stiffness as the cell proteolytic machinery is fully active activate [refer to Eq. (3.50)]. After the penetration of the cytosolic part of the cell, the MMPs are able to laterally enlarge the microtrack along its entire length, so that the resulting space matches the diameter of the (rigid) nuclear cluster. This way, the cell is then able to maintain the predefined direction of movement, see the left panels in Fig. 3.20c. The velocity of migration of the cell in such a subnuclear channel increases with the MMP secretion rate, until a threshold value, which, interestingly, matches the speed of the MMP-deprived cell within the intermediate

channel, as the reader can observe by comparing the bottom-right plot in Fig. 3.20 with the left graph in Fig. 3.19.

It is finally useful to remark that, at the end of the vertical channel, only a cell with a fully active proteolytic machinery would be able to create a *de novo* track large enough to maintain its directional movement. In all the other cases, it would slowly lose its polarity and start an isotropic Brownian movement (these model outcomes are not explicitly shown since they are very similar to the case of the intermediate 25 μm-channel).

3.4.4 Cell Migration in a Three-Dimensional Fibrous Scaffold

In order to get closer to the *in vivo* environment cells live in, we now apply the same modelling set-up to describe the motion of an isolated cell in isotropic 3D scaffolds, formed by a regular cubic mesh of virtual fibers that are arranged to create pores of different sizes, see Fig. 3.21a. The cell, initially placed in the middle of the scaffold, is a sphere with a diameter of 30 μm. Its nucleus is then a central spherical cluster with a diameter of 10 μm. The *hamiltonian* is defined as in Eq. (3.41). In particular, we assume that the cell cytosol is deformable (i.e., $\nu_C < 1$), whereas we vary, as usual, the elasticity of the nuclear compartment. Moreover, differently form the simulation settings presented so far, the adhesiveness between the cell and the ECM components enters the picture. In this respect, we set

$$0 < J^{ext}_{C,P} = 4.5 < J^{ext}_{C,M} = 6.5$$

because, as widely demonstrated in the experimental literature, most cell lines in standard conditions adhere more strongly to the polymeric (i.e., fibrous) part of the matrix than to its soluble component.

As summarized in Fig. 3.21, cell velocity is specifically determined by the correlation between the elastic properties of the nucleus and the dimension of matrix pores. In particular, at high pore sizes ($> 500\,\mu m^2$, i.e., in the same range of cell diameter), cell migratory behavior remains unaltered regardless of the deformation abilities of the nuclear compartment. In fact, the moving individual does not sense significative steric hindrances, since the distance from the nearest matrix fiber is too high to experience any interaction. As a consequence, in all cases, the cell exhibits a short-range movement with fluctuations in the interstitial medium around its initial position. This is consistent with the results previously presented. The formation of pore diameters of cellular or slightly subcellular ranges (say, $300\,\mu m^2$ and $100\,\mu m^2$, respectively) allows instead the cell to physically interact with fibers in all three spatial directions and is associated with the most efficient migration rates. In this case, the cell assumes an elongated morphology to pass through the matrix network. In particular, nuclear elasticity provides a further facilitation for cell movement (i.e., the speed slightly increases), since it allows the moving individual to more easily squeeze and stretch through the existing mesh. This result

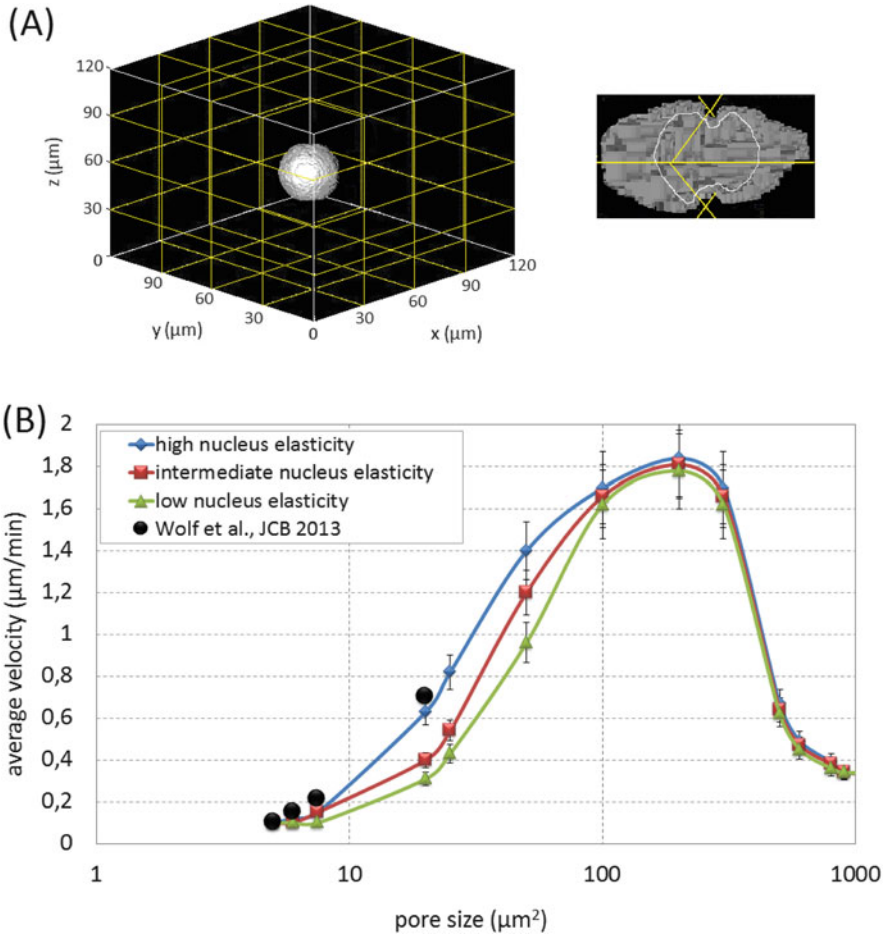

Fig. 3.21 Cell invasion within a 3D network structure, resembling an *in vivo* fibrous matrix. (**a**) Simulation domain $\Omega \subset \mathbb{R}^3$, containing both an isotropic cubic mesh of collagenous threads (*yellow stripes*) and the interstitial medium (*black*). For representative purposes, we depict a scaffold with a uniform distribution of pores of area of 900 μm^2 side length. *Inset*: Magnifications of the moving cell in the case of pores smaller than nucleus diameters. It is straightforward to see how the nucleus (manually *encircled*) has to squeeze to allow the entire individual to pass though the fiber network. (**b**) Velocity vs pore size in the case of cells with different nucleus elasticities: $\nu_N \gg 1$ (low elasticity, *green line*); $\nu_N \approx 1$ (intermediate elasticity, *red line*); $\nu_N < 1$ (high elasticity, *blue line*). The values are represented as means $\pm$ s.d. over 50 realizations. In the plot we also indicate the values of cell speed measured by Wolf and coworkers in [85] in the case of HT/MT1 cells seeded in 3D bovine dermal collagen lattices

is indeed consistent with the motile behavior of cells within intermediate channels or microtracks presented so far. Finally, an increment in the amount of matrix threads results in a scaffold characterized by small pores ($< 50\,\mu m^2$, i.e., smaller than nuclear size) and therefore by a limited available space. Indeed, only a soft nucleus

allows the cell to display an appreciable migration speed, which is not achieved in the other cases (see the inset in Fig. 3.21a). Analogous observations have previously emerged for cells moving in the subnuclear channels or microtracks.

As represented in the plot in Fig. 3.21b, the values of the cell average velocity in the case of sufficiently small pores (i.e., $\leq 20\,\mu m^2$) are also surprisingly similar to those measured by Wolf and coworkers for HT/MT1 cells, seeded in 3D bovine dermal collagen lattices [85]. Moreover, the bimodal behavior of cell speed in response to pore dimensions shown in Fig. 3.21 is consistent with the results presented in a number of experimental works focused on human adult vascular smooth muscle cells seeded in type-IV collagen scaffolds [13], human glioma cells plated on polyacrylamide ECMs [79] and different fibroblastic and cancerous cell lines migrating within 3D fibrous matrices of similar geometrical and structural properties, i.e., NR6 mouse fibroblasts in collagen-glycosaminoglycan matrices [26] or human melanoma cells in collagen lattices [18]. Moreover, neutrophil migration (both velocity and directional coefficient) has been reported to vary in a biphasic manner with the gel pore size [38], while mouse fibroblasts have been observed to migrate more significantly in collagen-glycosaminoglycan scaffolds featuring pore sizes somewhat smaller than cellular dimensions, whereas they have exhibited less dispersion in matrices with larger pores [26].

3.5 Multicomponent and Multiphase Modelling

As already mentioned in the introduction, macroscopic models based on continuum mechanics are more convenient (from a computational viewpoint) than microscopic approaches when dealing with large cell aggregates, tumor spheroids or tissues composed of millions of cells. In this respect, keeping also in mind that biological systems contain many components, the theory of mixtures appears to be a particularly suitable framework for modelling their behavior. This theory assumes that cellular and extracellular components are mixed so well that in each actual material point of the continuum matter there is a co-presence of several constituents. The proportions of the constituents can then vary from point to point and in time (see, for instance, [7, 50, 60]).

To define the percentage of volume occupied by a generic constituent α, usually called volume ratio, we can proceed as follows. Given a point in the mixture, let us consider a sequence of spheres centered in that point. Measuring the ratio between the volume occupied by the constituent α inside each sphere and the volume of the overall sphere of interest, one may observe the behavior shown in Fig. 3.22. For sample volumes (i.e., sample spheres) having the size of the microscopic constituent, the ratio is likely to oscillate very strongly due to microscopic inhomogenities. At the other extreme, macroscopic inhomogenities may affect the ratio for large sample volumes (i.e., large sample spheres). However, for intermediate sample volumes, i.e., larger than the characteristic cell size and smaller than the typical tissue scale, the ratio is nearly constant. Such a quantity

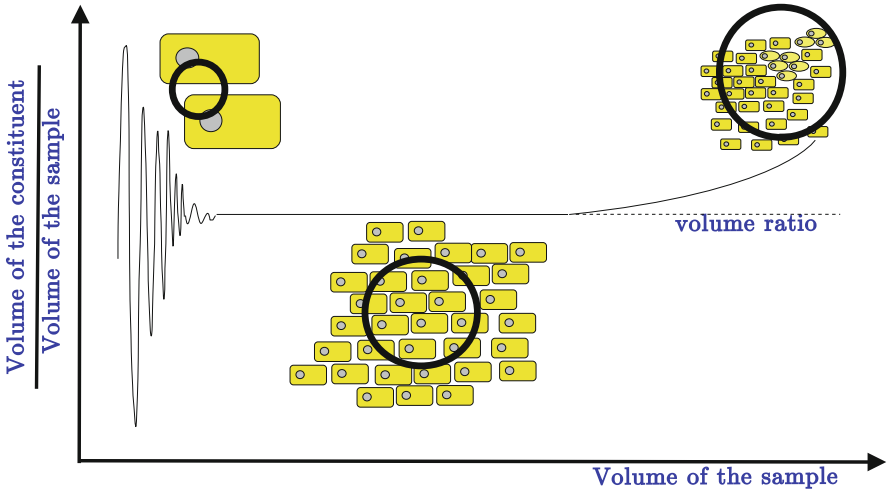

Fig. 3.22 Sample volumes to define the volume ratio

can be defined as the volume ratio of the constituent α and is labeled by ϕ_α. In this respect, it is useful to remark that the use of multiphase models at a scale comparable or even smaller than the cell size with the aim of describing the dynamics of the entire cell aggregate is at least questionable.

If one includes in the model all the constituents occupying the region of interest, then the mixture is said to be *saturated* and

$$\sum_\alpha \phi_\alpha = 1\,. \tag{3.54}$$

Otherwise, if one focuses only on some constituents, neglecting for instance the contribution of the others (for example, one may focuses only on cellular components neglecting the presence of the extracellular liquid or even of the vasculature and/or of the ECM), the mixture is said to be *unsaturated* and the unilateral constraint holds

$$\sum_\alpha \phi_\alpha \leq 1\,. \tag{3.55}$$

In this respect, in some cases, the upper constraint on the volume ratio (i.e., 1 in (3.54)) can replaced by a constant value $\overline{\phi} < 1$, possibly space dependent, allowing for some fixed portion of space to be occupied the constituents not considered in the mixture. To be more specific, if we are fixing the volume ratio $\overline{\phi}(\mathbf{x})$ occupied for example by vessels or by a general stroma Eqs. (3.54) and (3.55)

can be replaced by

$$\sum_{\alpha} \phi_{\alpha}(\mathbf{x}, t) = 1 - \overline{\phi}(\mathbf{x}) \,. \tag{3.56}$$

From the mathematical viewpoint this geometrical constraint still plays the same role as the saturation assumption (3.54). In all cases, however, the model, and in particular the growth terms and the dynamics related to the motion of the constituents, must be such that the solution always satisfies the proper constraint [56].

3.5.1 Mass Balance Equations

To define the mass balance equations for the different constituents, let us consider a general volume $\mathcal{V}$ fixed in space with boundary $\partial\mathcal{V}$. In more details, let us focus on a specific cell population c present in a soft tissue. If ρ_c is the density of the cell constituent within the host, the corresponding mass $\mathcal{V}$ is given by

$$M_c = \int_{\mathcal{V}} \rho_c \phi_c \, dV \,.$$

M_c can change in time because of

- Fluxes caused by the motion of the cell constituent through the boundary $\partial\mathcal{V}$

$$-\int_{\partial\mathcal{V}} \rho_c \phi_c \mathbf{v}_c \cdot \mathbf{n} \, d\Sigma \,,$$

  where $\mathbf{v}_c$ is the cell velocity and $\mathbf{n}$ is an external normal to the boundary $\partial\mathcal{V}$;
- Cell mitotic or death processes

$$G_c = \int_{\mathcal{V}} \rho_c \Gamma_c \, dV \,,$$

  where Γ_c is the growth/death rate of cells.

Indeed, the mass balance equation in the integral form reads as

$$\frac{dM_c}{dt} = -\int_{\partial\mathcal{V}} \rho_c \phi_c \mathbf{v}_c \cdot \mathbf{n} \, d\Sigma + \int_{\mathcal{V}} \rho_c \Gamma_c \, dV \,,$$

that, using Gauss's theorem, can be written as

$$\int_{\mathcal{V}} \left[\frac{\partial}{\partial t}(\rho_c \phi_c) + \nabla \cdot (\rho_c \phi_c \mathbf{v}_c) - \rho_c \Gamma_c \right] dV = 0 \,.$$

If the integrand is smooth, thanks to the arbitrariety of the volume of integration $\mathcal{V}$, we can get the mass balance equation in local form

$$\frac{\partial}{\partial t}(\rho_c \phi_c) + \nabla \cdot (\rho_c \phi_c \mathbf{v}_c) = \rho_c \Gamma_c \,, \tag{3.57}$$

where ρ_c can be taken constant and equal to the density of water ρ. In this case we can simplify (3.57) as

$$\frac{\partial \phi_c}{\partial t} + \nabla \cdot (\phi_c \mathbf{v}_c) = \Gamma_c \,. \tag{3.58}$$

The same procedure can be repeated for each cell population c_i, so that if ϕ_{c_i} is the related volume ratio, one has

$$\frac{\partial \phi_{c_i}}{\partial t} + \nabla \cdot (\phi_{c_i} \mathbf{v}_{c_i}) = \Gamma_{c_i} \,, \qquad i = 1, \ldots, I \,, \tag{3.59}$$

with the acceptable assumption that all cell constituents have a density that is close to that of water, i.e., all densities ρ_{c_i} are set equal to ρ. Actually, defining $\phi_c = \sum_i \phi_{c_i}$ as the total cell volume ratio, Eq. (3.58) can be viewed as the mass balance equation for the overall cell constituent of the mixture, where

$$\phi_c \mathbf{v}_c = \sum_i \phi_{c_i} \mathbf{v}_{c_i} \,, \quad \text{and} \qquad \Gamma_c = \sum_i \Gamma_{c_i} \,.$$

An identical procedure can be repeated for each other constituent, such as the different components m_j of the ECM, with volume ratio ϕ_{m_j} (possibly including blood and lymphatic vessels), and the liquid ℓ, with volume ratio ϕ_ℓ. Indeed, we can write

$$\frac{\partial \phi_{m_j}}{\partial t} + \nabla \cdot (\phi_{m_j} \mathbf{v}_{m_j}) = \Gamma_{m_j} \,, \qquad j = 1, \ldots, J \tag{3.60}$$

and

$$\frac{\partial \phi_\ell}{\partial t} + \nabla \cdot (\phi_\ell \mathbf{v}_\ell) = \Gamma_\ell \,. \tag{3.61}$$

Hence, in a compact way we can write the resulting set of mass balance equations as

$$\frac{\partial \phi_\alpha}{\partial t} + \nabla \cdot (\phi_\alpha \mathbf{v}_\alpha) = \Gamma_\alpha \,. \tag{3.62}$$

However, as already mentioned, the different ECM constituents and the blood and lymphatic vasculature form an intricate and interlinked network: in this respect, one can assume that there is no relative sliding and that all of them move with the same

velocity $\mathbf{v}_m$. This hypothesis, usually named *constrained sub-mixture assumption*, allows to simplify (3.60) to obtain

$$\frac{\partial \phi_{m_j}}{\partial t} + \nabla \cdot \left(\phi_{m_j} \mathbf{v}_m\right) = \Gamma_{m_j}\,, \qquad j = 1, \ldots, J\,, \tag{3.63}$$

which require the identification of only one velocity field, i.e., $\mathbf{v}_m$.

If it is not necessary to distinguish the specific role played by the different matrix and/or vasculature constituents, the equations above can be summed-up to get

$$\frac{\partial \phi_m}{\partial t} + \nabla \cdot (\phi_m \mathbf{v}_m) = \Gamma_m\,, \tag{3.64}$$

where

$$\sum_{j=1}^{J} m_j = m\,, \qquad \sum_{j=1}^{J} \Gamma_{m_j} = \Gamma_m\,. \tag{3.65}$$

When approaching tissue growth and remodelling, a crucial role is played by the growth terms, i.e., Γ_{c_i} and Γ_{m_j}. In particular, Γ_{c_i} includes terms both related to growth (or death) due to the absorption (or release) of mass from (or in) the extracellular liquid. Another important contribution in such terms is due to population transfers (i.e., processes resulting in the phenotypic differentiation of cells, that therefore pass from a clone to another of the same cell lines). In this case, the same term will appear in the growth term of the mass balance equations of two cell phenotypes, say c_h and c_k, but with opposite signs. However, it will not appear in the mass balance equation of the overall cell constituent, because the two mass transfer terms will cancel out.

Similarly, all terms used for instance to describe cell growth by liquid absorption should be present also in the mass balance equation for the liquid, but with the opposite sign.

If mass exchange occurs only between the constituents considered in the mixture, then the mixture itself is said to be *closed* and

$$\sum_{\alpha} \Gamma_\alpha = 0\,. \tag{3.66}$$

This is for instance the case of an avascular tumor when all constituents are taken into account, including the extracellular liquid. On the opposite, for a vascular malignancy, Eq. (3.66) does not hold, because of the fluid flowing in the blood vessels which is then perfusing the tissue and is absorbed by the lymphatic system. In this case, the mixture is said to be *open*. The same considerations are valid also for unsaturated cases when, for instance, the extracellular liquid may be not considered and may act as an "external reservoir".

3.5.2 Force Balance Equations

To determine the evolution of the velocities appearing in the mass balance equations, the theory of mixture requires to derive a momentum balance equation for each constituent. In this respect, at the end of the section we will exploit the fact that growth phenomena are so slow that inertial terms can be neglected in order to rewrite the equations in a force balance form.

Focusing again on the cellular constituent of the tissue, the momentum of the ensemble of cells in the fixed volume $\mathcal{V}$, i.e.,

$$\mathbf{Q}_c = \int_{\mathcal{V}} \rho_c \phi_c \mathbf{v}_c \, dV \,,$$

can change because of

- Momentum flux caused by the motion of the cells through the boundary $\partial\mathcal{V}$

$$-\int_{\partial\mathcal{V}} \rho_c \phi_c \mathbf{v}_c (\mathbf{v}_c \cdot \mathbf{n}) \, d\Sigma \,;$$

- Contact forces acting on the cells inside the volume $\mathcal{V}$ due to their contact with other cells outside $\mathcal{V}$ (i.e., through the boundary $\partial\mathcal{V}$)

$$\int_{\partial\mathcal{V}} \widetilde{\mathbf{T}}_c^T \mathbf{n} \, d\Sigma \,,$$

  where $\widetilde{\mathbf{T}}_c$ is called *partial stress tensor*;
- Interaction forces with the other constituents, e.g., ECM or liquid, through the microscopic interface separating the constituents, say the cell membrane wet by the extracellular liquid or in contact with the extracellular matrix through the adhesion sites, within the volume $\mathcal{V}$

$$\int_{\mathcal{V}} \widetilde{\mathbf{m}}_c \, dV \,,$$

  where $\widetilde{\mathbf{m}}_c$ is called *interaction force*;
- Momentum supply related to phase changes

$$\int_{\mathcal{V}} \rho_c \Gamma_c \mathbf{v}_c \, dV \,,$$

  e.g., fluid absorbed by a growing cell;
- Body forces

$$\int_{\mathcal{V}} \rho_c \phi_c \mathbf{b}_c \, dv.$$

Such a term may model for instance chemotaxis or haptotaxis although, as we shall see in Sect. 3.8, they in reality involve also the activation of internal subcellular mechanisms rather than only an external force (like gravity).

We can the write the integral form of the balance of momentum as

$$\frac{d\mathbf{Q}_c}{dt} = \int_{\partial\mathcal{V}} \left[-\rho\phi_c\mathbf{v}_c(\mathbf{v}_c\cdot\mathbf{n}) + \widetilde{\mathbf{T}}_c^T\mathbf{n}\right] d\Sigma + \int_{\mathcal{V}} (\rho\phi_c\mathbf{b}_c + \widetilde{\mathbf{m}}_c + \rho\Gamma_c\mathbf{v}_c)\, dV\,, \tag{3.67}$$

which using Gauss theorem can be written as

$$\int_{\mathcal{V}} \left[\frac{\partial}{\partial t}(\rho\phi_c\mathbf{v}_c) + \nabla\cdot(\rho\phi_c\mathbf{v}_c\otimes\mathbf{v}_c) - \nabla\cdot\widetilde{\mathbf{T}}_c - \rho\phi_c\mathbf{b}_c - \widetilde{\mathbf{m}}_c - \rho\Gamma_c\mathbf{v}_c\right] dV = 0\,. \tag{3.68}$$

Finally, if the integrand is sufficiently smooth, considering that (3.68) holds for any volume of integration $\mathcal{V}$, we can write the following local form of the momentum balance for the cell constituent in conservative form

$$\frac{\partial}{\partial t}(\rho\phi_c\mathbf{v}_c) + \nabla\cdot(\rho\phi_c\mathbf{v}_c\otimes\mathbf{v}_c) = \nabla\cdot\widetilde{\mathbf{T}}_c + \rho\phi_c\mathbf{b}_c + \widetilde{\mathbf{m}}_c + \rho\Gamma_c\mathbf{v}_c\,. \tag{3.69}$$

Actually, using the mass balance equation (3.58), Eq. (3.69) can be simplified to

$$\rho\phi_c\left(\frac{\partial\mathbf{v}_c}{\partial t} + \mathbf{v}_c\cdot\nabla\mathbf{v}_c\right) = \nabla\cdot\widetilde{\mathbf{T}}_c + \rho\phi_c\mathbf{b}_c + \widetilde{\mathbf{m}}_c\,. \tag{3.70}$$

The generalization to all cell populations gives

$$\rho\phi_{c_i}\left(\frac{\partial\mathbf{v}_{c_i}}{\partial t} + \mathbf{v}_{c_i}\cdot\nabla\mathbf{v}_{c_i}\right) = \nabla\cdot\widetilde{\mathbf{T}}_{c_i} + \rho\phi_{c_i}\mathbf{b}_{c_i} + \widetilde{\mathbf{m}}_{c_i}\,, \qquad i = 1,\ldots,I\,. \tag{3.71}$$

Similar equations hold for the interstitial liquid

$$\rho\phi_\ell\left(\frac{\partial\mathbf{v}_\ell}{\partial t} + \mathbf{v}_\ell\cdot\nabla\mathbf{v}_\ell\right) = \nabla\cdot\widetilde{\mathbf{T}}_\ell + \rho\phi_\ell\mathbf{b}_\ell + \widetilde{\mathbf{m}}_\ell\,, \tag{3.72}$$

and for the extra-cellular network

$$\rho\phi_m\left(\frac{\partial\mathbf{v}_m}{\partial t} + \mathbf{v}_m\cdot\nabla\mathbf{v}_m\right) = \nabla\cdot\widetilde{\mathbf{T}}_m + \rho\phi_m\mathbf{b}_m + \widetilde{\mathbf{m}}_m\,. \tag{3.73}$$

Of course, one could write a momentum equation for each component of the extra-cellular network, but the constrained sub-mixture assumption implies that it is sufficient to write a single equation for the common velocity $\mathbf{v}_m$. All the components of the extra-cellular network, possibly including vessels, will however contribute to the constitutive equation for the stress tensor according to their relative proportions.

Growth phenomena are very slow, so that all inertial terms of the equations above can be neglected and all momentum equations can be simplified to

$$\nabla \cdot \widetilde{\mathbf{T}}_\alpha + \rho \phi_\alpha \mathbf{b}_\alpha + \widetilde{\mathbf{m}}_\alpha = \mathbf{0}. \tag{3.74}$$

If the mixture is closed and therefore the momentum is exchanged only between the constituents taken into consideration, the mass supplies and the interaction forces are subject to the constraint [7, 60]

$$\sum_\alpha (\widetilde{\mathbf{m}}_\alpha + \rho \Gamma_\alpha \mathbf{v}_\alpha) = \mathbf{0}\,. \tag{3.75}$$

This results from the fact that if one sums up all momentum equations (3.71), (3.72), and (3.73) to obtain the momentum equation for the overall mixture, no supply terms should appear because they represent internal exchange terms of momentum.

However, as discussed in detail in [55], coherently with the fact that inertia can be neglected, the contribution due to mass exchange can be dropped in (3.75) (it is negligible with respect to that due to the interaction forces), so that

$$\sum_\alpha \widetilde{\mathbf{m}}_\alpha = \mathbf{0}\,. \tag{3.76}$$

The term $\widetilde{\mathbf{m}}_\alpha$ in Eq. (3.74) contains all forces acting on the constituent α due to its interactions with the other constituents, i.e., $\widetilde{\mathbf{m}}_\alpha = \sum_\beta \mathbf{m}_{\alpha\beta}$ where $\mathbf{m}_{\alpha\beta}$ is the force acting on the constituent α due to β. The application of an action-reaction principle for each interaction pair implies that $\mathbf{m}_{\alpha\beta} = -\mathbf{m}_{\beta\alpha}$. Considering in particular the interaction of the fluid with the other constituents, we can take it to be proportional to the velocity difference between the constituents, i.e.,

$$\mathbf{m}_{\ell\beta} = -\phi_\beta \phi_\ell \, \mu \mathbf{K}^{-1}(\phi_\ell)(\mathbf{v}_\ell - \mathbf{v}_\beta)\,, \tag{3.77}$$

where μ is the viscosity of the extra-cellular fluid and $\mathbf{K}$ is related to the permeability tensor. Notice that the permeability tensor is the same for all the constituents, as water is unable to distinguish whether it is flowing around a constituent or another. In many applications $\mathbf{K}$ is assumed independent of ϕ_ℓ. For instance, the classical Kozeny-Carman relation can be recovered assuming $\mathbf{K}(\phi_\ell) = \dfrac{\phi_\ell^2}{1-\phi_\ell}\hat{\mathbf{K}}$, where $\hat{\mathbf{K}}$ is independent of ϕ_ℓ. However, such slightly different choices give rise in practice to very little discrepancies, because biological applications are characterized by small variations of ϕ_ℓ .

The interaction forces involving cells and ECM or different types of cells are more complex to be modelled and require to account for the results of Sect. 3.3, because they depend on adhesive dynamics.

3.5.3 Model Reduction for the Saturated Case

In the unsaturated case, in which the presence of the interstitial liquid is neglected, there is no need for an equation for the liquid. Moreover, for each constituent α, $\widetilde{\mathbf{m}}_\alpha$ will only include the microscopic interactions not involving the interstitial fluid, i.e., those only occurring between cell types or between a cell type and a ECM component.

However, in this section we will show that one can obtain similar conclusions even in the saturated case, as the just mentioned simplifying assumption holds under proper physiological conditions on the stiffness of the tissue and the interstitial pressure drop.

Without entering in details that can be found for instance in [7, 60], it needs to be mentioned that in the saturated case the geometric constraint (3.54) implies (by thermodynamic arguments) the presence of a Lagrange multiplier that writes as a pressure term. Therefore, the force balance equations result as follows:

$$-\phi_\alpha \nabla P + \nabla \cdot \mathbf{T}_\alpha + \sum_{\beta \neq \alpha, \ell} \mathbf{m}_{\alpha\beta} + \phi_\alpha \phi_\ell \mu \mathbf{K}^{-1}(\mathbf{v}_\ell - \mathbf{v}_\alpha) + \rho \phi_\alpha \mathbf{b}_\alpha = \mathbf{0}\,, \quad \alpha \neq \ell\,, \tag{3.78}$$

$$-\phi_\ell \nabla P + \nabla \cdot \mathbf{T}_\ell - \sum_\alpha \phi_\alpha \phi_\ell \mu \mathbf{K}^{-1}(\mathbf{v}_\ell - \mathbf{v}_\alpha) + \rho \phi_\ell \mathbf{b}_\ell = \mathbf{0}\,. \tag{3.79}$$

Considering that the extracellular liquid is flowing in a porous material constituted by cells and extra-cellular network, its motion can be described using Darcy's law. This is classically obtained (see [7, 60]) from the assumption that the extra-stress $\mathbf{T}_\ell$ is negligible with respect, say, to the pressure gradient and the interaction forces, so that (3.79) can be simplified to

$$\sum_{\alpha \neq \ell} \phi_\alpha (\mathbf{v}_\ell - \mathbf{v}_\alpha) = -\frac{\mathbf{K}}{\mu}(\nabla P - \rho \mathbf{b}_\ell)\,. \tag{3.80}$$

In order to identify the relevant contributions in the momentum equations (3.78), it is convenient to scale the equations. From Darcy's law the characteristic velocity of the liquid is given by $\hat{v}_\ell = \dfrac{K \Delta P}{\mu d}$, where ΔP is the pressure drop within the tissue between regions close to the arterial and the venous/lymphatic system, K is a measure of the order of magnitude of the permeability tensor $\mathbf{K}$, and d is the intercapillary distance. In [12], Chary and Jain, for instance, measured $\hat{v}_\ell$ to be in the range 0.4–0.9 μm/s. On the other hand, the characteristic velocity of cell and matrix constituents (that move almost with the same speed during growth induced remodelling) is $\hat{v}_c = \hat{v}_m = \Gamma_c D$, where $D \approx 10\,\mu$m is a mean cell diameter and

$\Gamma_c \approx 1\ \text{day}^{-1} \approx 1.2 \cdot 10^{-5}\,\text{s}^{-1}$. Such a parameter setting results in $\hat{v}_c = \hat{v}_m \approx 10^{-4}\,\mu\text{m/s}$.

Dropping the body force acting on the liquid, we can then write the dimensionless form of (3.80) as

$$\mathbf{v}_\ell^* = \frac{V}{1-\phi_\ell}\sum_{\alpha\neq\ell}\phi_\alpha \mathbf{v}_\alpha^* - \frac{1}{1-\phi_\ell}\mathbf{K}^*\nabla^* P^*\,, \tag{3.81}$$

where $V = \dfrac{\hat{v}_c}{\hat{v}_\ell} = \dfrac{\mu\Gamma_c dD}{K\Delta P}$ that, considering the above-introduced estimates, is much smaller than 1.

Similarly, for instance, the dimensionless form of the other force balance equations can be written scaling the stress tensor with the Young modulus of the tissue E and the cell-ECM interaction force with the corresponding mechanical response E/d, as

$$\nabla\cdot\mathbf{T}_\alpha^* + \sum_{\beta\neq\alpha,\ell}\mathbf{m}_{\alpha\beta}^* + \frac{\Delta P}{E}\left[-\frac{\phi_\alpha}{1-\phi_\ell}\nabla^* P^* + V\sum_{\beta\neq\ell}\frac{\phi_\alpha\phi_\beta\phi_\ell}{1-\phi_\ell}(\mathbf{K}^*)^{-1}(\mathbf{v}_\beta^* - \mathbf{v}_\alpha^*)\right] = \mathbf{0}\,, \tag{3.82}$$

for $\alpha \neq \ell$.

Certainly, the last term in square parenthesis is negligible compared to the first one but, if also $\Delta P \ll E$, then the entire parenthesis can be dropped. This assumption holds in many cases. For instance, it is known that the elastic modulus of the softest fatty regions of a healthy breast is of the order of 20 kPa. Similarly for prostatic tissues the elastic modulus ranges between 40 and 70 kPA [37]. On the other hand, $\Delta P \approx 1$ kPa for normal tissues [32, 78]. In all cases, we have that $\dfrac{\Delta P}{E} < 0.1$. For tumor tissues, both values increase more or less one order of magnitude. For instance, for breast tumors and for prostatic cancerous tissues one has that $E > 100$ kPa [37] and that $\Delta P \approx 10$ kPa [5, 6, 32, 78, 81], so that again $\dfrac{\Delta P}{E} < 0.1$.

In such cases, it is possible to simplify the momentum equations, in the dimensional form, as

$$\nabla\cdot\mathbf{T}_\alpha + \sum_{\beta\neq\alpha,\ell}\mathbf{m}_{\alpha\beta} = \mathbf{0}\,, \qquad \alpha\neq\ell\,, \tag{3.83}$$

so that they depend neither on the interstitial pressure, nor on the liquid velocity. Therefore, they can be in principle solved without determining the evolution of the interstitial pressure, or of the interstitial velocity. In this case, the relative equations

are solvable *in cascade* after integrating Eqs. (3.83), jointly with the mass balance equations.

It is however useful to remark that this procedure might not be true in other dynamical phenomena which involve higher pressure gradients, such as fast compression of tissues (e.g., cartilage dynamics) or heart mechanics.

3.6 Linking Multiphase Models to the Result of Microscopic Models

In Sects. 3.3 and 3.4 we have discussed some models based on the observation that cell migration strongly depends on ECM stiffness and volume ratio, and in particular on the relative dimension of pores and channels characterizing the 3D matrix structures cells move through with respect to the dimension of their nucleus. In this respect, we have discussed the results of the experiments performed by Wolf and coworkers [84], who showed that there is a minimal pore (or channel) cross section (i.e., of about 5–10 μm^2) necessary to allow cell motion through three-dimensional ECMs. Above this critical threshold the mean cell speed depends almost linearly from the pore characteristic dimension, at least in the range considered (i.e., below 20 μm^2).

Wolf and colleagues observed that a threshold value of pore size exists also for multicellular spheroids invading across dense ECMs. In particular, the cells at the border of the spheroid try to penetrate the thick fiber network: however, while their cytoplasm is able to extend in the pores of the ECM, their nuclei remain trapped at the border of the aggregate (for instance, due to their rigidity, as previously commented). Indeed, there is no significant invasion of the tissue and the spheroid interface after 18 hours is still the same (see the bottom panels of Fig. 3.23). At this point, if cells are able to express metalloproteinases (MMPs), matrix fibers can be partially degraded with the consequent formation of paths within the collagen structure that can be used by the cells themselves for further invasion. Otherwise, cells with inhibited MMP-activity are able to invade only matrix environments characterized by a mean pore size that is not too sterically restrictive, as in the case of a GM6001 cell spheroid seeded within a bovine collagen network (see Fig. 3.23 top panels).

3.6.1 Cell Motility

The phenomenology described above can be properly described with a continuous model. In particular, we can consider the system as composed of three main constituents (cells, ECM, and liquid) where, as discussed in Sect. 3.5, the liquid has a negligible mechanical interaction with the other constituents. As we will see later on (in Sect. 3.6.3), the cellular population, c, can be possibly distinguished in

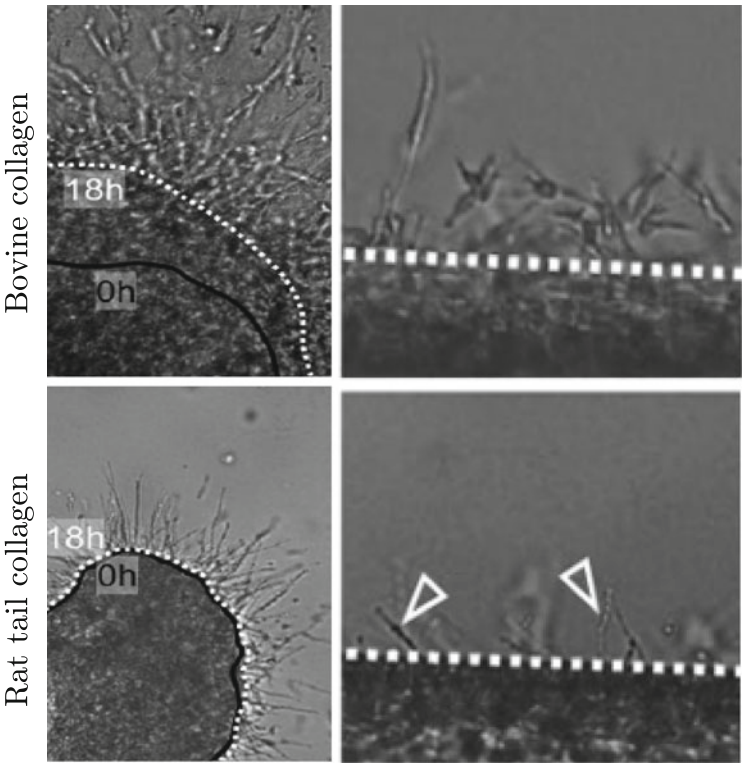

Fig. 3.23 Invasion into rat tail (*bottom*) and bovine (*top*) collagen when MMP activity is inhibited. Referring to Fig. 3.1, the rat tail collagen is characterized by a finer mesh that can not be penetrated by cells with a rigid nucleus. The *right panels* show a magnification of the region close to the spheroid interface. In the *bottom-right panel*, *arrowheads* indicate long cytoplasmic extensions of cells with the nucleus instead stuck below the collagen. Partially modified from [84] (with permission)

two sub-populations, namely normal and tumour cells, labeled by the subscript i. However, let us start from (3.83) and assume that the cell-ECM interaction force is proportional to the relative velocity, i.e.,

$$\mathbf{m}_{c_i m} = -\phi_{c_i}\phi_m \mathbf{M}_{im}^{-1}(\mathbf{v}_{c_i} - \mathbf{v}_m)\,, \tag{3.84}$$

or

$$\mathbf{v}_{c_i} - \mathbf{v}_m = -\frac{1}{\phi_{c_i}\phi_m}\mathbf{M}_{im}\mathbf{m}_{c_i m}\,. \tag{3.85}$$

Recalling the results given in Sect. 3.2, this assumption implies that, at the microscopic level, integrins constantly renew at the cell membrane independently from

the force exerted on the focal adhesion point. Of course, it is possible to use other more complex models, as described in Sect. 3.2.

As in (3.77), the multiplicative factor $\phi_{c_i}\phi_m$ takes into account of the fact that the interaction force is proportional to the volume ratios of the constituents. In fact, if there are no cells or no ECM, no interaction force can be exchanged as well. On the other hand, if the number of cells or the density of ECM increase, the interaction force will increase.

Given the specific problem of interest, the motility tensor $\mathbf{M}_{im}$ can not be considered constant or simply depending on the volume ratio, like in the Cozeny-Karman rule. It in fact vanishes below a threshold pore area, $\bar{A}_i$ that may depend on mechanical and geometrical properties of the invading cells, such as nucleus stiffness and size and cell traction abilities. Furthermore, for pore areas slightly above $\bar{A}_i$ it appears to be proportional to $A_m - \bar{A}_i$, where A_m is the characteristic pore area of the ECM of interest.

Considering then the isotropic case for sake of simplicity, the motility M_{im} can be assumed of this form:

$$M_{im} = \nu_i \left(A_m - \bar{A}_i\right)_+ , \tag{3.86}$$

where $(f)_+ = \frac{f+|f|}{2}$ stands for the positive part of f and the motility coefficient ν_i can be evaluated by the experiments in [84] from the slope of the curve giving the dependence of the cell velocity from the pore section of the pores in the gel.

Furthermore, we have seen in Sects. 3.3 and 3.4 that in both two- and three-dimensional environments cell velocity has a bimodal behavior depending on the ECM structure, porosity, density, adhesion, and stiffness, as shown also by experimental data [8, 13, 44, 45, 52, 86]. This means that there is a critical pore size above which traction is not so effective, because the number of focal adhesion points that cells can form is limited, so that they are unable to pull strongly on the ECM. Therefore, a generalization of (3.86) could be

$$M_{im} = \nu_i \frac{\left(A_m - \bar{A}_i\right)_+}{\left(1 + \frac{A_m - \bar{A}_i}{\hat{A}_i}\right)^n} , \tag{3.87}$$

that reduces to (3.86) for $n = 0$, saturates to $\nu_i \hat{A}_i$ for $n = 1$ and goes to zero for large pore areas if $n > 1$ after a maximum in $\left(\bar{A}_i + \frac{\hat{A}_i}{n-1}\right)$. Unfortunately, to our knowledge, there are no quantitative experiments that can help in evaluating neither $\hat{A}_i$ nor n. However, some hints can be obtained by the simulations described in Sect. 3.4.

Going in more detail, the threshold value $\bar{A}_i$ is not a constant but, as shown by both the experiments and the mathematical results in Sects. 3.3 and 3.4, it should at least depend on

- nucleus stiffness and dimension;
- cell traction ability and compression state of the cellular aggregate.

The former two dependencies measure the strength or the energy required by a cell in order to suitably change the shape of its nucleus to pass through pores of a given area. The latter two dependencies measure instead the force that a cell passively experiences as a consequence of the pressure of the other cells, or the force that a cell is able to exert by itself attaching and pulling on the ECM fibers, and therefore the work they can do. As discussed in Sect. 3.3, this last contribution will depend on the density of integrins expressed at the membrane, on the density of adhesive sites on the ECM, and on the active force due to myosin activation.

In analogy with Eq. (3.38), we define by

$$G_i = \frac{1}{3\mu_{n_i}} |\mathrm{tr}\, \mathbf{T}_{c_i}| \tag{3.88}$$

the ratio between an invariant measure of the stress acting on cells of type i and their nucleus elastic modulus μ_{n_i}. Then, using the results from [21] and reported in Sect. 3.3, we have that the threshold value $\bar{A}_i$ or, better, the ratio $\bar{A}_i/A_n$, where A_n is the cross section area of the cellular nucleus at rest, can be evaluated by formally inverting the relationship $G_i = g(\bar{A}_i/A_n)$, where, recalling the discussion in Sect. 3.3 and in particular Eq. (3.39)

$$g\left(\frac{\bar{A}_i}{A_n}\right) = \frac{2}{3} \frac{2\frac{\bar{A}_i}{A_n} + \frac{A_n^2}{\bar{A}_i^2} - 3}{2\frac{A_n}{\bar{A}_i} - 1 + \sqrt{1 - \frac{\bar{A}_i}{A_n}}} \sqrt{\frac{A_n}{\bar{A}_i}}, \qquad \text{for } \bar{A}_i < A_n\,. \tag{3.89}$$

that is drawn in Fig. 3.24.

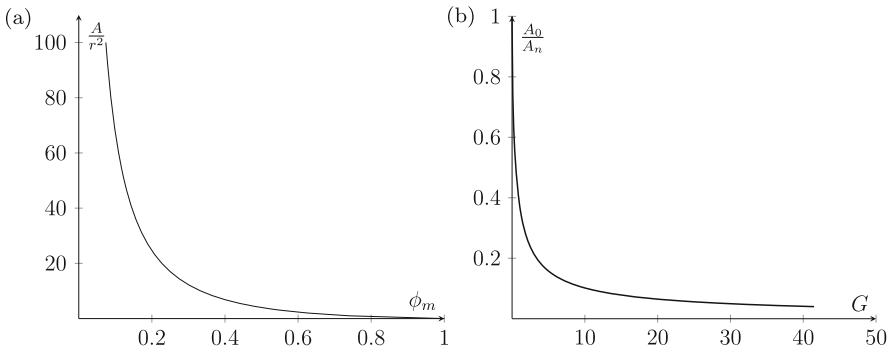

Fig. 3.24 Evaluation of the relationships between ECM pore area and volume ratio (in log ϕ_m) (**a**) and between the scaled threshold pore area and the ratio of stress versus nucleus stiffness, which is given by G (**b**)

For a given pore dimension $A_m(\phi_m)$ it will be also useful to denote by

$$T_i^m = \mu_{i_n} g \left(\frac{A_m}{A_n} \right) , \tag{3.90}$$

the traction necessary to pass through pores of area A_m.

In the study of problems where ECM remodelling plays an important role, for example in the case of MMP-dependent cell motion, it is important to evaluate how the volume ratio of ECM ϕ_m is related to the pore area of the ECM, a parameter that, as shown in Eq. (3.86) is fundamental in determining cell motility within the ECM. Real ECMs are characterized by randomly distributed fibers, so that the pore area is a random variable that, however, is strictly related to the volume ratio of the matrix.

An easier evaluation of the relationship between pore area and ϕ_m can be obtained for synthesized artificial scaffolds characterized by a regular structure. For instance, assuming that fibers are regularly distributed in a lattice-like manner, like that represented in Fig. 3.25, and that each collagenous thread has a square cross section with thickness $2r$, the following obvious relation holds:

$$A_m = (l - 2r)^2 = r^2 \left(\frac{1}{x} - 2 \right)^2 , \tag{3.91}$$

where $x = r/l$ and l is the side of each crystal component of the ECM.

To obtain a relation between ϕ_m and A_m, we can observe first of all that, in the case of the approximated ECM structure in Fig. 3.25,

$$\phi_m = \frac{12lr^2 - 16r^3}{l^3} = 4(3x^2 - 4x^3) . \tag{3.92}$$

Then Eq. (3.91) can be inverted to give

$$x = \frac{1}{\frac{\sqrt{A_m}}{r} + 2} ,$$

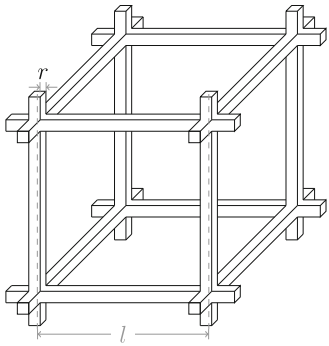

Fig. 3.25 Schematization of a regular structure of the ECM

and substituted back in (3.92) to obtain

$$\phi_m = 4\frac{3\frac{\sqrt{A_m}}{r}+2}{\left(\frac{\sqrt{A_m}}{r}+2\right)^3}\,. \tag{3.93}$$

From the experiments in [84], $\bar{A}_i \approx 5-10\,\mu\text{m}^2$. So, considering that single collagen fibrils have a radius of order $10^{-1}-10^{-2}\,\mu$m (see Fig. 3.1), then both x and r^2/A_m are much smaller than one. Even considering thick fiber bundles (i.e., that can reach a thickness of $1\,\mu$m) or artificially fabricated fibers, which can nowadays hardly reach thicknesses smaller than $1\,\mu$m, it results that $r^2/A_m \approx 0.05$. One can indeed get the approximate relationship

$$\phi_m \approx 12\frac{r^2}{A_m}\,, \qquad \text{for } A_m \gg r^2\,. \tag{3.94}$$

Results similar to (3.93) can be obtained replacing square section fibers with cylinders, or assuming that fibers do not cross. Actually, all evaluations collapse for $A_m \gg r^2$ to $A_m = 3A_f/\phi_m$, where A_f is the area of the cross section of the fibers.

3.6.2 Compartmentalization and Invasion

As an application of the proposed theory, in this section we model the growth of a tumor mass in a heterogeneous environment, characterized by the presence of a thick ECM layer that, in some situations, is able to compartmentalize the tumor while, under other conditions, can be penetrated by malignant cells that are then able to invade the tissue beyond it.

Keeping in mind the results of the experiments in [24, 40, 61] and of the mathematical models in Sects. 3.3 and 3.4, the threshold values both of the pore size $\overline{A}_i$ and of $\hat{A}_i$ in (3.87) are a function of cell geometrical and mechanical properties.

In order to explain the features of the model we first look at the one-dimensional case. In particular, we consider a single cell population (labeled by c without subscripts) growing in a liquid environment characterized by a region with lower ECM density ϕ_m^-, i.e., bigger pores, and a region with higher ECM density ϕ_m^+, i.e., smaller pores. This last region will be named Ω_m.

If cells are not able to degrade the ECM, then its density will remain constant in time. Therefore, we have only to focus on the cell population:

$$\begin{cases} \dfrac{\partial \phi_c}{\partial t} + \nabla\cdot(\phi_c \mathbf{v}_c) = \Gamma_c\,, \\ \nabla\cdot\mathbf{T}_c + \mathbf{m}_{cm} = \mathbf{0}\,. \end{cases} \tag{3.95}$$

In principle one could consider, as it will be done in the following section, the stress tensor split in a passive and an active part, the latter being related to the traction forces that cells are able to exert by adhering to the ECM and activating their cytoplasmic molecular motors (myosin). However, for sake of simplicity, this will not be done here.

We assume that nutrients are abundant everywhere and that growth is limited by cell-cell compression only, a phenomenon known as contact inhibition of growth [11]. Cell duplication and death is then regulated by

$$\Gamma_c = \left[\gamma \mathcal{H}_\varepsilon(\bar{\psi} - \psi) - \delta\right]\phi_c \,, \tag{3.96}$$

where γ is the duplication rate of cells, δ is the apoptotic rate and $\mathcal{H}_\varepsilon$ is a continuous mollificator of the Heaviside function defined as

$$\mathcal{H}_\varepsilon(\bar{\psi} - \psi) = \begin{cases} 1 \,, & \text{if } \psi \leq \bar{\psi} - \varepsilon; \\ \psi/\varepsilon \,, & \text{if } \bar{\psi} - \varepsilon < \psi < \bar{\psi}; \\ 0 \,, & \text{if } \psi \geq \bar{\psi} \,, \end{cases} \tag{3.97}$$

where $\psi := \phi_c + \phi_m$ and $\bar{\psi}$ is the threshold value that models contact inhibition.

For sake of simplicity, we assume that the cell aggregate behaves like an elastic fluid, i.e., $\mathbf{T}_c = -\Sigma(\psi)\mathbf{I}$ with

$$\Sigma(\psi) = E\frac{1 - \psi_{free}}{1 - \psi}(\psi - \psi_{free})_+ \,, \tag{3.98}$$

where E is an analogous of the Young modulus for low compression and ψ_{free} is the highest volume ratio below which cells do not experience compression. Obviously, more complex constitutive equations could be used [19, 20, 57, 58] resorting to the theory of evolving natural configuration.

Recalling Eqs. (3.85) and (3.87) that, in the case of rigid ECMs, rewrite as

$$\phi_c \mathbf{v}_c = \frac{M_{cm}}{\phi_m}\nabla \cdot \mathbf{T}_c = -\frac{\nu}{\phi_m}\frac{\left(A_m(\phi_m) - \bar{A}\right)_+}{\left(1 + \frac{A_m(\phi_m) - \bar{A}}{\hat{A}}\right)^n}\nabla\Sigma(\psi) \,,$$

one can get to the single equation

$$\frac{\partial \phi_c}{\partial t} + \nabla \cdot \left\{ \frac{\nu}{\phi_m}\frac{\left(A_m(\phi_m) - \bar{A}\right)_+}{\left(1 + \frac{A_m(\phi_m) - \bar{A}}{\hat{A}}\right)^n}\Sigma'(\psi)\nabla\psi \right\} = \left[\gamma \mathcal{H}_\varepsilon(\bar{\psi} - \psi) - \delta\right]\phi_c \,. \tag{3.99}$$

The solution of this equation would reproduce the behavior that in [84] has been observed for the so-called GM6001 cells, that are not able to produce MMPs. Figure 3.26 show two situations that differ only from the thickness of the ECM and

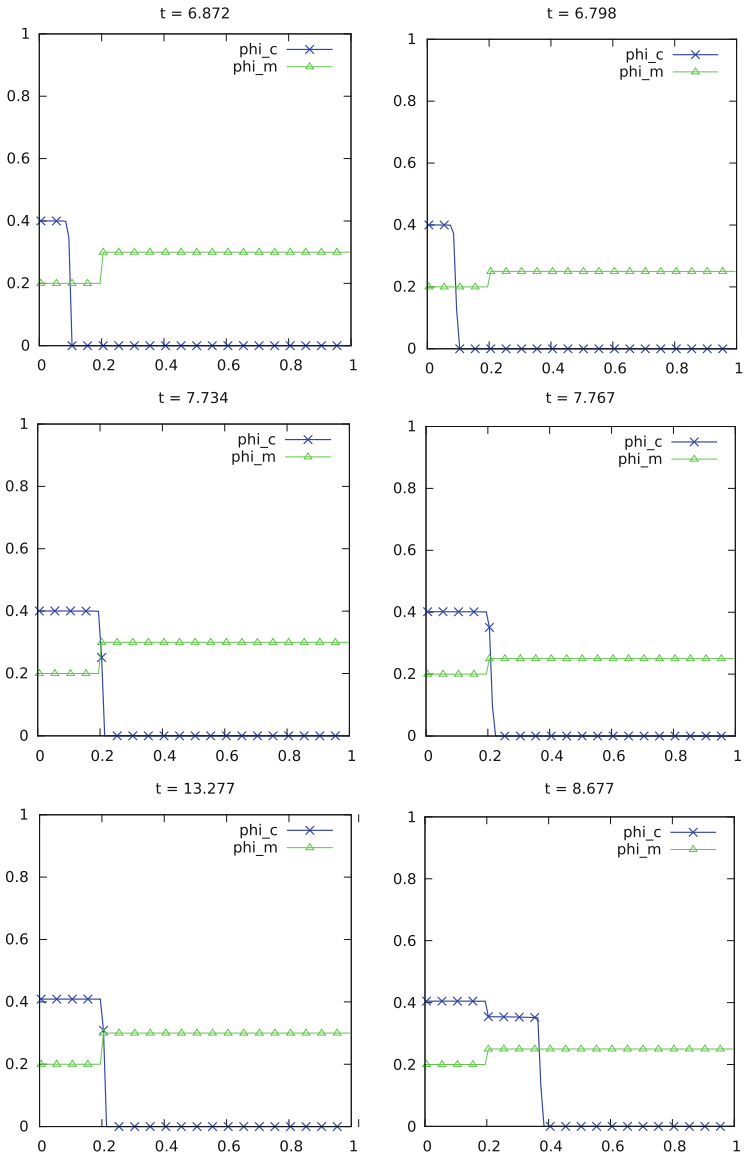

Fig. 3.26 Compartmentalization of growing aggregate when $\phi_m^- = 0.2, \delta_c/\gamma_c = 1/8, E/\mu = 25$, and $A_f/A_n = 0.16$, shown dimensionless times scaled with $1/\gamma$ on the left where $\phi_m^+ = 0.3$ and $t = 6.872, 7.7$. Lengths are scaled with $\sqrt{\nu A_n E/\gamma}$. When reaching the region characterized by a denser ECM, cells will stop invading because the network is too tight. Cells will also stop proliferating because of the contact inhibition of growth. On the right cells are able to pass through because the network is not thick enough as $\phi_m^+ = 0.25$

therefore from the characteristic size of the pores, i.e., A_m. On the left the ECM is too dense (i.e., $A_m < \bar{A}$) thereby hampering cell invasion, as cells remain segregated in the zone with lower ECM density. Proliferation eventually stops because of contact inhibition, having the cell population grown to confluence and filled the entire reachable space. On the right, the lower ECM density due to larger pores leads to $A_m > \bar{A}$: in this case, cells are able to penetrate the denser ECM that only slows down invasion.

3.6.3 A Two-Population Case

We now consider now the cell aggregate as formed by two cell clones: Normal cells with volume ratio ϕ_{c_1} and abnormal cancerous cells with volume ratio ϕ_{c_2}. With respect to the former, the latter are less sensitive to contact inhibition of growth and may have different mechanical properties, e.g., a softer nucleus. Such phenotypic differentiations arise from genetic mutations. As before the two cell clones live in a rigid ECM.

Still considering the MMP-inhibited case, we have only to focus on the following set of equations:

$$\begin{cases} \dfrac{\partial \phi_{c_1}}{\partial t} + \nabla \cdot (\phi_{c_1} \mathbf{v}_{c_1}) = \left[\gamma_1 \mathcal{H}_\varepsilon(\bar{\psi}_1 - \psi) - \delta_1\right] \phi_{c_1} \,, \\ \dfrac{\partial \phi_{c_2}}{\partial t} + \nabla \cdot (\phi_{c_2} \mathbf{v}_{c_2}) = \left[\gamma_2 \mathcal{H}_\varepsilon(\bar{\psi}_2 - \psi) - \delta_2\right] \phi_{c_2} \,, \\ \nabla \cdot \mathbf{T}_{c_1} + \mathbf{m}_{c_1 m} + \mathbf{m}_{c_1 c_2} = \mathbf{0} \,, \\ \nabla \cdot \mathbf{T}_{c_2} + \mathbf{m}_{c_2 m} - \mathbf{m}_{c_1 c_2} = \mathbf{0} \,, \end{cases} \tag{3.100}$$

where now $\psi := \phi_{c_1} + \phi_{c_2} + \phi_m$. It will be crucial in the following that the two subpopulations are characterized by different threshold values $\bar{\psi}_i$ leading to different contact inhibition responses.

Recalling (3.84) and assuming also that the interaction force between cell populations has a similar form, i.e.,

$$\mathbf{m}_{c_1 c_2} = -\phi_{c_1} \phi_{c_2} \mathbf{M}_{12}^{-1} (\mathbf{v}_{c_1} - \mathbf{v}_{c_2}) \,,$$

the two force balance equations write

$$\begin{aligned} \nabla \cdot \mathbf{T}_{c_1} - \phi_{c_1} \phi_m \mathbf{M}_{1m}^{-1} \mathbf{v}_{c_1} - \phi_{c_1} \phi_{c_2} \mathbf{M}_{12}^{-1} (\mathbf{v}_{c_1} - \mathbf{v}_{c_2}) &= \mathbf{0} \,, \\ \nabla \cdot \mathbf{T}_{c_2} - \phi_{c_2} \phi_m \mathbf{M}_{2m}^{-1} \mathbf{v}_{c_2} + \phi_{c_1} \phi_{c_2} \mathbf{M}_{12}^{-1} (\mathbf{v}_{c_1} - \mathbf{v}_{c_2}) &= \mathbf{0} \,. \end{aligned} \tag{3.101}$$

After some algebraic manipulation we can explicit the fluxes of the constituents as

$$\phi_{c_1}\mathbf{v}_{c_1} = \left(\phi_m\mathbf{M}_{1m}^{-1} + \phi_{c_2}\mathbf{M}_{12}^{-1} + \phi_{c_1}\mathbf{M}_{12}^{-1}\mathbf{M}_{2m}\mathbf{M}_{1m}^{-1}\right)^{-1}$$

$$\left[\nabla\cdot\mathbf{T}_{c_1} + \frac{\phi_{c_1}}{\phi_m}\mathbf{M}_{12}^{-1}\mathbf{M}_{2m}\nabla\cdot(\mathbf{T}_{c_1}+\mathbf{T}_{c_2})\right],$$

$$\phi_{c_2}\mathbf{v}_{c_2} = \left(\phi_m\mathbf{M}_{2m}^{-1} + \phi_{c_1}\mathbf{M}_{12}^{-1} + \phi_{c_2}\mathbf{M}_{12}^{-1}\mathbf{M}_{1m}\mathbf{M}_{2m}^{-1}\right)^{-1}$$

$$\left[\nabla\cdot\mathbf{T}_{c_2} + \frac{\phi_{c_2}}{\phi_m}\mathbf{M}_{12}^{-1}\mathbf{M}_{1m}\nabla\cdot(\mathbf{T}_{c_1}+\mathbf{T}_{c_2})\right],$$

that in the isotropic case simplify to

$$\phi_{c_1}\mathbf{v}_{c_1} = \frac{1}{\phi_m}\,\frac{M_{1m}[(\phi_m M_{12}+\phi_{c_1}M_{2m})\nabla\cdot\mathbf{T}_{c_1} + \phi_{c_1}M_{2m}\nabla\cdot\mathbf{T}_{c_2}]}{\phi_m M_{12}+\phi_{c_1}M_{2m}+\phi_{c_2}M_{1m}}, \tag{3.102}$$

$$\phi_{c_2}\mathbf{v}_{c_2} = \frac{1}{\phi_m}\,\frac{M_{2m}[\phi_{c_2}M_{1m}\nabla\cdot\mathbf{T}_{c_1} + (\phi_m M_{12}+\phi_{c_2}M_{1m})\nabla\cdot\mathbf{T}_{c_2}]}{\phi_m M_{12}+\phi_{c_1}M_{2m}+\phi_{c_2}M_{1m}}. \tag{3.103}$$

that could be inserted in the mass balance equations.

In principle, like there is a threshold value for the cell to penetrate in the ECM, there should be a threshold value for a cell to penetrate a layer of cells, which leads for instance to the segregation of tumor cells by epithelial layers, or hampering the transmigration of cells through the endothelial lining of vessel walls. However, the reader needs to be aware of the fact that the situation is much more complex in this case for several reasons. In order to understand that, we can think of the dynamics involved in the extravasation of an immune cell from the endothelial layer of a vessel wall, or the invasion of the mesothelium by ovarian cancer individuals. First of all, due the elasticity of the cytoplasm and plasma membrane, cells belonging to the endothelial or the epithelial layers are much softer and more deformable than ECM fibers. Therefore, a cell is facilitated to pass through a layer of other cells, as it can more easily deform the nearby individuals and pass in between. For instance, if the cell layer is compact, then the invading individual needs to interfere with cell-cell junction mechanisms (mediated by cadherins) to create a gap. The dynamics is therefore very complex and has not been modelled yet in a satisfactory way. In addition, the cell-cell motility coefficient probably is much larger than cell-ECM motility parameter, i.e., $M_{12} \gg M_{im}$, for any population $i = 1, 2$.

Only under this assumption, Eqs. (3.102) and (3.103) can be reduced to the much simpler form

$$\phi_{c_i}\mathbf{v}_{c_i} = \frac{M_{im}}{\phi_m}\nabla\cdot\mathbf{T}_{c_i} = -\frac{\nu_i}{\phi_m}\,\frac{\left(A_m-\bar{A}_i\right)_+}{\left(1+\frac{A_m-\bar{A}_i}{\hat{A}_i}\right)^n}\nabla\Sigma_i(\psi),$$

where

$$\Sigma_i(\psi) = E_i \frac{1-\psi_{free}}{1-\psi}(\psi - \psi_{free})_+ \,. \tag{3.104}$$

Notice that in (3.104) ψ_{free} is the same for both cell population as well as the shape of the cell response to stress, while E_i corresponding to the Young modulus for the two cell population might be different.

Taking all together, the equations that need to be integrated to simulate the evolution of the cell populations are

$$\frac{\partial \phi_{c_i}}{\partial t} + \nabla \cdot \left\{ \frac{\nu_i}{\phi_m} \frac{\left(A_m - \bar{A}_i\right)_+}{\left(1 + \frac{A_m - \bar{A}_i}{\hat{A}_i}\right)^n} \Sigma_i'(\psi) \nabla \psi \right\} = \left[\gamma_i \mathcal{H}_\varepsilon(\bar{\psi}_i - \psi) - \delta_i\right] \phi_{c_i} \,, \tag{3.105}$$

for $i = 1, 2$. We notice that the numerical integration of Eq. (3.105) is not straightforward at all, because of the following facts

- the equations present a cross diffusion term represented by the gradient of the sum of the two volume ratios;
- the equations might degenerate when $A_m(\phi_m) = \bar{A}_i$;
- the equations might change type from parabolic, in those time-dependent regions where $A_m(\phi_m) > \bar{A}_i$, to hyperbolic, in those time-dependent regions where $A_m(\phi_m) < \bar{A}_i$;
- the appearance of the degeneracy and the extension of the regions where the equation changes type will not be the same for the two cell populations, as they will depend on the evolution of the cell population volume ratios.

Considering that tumor cells typically derive from a genetic mutation of normal cells, it is consistent to assume that most of the model parameters are identical for the two populations, e.g., $E_i = E$, $\gamma_i = \gamma$, $\delta_i = \delta$, $\nu_i = \nu$ for $i = 1, 2$. Then we will focus on the different evolution of the cell system determined by selected changes either in the density of the ECM or in the nucleus stiffness μ_{n_i} which appears in the definition of $\bar{A}_i$ in Eqs. (3.88) and (3.89).

As a test case in the following simulations we consider the domain as divided by a horizontal stripe $\Omega_m = \{\mathbf{x} : y \in [0.45, 0.55]\}$ with higher density of ECM. The regions below and above Ω_m are initially filled with normal cells in equilibrium: they can not penetrate Ω_m because the corresponding pore area A_m is smaller than $\bar{A}_1$ at ψ_{free}.

Some cells in the bottom left corner initially lose the physiological contact inhibition of growth and because of that they start spreading within the tissue, as shown in Fig. 3.27. In fact, the misperception of the compression state induces an abnormal proliferation of tumor cells that, in turn, compress the neighboring normal individuals. Feeling overcompressed, normal cells do not proliferate. Indeed, only apoptosis occurs and the normal tissue is gradually replaced by the growing malignant mass.

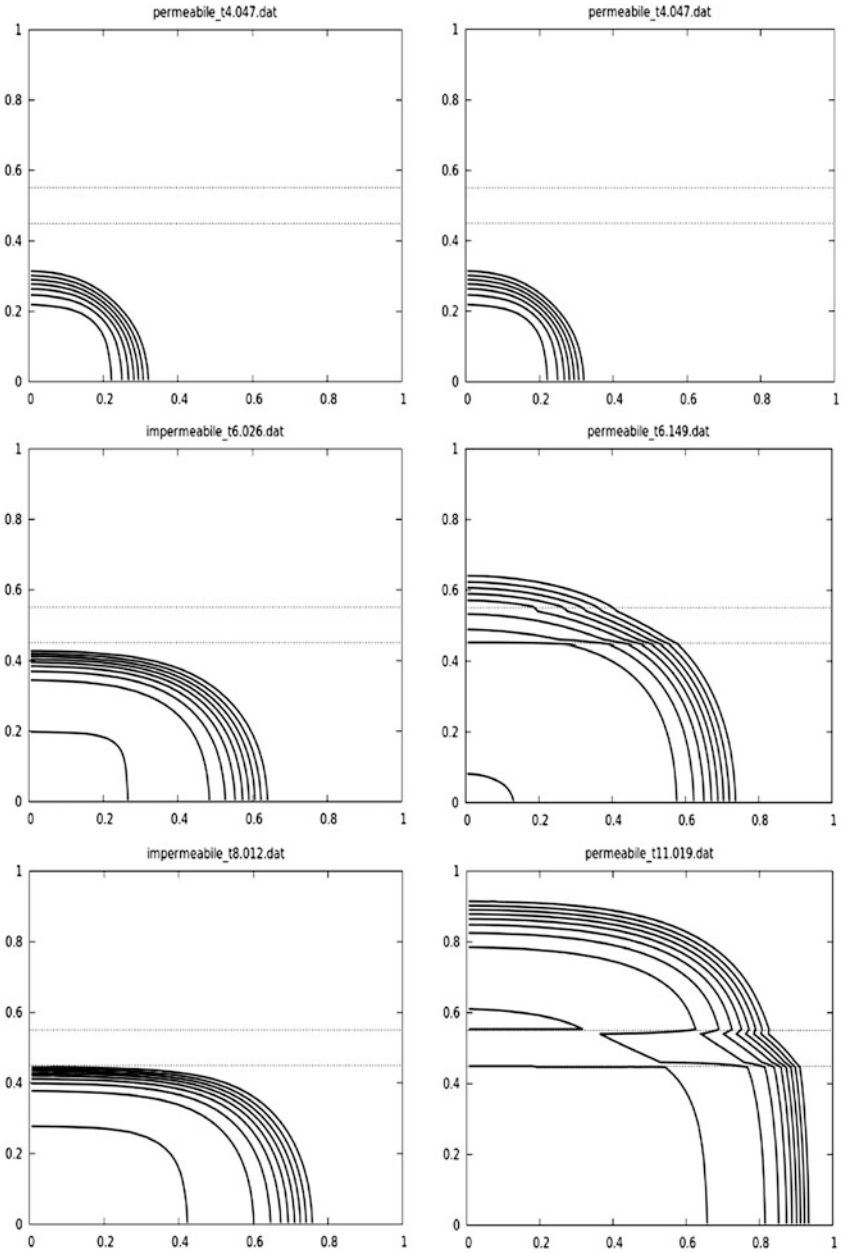

Fig. 3.27 Evolution of the volume ratio of MMP-inhibited tumor cells for $\delta/\gamma = 1/8$, $A_f/A_n = 0.16$, $E/\mu_{n_1} = 25$, and $\phi_m^+ = 0.3$ at scaled times $t = 4.046, 6.026, 8.021$ on the left while on the right $\phi_m^+ = 0.25$ and $t = 4.047, 6.149, 11.019$. Normal cells fill the remaining available space, but the region Ω_m with thick ECM. Before reaching the ECM denser region, the evolution in the two cases is similar, but on the left the ECM is too thick, tumor cells will stop invading but continue to grow along the denser region. On the right, cells are able to pass through, although their penetration is slowed down

Upon reaching the region Ω_m the tumor cells can not penetrate it because the pore size is smaller than the nucleus size and the compression of the growing tumor nearly at $\phi_2 \approx \psi_2 > \psi_{free}$ is not enough to let the nucleus squeeze into the microscopic pores. The tumour population then continues to grow along x below Ω_m to progressively fill the region. Eventually, the malignant mass will completely replace the normal tissue reaching a segregated equilibrium with tumor cells below Ω_m, normal cells above Ω_m and no cells in Ω_m.

Hence, the simulation shown on the left of Fig. 3.27 describes how under suitable conditions the development of a tumor mass might be segregated by the presence of a dense matrix in the region Ω_m, giving rise to a behavior that may represent a sort of growth of an *in situ* (ductal) carcinoma.

The following simulations shown on the right of Fig. 3.27 show how a change in a single parameter is able to substantially modify the situation and to induce invasion across the region Ω_m. We have already seen in Fig. 3.26 comparing the left and the right column how lowering the density of ECM might allow cells to pass through the region Ω_m. In this case we have two populations that behave differently in their interaction with the ECM. In particular, for the normal cells $A_m < \bar{A}_1$ even when the density of ECM in the stripe Ω_m is lowered to $\phi_m^+ = 0.25$, while for the tumor cells $A_m > \bar{A}_2$ and therefore they can invade Ω_m and invade the region above it. Cells are actually slowed down by the higher density of ECM but they can efficaciously reach out the upper region even in absence of activation of MMPs.

A qualitatively similar behavior is observed when we change other parameters that are able to influence the segregation rule. In this respect, we will present here only the case in which the nucleus of tumor cells is softer than the nucleus of sane cells, as it is known experimentally, i.e., $\mu_{n_2} < \mu_{n_1}$. This is a very interesting situation from the biomedical point of view, because it represents a differentiation of a purely mechanical origin that results in a dramatic change in cell invasive ability, as shown in Fig. 3.28. In particular, the simulation is represented in one dimension, in order to give a clear view of the evolution of the volume ratio of both populations (and of the overall volume ratio ψ as well). Upon reaching Ω_m, tumor cells not only are able to penetrate it but they also completely populate the matrix, so that the overall volume ratio is eventually constant everywhere.

The last simulation in Fig. 3.29 gives the tumor evolution in a heterogeneous tissue. In particular, as shown in the top-left figure, the host is divided in several subregions with three different ECM densities, namely $\phi_m = 0.2, 0.25, 0.3$. It is useful to underline that in this simulation setting, the stiffness of the nucleus is equal for both populations. As it is possible to see, all cells are able to move in the low density areas. On the opposite, only tumor individuals penetrate the medium density regions. Finally, neither malignant nor normal cells are instead able to invade the regions characterized by the highest density.

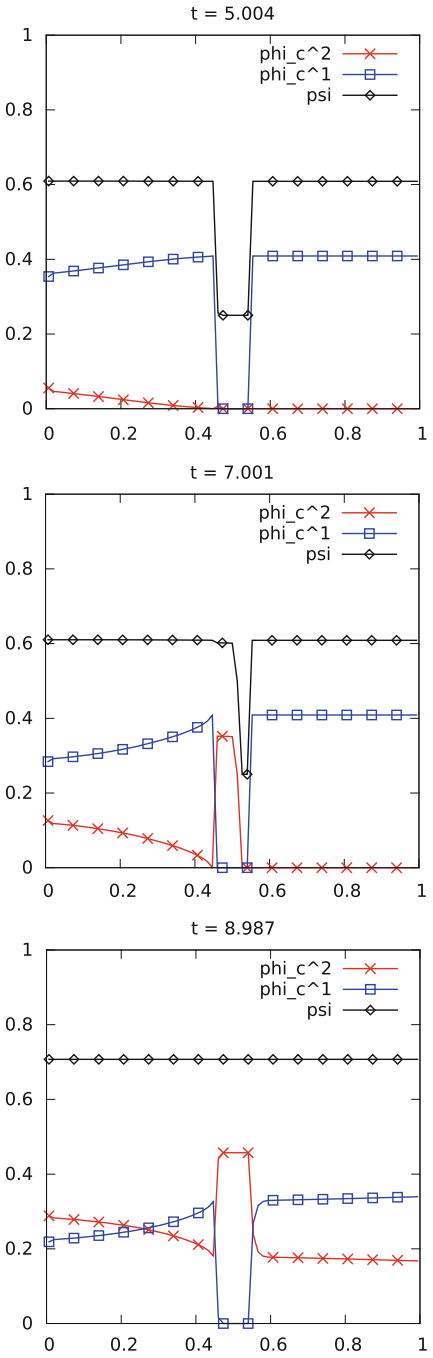

Fig. 3.28 Evolution of one-dimensional MMP-inhibited system for $E/\mu_{n_1} = 25$, $E/\mu_{n_2} = 37.5$, and $\phi_m^+ = 0.3$, other parameters being as in Fig. 3.27. Tumor cells, thanks to their softer nucleus, are able to invade the region Ω_m, that is too dense for the stiffer nucleus of sane cells, also in the compressed configuration. Tumor cells will also populate Ω_m because they are able to live in there. Hence the overall volume ratio is eventually constant everywhere

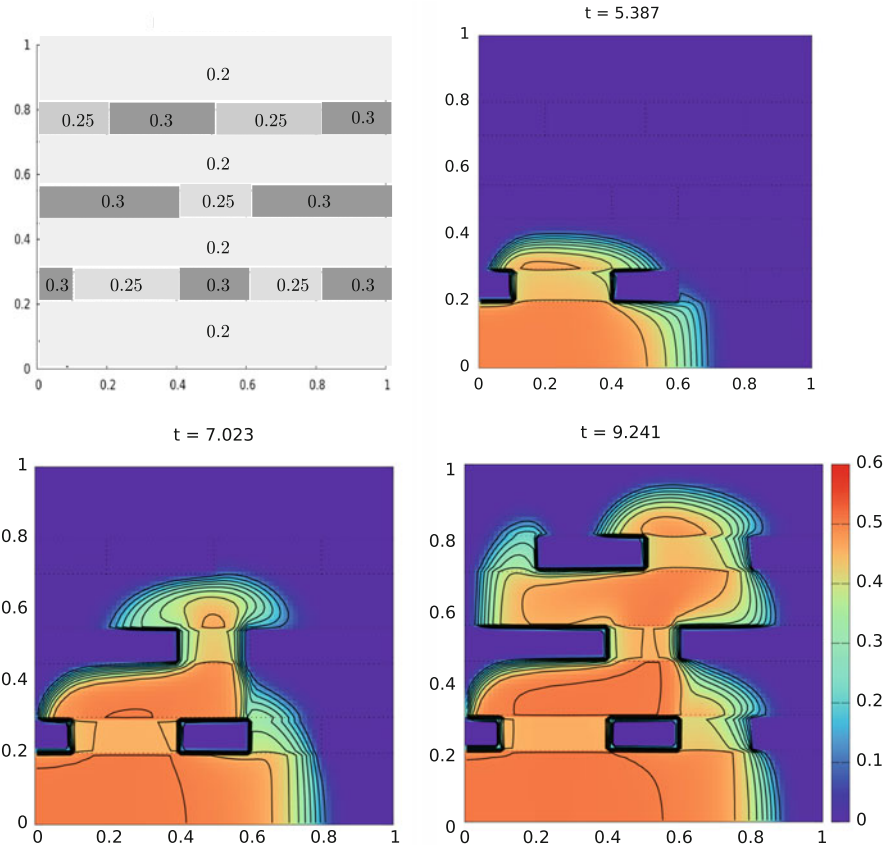

Fig. 3.29 Evolution of the volume ratio of MMP-inhibited tumor cells for a heterogeneous distribution of ECM as shown in the *top-left figure*, other parameters being as in Fig. 3.27. The tumor grows in the heterogeneous ECM avoiding denser regions

3.6.4 MMP-Induced Invasion

As already described in Sect. 3.4.3, when moving within ECMs cells can express matrix degrading enzymes, such as MMPs, to create paths for migration. In order to take into account of this effect, we still consider the ECM as rigid, but assume that it is now degradable.

Denoting the concentration of MMPs by C_{MMP} we need to add to (3.100) the following equations for the evolution of ϕ_m and C_{MMP}

$$\begin{cases} \dfrac{\partial \phi_m}{\partial t} = \Gamma_m \,, \\ \dfrac{\partial C_{MMP}}{\partial t} = \kappa \nabla^2 C_{MMP} + \Gamma_{MMP} \,, \end{cases} \tag{3.106}$$

where κ is the diffusion coefficient of MMPs. The ECM supply term Γ_m is modelled assuming both proteolytic fiber degradation and cell production of new peptidic filaments. In this respect, denoting by γ_m the deposition rate and δ_m the MMP degradation rate, we write

$$\Gamma_m = \gamma_m \phi_{c_2} - \delta_m c_{MMP} \phi_m \,. \tag{3.107}$$

Finally, the supply Γ_{MMP} of MMPs is modelled considering their production by tumor cells and their natural decay, i.e.,

$$\Gamma_{MMP} = \gamma_{MMP} \phi_{c_2} - \frac{C_{MMP}}{\tau} \,, \tag{3.108}$$

where γ_{MMP} is the secretion rate by the tumor cells and τ is the decay time.

Starting from the configuration of the control simulation on the left of Fig. 3.27, in Fig. 3.30 we observe that the activity of MMPs results in the digestion of the excessive part of the ECM that, however, is then restored after the passage of the tumor cells. Therefore, although slowed down, the tumoral invasion is successful again.

3.7 Chemotaxis as an Active Stress

In dealing with force balance in Eq. (3.70), we allowed the existence of an external body force acting on the cell populations. In fact, in many continuum models, chemotaxis, haptotaxis, and durotaxis are introduced either as body forces or by including in the definition of the velocity field a term proportional to the gradient of chemoattractants, of adhesion molecules, or of substrate rigidity. Focusing on chemotaxis as the only body force and neglecting inertia, we can for instance specialize (3.70) as

$$\nabla \cdot \mathbf{T}_c + \chi \phi_c \nabla C + \mathbf{m}_{cm} = \mathbf{0} \,, \tag{3.109}$$

where χ is the cell chemotactic sensitivity and C is the local concentration of chemoattractant.

To understand the consequences of this assumption, let us consider the simplest case of a cell population moving in a rigid ECM with an interaction force proportional to the relative velocity, as done in (3.84) with $\mathbf{v}_m = \mathbf{0}$, of course. Then we have

$$\nabla \cdot \mathbf{T}_c + \chi \phi_c \nabla C - \phi_c \phi_m \mathbf{M}_c^{-1} \mathbf{v}_c = \mathbf{0} \,. \tag{3.110}$$

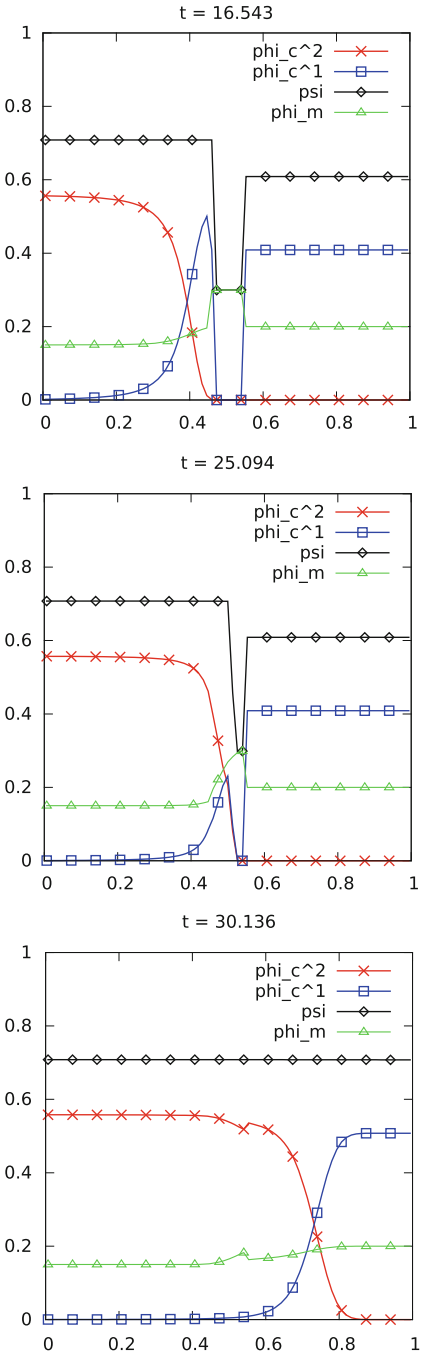

Fig. 3.30 Evolution of one-dimensional system for $\gamma_m/\gamma = 0.15$, $\kappa/(\nu A_n E) = 0.005$, $\gamma_{MMP}\delta_m/\gamma^2 = 50$, $\gamma\tau = 0.02$, other parameters being the same as in Fig. 3.27 (left). Tumour cells grow compressing the sane cells against the denser region Ω_m. When malignant individuals reach such an area, they remodel the ECM, opening their own way for further migration

This allows to readily explicit

$$\mathbf{v}_c = \frac{\mathbf{M}_c}{\phi_m}\left(\chi\nabla C + \frac{1}{\phi_c}\nabla\cdot\mathbf{T}_c\right). \tag{3.111}$$

Notice that the chemotactic component of cell motion is ineffective either if cells are not sensitive to the chemical gradient (i.e., $\chi = 0$), or if cells are not able to move even though their would like to (i.e., $\mathbf{M}_c = \mathbf{0}$, which might hold for frozen individuals, or for individuals pretreated with cytochalasin B, or for too dense ECMs, as described in Sect. 3.6).

The equation above can be then substituted in the mass balance equation (3.58) to get

$$\frac{\partial\phi_c}{\partial t} + \nabla\cdot\left(\frac{\phi_c}{\phi_m}\chi\mathbf{M}\nabla C\right) + \nabla\cdot\left(\frac{1}{\phi_m}\mathbf{M}_c\nabla\cdot\mathbf{T}_c\right) = \Gamma_c\,.$$

In this equation, it is possible to recognize in the second term of the l.h.s. the classical chemotactic term. If in addition $\mathbf{T}_c = -\Sigma_c(\phi_c)\mathrm{i}$, we then obtain a nonlinear advection-diffusion equation, which reduces to the classical chemotactic equation under a suitable assumption of isotropy and in the case of a special choice of $\Sigma_c(\phi_c)$ able to linearize the diffusion term.

In order to understand the consequences of treating chemotaxis as a body force, we consider now an ensemble of cells in a deformable ECM. This implies that we have to join (3.83), with $\alpha = m$, to (3.109) in order to describe the deformation of the ECM. So, for any general constitutive equation for the stress and for the cell-ECM interaction force the governing multiphase model will be

$$\begin{cases} \nabla\cdot\mathbf{T}_c + \mathbf{m}_{cm} + \phi_c\chi\nabla C = \mathbf{0}\,, \\ \nabla\cdot\mathbf{T}_m - \mathbf{m}_{cm} = \mathbf{0}\,, \end{cases} \tag{3.112}$$

which, if the two equations are summed up, results in the classical force balance equation for the overall mixture

$$\nabla\cdot(\mathbf{T}_c + \mathbf{T}_m) + \phi_c\chi\nabla C = \mathbf{0}\,. \tag{3.113}$$

To be specific, referring to Fig. 3.31, we consider a one-dimensional situation in which only the cells lying in a central interval of the domain, say $[a, b]$, are sensitive to the chemical signal, whereas the other individuals of the aggregate are insensitive to the chemical stimulus. Furthermore, we suppose that central cells respond with a constant chemotactic force, which means that the chemical gradient is constant. In this case (3.113) simplifies to

$$\frac{\partial}{\partial x}[T_c + T_m + F(x)] = 0\,,$$

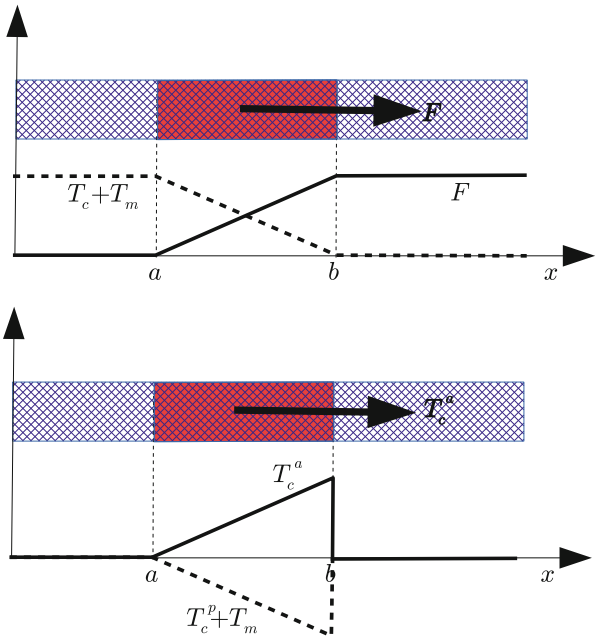

Fig. 3.31 Difference between passive response (*top*) and active pulling (*bottom*) to a chemotactic signal. F represents chemotaxis when treated as a body force

where

$$F(x) = \begin{cases} 0 & \text{if } x < a; \\ A(x-a) & \text{if } a \le x \le b; \\ A(b-a) & \text{if } x > b, \end{cases}$$

which can be easily solved to obtain that $T_c + T_m + F(x)$ is constant in space. Since $T_c + T_m$ and F are continuous across the interfaces between the two types of cells, i.e., at $x = a, b$, the assumption that the right border is stress-free implies that

$$T_c + T_m = F(b) - F(x)\,,$$

and in particular that $T_c + T_m > 0$. Similar results can be obtained replacing $A(x-a)$ with any increasing concentration field yielding to an $F(x)$ that vanishes below a and is continuous and constant above b.

Without going to the solution of the mass balance equations, by assuming that the cell response to the chemotactic force is mainly sustained by the matrix, i.e., $T_c \ll T_m$, we have that the ECM is in tension in the direction of the chemotactic force.

Such a conclusion is easily understandable if one thinks to a heavy ball placed within a deformable net. Due to gravity both the ball and the net will move downward thereby stretching the net in the direction of gravity. Even if the ball is deformable, it will fall down through the net pulling it downward.

Unfortunately, in biological experiments an opposite phenomenology is observed. In order to move in the direction of chemical gradients, cells in fact grab on the ECM and activate their internal motor proteins to move forward. This generates a relative fiber motion in the opposite direction. This is not far from our everyday walking experience, i.e., in order to move a step forward we are pulling the ground back. This is particularly evident when walking on a slippery and deformable surface like a slightly muddy soil.

An easy way to include this effect in continuum models consists in differentiating the stress tensor of the cellular component into an active and a passive part, that will be respectively named $\mathbf{T}_c^a$ and $\mathbf{T}_c^p$. The former is a way to model the internal activation of stresses. The latter is instead the classical response to deformation. To understand the difference, we can think to a spring having a rest length ℓ_0. If it is compressed to a length $\ell < \ell_0$, it will tend to passively respond to the deformation trying to go back to the length ℓ_0. If, instead, without any load, the spring anchored to two points having a distance ℓ_0 is able to shorten its rest length to $\ell_1 < \ell_0$, then its extrema will exert on the anchorages a traction force, that can be named active.

In this respect, Eq. (3.112) rewrites

$$\begin{cases} \nabla \cdot (\mathbf{T}_c^a + \mathbf{T}_c^p) + \mathbf{m}_{cm} = \mathbf{0}\,, \\ \nabla \cdot \mathbf{T}_m - \mathbf{m}_{cm} = \mathbf{0}\,, \end{cases} \tag{3.114}$$

which implies

$$\nabla \cdot (\mathbf{T}_c^a + \mathbf{T}_c^p + \mathbf{T}_m) = \mathbf{0}\,. \tag{3.115}$$

It is clear that Eqs. (3.113) and (3.115) are the same if $\mathbf{T}_c^a = \phi_c \chi \nabla C$ (if ϕ_c is constant in space). However mainly due to specific boundary conditions their solution is different. In fact, let us assume again a one-dimensional situation where the cells located in the interval $[a, b]$ are pulling on the ECM with an active traction $T_c^a = A(x - a)$. The continuity of the stress across the interfaces a and b and the no-stress boundary condition at the right hand side of the domain imply that

$$T_c^a + T_c^p + T_m = 0\,,$$

or that

$$T_c^p + T_m = -T_c^a\,,$$

which, differently from the previous case, implies that $T_c^p + T_m < 0$.

Finally, assuming again that the response to the chemotactic force is mainly sustained by the ECM, i.e., $T_c^p \ll T_m$ we have that

$$T_m \approx -T_c^a = -\phi_c \chi \nabla C \,,$$

which means that the ECM is pulled back in the direction opposite to the chemotactic force.

3.8 Perspectives on Mechanosensing and Mechanotransduction

As we have discussed so far, the deduction of models able to describe cell-ECM interactions gives rise to very interesting problems also from the mathematical point of view. In this respect, we end the chapter by proposing some ideas for further possible modelling developments, that directly arise from experimental and practical issues.

From the experimental observations, it turns out that selected interactions between cells and ECM are fundamental in governing cell fate, e.g., cell survival, migration, growth, and homeostasis. Hence, understanding such mechanisms is a fundamental issue in tissue engineering. In particular, the analysis of how cells sense and react to the mechanical properties of the surrounding environment is very important for the development of nature-inspired bioengineering mechanosensitive devices, tactile sensors and micro-sensors, e.g., of pressure and shear. In spite of the growing interest in this field very little is done from the matematical perspective.

A little more has been done in modelling the important role played by mechanics in tumor development, starting from the regulation of the contact inhibition of growth [9, 34] to the fact that ECM stiffness and tensile stresses enhance cell proliferation.

However, apart from cancer, several other diseases seem to be due to incorrect mechanosensing or mechanotransduction processes [30]: however, very few articles focus on the analysis of these mechanisms from the mechanical modelling point of view. Among others we can mention the following:

- Atrial fibrillation derives from an abnormal conversion of mechanical stress into intracellular gradient of electrical activity;
- Intimal hyperplasia is related to stretch-activated intracellular signalling cascades due to the presence of stents and grafts;
- Scleroderma and diabetic nephropathy might be due to abnormal accumulations of ECM components;
- Glomerulosclerosis is the consequence of the pathologic stretch of mesangial cells via ECM and integrins due to glomerular hypertension;
- Emphysema might be due to enhanced ECM breakdown;

- Pulmonary fibrosis and all other fibrosis characterizing many aging diseases might be due to an excessive production of ECM;
- Pulmonary hypertension might be due to cell hypercontractility;
- One of the causes of osteoporosis is insufficient mechanosensing;
- Many vascular diseases are due to the fact that vasculature remodels in response to wall shear stresses and indeed the pressure of blood flow and mechanosensing pathways of the endothelial cells building the vessel walls might be corrupted.

The computational and modeling literature has paid little attention to most of the above-cited problems. In fact, only few theoretical papers, which typically focused on cancer modelling, have dealt with the effect of the matrix microenvironment and on the possibility of healing tumors by normalizing the surrounding tissue (see, for instance, [11, 27] and references therein).

Understanding the mechanical interplay between cells and the surrounding environment is of crucial importance in tissue engineering as well. For instance, the fate of stem cells depends not only on genetic and molecular mediators, e.g., growth factors and transcription factors, but also on the interactions they have with the surroundings, which depend on ECM elasticity and morphology and include ECM-mediated stresses [33]. In this respect, one amazing evidence is the observation that stem cells differentiate according to the stiffness of the surrounding environment [9]. In particular, they are likely to become

- neurons, if the ECM rigidity is below 0.1 kPa;
- adipocytes, if the ECM rigidity is in the range 0.1–2 kPa;
- skeletal muscle cells, if the ECM rigidity is in the range 3–20 kPa;
- osteoblasts, if the ECM rigidity is above 20 kPa.

It seems that this is one of the reasons of the present unsuccessful use of stem cells in the treatment of neurodegenerative diseases (in spite of the suggestive idea and of its great potential [15, 41, 42]). Scars in the neural tissue are in fact too stiff for stem cells to be neurogenic.

While, as previously stated, there are not many papers devoted to modeling mechanosensing and mechanotransduction, there is an increasing effort to understand the mechanisms from the experimental point of view. In fact, the aim is the construction of proper niches that allow to culture stem cells and to control their differentiation, in order to build bioengineered tissues [69]. In this respect, a valuable support could be given by the development of proper mathematical, mechanical, and computational models.

Another area of interest is the optimization of the geometric characteristics of scaffolds in which cells can grow to build artificial tissues. In Sects. 3.3 and 3.4 we have focused on this aspect, stimulated by the practical aim to indentify the optimal morphological characteristics of an artificial scaffold able to enhance cell motility, having in mind those cells involved in wound healing. In order to do that, one need to understand selected aspects that can either favour or hamper cell motion. In this chapter we have for instance discussed in detail how the elasticity of the nucleus

plays a crucial role as well as the ability of the cell to actively exert traction forces via adhesion sites and to activate its proteolytic machinery.

References

1. A. Balter, R.M.H. Merks, N.J. Poplawski, M. Swat, J.A. Glazier, The Glazier-Graner-Hogeweg model: extensions, future directions, and opportunities for further study, in *Single-Cell-Based Models in Biology and Medicine, Mathematics and Biosciences in Interactions*, ed. by A.R.A. Anderson, M.A.J. Chaplain, K.A. Rejniak (Birkaüser, Basel, 2007), pp. 151–167
2. W. Baumgartner, P. Hinterdorfer, W. Ness, A. Raab, D. Vestweber, H. Schindler, D. Drenckhahn, Cadherin interaction probed by atomic force microscopy. Proc. Natl. Acad. Sci. U. S. A. **97**, 4005–4010 (2000)
3. C. Beadle, M.C. Assanah, P. Monzo, R. Vallee, S.S. Rosenfeld, P. Canoll, The role of myosin II in glioma invasion of the brain. Mol. Biol. Cell. **19**, 3357–3368 (2008)
4. M. Beil, A. Micoulet, G. Wichert, S. Paschke, P. Walther, M.B. Omary, P.P. Van Veldhoven, U. Gern, E. Wolff-Hieber, J. Eggermann, J. Waltenberger, G. Adler, J. Spatz, T. Seufferlei, Sphingosylphosphorylcholine regulates keratin network architecture and viscoelastic properties of human cancer cells. Nat. Cell Biol. **5**, 803–811 (2003)
5. Y. Boucher, L. Baxter, R.K. Jain, Interstitial pressure gradients in tissue-isolated and subcutaneous tumors: implications for therapy. Cancer Res. **50**, 4478–4484 (1990)
6. Y. Boucher, H. Salehil, B. Witwerl, G.R. Harsh, R.K. Jain, Interstitial fluid pressure in intracranial tumours in patients and in rodents. Br. J. Cancer **75**, 829–836 (1997)
7. R.M. Bowen, Theory of mixtures, in *Continuum Physics*, vol. 3, ed. by A.C. Eringen (Academic, New York, 1976)
8. B.T. Burgess, J.L. Myles, R.B. Dickinson, Quantitative analysis of adhesion-mediated cell migration in three-dimensional gels of RGD-grafted collagen. Ann. Biomed. Eng. **28**, 110–118 (2003)
9. D.T. Butcher, T. Alliston, V. Weaver, A tense situation: forcing tumour progression. Nat. Rev. Cancer **9**, 108–122 (2009)
10. S.B. Carter, Haptotaxis and the mechanism of cell motility. Nature **213**, 256–260 (1967)
11. M. Chaplain, L. Graziano, L. Preziosi, Mathematical modelling of the loss of tissue compression responsiveness and its role in solid tumour development. Math. Med. Biol. **23**, 197–229 (2006)
12. S.R. Chary, R.K. Jain, Direct measurement of interstitial convection and diffusion of albumin in normal and neoplastic tissues by fluorescence photobleaching. Proc. Natl. Acad. Sci. U. S. A. **86**, 5385–5389 (1989)
13. P.A. DiMilla, J.A. Stone, J.A. Quinn, S.M. Albelda, D.A. Lauffenburger, Maximal migration of human smooth-muscle cells on fibronectin and type-IV collagen occurs at an intermediate attachment strength. J. Cell Biol. **122**, 729–737 (1993)
14. A.D. Doyle, F.W. Wang, K. Matsumoto, K.M. Yamada, One-dimensional topography underlies three-dimensional fibrillar cell migration. J. Cell Biol. **184**, 481–490 (2009)
15. K. Franzé, The mechanical control of nervous system development. Development **140**, 3069–3077 (2013)
16. P. Friedl, E.B. Brocker, The biology of cell locomotion within three-dimensional extracellular matrix. Cell. Mol. Life Sci. **57**, 41–64 (2000)
17. P. Friedl, K. Wolf, Tumour-cell invasion and migration: diversity and escape mechanisms. Nat. Rev. Cancer **3**, 362–374 (2003)
18. P. Friedl, K. Maaser, C.E. Klein, B. Niggemann, G. Krohne, K.S. Zänker, Migration of highly aggressive MV3 melanoma cells in 3-dimensional collagen lattices results in local matrix reorganization and shedding of $\alpha 2$ and $\beta 1$ integrins and CD44. Cancer Res. **57**, 2061–2070 (1997)

19. C. Giverso, L. Preziosi, Modelling the compression and reorganization of cell aggregates. Math. Med. Biol. **29**, 181–204 (2012)
20. C. Giverso, L. Preziosi, Behaviour of cell aggregates under force-controlled compression. Int. J. Nonlinear Mech. **56**, 50–55 (2013)
21. C. Giverso, A. Grillo, L. Preziosi, Influence of nuclear deformability on cell entry into cylindrical structures. Biomech. Model. Mechanobiol. **13**, 481–502 (2014)
22. J.A. Glazier, F. Graner, Simulation of the differential adhesion driven rearrangement of biological cells. Phys. Rev. E **47**, 2128–2154 (1993)
23. F. Graner, J.A. Glazier, Simulation of biological cell sorting using a two dimensional extended Potts model. Phys. Rev. Lett. **69**, 2013–2017 (1992)
24. J. Guck, F. Lautenschläger, S. Paschke, M. Beil, Critical review: cellular mechanobiology and amoeboid migration. Integr. Biol. **2**, 575–583 (2010)
25. F. Guilak, D.M. Cohen, B.T. Estes, J.M. Gimble, W. Liedtke, C.S. Chen, Control of stem cell fate by physical interactions the extracellular matrix. Stem Cell **5**, 17–26 (2009)
26. B.A.C. Harley, H. Kim, M.H. Zaman, I.V. Yannas, D.A. Lauffenburger, L.J. Gibson, Microarchitecture of three-dimensional scaffolds influences cell migration behavior via junction interactions. Biophys. J. **95**, 4013–4024 (2008)
27. S. Hohme, D. Drasdo, Biomechanical and nutrient controls in the growth of mammalian cell populations. Math. Popul. Stud. **17**, 166–187 (2010)
28. S. Huang, C.P. Brangwynne, K.K. Parker, D.E. Ingber, Symmetry-breaking in mammalian cell cohort migration during tissue pattern formation: role of random-walk persistence. Cell Motil. Cytoskeleton **61**, 201–213 (2005)
29. O. Ilina, G.J. Bakker, A. Vasaturo, R.M. Hofmann, P. Friedl, Two-photon laser-generated microtracks in 3D collagen lattices: principles of MMP-dependent and -independent collective cancer cell invasion. Phys Biol. **8**, 015010 (2011). Erratum in: Phys Biol. **8**, 029501 (2011)
30. D. Ingber, Mechanobiology and diseases of mechanotransduction. Ann. Med. **35**, 1–14 (2009)
31. E. Ising, Beitrag zur theorie des ferromagnetismus. Z. Physik **31**, 253–258 (1925)
32. R.K. Jain, Transport of molecules in the tumor interstitium: a review. Cancer Res. **47**, 3039–3051 (1987)
33. D.L. Jones, A.J. Wagers, No place like home: anatomy and function of the stem cell niche. Nat. Rev. **9**, 11–22 (2008)
34. J. Kass, M. Erler, M. Dembo, V. Weaver, Mammary epithelial cell: influence of ECM composition and organization during development and tumorigenesis. Int. J. Biochem. Cell. Biol. **39**, 1987–1994 (2007)
35. A. Knapinska, G.B. Fields, Chemical biology for understanding matrix metalloproteinase function. Chembiochem. **13**, 2002–2020 (2012)
36. T.P. Kole, Y. Tseng, I. Jiang, J.L. Katz, D. Wirtz, Intracellular mechanics of migrating broblasts. Mol. Biol. Cell. **16**, 328–338 (2005)
37. T.A. Krouskop, T.M. Wheeler, F. Kallel, B.S. Garra, T. Hall, Elastic moduli of breast and prostate tissues under compression. Ultrason. Imaging **20**, 260–274 (1998)
38. R.M. Kuntz, W.M. Saltzman, Neutrophil motility in extracellular matrix gels: mesh size and adhesion affect speed of migration. Biophys. J. **72**, 1472–1480 (1997)
39. T. Lämmermann, B.L. Bader, S.J. Monkley, T. Worbs, R. Wedlich-Soldner, K. Hirsch, M. Keller, R. Förster, D.R. Critchley, R. Fässler, M. Sixt, Rapid leukocyte migration by integrin-independent flowing and squeezing. Nature **453**, 51–55 (2008)
40. F. Lautenschläger, S. Paschke, S. Schinkinger, A. Bruel, M. Beil, J. Guck, The regulatory role of cell mechanics for migration of differentiating myeloid cells. Proc. Natl. Acad. Sci. U. S. A. **106**, 15696–15701 (2009)
41. O. Lindvall, Z. Kokaia, Progress stem cells for the treatment of neurological disorders. Nature **441**, 1094–1096 (2006)
42. O. Lindvall, Z. Kokaia, Stem cells in human neurodegenerative disorders: time for clinical translation? J. Clin. Invest. **120**, 29–40 (2010)
43. C.M. Lo, H.B. Wang, M. Dembo, Y.L. Wang, Cell movement is guided by the rigidity of the substrate. Biophys. J. **79**, 144–152 (2000)

44. M.P. Lutolf, J.L. Lauer-Fields, H.G. Schmoekel, A.T. Metters, F.E. Weber, G.B. Fields, J.A. Hubbell, Synthetic matrix metalloproteinase-sensitive hydrogels for the conduction of tissue regeneration: engineering cell-invasion characteristics. Proc. Natl. Acad. Sci. U. S. A. **100**, 5413–5418 (2003)
45. K. Maaser, K. Wolf, C.E. Klein, B. Niggemann, K.S. Zänker, E.B. Bröcker, P. Friedl, Functional hierarchy of simultaneously expressed adhesion receptors: integrin $\alpha 2\beta 1$ but not CD44 mediates MV3 melanoma cell migration and matrix reorganization within three-dimensional hyaluronan-containing collagen matrices. Mol. Biol. Cell. **10**, 3067–3079 (1999)
46. R.M.H. Merks, J.A. Glazier, S.V. Brodsky, M.S. Goligorksy, S.A. Newman, Cell elongation is key to in silico replication of *in vitro* vasculogenesis and subsequent remodelling. Develop. Biol. **289**, 44–54 (2006)
47. R.M.H. Merks, E.D. Perryn, A. Shirinifard, J.A. Glazier, Contact-inhibited chemotactic motility: role in de novo and sprouting blood vessel growth. PLoS Comput. Biol. **4**, e1000163 (2008)
48. N. Metropolis, A.E. Rosenbluth, M.N. Rosenbluth, A.H. Teller, E.Teller, Equation of state calculations by fast computing machines. J. Chem. Phys. **21**, 1087–1092 (1953)
49. V. Milišic, D. Oelz, On a structured model for load-dependent reaction kinetics of transient elastic linkages mediating nonlinear friction. SIAM J. Math. Anal. **47**(3), 2104–2121 (2015)
50. I. Müller, A thermodynamic theory of mixture of fluids. Arch. Ration. Mech. Anal. **28**, 1–39 (1968)
51. D. Ölz, C. Schmeiser, V. Small, Modelling of the actin-cytoskeleton in symmetric lamellipodial fragments. Cell Adh. Migr. **2**, 117–126 (2008)
52. S.P. Palecek, J.C. Loftus, M.H. Ginsberg, D.A. Lauffenburger, A.F. Horwitz, Integrin-ligand binding properties govern cell migration speed through cell-substratum adhesiveness. Nature **385**, 537–540 (1997)
53. E.D. Perryn, A. Czirok, C.D. Little, Vascular sprout formation entails tissue deformations and VE-cadherin dependent cell-autonomous motility. Dev. Biol. **313**, 545–555 (2008)
54. R.B. Potts, Some generalized order-disorder transformations. Proc. Camb. Philos. Soc. **48**, 106–109 (1952)
55. L. Preziosi, A. Farina, On Darcy's law for growing porous media. Int. J. Nonlinear Mech. **37**, 485–491 (2001)
56. L. Preziosi, A. Tosin, Multiphase modelling of tumour growth and extracellular matrix interaction: mathematical tools and applications. J. Math. Biol. **58**, 625–656 (2009)
57. L. Preziosi, G. Vitale, A multiphase model of tumour and tissue growth including cell adhesion and plastic re-organisation. Math. Models Methods Appl. Sci. **21**, 1901–1932 (2011)
58. L. Preziosi, D. Ambrosi, C. Verdier, An elasto-visco-plastic model of cell aggregates. J. Theor. Biol. **262**, 35–47 (2010)
59. E.M. Purcell, Life at low Reynolds number. Am. J. Phys. **45**, 3–11 (1977)
60. K.R. Rajagopal, L. Tao, *Mechanics of Mixtures* (World Scientific, Singapore, 1995)
61. C.G. Rolli, T. Seufferlein, R. Kemkemer, J.P. Spatz, Impact of tumor cell cytoskeleton organization on invasiveness and migration: a microchannel-based approach. PLoS ONE **5**, e8726 (2010)
62. M. Scianna, L. Preziosi. Modeling the influence of nucleus elasticity on cell invasion in fiber networks and microchannels. J. Theor. Biol. **317**, 394–406 (2013)
63. M. Scianna, L. Preziosi, A cellular Potts model for the MMP-dependent and -independent cancer cell migration in matrix microtracks of different dimensions. Comput. Mech. **53**, 485–497 (2014)
64. M. Scianna, R.M.H. Merks, L. Preziosi, E. Medico, Individual cell-based models of cell scatter of ARO and MLP-29 cells in response to hepatocyte growth factor. J. Theor. Biol. **260**, 151–160 (2009)
65. M. Scianna, L. Preziosi, K. Wolf, A cellular Potts model simulating cell migration on and in matrix environments. Math. Biosci. Eng. **10**, 235–261 (2013)
66. S.A. Siefert, R. Sarkar, Matrix metalloproteinases in vascular physiology and disease. Vasc. Res. **20**, 210–216 (2012)

67. M.S. Steinberg, Reconstruction of tissues by dissociated cells. Some morphogenetic tissue movements and the sorting out of embryonic cells may have a common explanation. Science **141**, 401–408 (1963)
68. M.S. Steinberg, Does differential adhesion govern self-assembly processes in histogenesis? Equilibrium configurations and the emergence of a hierarchy among populations of embryonic cells. J. Exp. Zool. **173**, 395–433 (1970)
69. M.M. Stevens, J.H. George, Exploring and engineering the cell surface interface. Science **310**, 1135–1138 (2005)
70. Y. Sun, C.S. Chen, J. Fu, Forcing stem cells to behave: a biophysical perspective of the cellular microenvironment. Ann. Rev. Biophys. **41**, 519–542 (2012)
71. M. Sun, J. Graham, B. Hegedus, F. Marga, Y. Zhang, G. Forgacs, M. Grandbois, Multiple membrane tethers probed by atomic force microscopy. Byophys. J. **89**, 4320–4329 (2005)
72. A. Szabo, A. Czirok, The role of cell-cell adhesion in the formation of multicellular sprouts. Math. Model. Nat. Phenom. **5**, 106–122 (2010)
73. A. Szabo, E.D. Perryn, A. Czirok, Network formation of tissue cells via preferential attraction to elongated structures. Phys. Rev. Lett. **98**, 038102 (2007)
74. A. Szabo, E. Mehes, E. Kosa, A. Czirok, Multicellular sprouting *in vitro*. Biophys. J. **95**, 2702–2710 (2008)
75. A. Szabo, R. Unnep, E. Mehes, W. Twal, S. Argraves, Y. Cho, A. Czirok, Collective cell motion in endothelial monolayers. Phys. Biol. **7**, 046007 (2011)
76. A. Szabo, K. Varga, T. Garay, B. Hegedus, A. Czirok, Invasion from a cell aggregate: the roles of active cell motion and mechanical equilibrium. Phys. Biol. **9**, 016010 (2012)
77. P.A. Torzilli, J.W. Bourne, T. Cigler, C.T. Vincent, A new paradigm for mechanobiological mechanisms in tumor metastasis. Semin. Cancer Biol. **22**, 385–395 (2012)
78. I. Tufto, J. Lyng, E.K. Rofstad, Interstitial fluid pressure, perfusion rate and oxygen tension in human melanoma xenografts. Br. J. Cancer Suppl. **27**, S252–S255 (1996)
79. T.A. Ulrich, E.M. De Juan Pardo, S. Kumar, The mechanical rigidity of the extracellular matrix regulates th structure, motility, and proliferation of glioma cells. Cancer Res. **69**, 4167–4174 (2009)
80. M. Versaevel, T. Grevesse, S. Gabriele, Spatial coordination between cell and nuclear shape within micropatterned endothelial cells. Nat. Commun. **3**, 671 (2012)
81. P.S. Wellman, R.D. Howe, E. Dalton, K.A. Kern, Breast tissue stiffness in compression is correlated to histological diagnosis. Technical Report. Harvard BioRobotics Laboratory, 1–15 (1999)
82. K. Wolf, P. Friedl, Extracellular matrix determinants of proteolytic and non-proteolytic cell migration. Trends Cell. Biol. **21**, 736–744 (2011)
83. K. Wolf, I. Mazo, H. Leung, K. Engelke, U.H. von Andrian, E.I. Deryugina, A.Y. Strongin, E.B. Brocker, P. Friedl, Compensation mechanism in tumor cell migration mesenchymalamoeboid transition after blocking of pericellular proteolysis. J. Cell Biol. **160**, 267–277 (2003)
84. K. Wolf, Y.I. Wu, Y. Liu, J. Geiger, E. Tam, Multi-step pericellular proteolysis controls the transition from individual to collective cancer cell invasion. Nat. Cell. Biol. **9**, 893–904 (2007)
85. K. Wolf, M. te Lindert, M. Krause, S. Alexander, J. te Riet, A.L. Willis, R.M. Hoffman, C.G. Figdor, S.J. Weiss, P. Friedl, Physical limits of cell migration: control by ECM space and nuclear deformation and tuning by proteolysis and traction force. J. Cell Biol. **201**, 1069–1084 (2013)
86. M.H. Zaman, L.M. Trapani, A.L. Sieminski, D. Mackellar, H. Gong, R.D. Kamm, A. Wells, D.A. Lauffenburger, P. Matsudaira, Migration of tumor cells in 3D matrices is governed by matrix stiffness along with cell-matrix adhesion and proteolysis. Proc. Natl. Acad. Sci. U. S. A. **103**, 10889–10894 (2006)

Chapter 4
Mathematical Modeling of Morphogenesis in Living Materials

Valentina Balbi and Pasquale Ciarletta

Abstract From a mathematical viewpoint, the study of morphogenesis focuses on the description of all geometric and structural changes which locally orchestrate the underlying biological processes directing the formation of a macroscopic shape in living matter. In this chapter, we introduce a continuous chemo-mechanical approach of morphogenesis, deriving the balance principles and evolution laws for both volumetric and interfacial processes. The proposed theory is applied to the study of pattern formation for either a fluid-like or a solid-like biological system model, using both theoretical methods and simulation tools.

4.1 Introduction

In developmental biology, *morphogenesis* can be defined as the ensemble of the underlying biological processes directing the formation of a macroscopic shape in living matter. Morphogenetic events span over a wide range of molecular and cellular mechanisms, often inter-playing for controlling events at individual or collective level. Thus, the shape of an organism emerges over time as a morphological transition coordinated by these complex multi-scale interactions, revealing the intrinsic dynamic nature of its driving forces. Indeed, from a mathematical viewpoint, the study of morphogenesis focuses on the description of all geometric and structural changes which locally orchestrate the occurrence of a global shape in living materials. Accordingly, a mathematical model must consider the two most fundamental processes during tissue development, namely *growth* and *remodeling*, intended as the biological mechanisms determining any variation of the mass and of

V. Balbi
School of Mathematics, University of Manchester, Manchester M13 9PL, UK
e-mail: valentina.balbi@manchester.ac.uk

P. Ciarletta (✉)
Institut Jean le Rond d'Alembert, CNRS and Sorbonne Universités, Université Paris 6, UMR 7190, 4 place Jussieu case 162, 75005 Paris, France

Mox, Dipartimento di Matematica, Politecnico di Milano, piazza Leonardo da Vinci 33, 20133 Milano, Italy
e-mail: pasquale.ciarletta@upmc.fr; pasquale.ciarletta@polimi.it

L. Preziosi et al. (eds.), *Mathematical Models and Methods for Living Systems*,
Lecture Notes in Mathematics 2167, DOI 10.1007/978-3-319-42679-2_4

the micro-structural organization, respectively [110]. Nonetheless, morphogenesis is by far a more complex phenomenon, since these basic mechanisms often occur simultaneously, involving a cascade of inter-related developmental events from the molecular to the tissue scale, provoked by either genetic or epigenetic causes [31].

It is therefore mandatory for a mathematical theory of morphogenesis to provide a dynamic modelling of the morphology as a function of the interplay between geometry and physical forces, as well as chemical and biomolecular cues. Moreover, the suitability of a mathematical model should be evaluated not only for the accuracy of reproducing the observed morphology in the dynamical fashion, but also for the ability to identify the most relevant underlying causes, (*causas alias ex aliis aptas et necessitate nexas*).[1]

Before investigating in details the main building blocks for a suitable mathematical modelling, we briefly give an overview of the development of the morphogenetic theories over the centuries, highlighting the path towards the contemporary vision of morphogenesis and its most intriguing open challenges.

4.2 An Historical Overview of Morphogenetic Theories

The scope of this section is to provide an historical survey of the main events concerning evolutionary theories and biological discoveries, from the ancient times to the modern and contemporary approaches.

4.2.1 Epigenesis Versus Pre-formationism: From Ancient Times to the Advent of Microscopy

Although it is known that Babylonians and Egyptians made an earlier use of geometrical calculations for structural purposes, the first application of geometry for explaining the origin of a shape can be found in Euclid's Elements (Book VI, definition 3, ca.300 BC), where "a straight line is said to have been cut in extreme and mean ratio when, as the whole line is to the greater segment, so is the greater to the less". This definition highlighted a simple proportion already used almost two centuries earlier by the sculptor Phidia, who seemingly used it to construct the Parthenon's statues. The possibility of using such a simple geometrical rule to decrypt the harmony and symmetry behind several shapes commonly observed in Nature still creates much fascination in our times, explaining the Medieval belief

[1] In mathematical terms, this latin expression can be roughly translated as the set of the strictly necessary causes (from Cicero, *Rhetorica, Tusculanae Disputationes, Liber Quintus, 70).*

of a divine number.[2] Indeed, the theological doctrine of creationist prevailed for almost two millennia, and shape was considered as a pre-ordered organization of matter resulting from an act of divine creation. Opposed to such a pre-formationist view, Aristotle had already proposed in his books *Hystoria Animalium* and *De Generatione Animalium* (ca.350 BC) the so-called *epigenetic hypothesis*. According to Aristotele, after several steps of differentiation, the tissues forme structures which were not present at the initial steps of life [6]. Such works were mainly based on teleological concepts, but they reported an impressive number of biological observations on embryos, although methodologically very far from a rigorous modern scientific approach.

Notwithstanding, the predominance of *preformationism* persisted until the seventeenth century, where the advent of microscopy techniques opened a scientific debate between epigenetists and preformationists about the nature of embryonic structures. From one side, William Harvey retraced the Aristotelian ideas proposing the principle *ex ovo omnia*, i.e. that everything develops epigenetically from an egg [60]; on the opposite side, Marcello Malpighi and Nicolaas Hartsoeker claimed that a miniature structure of the adult organism, called *homunculus*, was present in the egg from the very beginning, and that the gestation period involved the growth and unfolding of that pre-existing structure [1, 59].

Few decades in advance, Galileo Galilei had hinted that the shape of organisms was somehow influenced by the load that they have to hold, proving that the changes in size of bones over mammals are actually governed by allometric scaling [47]. This seminal idea of mechanical causation would still take almost two centuries before influencing the scientific view of morphogenesis.

4.2.2 The Birth of Modern Embryology: Evolutionary Theories and Mechanical Causation

The nineteenth century was dominated by Darwinism and the advent of genetics, but also by the theory that plants and organisms are made of cells, and that reproduction is governed by cell division, according to the principle *omnis cellulae ex cellula* proposed by Rudolf Virchow [115]. Furthermore, the technical progress in microscopy determined the birth of the modern experimental embryology. Inspired by Darwinism, Ernst Haeckel proposed the *recapitulation theory*, claiming that the developmental steps of embryonic growth would be a reflection of the adult evolution of their ancestors [55]. This biogenetic law formulated that ontogeny (i.e. the development of an individual organism) recapitulates phylogeny (i.e. the evolution of a species). Although immediately rejected by Wilhelm His, who showed with experiments that the gut tube morphogenesis could be modeled by a

[2]This idea was enforced by Luca Pacioli, a student of Leonardo da Vinci, in his book *De divina proportione*, published in 1509.

mechanical causation principle [92], this biogenetic theory prevailed in the scientific community until the works of Wilhelm Roux towards the end of the nineteenth century. In particular, he shifted the focus of developmental biology from evolution (i.e. the final purpose) to the underlying mechanisms (i.e. the causes), performing several experiments on embryos in order to investigate the self-differentiation [99]. Although some of his deductions were incorrect [56], Roux inspired a new approach in experimental embryology, giving seminal results about *regulation*, i.e. the ability of the embryo to develop normally even if a part of it is removed, as well as *induction*, i.e. the influence of a cell or a tissue on the development of another. Interestingly, a definitive confirmation of the latter phenomenon had to wait till 1924, when Spemann and Mangold transplanted part of the embryonic tissue from a amphibian into an embryo of a different amphibian species [106]. They observed that a partial second embryo developed from the transplanted tissue: the hosting tissue induced the development of the hosted tissue.

Roux also extended the investigation about the mechanical causation of development establishing the concept of *functional adaptation* as a principle for dependent-differentiation: cells and tissues respond to change in external conditions in order to preserve their global organization and functions. Accordingly, any tissue would adapt under the action of external forces, regulating its growth in order to preserve lightness and structural robustness.

This fundamental principle contributed to the development of modern physiology, which considers that all life phenomena result from the mutual balance between the living matter and the surrounding media. In the same period, indeed, Claude Bernard first hypothesized that such a dynamic equilibrium might regulate living organisms despite the structural complexity of the constituting matter [10]. Initially focusing on anatomical, biochemical and symphato-adrenal stimuli, novel experiments highlighted the stable equilibrium between the interior matter of a living entity with respect to external perturbative agents. Accordingly, this physiological tendency towards a steady state was later called *homeostasis*, and found to drive the optimal structural remodelling of both bone to mechanical loading, also known as Wolff's law [117], and arterial endothelia to shear stress, also known as Murray's law [89].

4.2.3 The Contemporary Approaches to Morphogenesis

The twentieth century has been particularly rich in crucial discoveries and scientific contributions to the understanding of morphogenesis. In particular, the first half of the century was characterized by the introduction of mathematical modelling to investigate the relations between the physical forces exerted by the surroundings and the steady generation of shapes. The second half was instead dominated by the many astonishing discoveries in genetics and molecular biology, shifting the research focus to the dynamical aspects of morphogenesis.

4.2.3.1 The First Mathematical Approach on Growth and Form

In 1917, D'Arcy Wentworth Thompson published his masterpiece and only scientific book, entitled *On growth and form* [111], a compendium of more than a thousand pages, written in wartime, about the use of mathematical theory to describe the shape of living organisms.

Whilst other contemporary scientists focused on experimental analysis, D'Arcy Thompson's investigations were purely based on mathematical foundations. Being skeptical about a morphogenetic analysis based on evolution theories and natural selection, which were still dominant in the scientific community at that time, his original idea of morphogenetic development was instead focused on the role of physical forces in shaping organisms. The following quote from the Introduction section is fully explicative in this sense:

> *It is retained, somewhat crudely, in modern embryology*
> *[. . .]that the embryonic phenomena must be referred directly*
> *to their usefulness in building up the body of the future animal*
> *which is no more, and no less, to say, with Aristotle,*
> *that the organism is the* $\tau\epsilon\lambda o\varsigma$*, or final cause,*
> *of its own processes of generation and development.*
> *[. . .] Still, all the while, like warp and woof, mechanism and teleology*
> *are interwoven together, and we must not cleave to the one nor despise the other;*
> *for their union is rooted in the very nature of totality.*

Accordingly, the book investigates mechanical causation in the generation of many shapes in living matter, dealing with living organisms as material bodies subjected to physical forces and obeying to simple physical and geometrical laws. An illustrative example of the originality of D'Arcy Thompson's approach can be found in the second chapter of his book, where he focused on the physical scaling effects on the shape of animals of different sizes, complementing Galileo's first observations on allometric laws. He proved that, whilst big animals must have strong and heavy structures which allow to sustain the bulk gravitational load, the shapes and structures small animals can be calculated from a principle of functional adaptation to surface forces, e.g. surface tension. Furthermore, he proposed a grid transformation method, aimed at showing that physical forces can shape a living organism during either growth or evolution, as depicted in Fig. 4.1. D'Arcy Thompson's work had a seminal influence on modern biomechanics and his book is still read and published in reduced and revised versions. Among many other examples, it was a source of inspiration for Huxley's work on allometric growth [67] as well as for Gould's mechanistic theory of shape from an evolutionary viewpoint [51].

4.2.3.2 The Chemical Bases of Morphogenesis

The fast development of experimental techniques in biochemistry promoted an increasing attention to the chemical and molecular mechanisms underpinning morphogenetic processes. A new branch of applied mathematics especially focused

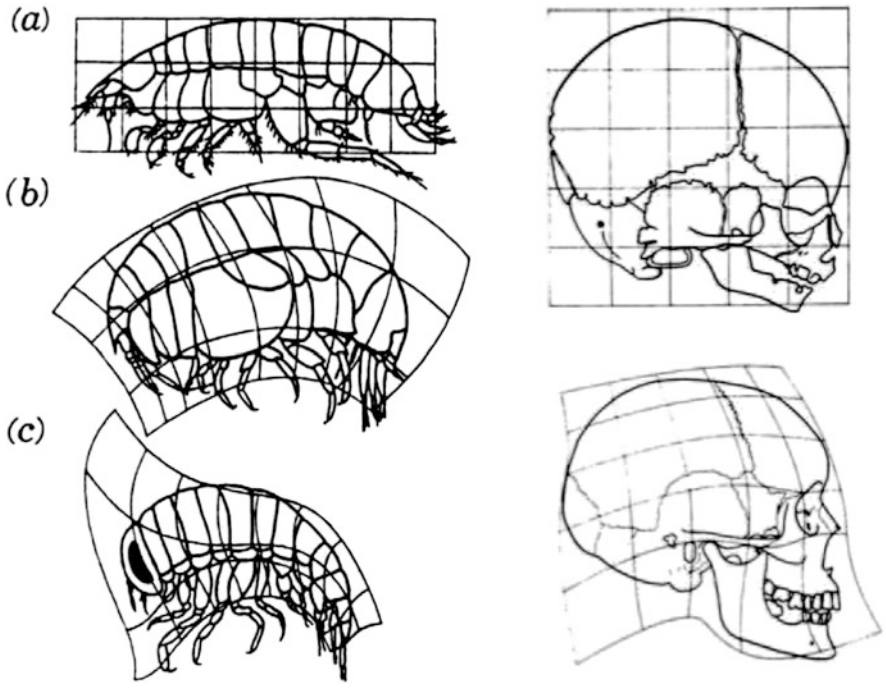

Fig. 4.1 *Left*: Transformation grid applied to the shape transformation of a small amphiopod (**a**) *Harpinia Plumosa* into the shapes of two other genera belonging to the same family (**b**) *Stegocephalus Inflatus*, and (**c**) *Hyperia Galba*, adapted from [29]. *Right*: Transformation grid applied to the growth of a skull in human foetus. In both examples the transformation is achieved by applying physical forces on the considered structure, during evolution and growth respectively

on the description of pattern formation, i.e. the emergence of organized living structures in space and time. A milestone in biomathematics is the paper by Alan Turing on the chemical bases of morphogenesis, published in 1952 [113]. Although it was his only contribution on morphogenesis, it is an extraordinary innovative work, especially since it proved how a mathematical theory could actually anticipate biological discoveries. Turing proposed a reaction-diffusion model of at least two chemical species which undergo chemical reaction within a living material: in order to highlight their role in generating a new pattern, he called them *morphogens*. They practically act as biochemical substances enabling certain shape control abilities in the embryonic tissue, closely resembling the *evocators* earlier hypothesized by Waddington [116]. In the absence of diffusion, the biological system is in a stable state defined by homogeneous concentrations of the two reactants. Under certain range of values of the reaction and diffusion parameters, an instability occurs and a stable non-homogenous pattern arises. This was a counter-intuitive result since it was thought that diffusion would rather introduce a chaotic behavior in the system, instead of generating an organized pattern.

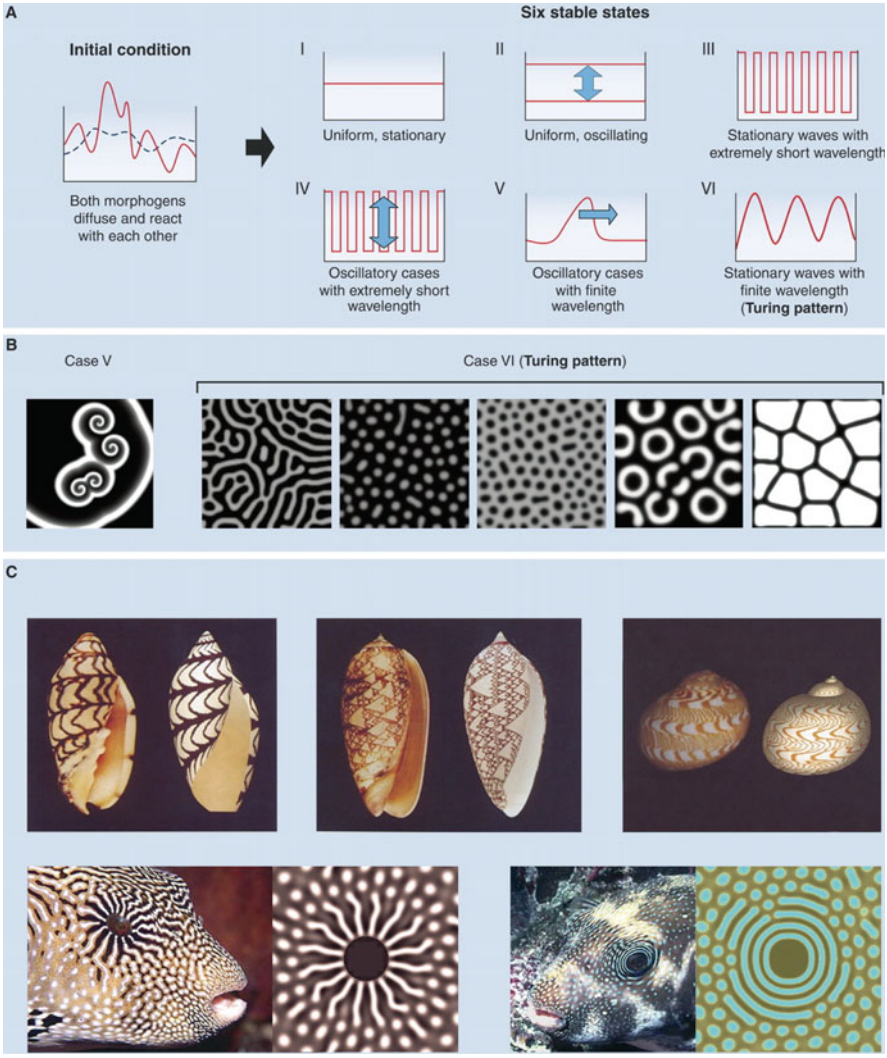

Fig. 4.2 Turing's reaction-diffusion model: (**a**) Examples of the six stable states solutions of Turing's model. (**b**) The so-called Turing's pattern is depicted as the Case VI where a stationary wave of finite wavelength develops. (**C**) Reproduction of biological patterns created by modified reaction-diffusion mechanisms. Adapted from [73]

In particular, Turing's model predicted the existence of six possible steady-states as shown in Fig. 4.2. The *uniform* stationary (I) and oscillatory (II) states, the *short wavelengths* stationary (III) and oscillatory (IV) states and the *finite wavelength* stationary (V) and oscillatory (VI) states. Of particular interest is Case VI, which occurs when the diffusion coefficients of the two morphogens differ substantially and initiate the so-called *short-range activation, long-range*

inhibition [48] mechanism. The two morphogens are seen as an activator and an inhibitor, respectively, which can act on themselves as well as on the other. A small perturbation in the homogeneous concentration can induce an increase in the activator concentration and initiate the feedback which lead to the formation of one of the Turing's patterns in Fig. 4.2b.

Turing's model has later been largely employed for modeling the emergence of several patterns in vertebrates such as the stripes in the zebra-fish pigmentation [72], the branching pattern in feathers [58], but also the fabulous seashell patterns [94] and the mechanism of plant phyllotaxis, i.e. the arrangement of leaves on a plant stem [105].

Nonetheless, Turing's work did not receive a great attention in the years right after its publication. Indeed, the problem of emergence of organized cellular patterns in the tissue was brought back to the attention of developmental biologists only in the 1970s, when Lewis Wolpert introduced the concept of *positional information* (PI). The main idea of Wolpert is that the position of a cell in the tissue specifies the information about the molecular changes the cell will undergo [118]. In this sense, morphogens display both positional information and growth orchestration properties. The key elements of Wolpert's theory can be summarized in the definition of:

- A mechanism which specifies the *polarity* in the tissue. Polarity is the direction in which PI is specified and is defined with respect to one or more reference points.
- A mechanism for specifying the different responses of the cell.

PI can be specified by a quantitative variation of some factor such as the concentration, or a qualitative variation of some cell parameters such as a combination of genes or enzymes. A set of cells which have their PI specified with respect to the same reference points constitutes a field. *Interpretation* of PI is the process by which PI specifies the cell state and *conversion* is the mechanism by which PI is translated in a particular cellular activity. Furthermore, PI is universal in organisms and size invariant, meaning that if a part of the tissue is removed, the tissue is still able to pattern and interpret the PI.

The concept of positional information is well clarified in the French flag model depicted in Fig. 4.3. In this example, the mechanism which specifies polarity is the monotonic variation of the morphogen concentration C. T_1 and T_2 identify the mechanism for the differential response of the cells. The interpretation acts according to the following rule: cells with position in the region where $C < T_1$ express the blue pigment, a cell in the region where $T_1 < C < T_2$ expresses the white pigment and cells in the region where $C > T_2$ express the red pigment. This apparently simplistic model was later confirmed by experimental observations on the early Drosophila embryo, where the concentration gradient of the protein Bicoid (i.e. a transcription factor, being the first molecules found to act as a morphogen in 1988 [36]) drives an antero-posterior differentiation in three separated domains [68].

The models proposed by Turing and Wolpert offer two different points of view on pattern formation. A first difference comes from the fact that Turing aimed at modeling spontaneous formation of a pattern, while Wolpert asked how a more

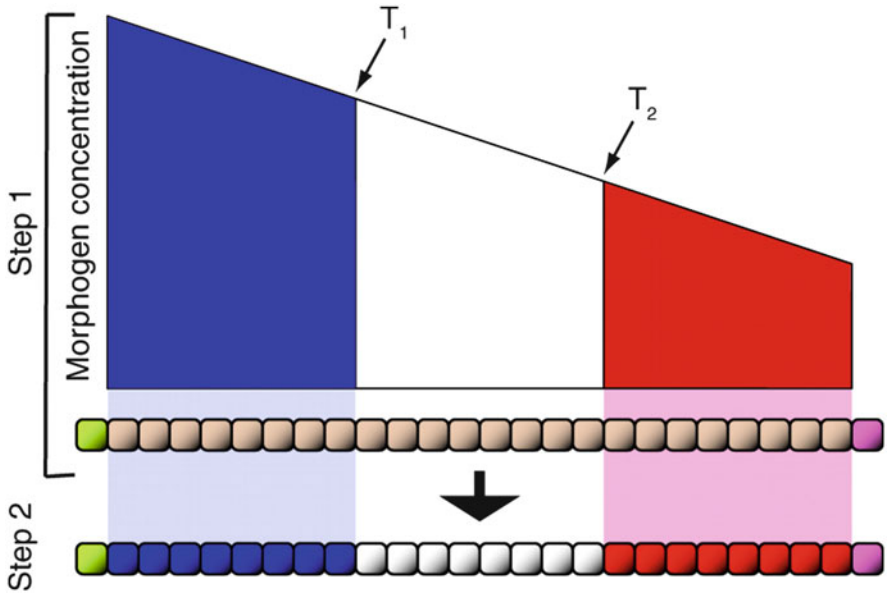

Fig. 4.3 The French Flag model: positional information is specified by the gradient of a morphogen concentration. Adapted from [69]

complex pattern can arise from an asymmetry (i.e. polarity) within the tissue. Furthermore, in Turing's model the concentration of morphogens is directly related to the spatial pattern, in this sense it is a *pre-pattern*. Conversely, Wolpert introduced an interpretation step where the cell activity is specified by the concentration gradient. Moreover, Wolpert himself later argued that morphogenetic movements are rather determined by other transport mechanisms than passive diffusion, such as planar transcytosis and cytonemes [119]. Furthermore, morphogens should be generally subjected to fluctuations on short length-scales whilst travelling through individual cells, yet finally delivering precise positional information. Without discussing in further details such limiting aspects, it is now generally accepted that more complicated morphogenetic models are needed in the wide scenario of embryogenesis. For example, recent works have proposed a different mechanism through which the two models can cooperate in pattern formation [52].

4.2.3.3 The New Course of Genetics and the Return of an Ancient Dichotomy

Although the origins of genetics date back to the second half of the nineteenth century, when Gregor Mendel discovered the inheritance of biological traits [87], its fundamental role in morphogenesis finally emerged only during the twentieth century [120]. Indeed, the earlier vision of genetics uniquely concerned studying

the transmission of hereditary properties in the embryo, since Mendel's theory was based on the idea that the hereditary package is transmitted from parents to offspring through a set of discrete hereditary factors. Although proved by experimenting on pea plants, Mendel's theory was unable to provide any concrete description of the nature of such factors. A breakthrough occurred with the discovery that the DNA carries the genetic information and that genes encode proteins. Thus, the properties of a cell are determined by the proteins they contain, genes control and act on proteins in order to drive the cell fate and consequently, the development of a shape. Right after these discoveries, a lot of experiments focused on finding the genes responsible for several morphogenetic events in the embryo. The strategy adopted was to introduce changes in the molecular organization of the DNA in order to observe abnormal changes in a final structure. In this way, it has been possible to identify which genes play an active role in the formation of an emerging pattern.

These novel discoveries puzzled researchers about the genetic bases of morphogenesis. Interestingly, the ancient dichotomy between pre-formationism and epigenesis rephrased in a modern key, whether the shape of an organism emerges as a results of a set of fixed genetic instructions or it can be influenced by environmental factors, both at the individual level and during evolution.

Even if many open questions exist in the rapidly developing research branches of morphogenesis, it is now acknowledged that both the genetic and the epigenetic factors influence shape at different levels [7]. In the absence of mutations, each cell within a given organism has the same set of genes, called genotype, whilst only a small subset is expressed as a function of the environment, defining the phenotype. Therefore, the epigenetic adaptation can occur both at the level of individual organism as a change of phenotype and at the evolutionary level as a switch of ontogenic programs [2]. In summary, it is now clear that the morphogenetic processes (e.g. cell division and differentiation) are driven by genetic signals, as well as that the genetic expression involves epigenetic processes by means of morpho-regulatory biomolecules, that interact with genes through a complex network of feedback regulatory mechanisms [38].

4.2.4 The Open Quest for the Chemo-Mechanical Cues of Morphogenesis

Nowadays, there is an increasing research interest in life sciences concerning the biomolecular mechanisms directing the adaptation of living matter to the physical forces exerted by the surrounding micro-environment. The ensemble of biologically processes converting mechanical forces into biochemical factors is called *mechano-transduction*. This is a typical multi-scale phenomenon, since living cells may sense from nano-scale to macroscopic forces often driving the transition from physiological to pathological conditions [37]. The nano-scale force transduction occurs by means of cell membrane molecules, typically focal adhesion proteins and

integrins, converting the mechanical stimulus into a change of membrane potential through the formation of a ionic current. In physiological condition, a feedback mechanism, known as *mechano-reciprocity*, acts for activating the acto-myosin machinery in order to restore a tensional homeostasis at the macro-scale (e.g. tissue), i.e. globally balancing endogenous and exogenous forces. Conversely, a loss of tensional homeostasis often characterizes a hallmark of disease, e.g. directing both the initiation of solid tumours and the formation of metastasis [15].

Mechano-transduction plays a fundamental role in the modern view of morphogenesis, since it allows the regulation of epigenetic and genomic factors at different time-scales. In fact, it controls the dynamic adaptation of living cells by means of both switch-like events at their trans-membrane structures [121] and the activation dynamic molecular processes in response to long time-varying mechanical stimuli [61]. Many seminal experiments highlighting the crucial role of chemo-mechanical cue in morphogenesis have been performed in the last decades by the research group lead by Lev Beloussov. In particular, these works have reported that the active responses of living matter may overshoot the passive mechanical stimuli, proposing a *hyper-restoration principle* for homeostasis [8]. Another open area of investigation concerns the identification of the local regulation mechanisms, mainly signalling pathways that spatially and temporally control cell behaviour, which allow the global orchestration of a macroscopic shape [76]. Therefore, the current understanding of morphogenetic events gained a further complexity in the underlying phenomena with respect to the purely chemical bases earlier assumed. For example, the local concentration of morphogens can trigger growth as a random cellular proliferation. Nonetheless, polarity can induce preferred orientations in cellular division, possibly affected also both by competition between different cell populations and by physical forces, e.g. growth inhibition by compression [77]. At a more macroscopic level, unknown chemo-mechanical orchestration mechanisms should transform random or oriented local proliferations into a uniform growth, which must ultimately cease as the final size is reached. Thus, the morphological control may depend on both the cell number and the overall size, suggesting that the spatial gradient of morphogens can provide cells a dimension-sensing mechanism.

The quest for the chemo-mechanical cues in morphogenesis is therefore a mandatory step for the development of refined mathematical theories [66]. This was somewhat hinted by Turing himself in his original paper:

> *In the continuous form of the theory [..] one should take into account*
> *(i) The changes of position and velocity as given by Newton's laws of motion.*
> *(ii) The stresses as given by the elasticities and motions[. . .].*
> *(iii) The chemical reactions.*
> *(iv) The diffusion of the chemical substances[. . .].*
> *This account of the problem omits many features, [. . .] but even so it is a problem of formidable mathematical complexity. The interdependence of the chemical and mechanical data adds enormously to the difficulty [. . .].*

Well aware of such unavoidable complications, we will sketch in the next section the balance laws for a continuous theory of morphogenesis, using the thermodynamics of open systems to take into account for the chemo-mechanical coupling.

4.3 A Continuous Chemo-Mechanical Theory of Morphogenesis

The thermo-mechanics of open systems is a natural framework for a macroscopic mathematical description of morphogenesis in living matter, which is hereafter considered as a continuous distribution of matter. Accordingly, we disregard the microscopic dynamics of the underlying biological phenomena acting at the subcellular or cellular level, and we model the relevant chemo-mechanical properties by averaged fields at the tissue scale. In the following, we provide some basic kinematic notions and we derive the physical balance laws that govern the morphogenetic processes within living matter as a function of both the mechanical and the chemical cues.

4.3.1 Basic Kinematic Notions

Denoting by $\mathscr{E} \subset \mathbb{R}^3$ be a three-dimensional Euclidean space, let $\mathscr{B}_0, \mathscr{B}_a \subset \mathscr{E}$ be two regions occupied by the living body in two different instants of time. Let $\boldsymbol{\chi}$ be the mapping which transforms the tissue from its initial configuration $\mathscr{B}_0$ to its final configuration $\mathscr{B}_a$, which can be defined as the following $\mathscr{C}^1$-diffeomorphism:

$$\boldsymbol{\chi} : \mathscr{B}_0 \to \mathscr{B}_a \qquad \mathbf{x} = \boldsymbol{\chi}(\mathbf{X}), \qquad \text{with inverse} \quad \mathbf{X} = \boldsymbol{\chi}^{-1}(\mathbf{x}) \tag{4.1}$$

where $\mathbf{X}$, $\mathbf{x}$ are the position vectors in the reference and actual configurations $\mathscr{B}_0$ and $\mathscr{B}_a$, respectively. The deformation gradient, associated to the deformation in Eq. (4.1), is the second order two-point tensor defined as:

$$\mathbf{F} : T\mathscr{B}_0 \to T\mathscr{B}_a \qquad \mathbf{F} = \mathrm{Grad}\,\mathbf{x} = \frac{\partial \boldsymbol{\chi}(\mathbf{X})}{\partial \mathbf{X}} = \frac{\partial x_i}{\partial X_j}\mathbf{e}_i \otimes \mathbf{E}_j, \tag{4.2}$$

where $\mathbf{E}_j, \mathbf{e}_i$ (with $i, j \in \{1, 2, 3\}$) are the basis unit vectors in the reference and actual configurations, respectively, and $T\mathscr{B}_0, T\mathscr{B}_a$ are the collections of all tangent spaces on $\mathscr{B}_0$ and $\mathscr{B}_a$, respectively. A tangent space is the set of all line elements attached to a body point. The capital notation Grad in Eq. (4.2) indicates the gradient operator with respect to the material position X_j in the reference configuration $\mathscr{B}_0$ and the symbol $\otimes$ indicates the dyadic product between two vectors, in indicial form : $(\mathbf{a} \otimes \mathbf{b})_{\alpha\beta} = a_\alpha b_\beta$.

According to Eq. (4.2), the following relations for the transformation of line, surface and volume elements, respectively, hold:

$$\mathbf{dx} = \mathbf{F}\mathbf{dX} \tag{4.3}$$

$$\mathbf{n}\mathrm{d}s = J\mathbf{F}^{-T}\mathbf{N}\mathrm{d}S \tag{4.4}$$

$$\mathrm{d}v = J\mathrm{d}V \tag{4.5}$$

where $J = \det \mathbf{F}$ and the quantities $\mathbf{dX}, \mathbf{N}\mathrm{d}S, \mathrm{d}V$ and $\mathbf{dx}, \mathbf{n}\mathrm{d}s, \mathrm{d}v$ are defined in the reference and actual configurations, respectively, with $\mathbf{N}$ and $\mathbf{n}$ being the unit normal vectors to dS and ds, respectively. Eq. (4.5) can be directly derived from Eq. (4.3), while Eq (4.4) is also known as *Nanson's Formula*.

Before deriving the thermo-mechanical laws for a morphogenetic process, it is useful to introduce some relations that will be used in the following.

Let $\mathbf{f}(\mathbf{x}, t)$ be a continuously differentiable spatial vector field, its total time derivative writes as:

$$\dot{\mathbf{f}}(\mathbf{x}, t) = \frac{d\mathbf{f}(\mathbf{x}, t)}{dt} = \frac{\partial \mathbf{f}(\mathbf{x}, t)}{\partial t} + \mathbf{v}(\mathbf{x}, t) \operatorname{grad} \mathbf{f}(\mathbf{x}, t), \tag{4.6}$$

Moreover, considering the integral of the spatial field $\mathbf{f}$ on a volume changing with time, the Reynolds theorem allows for the time derivative to be calculated as:

$$\frac{d}{dt} \int_{\mathscr{B}_a} \mathbf{f}(\mathbf{x}, t)\, \mathrm{d}v = \int_{\mathscr{B}_a} [\dot{\mathbf{f}}(\mathbf{x}, t) + \mathbf{f}(\mathbf{x}, t) \operatorname{div} \mathbf{v}(\mathbf{x}, t)]\, \mathrm{d}v, \tag{4.7}$$

where $\mathbf{v}(\mathbf{x}, t)$ is the spatial velocity, and div is the spatial divergence operator. Moreover, we will use the divergence theorem in the form :

$$\int_{\partial \mathscr{B}_a} \mathbf{n} \cdot \mathbf{f}(\mathbf{x}, t)\, \mathrm{d}s = \int_{\mathscr{B}_a} \operatorname{div} \mathbf{f}(\mathbf{x}, t)\, \mathrm{d}v, \tag{4.8}$$

so that $\operatorname{div}(\mathbf{f}) = \mathrm{f}_{ih,i}$ for any given tensor field $\mathbf{f}$, assuming saturation on repeated indices unless explicitly stated.

4.3.1.1 Balance of Mass

Since morphogenetic processes usually involve growth and remodelling, let us first derive the mass balance for a living material as a function of the biochemical factors [23, 40]. The global form of the mass balance for a growing body X in spatial coordinates reads:

$$\frac{d}{dt} \int_{\mathscr{B}_a} \rho\, \mathrm{d}v = \int_{\mathscr{B}_a} \omega\, \mathrm{d}v \tag{4.9}$$

where ρ is the spatial mass density and d/dt denotes the total time material derivative. Accordingly, ω is the internal mass production rate per unit current volume, and we neglected any non-convective mass flux for the sake of brevity. The interested reader is referred to [39] for the introduction of mass self-diffusion terms.

The mass production rate represents the cellular proliferation within the material which is possibly driven by some biochemical fields, e.g. growth signals, nutrients, morphogens. Indicating with $c_i(\mathbf{x}, t)$ the concentration of the generic $i - th$ species

per unit volume, we can generically assume that $\omega = \omega(c_i, \mathbf{F})$. Moreover, since we deal with signals or low weight molecules, such species can me modeled as internal variables with negligible inertia [24], having the following balance laws:

$$\frac{d}{dt}c_i - \operatorname{div} \mathbf{J}_{ci} = -\xi_i(\mathbf{F}, Grad\mathbf{F}) \tag{4.10}$$

where ξ_i is the absorption rate of the $i-th$ species, whose value may depend both on the first and on the second gradient of the deformation field, the latter reproducing, for example, curvature-dependent effects in the absorption of angiogenetic factors [79]. The diffusion of a morphogen from the source through the extracellular matter, with a sink function possibly regulated by receptor endocytosis, has been proved to describe the morphogens gradient in multicellular embryonic tissues [122]. As discussed in [4], the simpler expression for the flux of nutrients $\mathbf{J}_c$ is given:

$$\mathbf{J}_{ci} = D(c_i)J \operatorname{grad} c_i \tag{4.11}$$

where $D(c_i)$ represents a diffusion tensor, whose positive definiteness and monotonicity on c_i ensure the well posedness of the mathematical problem.

The local spatial form of Eq. (4.51), can now be easily derived by substituting Eq. (4.7) and permuting integration and differentiation, being:

$$\dot{\rho} + \rho \operatorname{div} \mathbf{v} = \omega(c_i, \mathbf{F}), \tag{4.12}$$

where the dot symbol indicates the total time derivative defined in Eq. (4.6). For problems involving solids, it is useful to derive its material counterpart using a similar procedure after recasting Eq. (4.51) in the reference volume. It reads:

$$\dot{\rho}_0 = \Omega. \tag{4.13}$$

where $\rho_0 = J\rho$ is the material density and $\Omega = J\omega$ is the internal mass production rate per unit reference volume.

In summary, Eqs. (4.12) and (4.13) are the mass balance laws of biological material during a morphogenetic process guided by the reaction diffusion Eq. (4.10). We remark that the driving chemo-mechanical cues will be defined by the proper constitutive choices of the coupling terms ω and ξ.

4.3.2 Balance of Linear and Angular Momentum

Let us first consider the balance of the physical linear momentum $\mathbf{p} = \rho\mathbf{v}$ inside the biological system. Its conservation law in the global form rewrites:

$$\frac{d}{dt}\left(\int_{\mathscr{B}_a} \mathbf{p} dv\right) = \int_{\mathscr{B}_a} (\rho \mathbf{b}_v + \omega \mathbf{v}) dv + \int_{\partial\mathscr{B}_a} \mathbf{n}.\boldsymbol{\sigma}\, ds \tag{4.14}$$

where $\boldsymbol{\sigma}$ is the Cauchy stress tensors , and $\mathbf{b}_v$ is an external bulk force. Substituting Eq. (4.12) while developing the integral terms in Eq. (4.14), we obtain after some standard manipulations the following local form in the spatial configuration:

$$\rho \frac{d\mathbf{v}}{dt} = \rho \mathbf{b}_v + \operatorname{div} \boldsymbol{\sigma} \tag{4.15}$$

In order to derive the material counterpart of Eq. (4.14), let us substitute the Nanson's formula in Eq. (4.4), so that:

$$\frac{D}{Dt} \int_{\mathscr{B}_0} \rho_0 \mathbf{v} \, \mathrm{dV} = \int_{\partial \mathscr{B}_0} \mathbf{N}.\mathbf{S} \, \mathrm{dS} + \int_{\mathscr{B}_0} (\rho_0 \mathbf{b}_v + \omega \mathbf{v}) \, \mathrm{dV} \tag{4.16}$$

where the volume element transformation in Eq. (4.5) and the relation in Eq. (4.12) have been used. The stress tensor $\mathbf{S}$ in Eq. (4.16) is called the Nominal stress and is related to the Cauchy stress by $\mathbf{S} = J\mathbf{F}^{-1}\boldsymbol{\sigma}$.[3] Thus, its local form in material coordinates reads:

$$\rho_0 \frac{d\mathbf{v}}{dt} = \rho_o \mathbf{b}_v + \operatorname{Div} \mathbf{S} \tag{4.17}$$

where Div is the material divergence.

Furthermore, the global form of the angular momentum balance in presence of growth can be written in spatial coordinates as:

$$\frac{D}{Dt} \int_{\mathscr{B}_a} \mathbf{y} \times \rho \mathbf{v} \, \mathrm{d}v = \int_{\partial \mathscr{B}_a} \mathbf{y} \times \boldsymbol{\sigma} \mathbf{n} \, \mathrm{ds} + \int_{\mathscr{B}_a} \mathbf{y} \times (\rho \mathbf{b}_v + \omega \mathbf{v}) \, \mathrm{d}v \tag{4.18}$$

where $\times$ is the cross product and the position vector $\mathbf{y}$ has been introduced as $\mathbf{y} = \mathbf{x} - \mathbf{x}_0$ with $\mathbf{x}_0$ being a fixed vector position. Using the Reynolds theorem in Eq. (4.7), the l.h.s of Eq. (4.18), rewrites:

$$\frac{D}{Dt} \int_{\mathscr{B}_a} \mathbf{y} \times \rho \mathbf{v} \, \mathrm{d}v = \int_{\mathscr{B}_a} [\mathbf{y} \times (\dot{\rho} \mathbf{v} + \rho \dot{\mathbf{v}}) + (\mathbf{y} \times \rho \mathbf{v}) \operatorname{div} \mathbf{v}] \, \mathrm{d}v \tag{4.19}$$

where the second equality follows from $\dot{\mathbf{y}} = \dot{\mathbf{x}} = \mathbf{v}$ and the product differentiation rule of the cross product.

Using the divergence theorem in Eq. (4.8) and the properties of the cross product, the first term in the r.h.s of Eq. (4.18) transforms into the volume integral:

$$\int_{\partial \mathscr{B}_a} \mathbf{y} \times \boldsymbol{\sigma} \mathbf{n} \, \mathrm{ds} = \int_{\mathscr{B}_a} [\mathbf{y} \times \operatorname{div} \boldsymbol{\sigma} + \mathscr{E} : \boldsymbol{\sigma}^T] \, \mathrm{dV} \tag{4.20}$$

[3] Since $\mathbf{S}$ is related to $\boldsymbol{\sigma}$ through a Piola transformation, it is often called first Piola-Kirchhoff stress tensor [85]. Nonetheless, some authors consider the latter being the transpose of $\mathbf{S}$ [90]. Accordingly we prefer to call it nominal stress in order to avoid misunderstanding to the readers.

where $\mathscr{E} = \epsilon_{jkl}\mathbf{e}_j \otimes \mathbf{e}_k \otimes \mathbf{e}_l$ is the third-order permutation tensor with components $\epsilon_{jkl} = (\mathbf{e}_j \times \mathbf{e}_k) \cdot \mathbf{e}_l$. Now, using the mass balance in Eq. (4.12), the balance of linear momentum in Eq. (4.15) and substituting Eqs. (4.19) and (4.20) into Eq. (4.18), it follows that:

$$\int_{\mathscr{B}_a} \mathscr{E} : \boldsymbol{\sigma}^T \, \mathrm{dV} = \mathbf{0} \tag{4.21}$$

whose local eulerian form is:

$$\boldsymbol{\sigma} = \boldsymbol{\sigma}^T \tag{4.22}$$

with material counterpart:

$$\mathbf{FS} = \mathbf{S}^T\mathbf{F}^T \tag{4.23}$$

Hence, the Cauchy stress tensor $\boldsymbol{\sigma}$ must be symmetric whilst the Nominal stress $\mathbf{S}$ is not. In the following, we will derive the thermodynamic principles for the growing biological system.

4.3.3 Balance of Internal Energy and Entropy Inequality

Following the approach in [40], let ε be the internal energy per unit mass and with μ_i a scalar function representing the source of internal energy associated with the $i-th$ solute c_i. Accordingly, the global form of the first law of thermodynamics can be expressed as follows:

$$\frac{d}{dt}\int_{\mathscr{B}_a} \rho\varepsilon dv = \int_{\mathscr{B}_a} (\omega\varepsilon - \xi_i c_i \mu_i + r_0 + tr(\boldsymbol{\sigma}\,\mathbf{d}))\, dv + \int_{\partial\mathscr{B}_a} \mathbf{n}.(\mu_i \mathbf{J}_{ci} - \mathbf{Q}) ds \tag{4.24}$$

were $\mathbf{d} = (\mathrm{grad}\,\mathbf{v} + (\mathrm{grad}\,\mathbf{v})^T)/2$, r_0 is the external heat supply per unit of volume, $\mathbf{Q}$ is the heat flux, μ_i is the chemical potential of the i-th species and represents the increase of the internal energy of the continuum by physical absorption of the diffusing chemicals. Irreversible terms and the temperature gradient dependence have been neglected for the sake of simplicity. Substituting Eqs. (4.10), (4.12) and (4.15) in Eq. (4.24), we obtain the following local form for the balance of the internal energy in a growing material:

$$\rho\dot{\varepsilon} = tr(\boldsymbol{\sigma}\,\mathbf{d}) + \mu_i \dot{c}_i - \mathrm{div}\mathbf{Q} + r_0 + \mathbf{J}_{ci}.\,\mathrm{grad}\,\mu_i \tag{4.25}$$

The global form of Clausius-Duhem entropy inequality reads:

$$\frac{d}{dt}\int_{\mathscr{B}_a} \rho_0 \eta \, dv \geq \int_{\mathscr{B}_a} \left(\omega\eta - \eta_i \xi_i \dot{c}_i + \frac{r_0}{\Theta}\right) dv + \int_{\partial\mathscr{B}_a} \mathbf{n}.\left(\mathbf{J}_{ci}\eta_i - \frac{\mathbf{Q}}{\Theta}\right) ds \tag{4.26}$$

where η, η_i are the entropy density per unit mass and per unit of solvent concentration, respectively. Substituting Eq. (4.12) in Eq. (4.26), the local form of the entropy inequality, reads:

$$\rho\dot{\eta} \geq \eta_i\dot{c}_i + \mathbf{J}_{ci}.\,\mathrm{grad}\,\eta_i + \frac{r_0}{\Theta} - \mathrm{div}\left(\frac{\mathbf{Q}}{\Theta}\right) \tag{4.27}$$

Recalling the expression of the Helmholtz free energy per unit of mass, $\Psi = (\varepsilon - \Theta\eta)$, and per unit of solvent concentration, $\Psi_i = (\mu_i - \Theta\eta_i)$, we can put together Eqs. (4.25) and (4.27) in order to obtain an equivalent form of the entropy inequality:

$$\rho(\dot{\Psi} + \dot{\Theta}\eta) \leq tr(\boldsymbol{\sigma}\,\mathbf{d}) + \Psi_i\dot{c}_i + \mathbf{J}_{ci}\cdot(\nabla_R\Psi_i + \eta_i\nabla_R\Theta) - \frac{\mathbf{Q}}{\Theta}\cdot\nabla_R\Theta \tag{4.28}$$

The latter inequality describes the thermodynamical consistency for the energy dissipation during a morphogenetic process, accounting both for mass production and for the reaction-diffusion of the biochemical species. Once defined the constitutive equation for the stresses, Eq. (4.28) gives a suitable chemo-mechanical coupling regulating the evolution of the biological system. An extension of the presented thermo-mechanic framework to strain gradient continua can be found in [25].

4.3.4 Balance Laws for Interfacial Morphogenetic Processes

Morphogenetic processes can occur at different scales, which are governed by the typical lengths characterizing the local interplay between mass production and the reaction- diffusion properties of biomolecules. For example, cells duplicate inside narrow regions created by the diffusion fronts of morphogenetic signals, whilst a macroscopic remodelling occurs in order to reach an homeostatic state at the tissue level [76]. It is therefore useful to extend the balance laws derived in the previous paragraphs to the case in which the bulk mass changes are localised into a small volume. For the sake of clarity, let us consider a biological system made by two different materials occupying growing adjacent regions $V^-(t)$ and $V^+(t)$, separated by the moving surface $\Sigma(t)$ with outer normal $\mathbf{n}_\Sigma$. Such surface will be considered as a non-material interface [27], i.e. carrying thermo-mechanical properties. It can be described by using a local parametrization expressing its spatial position as $\mathbf{x} = \mathbf{x}(u^1, u^2)$, with tangent bases $\mathbf{a}_l = \mathbf{x}_{,u^l}$ and $l = (1, 2)$. The parametric velocity $\bar{\mathbf{v}}_\Sigma$ of the surface can be decomposed as:

$$\bar{\mathbf{v}}_\Sigma = \bar{\mathbf{v}}_{\Sigma s} + \bar{v}_{\Sigma n}\,\mathbf{n}_\Sigma \tag{4.29}$$

where $\bar{\mathbf{v}}_{\Sigma s}$ is assumed to correspond to the projection of the physical velocity on the surface, whose value depends on the parametrization. Moreover, every point on $\Sigma(t)$ has a physical velocity $\mathbf{v}_\Sigma$, and we assume that the compatibility condition $v_{\Sigma s} = \bar{v}_{\Sigma s}$ holds. In the following the superscripts $-$ and $+$ will be used to indicate the physical fields inside the volumes having outer normal $\mathbf{n}^- = -\mathbf{n}^+ = \mathbf{n}_\Sigma$, respectively. The volumetric physical fields must obey the balance principles previously derived.

Morphogenetic processes occur in a very narrow layer of thickness ε, defined as:

$$\Delta V_\varepsilon = \bigcup (\mathbf{x} + \nu \mathbf{n}_\Sigma)\,;\ \forall\, \mathbf{x} \in \Sigma(t),\ -\varepsilon/2 \le \nu \le \varepsilon/2 \tag{4.30}$$

so that we can obtain surface fields on $\Sigma(t)$ by homogenization of the volume fields, calculating their finite limit for $\varepsilon \to 0$. Indicating with the subscript Σ such interfacial physical fields, we can therefore derive the mechanical balance laws and write the thermo-dynamic principles for the entire system. Dealing with a moving discontinuity, we define the Thomas derivative as $\frac{\delta_t(\cdot)}{\delta_t t} = \frac{\partial(\cdot)}{\partial t} + \bar{v}_{\Sigma n}\mathbf{n}_\Sigma.\nabla(\cdot)$, and we introduce the jump operator $[\![\cdot]\!] = (\cdot)^+ - (\cdot)^-$.

For matters of generality, we assume that generic mass fluxes $\mathbf{m}^-$ and $\mathbf{m}^+$ may exist between the volumes and the moving interface.[4] Therefore, by applying the transport and divergence theorems to a system with a non-material discontinuity [98], the surface mass balance takes the following form:

$$\frac{\delta_t \rho_\Sigma}{\delta_t t} + \operatorname{div}_\Sigma .(\rho_\Sigma \mathbf{v}_{\Sigma s}) - K\rho_\Sigma \bar{v}_{\Sigma n} = \rho_\Sigma \omega_\Sigma + [\![\rho(\bar{v}_{\Sigma n} - v_n) + \mathbf{n}_\Sigma.\mathbf{m}]\!] \tag{4.31}$$

where $\operatorname{div}_\Sigma \cdot$ is the surface divergence, K is twice the local mean curvature, v_n is the normal component of the physical velocity and ω_Σ is the surface mass source.

Using Eq. (4.31) and neglecting surface external forces, the balance of linear momentum on $\Sigma(t)$ reads:

$$\begin{aligned} \rho_\Sigma \frac{\delta_t \mathbf{v}_\Sigma}{\delta_t t} + (\rho_\Sigma \mathbf{v}_{\Sigma s}.\operatorname{grad}_\Sigma)\mathbf{v}_\Sigma = \operatorname{div}_\Sigma .\boldsymbol{\sigma}_\Sigma + \\ [\![(\mathbf{v} - \mathbf{v}_\Sigma)\,(\rho(\bar{v}_{\Sigma n} - v_n) + \mathbf{n}_\Sigma.\mathbf{m}) + \mathbf{n}_\Sigma.\boldsymbol{\sigma}]\!] \end{aligned} \tag{4.32}$$

where $\boldsymbol{\sigma}_\Sigma$ is the Cauchy stress tensor acting on the surface. We remark that Eq. (4.32) generalizes the Young-Laplace law for a growing non-material interface.

The balance of angular momentum on the surface reads:

$$\mathbf{a}^l.\boldsymbol{\sigma}_\Sigma \times \mathbf{a}_l = 0 \qquad l = (1, 2) \tag{4.33}$$

where $\times$ is the cross-product and $\mathbf{a}^l$ indicate the reciprocal tangent bases. Thus, $\boldsymbol{\sigma}_\Sigma$ must be a tangential field on $\Sigma(t)$ with symmetric surface components.

[4] We remark that for Galilean invariance they should be somehow dependent on a relative velocity field.

The first and second laws of thermodynamics after standard manipulations rewrite:

$$\rho_\Sigma \dot{\epsilon}_\Sigma = \mathbf{a}^l.\boldsymbol{\sigma}_\Sigma.\,\mathrm{grad}_\Sigma\,\mathbf{v}_\Sigma - \mathrm{div}_\circ\,.\,\mathbf{Q}_\Sigma + r_\Sigma + \left[\!\left[\mathbf{n}_\Sigma.\boldsymbol{\sigma}.(\mathbf{v}-\mathbf{v}_\Sigma) + \left(\frac{(\mathbf{v}-\mathbf{v}_\Sigma)^2}{2} + \epsilon - \epsilon_\Sigma\right)(\rho(\bar{v}_{\Sigma n} - v_n) + \mathbf{n}_\Sigma.\mathbf{m}) - \mathbf{n}_\Sigma.\mathbf{Q}\right]\!\right] \tag{4.34}$$

$$\rho_\Sigma \dot{\eta}_\Sigma \geq \frac{r_\Sigma}{\Theta} - \nabla.\left(\frac{\mathbf{Q}_\Sigma}{\Theta}\right) - \left[\!\left[\mathbf{n}_\Sigma.\left(\frac{\mathbf{Q}}{\Theta} + \bar{\mathbf{Q}}\right) - (\eta - \eta_\Sigma)\,(\rho(\bar{v}_{\Sigma n} - v_n) + \mathbf{n}_\Sigma.\mathbf{m})\right]\!\right] \tag{4.35}$$

where $\bar{\mathbf{Q}}$ represents a bulk extra-entropy flux, whose jump may represent the transfer of biochemical energy within the interface. Putting together Eqs. (4.34) and (4.35) and defining a surface free energy Ψ_Σ per unit mass, the dissipation inequality on the surface can be written as:

$$\rho_\Sigma \dot{\Psi}_\Sigma \leq \mathbf{a}^l.\boldsymbol{\sigma}_\Sigma.\mathbf{v}_{\Sigma,l} + \left[\!\left[\mathbf{n}_\Sigma.\boldsymbol{\sigma}.(\mathbf{v}-\mathbf{v}_\Sigma) - \Theta\mathbf{n}_\Sigma.\bar{\mathbf{Q}} + \left(\tfrac{(\mathbf{v}-\mathbf{v}_\Sigma)^2}{2} + \Psi - \Psi_\Sigma\right)(\rho(\bar{v}_{\Sigma n} - v_n) + \mathbf{n}_\Sigma.\mathbf{m})\right]\!\right] \tag{4.36}$$

where we have assumed isothermal, uniform conditions for simplicity of notation. In particular the term between the bracket operator represents the flux of the chemo-mechanical energy flux vector, i.e. a generalization of the Poynting vector for the moving non-material interface. In summary, once defined the constitutive equation for the surface stress, the dissipation inequality in Eq. (4.36) allows defining thermodynamically consistent evolution laws for the interfacial morphogenesis.

An Application: Morphogenesis of Seashells Let us consider the proposed thermo-mechanical model of interfacial growth to describe the morphogenesis of seashells [26]. As accurately investigated by D'Arcy Thompson [111], seashells also display a great variety of shapes and patterns, often characterized by a self-similar geometric structure, following a logarithmic (equiangular) helico-spiral.

The growing shell is generated by a tongue-like protrusion of the mollusc, known as the mantle, which wraps around the grown shell edge for depositing both new material and pigments. The surface growth process here occurs at a moving surface $\Sigma(t)$ at the edge of the shells, and the secretion velocity is found to be controlled by the neural system of the mantle [12]. Indeed, the position $\rho(\theta)=\sqrt{x^2+y^2+z^2}$ of the mantle can be expressed in a logarithmic helico-spiral as a function of the turning angle θ, reading:

$$\begin{cases} x = \rho_0 sin\beta\ cos\theta\ e^{\theta cot\alpha} \\ y = \rho_0 sin\beta\ sin\theta\ e^{\theta cot\alpha} \\ z = \rho_0 cos\beta\ e^{\theta cot\alpha} \end{cases} \tag{4.37}$$

where β is the enlarging angle and α the wrapping (equiangular) angle of the spiral, as shown in Fig. 4.4a. In practice, if $R = \sqrt{x^2 + y^2}$, the components of the mantle velocity are linked by the following relation: $\dot{z}\, tan\beta = \dot{R}$.

Considering a moving reference framework whose origin represents the mantle position, the deposition of new material occurs on a generating curve on the moving surface $\Sigma(t)$, with unit vectors $\mathbf{e}_z$ and $\mathbf{e}_\rho = \mathbf{e}_x cos\theta + \mathbf{e}_y sin\theta$. The volumetric mass balance equation in Eq. (4.12) for the shell imposes:

$$\rho^- \operatorname{div} \mathbf{v}^- = 0 \tag{4.38}$$

where ρ^- is the constant volume density of the fabricated material. Choosing a generating circular section for the sake of simplicity, its outer radius $r(\theta)$ can be given on a polar parametric representation (r, s) on $\Sigma(t)$. If the mantle deposit a surface mass source γ_Σ, a solution of the surface mass balance in Eq. (4.38) is given by:

$$\mathbf{m}^- = [\rho^-(\mathbf{v}^- - \bar{\mathbf{v}}_\Sigma)\cdot \mathbf{e}_n]\mathbf{e}_n; \qquad \operatorname{div}_\Sigma . \bar{\mathbf{v}}_{\Sigma s} = \gamma_\Sigma \quad \Rightarrow \quad r(t) = r(0) e^{\frac{\gamma_\Sigma t}{2}} \tag{4.39}$$

with $\mathbf{e}_n = \mathbf{e}_z \wedge \mathbf{e}_\rho$ being the normal unit vector of the growing surface, setting $\bar{v}_{\Sigma n} = (\bar{\mathbf{v}}_\Sigma \cdot \mathbf{e}_n) = \rho(\theta)\dot{\theta}$ in virtue of Eq. (4.37). Moreover, the parametrization is chosen such that the $\Sigma(t)$ moves with the center of mass of the growing mass, i.e. $\bar{v}_{\Sigma n} = v_{\Sigma n}$. Under these assumptions, Eq. (4.36) ensures that the seashell growth is thermodynamically consistent.

The shell morphology depends on the combination of the helico-spiral movement of the mantle, through the angles α, β in Eq. (4.37), and the displacement of the edge radius, given by the surface mass source γ_Σ in Eq. (4.39). Assuming that the spiral velocity of the mantle is constant, so that $\dot{\theta} = m$, we can impose that the growing material is always deposited tangentially to the shell, reading:

$$\begin{aligned} \rho(\theta + 2\pi) - \rho(\theta) &= r\left(\frac{\theta + 2\pi}{m}\right) + r\left(\frac{\theta}{m}\right); \\ \rho_0\, e^{\theta cot\alpha}\left(e^{2\pi cot\alpha} - 1\right) &= r(0) e^{\frac{\gamma_\Sigma \theta}{2k}}\left(e^{\frac{\gamma_\Sigma \pi}{m}} + 1\right) \end{aligned} \tag{4.40}$$

The proposed model is applied to describe the shape of *Turritella communis*, a marine gastropod of the family of the Turritellidae, depicted in Fig. 4.4b. Its coiling edge remains tangent to the z axis, so that $\rho(\theta) = r(\theta/k) sin\beta$.

This geometrical property, used in combination with Eq. (4.40), allows a correlation between the movement of the mantle and its mass supply, being:

$$2\pi \cot\alpha = \log\left(\frac{1 + \sin\beta}{1 - \sin\beta}\right); \qquad \gamma_\Sigma = 2k \cot\alpha \tag{4.41}$$

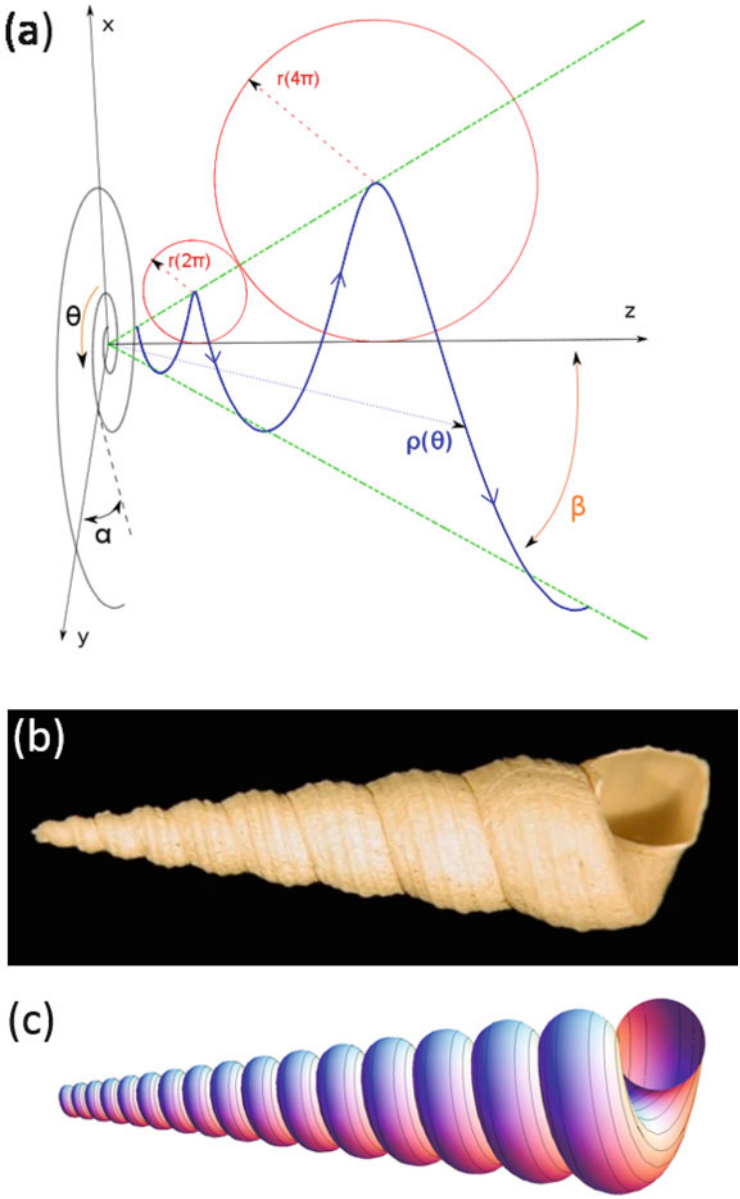

Fig. 4.4 (**a**) Parametric description of the growing seashell: the generating line is given by the mantle position $\rho(\theta)$ along a helico-spiral (*blue line*), while new material is deposited on a circular border with radius $r(\theta)$ (*red circles*). (**b**) Picture of the seashell *turritella communis* (**b**) and its simulated morphology (**c**). The simulation is performed using Eqs. (4.38)–(4.41), setting the values $\mathbf{v}^- = 0, \beta = 4^o, \alpha = \cot^{-1}\left(log\left(\frac{1+sin\beta}{1-sin\beta}\right)/2\pi\right) = 87.72^o, m = 1, \gamma = 2mcot\alpha = 0.044$

The resulting simulated morphology is depicted in Fig. 4.4c, demonstrating that the neural system of the gastropod is somehow able to regulate mass production with respect to the coiling angle.

4.4 Free-Boundary Morphogenesis for Fluid-Like Living Matter

In the previous section, we have introduced a general chemo-mechanical theory of morphogenesis, which requires the specification of the constitutive equations describing the biorheological properties of living matter, possibly spanning from viscous fluids to soft solids. Let us first discuss a simple free-boundary morphogenetic problem for a fluid-like biological system as in [18]. In particular, we will consider the chemotactic expansion of an aggregate of living cells, which will be modelled as an incompressible newtonian fluid, such that:

$$\boldsymbol{\sigma} = -p\mathbf{I} + \eta\mathbf{d} \tag{4.42}$$

where p is an hydrostatic pressure and η is the fluid viscosity.

From Eq. (4.15), the motion is governed by the Navier-Stokes equations:

$$\rho\frac{d\mathbf{v}}{dt} = \rho\mathbf{b}_v - \operatorname{grad} p + \eta\nabla^2\mathbf{v} \tag{4.43}$$

where ∇^2 is the spatial laplacian operator, and ρ is the constant spatial density of the cell, which is almost equal to the one of water.

4.4.1 Definition of the Chemotactic Model in a Hele Shaw Cell

We consider an aggregate of living cells occupying the domain $x \leq x_b$, where x_b is the rectilinear border, of an Hele Shaw cell, i.e. confined between two parallel flat plates separated by an small gap of length ℓ. The cells are bounded by an inviscid fluid which occupies the domain $x > x_b$, as sketched in Fig. 4.5a. Let $z = 0$ be the plane in between the plates and $\ell << L$, where L is the characteristic macroscopic size of the morphogenetic pattern that we aim to observe. Accordingly, the component of the velocity in z is much smaller than the two others, which are also governed by the following scaling [54]:

$$\frac{\partial^2 v_i}{\partial x^2} << \frac{\partial^2 v_i}{\partial z^2} \tag{4.44}$$

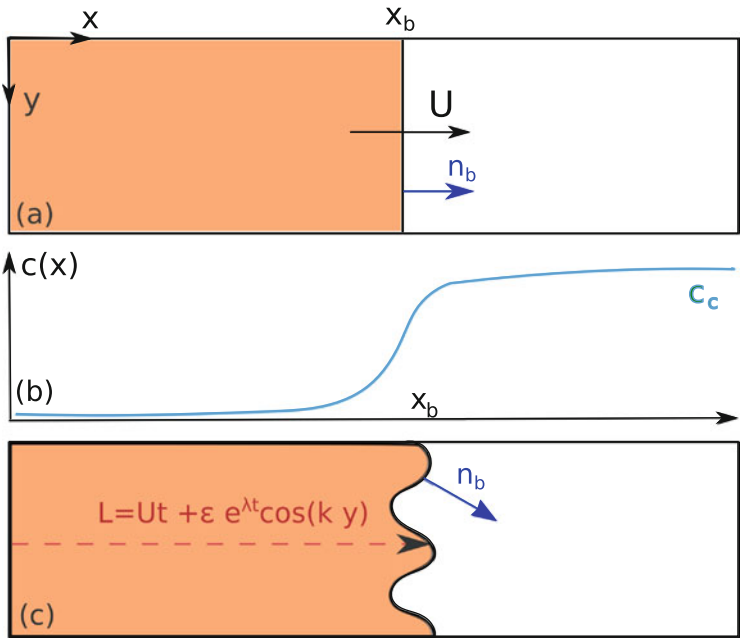

Fig. 4.5 Schematics of the Hele Shaw cell containing a living material (*orange*) expanding with a rectilinear free border at $x = x_b$ (**a**). Distribution of the morphogen concentration n (*green line*) inside the cell (**b**). Perturbation of the rectilinear border with wavenumber k and growth rate λ (**c**)

where the subscript $i = (x, y)$ indicates the component of the velocity. Since the typical duplication time of cells is about a day and the fluid is highly viscous, the corresponding flow occurs at a low Reynolds number, so that the terms $\eta\nabla^2\mathbf{v}$ dominate with respect to convective and gravitational effects. Therefore Eq. (4.43) simplifies in virtue of Eq. (4.44) as:

$$\operatorname{grad} p = \eta \frac{\partial^2 v_i}{\partial z^2} \tag{4.45}$$

We assume that the necessary symmetry and boundary conditions at the plates hold. We can therefore assume that:

$$v_i(x, y, z; t) = v_i(x, y, 0; t)\left(1 - \frac{4z^2}{\ell^2}\right) \qquad i = (x, y) \tag{4.46}$$

so that Eq. (4.45) reduces to a classical Darcy equation for the planar velocity $\mathbf{v} = \mathbf{v}(x, y, 0, ; t)$, being:

$$\mathbf{v} = \frac{\ell^2}{8\eta} \operatorname{grad} p = K_p \operatorname{grad} p \tag{4.47}$$

where all fields and operators are planar. The parameter $K_p = \ell^2/(8\eta)$ is the equivalent of the porosity coefficient, and represents here the friction forces resulting from the shallow geometry. It is therefore possible to solve the problem using a fully two-dimensional model.

We assume that the cell proliferation if driven by a morphogenetic signal diffusing inside the Hele-Shaw cell, and possessing an infinite reservoir at $x \to \infty$, which is independent on the local dynamics (Fig. 4.5b). The cells possess specific surface receptors which capture the morphogen at a typical uptake rate γ_c. Accordingly, the concentration $c = c(x, y; t)$ of the morphogen is governed by the following reaction-diffusion equations inside the Hele-Shaw cell:

$$\dot{c} = \begin{cases} D_c \nabla^2 c - \gamma_c c & \text{if} \quad x \leq x_b \\ D_c \nabla^2 c & \text{if} \quad x > x_b \end{cases} \tag{4.48}$$

where D_c is the diffusion coefficient inside the cell.

The living cells respond to a gradient of the morphogen concentration by generating a mass flux $\mathbf{m}$. In particular, we assume the classical Keller-Siegel constitutive equation [71], being:

$$\mathbf{m} = K_c \operatorname{grad} c \tag{4.49}$$

where K_c is a positive definite mobility parameter. Although possibly dependent on c for representing a degenerate mobility in different classes of biochemical reactions, for the sake of simplicity we assume K_c to be a constant. From Eq. (4.12), the balance of mass within the expanding cellular domain is given by:

$$\frac{d\rho}{dt} = \operatorname{div}\mathbf{m} - \rho \operatorname{div}\mathbf{v} = 0 \tag{4.50}$$

which vanishes in virtue of the incompressibility of the living cells. In Eq. (4.50) we considered that the morphogenesis only resides on mass diffusion, neglecting the presence of volumetric sources of mass.

Substituting Eqs. (4.47) and (4.49) in Eq. (4.50), the equation of motion reads:

$$K_p \rho \nabla^2 p - K_c \nabla^2 c = 0 \tag{4.51}$$

Thus, the Eqs. (4.48) and (4.51) govern the morphogenesis of the free boundary domain in this model. The mathematical model is complemented by four boundary conditions at the free border. First, the Young-Laplace equation imposes the mechanical equilibrium at the interface, being:

$$p = p_0 - \sigma C \qquad at \quad x = x_b \tag{4.52}$$

where C is the local curvature (initially equal to zero for a planar front), σ is the surface tension and p_0 is the constant outer pressure of the inviscid fluid. Second, for compatibility we must impose the continuity of the normal velocity at the interface:

$$\frac{d\mathbf{x}_b}{dt} \cdot \mathbf{n}_b = \mathbf{v}(x_b) \cdot \mathbf{n}_b \qquad at \quad x = x_b \tag{4.53}$$

where $\mathbf{n}_b$ is the outward unit vector at the free surface. Finally, two conditions must be imposed for c and its normal gradient at the interface:

$$c(x_b^-) = c(x_b^+); \qquad \text{grad}\, c(x_b^-) \cdot \mathbf{n}_b = \text{grad}\, c(x_b^+) \cdot \mathbf{n}_b \tag{4.54}$$

Eq. (4.54) enforces the continuity of the morphogen concentration and of the chemical flux across the free boundary, given the absence of any interfacial phenomenon.

4.4.2 Dimensionless Form of the Governing Equations

The governing equations can be recast in a dimensionless form using the following values:

$$t_c = \gamma_n^{-1}; \qquad L_c = \sqrt{\frac{D_c}{\gamma_c}}; \qquad v_c = \sqrt{D_c \gamma_c}; \tag{4.55}$$

$$p_c = \frac{D_c}{K_p}; \qquad c_c = c(x \to \infty)$$

where t_c, L_c, v_c, p_c, c_c are characteristic time, length, velocity, pressure, and chemical concentration, respectively. Defining dimensionless variables with respect to such characteristic values to obtain, we can rewrite the Eqs. (4.48), (4.15) and (4.51) in their dimensionless form as follows:

$$\dot{\bar{c}} = \begin{cases} \bar{\nabla}^2 \bar{c} - \bar{c} & if \quad \bar{x} \le \bar{x}_b \\ \bar{\nabla}^2 \bar{c} & if \quad \bar{x} > \bar{x}_b \end{cases} \tag{4.56}$$

$$\bar{\mathbf{v}} = -\bar{\text{grad}}\bar{p} \tag{4.57}$$

$$\bar{\nabla}^2 \bar{\text{p}} = -\bar{\nabla}^2 \bar{c}; \quad \text{with} \qquad \text{G} = \frac{\text{K}_\text{c}\text{c}_\text{c}}{\rho \text{D}_\text{n}} \tag{4.58}$$

where the bar indicates dimensionless variables. Interestingly, the only resulting dimensionless parameter is G in Eq. (4.58), which represents a ratio between morphogen-driven mass production and the mass evacuation rate driven by viscous

effects. Furthermore, the boundary conditions given by Eqs. (4.52)–(4.54) rewrite as:

$$\bar{p} = \bar{p}_0 - \bar{\sigma}\bar{C}; \quad \text{with} \quad \bar{\sigma} = \frac{\sigma K_p}{D_n}\sqrt{\frac{\gamma_n}{D_n}} = \frac{\sigma \ell^2}{8\eta v_c L_c^2} \quad at \quad \bar{x} = \bar{x}_b \tag{4.59}$$

$$\frac{d\bar{\mathbf{x}}_b}{d\bar{t}} \cdot \mathbf{n}_b = \bar{\mathbf{v}}(x_b) \cdot \mathbf{n}_b \tag{4.60}$$

$$\bar{c}(\bar{x}_b^-) = \bar{c}(\bar{x}_b^+); \qquad \bar{\nabla}\bar{c}(\bar{x}_b^-) \cdot \mathbf{c}_b = \bar{\nabla}\bar{c}(\bar{x}_b^+) \cdot \mathbf{n}_b \tag{4.61}$$

In accordance with the Buckingham Π theorem [13], the mathematical model given by Eqs. (4.56)–(4.61) is entirely governed by the dimensionless parameters G and $\bar{\sigma}$ defined in Eqs. (4.58) and (4.59), which will control the evolution of the biological system during morphogenesis. In physical terms, $\bar{\sigma}$ represents the ratio between the surface tension and the viscous forces.

For simplicity of notation, we'll drop the bars in the following analysis.

4.4.3 Traveling Wave Solution

Equations (4.56)–(4.61) allow the existence of a traveling wave solution of the problem. Thus, we hypothesize that the front moves with a constant dimensionless velocity U going from left to right, i.e. assuming a positive chemotaxis driving towards the highest concentration of the morphogen. Considering a dimensionless variable $\zeta = (x - U\,t)$, we can solve the reaction-diffusion dynamics in Eqs. (4.56) and (4.61), deriving the following morphogen concentration:

$$c_0(\zeta) = \begin{cases} c_0(0) \cdot e^{\frac{-U+\sqrt{U^2+4}}{2}\zeta} & if \quad \zeta \leq 0 \\ 1 + (c_0(0) - 1) \cdot e^{-U\zeta} & if \quad \zeta > 0 \end{cases} \tag{4.62}$$

where $c(-\infty) = 0$, $c(\infty) = 1$ and $c_0(0) = \frac{2U}{U+\sqrt{U^2+4}}$ is the morphogen concentration at the rectilinear front. We remark that c_0 must be positive definite, so that the boundary expands with $U > 0$. Imposing in Eqs. (4.58) and (4.59) that $p_0(0) = p_0$ and that $p(-\infty)$ must be bounded, the traveling wave for the pressure field reads:

$$p_0(\zeta) = -G(c_0(\zeta) - c_0(0)) + p_0 \qquad if \quad \zeta \leq 0 \tag{4.63}$$

Finally, the Dirichlet condition at the free boundary in Eq. (4.60) gives the velocity of the traveling wave as:

$$U = \frac{G-1}{\sqrt{G}} \tag{4.64}$$

revealing that a traveling wave solution can appear if and only if $G > 1$, i.e. if the chemotactic growth production is faster than diffusion-driven mass evacuation.

4.4.4 Linear Stability Analysis

Let us now study the stability of the traveling wave solution given by Eqs. (4.62) and (4.63), in order to investigate the existence of a morphological transition during the morphogenetic process. For this purpose, we impose a perturbation $\zeta(0)$ at the free boundary, whose dimensionless expression in the moving frame is given by :

$$\zeta(0) = x_b - Ut = \epsilon \cdot e^{\lambda t} cos(\kappa y) \tag{4.65}$$

where κ is the spatial wavenumber and λ is its time growth rate, as depicted in Fig. 4.5c and $\epsilon \ll 1$ is a small parameter.

We write p and c as a series expansion around the traveling wave solution in the moving frame, as follows:

$$p(x, y; t) = p_0(\zeta) + \epsilon \cdot p_1(\zeta) e^{\lambda t} cos(\kappa y) \tag{4.66}$$

$$c(x, y; t) = c_0(\zeta) + \epsilon \cdot c_1(\zeta) e^{\lambda t} cos(\kappa y) \tag{4.67}$$

where $p_0(Z), c_0(Z)$ are the known traveling wave solutions.

The solution for $c_1(\zeta)$ can be found from Eq. (4.56), imposing the continuity of the chemical concentration and its flux across the boundary:

$$c_1(\zeta) = \begin{cases} c_1(0) \cdot e^{\frac{-U+\sqrt{U^2+4(1+\lambda+\kappa^2)}}{2}\zeta} & if \quad \zeta \leq 0 \\ c_1(0) \cdot e^{\frac{-U-\sqrt{U^2+4(\lambda+\kappa^2)}}{2}\zeta} & if \quad \zeta > 0 \end{cases} \tag{4.68}$$

where:

$$c_1(0) = -\frac{4U \cdot (U + \sqrt{U^2+4})^{-1}}{\sqrt{U^2+4(1+\lambda+\kappa^2)} + \sqrt{U^2+4(\lambda+\kappa^2)}} \tag{4.69}$$

Substituting the solution for $c_1(\zeta)$ in Eq. (4.58), we derive the leading order governing equation for the perturbed pressure field, being:

$$p_1''(\zeta) - \kappa^2 p_1(\zeta) + \\ + Bc_1(0) \cdot \left[\left(\frac{-U + \sqrt{U^2 + 4(1+\lambda+\kappa^2)}}{2} \right)^2 - \kappa^2 \right] e^{\frac{-U+\sqrt{U^2+4(1+\lambda+\kappa^2)}}{2}\zeta} = 0 \tag{4.70}$$

which is valid for $\zeta \leq 0$.

The prime denotes derivative on ζ. Eq. (4.70) has the following general solution:

$$p_1(\zeta) = -Gc_1(0) e^{\frac{-U+\sqrt{U^2+4(1+\lambda+\kappa^2)}}{2}\zeta} + A \cdot e^{\kappa\zeta} \tag{4.71}$$

The constant A in Eq. (4.71) can be fixed imposing the boundary solution in Eq. (4.59). Recalling that the curvature can be written as:

$$C = \frac{\partial^2 \zeta(0)/\partial y^2}{\left[1 + (\partial \zeta(0)/\partial y)^2\right]^{3/2}}, \tag{4.72}$$

we find that :

$$p_1(\epsilon \cdot e^{\lambda t} cos(\kappa y)) = p_0(0) + (p_0'(0) + p_1(0))\epsilon \cdot e^{\lambda t} = p_o + \bar{\sigma}\kappa^2 \epsilon \cdot e^{\lambda t} cos(\kappa y) \tag{4.73}$$

giving at the leading order:

$$A = \bar{\sigma}\kappa^2 + G[c_1(0) + c_0'(0)] = \bar{\sigma}\kappa^2 + U + Gc_1(0) \tag{4.74}$$

Finally, the boundary condition in Eq. (4.60) allows to derive the dispersion equation for the perturbed mode. Accordingly, we find that:

$$-p_0''(0) - p_1'(0) = \lambda \tag{4.75}$$

which can be simplified as:

$$\lambda = -\bar{\sigma}\kappa^3 - \kappa U + G\left[c_0''(0) + c_1(0) \left(-\kappa + \frac{-U + \sqrt{U^2 + 4(1+\lambda+\kappa^2)}}{2} \right) \right] \tag{4.76}$$

Substituting Eqs. (4.64) and (4.69) in Eq. (4.76), we can write an implicit dispersion equation uniquely as a function of the two dimensionless parameters $G, \bar{\sigma}$ of the problem, reading:

$$\lambda = -\bar{\sigma}\kappa^3 - \kappa\frac{G-1}{\sqrt{G}} + \frac{G-1}{G} - \frac{(G-1)\cdot\left(-2\kappa - \frac{G-1}{\sqrt{G}} + \sqrt{\frac{(G+1)^2}{G} + 4(\lambda+\kappa^2)}\right)}{\sqrt{\frac{(G-1)^2}{G} + 4(\lambda+\kappa^2)} + \sqrt{\frac{(G+1)^2}{G} + 4(\lambda+\kappa^2)}} \tag{4.77}$$

Since Eq. (4.77) involves the dimensionless growth mode λ and wavenumber κ in an implicit way, we solved it numerically. The resulting curves are depicted in Figs. 4.6 and 4.7 for different values of G and $\bar{\sigma}$. Even if both the surface tension and the boundary velocity have a stabilizing effect at small wavelengths, the rectilinear front is always unstable at large wavelengths, having a maximum value λ_{max} of the time growth rate. Although the a nonlinear stability analysis would be required for investigating the pattern dynamics, we expect the emergence of undulated structures with a typical length of about $2\pi/\kappa(\lambda_{max}) \cdot \sqrt{D_n/\gamma_n}$.

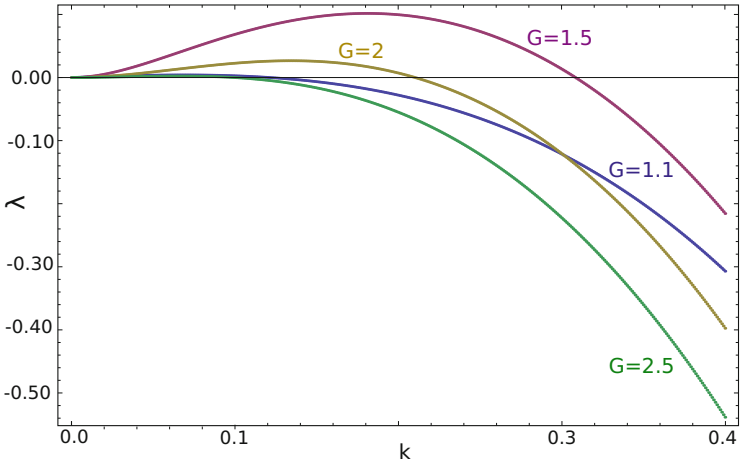

Fig. 4.6 Dispersion diagrams shown at different values of the dimensionless parameter $G = \frac{K_m K_\psi n_c}{\rho D_n}$. The curves have been numerically obtained using the Newton algorithm, setting σ=0.5

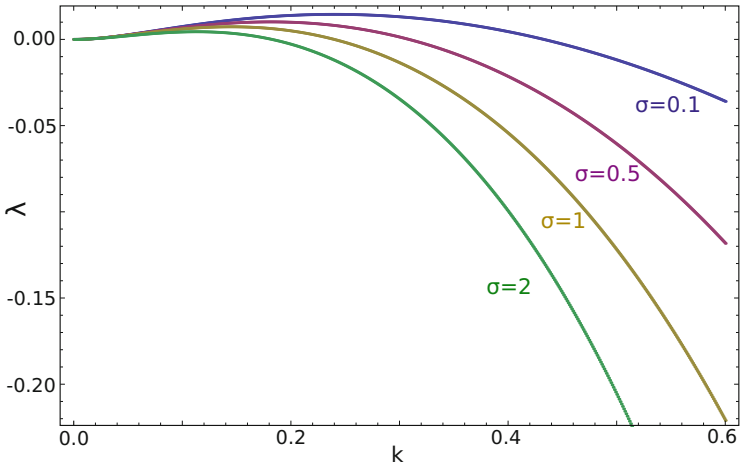

Fig. 4.7 Dispersion diagrams shown at different values of the dimensionless parameter $\bar{\sigma} = \frac{\sigma K_p}{D_n}\sqrt{\frac{\gamma_n}{D_n}}$. The curves have been numerically obtained using the Newton algorithm, setting G=1.5

4.4.5 Pattern Formation in the Nonlinear Regime

The dispersion diagrams resulting from the linear stability analysis highlighted that the rectilinear border is always unstable at large wavelengths. The dispersion curves are qualitatively similar to the one encountered in other hydrodynamic problems, such as the Saffmann-Taylor [100] or the Mullins-Sekerka [88] instabilities. Similarly, we expect that the moving front will rapidly develop growing undulations, whose shape will be fixed by fully nonlinear effects. In the following we numerically investigate the nonlinear pattern formation for the proposed model in order to describe some experimental results on epithelial cells [93].

The results show the formation of fingering instabilities in expanding free rectilinear surfaces of cellular monolayers. In order to provide a computational solution, we implemented the problem into a finite element code [49]. Equations (4.56) and (4.58) have been solved on a triangular grid, fitting at every iteration the moving interface. Briefly, given the concentration of nutrients at time t_m, the pressure p_m is first computed, through Eq. (4.58) and then the velocity field, using the Darcy's law. Thus, the boundary can be explicitly moved and Eq. (4.56) can be solved for the concentration at time t_{m+1}, using an implicit-Euler scheme. In order to guarantee the robustness of the semi-implicit algorithm, at every iteration the time step $\Delta t = (t_{m+1} - t_m)$ is set equal to the ratio between the minimum mesh size and the modulus of the maximum boundary velocity at the m^{th} iteration. Finally, a spatial discretization with finite element is performed using continuous piecewise quadratic $P2$ Lagrangian elements. Since the mesh size affects the minimum observable unstable wavelength, we adaptively refined the mesh in order to control the number of elements on the contour at every time step.

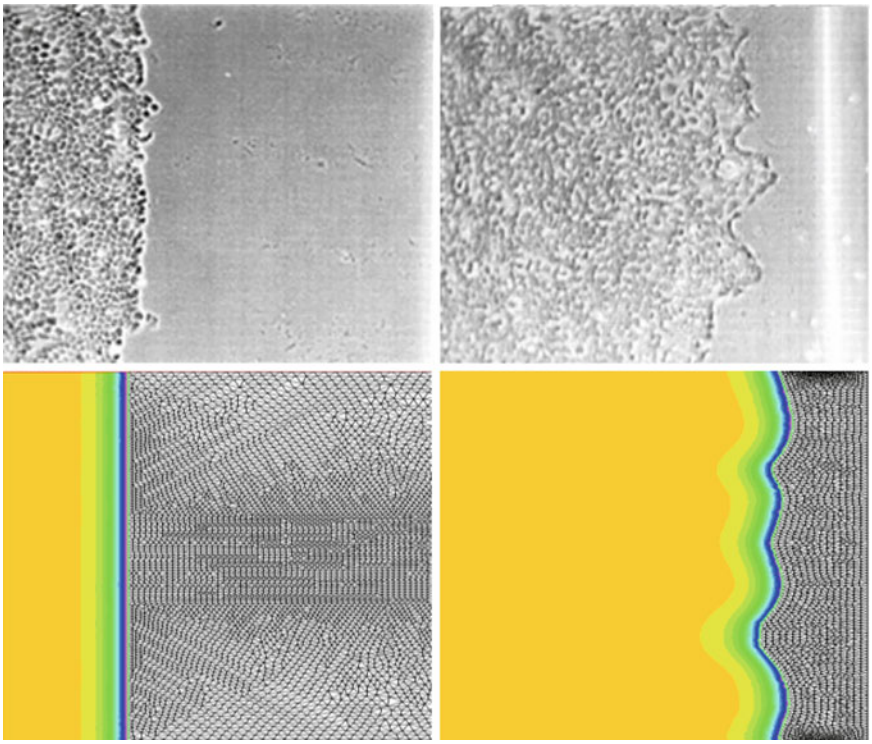

Fig. 4.8 (**a**) Wound healing experiment showing the propagation over 24 h of a monolayer of tumour cells. Adapted from [107]. (**b**) Fully nonlinear numerical simulation of the proposed free-boundary morphogenetic model

Simulation results are shown in Fig. 4.8 together with some pictures of a wound healing experiment showing the propagation over 24 h of a monolayer of tumour cells. The qualitative agreement of the emerging morphology highlights the importance of chemo-mechanical cues on the dynamics of the wound healing processes, whose effectiveness is known depend on the coupling between the motility and the cell proliferation rate [81].

4.5 Growth, Remodelling and Morphogenesis for Soft Elastic Matter

The proposed morphogenetic theory should be refined to account for further important issues arising when dealing with solid living matter. Firstly, biological tissues undergo *large deformations*. Therefore, the undeformed and deformed configurations are not necessarily close, so that the classical infinitesimal elastic

theory cannot be used. Secondly, soft biological matter exhibits *residual stresses*, i.e. a self-equilibrated distribution of internal stresses persists in the tissue when all external loads have been removed. Indeed, as discussed in the previous sections, living materials have the striking ability to change actively their micro-structure for adjusting to the surrounding media, developing a state of internal tension aimed at optimizing their structural behavior. Residual stresses in living materials, closely resembling the ones originated by misfits within inert matter [3], are almost ubiquitous in Nature. Their magnitude has been measured in several tissues (e.g. arteries [17], airways [57], hearth [123], gastro-intestinal tissues [53]), using simple cutting experiments. In arteries, for instance, they can be inferred by measuring the opening angle of an excised tissue ring after a radial cut. Thirdly, residual stress may accumulate in the tissue during a morphogentic process, possibly triggering an elastic instability beyond a critical value. Accordingly, they can orchestrate a morphological transition even in the absence of either external loads or geometrical constraints. Lastly, soft tissues exhibit a *nonlinear elastic behavior* which should be taken into account when making constitutive assumptions.

In the following, we will extend the proposed chemo-mechanical theory of open systems in view of these key considerations.

4.5.1 An Interpretation of Morphogenesis in Solids Using the Theory of Configurational Forces

The theory of configurational forces allows to provide a straightforward interpretation of the driving forces acting during the morphogenetic processes in living matter [82]. For a soft elastic solid, we can postulate the existence of an Helmholtz free energy Ψ having the following functional form:

$$\Psi = \Psi(\mathbf{F}, c_i, \Theta; \mathbf{X}, t) \tag{4.78}$$

where the explicit dependence on $\mathbf{X}$ and t may represent growth and ageing phenomena, respectively. Applying the chain rule for the differentiation of Ψ in in Eq. (4.28), we obtain the following set of constitutive equations [30] :

$$\mathbf{S} = \rho_0 \frac{\partial \Psi}{\partial \mathbf{F}}; \qquad \Psi_i = \rho_0 \frac{\partial \Psi}{\partial c_i}; \qquad \eta = -\frac{\partial \Psi}{\partial \Theta} \tag{4.79}$$

Accordingly, the reduced Clausius-Duhem inequality rewrites:

$$\mathbf{J}_{ci} \cdot (\mathrm{Grad}\, \Psi_i + \eta_i \,\mathrm{Grad}\, \Theta) - \rho_0 \frac{\partial \Psi}{\partial t}|_{expl} - \frac{\mathbf{Q}}{\Theta} \cdot \mathrm{Grad}\, \Theta \geq 0 \tag{4.80}$$

where the explicit derivative over time accounts for the possible dissipation during ageing phenomena [84].

According to the theory of configurational forces, the canonical projection of the balance of the linear momentum in the material setting allows to account for the momentum associated to all the degrees of freedom of the deformation field, whilst the balance of **p** involves only the translational momentum [86]. This is of fundamental importance for morphogenetic processes, which are characterized by the presence of inhomogeneities in the material set.

Let $\mathbf{V} = \frac{\partial \mathbf{X}}{\partial t}|_x = -\mathbf{F}^{-1}\mathbf{v}$ be the inverse motion velocity, i.e. the material velocity field, we can define a pseudomomentum density or canonical momentum density as follows:

$$\mathbf{P}_m = \frac{\partial K}{\partial \mathbf{V}} = \rho_0 \mathbf{F}^T \mathbf{F}\mathbf{V} = -\mathbf{F}^T \mathbf{p} = -\mathbf{p}\mathbf{F} \tag{4.81}$$

where $K = 1/2\rho_0 \mathbf{v}^2$ is the kinetic energy. Let us now perform a right-multiplication of Eq. (4.17) times **F**, as follows:

$$\frac{d}{dt}(\rho_0 \mathbf{v})\mathbf{F} = -\frac{d\mathbf{P}_m}{dt} - \rho_0 \mathbf{v}\dot{\mathbf{F}} = \mathbf{b}_v \mathbf{F} - \frac{\Omega}{\rho_0}\mathbf{P}_m + (\mathrm{Div}\,\mathbf{S})\mathbf{F} \tag{4.82}$$

Using the constitutive assumptions in Eq. (4.142), let us recall the useful identities:

$$(\mathrm{Div}\,\mathbf{S})\,.\mathbf{F} = \mathrm{Div}(\mathbf{S}\mathbf{F}) - tr(\mathbf{S}\,\mathrm{Grad}\mathbf{F}) \tag{4.83}$$

$$tr(\mathbf{S}\,\mathrm{Grad}\mathbf{F}) = \mathrm{Div}(\rho_0 \Psi \mathbf{I}) - \frac{\partial(\rho_0 \Psi)}{\partial \mathbf{X}}|_{expl} - \mu_i\,\mathrm{Grad}c_i + \eta\,\mathrm{Grad}\Theta \tag{4.84}$$

$$\rho_0 \mathbf{v}\dot{\mathbf{F}} = \mathrm{Grad}\,K - \frac{1}{2}\mathbf{v}^2(\mathrm{Grad}\,\rho_0) \tag{4.85}$$

By substituting Eqs. (4.13) (4.83)–(4.85) in Eq. (4.82), we find the the canonical balance of pseudomomentum density in the material framework:

$$\frac{d\mathbf{P}_m}{dt} = \mathbf{f}^{ext} + \mathbf{f}^g + \mathbf{f}^{inh} + \mathbf{f}^c + \mathbf{f}^{\Theta} + \mathrm{Div}\,\mathbf{b} \tag{4.86}$$

Equation (4.86) states that there are five sources of material inhomogeneities: the convection of the body forces in $\mathbf{f}^{ext}$, the mass growth in $\mathbf{f}^g$, the true material inhomogeneities in $\mathbf{f}^{inh}$, the internal variables in $\mathbf{f}^c$, and the temperature in $\mathbf{f}^{\Theta}$. They are defined as:

$$\begin{cases} \mathbf{f}^{ext} = -\mathbf{b}_v \mathbf{F} \\ \mathbf{f}^g = \frac{\dot{\rho}_0}{\rho_0}\mathbf{P}_m \\ \mathbf{f}^{inh} = \frac{\partial(K-\rho_0\Psi)}{\partial \mathbf{X}}|_{expl} \\ \mathbf{f}^c = -\mu_i \mathrm{Grad}c_i \\ \mathbf{f}^{\Theta} = \rho_0 \eta \mathrm{Grad}\Theta \end{cases} \tag{4.87}$$

Moreover, we find the stress measure that drives the evolution of material inhomogeneities is the Eshelby tensor **b**, defined as:

$$\mathbf{b} = -[(K - \rho_0 \Psi)\mathbf{I} + \mathbf{SF}] \tag{4.88}$$

This stress measure is a fundamental importance since it governs the configurational changes during morphogenesis, as it will be highlighted in the following. Finally, we recall that the frame indifference of the Helmholtz free energy in Eq. (4.79) with respect of arbitrary rotations of the actual configuration allows to derive the conservation of the angular momentum.

4.5.2 Mathematical Theory of Volumetric Growth in Soft Solids

At the beginning of the 1980s, Skalak and coworkers proposed the first kinematic descriptions of finite volumetric and surface growth [102, 103] in a continuum mechanics framework. They introduced the idea that growth can induce geometric incompatibilities in the microstructure, which would provoke the transition from an unloaded stress-free configuration to a pre-stressed reference configuration. Conversely, no internal stresses arise in the tissue if the growth strains are *compatible*, i.e. do not induce material distortions.

The seminal work of Skalak opened the door to a number of experimental studies which aimed at characterizing the residual stress distribution in biological tissues. From a modeling viewpoint, much work has been done by Anne Hoger and coworkers [62–65, 70] to define a hyperelastic constitutive theory of soft materials with residual stresses. In particular, a multiplicative decomposition has been proposed for dealing with volumetric growth in living materials [97, 104]. The mechanical approach based on a multiplicative decomposition was first introduced in the theory of elasto-plasticity by Kröner [74] and Lee [78] in order to split the inelastic and the elastic components and it has been widely employed in continuum mechanics models.

According to this mathematical theory, the mapping $\boldsymbol{\chi}$ introduced in Eq. (4.1) can be split into two components. The first is associated to the a change of the unstressed state of the material and it transforms the tissue from its initial stress free configuration $\mathscr{B}_0$ into a new stress-free grown (remodeled) state, denoted as $\mathscr{B}_g$ in Fig. 4.9. In mathematical terms, the deformation gradient **F** defined in Eq. (4.2) can be split into two components, as follows:

$$\mathbf{F} = \mathbf{F}_e \mathbf{F}_g \tag{4.89}$$

where $\mathbf{F}_g$ represents the volumetric growth (remodeling) tensor and $\mathbf{F}_e$ is the elastic tensor. We remark that the intermediate state is not necessarily a configuration that could be physically observable for the material. Indeed, this grown or remodeled state $\mathscr{B}_g$ can be seen as the collection of local states obtained at each material point

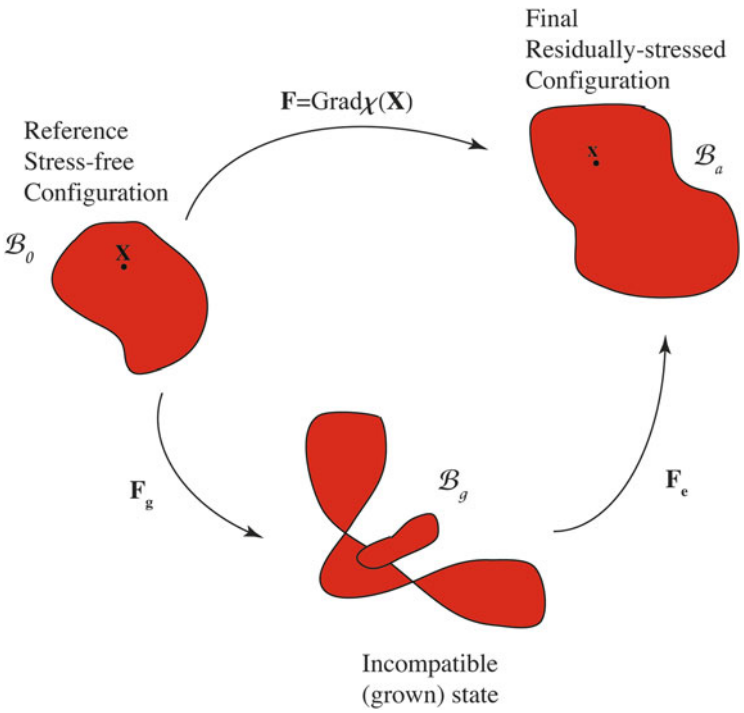

Fig. 4.9 The multiplicative decomposition of the deformation gradient $\mathbf{F}$: the growth (remodeling) component $\mathbf{F}_g$ defines a natural grown or remodeled state $\mathscr{B}_g$, in which geometrical incompatibilities are allowed, and the elastic component $\mathbf{F}_e$, which restores the physical compatibility in the spatial configuration

if all the surrounding constraints would be removed. The ensemble of these stress-free parts defines the natural grown state of the tissue $\mathscr{B}_g$. Since they may not be geometrically compatible with each other, overlapping and intersections are allowed in $\mathscr{B}_g$. The elastic component later restores the global compatibility in the spatial configuration $\mathscr{B}_a$ from the intermediate state $\mathscr{B}_g$.

It is worth noting that even if $\mathbf{F}$ is the geometrical gradient of a deformation, this may not be the case for its components $\mathbf{F}_g$ and $\mathbf{F}_e$, which are defined as tangent maps as follows:

$$\mathbf{F}_g : T\mathscr{B}_0 \to T\mathscr{B}_g \qquad \mathbf{F}_e : T\mathscr{B}_g \to T\mathscr{B}_a. \tag{4.90}$$

The multiplicative decomposition in Eq. (4.89) implies that the morphogenetic effects on the tissue strain can be considered separately from the elastic deformations. This assumption resides on the physical observation that the typical time-scales involving elasticity and growth (remodeling) are very different.

Let $\tau_g, \tau_v, \tau_l, \tau_e$ be the four characteristic times of the growth elastic problem:

- The characteristic time of growth τ_g can range from hours to days, e.g. being characterized by the typical doubling time of living cells.
- The viscoelastic characteristic time τ_v is of the order of hundreds of seconds and is considered as the relaxation time of the tissue [46].
- The elastic time τ_e is associated to the characteristic propagation time of elastic waves, in the order of seconds.
- The loading time τ_l of the external loading.

Therefore the growth time scale is much bigger than the others, so that the growth strains can be separated from the elastic deformations. Furthermore, since the elastic response is much faster than the growth processes, the soft matter is always in a state of elastic equilibrium at times comparable to τ_g [50].

Under these assumptions, it is possible to introduce a material isomorphism for the Helmholtz free energy [40], so that:

$$\rho_0 \Psi(\mathbf{F}, c_i, \Theta; \mathbf{X}, t) = \rho_0 \Psi(\mathbf{F}, \mathbf{F}_g(\mathbf{X}; t), c_\beta, \Theta, t) = \rho_g (det\mathbf{F}_g)\, \Psi_0(\mathbf{F}_e, c_\beta, \Theta, t) \tag{4.91}$$

where $\rho_g = (\rho_0 / det\mathbf{F}_g)$ represents the mass density with respect the intermediate state. In practice, the mechanical behavior of the materials uniquely depends on the elastic part of the deformation gradient, whilst the growth tensor may introduce volume changes and geometrical distortions.

Before considering the constitutive equation and the evolution laws for the growth tensor in the next paragraph, let us finally clarify the morphogenetic information carried within $\mathbf{F}_g$. Since most living materials are mainly composed by water, the incompressibility constraint reads:

$$det\mathbf{F}_e - 1 = 0 \tag{4.92}$$

so that in general $\rho = \rho_g$. Accordingly $\det \mathbf{F}_g$ represent the volume ratio between the grown and the ungrown matter. If we assume that the material is produced at a constant density ρ, the mass balance in Eq. (4.13) rewrites:

$$\frac{\dot{\rho}_0}{\rho_0} = \frac{\Omega}{\rho_0} = \frac{(\dot{det\mathbf{F}_g})}{det\mathbf{F}_g} = tr(\dot{\mathbf{F}}_g \mathbf{F}_g^{-1}) \tag{4.93}$$

Equation (4.93) highlights a fundamental issue: for an incompressible material, the specification of the functional dependence of $\mathbf{F}_g$ over time is equivalent to a constitutive assumption on Ω. Therefore, only one of the two can be constitutively imposed. Whilst modeling fluid-like materials it was mandatory to define Ω, in solid materials this could be equivalently done by imposing an evolution law for $\mathbf{F}_g$.

4.5.3 Constitutive Assumptions and Evolution Laws for Growth and Remodelling

Let us now discuss the thermodynamic restrictions arising from the application of the multiplicative decomposition in Eq. (4.89) with the material isomorphism in Eq. (4.91). Substituting Eq. (4.91) in the reduced dissipation inequality in Eq. (4.28), developing the derivatives using the chain rule one obtains after straightforward calculation the following constitutive laws:

$$\boldsymbol{\sigma} = \rho \mathbf{F}_e \frac{\partial \Psi_0}{\partial \mathbf{F}_e} \tag{4.94}$$

$$\mathbf{S} = \rho_0 \mathbf{F}_g^{-1} \frac{\partial \Psi_0}{\partial \mathbf{F}_e} \tag{4.95}$$

Using Eqs. (4.95) and (4.93), the residual dissipation inequality inside the control volume reads:

$$-\operatorname{tr}[\mathbf{b}(\mathbf{F}_g^{-1}\dot{\mathbf{F}}_g)] + \dot{\rho}_0 \Psi_0 - \rho_0 \frac{\partial \Psi_0}{\partial t} \geq 0 \tag{4.96}$$

Equation (4.96) highlights that the static material Eshelby stress tensor $\mathbf{b} = \rho_0 \Psi_0 \mathbf{I} - \mathbf{S}\mathbf{F}$ is the driving stress measure directing the evolution dynamics of the morphogenetic processes. The frame indifference for the material isomorphism in Eq. (4.91) imposes that $\boldsymbol{b}$ is a symmetric tensor. Accordingly, thermodynamically consistent evolution laws for growth and remodelling read:

$$\dot{\mathbf{F}}_g = -f^+(c_i, \Theta)\rho_0 \mathbf{F}_g \mathbf{b} \tag{4.97}$$

where $f^+(c_i, \Theta)$ is a positive definite scalar function, whose expression may represents a specific temperature-dependent (e.g. Arrhenius-based relations) chemical kinetics in the reactions occurring during the morphogenetic processes [25]. The evolution law in Eq. (4.97) is a generalization of the classical results obtained for inelastic continua, since the Eshelby tensor is the symmetric stress conjugate of the growth velocity gradient [83]. Moreover, the symmetry of the driving force expressed by $\mathbf{b}$ is a necessary requirement, as pointed out by Skalak [102]: indeed, the symmetric part of $\mathbf{F}_g$ is the only shape-changing deformation of the growth tensor.

Let us now provide a geometrical interpretation of the coupling between stress and growth in the proposed mathematical model. For this purpose, we perform the explicit gradient of the free energy expressed by Eq. (4.91), and we derive the quasi-static driving force $\mathbf{f}_{inh}$ of true material inhomogeneities in Eq. (4.87):

$$\mathbf{f}_{inh} = -\rho_0 \frac{\partial \Psi_0}{\partial \mathbf{X}}|_{expl} = -\rho_0 \left(\frac{\partial \Psi}{\partial \mathbf{F}_g} : \operatorname{Grad} \mathbf{F}_g \right) = -\rho_0 \mathbf{b} : \mathscr{T} \tag{4.98}$$

where we used the two dots to indicate double contraction, i.e. $(\mathbf{b} : \mathscr{T})_k = \mathbf{b}_{ji}(\mathscr{T})_{ijk}$. In Eq. (4.98), the third-order tensor $\mathscr{T} = \mathbf{F}_g^{-1}\,\mathrm{Grad}\,\mathbf{F}_g$ is the generally not-symmetric torsional material connection associated with $\mathbf{F}_g$. Accordingly, the expression of the driving force in Eq. (4.98) reflects the geometrical interpretation that the Eshelby force is the stress measure driving the torsion of the material connection during morphogenesis. Evolution laws coupling stress, growth and mass transport, extended to the second gradient of the deformation have been discussed in further details in [25], showing that the strain gradient Eshelby stress is associated to the curvature of the material connection.

4.5.4 Morpho-Elasticity of Growing Living Matter

Morpho-elasticity is the recently developed branch of continuum mechanics investigating the emergence of complex patterns in living matter after the occurrence of an elastic instability. Indeed, the accumulation of residual stresses during morphogenetic processes can trigger a morphological transition within the biological material as a result of an elastic bifurcation. In the following, we will present the basic theoretical tools in the field.

4.5.4.1 Basic Solution of the Quasi-Static Elastic Problem

In previous sections of this section, we have shown that the thermo-mechanics of open systems and the theory of configurational forces are useful frameworks to model the chemo-mechanical cues of morphogenesis in soft elastic tissues.

Summarizing, the resulting boundary value problem in nonlinear elasticity is given by the following set of equations in the current configuration $\mathscr{B}_a$:

$$\begin{cases} \rho\dot{\mathbf{v}} - \mathrm{div}\,\boldsymbol{\sigma} - \mathbf{b}_v = \mathbf{0} \\ \omega = \rho\ \mathrm{tr}(\dot{\mathbf{F}}_g\mathbf{F}_g^{-1}) \\ \det\mathbf{F}_e = 1 \\ \boldsymbol{\sigma} = \rho\mathbf{F}_e\dfrac{\partial\psi_0}{\partial\mathbf{F}_e} - p\mathbf{I} \\ \dot{\mathbf{F}}_g = -f^+(c_i,\Theta)\rho_0\mathbf{F}_g\mathbf{b} \end{cases} \tag{4.99}$$

which contains the balances of linear momentum and mass, the incompressibility constraint, the constitutive equation for the Cauchy stress tensor and the evolution law for the growth tensor, respectively. Such governing equations are typically complemented by three possible sets of boundary conditions, which will be briefly discussed.

Let $\partial\mathscr{B}_0, \partial\mathscr{B}_0^{\mathbf{x}}, \partial\mathscr{B}_0^{\boldsymbol{\sigma}}$ be the boundary in the reference configuration and two portions of the boundary, respectively, such that $\partial\mathscr{B}_0 = \partial\mathscr{B}_0^{\mathbf{x}} \cup \mathscr{B}_0^{\boldsymbol{\sigma}}$. Let $\partial\mathscr{B}_a, \partial\mathscr{B}_a^{\mathbf{x}}, \partial\mathscr{B}_a^{\boldsymbol{\sigma}}$ the associated quantities in the actual configuration, where $\partial\mathscr{B}_a = \partial\mathscr{B}_a^{\mathbf{x}} \cup \mathscr{B}_a^{\boldsymbol{\sigma}}$. Let us consider a quasi-static growth process, so that we are not interested in determining the evolution of the growth tensor $\mathbf{F}_g$ over time, but we aim at deriving the elastic solution at a fixed value of $\mathbf{F}_g$. Under this assumption, the three possible sets of boundary conditions read:

- **Dirichlet boundary conditions**: the displacements for all points belonging to $\partial\mathscr{B}_0$ and $\partial\mathscr{B}_a$ are specified in the following forms, respectively:

$$\begin{cases} \mathbf{u}_0(\mathbf{X}) = \mathbf{x}(\mathbf{X}) - \mathbf{X} = \mathbf{u}_0^* & \text{on } \partial\mathscr{B}_0 \\ \mathbf{u}_a(\mathbf{x}) = \mathbf{x} - \mathbf{X}(\mathbf{x}) = \mathbf{u}_0^* & \text{on } \partial\mathscr{B}_a \end{cases} \tag{4.100}$$

  where $\mathbf{u}_0, \mathbf{u}_a$ are the displacements in material and spacial form, respectively and $\mathbf{u}_0^*$ is the displacement vector to be assigned at the boundaries.
- **Neumann boundary conditions**: the traction loads at all points belonging to $\partial\mathscr{B}_0$ and $\partial\mathscr{B}_a$ are given in the following forms, respectively:

$$\begin{cases} \mathbf{S}^T\mathbf{N} = \mathbf{t}_0^* & \text{on } \partial\mathscr{B}_0 \\ \boldsymbol{\sigma}\mathbf{n} = \mathbf{t}^* & \text{on } \partial\mathscr{B}_a, \end{cases} \tag{4.101}$$

  where $\mathbf{S}, \boldsymbol{\sigma}$ are the Nominal and Cauchy stress respectively and $\mathbf{t}_0^*, \mathbf{t}^*$ are traction vectors to be assigned.
- **Mixed boundary conditions**: the displacements are specified on a portion of the boundary $\partial\mathscr{B}_0^{\mathbf{x}}$, $\partial\mathscr{B}_a^{\mathbf{x}}$ and traction loads are given on the remaining subset $\partial\mathscr{B}_0^{\boldsymbol{\sigma}}$,$\partial\mathscr{B}_a^{\boldsymbol{\sigma}}$, in the following forms:

$$\begin{cases} \mathbf{u}_0(\mathbf{X}) = \mathbf{u}_0^* & \text{on } \partial\mathscr{B}_0^{\mathbf{x}} \\ \mathbf{S}^T\mathbf{N} = \mathbf{t}_0^* & \text{on } \partial\mathscr{B}_0^{\boldsymbol{\sigma}}, \end{cases} \tag{4.102}$$

  in the reference configuration or:

$$\begin{cases} \mathbf{u}_a(\mathbf{x}) = \mathbf{u}_0^* & \text{on } \partial\mathscr{B}_a^{\mathbf{x}} \\ \boldsymbol{\sigma}\mathbf{n} = \mathbf{t}^* & \text{on } \partial\mathscr{B}_a^{\boldsymbol{\sigma}}, \end{cases} \tag{4.103}$$

  in the actual configuration.

In quasi-static conditions, let $\mathbf{x}^{(0)} = \boldsymbol{\chi}^{(0)}(\mathbf{X})$ be the basic solution of the governing equation in Eq. (4.99) with one of the possible sets of boundary conditions in Eqs. (4.100)–(4.103). The solution $\mathbf{x}^{(0)}$ depends on a control parameter which is related to the given expression of $\mathbf{F}_g$. In the following, we will introduce the theory of incremental deformations superposed on finite strains to investigate the linear stability analysis of this basic solution.

4.5.4.2 Method of Incremental Deformations Superposed on Finite Deformations

Following Ogden [90], the fundamental idea of *the method of incremental deformations superposed on finite deformations* is to perturb the basic solution $\mathbf{x}^{(0)}$ to the elastic problem, with a small incremental deformation. Performing a series expansion, the zeroth order term is a finite deformation, representing the basic solution with the initial shape of the material. The first order term is an incremental deformation, defining the possible morphology after an elastic bifurcation.

Kinematics of the Incremental Deformation Let $\mathbf{x}^{(0)}$ be the *basic* position vector in $\mathscr{B}_a$ identified by the basic finite deformation $\boldsymbol{\chi}^{(0)}$ and let $\varepsilon\hat{\mathbf{x}}$ be a small displacement from $\mathbf{x}^{(0)}$. Accordingly, the perturbed position $\bar{\mathbf{x}}$ can be written as:

$$\bar{\mathbf{x}} = \mathbf{x}^{(0)} + \varepsilon\hat{\mathbf{x}} = \boldsymbol{\chi}^{(0)}(\mathbf{X}) + \varepsilon\boldsymbol{\chi}^{(1)}(\mathbf{x}^{(0)}) \tag{4.104}$$

where $|\varepsilon| \ll 1$ and $\varepsilon\boldsymbol{\chi}^{(1)}(\mathbf{x}^{(0)})$ is a small deformation which in the following will be referred to as the *incremental* deformation. Note that $\boldsymbol{\chi}^{(1)}$ maps the basic position vector $\mathbf{x}^{(0)}$ into its incremental displacement $\hat{\mathbf{x}}$ in the perturbed actual configuration $\hat{\mathscr{B}}_a$. Adopting the convention of summation on repeated indexes, the incremental deformation can be written:

$$\boldsymbol{\chi}^{(1)}(\mathbf{x}) = u_j(\mathbf{x})\mathbf{e}_j \tag{4.105}$$

where the components u_j ($j = 1, 2, 3$) are the displacements along the principal directions $\mathbf{e}_j$ ($j = 1, 2, 3$), respectively. Figure 4.10 gives a graphical representation of the basic and perturbed fields. In the following, the variables after perturbation will be indicated with the symbol $(\bar{\bullet})$, and the incremental variables with the symbol $(\hat{\bullet})$. Using the definition of deformation gradient in Eq. (4.2), the *perturbed deformation gradient* $\bar{\mathbf{F}}$ rewrites:

$$\begin{aligned}\bar{\mathbf{F}} = \mathbf{F}^{(0)} + \varepsilon\hat{\mathbf{F}} = \frac{\partial\boldsymbol{\chi}^{(0)}(\mathbf{X})}{\partial\mathbf{X}} + \varepsilon\frac{\partial\boldsymbol{\chi}^{(1)}(\mathbf{x}^{(0)})}{\partial\mathbf{X}} = \\ = \frac{\partial\boldsymbol{\chi}^{(0)}(\mathbf{x}^{(0)})}{\partial\mathbf{X}} + \varepsilon\frac{\partial\boldsymbol{\chi}^{(1)}(\mathbf{x}^{(0)})}{\partial\mathbf{x}^{(0)}}\frac{\partial\mathbf{x}^{(0)}}{\partial\mathbf{X}} = \mathbf{F}^{(0)} + \varepsilon\boldsymbol{\Gamma}\mathbf{F}^{(0)}\end{aligned} \tag{4.106}$$

where the material and the spatial displacement gradient $\hat{\mathbf{F}} = \mathrm{Grad}(\boldsymbol{\chi}^{(1)}(\mathbf{x}^{(0)}))$ and $\boldsymbol{\Gamma} = \mathrm{grad}(\boldsymbol{\chi}^{(1)}(\mathbf{x}^{(0)}))$ respectively, have been introduced and are related through the following relation:

$$\hat{\mathbf{F}} = \boldsymbol{\Gamma}\mathbf{F}^{(0)}. \tag{4.107}$$

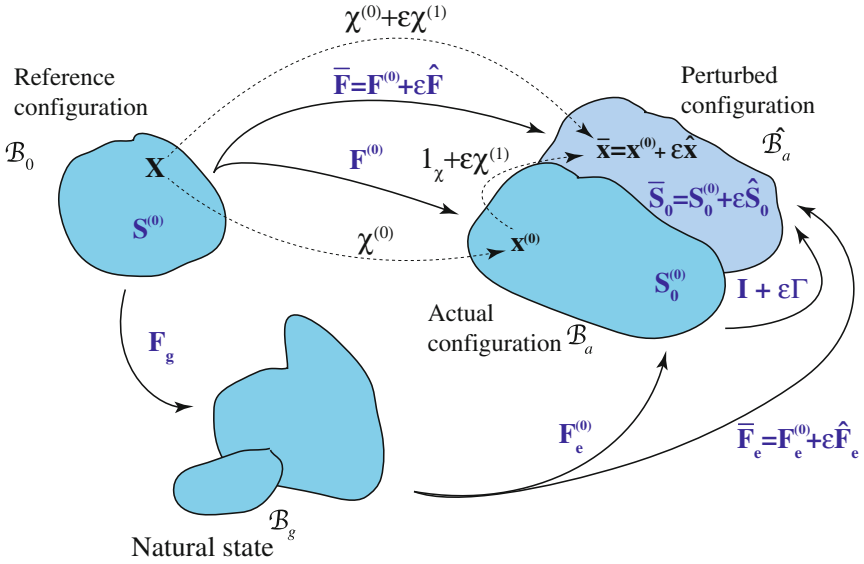

Fig. 4.10 Schematic diagram of the incremental deformation superposed on a finite strain. The zeroth order fields are the finite deformation $\boldsymbol{\chi}^{(0)}$, the basic position vector $\mathbf{x}^{(0)}$, the basic deformation gradient $\mathbf{F}^{(0)}$ and its elastic component $\mathbf{F}_e^{(0)}$, the basic Nominal stress $\mathbf{S}^{(0)}$ and its push-forward $\mathbf{S}_0^{(0)}$. The perturbed fields after the introduction of the incremental deformation $\boldsymbol{\chi}^{(1)}$ are the perturbed position vector $\bar{\mathbf{x}}$, the perturbed deformation gradient $\bar{\mathbf{F}}$ and its elastic component $\bar{\mathbf{F}}_e$, the push forward of the perturbed Nominal stress $\bar{\mathbf{S}}^{(0)}$

Accordingly, the *incremental incompressibility condition* in Eq. (4.92) reads:

$$\operatorname{tr}\boldsymbol{\Gamma} = 0. \tag{4.108}$$

Incremental Equilibrium Equations Let us now consider the incremental constitutive equation for the stress tensor fields. The *perturbed Nominal stress* $\bar{\mathbf{S}}$ is given by:

$$\bar{\mathbf{S}} = \mathbf{S}^{(0)} + \varepsilon\hat{\mathbf{S}}, \tag{4.109}$$

where the $\mathbf{S}^{(0)}$ is the zeroth order term of the series expansion of the Nominal stress in Eq. (4.99). The leading order increment $\hat{\mathbf{S}}$ can be derived by differentiating the constitutive equation in Eq. (4.95) and it reads:

$$\hat{\mathbf{S}} = \mathscr{A}^1\hat{\mathbf{F}} + p(\mathbf{F}^{(0)})^{-1}\hat{\mathbf{F}}(\mathbf{F}^{(0)})^{-1} - q(\mathbf{F}^{(0)})^{-1}. \tag{4.110}$$

In Eq. (4.110), the term $q = \hat{p}$ is the increment in p and $\mathscr{A}^1$ is the fourth-order tensor of the elastic moduli, defined as:

$$\mathscr{A}^1 = \frac{\partial \psi_0}{\partial \mathbf{F} \partial \mathbf{F}}, \quad \text{with} \qquad \mathscr{A}^1_{\gamma k \beta j} = \frac{\partial^2 \psi_0}{\partial F_{k\gamma} \partial F_{j\beta}}. \tag{4.111}$$

The *perturbed Cauchy stress* tensor in the perturbed configuration $\hat{\mathscr{B}}_a$, is given by $\bar{\boldsymbol{\sigma}} = \bar{\mathbf{F}}\bar{\mathbf{S}}$, but since $\hat{\mathscr{B}}_a$ is unknown, it is more practical to use the *push-forward of the perturbed Nominal stress*, defined as:

$$\bar{\mathbf{S}}_0 = \mathbf{F}^{(0)}\bar{\mathbf{S}} = \mathbf{S}_0^{(0)} + \varepsilon \hat{\mathbf{S}}_0 \tag{4.112}$$

where, $\mathbf{S}_0^{(0)} = \mathbf{F}^{(0)}\mathbf{S}^{(0)}$ is the push forward of the zeroth-order term $\mathbf{S}^{(0)}$. Using Eq. (4.107) the push-forward $\hat{\mathbf{S}}_0$ of the first order term $\hat{\mathbf{S}}$ is given by:

$$\hat{\mathbf{S}}_0 = \mathbf{F}^{(0)}\hat{\mathbf{S}} = \mathscr{A}^1_0 \boldsymbol{\Gamma} + p\boldsymbol{\Gamma} - q\mathbf{I} \tag{4.113}$$

with:

$$\mathscr{A}^1_{0hklj} = F^{(0)}_{h\gamma} F^{(0)}_{l\beta} \mathscr{A}^1_{\gamma k \beta j}. \tag{4.114}$$

being the component of the fourth-order tensor $\mathscr{A}^1_0$, also known as *the fourth-order tensor of instantaneous elastic moduli*.

Using the properties of the Piola transformation, the *incremental equilibrium equations* in $\mathscr{B}_a$ simplify as:

$$\operatorname{div} \hat{\mathbf{S}}_0 = \mathbf{0}, \tag{4.115}$$

where $\hat{\mathbf{S}}_0$ is given by Eq. (4.113).

Let $\hat{\mathbf{u}}_0^*$ and $\hat{\mathbf{t}}_0^*$ be the increments of the assigned displacement and traction vectors $\mathbf{u}_0^*$ and $\mathbf{t}_0^*$ respectively and $\hat{\mathbf{t}}^*$ the increment of the assigned traction vector $\mathbf{t}^*$. The Dirichlet boundary conditions in the incremental form rewrite:

$$\hat{\mathbf{x}}(\mathbf{X}) = \hat{\mathbf{u}}_0^* \qquad \text{on } \partial\mathscr{B}_0^{\mathbf{x}} \tag{4.116}$$

$$\hat{\mathbf{x}}(\mathbf{x}) = \boldsymbol{\chi}^{(1)}(\mathbf{x}) = \hat{\mathbf{u}}_0^* \qquad \text{on } \partial\mathscr{B}_a^{\mathbf{x}} \tag{4.117}$$

and the corresponding incremental boundary conditions for traction loads read:

$$\hat{\mathbf{S}}^T\mathbf{N} = \hat{\mathbf{t}}_0^* \qquad \text{on } \partial\mathscr{B}_0^{\boldsymbol{\sigma}} \tag{4.118}$$

$$\hat{\mathbf{S}}_0^T\mathbf{n} = \hat{\mathbf{t}}^* \qquad \text{on } \partial\mathscr{B}_a^{\boldsymbol{\sigma}}. \tag{4.119}$$

We remark that the increment $\hat{\mathbf{t}}^*$ in the nominal traction depends in general on the incremental deformation other than on any loading parameter.

4.5.4.3 Summary of the Incremental Boundary Value Problem

In summary, the emergence of a morphological transition in living materials resulting from an elastic instability can be studied by solving the following boundary value problem in nonlinear elasticity:

$$\begin{cases} \operatorname{div} \hat{\mathbf{S}}_0 = \mathbf{0} \\ \operatorname{tr} \boldsymbol{\Gamma} = 0 \end{cases} \tag{4.120}$$

with boundary conditions in the general mixed form:

$$\hat{\mathbf{x}}(\mathbf{x}) = \boldsymbol{\chi}^{(1)}(\mathbf{x}) = \hat{\mathbf{u}}_0^* \text{ on } \partial\mathscr{B}_a^{\mathbf{x}}, \qquad \hat{\mathbf{S}}_0^T \mathbf{n} = \hat{\mathbf{t}}^* \qquad \text{on } \partial\mathscr{B}_a^{\boldsymbol{\sigma}}. \tag{4.121}$$

Equations (4.120) and (4.121) represent a system of four partial differential equations, where the four unknowns are the three incremental displacements $u_1(\mathbf{x}), u_2(\mathbf{x}), u_3(\mathbf{x})$ in Eq. (4.105) and the increment q of the Lagrange multiplier.

4.6 Pattern Formation in a Growing Bilayer Under Lateral Constraint

During embryogenesis, a differential growth between the layers constituting a soft tissue has been found to control the emergence of a pre-patterning, which may drive the later tissue differentiation. For example, it has been shown that both elastic properties and the geometry of the growing layers are key factors determining the pattern selection and the emergence of several functional structures on the epithelium of gastro-intestinal tissues [28, 101].

In the following, we define a morpho-elastic model of a hyperelastic soft tissue made of two flat layers growing under a spatial constraint. Such a bilayered geometry is widely encountered in epithelial tissues, e.g. the dermis and the epidermis for the skin [20, 75]. Our aim is to investigate the pattern formation in this system model in the absence of differential growth process, simply considering a uniform, homogeneous swelling constrained by the presence of lateral rigid walls.

4.6.1 Definition of the Model and Basic Morpho-Elastic Solution

In a Cartesian coordinate system with unit base vectors $\mathbf{e}_i$, with $i = (x, y, z)$, let us consider a soft elastic tissue attached at the surface $Z = 0$, and having a vertical thickness H much smaller than the horizontal lengths L_x, L_y. Moreover, we assume $L_y >> L_x$ so that a plain strain condition applies in fulfillment of symmetry

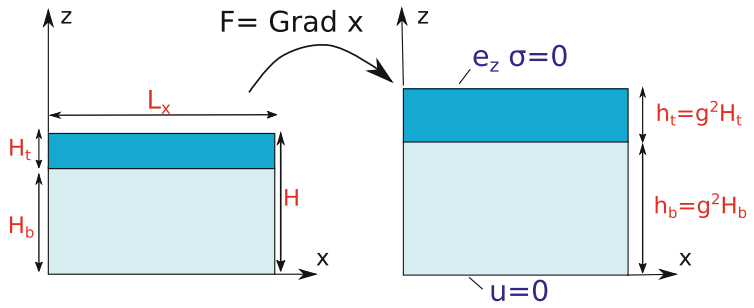

Fig. 4.11 Schematic diagram of the reference (*left*) and the basic spatial (*right*) configurations of a soft bi-layered materials with lateral constraint along the x-axis. Both the layers are subjected to a isotropic volumetric growth with $\mathbf{F}_g = g\mathbf{I}$, where the scalar g indicates the growth rate

requirements. Accordingly, we will consider the equivalent 2D problem in (x, z) in the following, unless explicitly stated, as depicted in Fig. 4.11.

The tissue is composed by two layers, with thicknesses H_b and H_t, so that $(H_b + H_t) = H$. In the following, we will denote with subscripts b and t the fields related to the bottom and top layer, respectively. Indicating with $\mathbf{X} = \mathbf{X}(X, Z)$ and $\mathbf{x} = \mathbf{x}(x, z)$ its material and spatial position vectors, respectively, the kinematics is described by the geometrical deformation tensor $\mathbf{F} = \partial\mathbf{x}/\partial\mathbf{X}$. The elastic layers can undergo a isotropic volume variation (e.g. swelling for a polymeric gel, or growth for a living material). Assuming the multiplicative decomposition in Eq. (4.122), their grown natural states are defined by the growth tensor:

$$\mathbf{F}_g = g\mathbf{I}, \qquad \text{with g} > 1 \tag{4.122}$$

where g is the isotropic growth rate and $\mathbf{I}$ is the unit tensor. Considering the presence on rigid walls at $X = -L_x/2, L_x/2$, $\mathbf{F}_g$ is not compatible with such spatial constraints, therefore an elastic deformation must restores the overall compatibility of the tissue deformation, whilst residual stresses arise.

From a constitutive viewpoint, each layer is modeled as an isotropic neo-Hookean incompressible material, so that strain energy Ψ_0 per unit mass reads

$$\Psi_0 = \frac{\mu}{2} \iint \left(\text{tr}\, \mathbf{F}_e \mathbf{F}_e^T - 3\right) \mathrm{d}X \;\; \mathrm{d}Z, \tag{4.123}$$

where μ is the shear modulus.

The base solution for a growing layer, whose fields are indicated with superscript (0) in the following, corresponds to a homogeneous elastic deformation:

$$\mathbf{F}_e^{(0)} = \mathbf{F}^{(0)} \mathbf{F}_g^{-1} = \text{diag}(\lambda_x, \lambda_z) = \text{diag}(1/g, g) \tag{4.124}$$

whose principal stretches $\lambda_x = 1/g$ and $\lambda_z = g$ enforce the incompressibility constraint , i.e. $\det \mathbf{F}_e^{(0)} = 1$. Using the constitutive assumptions in Eqs. (4.94) and (4.95), the residual Cauchy stress $\boldsymbol{\sigma}^{(0)}$ and first Piola-Kirchoff stress tensor $\mathbf{P}^{(0)}$ for each layer read:

$$\boldsymbol{\sigma}^{(0)} = \mu \mathbf{F}_e^{(0)} \mathbf{F}_e^{(0)T} - p_0 \mathbf{I}, \qquad \mathbf{S}^{(0)} = \mu \mathbf{F}_e^{(0)^T} - p_0 \mathbf{F}_e^{(0)^{-1}} \tag{4.125}$$

where p_0 is the basic Lagrange multiplier, which can be fixed through the boundary conditions. In particular, considering a stress-free surface at $Z = H$, we have $p_{0t} = \mu_t \lambda_z^2 = \mu_t g^2$. Moreover, the continuity of the normal stress and displacements at the layers' interface read:

$$\boldsymbol{\sigma}_t^{(0)} e_z = \boldsymbol{\sigma}_b^{(0)} e_z; \qquad \mathbf{x}_t(x, H_b) = \mathbf{x}_b(x, H_b) \tag{4.126}$$

so that $p_{0b} = \mu_b \lambda_z^2 = \mu_b g^2$. Therefore each layer is subjected to a uniaxial stress with:

$$\mathbf{S}_{xx}^{(0)} = \mu(g^{-1} - g^3); \qquad \sigma_{xx}^{(0)} = \mu(g^{-2} - g^2) \tag{4.127}$$

which is compressive if $g > 1$, i.e. if the tissue is increasing its volume. Therefore, such a uniaxial compressive stress is discountinous within the tissue if the layers have different shear moduli. The goal of the next section is to perform a linear stability analysis of this basic solution, with the aim to investigate the condition driving the onset of a morphological transition.

4.6.2 Linear Stability Analysis

Let us now apply the theory of incremental deformations superposed on the finite homogeneous solution given by Eq. (4.124). Hence, let $\mathbf{u}^{(1)}(x, z, t)$ be the infinitesimal incremental displacement field. In the case of a neo-Hookean material as in Eq. (4.123), it is easy to check that the components of the elastic tensor of instantaneous moduli in Eq. (4.114) read:

$$\mathscr{A}_{0jikl}^{1} = \mu \lambda_j^2 \delta_{jk} \delta_{il} \tag{4.128}$$

where the subscripts run over (x, z) and δ is the Kronecker delta. Equation (4.128) applies in a coordinate system aligned with the directions of the principal stretches, whilst higher order instantaneous moduli vanish. Accordingly, the neo-Hookean constitutive equation allows to take into account only for geometrical non-linearities. From Eq. (4.113), the constitutive equation for the incremental stress reads:

$$\hat{\mathbf{S}}_0 = \mu(\tilde{\text{grad}}\mathbf{u}^{(1)})^T + p_0 \ \text{grad}\,\mathbf{u}^{(1)} - q\mathbf{I} \tag{4.129}$$

where q is the linear increment in the Lagrange multiplier and we defined the operator $\tilde{\text{grad}} = [\lambda_x^2 \partial_x, \lambda_z^2 \partial_z]^T$. In the absence of body forces, the equations of motion in Eq. (4.115) rewrite:

$$\text{div}\, \hat{\mathbf{S}}_0 = \mathbf{0}. \tag{4.130}$$

Using Eq. (4.129), the incremental equations of in Eq. (4.130) take the following simplified expressions:

$$-q_{,x} + \mu \lambda_i^2 u_{x,ii}^{(1)} = 0, \qquad -q_{,z} + \mu \lambda_i^2 u_{z,ii}^{(1)} = 0, \tag{4.131}$$

where the comma denote partial differentiation and Einstein's summation rule on repeated indices is assumed. Differentiating these incremental equations of motion with respect to x, and z, respectively, and using the incremental incompressibility condition in Eq. (4.134), we find that:

$$\nabla^2 q = 0, \tag{4.132}$$

implying that the incremental Lagrange multiplier is a Laplacian field [41].

Conversely, by differentiating the first and second of Eq. (4.131) by z and x, respectively, and subtracting the resulting equations, we find that:

$$\lambda_x^2 u_{x,zxx}^{(1)} + \lambda_z^2 u_{x,zzz}^{(1)} - \lambda_z^2 u_{z,xzz}^{(1)} - \lambda_x^2 u_{z,xxx}^{(1)} = 0, \tag{4.133}$$

At the leading order, the linear incremental incompressibility condition rewrites:

$$\text{div}\, \mathbf{u}^{(1)} = u_{x,x}^{(1)} + u_{z,z}^{(1)} = 0. \tag{4.134}$$

The bulk Eqs. (4.133) and (4.134) will be solved in the following using two different methods: the stream function approach and the Stroh formalism.

4.6.2.1 Solution Using an Elastic Stream Functions

First, let us define an elastic stream function $\phi = \phi(x, z)$, so that [90]:

$$u_x^{(1)} = -\phi_{,z}, \qquad u_z^{(1)} = \phi_{,x}, \tag{4.135}$$

and Eq. (4.134) is automatically satisfied. Thus, substituting Eq. (4.135) in Eq. (4.133), the incremental equilibrium is governed by the following bulk equation:

$$\lambda_z^2 \phi_{,zzzz} + (\lambda_x^2 + \lambda_z^2)\phi_{,zzxx} + \lambda_x^2 \phi_{,xxxx} = 0, \tag{4.136}$$

In particular, it is useful to recast the previous equation in the following form [9]:

$$\nabla^2\tilde{\nabla}^2\phi = 0, \tag{4.137}$$

where $\tilde{\nabla}^2(.) = \lambda_x^2(.)_{,xx} + \lambda_z^2(.)_{,zz} = (.)_{,XX} + (.)_{,ZZ}$. Accordingly, Eq. (4.137) states that the equilibrium is governed by a forth order partial differential equation obtained by combination of the material and spatial Laplacian operators. Thus, the growth tensor acts as a distortion of the original metrics which changes the differential incremental problem. In the absence of growth Eq. (4.137) would represent the classical bilaplacian problem found for plane strain problems in linear elasticity.

Let us now impose the required set of boundary conditions. First, since the bottom $z = 0$ of the bilayer is fixed, the two corresponding incremental boundary conditions read:

$$\mathbf{u}_b^{(1)}(x, 0) = 0. \tag{4.138}$$

The top surface $z = (\lambda_z/\lambda_x)H = g^2H = h$ is free of incremental tractions, thus:

$$\begin{aligned} (u_t^{(1)})_{x,z} + (u_t^{(1)})_{z,x} &= 0, \\ -\lambda_z^2 q_t^{(1)} + 2\mu_t\lambda_z^2(u_t^{(1)})_{z,z} &= 0. \end{aligned} \tag{4.139}$$

Moreover, the four remaining equations are given by the continuity of the incremental displacements and the normal stresses across the interface at $z = g^2H_b$, being:

$$\begin{aligned} \mathbf{u}_b^{(1)} &= \mathbf{u}_t^{(1)}, \\ \mu_t((u_t^{(1)})_{x,z} + (u_t^{(1)})_{z,x}) &= \mu_b((u_b^{(1)})_{x,z} + (u_b^{(1)})_{z,x}), \\ -\lambda_z^2 q_t^{(1)} + 2\mu_t\lambda_z^2(u_t^{(1)})_{z,z} &= -\lambda_z^2 q_b^{(1)} + 2\mu_b\lambda_z^2(u_b^{(1)})_{z,z}. \end{aligned} \tag{4.140}$$

Let us search for a solution to Eq. (4.137) using the variable separation.
Thus we set:

$$\phi(x, z) = \Phi(z)e^{\imath kx} + c.c., \tag{4.141}$$

corresponding to the occurrence of a surface undulation with wavenumber k along the x-axis, where $\imath$ is the imaginary unit and *c.c.* indicates the complex conjugate. the corresponding solution is given by:

$$\Phi_i(z) = a_{1i}e^{-kz} + a_{2i}e^{kz} + a_{3i}e^{-\frac{\lambda_x}{\lambda_z}kz} + a_{4i}e^{\frac{\lambda_x}{\lambda_z}kz}; \qquad \text{with } i = (t, b) \tag{4.142}$$

where $a_{1i}, a_{2i}, a_{3i}, a_{4i}$ are coefficient to be determined by boundary conditions, and we remind that $\lambda_x/\lambda_z = 1/g^2$. Substituting Eqs. (4.135) and (4.142) in Eqs. (4.138) and (4.140), the boundary conditions can be rewritten in the following form:

$$\mathbf{Ma} = \mathbf{0} \tag{4.143}$$

where $\mathbf{a} = [a_{1t}, a_{2t}, a_{3t}, a_{4t}, a_{1b}, a_{2b}, a_{3b}, a_{4b}]^T$ and $\mathbf{M}$ is a 8x8 square matrix, whose detailed expression is given by:

$$\mathbf{M} = \begin{bmatrix} \mathbf{M}_1, \mathbf{M}_2 \\ \mathbf{M}_3, \mathbf{M}_4 \end{bmatrix} \tag{4.144}$$

with sub-blocks given by:

$$\mathbf{M}_1 = \begin{bmatrix} 0 & 0 & 0 & 0 \\ 0 & 0 & 0 & 0 \\ -\frac{e^{-\frac{ikh_b\lambda_x}{\lambda_z}}}{2k\lambda_z^2\mu_t} & -\frac{e^{\frac{ikh_b\lambda_x}{\lambda_z}}}{2k\lambda_z^2\mu_t} & -\frac{e^{-ikh_b}}{k\mu_t\lambda_x^2+k\lambda_z^2\mu_t} & -\frac{e^{ikh_b}}{k\mu_t\lambda_x^2+k\lambda_z^2\mu_t} \\ \frac{e^{-\frac{ikh_b\lambda_x}{\lambda_z}}}{2k\lambda_x\lambda_z\mu_t} & -\frac{e^{\frac{ikh_b\lambda_x}{\lambda_z}}}{2k\lambda_x\lambda_z\mu_t} & \frac{e^{-ikh_b}}{k\mu_t\lambda_x^2+k\lambda_z^2\mu_t} & -\frac{e^{ikh_b}}{k\mu_t\lambda_x^2+k\lambda_z^2\mu_t} \end{bmatrix}, \tag{4.145}$$

$$\mathbf{M}_2 = \begin{bmatrix} \frac{1}{2k\lambda_z^2\mu_b} & \frac{1}{2k\lambda_z^2\mu_b} & \frac{1}{k\mu_b\lambda_x^2+k\lambda_z^2\mu_b} & \frac{1}{k\mu_b\lambda_x^2+k\lambda_z^2\mu_b} \\ -\frac{1}{2k\lambda_x\lambda_z\mu_b} & \frac{1}{2k\lambda_x\lambda_z\mu_b} & -\frac{1}{k\mu_b\lambda_x^2+k\lambda_z^2\mu_b} & \frac{1}{k\mu_b\lambda_x^2+k\lambda_z^2\mu_b} \\ \frac{e^{-\frac{ikh_b\lambda_x}{\lambda_z}}}{2k\lambda_z^2\mu_b} & \frac{e^{\frac{ikh_b\lambda_x}{\lambda_z}}}{2k\lambda_z^2\mu_b} & \frac{e^{-ikh_b}}{k\mu_b\lambda_x^2+k\lambda_z^2\mu_b} & \frac{e^{ikh_b}}{k\mu_b\lambda_x^2+k\lambda_z^2\mu_b} \\ -\frac{e^{-\frac{ikh_b\lambda_x}{\lambda_z}}}{2k\lambda_x\lambda_z\mu_b} & \frac{e^{\frac{ikh_b\lambda_x}{\lambda_z}}}{2k\lambda_x\lambda_z\mu_b} & -\frac{e^{-ikh_b}}{k\mu_b\lambda_x^2+k\lambda_z^2\mu_b} & \frac{e^{ikh_b}}{k\mu_b\lambda_x^2+k\lambda_z^2\mu_b} \end{bmatrix}, \tag{4.146}$$

$$\mathbf{M}_3 = \begin{bmatrix} -\frac{e^{-\frac{ikh_b\lambda_x}{\lambda_z}}(\lambda_x^2+\lambda_z^2)}{2\lambda_x\lambda_z} & \frac{e^{\frac{ikh_b\lambda_x}{\lambda_z}}(\lambda_x^2+\lambda_z^2)}{2\lambda_x\lambda_z} & -\frac{2e^{-ikh_b}\lambda_z^2}{\lambda_x^2+\lambda_z^2} & \frac{2e^{ikh_b}\lambda_z^2}{\lambda_x^2+\lambda_z^2} \\ -e^{-\frac{ikh_b\lambda_x}{\lambda_z}} & -e^{\frac{ikh_b\lambda_x}{\lambda_z}} & -e^{-ikh_b} & -e^{ikh_b} \\ \frac{ie^{-\frac{ihk\lambda_x}{\lambda_z}}(\lambda_x^2+\lambda_z^2)}{2\lambda_x\lambda_z} & -\frac{ie^{\frac{ihk\lambda_x}{\lambda_z}}(\lambda_x^2+\lambda_z^2)}{2\lambda_x\lambda_z} & \frac{2ie^{-ihk}\lambda_z^2}{\lambda_x^2+\lambda_z^2} & -\frac{2ie^{ihk}\lambda_z^2}{\lambda_x^2+\lambda_z^2} \\ e^{-\frac{ihk\lambda_x}{\lambda_z}} & e^{\frac{ihk\lambda_x}{\lambda_z}} & e^{-ihk} & e^{ihk} \end{bmatrix}, \tag{4.147}$$

$$\mathbf{M}_4 = \begin{bmatrix} \frac{e^{-\frac{ikh_b\lambda_x}{\lambda_z}}(\lambda_x^2+\lambda_z^2)}{2\lambda_x\lambda_z} & -\frac{e^{\frac{ikh_b\lambda_x}{\lambda_z}}(\lambda_x^2+\lambda_z^2)}{2\lambda_x\lambda_z} & \frac{2e^{-ikh_b}\lambda_z^2}{\lambda_x^2+\lambda_z^2} & -\frac{2e^{ikh_b}\lambda_z^2}{\lambda_x^2+\lambda_z^2} \\ e^{-\frac{ikh_b\lambda_x}{\lambda_z}} & e^{\frac{ikh_b\lambda_x}{\lambda_z}} & e^{-ikh_b} & e^{ikh_b} \\ 0 & 0 & 0 & 0 \\ 0 & 0 & 0 & 0 \end{bmatrix}. \tag{4.148}$$

Accordingly, the onset of a marginal stability is given by the following condition:

$$\det \mathbf{M} = 0 \tag{4.149}$$

which gives an implicit relation between the marginally stable growth rate g for each wavenumber k as a function of two dimensionless parameters governing the elastic problem, namely the shear ratio μ_t/μ_b and the aspect ratio H_t/H_b.

4.6.2.2 Solution Using the Stroh Formalism

Let us now solve the incremental boundary value problem by recasting the governing equations and by using the so-called *S*troh formalism, originally developed by Stroh [109] for steady state elastic problems. Let the traction vector in the direction $\mathbf{e}_z$ be:

$$\mathbf{t} = \hat{\mathbf{S}}_0^T \mathbf{e}_z = [\hat{S}_{0zx}, \hat{S}_{0zz}]^T. \tag{4.150}$$

In a Cartesian reference system, we can write:

$$\mathbf{t} = \tilde{\mathbf{A}}_{zz}\mathbf{u}_{,z} + \tilde{\mathbf{A}}_{zx}^T\mathbf{u}_{,x} - q\,\mathbf{e}_z \tag{4.151}$$

$$\mathbf{t}_x = \hat{\mathbf{S}}_0^T \mathbf{e}_x = \tilde{\mathbf{A}}_{zx}\mathbf{u}_{,z} + \tilde{\mathbf{A}}_{xx}\mathbf{u}_{,x} - q\,\mathbf{e}_x, \tag{4.152}$$

where the following matrices have been introduced:

$$\begin{aligned} &\tilde{\mathbf{A}}_{xx} = \mathscr{A}^1_{0zjzl} + p\,\mathbf{e}_z \otimes \mathbf{e}_z, \quad \tilde{\mathbf{A}}_{zz} = \mathscr{A}^1_{0xjxl} + p\,\mathbf{e}_x \otimes \mathbf{e}_x, \\ &\tilde{\mathbf{A}}_{zx} = \mathscr{A}^1_{0zjxl} + p\,\mathbf{e}_z \otimes \mathbf{e}_x. \end{aligned} \tag{4.153}$$

The incompressibility condition in Eq. (4.134) rewrites:

$$\mathbf{e}_z \cdot \mathbf{u}_{,z} + \mathbf{e}_x \cdot \mathbf{u}_{,x} = 0. \tag{4.154}$$

Substituting Eqs. (4.151) and (4.152) into Eq. (4.130), the equilibrium equations rewrite:

$$\mathbf{t}_{,z} + \tilde{\mathbf{A}}_{zx}\mathbf{u}_{,zx} + \tilde{\mathbf{A}}_{xx}\mathbf{u}_{,xx} - q_{,x}\,\mathbf{e}_x = \mathbf{0}. \tag{4.155}$$

Now, $\mathbf{u}_{,z}$ can be calculated from Eq. (4.151) as:

$$\mathbf{u}_{,z} = \tilde{\mathbf{A}}_{zz}^{-1}(\mathbf{t} - \tilde{\mathbf{A}}_{zx}^T\mathbf{u}_{,x} + q\,\mathbf{e}_z) \tag{4.156}$$

Deriving Eq. (4.156), it follows:

$$\mathbf{u}_{,zx} = \tilde{\mathbf{A}}_{zz}^{-1}(\mathbf{t}_{,x} - \tilde{\mathbf{A}}_{zx}^T\mathbf{u}_{,xx} + q_{,x}\,\mathbf{e}_z) \tag{4.157}$$

Substituting Eq. (4.157) into Eq. (4.155), the equilibrium equations in Eq. (4.155) rewrite:

$$\begin{aligned}\mathbf{t}_{,z} &+\tilde{\mathbf{A}}_{zx}\tilde{\mathbf{A}}_{zz}^{-1}(\mathbf{t}_{,x}-\tilde{\mathbf{A}}_{zx}^{T}\mathbf{u}_{,xx}+q_{,x}\,\mathbf{e}_z)+\\ &+\tilde{\mathbf{A}}_{xx}\mathbf{u}_{,xx}-q_{,x}\,\mathbf{e}_x=\mathbf{0}.\end{aligned} \tag{4.158}$$

Now, the aim is to eliminate the unknown q from Eq. (4.158).

Therefore, the scalar product $\mathbf{e}_1\cdot$ is applied to Eq. (4.156). Then, using the incompressibility condition in Eq. (4.154) the term $\mathbf{e}_1\cdot\mathbf{u}_{,1}$ can be eliminated and after some rearrangements the expression for q can be derived as follows:

$$q=\xi\left(\mathbf{e}_1\cdot\tilde{\mathbf{A}}_{zz}^{-1}\tilde{\mathbf{A}}_{zx}^{T}\mathbf{u}_{,x}-\mathbf{e}_x\cdot\mathbf{u}_{,x}-\mathbf{e}_z\cdot\tilde{\mathbf{A}}_{zz}^{-1}\mathbf{t}\right), \tag{4.159}$$

where $\xi=1/(\mathbf{e}_z\cdot\tilde{\mathbf{A}}_{zz}^{-1}\mathbf{e}_z)$.

Assuming that separation of variables holds, wee search for solutions a in the form:

$$\begin{aligned}\mathbf{u}&=\mathbf{U}(z)\;e^{ikx}\\ \mathbf{t}&=\mathbf{S}(z)\;e^{ikx},\end{aligned} \tag{4.160}$$

where k is the wavenumber in the x direction, i is the imaginary unit and $\mathbf{U}(z)$, $\mathbf{S}(z)$ are the amplitude of the incremental displacement and traction vectors, respectively. Using Eqs. (4.159)–(4.160), (4.156) and (4.158) rewrite:

$$\begin{aligned}\frac{d}{dz}\mathbf{U}(z)=&-i\left\{\tilde{\mathbf{A}}_{zz}^{-1}\left[\tilde{\mathbf{A}}_{zx}^{T}(k)+\xi\mathbf{e}_z\otimes(k\boldsymbol{\alpha})\right]\right\}\mathbf{U}(z)+\\ &-i\left\{\tilde{\mathbf{A}}_{zz}^{-1}-\xi\mathbf{e}_z\otimes\mathbf{e}_z\tilde{\mathbf{A}}_{zz}^{-1}\right\}(i\mathbf{S}(z))\end{aligned} \tag{4.161}$$

$$\begin{aligned}\frac{d}{dz}(i\mathbf{S}(z))=&\,i\left\{-k^2\left[\tilde{\mathbf{A}}_{zx}\tilde{\mathbf{A}}_{zz}^{-1}\tilde{\mathbf{A}}_{zx}^{T}-\tilde{\mathbf{A}}_{xx}-\xi\boldsymbol{\alpha}\otimes\boldsymbol{\alpha}\right]\right\}\mathbf{U}(z)+\\ &-i\left\{\left[\tilde{\mathbf{A}}_{zx}(k)+\xi k\boldsymbol{\alpha}\otimes\mathbf{e}_z\right]\tilde{\mathbf{A}}_{zz}^{-1}\right\}(i\mathbf{S}(z))\end{aligned} \tag{4.162}$$

respectively, where $\boldsymbol{\alpha}=(\mathbf{e}_x-\tilde{\mathbf{A}}_{zx}\tilde{\mathbf{A}}_{zz}^{-1}\mathbf{e}_z)$. Equivalently, we can use the compact form:

$$\frac{d}{dz}\boldsymbol{\eta}(z)=i\mathbf{G}\boldsymbol{\eta}(z)\qquad\text{with}\qquad\boldsymbol{\eta}(z)=\begin{bmatrix}\mathbf{U}(z)\\ i\mathbf{S}(z)\end{bmatrix} \tag{4.163}$$

where the vector $\boldsymbol{\eta}(z)$ is the six-component displacement-traction vector and $\mathbf{G}$ is the so-called Stroh matrix, having the following block-type structure:

$$\mathbf{G} = \begin{bmatrix} \mathbf{G}_1 & \mathbf{G}_2 \\ \mathbf{G}_3 & \mathbf{G}_4 \end{bmatrix} \tag{4.164}$$

Therefore, the blocks which constitute the Stroh matrix in the case of incompressible materials take the form:

$$\begin{aligned} \mathbf{G}_1 &= -\tilde{\mathbf{A}}_{zz}^{-1}\left[\tilde{\mathbf{A}}_{zx}^{T}(k) + \xi \mathbf{e}_z \otimes (k\boldsymbol{\alpha})\right] \\ \mathbf{G}_2 &= -\tilde{\mathbf{A}}_{zz}^{-1} + \xi \mathbf{e}_z \otimes \mathbf{e}_z \tilde{\mathbf{A}}_{zz}^{-1} \\ \mathbf{G}_3 &= -k^2\left[\tilde{\mathbf{A}}_{zx}\tilde{\mathbf{A}}_{zz}^{-1}\tilde{\mathbf{A}}_{zx}^{T} - \tilde{\mathbf{A}}_{xx} - \xi \boldsymbol{\alpha} \otimes \boldsymbol{\alpha}\right] \\ \mathbf{G}_4 &= \mathbf{G}_1^{+}, \end{aligned} \tag{4.165}$$

In particular, the hermitian property $\mathbf{G}_4 = \mathbf{G}_1^{+}$ is crucial for the Stroh formalism to provide an optimal form in a great variety of elasticity problems. Optimal here is used in the sense that an efficient numerical procedure can be implemented in order to solve the incremental problem [21, 33, 34]. The hermitian property, also implies that the matrix $i\hat{\mathbf{I}}\mathbf{G}$ is symmetric, where $\hat{\mathbf{I}}$ is defined as the block matrix with 0-blocks on the diagonal and identity blocks elsewhere. This property can be used to derive the orthogonality and closure relations which provide useful information on the nature of the blocks of the Stroh matrix [112]. Furthermore, the hermitian property is a direct consequence of the Hamiltonian nature of the Stroh formalism. Indeed, every Hamiltonian system in which the variables $\mathbf{u}$ and $\mathbf{t}$ are work conjugates owns this fundamental property [42, 43].

In the case of the incremental problem for the growing bilayer, the blocks of the Stroh matrix simplify as follows:

$$\begin{aligned} \mathbf{G}_1 &= \begin{bmatrix} 0 & -m \\ -m & 0 \end{bmatrix}; \qquad \mathbf{G}_2 = \begin{bmatrix} -1/(\mu\lambda_z^2) & 0 \\ 0 & 0 \end{bmatrix}; \\ \mathbf{G}_3 &= \begin{bmatrix} k^2\mu(\lambda_x^2 + 3\lambda_z^2) & 0 \\ 0 & k^2\mu(\lambda_x^2 - \lambda_z^2) \end{bmatrix}. \end{aligned} \tag{4.166}$$

The Stroh formalism allows to transform the boundary value problem into a first-order system of ordinary differential equation. In particular, its solution is given in terms of displacements as [32]:

$$\boldsymbol{\eta}_i(z) = \sum_{j=1}^{4} a_{ji}\boldsymbol{\xi}_j e^{\beta_j z}; \qquad \text{with } i = (t, b) \tag{4.167}$$

where $\beta = \{-k, k, -k\lambda_x/\lambda_z, k\lambda_x/\lambda_z\}$ and $\boldsymbol{\xi}_j$ are the eigenvalues and the $j-th$ eigenvector ($j = 1, 2, 3, 4$) of $\mathbf{G}$, respectively. Thus, Eq. (4.167) corresponds to the previous result in Eq. (4.78) found with the stream function approach. Similarly, it is possible to recast the eight boundary conditions in the form of Eq. (4.143), and obtain the dispersion relation expressed in Eq. (4.149).

4.6.2.3 Theoretical Results: Critical Growth Threshold and Pattern Selection

We implemented an iterative numerical scheme to solve the dispersion relation in Eq. (4.149) as a function of the marginal value $\epsilon = (1 - \lambda_x) = (g - 1)/g$ for each wavenumber $k = 2\pi n_x/L$, with n_x integer, at given values of the elastic ratio μ_t/μ_b and aspect ratio H_t/H_b. We identify the critical strain ϵ_{cr} as the highest marginally stable value associated to the critical wavelength k_{cr}, which will be considered in the following as a continuous function for the sake of graphical clarity.

In Fig. 4.12, we depict the corresponding critical threshold for the onset of a morphological transition for a growing bi-layered material with $H_b = 10H_t$ (blue curves) and $H_b = 20H_t$ (green curves) as a function of the elastic ratio μ_t/μ_b. In particular, we observe that if the top layer is stiffer, the critical strain and the corresponding wavenumber decrease for increasing μ_t/μ_b. Moreover, we find that the emerging pattern wavelength is of the order of the thickness of the top layer, whilst the results do not depend much on the aspect ration if $H_t << H_b$.

We also note that the marginally stable curve for $k_{cr}H_t$ has a singular behaviour for $\mu_t/\mu_b \to 1$ and $\mu_t/\mu_b \to 0$. Both cases represent the confined compression of a homogeneous slab, which is known to experience a surface instability at $k_{cr} \to \infty$, as first predicted for an elastic half-space by Biot [11]. In this case, the dispersion relation in Eq. (4.149) can be greatly simplified, and its marginally stable solution

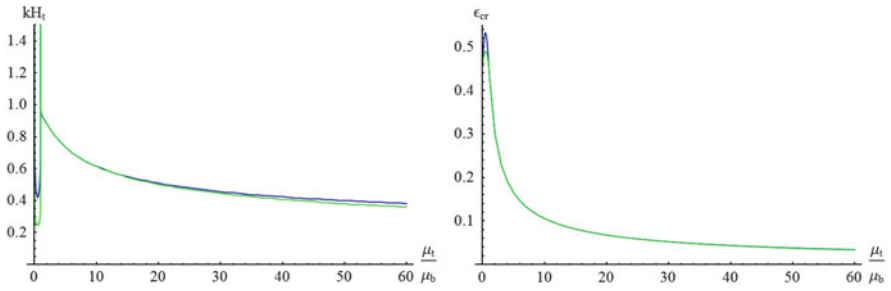

Fig. 4.12 Curves of the critical dimensionless wavenumber $k_{cr}H_t$ (*left*) and compressive strain $\epsilon_{cr} = (1 - \lambda_x) = (g - 1)/g$ (*right*) for a growing bi-layered material with $H_b = 10H_t$ (*blue curves*) and $H_b = 20H_t$ (*green curves*) as a function of the elastic ratio μ_t/μ_b

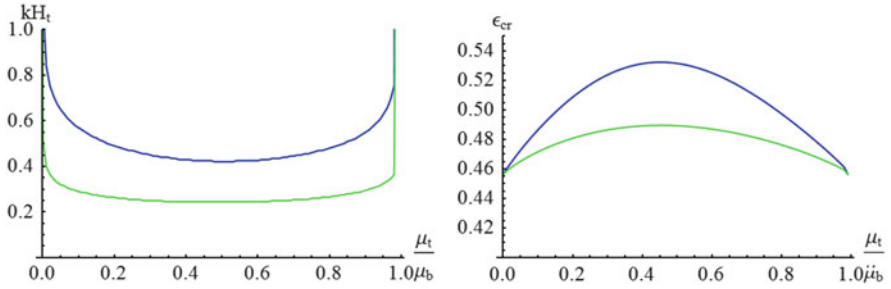

Fig. 4.13 Zoom of the marginally stable curves for the critical dimensionless wavenumber $k_{cr}H_t$ (*left*) and compressive strain $\epsilon_{cr} = (1 - \lambda_x) = (g - 1)/g$ (*right*) for a growing bi-layered material with $H_b = 10H_t$ (*blue curves*) and $H_b = 20H_t$ (*green curves*) as a function of the elastic ratio μ_t/μ_b

occurs at $k_{cr} \to \infty$ for the real root of $(\lambda_x^6 + \lambda_x^4 + 3\lambda_x^2 - 1) = 0$, being:

$$(\lambda_x)_{cr} = \frac{1}{3}\left(\sqrt[3]{17 + 3\sqrt{33}} - \frac{2}{\sqrt[3]{17 + 3\sqrt{33}}} - 1\right) \cong 0.5436. \tag{4.168}$$

Eq. (4.168) implies a critical growth ratio of $g_{cr} \cong 1.8393$ or a critical strain of $\epsilon_{cr} \cong 0.4563$, as depicted in greated detail in Fig. 4.13.

It is also possible to show that the critical wavenumbers in such singular branches have a logarithmic dependence on the surface stiffening effect given by the top layer [9, 20].

From an energetic viewpoint, the onset of a morphological transition is driven by a competition between the two bulk elastic energies, through a complex interplay between geometric and elastic parameters. The linear stability analysis allows to identify the critical threshold of such a bifurcation, but it cannot describe its evolution beyond this threshold value. For this purpose, it would be necessary to solve the incremental problem beyond the linear approximation. Although out of the scopes of this chapter, we highlight that a weakly nonlinear stability analysis could be performed using a multiple scale expansion [19]. Accordingly, it is possible to derive a compatibility condition by imposing the vanishing of secular terms in higher-order elastic solutions, thus unveiling the nature of the elastic bifurcation [22]. For example, instead of a substrate of finite thickness we could consider a half space, i.e. we could assume $H_b << H_t$. In this case, the elastic bifurcation would be supercritical if $\mu_t/\mu_b > 1.74$ and subcritical if $\mu_t/\mu_b < 1.74$. In the subcritical regime for $\mu_t \to \mu_b$ there exists a localized solution that arises as the limit of modulated periodic solutions with increasingly longer and longer decaying tails. The evolution of each modulated periodic solution can be followed as μ_t/μ_b

decreases, finding that there exists a critical value at which the deformation gradient develops a discontinuity and the solution becomes a static shock, highlighting the spontaneous formation of a crease [45].

4.6.2.4 Numerical Results: Post-buckling Behavior

In order to explore the behavior of the system in the post-critical regime, we implemented numerical simulations using a user defined finite element (FE) code implemented in Matlab (The MathWorks, Inc., Natick, Massachusetts, United States; version 2013a). The geometrical model is composed by two layers, a top layer superposed on a substrate with initial thicknesses H_t and H_b, respectively. The bi-layer has initial width L_x. Since the value of k is predicted by the linear stability analysis, L_x can be calculated at n_x arbitrarily fixed. The two layers are modeled as incompressible and hyperelastic materials. A neo-Hookean model is used, and boundary conditions of zero-displacement at the bottom of the bi-layer and zero-horizontal displacement at the side edges are imposed.

We model the growth using a pseudo-dynamic method similar to the one classically implemented for thermal dilatation. We adopt the following linear evolution law:

$$g(t) = g(t_{n-1})dt, \tag{4.169}$$

with $g(0) = 1$ and where t is the time and $dt = (t_n - t_{n-1})$ is the time increment. An *ad hoc* time adaptive scheme is implemented, where the time step automatically decreases by 50% once the number of Newton iterations exceeds seven, and increases the time step size by 10% otherwise, as done in [91]. The initial, the minimum and the maximum time steps are manually set to 10^2, 10^3 and 10^2, respectively. A sinusoidal perturbation is introduced as a small imperfection in the initial mesh, with a small amplitude of $0.005H_t$ and the critical wavenumber predicted by the linear stability analysis.

We used linear elements with 4 integration points, building the mesh with 400 elements in the x-direction and 150 elements in the z-direction, respectively 100 elements for the substrate and 50 for the film.

Validation of the Numerical Code Against the Theoretical Results First, we validate the FE code by comparing the critical strain values in numerical simulation with the theoretical predictions from the linear stability analysis. The criterion for such a comparison is based on the energy considerations, since we expect that the selected pattern will minimizes the total elastic energy of the system. Before the onset of the pattern transition, the solution with the minimal elastic energy is the basic homogeneous deformation. Due to the spatial incompatibility of the growth process, residual stresses accumulate until a marginally stable growth value

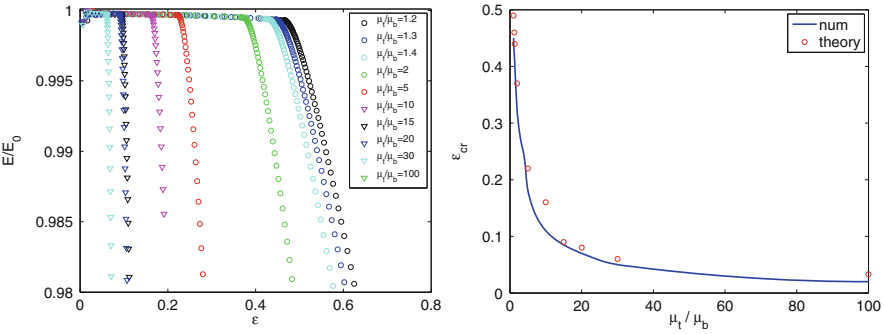

Fig. 4.14 *Left*: Ratio between the total current elastic energy in the numerical simulations E and the elastic energy of the basic homogeneous solution E_0 versus the axial strain $\epsilon = (1 - \lambda_x)$ at different values of the elastic ratio μ_t/μ_b . *Right*: Comparison between the marginally stable thresholds in numerical FE simulations (*circles*) and the theoretical predictions (*solid line*) from the linear stability analysis. We set $H_b = 10H_t$ in all the simulations

is reached. At this point, the system bifurcates into a solution with a lower energy than the one associated with the basic homogeneous solution.

Here we identify the critical strain as the value of $\epsilon_{cr} = (1 - \lambda_x) = (g - 1)/g$ at which the ratio E/E_0 between the total current elastic energy and the basic elastic energy has decreased by more than 1% of its initial value. The corresponding energy plots are depicted in Fig. 4.14(left) at different values of the elastic ratio μ_t/μ_b.

In particular, Fig. 4.14(right) shows that the critical values resulting from the numerical simulations are in good agreement with the corresponding theoretical predictions, thus validating the numerical code.

FE Simulations of the Post-critical Regime Once the FE code has been validated, we performed numerical simulations in order to investigate the nonlinear pattern evolution in the post-critical regime. We depict the emerging morphology of the growing bi-layer for $\mu_t/\mu_b = 30{,}100$ in Figs. 4.15 and 4.16 respectively.

Before the critical point is reached, the bi-layered material remains flat. As soon as the compression reaches the critical value, an undulated pattern develops at the top surface, forming wrinkles with wavenumber k_{cr}. The depth of the wrinkles increases whilst increasing the growth, which increases the axial compression. In both cases we set $H_b = 10H_t$. The critical values for the wavenumber and the compression given by the linear stability analysis are $k^{cr} = 0.4$, $\epsilon^{cr} = 0.05$ for $\mu_t/\mu_b = 30$, and $k^{cr} = 0.23$, $\epsilon^{cr} = 0.02$ for $\mu_t/\mu_b = 100$.

In practice, we observe that the surface undulation rapidly grows to form a stable fold, whose amplitude increases whilst increasing the growth ratio. The amplitude of the emerging surface fold is depicted in Fig. 4.17 for different values of the elastic ratio μ_t/μ_b. In particular, we show that for $\mu_t >> \mu_b$ the amplitude grows continuously, thus highlighting the existence of a supercritical bifurcation, as predicted for the coated elastic half-space.

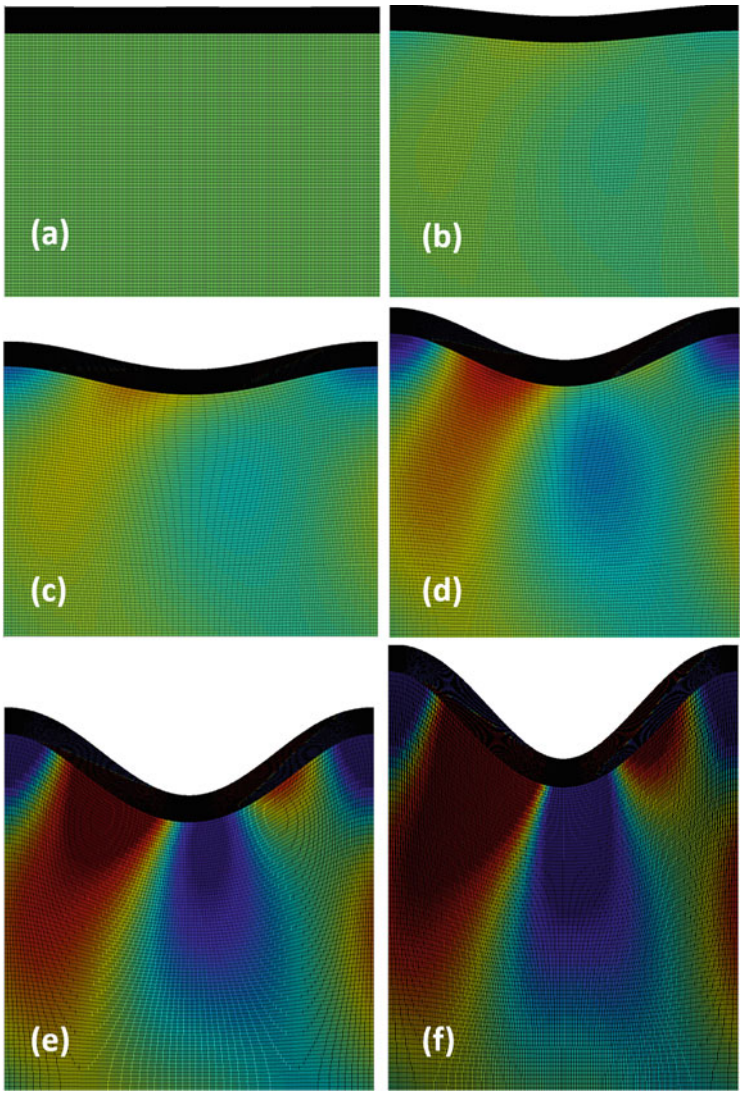

Fig. 4.15 Morphological evolution of the bi-layered material at different growth ratios. We set $\mu_t/\mu_b = 30$, $H_b = 10H_t$, $n_x = 1$, for which the linear stability analysis predicts $k^{cr} = 0.4$, $\epsilon^{cr} = 0.05$. The snapshots are taken for $\epsilon = (g-1)/g = 0$ (**a**), 0.063004 (**b**), 0.075409 (**c**), 0.108321 (**d**), 0.165309 (**e**), 0.283784 (**f**)

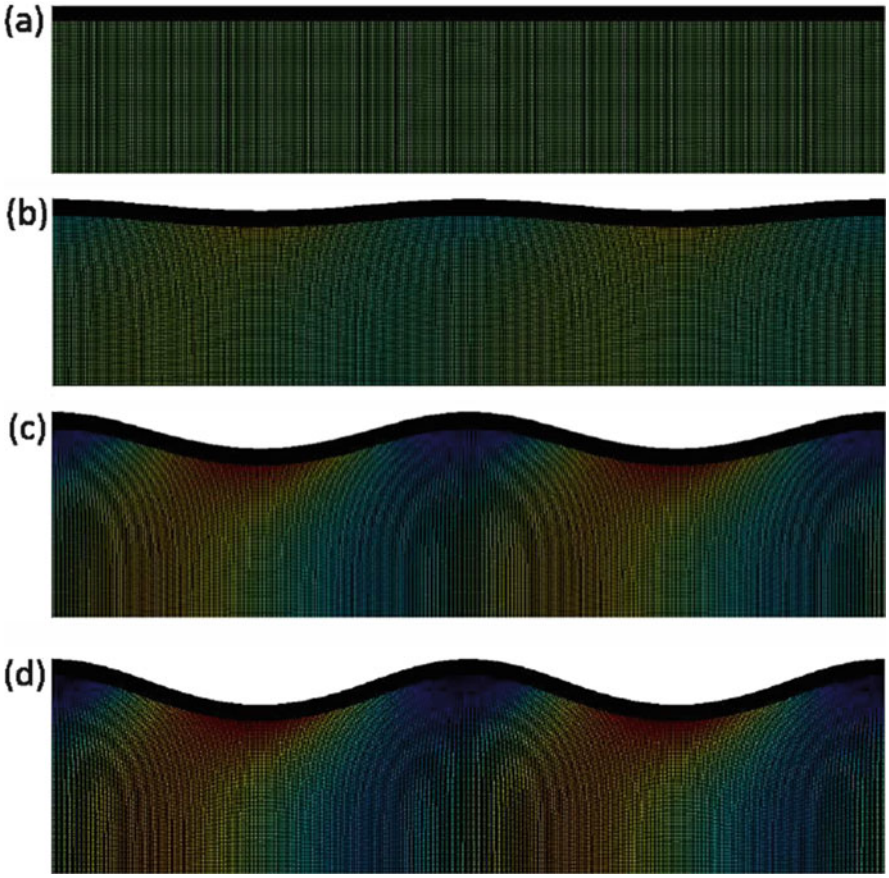

Fig. 4.16 Morphological evolution of the bi-layered material at different growth ratios. We set $\mu_t/\mu_b = 100$, $H_b = 10H_t$, $n_x = 2$, for which the linear stability analysis predicts $k^{cr} = 0.23$, $\epsilon^{cr} = 0.02$. The snapshots are taken for $\epsilon = (g-1)/g = 0$ (**a**), 0.033173 (**b**), 0.042321 (**c**), 0.059083 (**d**)

It is important to highlight that we used linear elements for illustrative purposes. Nonetheless, it is known that they do not allow to capture the occurrence of secondary bifurcations, which have been observed in bi-layered materials, possibly leading to the emergence of more complex patterns characterized by sub-harmonic resonances [14]. Although out of the scopes of this work, we remind that secondary bifurcations can be studied using analytic perturbation techniques [44] or more advanced numerical tools [80].

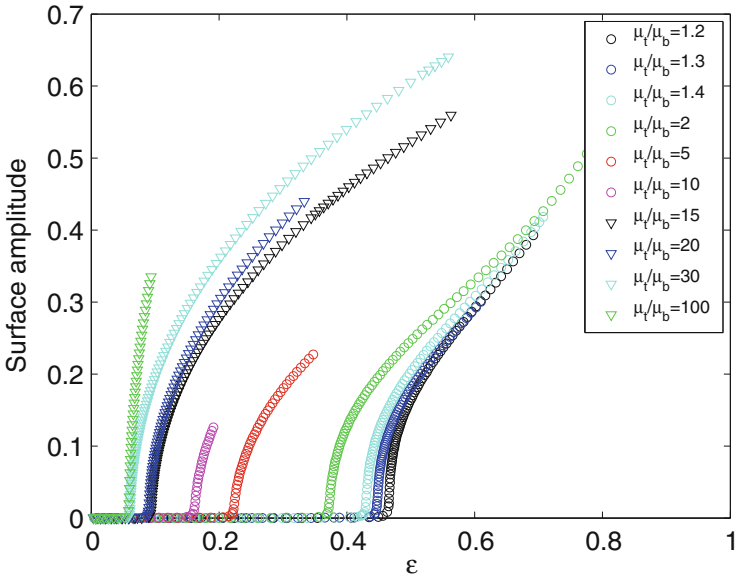

Fig. 4.17 Amplitude of the surface folds in numerical simulations for different values of the elastic ratio μ_t/μ_b at $H_b = 10H_t$

4.7 Concluding Remarks

In this chapter, we have introduced a continuous chemo-mechanical approach of morphogenesis, deriving the balance principles and evolution laws for both volumetric and interfacial processes. The proposed theory has been applied to the study of pattern formation for either a fluid-like and a solid-like biological system model, using both theoretical methods and simulation tools. Nonetheless, it should be reminded that biological materials have a wide range of rheological properties in between such limiting ideal behaviors [114]. Furthermore, it has been recently highlighted that morphogenetic processes may involve microstructural rearrangement processes, such cell duplication and/or migration, which provoke fluid-like stress relaxation phenomena up to the timescale of days [95, 96]. Thus, there will be the necessity to integrate the continuous approach with methods of individual cell-based models in order to capture the microscopic processes at the grain cell scale [35].

Finally, further modelling work should be done to investigate the role of morphogens in the regulation of growth, shape and size. On one hand, their local concentration can trigger an increase of mass resulting from a random cellular proliferation. Preferred orientation may exists in cellular division as well as competition between different cell populations. On the other hand, further spatial orchestration is needed in order to transform random proliferations into a uniform growth, which must ultimately ceases as the correct size is reached. The

control of shape can therefore depend both on cell number and on overall size, suggesting that the spatial gradient of morphogens can provide cells a dimension-sensing mechanism. This early vision was also supported by the discovery that cells have the ability to measure gradients comparing their own signalling level with those of their neighbours through specific regulatory pathways [124]. Nevertheless other interpretations are also possible. In fact, cells can change relative position undergoing a rearrangement process (e.g. during intercalation), implying that they are able to remodel their adhesive contacts making use of a mechanical feedback with their environment to adjust their position [76]. Giving a practical example, the stop signal for growth, thus determining the final size, could be triggered by a morphogen gradient level below a minimal threshold, as well as by a critical increase in tissue compression, causing a progressive inhibition of growth [5]. In summary, the orchestration of shape and size in the biological realm is more likely based on a combination of mechanical and biochemical feedbacks. Despite of the explosive rate of new knowledge on the biochemistry of morphogenesis, a major challenge for mathematical modeling is to understand the local coordination between mechanical properties of the cells and the morphogenetic signals for the global orchestration of a macroscopic shape [108].

Acknowledgements We are thankful to Chiara Giverso for performing the numerical simulations shown in Fig. 4.8, and to Ellen Kuhl for sharing the numerical FE code used in Sect. 4.6.2.4. Partial funding by the European Community grant ERG-256605, FP7 program, and by the "Start-up Packages and PhD Program" project, co-funded by Regione Lombardia through the "Fondo per lo sviluppo e la coesione 2007-2013", formerly FAS program, is gratefully acknowledged by the corresponding author.

References

1. H.B. Adelmann, M. Malpighi, et al., *Marcello Malpighi and the Evolution Of Embryology* (Cornell University Press, New York, 1966)
2. P. Alberch, Developmental constraints in evolutionary processes, in *Evolution and Development* (Springer, New York, 1982), pp. 313–332
3. J.O. Almen, P.H. Black, *Residual Stresses and Fatigue in Metals* (McGraw-Hill, New York, 1963)
4. D. Ambrosi, F. Mollica, On the mechanics of a growing tumor. Int. J. Eng. Sci. **40**(12), 1297–1316 (2002)
5. D. Ambrosi, V. Pettinati, P. Ciarletta, Active stress as a local regulator of global size in morphogenesis. Int. J. Non-Linear Mech. **75**, 5–14 (2015)
6. D. Balme, Aristotle, in *History of Animals. Books VII–X* (Harvard University Press, Cambridge, 1991)
7. J.B. Bard, J. Bard, *Morphogenesis: the Cellular and Molecular Processes of Developmental Anatomy*, vol. 23 (Cambridge University Press, Cambridge, 1992)
8. L. Beloussov, The interplay of active forces and passive mechanical stresses in animal morphogenesis, in *Biomechanics of Active Movement and Division of Cells* (Springer, New York, 1994), pp. 131–180
9. M. Ben Amar, P. Ciarletta, Swelling instability of surface-attached gels as a model of soft tissue growth under geometric constraints. J. Mech. Phys. Solids **58**(7), 935–954 (2010)

10. C. Bernard, É. Alglave, *Leçons sur les propriétés des tissus vivants* (Baillière, Paris, 1866)
11. M. Biot, Surface instability of rubber in compression. Appl. Sci. Res. Sec. A **12**(2), 168–182 (1963)
12. A. Boettiger, B. Ermentrout, G. Oster, The neural origins of shell structure and pattern in aquatic mollusks. Proc. Natl. Acad. Sci. **106**(16), 6837–6842 (2009)
13. E. Buckingham, On physically similar systems; illustrations of the use of dimensional equations. Phys. Rev. **4**(4), 345–376 (1914)
14. S. Budday, E. Kuhl, J.W. Hutchinson, Period-doubling and period-tripling in growing bilayered systems. Philos. Mag. (ahead-of-print), 1–17 (2015)
15. D.T. Butcher, T. Alliston, V.M. Weaver, A tense situation: forcing tumour progression. Nat. Rev. Cancer **9**(2), 108–122 (2009)
16. Z. Cai, Y. Fu, On the imperfection sensitivity of a coated elastic half-space, in *Proceedings of the Royal Society of London A: Mathematical, Physical and Engineering Sciences*, vol. 455 (The Royal Society, London, 1999), pp. 3285–3309
17. C. Chuong, Y. Fung, Residual stress in arteries, in *Frontiers in Biomechanics* (Springer, New York, 1986), pp. 117–129
18. P. Ciarletta, Free boundary morphogenesis in living matter. Eur. Biophys. J. **41**(8), 681–686 (2012)
19. P. Ciarletta, Wrinkle-to-fold transition in soft layers under equi-biaxial strain: a weakly nonlinear analysis. J. Mech. Phys. Solids **73**, 118–133 (2014)
20. P. Ciarletta, M.B. Amar, Papillary networks in the dermal–epidermal junction of skin: a biomechanical model. Mech. Res. Commun. **42**, 68–76 (2012)
21. P. Ciarletta, M. Destrade, Torsion instability of soft solid cylinders. IMA J. Appl. Math. **79**(5), 804–819 (2014)
22. P. Ciarletta, Y. Fu, A semi-analytical approach to biot instability in a growing layer: strain gradient correction, weakly non-linear analysis and imperfection sensitivity. Int. J. Non-Linear Mech. **75**, 38-45 (2015)
23. P. Ciarletta, G.A. Maugin, Elements of a finite strain-gradient thermomechanical theory for material growth and remodeling. Int. J. Non-Linear Mech. **46**(10), 1341–1346 (2011)
24. P. Ciarletta, D. Ambrosi, G. Maugin, Configurational forces for growth and shape regulations in morphogenesis. Bull. Pol. Acad. Sci.: Tech. Sci. **60**(2), 253–257 (2012)
25. P. Ciarletta, D. Ambrosi, G. Maugin, Mass transport in morphogenetic processes: a second gradient theory for volumetric growth and material remodeling. J. Mech. Phys. Solids **60**(3), 432–450 (2012)
26. P. Ciarletta, L. Preziosi, G. Maugin, Thermo-mechanics of growth and mass transfer: morphogenesis of seashells. Comput. Methods Biomech. Biomed. Eng. **15**(sup1), 110–112 (2012)
27. P. Ciarletta, L. Preziosi, G. Maugin, Mechanobiology of interfacial growth. J. Mech. Phys. Solids **61**(3), 852–872 (2013)
28. P. Ciarletta, V. Balbi, E. Kuhl, Pattern selection in growing tubular tissues. Phys. Rev. Lett. **113**(24), 248101 (2014)
29. C. Cohen, Gould et d'arcy thompson. C.R. Palevol **3**(5), 421–431 (2004)
30. B.D. Coleman, W. Noll, The thermodynamics of elastic materials with heat conduction and viscosity. Arch. Ration. Mech. Anal. **13**(1), 167–178 (1963)
31. J. Davies, *Mechanisms of Morphogenesis* (Academic, Amsterdam, 2013)
32. M. Destrade, M. Gilchrist, D. Prikazchikov, G. Saccomandi, Surface instability of sheared soft tissues. J. Biomech. Eng. **130**(6), 061007 (2008)
33. M. Destrade, A.N. Annaidh, C.D. Coman, Bending instabilities of soft biological tissues. Int. J. Solids Struct. **46**(25), 4322–4330 (2009)
34. M. Destrade, J.G. Murphy, R.W. Ogden, On deforming a sector of a circular cylindrical tube into an intact tube: existence, uniqueness, and stability. Int. J. Eng. Sci. **48**(11), 1212–1224 (2010)

35. D. Drasdo, S. Hoehme, M. Block, On the role of physics in the growth and pattern formation of multi-cellular systems: what can we learn from individual-cell based models. J. Stat. Phys. **128**(1–2), 287–345 (2007)
36. W. Driever, C. Nüsslein-Volhard, The bicoid protein determines position in the drosophila embryo in a concentration-dependent manner. Cell **54**(1), 95–104 (1988)
37. C.C. DuFort, M.J. Paszek, V.M. Weaver, Balancing forces: architectural control of mechanotransduction. Nat. Rev. Mol. Cell Biol. **12**(5), 308–319 (2011)
38. G.M. Edelman, Morphoregulatory molecules. Biochemistry **27**(10), 3533–3543 (1988)
39. M. Epstein, A. Goriely, Self-diffusion in remodeling and growth. Z. Angew. Math. Phys. **63**(2), 339–355 (2012)
40. M. Epstein, G.A. Maugin, Thermomechanics of volumetric growth in uniform bodies. Int. J. Plast. **16**(7), 951–978 (2000)
41. J. Flavin, Surface waves in pre-stressed mooney material. Q. J. Mech. Appl. Math. **16**(4), 441–449 (1963)
42. Y. Fu, Existence and uniqueness of edge waves in a generally anisotropic elastic plate. Q. J. Mech. Appl. Math. **56**(4), 605–616 (2003)
43. Y. Fu, D. Brookes, Edge waves in asymmetrically laminated plates. J. Mech. Phys. Solids **54**(1), 1–21 (2006)
44. Y. Fu, Z. Cai, An asymptotic analysis of the period-doubling secondary bifurcation in a film/substrate bilayer. SIAM J. Appl. Math. **75**(6), 2381–2395 (2015)
45. Y. Fu, P. Ciarletta, Buckling of a coated elastic half-space when the coating and substrate have similar material properties, in *Proceedings of the Royal Society of London A: Mathematical, Physical and Engineering Sciences*, vol. 471 (The Royal Society, London, 2015), pp. 20140979
46. Y.-C. Fung, *Biomechanics: Mechanical Properties of Living Tissues* (Springer Science and Business Media, New York, 2013)
47. G. Galilei, Discorsi e Dimostrazioni Matematiche Intorno a Due Nuove Scienze (Elzeviro, 1638)
48. A. Gierer, H. Meinhardt, A theory of biological pattern formation. Kybernetik **12**(1), 30–39 (1972)
49. C. Giverso, M. Verani, P. Ciarletta, Branching instability in expanding bacterial colonies. J. R. Soc. Interface **12**(104), 20141290 (2015)
50. A. Goriely, M.B. Amar, On the definition and modeling of incremental, cumulative, and continuous growth laws in morphoelasticity. Biomech. Model. Mechanobiol. **6**(5), 289–296 (2007)
51. S.J. Gould, *Ontogeny and Phylogeny* (Harvard University Press, Cambridge, 1977)
52. J.B. Green, J. Sharpe, Positional information and reaction-diffusion: two big ideas in developmental biology combine. Development **142**(7), 1203–1211 (2015)
53. H. Gregersen, G. Kassab, Y. Fung, Review: the zero-stress state of the gastrointestinal tract. Dig. Dis. Sci. **45**(12), 2271–2281 (2000)
54. E. Guyon, J.-P. Hulin, L. Petit, P.G. de Gennes, *Hydrodynamique Physique* (EDP Sciences Les Ulis, France, 2001)
55. E.H. Haeckel, *Generelle Morphologie der Organismen allgemeine Grundzuge der organischen Formen-Wissenschaft, mechanisch begrundet durch die von Charles Darwin reformirte Descendenz-Theorie von Ernst Haeckel: Allgemeine Entwickelungsgeschichte der Organismen kritische Grundzuge der mechanischen Wissenschaft von den entstehenden Formen der Organismen, begrundet durch die Descendenz-Theorie*, vol. 2 (Verlag von Georg Reimer, Berlin, 1866)
56. V. Hamburger, Wilhelm roux: visionary with a blind spot. J. Hist. Biol. **30**(2), 229–238 (1997)
57. H. Han, Y. Fung, Residual strains in porcine and canine trachea. J. Biomech. **24**(5), 307–315 (1991)
58. M.P. Harris, S. Williamson, J.F. Fallon, H. Meinhardt, R.O. Prum, Molecular evidence for an activator–inhibitor mechanism in development of embryonic feather branching. Proc. Natl. Acad. Sci. U. S. A. **102**(33), 1734–11739 (2005)

59. N. Hartsoeker, *Conjectures Physiques*, vol. 2 (H. Desbordes, Amsterdam, 1708)
60. W. Harvey, R. Willis, *The Works of William Harvey*, vol. 11 (Sydenham Society, London, 1847)
61. B.D. Hoffman, C. Grashoff, M.A. Schwartz, Dynamic molecular processes mediate cellular mechanotransduction. Nature **475**(7356), 316–323 (2011)
62. A. Hoger, On the residual stress possible in an elastic body with material symmetry. Arch. Ration. Mech. Anal. **88**(3), 271–289 (1985)
63. A. Hoger, On the determination of residual stress in an elastic body. J. Elast. **16**(3), 303–324 (1986)
64. A. Hoger, Residual stress in an elastic body: a theory for small strains and arbitrary rotations. J. Elast. **31**(1), 1–24 (1993)
65. A. Hoger, The elasticity tensor of a transversely isotropic hyperelastic material with residual stress. J. Elast. **42**(2), 115–132 (1996)
66. J. Howard, S.W. Grill, J.S. Bois, Turing's next steps: the mechanochemical basis of morphogenesis. Nat. Rev. Mol. Cell Biol. **12**(6), 392–398 (2011)
67. J.S. Huxley, *Problems of Relative Growth* (Methuen, London, 1932)
68. J. Jaeger, S. Surkova, M. Blagov, H. Janssens, D. Kosman, K.N. Kozlov, E. Myasnikova, C.E. Vanario-Alonso, M. Samsonova, D.H. Sharp, et al. Dynamic control of positional information in the early drosophila embryo. Nature **430**(6997), 368–371 (2004)
69. J. Jaeger, D. Irons, N. Monk, Regulative feedback in pattern formation: towards a general relativistic theory of positional information. Development **135**(19), 3175–3183 (2008)
70. B.E. Johnson, A. Hoger, The dependence of the elasticity tensor on residual stress. J. Elast. **33**(2), 145–165 (1993)
71. E.F. Keller, L.A. Segel, Model for chemotaxis. J. Theor. Biol. **30**(2), 225–234 (1971)
72. S. Kondo, R. Asai, A reaction-diffusion wave on the skin of the marine angelfish pomacanthus. Nature **376**(6543), 765–768 (1995)
73. S. Kondo, T. Miura, Reaction-diffusion model as a framework for understanding biological pattern formation. Science **329**(5999), 1616–1620 (2010)
74. E. Kröner, Allgemeine kontinuumstheorie der versetzungen und eigenspannungen. Arch. Ration. Mech. Anal. **4**(1), 273–334 (1959)
75. M. Kücken, A.C. Newell, Fingerprint formation. J. Theor. Biol. **235**(1), 71–83 (2005)
76. T. Lecuit, P.-F. Lenne, Cell surface mechanics and the control of cell shape, tissue patterns and morphogenesis. Nat. Rev. Mol. Cell Biol. **8**(8), 633–644 (2007)
77. T. Lecuit, P.-F. Lenne, E. Munro, Force generation, transmission, and integration during cell and tissue morphogenesis. Annu. Rev. Cell Dev. Biol. **27**, 157–184 (2011)
78. E.H. Lee, Elastic-plastic deformation at finite strains. J. Appl. Mech. **36**(1), 1–6 (1969)
79. H. Levine, S. Pamuk, B. Sleeman, M. Nilsen-Hamilton, Mathematical modeling of capillary formation and development in tumor angiogenesis: penetration into the stroma. Bull. Math. Biol. **63**(5), 801–863 (2001)
80. J. Liu, K. Bertoldi, Bloch wave approach for the analysis of sequential bifurcations in bilayer structures, in *Proceedings of the Royal Society A*, vol. 471 (The Royal Society, London, 2015), pp. 20150493
81. P.K. Maini, D.S. McElwain, D.I. Leavesley, Traveling wave model to interpret a wound-healing cell migration assay for human peritoneal mesothelial cells. Tissue Eng. **10**(3–4), 475–482 (2004)
82. G.A. Maugin, *Material Inhomogeneities in Elasticity*, vol. 3 (CRC Press, Boca Raton, 1993)
83. G.A. Maugin, Eshelby stress in elastoplasticity and ductile fracture. Int. J. Plast. **10**(4), 393–408 (1994)
84. G. Maugin, On inhomogeneity, growth, ageing and the dynamics of materials. J. Mech. Mater. Struct. **4**(4), 731–741 (2009)
85. G.A. Maugin, *Configurational Forces: Thermomechanics, Physics, Mathematics, and Numerics* (CRC Press, Boca Raton, 2010)
86. G. Maugin, C. Trimarco, Pseudomomentum and material forces in nonlinear elasticity: variational formulations and application to brittle fracture. Acta Mech. **94**(1–2), 1–28 (1992)

87. G. Mendel, Versuche über pflanzenhybriden, in *Verhandlungen des naturforschenden Vereines in Brunn 4: 3*, vol. 44 (1866)
88. W.W. Mullins, R. Sekerka, Stability of a planar interface during solidification of a dilute binary alloy. J. Appl. Phys. **35**(2), 444–451 (1964)
89. C.D. Murray, The physiological principle of minimum work: I. the vascular system and the cost of blood volume. Proc. Natl. Acad. Sci. U. S. A. **12**(3), 207 (1926)
90. R.W. Ogden, *Non-linear Elastic Deformations* (Courier Corporation, New York, 1997)
91. A. Papastavrou, P. Steinmann, E. Kuhl, On the mechanics of continua with boundary energies and growing surfaces. J. Mech. Phys. Solids **61**(6), 1446–1463 (2013)
92. S. Pivar, *On the Origin of Form: Evolution by Self-Organization* (North Atlantic Books, Berkeley, 2009)
93. M. Poujade, E. Grasland-Mongrain, A. Hertzog, J. Jouanneau, P. Chavrier, B. Ladoux, A. Buguin, P. Silberzan, Collective migration of an epithelial monolayer in response to a model wound. Proc. Natl. Acad. Sci. **104**(41), 15988–15993 (2007)
94. P. Prusinkiewicz, D.R. Fowler, H. Meinhardt, *The Algorithmic Beauty of Sea Shells* (Springer Science and Business Media, New York, 2009)
95. A. Puliafito, L. Hufnagel, P. Neveu, S. Streichan, A. Sigal, D.K. Fygenson, B.I. Shraiman, Collective and single cell behavior in epithelial contact inhibition. Proc. Natl. Acad. Sci. **109**(3), 739–744 (2012)
96. J. Ranft, M. Basan, J. Elgeti, J.-F. Joanny, J. Prost, F. Jülicher, Fluidization of tissues by cell division and apoptosis. Proc. Natl. Acad. Sci. **107**(49), 20863–20868 (2010)
97. E.K. Rodriguez, A. Hoger, A.D. McCulloch, Stress-dependent finite growth in soft elastic tissues. J. Biomech. **27**(4), 455–467 (1994)
98. A. Romano, *Thermomechanics of Phase Transitions in Classical Field Theory*, vol. 13 (World Scientific, Singapore, 1993)
99. W. Roux, Beiträge zur entwickelungsmechanik des embryo. Arch. Pathol. Anat. Physiol. klin. Med. **114**(2), 246–291 (1888)
100. P.G. Saffman, G. Taylor, The penetration of a fluid into a porous medium or hele-shaw cell containing a more viscous liquid, in *Proceedings of the Royal Society of London A: Mathematical, Physical and Engineering Sciences*, vol. 245 (The Royal Society, London, 1958), pp. 312–329
101. A.E. Shyer, T. Tallinen, N.L. Nerurkar, Z. Wei, E.S. Gil, D.L. Kaplan, C.J. Tabin, L. Mahadevan, Villification: how the gut gets its villi. Science **342**(6155), 212–218 (2013)
102. R. Skalak, Growth as a finite displacement field, in *Proceedings of the IUTAM Symposium on Finite Elasticity* (Springer, Dordrecht, 1982), pp. 347–355
103. R. Skalak, G. Dasgupta, M. Moss, E. Otten, P. Dullemeijer, H. Vilmann, Analytical description of growth. J. Theor. Biol. **94**(3), 555–577 (1982)
104. R. Skalak, S. Zargaryan, R.K. Jain, P.A. Netti, A. Hoger, Compatibility and the genesis of residual stress by volumetric growth. J. Math. Biol. **34**(8), 889–914 (1996)
105. R.S. Smith, S. Guyomarc'h, T. Mandel, D. Reinhardt, C. Kuhlemeier, P. Prusinkiewicz, A plausible model of phyllotaxis. Proc. Natl. Acad. Sci. U. S. A. **103**(5), 1301–1306 (2006)
106. H. Spemann, H. Mangold, Über induktion von embryonalanlagen durch implantation artfremder organisatoren. Dev. Genes Evol. **100**(3), 599–638 (1924)
107. M. Stähle, C. Veit, U. Bachfischer, K. Schierling, B. Skripczynski, A. Hall, P. Gierschik, K. Giehl, Mechanisms in lpa-induced tumor cell migration: critical role of phosphorylated erk. J. cell Sci. **116**(18), 3835–3846 (2003)
108. A. Stathopoulos, D. Iber, Studies of morphogens: keep calm and carry on. Development **140**(20), 4119–4124 (2013)
109. A. Stroh, Steady state problems in anisotropic elasticity. J. Math. Phys. **41**(2), 77–103 (1962)
110. L.A. Taber, Biomechanics of growth, remodeling, and morphogenesis. Evolution **490**, 6 (1995)
111. D.W. Thompson, *On Growth and Form* (Cambridge University Press, Cambridge, 1917)
112. T.C. Ting, C. Horgan, Anisotropic elasticity: theory and applications. J. Appl. Mech. **63**, 1056 (1996)

113. A.M. Turing, The chemical basis of morphogenesis. Philos. Trans. R. Soc. Lond. B Biol. Sci. **237**(641), 37–72 (1952)
114. C. Verdier, J. Etienne, A. Duperray, L. Preziosi, Review: rheological properties of biological materials. C. R. Phys. **10**(8), 790–811 (2009)
115. R.L.K. Virchow, *Cellular Pathology* (John Churchill, London, 1860)
116. C.H. Waddington, Canalization of development and the inheritance of acquired characters. Nature **150**(3811), 563–565 (1942)
117. J. Wolff, Das gesetz der transformation der knochen. DMW-Dtsch. Med. Wochenschr. **19**(47), 1222–1224 (1892)
118. L. Wolpert, Positional information and the spatial pattern of cellular differentiation. J. Theor. Biol. **25**(1), 1–47 (1969)
119. L. Wolpert, Positional information and patterning revisited. J. Theor. Biol. **269**(1), 359–365 (2011)
120. L. Wolpert, C. Tickle, A.M. Arias, *Principles of Development* (Oxford University Press, Oxford, 2015)
121. M.A. Wozniak, C.S. Chen, Mechanotransduction in development: a growing role for contractility. Nat. Rev. Mol. Cell Biol. **10**(1), 34–43 (2009)
122. S.R. Yu, M. Burkhardt, M. Nowak, J. Ries, Z. Petrášek, S. Scholpp, P. Schwille, M. Brand, Fgf8 morphogen gradient forms by a source-sink mechanism with freely diffusing molecules. Nature **461**(7263), 533–536 (2009)
123. E.A. Zamir, L.A. Taber, Material properties and residual stress in the stage 12 chick heart during cardiac looping. J. Biomech. Eng. **126**(6), 823–830 (2004)
124. A.J. Zhu, M.P. Scott, Incredible journey: how do developmental signals travel through tissue? Genes Dev. **18**(24), 2985–2997 (2004)

Chapter 5
Multiscale Computational Modelling and Analysis of Cancer Invasion

Dumitru Trucu, Pia Domschke, Alf Gerisch, and Mark A.J. Chaplain

Abstract Recognised as a key stage in cancer growth and spread in the human body, the cancer cell invasion process is crucial for metastatic spread and the subsequent development of secondary cancers. Tissue scale proliferation and migration in conjunction with a pallet of arising cell-scale dynamics including altered adhesion and secretion of matrix degrading enzymes enable the cancer cells to actively spread locally into the surrounding tissue. This biological multiscale character that cancer invasion exhibits therefore explores the natural two-way link between the molecular processes occurring at the level of individual cells (micro-scale) and the processes occurring at the level of cell population (macro-scale). This chapter will address these multiscale biological processes from a mathematical modelling and analysis perspective, gradually paving the way towards an integrated multiscale framework that explores the tight connection between the tissues scale changes in tumour morphology and the cell-scale dynamics of proteolytic enzymes in the neighbourhood of the tumour interface.

5.1 Introduction

Known as one of the hallmarks of cancer [22], cancer invasion is a complex, multiscale phenomenon involving many inter-related genetic, biochemical, cellular and tissue processes at different spatial and temporal scales. Its complicated spatio-temporal multiscale dynamics enables a localised solid tumour to transform into a

D. Trucu (✉)
Division of Mathematics, University of Dundee, Dundee, DD1 4HN, UK
e-mail: trucu@maths.dundee.ac.uk

P. Domschke • A. Gerisch
Fachbereich Mathematik, Technische Universität Darmstadt, Dolivostrasse 15, 64293 Darmstadt, Germany
e-mail: domschke@mathematik.tu-darmstadt.de; gerisch@mathematik.tu-darmstadt.de

M.A.J. Chaplain
School of Mathematics and Statistics, Mathematical Institute (MI), University of St Andrews, St Andrews KY16 9SS, UK
e-mail: majc@st-andrews.ac.uk

L. Preziosi et al. (eds.), *Mathematical Models and Methods for Living Systems*, Lecture Notes in Mathematics 2167, DOI 10.1007/978-3-319-42679-2_5

systemic, metastatic and fatal disease. This process explores and takes advantage of the reciprocal relation that the solid tumours establish with the extracellular matrix (ECM) components and other multiple distinct cell types from the surrounding microenvironment. Combining abnormal proliferation and migration, which is enabled and enhanced by altered cell-cell and cell-matrix adhesion and the secretion of various proteolitic enzymes, the cancer cells population affects the configuration of the surrounding ECM composition and overcomes the physical barriers to ultimately achieve local cancer spread into the surrounding tissue.

During the growth and spread of malignant tumours, several classes of matrix-degrading enzymes (MDEs) [17, 55] such as matrix metalloproteinases (MMPs) [38] or the urokinase-type plasminogen activator (uPA) are secreted by the cancer cells and contribute to significant degradation or changes in the composition of the extracellular matrix (ECM) [2, 3, 41]. The degradation of the matrix by these proteolytic enzymes creates space that can be exploited by highly migratory cancer cells, leading to further local expansion of the tumour [37]. Whether distributed freely in the ECM or bound to the cancer cell membrane, once secreted, the different MMPs degrade at least one component of the ECM enabling further tumour progression [45, 46, 52].

In parallel to secreting proteolytic enzymes, the processes of cell-cell and cell-matrix adhesion play a particularly important role during cancer invasion [5, 8, 31, 32, 50, 58]. In vivo and in vitro investigations focused on exploring the impact of adhesion on the morphology and direction of migratory tumour cell patterns arising in cancer invasion [16, 30, 42]. In this regard, a major contribution to cell adhesion was identified to be brought by the calcium-dependent adhesion molecules called *cadherins* [54]. These interact with intra-cellular proteins, most notably β*-catenin*, to form adherence junctions between cells in human tissue [28]. This important molecular process is strongly perturbed during cancer growth. It has been observed that reduced cell-cell adhesion levels favour an increase in motility of the invading cancer cells [50]. A significant contribution to the cell-cell adhesion is featured by cell-cell signalling mechanisms based on the interactive dynamics occurring between the Ca^{2+} ions from the ECM and the calcium-sensing receptor distribution on the cell surface [24, 25, 29], this process being strongly altered during cancer invasion, as observed for instance in colon carcinoma [7].

Alongside cell-cell adhesion, cell-matrix adhesion is equally important in individual and collective cancer cell motility during cancer growth [57]. This is enabled by a class of cell-surface receptors known as integrins that bind to ECM ligands [6]. Furthermore, the integrins interact with various intracellular actin-based dynamics, which enable the cells to acquire directionality by establishing a leading edge and a trailing edge [36]. In addition to mediating the creation of new protrusions at the leading edge, actin molecules also influence the contractile properties of the cell, which are then exploited by the cancer cells to enhance their migration [35, 43]. Additionally, tumour cells exploit the ECM confinement and facilitate changes in the ECM stiffness to invade the surrounding tissue [26, 39, 56].

Despite the progress made through in vivo and in vitro research, the profound understanding of the cross-talk between the molecular signalling mechanisms and the individual and collective cell dynamics either in pathological situations such as cancer and would healing or in general human tissue remains a great scientific challenge. In this context, modelling the coupling between the collective cell dynamics and the contribution of the signalling molecules that are traveling along and are exercising their dynamics in conjunction with the moving cell population remains a particularly difficult open question. The active interplay between the tissue-scale tumour dynamics and the molecular mechanics of the involved proteolitic enzymes at cell-scale underlines the biologically multiscale character of invasion, and raises the challenge of modelling this process with an appropriate multiscale approach. The development of a suitable theoretical framework coupling dynamics at the cell population level with dynamics at the level of cell-surface receptors and molecules is crucial in understanding many important normal and pathological cellular processes. These are naturally spatially multi-scale processes where the structural information at each scale plays a major role in the overall dynamics.

In this chapter we will assume a systematic modelling approach to cancer invasion, ranging from *"classical"* and *"structural"* single scale modelling considerations exploring cell adhesion and the effect of the secreted proteolytic enzymes to a general multiscale modelling framework where the spatial scale are linked together in a three-scale approach. This will start in Sect. 5.2 by formulating a basic cancer invasion modelling for two cancer cell subpopulation that accounts for the adhesion properties and explore its possible extensions to n subpopulations.

Section 5.3 will address the molecular binding in the uPA system, which gives rise to general macroscale spatio-temporal-structural modeling framework. This framework will be able to explore the binding, activation and inhibition processes that occur between cell surface-bound and free molecular species and their effect on the overall cell-population dynamics.

Section 5.4 will detail a multiscale moving boundary modelling platform which links the macro-scale dynamics to the micro-scale molecular processes exercised by matrix degrading enzymes. This will explore the multiscale moving boundary method proposed in [47], allowing us to characterize the changes in tissue-scale (macro) tumour morphology caused by the cell-scale matrix degrading enzymes micro-dynamics occurring in a cell-scale (micro) neighbourhood of the tumour invasive edge.

Finally, Sect. 5.5 will comment on the conclusions that can be drawn from each of the modelling approaches exposed in the chapter and reflect on the future research perspectives in this area.

5.2 A Basic Tissue-Scale Cancer Invasion Model

5.2.1 Model Formulation

The past two decades have witnessed intensive efforts in macro-scale modelling of cancer invasion. In this section we will describe the model proposed in [13] which builds on the earlier modelling framework introduced in [4, 18]. This explores the effects of varying the cell-cell and cell-matrix adhesion properties of the cancer cells through time-dependent parameters within the context of n cancer cell sub-populations $c_1, c_2, \ldots c_n$, which may mutate sequentially into each other, $c_i \to c_{i+1}$.

In order to describe the general framework of the modelling approach, let us consider a fixed tissue region $\Omega \subset \mathbb{R}^p$, $p \in \{1, 2, 3\}$ and a time interval $\mathscr{I}_T = (0, T]$, $0 < T \in \mathbb{R}$. The macroscopic model that we describe in this section has three time- and space-dependent variables, namely:

- the vector-valued cancer cell density $\mathbf{c} = (c_i) : \mathscr{I}_T \times \Omega \to \mathbb{R}^n$ representing several cell populations;
- the extracellular matrix (ECM) density, $v : \mathscr{I}_T \times \Omega \to \mathbb{R}$; and
- a matrix-degrading enzyme (MDE) density, $m : \mathscr{I}_T \times \Omega \to \mathbb{R}$.

For a compact notation, we define the combined vector of the cell and ECM densities

$$\mathbf{u}(t,x) := (\mathbf{c}(t,x)^{\mathsf{T}}, v(t,x))^{\mathsf{T}} .$$

The spatial considerations play an important role in this model. While assuming that we assume that the amount of MDEs occupy a negligible amount of space, the *volume fraction of occupied space* is defined here as

$$\rho(t,x) \equiv \rho(\mathbf{u}(t,x)) := \vartheta_v v(t,x) + \vartheta_c \sum_{i=1}^{n} c_i(t,x) ,$$

where $\vartheta_c c_i$ represents the volume fraction occupied by c_i, and $\vartheta_v v$ represents volume fraction of ECM consisting of various *fibrous proteins*, such as collagen.

We will now present the mathematical model proposed in [13] to capture the spatio-temporal dynamics of $\mathbf{c}$, v, and m. The evolution of the cancer cell sub-population densities is assumed to be driven by cell random motility, cell-cell and cell-matrix adhesion-mediated directed migration, proliferation, and mutations between the cancer cell sub-populations. This can be expressed as

$$\frac{\partial \mathbf{c}}{\partial t} = \nabla \cdot [\mathbf{D}\nabla\mathbf{c} - \mathrm{diag}(\mathbf{c})\mathscr{A}(t,x,\mathbf{u}(t,\cdot))] + \mathbf{P}(t,\mathbf{u})\mathbf{c} + \mathbf{M}(t,\mathbf{u})\mathbf{c} . \tag{5.1}$$

where $\nabla\mathbf{c}(t,x) \in \mathbb{R}^{n,p}$ and $\nabla m(t,x) \in \mathbb{R}^{1,p}$ denote the Jacobian matrices in (t,x) of the vector field $\mathbf{c}$ and of m, respectively, with $\nabla\cdot$ notation standing for the

divergence operator. The diagonal matrix $\mathbf{D} = \mathrm{diag}(D_{1,1}, \ldots, D_{1,n}) \in \mathbb{R}^{n,n}$ contains the constant diffusion coefficients $D_{1,i} > 0$ of the tumour sub-populations c_i.

The influence of cell adhesion in cancer cell migration is represented in (5.1) via the non-local operator

$$\mathscr{A}(t, x, \mathbf{u}(t, \cdot)) := \begin{bmatrix} \mathscr{A}_1(t, x, \mathbf{u}(t, \cdot))^\mathsf{T} \\ \mathscr{A}_2(t, x, \mathbf{u}(t, \cdot))^\mathsf{T} \\ \vdots \\ \mathscr{A}_n(t, x, \mathbf{u}(t, \cdot))^\mathsf{T} \end{bmatrix} \in \mathbb{R}^{n,p},$$

which maps any triplet formed by a given spatio-temporal node (t, x) together with the space-dependent function $\mathbf{u}(t, \cdot)$ to an $n \times p$ matrix. Row i in that matrix, i.e. $\mathscr{A}_i(t, x, \mathbf{u}(t, \cdot))^\mathsf{T}$, represents the velocity of directed cancer cell migration of sub-population c_i that is induced by its cell-cell and cell-matrix adhesion properties. Here the cell-cell adhesion aggregate both adhesion between cells of the same sub-population c_i, referred to as *self-adhesion*, and adhesion between cells of different sub-populations c_i and c_j, which is usually called *cross-adhesion*. Therefore, using the ideas introduced in [4, 18], the velocity of c_i due to adhesion is defined by

$$\mathscr{A}_i(t, x, \mathbf{u}(t, \cdot)) = \frac{1}{R} \int_{B(0,R)} \mathfrak{n}(y) \cdot \mathscr{K}_i(\|y\|_2) \cdot g_i(t, \mathbf{u}(t, x+y)) \cdot \chi_\Omega(x+y) \, \mathrm{d}y \,. \tag{5.2a}$$

Here, $R > 0$ is the *sensing radius*, $B(0, R) \subset \mathbb{R}^p$ is the ball of radius R centred at zero, thus for $x \in \Omega$ the set $x + B(0, R)$ is the *sensing region* at x. Finally, $\chi_\Omega(\cdot)$, which represents the characteristic function of Ω, ensures that we account only for adhesion signals within the domain Ω. For $y \in B(0, R)$, the unit vector pointing from x to $x + y$, is denoted by $\mathfrak{n}(y)$, i.e.

$$\mathfrak{n}(y) := \begin{cases} y / \|y\|_2 & \text{if } y \neq 0 \\ 0 \in \mathbb{R}^p & \text{otherwise} \end{cases} . \tag{5.2b}$$

Furthermore, $\mathscr{K}_i(r)$ is a *radial dependency kernel* for that characterizes the relative importance of points at distance $r \in (0, R)$ from x for adhesion-mediated cell migration of sub-population c_i. This function is non-negative and normalised such that

$$1 = \int_{B(0,R)} \mathscr{K}_i(\|y\|_2) \, \mathrm{d}y \,, \tag{5.2c}$$

and specific instances of $\mathscr{K}_i$ are specified later. Finally, the function $g_i(t, \mathbf{u})$ is the ith component of

$$\mathbf{g}(t, \mathbf{u}) \equiv \mathbf{g}(t, \mathbf{c}, v) = [\mathbf{S_{cc}}(t)\mathbf{c} + \mathbf{S_{cv}}(t)\mathbf{1}v] \cdot (1 - \rho(\mathbf{u}))^+ \,. \tag{5.2d}$$

where $\mathbf{1} \in \mathbb{R}^n$ is the all-one vector, $\mathbf{S_{cv}}(t) \in \mathbb{R}^{n,n}$ is the diagonal matrix containing the non-negative cell-matrix adhesion coefficients of all cancer cell sub-populations with the ECM, and $\mathbf{S_{cc}}(t) \in \mathbb{R}^{n,n}$ represents the symmetric matrix containing the non-negative cell-cell adhesion coefficients. Specifically, in this notation, we have that

$$S_{c_i,c_j} := (\mathbf{S_{cc}})_{i,j} = \begin{cases} \text{self-adhesion coefficient of } c_i & \text{if } i = j, \\ \text{cross-adhesion coefficient of } c_i \text{ and } c_j & \text{if } i \neq j. \end{cases} \tag{5.2e}$$

and

$$S_{c_i,v} := (\mathbf{S_{cv}})_{i,i} \text{ is the cell-matrix adhesion coefficient of } c_i. \tag{5.2f}$$

Finally, as usual, the positive part of an expression is denoted by $(\cdot)^+ := \max\{0, \cdot\}$, and in this context the factor $(1 - \rho(\mathbf{u}))^+$ models an inhibition of migration due to volume filling effects, see e.g. [23].

The diagonal matrix $\mathbf{P}(t, \mathbf{u}(t, x)) \in \mathbb{R}^{n,n}$ multiplied by $\mathbf{c}$ in (5.1) represents cancer cell proliferation. With the factor $\mathbf{c}$ we make explicit that cells of sub-population i may proliferate only if they already exist.

Finally, in (5.1) we assume that cancer cells mutate from one cancer cell sub-population to another one and we capture this through the term $\mathbf{M}(t, \mathbf{u}(t, x)) \in \mathbb{R}^{n,n}$ multiplied by $\mathbf{c}$, where $\mathbf{M}$ is the matrix of mutation coefficients. As in the case of the proliferation term, the factor $\mathbf{c}$ makes explicit that cells of sub-population i may mutate only if they already exist. Since mutations of cells of sub-population i correspond to a loss of cells in c_i and mutations of other cells into cells of sub-population i correspond to a gain of cells in c_i, the diagonal elements of $\mathbf{M}$ must be non-positive and the off-diagonal elements of $\mathbf{M}$ must be non-negative. Hence, due to cell mass conservation reasons for each sub-population c_j, we obtain that the matrix $\mathbf{M}$ must have the property that

$$\sum_{i=1}^{n} M_{ij} = 0\,, \quad \text{for } j = 1, 2, \ldots, n.$$

As in this work we consider only mutations $c_i \to c_{i+1}$, $i = 1, 2, \ldots, n-1$, here the matrix $\mathbf{M}$ is lower bidiagonal. However, in other situations different structural cell population conditions may apply and give rise to a lower triangular or even a full matrix $\mathbf{M}$.

The evolution of the ECM density is governed by MDE-mediated matrix degradation as well as ECM remodelling. This is expressed as

$$\frac{\partial v}{\partial t} = -\gamma m v + \psi(t, \mathbf{u}), \tag{5.3}$$

where $\psi(t, \mathbf{u})$ represents the ECM remodelling term, and γ is the rate constant of ECM degradation due to the presence of MDEs. We require that $v = 0$ implies that $\psi(t, \mathbf{u}) \geq 0$ as this will ensure the non-negativity of the ECM density.

Finally, the evolution of the MDE concentration is determined by molecular diffusion of the enzymes, by natural decay, and by the secretion of MDEs by the cancer cell sub-populations into the tumour microenvironment. Hence we obtain

$$\frac{\partial m}{\partial t} = \nabla \cdot [D_3 \nabla m] + \boldsymbol{\alpha}^{\mathsf{T}} \mathbf{c} - \lambda m \,. \tag{5.4}$$

In the above equation, D_3 is the positive MDE diffusion constant, $\boldsymbol{\alpha} \in \mathbb{R}^n$ is the non-negative vector of MDE secretion rates by the cancer cell sub-populations, and λ is the non-negative decay constant.

The system (5.1)–(5.4) is supposed to hold for $x \in \Omega$ and $t \in \mathscr{I}_T$ and is complemented with zero-flux boundary conditions for $\mathbf{c}$ and m, that is

$$\begin{aligned} [\mathbf{D}\nabla \mathbf{c} - \operatorname{diag}(\mathbf{c}) \mathscr{A}(t, x, \mathbf{u}(t, \cdot))] \cdot \mathfrak{n}(x) &= \mathbf{0} \\ \nabla m \cdot \mathfrak{n}(x) &= 0 \end{aligned} \qquad \text{for } t \in \mathscr{I}_T \,, x \in \partial\Omega \,, \tag{5.5}$$

where $\mathfrak{n}(x)$ denotes here the unit outer normal vector on $\partial\Omega$ in $x \in \partial\Omega$, and initial conditions for all equations

$$\mathbf{c}(0, x) = \mathbf{c}_0(x) \,, \quad v(0, x) = v_0(x) \,, \quad m(0, x) = m_0(x) \qquad \text{for } x \in \overline{\Omega} \,. \tag{5.6}$$

The zero-flux boundary conditions for the cancer cell sub-populations imply that cells cannot cross the boundary of the domain Ω and in particular cannot sense any adhesive signals outside Ω.

5.2.2 *Specific Choices for Simulations in Two Spatial Dimensions*

In this study we consider spatially two-dimensional ($p = 2$) simulations. The spatial domain $\Omega = (-1.5, 1.5)^2$ and the final simulation time is set to $T = 60$. However, in all figures with simulation results in this subsection, in all plots, as in [13], we display the central part $(-1, 1)^2$ of Ω only. In this region the formation of the different patterns can be seen and in most of the plots the invasion of the cancer cells has not yet reached the boundary of Ω at final time $T = 60$ such that influences of the boundary conditions on the invasion patterns are negligible.

In the definition of the non-local term, Eq. (5.2a), we use the radial dependency kernel, see [13, 18],

$$\mathscr{K}_i(r) := \mathscr{K}(r) = \frac{3}{\pi R^2} \left(1 - \frac{r}{R}\right) \quad \text{for } i = 1, \ldots, n \,. \tag{5.7}$$

This implies that points in the sensing region at x have, with increasing distance r from x, a decreasing influence on adhesion-driven migration in x.

In our simulations we use the following initial functions in (5.6). First of all, only cancer cell sub-population c_1 is present initially forming a cancerous mass centred at the origin

$$c_{1,0}(x) := \exp(-\|x\|_2^2/\epsilon)\,, \epsilon := 10^{-2}\,, \quad c_{i,0}(x) := 0\,,\ i = 2, \ldots, n\,. \tag{5.8a}$$

For the initial ECM density we assume a heterogeneous distribution such that $\rho(\mathbf{u}(0,x)) \leq 1$ is satisfied. This is achieved using

$$\begin{aligned}(x_1, x_2) &:= \frac{1}{3}(x + 1.5) \in [0,1]^2 \text{ for } x \in \Omega\,, \quad \zeta := 6\pi\,,\\ h(x_1, x_2) &:= \frac{1}{2} + \frac{1}{2}\sin(\zeta x_1/(x_2+1)) \cdot \sin(\zeta x_1 x_2) \cdot \sin(\zeta(1-x_1)/(x_2+1))\\ &\quad \cdot \sin(\zeta(x_1-1)(x_2-1))\,,\\ v_0(x) &:= \min\left\{h(x_1,x_2), \frac{1-\vartheta_c c_{1,0}(x)}{\vartheta_v}\right\}\,.\end{aligned} \tag{5.8b}$$

Finally, we assume that cancer cells have already released some MDE into their environment and set

$$m_0(x) := 0.5 c_{1,0}(x)\,. \tag{5.8c}$$

In the simulations that we show in the following two subsections, a parameter p that will be specified in each of the considered cases will observe changes in its values from an initial value p_- to a final value p_+ around a given time point t_*. In order to express this parameter behaviour, we consider the following transition function

$$p^{(T)}(t; p_-, p_+, t_*) := \frac{1}{2}(p_- + p_+) - \frac{1}{2}(p_- - p_+)\tanh\left(C(t - t_*)\right)\,, \tag{5.9}$$

which enable a gradual, smooth change from p_- to p_+ around t_*. The constant $C > 0$ accounts for the width of the "transition" from p_- to p_+ and is chosen to be $C = 1/3$ in all simulations.

In the following two sub-sections, we explore of the macro-scale cancer invasion modelling framework given in (5.1)–(5.4). Specifically, we focus on one and two cancer cell sub-populations situations, with both constant and time-dependent adhesion coefficients.

5.2.3 The Non-local Model for a Single Cancer Cell Population

Considering a single cancer cell population $c_1 =: c$, the model equations (5.1), (5.3), and (5.4) translate in this situation as follows:

$$\begin{aligned}
\frac{\partial c}{\partial t} &= \nabla \cdot [D_{1,1} \nabla c - c \mathscr{A}(t, x, \mathbf{u}(t, \cdot))] + \mu_{1,1}(t) c (1 - \rho(\mathbf{u})) \,, \\
\frac{\partial v}{\partial t} &= -\gamma m v + \mu_2 (1 - \rho(\mathbf{u}))^+ \,, \\
\frac{\partial m}{\partial t} &= \nabla \cdot [D_3 \nabla m] + \alpha_1 c - \lambda m \,,
\end{aligned} \tag{5.10}$$

with the non-local term $\mathscr{A}$ as given in (5.2a), and the function g defined in (5.2d) is specified by:

$$g(t, \mathbf{u}) = [S_{cc}(t) c + S_{cv}(t) v] \cdot (1 - \rho(\mathbf{u}))^+ \,.$$

We have further chosen $\mathbf{P}(t, \mathbf{u}) = \mu_{1,1}(t)(1 - \rho(\mathbf{u}))$ yielding a logistic-type growth law for the cancer cells with competition for space with the ECM, $\mathbf{M}(t, \mathbf{u}) = 0$ since with a single cancer cell sub-population we have no mutations, and $\psi(t, \mathbf{u}) = \mu_2 (1 - \rho(\mathbf{u}))^+$ for the remodelling of ECM. Finally, we note that for $\mu_2 > 0$ the ECM remodelling process takes place as long as the locally available space is not entirely occupied, i.e., as long as $1 - \rho(\mathbf{u}) > 0$.

The basic parameter set Σ_1 that we use in the simulations is the one considered in [13], namely:

$$\begin{array}{lllll}
D_{1,1} = 10^{-4} & \mu_{1,1} = 0.1 & \gamma = 10 & \mu_2 = 0.05 & D_3 = 10^{-3} \\
\alpha_1 = 0.1 & \lambda = 0.5 & R = 0.1 & S_{cc} = 0.5 & S_{cv} = 0.1 \,.
\end{array} \tag{Σ_1}$$

The values given in (Σ_1) apply whenever no other values for a certain parameter are specified. Also, as indicated in (5.10), the parameters $\mu_{1,1}$, S_{cc}, and S_{cv} can be time-dependent, and in that case their default constant values, as given in (Σ_1), do not apply. Finally, using Eq. (5.9), we will be able to define the time dependent adhesion matrices

$$S_{cc}(t) = S_{cc}^{(T)}(t; S_{cc,-}, S_{cc,+}, t_{cc}) \tag{5.11}$$

$$S_{cv}(t) = S_{cv}^{(T)}(t; S_{cv,-}, S_{cv,+}, t_{cv}) \tag{5.12}$$

for values of the parameter triplets $(S_{cc,-}, S_{cc,+}, t_{cc})$ and $(S_{cv,-}, S_{cv,+}, t_{cv})$ that will be appropriately specified in the considered context.

5.2.3.1 Constant Cell-Cell Adhesion Coefficient

In what follows, we focus on assessing the effect of ECM remodelling on the invasive behaviour. We use the basic parameter set (Σ_1) with the constant cell-cell adhesion coefficient $S_{cc} = 0.5$. The cell-matrix adhesion coefficient function $S_{cv}(\cdot)$ is chosen according to (5.11) with the parameters $(S_{cv,-}, S_{cv,+}, t_{cv}) = (0.1, 0.3, 10)$.

In the simulation results shown in Fig. 5.1, we observe a well-defined pattern that the cancer cell population follows in its evolution. Because of the remodelling of the ECM inside the outer boundary of the evolving cancer cells, i.e. within the developing tumour mass, the cancer cells invade not only outward into surrounding tissue but also tend to move back inwards. Furthermore, due to the disappearance of the heterogeneous, structured ECM due to remodelling, the invasive cell front is much more uniform.

5.2.3.2 Time-Dependent Cell-Cell Adhesion Coefficient

We now explore the cancer cell dynamics by incorporating the remodelling of the ECM in the context of time-dependent cell-cell and cell-matrix adhesive properties and set the corresponding parameter $\mu_2 = 0.05$. We consider two different settings of the time-dependent cell-matrix adhesion parameter, in both cases using the same time-dependent cell-cell adhesion parameter of the form given in (5.11). Figure 5.2 shows the corresponding simulation results in two subplots, namely:

$$\text{Fig. 5.2a:} \quad S_{cv}(t) = S_{cv}^{(T)}(t; 0.1, 0.3, 10)\,, \qquad S_{cc}(t) = S_{cc}^{(T)}(t; 0.5, 0.25, 40)\,,$$

$$\text{Fig. 5.2b:} \quad S_{cv}(t) = S_{cv}^{(T)}(t; 0.25, 0.5, 10)\,, \qquad S_{cc}(t) = S_{cc}^{(T)}(t; 0.5, 0.25, 40)\,.$$

We observe that, while the main features of the invasive pattern that are present in Fig. 5.1 are preserved in the current simulations, the additional time-dependent

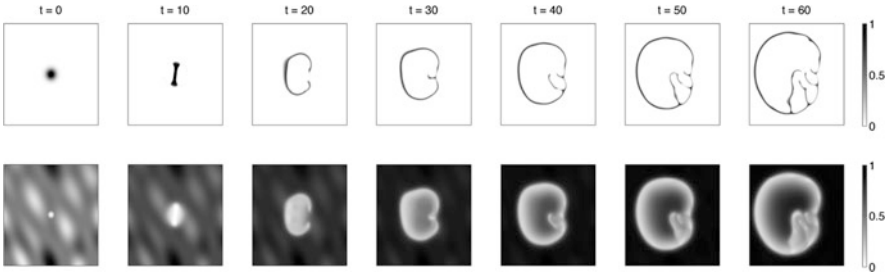

Fig. 5.1 This figure is a reproduction under **granted copyright from JTB** of Fig. 7 from [13]. This shows simulation results of model (5.10) with cell-matrix adhesion coefficient $S_{cv}(t) = S_{cv}^{(T)}(t; 0.1, 0.3, 10)$ and parameter set Σ_1

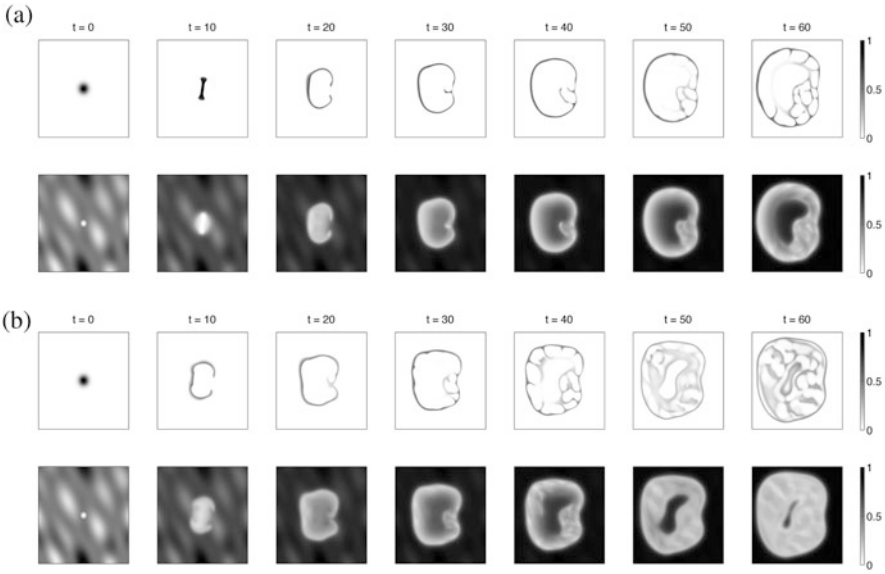

Fig. 5.2 This figure is a reproduction under **granted copyright from JTB** of Fig. 9 from [13]. This shows simulation results of model (5.10) with cell-cell and cell-matrix adhesion coefficients as given in each subplot and parameter set Σ_1. (**a**) $S_{cv}(t) = S_{cv}^{(T)}(t; 0.1, 0.3, 10)$ and $S_{cc}(t) = S_{cc}^{(T)}(t; 0.5, 0.25, 40)$. (**b**) $S_{cv}(t) = S_{cv}^{(T)}(t; 0.25, 0.5, 10)$ and $S_{cc}(t) = S_{cc}^{(T)}(t; 0.5, 0.25, 40)$

decrease of $S_{cc}(t)$ causes a more diffuse and heterogeneous invasive pattern in Fig. 5.2. Furthermore, as can be observed in Fig. 5.2b, increasing $S_{cv}(t)$ further compared to the simulation shown in Fig. 5.2a, leads to an even more pronounced heterogeneous pattern with cancer cells and ECM inter-mixed throughout the domain.

5.2.4 *The Non-local Model with Two Cancer Cell Sub-Populations*

It is well known that over time cancers become more malignant, with some of the cancer cells mutating into more aggressive phenotypes. In this subsection, we explore this situation by modelling the overall tumour dynamics where there are two cancer cell sub-populations, c_1 and c_2. During the development of the cancer, we assume that the second sub-population emerging in the tumour mass arises from mutations in the cells of the first sub-population. Using the general model

formulation (5.1), (5.3), and (5.4), we consider the following (nondimensionalized) model for the two sub-populations c_1 and c_2:

$$\begin{aligned}
\frac{\partial c_1}{\partial t} &= \nabla \cdot [D_{1,1}\nabla c_1 - c_1 \mathscr{A}_1(t,x,u(t,\cdot))] + \mu_{1,1}c_1(1-\rho(\mathbf{u})) + M_{1,1}(t,\mathbf{u})c_1\,,\\
\frac{\partial c_2}{\partial t} &= \nabla \cdot [D_{1,2}\nabla c_2 - c_2 \mathscr{A}_2(t,x,u(t,\cdot))] + \mu_{1,2}c_2(1-\rho(\mathbf{u})) + M_{2,1}(t,\mathbf{u})c_1\,,\\
\frac{\partial v}{\partial t} &= -\gamma m v + \mu_2(1-\rho(\mathbf{u}))^+\,,\\
\frac{\partial m}{\partial t} &= \nabla \cdot [D_3\nabla m] + \alpha_1 c_1 + \alpha_2 c_2 - \lambda m\,.
\end{aligned} \tag{5.13}$$

In the above, as in the case of a single cancer cell population, we have chosen a logistic-type growth law for each cancer cell sub-population; note however that the proliferation rates $\mu_{1,1}$ and $\mu_{1,2}$ are constants here. The mutation of cancer cells from type c_1 to type c_2 is modelled as in [1], that is, the non-zero elements of the matrix $\mathbf{M}(t,\mathbf{u}(t,x))$ are given by

$$-M_{1,1}(t,\mathbf{u}) = M_{2,1}(t,\mathbf{u}) = \delta H(t-t_{1,2})\cdot H(v(t,x)-v_{\min})\,.$$

Here, $H(\cdot)$ denotes the Heaviside function, $t_{1,2}$ is the time point after which mutations from sub-population 1 to sub-population 2 begin to occur, $v_{\min}$ is the minimum ECM density that is needed for mutations to take place, and $\delta > 0$ is the mutation rate. The non-local terms $\mathscr{A}_1$ and $\mathscr{A}_2$ are as defined in (5.2a) with the function $\mathbf{g}$, cf. (5.2d), fully specified when the 2×2 matrices $\mathbf{S_{cc}}(t)$ and $\mathbf{S_{cv}}(t)$ are given. We note already here that only the components S_{c_2,c_2} and $S_{c_2,v}$ are considered time-dependent in our simulations below; all other components of these matrices are constants. The ECM remodelling process is represented as in the case of a single cell population, that is $\psi(t,\mathbf{u}) = \mu_2(1-\rho(\mathbf{u}))^+$.

In this section we use the basic parameter set (Σ_2), which is an extension of the basic parameter set (Σ_1) used in Sect. 5.2.3 and is given by:

Parameter values defined in basic parameter set (Σ_1) together with

$$\begin{aligned}
&D_{1,2} = 10^{-4}\,, \quad \mu_{1,2} = 0.25\,, \quad \alpha_2 = 0.1\,, \quad \mathbf{S_{cc}} = \begin{pmatrix} 0.5 & 0 \\ 0 & 0.3 \end{pmatrix}\,,\\
&\delta = 0.3\,, \quad t_{1,2} = 10\,, \quad v_{\min} = 0.3\,, \quad \mathbf{S_{cv}} = \begin{pmatrix} 0.1 & 0 \\ 0 & 0.5 \end{pmatrix}\,.
\end{aligned} \tag{Σ_2}$$

The values given in (Σ_2) apply whenever no other values for a certain parameter are specified. Finally, in the following simulations, sub-population c_1 is shown in black, while sub-population c_2 is shown in red.

5.2.4.1 The Effect of ECM Remodelling and the Influence of the Cross-Adhesion Coefficient

We consider again the effect that ECM remodelling has on the cancer cell dynamics. Figure 5.3 shows the results obtained using the basic parameter set (Σ_2). Despite the fact that we have time-independent adhesive properties in this simulation, the two cancer cell sub-populations alongside the continuously remodelling ECM form together a strongly heterogeneous pattern. We also observe that since the cell-cell cross-adhesion parameter $S_{c_1,c_2} = 0$, the two sub-populations do not mix.

However, by increasing the cross-adhesion coefficient S_{c_1,c_2} from its default value zero, the results that we obtain, shown here in Fig. 5.4a–c, reveal that the two cancer cell sub-populations get generally closer to each other. The dominant features in the distributions of the two cancer cell sub-populations shown in Fig. 5.4a–c complement each other within close proximity, and as observed in [19] for two species without ECM, cell sub-populations mixing may occur here as well for high cross-adhesion values.

If we consider a higher cell-matrix adhesion value for the first cancer cell sub-population, we observe a faster spread of both cancer cell sub-populations and an increased number of cancer/ECM nests inside the tumour. Figure 5.5 shows the result for the same set of parameters as for Fig. 5.4a except that the cell-matrix adhesion coefficient of the first sub-population is increased to $S_{c_1,v} = 0.3$. If we further increase the cross-adhesion parameter, as was done in Figs. 5.3 and 5.4, the results follow the same principle from separation towards mixing of cancer cell sub-populations (not shown).

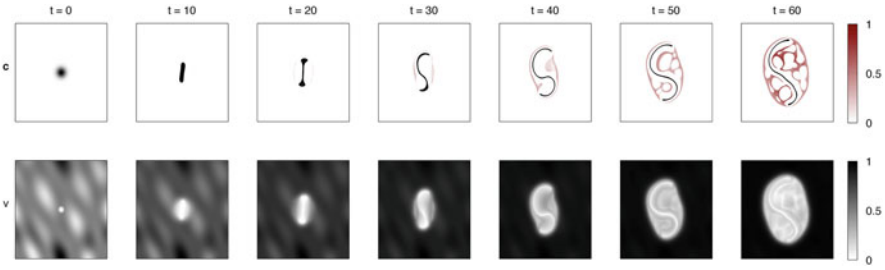

Fig. 5.3 This figure is a reproduction under **granted copyright from JTB** of Fig. 11 from [13]. This shows simulation results of model (5.13) for the parameter set (Σ_2)

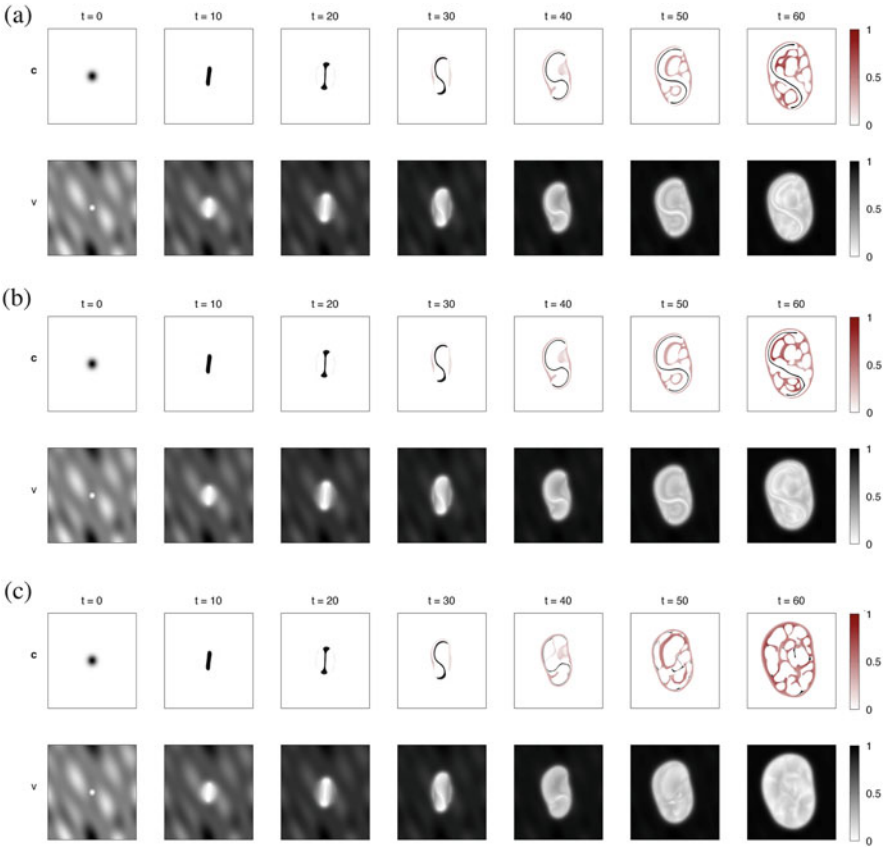

Fig. 5.4 This figure is a reproduction under **granted copyright from JTB** of Fig. 12 from [13]. This shows simulation results of model (5.13) for the parameter set (Σ_2), but with positive cross-adhesion coefficient S_{c_1,c_2} as indicated in the subplots. (**a**) $S_{c_1,c_2} = 0.075$. (**b**) $S_{c_1,c_2} = 0.15$. (**c**) $S_{c_1,c_2} = 0.3$

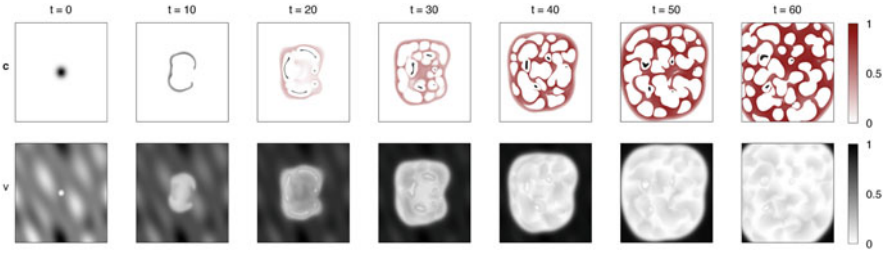

Fig. 5.5 This figure is a reproduction under **granted copyright from JTB** of Fig. 13 from [13]. This shows simulation results of model (5.13) for the parameter set (Σ_2), but with cross-adhesion coefficient $S_{c_1,c_2} = 0.075$ and cell-matrix adhesion coefficient $S_{c_1,v} = 0.3$

5.3 Macroscopic Spatio-Temporal-Structural Modelling Approach with Application to the uPA System

Expanding now the modelling perspective of the previous section, in the following we will describe the fundamentals of a general framework proposed initially in [14] that captures the overall coupled interaction of a *spatio-temporal-structurally* distributed cell population accompanied by a number of binding spatio-temporal distributed molecular species. This will explore the binding, activation and inhibition processes between cell surface-bound and free molecular species and their effect on the overall cell-population dynamics.

5.3.1 General Spatio-Temporal-Structured Cell Population Modelling Framework

In order to describe the general spatio-temporal-structural modelling framework proposed initially in [14], we start by introducing the necessary concepts and notations. Let $\Omega \subset \mathbb{R}^d$, $d \in \{1, 2, 3\}$, be a bounded spatial domain, $\mathscr{I} = (0, T]$, $0 < T \in \mathbb{R}$, be the time interval, and $\mathscr{P} \subset \mathbb{R}^p$, $p \in \mathbb{N}$, be a convex domain of admissible molecular binding structure states that contains $\mathbf{0} \in \mathbb{R}^p$ as accumulation point. The set $\mathscr{P}$ will be referred to as the *i*-state space (= *individual's state*) [34].

In this context, we aim to explore the *spatio-temporal-structural dynamics* of a tissue consisting of

- the structured cell population density $c(t, x, y)$, with $(t, x, y) \in \mathscr{I} \times \Omega \times \mathscr{P}$;
- the extracellular matrix (ECM) density $v(t, x)$, with $(t, x) \in \mathscr{I} \times \Omega$;
- q free molecular species, of concentration $m_i(t, x)$, with $(t, x) \in \mathscr{I} \times \Omega$, $i = 1, \ldots, q$, which may be written in vector notation as

$$\mathbf{m} = (m_1, \ldots, m_q)^{\mathsf{T}} : \mathscr{I} \times \Omega \to \mathbb{R}^q .$$

We consider that $p \leq q$ out of the total number of q molecular species are able to bind to the cell surface, and so, without loss of generality, these are assumed to be m_i, $i = 1, \ldots, p$. The binding of the p molecular species affects the macroscopic dynamics of the cell population density, and therefore at each spatio-temporal node (t, x), this gives rise to a *cell-surface binding signature*

$$c(t, x, \cdot) : \mathscr{P} \to \mathbb{R}$$

of the p molecular species attached to the cell mass distributed at (t, x). Adopting a similar approach to size-structured population models, see for example [11, 12] or [48], the surface concentration of bound molecules on the surface of the cells is represented here by the structure or *i*-state variable $y \in \mathscr{P}$, which leads to

the structured cell population density $c(t,x,y)$. Therefore, if we ignore the binding structure, the total cell density at (t,x) is given by

$$C(t,x) = \int_{\mathscr{P}} c(t,x,y)\,\mathrm{d}y\,. \tag{5.14}$$

Denoting the combined vector of the cell and ECM densities with

$$\mathbf{u}(t,x) := (c(t,x,\cdot), v(t,x))^{\mathsf{T}}\,, \tag{5.15}$$

we define the *volume fraction of occupied space* by

$$\hat{\rho}(t,x) \equiv \rho(\mathbf{u}(t,x)) := \vartheta_c \int_{\mathscr{P}} c(t,x,y)\,\mathrm{d}y + \vartheta_v v(t,x) = \vartheta_c C(t,x) + \vartheta_v v(t,x)$$

for suitable parameters ϑ_c and ϑ_v. This definition assumes therefore that the amount of free and bound molecular species is negligible for the volume fraction of occupied space.

Of further interest for us is also the concentration of *surface-bound reactants* per volume fraction at, i.e., the part of molecular species that are bound to the cell surface. To this end, assuming a fixed cell surface ε for all cells in the tissue, the *surface density* per i-state at (t,x) is therefore given by

$$s(t,x,y) = \varepsilon c(t,x,y)\,.$$

Thus, the total concentration of all bound molecular species at $(t,x) \in \mathscr{I} \times \Omega$ is the expectation vector of the surface density s with respect to the structural variable y, namely

$$E(t,x) := \int_{\mathscr{P}} y s(t,x,y)\,\mathrm{d}y \quad \in \mathbb{R}^p\,. \tag{5.16}$$

Obviously, for each individual bound molecular species m_i, this expectation specialises to

$$E_i(t,x) := \int_{\mathscr{P}} y_i s(t,x,y)\,\mathrm{d}y\,,$$

and we can immediately observe that $E(t,x) = (E_1(t,x), \ldots, E_p(t,x))^{\mathsf{T}}$. Finally, for a compact notation, we define the combined vector of bound and free molecular

species to be

$$\mathbf{r}(t,x) = \begin{pmatrix} E(t,x) \\ \mathbf{m}(t,x) \end{pmatrix} \in \mathbb{R}^{p+q}\,. \tag{5.17}$$

In the following, we discuss the model equations for the evolution of c, v and $\mathbf{m}$.

5.3.2 Cell Population Dynamics

Let us start by considering an arbitrarily small control volume $V \times W$ inside the *spatio-structural* space $\Omega \times \mathscr{P}$, with V and W assumed to be compact and with piecewise smooth boundaries ∂V and ∂W. In this context, the total amount of cells in $V \times W$ at time t is

$$\bar{c}(t) = \int_W \int_V c(t,x,y)\,\mathrm{d}x\,\mathrm{d}y\,.$$

Per unit time, the rate of change in $\bar{c}(t)$ is given by the combined effect of the sources of cells of the structural types considered over the control volume and the flux of cells into the control volume over the spatial and structural boundaries. Therefore, this is given by

$$\frac{d\bar{c}}{dt} = \underbrace{\int_W \int_V S(t,x,y)\,\mathrm{d}x\,\mathrm{d}y}_{\text{source}} - \underbrace{\int_W \int_{\partial V} F(t,x,y)\cdot \mathfrak{n}(x)\,\mathrm{d}\sigma_{n-1}(x)\,\mathrm{d}y}_{\text{flux over spatial boundary}}$$
$$- \underbrace{\int_V \int_{\partial W} G(t,x,y)\cdot \mathfrak{n}(y)\,\mathrm{d}\sigma_{p-1}(y)\,\mathrm{d}x}_{\text{flux over structural boundary}}\,,$$

where σ_{n-1} and σ_{p-1} are the surface measures on ∂V and ∂W, respectively. Assuming now that the vector fields F and G are and continuously differentiable, via Divergence Theorem we obtain that

$$\frac{d\bar{c}}{dt} = \int_W \int_V S(t,x,y)\,\mathrm{d}x\,\mathrm{d}y - \int_W \int_V \nabla_x \cdot F(t,x,y)\,\mathrm{d}x\,\mathrm{d}y$$
$$- \int_V \int_W \nabla_y \cdot G(t,x,y)\,\mathrm{d}y\,\mathrm{d}x\,.$$

Assuming further that c and c_t are continuous, the Dominated Convergence Theorem allows us to interchange the derivative with the integral [21], and so we obtain that

$$\int_W \int_V \frac{\partial}{\partial t} c(t,x,y)\,\mathrm{d}x\,\mathrm{d}y = \int_W \int_V S(t,x,y)\,\mathrm{d}x\,\mathrm{d}y - \int_W \int_V \nabla_x \cdot F(t,x,y)\,\mathrm{d}x\,\mathrm{d}y - \int_W \int_V \nabla_y \cdot G(t,x,y)\,\mathrm{d}x\,\mathrm{d}y\,.$$

This can be equivalently written as

$$\begin{aligned}\int_{\mathbb{R}^{d+p}} \frac{\partial}{\partial t} c(t,x,y)\mathbf{1}_{V\times W}(x,y)\,\mathrm{d}x\,\mathrm{d}y = &\int_{\mathbb{R}^{d+p}} S(t,x,y)\mathbf{1}_{V\times W}(x,y)\,\mathrm{d}x\,\mathrm{d}y \\ &- \int_{\mathbb{R}^{d+p}} [\nabla_x \cdot F(t,x,y)]\mathbf{1}_{V\times W}(x,y)\,\mathrm{d}x\,\mathrm{d}y \\ &- \int_{\mathbb{R}^{d+p}} [\nabla_y \cdot G(t,x,y)]\mathbf{1}_{V\times W}(x,y)\,\mathrm{d}x\,\mathrm{d}y\,,\end{aligned}$$

where $\mathbf{1}_A$ generally denotes the indicator function of an arbitrary subset A of $\Omega \times \mathscr{P}$. Therefore, since

$$\{V \times W \subset \Omega \times \mathscr{P} |\ V \text{ and } W \text{ - compact with piecewise smooth boundaries}\}$$
$$\text{is a family of generators for the borelian } \sigma-\text{algebra on } \Omega \times \mathscr{P},$$

we obtain that

$$\begin{aligned}\int_{\mathbb{R}^{d+p}} \frac{\partial}{\partial t} c(t,x,y)\mathbf{1}_{A}(x,y)\,\mathrm{d}x\,\mathrm{d}y = &\int_{\mathbb{R}^{d+p}} S(t,x,y)\mathbf{1}_{A}(x,y)\,\mathrm{d}x\,\mathrm{d}y \\ &- \int_{\mathbb{R}^{d+p}} [\nabla_x \cdot F(t,x,y)]\mathbf{1}_{A}(x,y)\,\mathrm{d}x\,\mathrm{d}y \\ &- \int_{\mathbb{R}^{d+p}} [\nabla_y \cdot G(t,x,y)]\mathbf{1}_{A}(x,y)\,\mathrm{d}x\,\mathrm{d}y\,,\end{aligned}$$

for any borelian set A in the $\sigma-$algebra on $\Omega \times \mathscr{P}$. Thus, this equality remains valid if we replace $\mathbf{1}_A(x,y)$ with any simple function, and so using now the fact that the family of simple functions is dense within $L^1(\Omega \times \mathscr{P})$ in the family of test functions

with respect to the L^1-norm on $\Omega \times \mathscr{P}$ [21], we obtain

$$\int_{\mathbb{R}^{d+p}} \frac{\partial c}{\partial t} \upsilon(x,y)\,\mathrm{d}x\,\mathrm{d}y = \int_{\mathbb{R}^{d+p}} S(t,x,y)\upsilon(x,y)\,\mathrm{d}x\,\mathrm{d}y - \int_{\mathbb{R}^{d+p}} [\nabla_x \cdot F(t,x,y)]\upsilon(x,y)\,\mathrm{d}x\,\mathrm{d}y$$
$$- \int_{\mathbb{R}^{d+p}} [\nabla_y \cdot G(t,x,y)]\upsilon(x,y)\,\mathrm{d}x\,\mathrm{d}y\,, \quad \forall \upsilon \in \mathscr{C}_0^\infty(\Omega \times \mathscr{P}).$$

Since this equality holds for any test function $\upsilon \in \mathscr{C}_0^\infty(\Omega \times \mathscr{P})$, we obtain the following *spatio-temporal-structural* governing partial differential equation for the structured cell population dynamics, namely:

$$\frac{\partial}{\partial t} c(t,x,y) = S(t,x,y) - \nabla_x \cdot F(t,x,y) - \nabla_y \cdot G(t,x,y)\,. \tag{5.18}$$

5.3.2.1 Source

For simplicity, we ignore apoptosis and we assume here that the source of the cell population is determined only by the cell proliferation process enabled by cell division. In this context, denoting by $\Phi(y,\mathbf{u})$ the rate at which cells undergo mitosis (proliferation rate), we assume that, as cells divide, the daughter cells share the p different bounded molecular species uniformly. This means that the cells distributed at (t,x,y) divide into pairs of daughter cells distributed at $(t,x,\frac{1}{2}y)$, as shown in Fig. 5.6.

Let us now consider an arbitrary compact subset with piecewise smooth boundary $W \subset \mathscr{P}$. Considering now the extended mapping $\hat{c}(t,x,\tilde{y})$ given by

$$\hat{c}(t,x,\tilde{y}) = \begin{cases} c(t,x,\tilde{y}), & \tilde{y} \in \mathscr{P}, \\ 0, & \tilde{y} \notin \mathscr{P}, \end{cases} \tag{5.19}$$

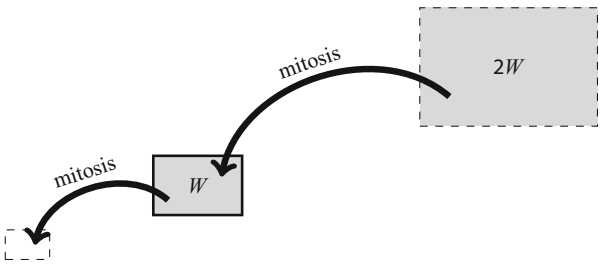

Fig. 5.6 This figure is a reproduction of Fig. 1 from [14]. This illustrate individuals leaving and entering the control volume $W \subset \mathscr{P}$ through mitosis

at any $(t,x) \in \mathscr{I} \times \Omega$, the source of cells in the structural region W is given by

$$\int_W S(t,x,y)\,\mathrm{d}y = 2\int_{2W} \Phi(\tilde{y},\mathbf{u})\hat{c}(t,x,\tilde{y})\,\mathrm{d}\tilde{y} - \int_W \Phi(y,\mathbf{u})\hat{c}(t,x,y)\,\mathrm{d}y\,.$$

Thus, using now the change of variables $\tilde{y}(y) = 2y$, for which $\det(J_{\tilde{y}}) = 2^p$, we get

$$\int_W S(t,x,y)\,\mathrm{d}y = \int_W 2^{p+1}\Phi(2y,\mathbf{u})\hat{c}(t,x,2y)\,\mathrm{d}y - \int_W \Phi(y,\mathbf{u})\hat{c}(t,x,y)\,\mathrm{d}y\,.$$

Therefore, since

$$\{W \subset \mathscr{P} \,|\, W \text{ - compact with piecewise smooth boundaries}\}$$
$$\text{is a family of generators for the borelian } \sigma-\text{algebra on } \mathscr{P}$$

we obtain that

$$\int_{\mathbb{R}^p} S(t,x,y)\mathbf{1}_B(y)\,\mathrm{d}y = \int_{\mathbb{R}^p} 2^{p+1}\Phi(2y,\mathbf{u})\hat{c}(t,x,2y)\mathbf{1}_B(y)\,\mathrm{d}y - \int_{\mathbb{R}^p} \Phi(y,\mathbf{u})\hat{c}(t,x,y)\mathbf{1}_B(y)\,\mathrm{d}y\,.$$

for any borellian set B in the $\sigma-$algebra on $\mathscr{P}$. Thus, this equality remains valid if we replace the indicator $\mathbf{1}_B(y)$ with any simple function, and so using again the fact that the simple functions are dense within $L^1(\mathscr{P})$ in the family of test functions, we obtain

$$\int_{\mathbb{R}^p} S(t,x,y)\tilde{\upsilon}(y)\,\mathrm{d}y = \int_{\mathbb{R}^p} 2^{p+1}\Phi(2y,\mathbf{u})\hat{c}(t,x,2y)\tilde{\upsilon}(y)\,\mathrm{d}y - \int_{\mathbb{R}^p} \Phi(y,\mathbf{u})\hat{c}(t,x,y)\tilde{\upsilon}(y)\,\mathrm{d}y\,,$$

for all $\tilde{\upsilon} \in \mathscr{C}_0^\infty(\mathscr{P})$. Therefore, we finally obtain that, for any $(t,x) \in \mathscr{I} \times \Omega$, we have

$$S(t,x,y) = 2^{p+1}\Phi(2y,\mathbf{u})\hat{c}(t,x,2y) - \Phi(y,\mathbf{u})\hat{c}(t,x,y)\,, \qquad \forall y \in \mathscr{P}. \tag{5.20}$$

5.3.2.2 Spatial Flux

There are various processes that lead to the flux over the spatial boundary. These include diffusion (random motion), chemotaxis with respect to various chemoattractants or haptotaxis with respect to the ECM, as well as cell adhesion. A combination of these spatial flux contributing factors can for example be chosen as in [1, 13, 18],

and can be formulated as

$$F(t,x,y) = F_D + F_T + F_A$$
$$= -D_c \nabla_x c + c(1-\rho(\mathbf{u}))\left(\sum_{k=1}^{q} \chi_k \nabla_x m_k + \chi_v \nabla_x v\right) + c\mathscr{A} \tag{5.21}$$

where the free molecular species m_k are either chemoattractants or chemorepellents. Here we assume that the diffusion coefficient $D_c(\cdot)$ as well as the taxis coefficients $\chi_v(\cdot)$ and $\chi_k(\cdot)$, $k = 1,\ldots,q$, are dependent on the i-state $y \in \mathscr{P}$. Under similar considerations those that led to (5.2a), the adhesion term $\mathscr{A}$ is defined also in this case as

$$\mathscr{A}(t,x,y,\mathbf{u}(t,\cdot)) = \frac{1}{R}\int_{B(0,R)} \mathfrak{n}(\tilde{x})\mathscr{K}(\|\tilde{x}\|_2) g(t,y,\mathbf{u}(t,x+\tilde{x}))\,\mathrm{d}\tilde{x}$$

with the sensing radius $R > 0$, $\mathfrak{n}(\tilde{x})$ a unit normal vector pointing from x to $x+\tilde{x}$, and the radial dependency kernel $\mathscr{K}(r)$ with $r := \|\tilde{x}\|_2$. Finally, using the same arguments that led to (5.2d), the adhesion coefficient function $g(t,y,\mathbf{u}(t,x^*))$ is given here by

$$g(t,y,\mathbf{u}(t,x^*)) = \left(\int_{\mathscr{P}} S_{cc}(t,y,\tilde{y})c(t,x^*,\tilde{y})\,\mathrm{d}\tilde{y} + S_{cv}(t,y)v(t,x^*)\right)$$
$$\cdot\,(1-\rho(\mathbf{u}(t,x^*)))^+,$$

where $S_{cc}(t,y,\tilde{y})$ represents the cell-cell adhesion coefficient between cells of i-states y and $\tilde{y}$, and $S_{cv}(t,y)$ denotes the cell-matrix adhesion coefficient between cells with i-state y and the ECM.

5.3.2.3 Structural Flux

The flux over the structural boundary arises from the binding and unbinding processes of the p molecular species to the cells surface. Thus, denoting by $\mathscr{B}(\mathscr{P})$ the Borel $\sigma-$algebra on $\mathscr{P}$, given a density of molecular species $\mathbf{m}(t,x)$, the structural measure of their binding process to the total cell density $C(t,x)$ is denoted by

$$\eta_{\mathbf{b}}(\cdot;\mathbf{m}) : \mathscr{B}(\mathscr{P}) \to \mathbb{R}^p$$

and is assumed to be known and absolutely continuous with respect to the Lebesgue measure on $\mathscr{P}$. Therefore, the induced Lebesgue-Radon-Nikodym density

$$\mathbf{b}(\cdot;\mathbf{m}) = \begin{pmatrix} b_1(\cdot;\mathbf{m}) \\ \vdots \\ b_p(\cdot;\mathbf{m}) \end{pmatrix} : \mathscr{P} \to \mathbb{R}^p \tag{5.22}$$

is uniquely defined by

$$\eta_{\mathbf{b}}(W;\mathbf{m}) = \int_W \mathbf{b}(\gamma;\mathbf{m})\,\mathrm{d}\gamma\,, \quad \forall W \in \mathscr{B}(\mathscr{P})\,, \tag{5.23}$$

[21], and represents the binding rate of the molecular species $\mathbf{m}$ to the total cell population density C.

Similarly, the structural measure of the unbinding process of the bound molecular species $E(t,x)$ is denoted by

$$\eta_{\mathbf{d}}(\cdot) : \mathscr{B}(\mathscr{P}) \to \mathbb{R}^p$$

and is again assumed to be absolutely continuous with respect to the Lebesgue measure on $\mathscr{P}$. Thus, this leads to an unbinding rate depending only on the i-state given by the Lebesgue-Radon-Nikodym density

$$\mathbf{d}(\cdot) = \begin{pmatrix} d_1(\cdot) \\ \vdots \\ d_p(\cdot) \end{pmatrix} : \mathscr{P} \to \mathbb{R}^p \tag{5.24}$$

which is uniquely defined by

$$\eta_{\mathbf{d}}(W) = \int_W \mathbf{d}(\gamma)\,\mathrm{d}\gamma\,, \quad \forall W \in \mathscr{B}(\mathscr{P})\,. \tag{5.25}$$

and represents the unbinding rate of the molecular species $\mathbf{m}$ from the total cell population density C. Hence, these binding and unbinding rates lead to an associated *net variation* of the i-state given by

$$\mathbf{b}(y,\mathbf{m}) - \mathbf{d}(y)\,.$$

Thus adopting the same interpretation of the flux $G(t,x,y)$ as *growth* in size-structured populations [11, 34, 48, 53], this is then given by the product of the density of the population/species and the net growth rate. Therefore, the structural flux has the form

$$G(t,x,y) = c(t,x,y)\big(\mathbf{b}(y,\mathbf{m}) - \mathbf{d}(y)\big)\,. \tag{5.26}$$

5.3.3 Extracellular Matrix

Given the constitutive structure of the ECM, this is not considered to be diffusing. However, the ECM is assumed to be degraded by one or more of the free molecular species or the surface-bound molecules and is remodelled by the stroma cells present in the tissue (which are not modelled here explicitly). Thus, in this context, the governing equation for ECM is

$$\frac{\partial}{\partial t} v(t,x) = -\underbrace{\boldsymbol{\delta}_v^{\mathsf{T}} \mathbf{r}(t,x) v(t,x)}_{\text{degradation}} + \underbrace{\psi_v(t, \mathbf{u}(t,x))}_{\text{remodelling}},$$

where $\boldsymbol{\delta}_v \in \mathbb{R}^{p+q}$ is an appropriate non-negative vector of ECM degradation rates and $\psi_v(t, \mathbf{u})$ represents the remodelling term. We note that this generalises Eq. (5.3) where we only considered one type of molecular species, namely the MDEs. Finally, to ensure positivity of the ECM density, we require $\psi_v(t, \mathbf{u}) \geq 0$ for $v = 0$.

5.3.4 Molecular Species

Adopting a similar line of reasoning as for (5.4), we assume here that the molecular species m_i, $i = 1, \ldots, q$ are driven by diffusion, are produced by either the cells or by chemical reactions, and are subject to natural decay. However, depending on the i-state y, the first p species m_i, $i = 1, \ldots, p$, may also bind to the cells surface with the binding rates b_i. Further, due to the unbinding processes for each of the bound m_i with rates η_i, part of the previously bounded molecular species reenter the molecular dynamics. Therefore, under these considerations, by extending the vectors $\mathbf{b}(y, \mathbf{m})$ and $\mathbf{d}(y)$ by an appropriate number of zero components, i.e.,

$$\hat{\mathbf{b}}(y, \mathbf{m}) = \begin{pmatrix} \mathbf{b}(y, \mathbf{m}) \\ \mathbf{0} \end{pmatrix} \in \mathbb{R}^q \text{ and } \hat{\mathbf{d}}(y) = \begin{pmatrix} \mathbf{d}(y) \\ \mathbf{0} \end{pmatrix} \in \mathbb{R}^q,$$

the spatio-temporal dynamics of the molecular species is considered to be described by

$$\begin{aligned} \frac{\partial}{\partial t} \mathbf{m}(t,x) = \underbrace{\nabla_x \cdot \mathbf{D}_{\mathbf{m}} \nabla_x \mathbf{m}(t,x)}_{\text{diffusion}} - \underbrace{\int_{\mathscr{P}} \left(\hat{\mathbf{b}}(y, \mathbf{m}) - \hat{\mathbf{d}}(y) \right) s(t,x,y) \, \mathrm{d}y}_{\text{binding/unbinding}} \\ + \underbrace{\boldsymbol{\psi}_{\mathbf{m}}(\mathbf{u}(t,x), \mathbf{r}(t,x))}_{\text{production}} - \underbrace{\operatorname{diag}(\boldsymbol{\delta}_{\mathbf{m}}) \mathbf{m}(t,x)}_{\text{decay}}. \end{aligned} \tag{5.27}$$

Here, $\mathbf{D}_{\mathbf{m}} = \operatorname{diag}(D_{m_1}, \ldots, D_{m_2}) \in \mathbb{R}^{q,q}$ denotes the diagonal matrix containing the diffusion constants of the individual species. The vector $\boldsymbol{\psi}_{\mathbf{m}} = \boldsymbol{\psi}_{\mathbf{m}}(\mathbf{u}, \mathbf{r})$ represents

the production term, and $\boldsymbol{\delta}_{\mathbf{m}}$ is the vector of non-negative rates of decay for each molecular species m_i, $i = 1, \ldots, q$.

5.3.5 *Summary of the General Spatio-Temporal-Structural Model for Cell Migration*

The structured-population model introduced in Sects. 5.3.2–5.3.4 for the cell and ECM density and the molecular species densities reads as follows:

$$\begin{aligned}\frac{\partial c}{\partial t} &= \nabla_x \cdot \left[D_c \nabla_x c - c(1-\rho(\mathbf{u})) \left(\sum_{k=1}^{q} \chi_k \nabla_x m_k + \chi_v \nabla_x v \right) + c\mathscr{A} \right] \\ &\quad - \nabla_y \cdot \left[(\mathbf{b}(y,\mathbf{m}) - \mathbf{d}(y))\, c \right] \\ &\quad + 2^{p+1} \Phi(2y, \mathbf{u}) c(t, x, 2y) - \Phi(y, \mathbf{u}) c(t, x, y).\end{aligned} \tag{5.28a}$$

$$\frac{\partial v}{\partial t} = -\boldsymbol{\delta}_v^{\mathsf{T}} \mathbf{r} v + \psi_v(t, \mathbf{u}) \tag{5.28b}$$

$$\begin{aligned}\frac{\partial \mathbf{m}}{\partial t} &= \nabla_x \cdot [\mathbf{D}_{\mathbf{m}} \nabla_x \mathbf{m}] - \int_{\mathscr{P}} \left(\hat{\mathbf{b}}(y, \mathbf{m}) - \hat{\mathbf{d}}(y) \right) s(t, x, y)\, \mathrm{d}y \\ &\quad + \boldsymbol{\psi}_{\mathbf{m}}(\mathbf{u}, \mathbf{r}) - \mathrm{diag}(\boldsymbol{\delta}_{\mathbf{m}}) \mathbf{m}\end{aligned} \tag{5.28c}$$

where, for notational simplicity, we omitted here the $\hat{}$ notation that we introduced in Eq. (5.19) to extend the mapping c (but we assume that the extended mapping $\hat{c}$ is used implicitly wherever this is necessary).

System (5.28) is assumed to hold for $t \in \mathscr{I}$, $x \in \Omega$ and $y \in \mathscr{P}$ and is complemented by initial conditions

$$c(0, x, y) = c_0(x, y)\,, \quad v(0, x) = v_0(x)\,, \quad \mathbf{m}(0, x) = \mathbf{m}_0(x) \quad \text{for } x \in \overline{\Omega},\ y \in \overline{\mathscr{P}}\,, \tag{5.29a}$$

and zero-flux boundary conditions in space, that is

$$\begin{aligned}\left[D_c \nabla_x c - c(1-\rho(\mathbf{u})) \left(\sum_{k=1}^{q} \chi_k \nabla_x m_k + \chi_v \nabla_x v \right) + c\mathscr{A} \right] \cdot \mathfrak{n}(x) = 0 \\ [\mathbf{D}_{\mathbf{m}} \nabla_x \mathbf{m}] \cdot \mathfrak{n}(x) = \mathbf{0}\end{aligned} \tag{5.29b}$$

for $t \in \mathscr{I}$, $x \in \partial\Omega$, $y \in \mathscr{P}$, where $\mathfrak{n}(x)$ denotes the outer normal vector on ∂D in $x \in \partial\Omega$. Since we assume that no cells with i-states outside $\mathscr{P}$ exist, the boundary

condition for the i-state space is

$$c(t,x,y) = 0 \qquad \text{for } t \in \mathscr{I},\ x \in \Omega,\ y \in \partial\mathscr{P}. \tag{5.29c}$$

5.3.6 Application of the Structured-Population Approach to a Model of Cancer Invasion Based on the uPA System

A key enzymatic system in cancer invasion is the urokinase plasminogen activation system, known as *the uPA system* [3, 15, 44, 49, 51]. Playing a major role in ECM degradation during cancer invasion, this is a proteolytic system that is based on the dynamic interplay of four major populations on molecules, namely: (1) urokinase plasminogen activator (uPA); (2) plasminogen activator inhibitor type-1 (PAI-1) proteins; (3) the urokinase plasminogen activator receptors (uPAR) which are bound to the cancer cell membranes; and (4) the matrix degrading enzyme plasmin.

In a brief description, the uPA is an extracellular serine protease produced by cancer cells and that has two major functional domains namely: (1) the protease domain; and (2) the growth factor domain. The protease domain activates plasmin from its pro-enzyme plasminogen form which is then able to bind to the uPAR receptors on the cancer cells. At the same time, the inhibitor PAI-1 is able to bind to membrane-bound uPA, and this way to inhibit plasminogen activation into plasmin. Finally, once activated, plasmin is able to degrade several classes of ECM proteins such as fibronectin, laminin, vitronectin and thrombospondin.

While over the past decade the role of uPA system in cancer invasion attracted significant non-structured mathematical modelling [1, 9, 10, 40], in this subsection we address the following structural dynamics. Under the assumption that cancer cells carry an amount M of uPAR bound to their surface, free uPA molecules may bind to these receptors and free PAI-1 enzymes bind to the bound uPA, and so denoting

$y_1 :=$ the amount of uPA that gets bound to the cell surface receptors,
$y_2 :=$ the amount of bound inhibitor PAI-1 attached to the bound uPA enzymes,

we arrive at the following 2-dimensional binding structure i-state space:

$$\mathscr{P} = \{y \in [0,M]^2 \,|\, y_2 \le y_1\} \tag{5.30}$$

which is illustrated in Fig. 5.7. Therefore, in the following we explore the particular spatio-temporal-structural modelling formulation that the general framework (5.28) induces for cancer invasion when the uPA system is considered. In this context, the tumour assumes a tissue-scale configuration consisting of:

- a structured cancer cell distribution $c(t,x,y)$;
- an extracellular matrix density $v(t,x)$;

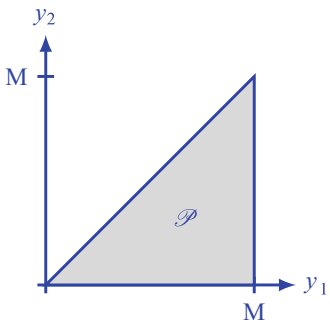

Fig. 5.7 This figure is a modified reproduction of a part of Fig. 5 from [14]. This is a schematic diagram of binding structure i-state space $\mathscr{P}$

- three molecular species, written as in vector form as

$$\mathbf{m} = \begin{pmatrix} m_1 \\ m_2 \\ m_3 \end{pmatrix},$$

  where $m_1(t,x)$ represents the uPA that binds to cell surface, $m_2(t,x)$ stands for the PAI-1 that attach to and this way inhibit the bounded uPA , and $m_3(t,x)$ is the plasmin that is not able to bind to the cell surface.

Therefore, using the terminology from Sect. 5.3.1, m_1 and m_2 are the species that are able to bind and unbind from the cell surface, while m_3 is not assumed to bind, and so the number of bound molecular species is $p = 2$, the total number of molecular populations that are considered here is $q = 3$. Moreover, the vector of the binding rates defined in (5.22)–(5.23) translates here as

$$\mathbf{b}(y, \mathbf{m}) = \begin{pmatrix} b_1(y, \mathbf{m}) \\ b_2(y, \mathbf{m}) \end{pmatrix},$$

which are derived as follows. On one hand, the binding rate of free uPA is assumed to be proportional to the available amount of $\mathscr{P}-$distributed unoccupied receptors $M - y_1$, and so this way obtain that

$$b_1(y, \mathbf{m}) = \frac{(M - y_1)}{\int\limits_{\mathscr{P}} (M - y_1)\, \mathrm{d}y} \beta_1 m_1 = \frac{6}{M^3}(M - y_1)\beta_1 m_1 \,. \tag{5.31}$$

On the other hand, the binding rate of the free inhibitor PAI-1 is assumed to be proportional to the available $\mathscr{P}-$distributed amount of uninhibited bound uPA molecules $y_1 - y_2$, and so we obtain that

$$b_2(y, \mathbf{m}) = \frac{(y_1 - y_2)}{\int\limits_{\mathscr{P}} (y_1 - y_2)\, \mathrm{d}y} \beta_2 m_2 = \frac{6}{M^3}(y_1 - y_2)\beta_2 m_2 \,. \tag{5.32}$$

Finally, while the uPA is produced by the cancer cells, and the inhibitor PAI-1 is produced via plasmin activation, plasmin itself is activated from plasminogen by uninhibited bound uPA. Thus, in the notations from Sects. 5.3.1–5.3.5, we obtain that the vector of molecular production terms $\boldsymbol{\psi}_{\mathbf{m}}(\mathbf{u}, \mathbf{r})$ is given by

$$\boldsymbol{\psi}_{\mathbf{m}}(\mathbf{u}, \mathbf{r}) = \begin{pmatrix} \alpha_{m_1} C \\ \alpha_{m_2} m_3 \\ \alpha_{m_3}(E_1 - E_2) \end{pmatrix}$$

Therefore, in the special case of uPA based cancer invasion, under the presence of logistic proliferation law $\Phi(c, v) = \mu_c(1 - \rho(c, v))$, the general framework (5.28) gives the following spatio-temporal-structural dynamics, namely:

$$\begin{aligned} \frac{\partial c}{\partial t} &= \nabla_x \cdot \Big(D_c \nabla_x c - c(1 - \rho(c, v)) \left(\chi_1 \nabla_x m_1 + \chi_2 \nabla_x m_2 + \chi_v \nabla_x v\right) \Big) \\ &\quad - \nabla_y \cdot \Big(c\mathbf{b}(y, \mathbf{m}) \Big) + \Phi(\mathbf{u}) \left(8c(2y, t, x) - c(y, t, x)\right) , \end{aligned} \tag{5.33a}$$

$$\frac{\partial v}{\partial t} = -\delta_v m_3 v + \mu_v (1 - \rho(c, v))^+ , \tag{5.33b}$$

$$\frac{\partial m_1}{\partial t} = \nabla_x \cdot [D_{m_1} \nabla_x m_1] - \int_{\mathscr{P}} b_1(y, \mathbf{m}) s(t, x, y) \, \mathrm{d}y + \alpha_{m_1} C , \tag{5.33c}$$

$$\frac{\partial m_2}{\partial t} = \nabla_x \cdot [D_{m_2} \nabla_x m_2] - \int_{\mathscr{P}} b_2(y, \mathbf{m}) s(t, x, y) \, \mathrm{d}y + \alpha_{m_2} m_3 , \tag{5.33d}$$

$$\frac{\partial m_3}{\partial t} = \nabla_x \cdot [D_{m_3} \nabla_x m_3] + \alpha_{m_3}(E_1 - E_2) - \delta_{m_3} m_3 , \tag{5.33e}$$

which is assumed to be appropriately accompanied by initial and boundary conditions of the type described in (5.29).

Finally, we would like to conclude this section by remarking that by performing an i-state integration of the system (5.33), see [14] for details, the resulting unstructured model is similar in flavour to the one initially proposed by Chaplain and Lolas [9, 10], which, in the above notations, is briefly stated here as

$$\frac{\partial C}{\partial t} = D_C \Delta C - \nabla \cdot [\chi_1 C \nabla m_1 + \chi_2 C \nabla m_2 + \chi_v C \nabla v] + \mu_1 C(1 - C) , \tag{5.34a}$$

$$\frac{\partial v}{\partial t} = -\delta v m_3 + \phi_{21} u m_2 - \phi_{22} v m_2 + \mu_2 v(1 - v) , \tag{5.34b}$$

$$\frac{\partial m_1}{\partial t} = D_{m_1}\Delta m_1 - \phi_{31} m_1 m_2 - \phi_{33} c m_1 + \alpha_{31} C, \tag{5.34c}$$

$$\frac{\partial m_2}{\partial t} = D_{m_2}\Delta m_2 - \phi_{41} m_1 m_2 - \phi_{42} v m_2 + \alpha_{41} m_3, \tag{5.34d}$$

$$\frac{\partial m_3}{\partial t} = D_{m_3}\Delta m_3 + \phi_{52} v m_2 + \phi_{53} C m_1 - \phi_{54} m_3 . \tag{5.34e}$$

5.4 Multiscale Moving Boundary Modelling Framework for Tumour Invasion

Extending the single-scale modelling perspective discussed so far, in this section we present the general multiscale modelling framework for cancer invasion introduced in [47] and its application to the specific case of the uPA proteolitic system discussed in [40]. This aims to explore the inherently a multi-scale character of cancer invasion, whose processes occurring at several spatial and temporal scales e.g. molecular, cellular and tissue levels.

The general modeling approach introduced in [47] explores in an integrated manner the tissue-scale cell population dynamics and relevant cell-scale molecular mechanics together with the permanent link between these two biological scales. This explores the biological evidence that specific MDEs, such as the matrix metalloproteinases (MMPs or the uPA) (secreted from the outer proliferating rim and released within the tumour microenvironment), play a crucial role in the local cancer invasion [22, 54]. The tissue-scale progression of tumour morphology is captured here in a multiscale moving boundary approach where the contribution arriving from the cell-scale activity to the cancer invasion pattern is realised by the micro-scale MDEs dynamics (occurring along the tumour invasive edge), which, for its part, is induced by the cancer macro-dynamics.

5.4.1 Modelling Framework Set-Up: The Macroscopic Dynamics and Top-Down Link

As from a topological perspective, we regard an invading solid tumour within a human body as a growing compact $\Omega(t)$, it is therefore natural to assume that its development is taking place within a large enough spatial cube $Y \subset \mathbb{R}^n (n = 2, 3)$ (say, in 3D, of the size of a classroom), i.e., $\Omega(t) \subset Y$, $\forall t > 0$. Without loss of generality, we set the origin of the space at the centre of Y, and let t_0 be an arbitrarily chosen time during tumour evolution. In this context, we assume that the tissue-scale macro-dynamics is given by a coupled system of reaction-diffusion-taxis equations, generally written in terms of differential operators as

$$\mathfrak{M}(c, v, \mathbf{m}, t) = 0, \quad t \in [0, T], \tag{5.35}$$

where $c, v, \mathbf{m}$ are the cancer cell population, the ECM density, and the vector of proteolytic enzymes densities, respectively. Depending on the particular question under investigation, examples of such tissue scale operator equations include for instance the spatio-temporal system (5.1)–(5.4) discussed in Sect. 5.2.1, or the spatio-temporal-structural dynamics (5.28) in summarised in Sect. 5.3.5, or other macroscopic systems proposed in the literature such as the one introduced in initially in [9, 10] and summarised here in (5.34).

However, large biological evidence [2, 3, 15, 22, 41, 49, 54] reveal that the invasive edge cell-scale molecular dynamics exercised by several classes of MDEs, such as MMPs or the uPA system, play a key role in local cancer invasion. Specifically, those cancer cells that during their dynamics arrive within the tumour outer proliferating rim are able to secrete these MDEs, and once secreted, these molecular populations of enzymes are exercising a local parabolic dynamics in a cell-scale neighbourhood of the tumour interface $\partial\Omega(t_0)$, degrading the surrounding tissue and this way causing further tumour progression.

To formalise mathematically this top-down link between tissue-scale dynamics of cell population and the cell scale dynamics of a generic MDE m that is secreted by the cancer, let us denote by $\gamma > 0$ the maximal thickness of the outer proliferating rim. Therefore, considering now a cell-scale neighbourhood $\mathscr{H}$ of $\partial\Omega(t_0)$, at any point $y \in \partial\Omega(t_0) \cap \mathscr{H}$ and any instance $\tau \in [0, \Delta t]$ during the tumour evolution over the period $[t_0, t_0 + \Delta t]$, a source of MDEs $f_{\mathscr{H}} : [0, \Delta t] \times \mathscr{H} \to \mathbb{R}_+$ arises as a collective contribution of all the cancer cells within distance γ. Thus, using the Smooth Urysohn Theorem [20], we obtain a space-wise smooth compact support source $f_{\mathscr{H}}$ such that, for any $\tau \in [0, \Delta t]$, $f_{\epsilon Y}(\cdot, \tau)$ has the following properties:

$$
\begin{aligned}
&1.\, f_{\mathscr{H}}(\tau, y) = \frac{1}{\lambda(\mathbf{B}(y,\gamma) \cap \Omega(t_0))} \int\limits_{\mathbf{B}(y,\gamma)\cap\Omega(t_0)} c_{\Omega(t_0)}(x, t_0 + \tau), dx, \quad y \in \mathscr{H} \cap \Omega(t_0), \\
&2.\, f_{\mathscr{H}}(\tau, y) = 0, \quad y \in \mathscr{H} \setminus \big(\Omega(t_0) + \{z \in Y \mid \|z\|_2 < \zeta\}\big),
\end{aligned}
\tag{5.36}
$$

where $\lambda(\cdot)$ is the standard Lebesgue measure on $\mathbb{R}^n$, $\mathbf{B}(y, \gamma)$ is the usual L^∞-ball, i.e., $\mathbf{B}(y, \gamma) := \{x \in Y \mid \|y - x\|_\infty \leq \gamma\}$, and ζ is a small enough constant that enable fast and smooth decay to 0 of the $f_{\mathscr{H}}(\tau, y)$ outside the tumour region $\Omega(t_0)$.

In the following subsection we will focus on the development of a constructive topological approach that will allow us to obtain a cell-scale neighbourhood of $\partial\Omega(t_0)$ which will enable the exploration of the MDEs molecular dynamics.

5.4.2 *Exploring the MDEs Micro-Dynamics*

Given the importance of the interface cell-scale processes in the overall cancer invasion, in the following we will develop a mathematical setting that will enable us to explore the micro-scale MDEs dynamics in a computationally feasible way. For this purpose, we focus first on developing a flexible boundary tracking technique that will enable the decoupling the micro-dynamics occurring in a cell-

scale neighbourhood of the tumour interface in a bundle of reaction-diffusion-type processes occurring on finite family of *half-way overlapping micro-domains*.

Given a fixed ϵ representing a negative power of 2 (i.e., $0 < \epsilon < 1$), we decompose uniformly the cube Y in the corresponding collection of ϵ-size cubes, ϵY, whose union will provide an ϵ-resolution of Y. For any small cube ϵY from this decomposition, for any triplet $(i,j,k) \in \{(i,j,k)|i,j,k \in \{-1,0,1\}\}$, we define the "half-way shifted" cubes in the direction $i\bar{e}_1 + j\bar{e}_2 + k\bar{e}_3$ as

$$\epsilon Y_{\frac{i}{2},\frac{j}{2},\frac{k}{2}} = \epsilon Y + \frac{\epsilon(i\bar{e}_1 + j\bar{e}_2 + k\bar{e}_3)}{2}, \tag{5.37}$$

where,

$$\bar{e}_1 := e_1, \qquad \bar{e}_2 := e_2, \qquad \text{and,} \qquad \bar{e}_3 := \begin{cases} e_3 \text{ for } & N = 3, \\ 0 \text{ for } & N = 2, \end{cases} \tag{5.38}$$

and $\{e_1, e_2, e_3\}$ is the standard Euclidean basis of $\mathbb{R}^3$. Collecting now all the cubes from the initial ϵ-resolution together with the associated half-way shifted cubes, we obtain the following family of $\epsilon-$cubes

$$\mathscr{F}_\epsilon := \bigcup_{i,j,k\in\{-1,0,1\}} \left\{\epsilon Y_{\frac{i}{2},\frac{j}{2},\frac{k}{2}} \middle| \epsilon Y \text{ is in the } \epsilon\text{-resolution of } Y\right\}. \tag{5.39}$$

The mathematical setting constructed so far is schematically illustrated in 3D in Fig. 5.8.

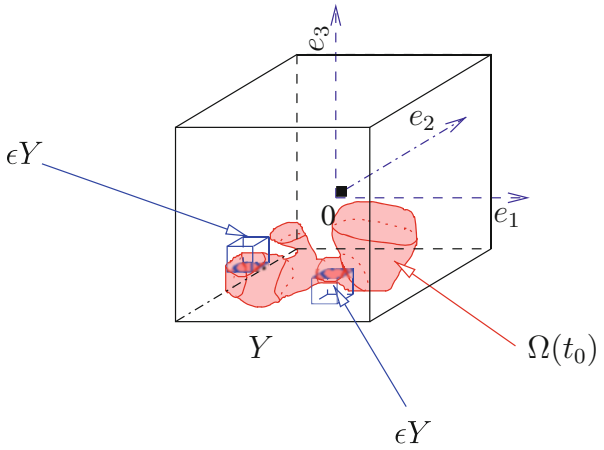

Fig. 5.8 This figure is a reproduction under **granted copyright from SIAM MMS** of Fig. 1 from [47]. This is a schematic diagram showing the cubic region Y centred at $0 \in \mathbb{R}^3$. The *dashed blue lines* represent the Euclidean directions $\{e_1, e_2, e_3\}$, the *pink* region illustrates the cancer cluster $\Omega(t_0)$, and the *solid blue line* represents the family of microscopic cubic domains ϵY placed at the boundary of $\Omega(t_0)$.

As at this stage our focus is to characterise the microdynamics occurring in a cell-scale neighbourhood of the tumour boundary $\partial\Omega(t_0)$, we select a subfamily denoted by $\mathscr{F}_{\epsilon,\Omega(t_0)} \subset \mathscr{F}_\epsilon$, consisting only the $\epsilon-$cubes from $\mathscr{F}_\epsilon$ that cross the tumour interface $\partial\Omega(t_0)$ and have exactly one face included in the interior of $\Omega(t_0)$, namely

$$\begin{aligned}\mathscr{F}_{\epsilon,\Omega(t_0)} := \{\epsilon Y \in \mathscr{F}_\epsilon | \epsilon Y \cap (Y \backslash \Omega(t_0)) \neq \emptyset,\\ \text{and } \epsilon Y \text{ has only one face included in int}(\Omega(t_0))\},\end{aligned} \tag{5.40}$$

where $\text{int}(\Omega(t_0))$ is the topological interior of $\Omega(t_0)$ with respect to the natural topology on $\mathbb{R}^n$.

By taking now a closer look at each $\epsilon Y \in \mathscr{F}_{\epsilon,\Omega(t_0)}$, we distinguish several geometrical features, and we denote these as follows:

$$\begin{cases} \Gamma_{\epsilon Y}^{int} \text{ denotes the face of } \epsilon Y \text{ that is included in int}(\Omega(t_0)), \\ \Gamma_{\epsilon Y}^{j,\perp}, j = 1, \ldots, 2^{N-1}, \text{ denote the faces of } \epsilon Y \text{ that are perpendicular to } \Gamma_{\epsilon Y}^{int} \\ \Gamma_{\epsilon Y}^{\parallel} \text{ denotes the face of } \epsilon Y \text{ that is parallel to } \Gamma_{\epsilon Y}^{int}. \end{cases} \tag{5.41}$$

Furthermore, for each $\epsilon Y \in \mathscr{F}_{\epsilon,\Omega(t_0)}$, as illustrated in Fig. 5.9, while it is possible to have a multiple connected component intersection between $\Omega(t_0)$ and ϵY, there is only one connected component that contains the face included in $int(\Omega(t_0))$. The topological closure of this particular connected component of $\Omega(t_0) \cap \epsilon Y$, which is confined between $\partial\Omega(t_0) \cap \epsilon Y$ and $\Gamma_{\epsilon Y}^{int}$, is denoted by $[\Omega(t_0)]_{\epsilon Y}$, i.e.,

$$[\Omega(t_0)]_{\epsilon Y} := \overline{\left\{ x \in \Omega(t_0) \cap \epsilon Y \;\middle|\; \begin{array}{c} \forall y \in \Gamma_{\epsilon Y}^{int},\ \exists\, \gamma_{x,y} : [0,1] \to \Omega(t_0) \cap \epsilon Y \\ \text{such that } \gamma_{x,y} \text{ is continuous and} \\ \gamma_{x,y}(0) = x \text{ and } \gamma_{x,y}(1) = y \end{array} \right\}} \tag{5.42}$$

Additionally, denoting by $[\partial\Omega(t_0)]_{\epsilon Y}$ the connected component part of $\partial\Omega(t_0) \cap \epsilon Y$ that corresponds to $[\Omega(t_0)]_{\epsilon Y}$, i.e.,

$$[\partial\Omega(t_0)]_{\epsilon Y} := [\Omega(t_0)]_{\epsilon Y} \cap \partial\Omega(t_0) \tag{5.43}$$

we can immediately observe that this is the only connected component of the set $\partial\Omega(t_0) \cap \epsilon Y$ that has non-empty intersection with any of the $\Gamma_{\epsilon Y}^{j,\perp}$, $j = 1, \ldots, 2^{n-1}$. Therefore, since we are interested in characterising the MDEs microdynamics occurring on both sides of tumour interface, using these last topological observations, we perform now a filtering of the family $\mathscr{F}_{\epsilon,\Omega(t_0)}$ and select a special subfamily, denoted by $\mathscr{F}^*_{\epsilon,\Omega(t_0)} \subset \mathscr{F}_{\epsilon,\Omega(t_0)}$, which consists only of those $\epsilon-$cubes

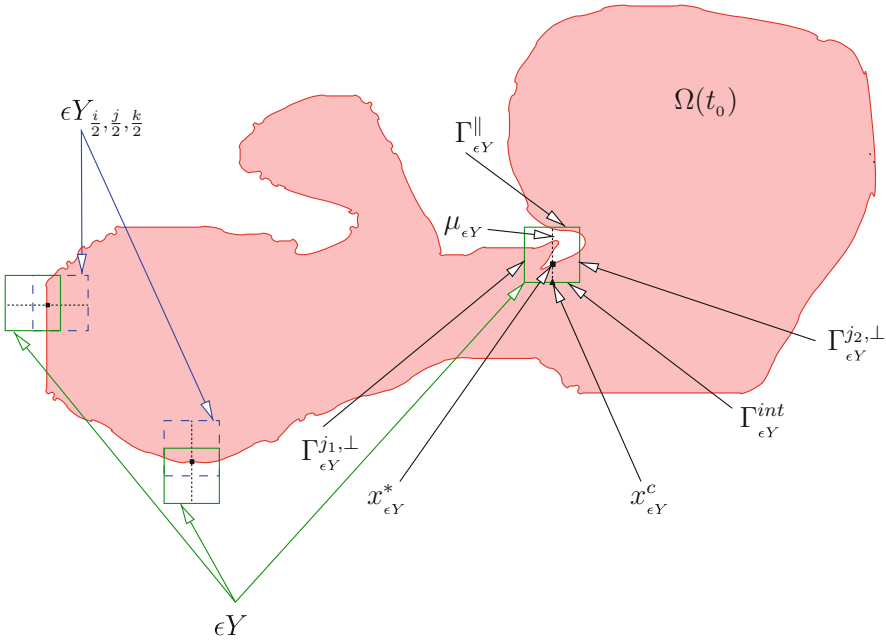

Fig. 5.9 This figure is a reproduction under **granted copyright from SIAM MMS** of Fig. 2 from [47]. This is a schematic diagram illustrating the notations introduced in Eqs. (5.37)–(5.41) and (5.45). For the arbitrary micro-domain ϵY, we indicate with a *black arrow* the features: $\Gamma^{int}_{\epsilon Y}$, $\Gamma^{j_1,\perp}_{\epsilon Y}$ and $\Gamma^{j_2,\perp}_{\epsilon Y}$, $j_1, j_2 \in \{1,\ldots,2^{n-1}\}$, $\Gamma^{\parallel}_{\epsilon Y}$, $x^{c}_{\epsilon Y}$, $\mu_{\epsilon Y}$, and $x^{*}_{\epsilon Y}$. Copyright ©2013 Society for Industrial and Applied Mathematics. Reprinted with permission. All rights reserved

that have the connected component $[\Omega(t_0)]_{\epsilon Y}$ not intersecting $\Gamma^{\parallel}_{\epsilon Y}$, namely:

$$\mathscr{F}^{*}_{\epsilon,\Omega(t_0)} := \{\epsilon Y \in \mathscr{F}_{\epsilon,\Omega(t_0)} |\ [\Omega(t_0)]_{\epsilon Y} \subset \epsilon Y \text{ and } [\partial\Omega(t_0)]_{\epsilon Y} \cap \Gamma^{\parallel}_{\epsilon Y} = \emptyset\}. \tag{5.44}$$

We can immediately remark that, for the fixed ϵ that we started with, due to the topological constraints imposed in selecting the ϵ-cubes, the resulting family $\mathscr{F}^{*}_{\epsilon,\Omega(t_0)}$ may not be able to provide us with a complete covering of the entire tumour interface. However, leaving now ϵ to take all the negative powers of 2, the union

$$\bigcup_{\epsilon\in\{2^{-k}\,|\,k\in\mathbb{N}\}} \mathscr{F}^{*}_{\epsilon,\Omega(t_0)}$$

provides an infinite covering of $\partial\Omega(t_0)$. Since $\partial\Omega(t_0)$ is compact, using standard compactness arguments combined with the dyadic structure of the ϵ-cubes from

the infinite covering of $\partial\Omega(t_0)$, we obtain that we can sub-select a finite complete sub-covering

$$\mathscr{H} \subset \bigcup_{\epsilon\in\{2^{-p}|p\in\mathbb{N}\}} \mathscr{F}^{*}_{\epsilon,\Omega(t_0)} \quad \text{formed of small cubes of equal size } \epsilon_{\mathscr{H}}$$
$$\text{such that} \quad \bigcup_{\epsilon_{\mathscr{H}} Y\in\mathscr{H}} \epsilon_{\mathscr{H}} Y \supset \partial\Omega(t_0).$$

Therefore, the size of the micro-scale $\epsilon_{\Omega(t_0)}$ will be given by the coarsest finite interface covering of this kind, namely

$$\epsilon_{\Omega(t_0)} := \sup\left\{ \epsilon \;\middle|\; \begin{array}{c} \exists\, \mathscr{H}_\epsilon \subset \bigcup\limits_{\epsilon\in\{2^{-p}|p\in\mathbb{N}\}} \mathscr{F}^{*}_{\epsilon,\Omega(t_0)}, \text{ with } |\mathscr{H}_\epsilon| < \infty, \\ \text{formed of small cubes of equal size } \epsilon \\ \text{such that } \bigcup\limits_{\epsilon Y\in\mathscr{H}_\epsilon} \epsilon Y \supset \partial\Omega(t_0) \end{array} \right\},$$

and the corresponding family of $\epsilon_{\Omega(t_0)}$-cubes, $\mathscr{H}_{\epsilon_{\Omega(t_0)}}$, represents the desired cell-scale covering of the tumour interface $\partial\Omega(t_0)$. Thus, together with the covering bundle of the interface we also obtain the size of the micro-scale [47].

For simplicity of notation, for the rest of the discussion in this chapter, we will drop the index notation $_{\Omega(t_0)}$ for the size of the micro-scale $\epsilon_{\Omega(t_0)}$, and we will simply denote this by ϵ. As a consequence, for the rest of the chapter, also the associated covering bundle $\mathscr{H}_{\epsilon_{\Omega(t_0)}}$ will be correspondingly denoted simply by $\mathscr{H}_\epsilon$. Moreover, any ϵY cube in $\mathscr{H}_\epsilon$ will be referred to as *micro-cube* or *micro-domain*. Finally, for any micro-domain $\epsilon Y \in \mathscr{H}_\epsilon$, we distinguish the following topological details:

$$\left\{ \begin{array}{l} x^{c}_{\epsilon Y} \text{ denotes the centre of the face } \Gamma^{int}_{\epsilon Y}, \\ \\ \mu_{\epsilon Y}, \text{ is the line that passes through } x^{c}_{\epsilon Y} \text{ and is perpendicular on } \Gamma^{int}_{\epsilon Y} \\ \\ x^{*}_{\epsilon Y} \in [\partial\Omega(t_0)]_{\epsilon Y} \text{ which will be referred to as the "midpoint" of } [\partial\Omega(t_0)]_{\epsilon Y}, \\ \text{represents the point from the intersection } \mu_{\epsilon Y} \cap [\partial\Omega(t_0)]_{\epsilon Y} \text{ that is located} \\ \text{at the smallest distance with respect to } x^{c}_{\epsilon Y}. \end{array} \right. \tag{5.45}$$

which are illustrated in Fig. 5.9, with further discussions on their well-posedness being available in [47].

Given the particular overlapping micro-domains structure of the covering $\mathscr{H}_\epsilon$ for $\partial\Omega(t_0)$, the local cell-scale cross-interface parabolic dynamics of the MDEs that arises on $\mathscr{H}_\epsilon$ in the presence of source defined (5.36) can this way be decomposed into a bundle of micro-processes occurring on each micro-domain $\epsilon Y \in \mathscr{H}_\epsilon$. The midpoints introduced above will turn out to play a key role in the forthcoming discussion as the *choreographic movement* of the tumour interface captured by a

given micro-domain ϵY will be characterised and represented back at macro-scale through the movement of the associated $x^*_{\epsilon Y}$.

In the following, we describe the MDEs dynamics that emerges at micro-scale when considering the uPA system as the main cell-scale proteolytic process that is responsible for the ECM degradation at the invasive edge $\partial\Omega(t)$ of the tumour $\Omega(t)$. This, of course, is just one example of micro-scale MDEs processes, however, the modelling techniques remains unchanged should other proteolytic enzymes need to be considered.

5.4.2.1 The uPA Micro-Dynamics on Each Micro-Domain in $\mathscr{H}_\epsilon$

On any micro-domain ϵY, at any instance $\tau \in [0, \Delta t]$ and any micro-scale spatial point $y \in \epsilon Y \cap \Omega(t_0)$, a source of uPA arises as a collective contribution of the cancer cell population that arrive within its neighbourhood, and so this is given by the following particular form general MDEs source operator defined in (5.36), namely by a smooth function $f^1_{\epsilon Y} : [0, \Delta t] \times \epsilon Y \to \mathbb{R}_+$ that is defined by

$$1.\, f^1_{\epsilon Y}(\tau, y) = \frac{1}{\lambda(\mathbf{B}(y,\gamma)\cap\Omega(t_0))} \int\limits_{\mathbf{B}(y,\gamma)\cap\Omega(t_0)} c_{\Omega(t_0)}(x, t_0 + \tau), dx, \quad y \in \epsilon Y \cap \Omega(t_0),$$

$$2.\, f^1_{\epsilon Y}(\tau, y) = 0, \quad y \in \epsilon Y \setminus \big(\Omega(t_0) + \{z \in Y \mid \|z\|_2 < \zeta\}\big), \tag{5.46}$$

with the parameters γ and ζ considered as in (5.36). Per unit time, under the presence of the source (5.46), the uPA molecular population $h_1(\cdot,\cdot)$ exercises a local diffusion is inhibited by the interaction with the $h_2(\cdot,\cdot)$ density of PAI-1 inhibitors and binds to the cell receptors uPAR (to activate plasmin). Therefore, the uPA dynamics on the micro-domain ϵY is governed by

$$\frac{\partial h_1}{\partial \tau} = \underbrace{D_{h_1}\Delta h_1}_{\text{diffusion}} - \underbrace{\xi_{11} h_1 h_2}_{\text{uPA/PAI-1}} + \underbrace{(\ \alpha_1}_{\text{production}} - \underbrace{\xi_{12} u)}_{\text{uPA/uPAR}} f^1_{\epsilon Y}(y, \tau) \tag{5.47}$$

Further, per unit time, the change in the inhibitor PAI-1 density $h_2(\cdot,\cdot)$ is due to diffusion, production caused by plasmin activation density $h_3(\cdot,\cdot)$, and loss triggered by binding to uPA and ECM. As the binding of PAI-1 to ECM corresponds to the local distribution of ECM distribution in the neighbourhood of any point $y \in \epsilon Y$, proceeding similarly to the case of the source term (5.46), we explore this aspect by accounting for a *binding* coefficient that is defined as

$$f^2_{\epsilon Y}(y, \tau) = \frac{1}{\lambda(\mathbf{B}(y,\gamma))} \int\limits_{\mathbf{B}(y,\gamma)} v\ (x, t_0 + \tau)\ dx, \quad y \in \epsilon Y,$$

where the involved notations have the same meaning as in (5.46). Therefore, the micro-dynamics of the PAI-1 inhibitor in ϵY is given by

$$\frac{\partial h_2}{\partial \tau} = \underbrace{D_{h_2}\Delta h_2}_{\text{diffusion}} - \underbrace{\xi_{21}h_1h_2}_{\text{uPA/PAI-1}} - \underbrace{\xi_{22}h_2 f^2_{\epsilon Y}(y,\tau)}_{\text{PAI-1/ECM}} + \underbrace{\alpha_2 h_3}_{\text{production}} . \tag{5.48}$$

Finally, under the presence of appropriate sources and natural decay, per unit time the evolution of the plasmin density $h_3(\cdot,\cdot)$ is governed by local diffusion. Specifically, as the molecular proteolytic activity requires the binding of uPA to the cell receptors uPAR, a direct source of plasmin density h_3 results from the binding of uPA to the surface of the readily available cells from the same maximal spatial neighbourhood where the uPA is secreted in the first place. On the other hand, the binding of PAI-1 to the neighbouring ECM enables additional opportunities for uPA to bind the cell receptors uPAR, and so this indirectly results in a corresponding formation of plasmin. Therefore, the dynamics of plasmin on ϵY is given by

$$\frac{\partial h_3}{\partial \tau} = \underbrace{D_{h_3}\Delta h_3}_{\text{diffusion}} + \underbrace{\xi_{31}h_1 f^1_{\epsilon Y}(y,\tau)}_{\text{uPA/uPAR}} + \underbrace{\xi_{32}h_2 f^2_{\epsilon Y}(y,\tau)}_{\text{PAI-1/ECM}} - \underbrace{\alpha_3 h_3}_{\text{degradation}} \tag{5.49}$$

During its dynamics, plasmin degrades the ECM that it meets within the micro-domain ϵY, this way enabling the progression of the tumour in the space created. It is therefore the pattern of the ECM degradation caused by the micro-dynamics of the matrix degrading enzyme plasmin that we are seeking to characterise in order to learn the way the macro-scale tumour boundary will evolve. In the following subsection we focus on exploring the law for the tissue scale boundary movement that is induced by the micro-dynamics on each micro-domain ϵY.

5.4.3 *The Macroscale Boundary Movement Induced by the Invasive Edge MDE Micro-Dynamics*

In the following, we focus on characterising the *choreographic movement* of the part of the tumour interface captured by a given micro-domain $\epsilon Y \in \mathscr{H}_\epsilon$, i.e., the evolution of $[\partial\Omega(t_0)]_{\epsilon Y}$, that will be represented back at macro-scale through the movement of the associated midpoint $x^*_{\epsilon Y}$.

Based on biological evidence, on any micro domain $\epsilon Y \in \mathscr{H}_\epsilon$, the pattern of ECM degradation corresponds to the pattern of the front of the advancing spatial distribution of the matrix-degrading enzyme plasmin. This determines the evolution of $[\partial\Omega(t_0)]_{\epsilon Y}$ and paves the way for defining appropriate movement laws for the associated midpoint $x^*_{\epsilon Y}$ that will represent this back at macro-scale. However, in order to characterise this pattern of significant ECM degradation globally, on the entire bundle of micro-domains $\mathscr{H}_\epsilon$, it of interest to identify with the same fixed

accuracy $\rho > 0$ the part of the level set of the expectation of degrading enzyme plasmin on $\epsilon Y \setminus \Omega(t_0)$ distributed during the entire micro-dynamics that is located at the biggest possible distance from $x^*_{\epsilon Y}$.

For any given $\rho > 0$, we use the regularity property of Lebesgue measure [21] as a stopping criterion to select the first dyadic decomposition $\{D_j\}_{j\in \mathscr{J}_\rho}$ of ϵY such that

$$\lambda\left([\epsilon Y\setminus\Omega(t_0)] \setminus \bigcup_{\{j\in \mathscr{J}_\rho \,|\, D_j\subset \epsilon Y\setminus\Omega(t_0)\}} D_j\right) \leq \rho. \tag{5.50}$$

This simply means that the union of all the dyadic cubes from $\{D_j\}_{j\in \mathscr{J}_\rho}$ that are included in $\epsilon Y \setminus \Omega(t_0)$ approximates $\epsilon Y \setminus \Omega(t_0)$ to accuracy ρ. Further, let us denote by y_j the barycenters of D_j, for all $j \in \mathscr{J}_\delta$. As announced earlier and widely explained in [47], for all $\epsilon Y \in \mathscr{H}_\epsilon$, this provides a resolution for the ϵY at which we identify the part of the level set $\frac{1}{\lambda(\epsilon Y\setminus\Omega(t_0))}\int_{\epsilon Y\setminus\Omega(t_0)} h_3(y,\cdot)dy$ in the distribution of the advancing front of degrading enzymes $h_3(\cdot,\cdot)$ outside $\Omega(t_0)$ that is located at maximal distance in radial direction with respect to the midpoint $x^*_{\epsilon Y}$. Thus, this resolution allows us to identify the dyadic pixels D_l that support the peaks at the tip of the plasmin front at the final time of micro-dynamics $\tau_f = \Delta t$ that still have significant contribution in degrading the ECM. Hence, as described in [40, 47], the pixels supporting these peaks represent the furthest away part of the level set $\frac{1}{\lambda(\epsilon Y\setminus\Omega(t_0))}\int_{\epsilon Y\setminus\Omega(t_0)} h_3(y,\cdot)dy$ with respect to $x^*_{\epsilon Y}$ and are identified by the following subset of indices, namely

$$\mathscr{I}_\rho := \left\{ l \in \mathscr{J}_\rho \;\middle|\; \begin{array}{l} \exists r \in S^1 \text{ such that, if the index } i \in \mathscr{J}_\rho \text{ has the properties:} \\ 1)\ D_i \cap \{x \in \mathbb{R}^n \,|\, x = x^*_{\epsilon Y} + \alpha r, \alpha \in \mathbb{R}\} \neq \emptyset, \\ 2)\ D_i \subset \epsilon Y\setminus\Omega(t_0), \\ 3)\ \frac{1}{\lambda(D_i)}\int_{D_i} h_3(y,\tau_f)dy \geq \frac{1}{\lambda(\epsilon Y\setminus\Omega(t_0))}\int_{\epsilon Y\setminus\Omega(t_0)} h_3(y,\tau_f)dy, \\ \text{then} \\ l = argmax\{d(x^*_{\epsilon Y}, y_i) \,|\, i \in \mathscr{J}_\rho \text{ satisfies:} 1), 2), \text{ and } 3)\} \end{array} \right\}, \tag{5.51}$$

where $S^1 \subset \mathbb{R}^n$ is represents the unit sphere, and $d(\cdot,\cdot)$ is the standard Euclidean distance on $\mathbb{R}^n$, $n = 2, 3$.

Thus, as the local ECM degradation driven by each of these peaks at the tip of advancing front of plasmin depends directly both on the location of the supporting pixel D_l and on the amount on plasmin distributed on D_l, the direction $\eta_{\epsilon Y}$ for the potential displacement of $x^*_{\epsilon Y}$ is defined by the revolving direction determined by the position vectors $\overrightarrow{x^*_{\epsilon Y}, y_l}$ that are appropriately magnified by the corresponding plasmin mean-value on D_l, $\forall l \in \mathscr{I}_\rho$, namely

$$\eta_{\epsilon Y} = x^*_{\epsilon Y} + \nu \sum_{l\in\mathscr{I}_\rho}\left(\frac{1}{\lambda(D_j)}\int_{D_l} h_3(y,\tau_f)dy\right)(y - x^*_{\epsilon Y}), \quad \nu \in [0,\infty). \tag{5.52}$$

Furthermore, the displacement magnitude of the point $x^*_{\epsilon Y}$ is obtained as a convex combination of the magnitudes of these position vectors whose weight accounts for the relative MDEs strength of the peak supported by a given D_l with respect to all the selected peaks supported by $\{D_l\}_{l\in\mathscr{I}_\rho}$, and so this is defined by:

$$\xi_{\epsilon Y} := \sum_{l\in\mathscr{I}_\rho} \frac{\int_{\mathscr{D}_l} h_3(y,\tau_f)dy}{\sum\limits_{l\in\mathscr{I}_\rho}\int_{\mathscr{D}_l} h_3(y,\tau_f)dy} |\overrightarrow{x^*_{\epsilon Y} y_l}|. \tag{5.53}$$

Finally, as discussed in [40, 47], although a displacement magnitude and a moving direction is derived for each $x^*_{\epsilon Y}$, with $\epsilon Y \in \mathscr{H}_\epsilon$, this will only exercise the movement if and only if the ECM degradation attain a certain local strength. The local strength of ECM degradation within a given cross-interface region $A\epsilon Y$ corresponds to the amount of MDEs release on $\epsilon Y \setminus \Omega(t_0)$ relative to the total amount of MDEs on A and is explored by the local transitional probability

$$q^* : \mathscr{B}(\epsilon Y) \to \mathbb{R}_+$$

defined as

$$q^*(G) := \frac{1}{\int\limits_{\epsilon Y} h_3(y,\tau_f)dy} \int\limits_G h_3(y,\tau_f)dy, \qquad \text{for all } G \in \mathscr{B}(\epsilon Y) \tag{5.54}$$

where $\mathscr{B}(\epsilon Y)$ represents the Borel $\sigma-$algebra of ϵY. In conjunction with the local tissue conditions, this characterises whether the point $x^*_{\epsilon Y}$ is likely to relocate to the new spatial position $\widetilde{x^*_{\epsilon Y}}$ or not. Thus, the midpoint $x^*_{\epsilon Y}$ is moved to the new position $\widetilde{x^*_{\epsilon Y}}$ if and only if

$$q^*(x^*_{\epsilon Y}) := q^*(\epsilon Y \setminus \Omega(t_0)) \text{ exceeds a certain threshold } \omega_{\epsilon Y} \in (0,1).$$

Therefore, we finally obtain that the new tumour boundary $\partial\Omega(t_0+\Delta t)$ will be the interpolation of the following set of points:

$$\{x^*_{\epsilon Y} | \epsilon Y \in \mathscr{H}_\epsilon \text{ and } q^*(x^*_{\epsilon Y}) < \omega_{\epsilon Y}\} \cup \{\widetilde{x^*_{\epsilon Y}} | \epsilon Y \in \mathscr{H}_\epsilon \text{ and } q^*(x^*_{\epsilon Y}) \geq \omega_{\epsilon Y}\} \tag{5.55}$$

Therefore, the invasion process will now continue on the new expanded domain $\Omega(t_0+\Delta t)$, with a new macro-micro stage dynamics on the next multiscale timeframe $[t_0+\Delta t, t_0+2\Delta t]$, as detailed in [47].

5.4.4 Multiscale Computational Simulation Results

We implemented the multiscale model of cancer invasion described in this section using the multiscale numerical approach introduced in [47], which involves finite differences at macro-scale combined with finite element at micro-scale [40]. Here we consider that the cancer cell population is initially distributed on the tumour region $\Omega(0) := \mathbf{B}_{\|\cdot\|_2}((2,2),0.5)$, centred at the centre of the environmental cube $Y := [0,4] \times [0,4]$, and is assumed to be given by

$$c(x,0) = \frac{\left(\exp\left(-\frac{||x-(2,2)||_2^2}{\sqrt{\Delta x \Delta y}}\right) - \exp(-28.125)\right)\left(\chi_{\mathbf{B}_{\|\cdot\|_2}((2,2),0.5-r)} * \psi_r\right)(x)}{2}, \quad x \in Y, \tag{5.56}$$

where $\mathbf{B}_{\|\cdot\|_2}(\xi, r)$ represents the usual L^2-ball centred at $\xi \in \mathbb{R}^n$ and of radius r, $\chi_{\mathbf{B}_{\|\cdot\|_2}((2,2),0.5-r)}$ represents the characteristic function, and ψ_γ is defined by the standard mollifier $\psi : \mathbb{R}^n \to \mathbb{R}_+$,

$$\psi(x) := \begin{cases} \frac{\exp\left(\frac{1}{x^2-1}\right)}{\int_{\mathbf{B}_{\|\cdot\|_2}(0,1)} \exp\left(\frac{1}{z^2-1}\right) dz} & \text{if} \quad \|x\|_2 < 1, \\ 0 & \text{if} \quad \|x\|_2 \geq 1, \end{cases} \tag{5.57}$$

via the formula

$$\psi_r(x) := \frac{1}{r^n}\psi\left(\frac{x}{r}\right). \tag{5.58}$$

Further, given the heterogeneous nature of both the tumour and the tissue, to illustrate the modelling described in the previous section we consider here the following initial conditions for the ECM, namely

$$v(x,0) = \frac{1+0.3\sin(4\pi||x||_2)+\sin(4\pi||(4,0)-x||_2)}{2}, \quad x \in Y. \tag{5.59}$$

Figure 5.10 shows the initial conditions (5.56) and (5.59) of ECM and cancer cell distributions that are used in all the simulations presented in this chapter.

For the enzymatic components entering the system (5.34), we consider the following initial conditions, namely:

$$\begin{aligned} u(x,0) &= 1 - \tfrac{1}{2}c(x,0), && x \in Y \\ p(x,0) &= \tfrac{1}{2}c(x,0), && x \in Y \\ m(x,0) &= \tfrac{1}{20}c(x,0), && x \in Y \end{aligned} \tag{5.60}$$

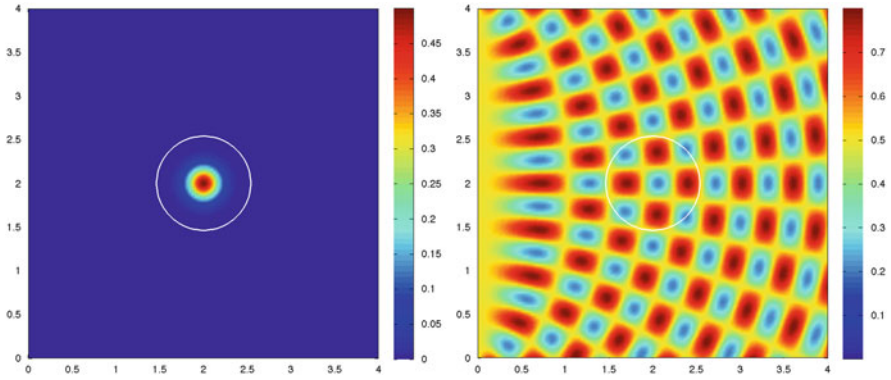

Fig. 5.10 This is a partial reproduction of Fig. 1 from [40]. It shows initial conditions of the distributions of cancer cells (*left column*) and ECM (*right column*) and the invasive boundary of the tumour (*white line*)

Finally, in the absence of tissue data at the invasive edge of the tumour, the tissue threshold ω_{ϵ_Y} controlling whether or not a point on the boundary exercises the movement is taken here in the following functional form:

$$\omega_{\epsilon_Y}(\beta) := \begin{cases} \sin\left(\frac{\pi}{2}\left(1-\frac{1}{\beta}\frac{v_{\omega(t_0)}(x^*_{\epsilon_Y},t_0+\Delta t)}{\sup\limits_{\xi\in\partial\Omega(t_0)} v_{\Omega(t_0)}(\xi,t_0+\Delta t)}\right)\right) & \text{if } \frac{v_{\omega(t_0)}(x^*_{\epsilon_Y},t_0+\Delta t)}{\sup\limits_{\xi\in\partial\Omega(t_0)} v_{\Omega(t_0)}(\xi,t_0+\Delta t)} \leq \beta \\ \sin\left(\frac{\pi}{2(1-\beta)}\left(\frac{v_{\omega(t_0)}(x^*_{\epsilon_Y},t_0+\Delta t)}{\sup\limits_{\xi\in\partial\Omega(t_0)} v_{\Omega(t_0)}(\xi,t_0+\Delta t)}-\beta\right)\right) & \text{if } \frac{v_{\omega(t_0)}(x^*_{\epsilon_Y},t_0+\Delta t)}{\sup\limits_{\xi\in\partial\Omega(t_0)} v_{\Omega(t_0)}(\xi,t_0+\Delta t)} > \beta \end{cases} \tag{5.61}$$

where $\beta \in (0,1)$ is a parameter that explores the level of ECM degradation, indicating the most favourable conditions for invasion in the peritumoural region, [47]. We can immediately observe that this functional form of $\omega_{\epsilon_Y}(\cdot)$ does not allow for any invasion if the MDEs cause either a complete destruction or a very superficial degradation of the surrounding ECM.

In this context, the following three figures present here the computational results published first in [40], Figs. 7, 8, and 9.

Figure 5.11 show the results of the evolving cancer cell and ECM spatial distributions and of the invasive tumour boundary at macro-time stage 20, 40, 60. Even though we started from the symmetric distribution of cancer cells shown in Fig. 5.10, in each macro-micro stage of the multiscale invasion process, the macro-scale cancer dynamics gives rise to a heterogeneous distribution of sources for the bundle of micro-processes occurring at the tumour invasive edge. As described by the model, these micro-processes determine the macro-scale movement characteristics of the tumour boundary, ultimately resulting in pronounced changes in tumour morphology. These morphological changes lead to the pronounced fingering and lobular patterns in the evolution of the invading tumour shown in Fig. 5.11. Furthermore, focussing now on the effect of the ECM proliferation rate μ_2 and ECM

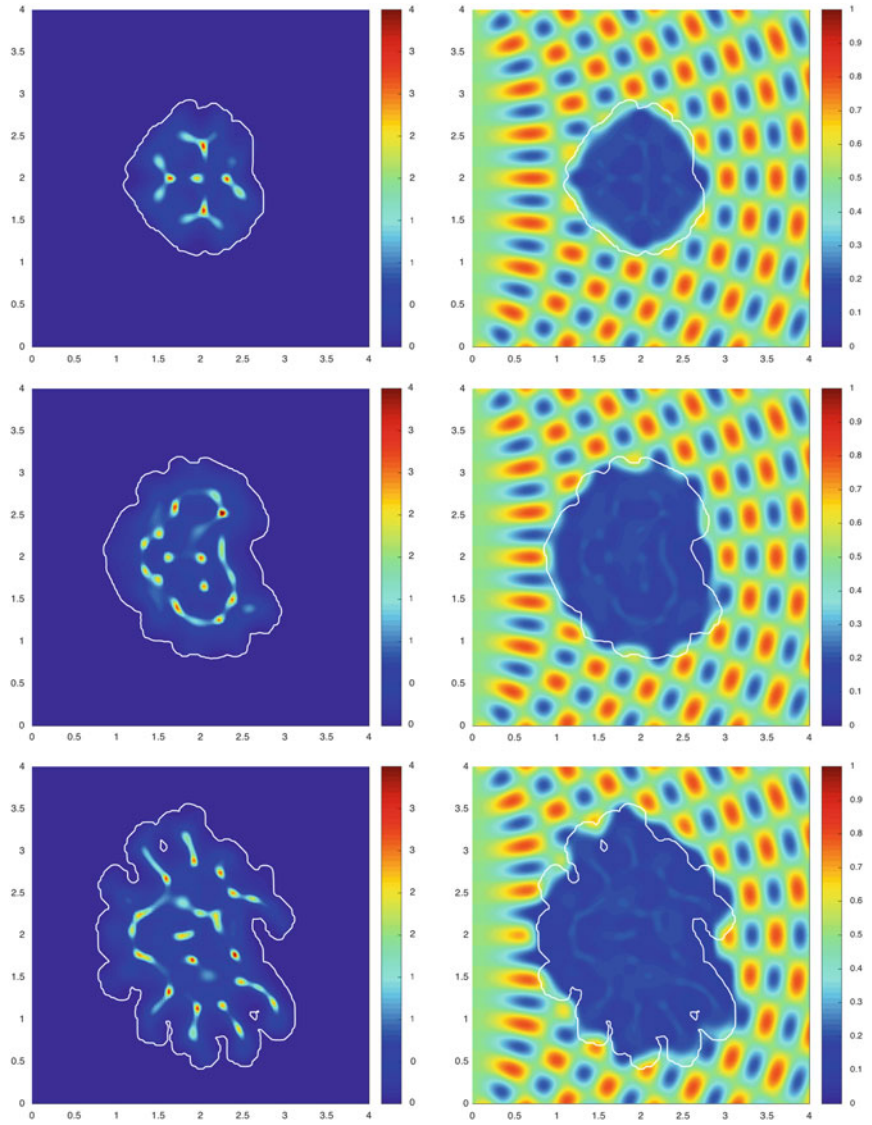

Fig. 5.11 This is a reproduction of Fig. 7 from [40]. It consists of simulation results showing distributions of cancer cells (*left column*) and ECM (*right column*) and the invasive boundary of the tumour (*white line*) at various macro-micro stages: Stage 20, 40, 60. Starting from the initial conditions shown in Fig. 5.10 in this chapter, these results were obtained for the standard parameter set considered in [40], with $D_c = 4.3 \times 10^{-3}$, $\beta = 0.7625$, $\mu_2 = 0$ and $\delta = 0.75$

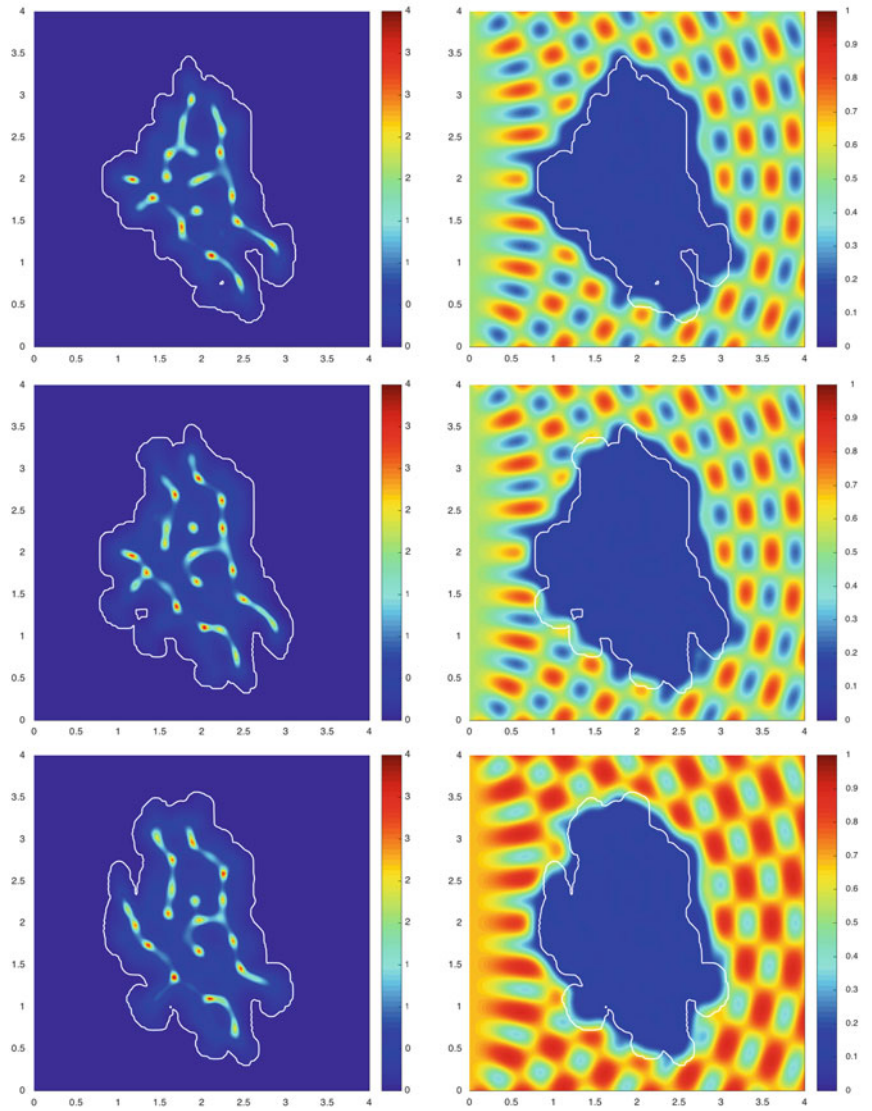

Fig. 5.12 This is a reproduction of Fig. 8 from [40]. It consists of simulation results showing distributions of cancer cells (*left column*) and ECM (*right column*) and the invasive boundary of the tumour (*white line*) at macro-micro stage 60. Starting from the initial conditions shown in Fig. 5.10 in this chapter, these results were obtained for the standard parameter set considered in [40], with $D_c = 4.3 \times 10^{-3}$, $\beta = 0.7625$, $\delta = 1.5$, and for rows 1–3 of images we consider $\mu_2 = 0.0005$, $\mu_2 = 0.001$, and $\mu_2 = 0.005$, respectively

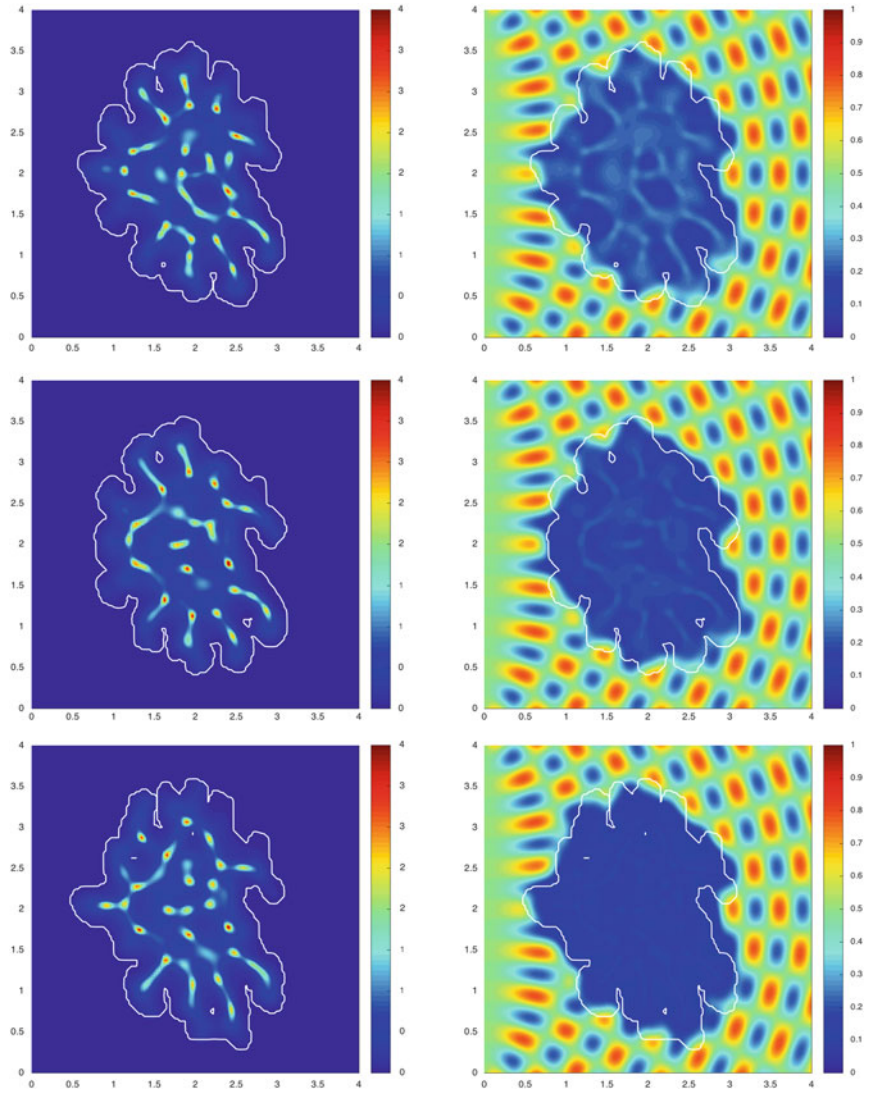

Fig. 5.13 This is a reproduction of Fig. 9 from [40]. It consists of simulation results showing distributions of cancer cells (*left column*) and ECM (*right column*) and the invasive boundary of the tumour (*white line*) at macro-micro stage 60. Starting from the heterogeneous initial conditions shown in Fig. 5.10 in this chapter, these results were obtained for the standard parameter set considered in [40], with $D_c = 4.3 \times 10^{-3}$, $\mu_2 = 0$, $\beta = 0.7625$, and for rows 1–3 of images we consider $\delta = 0.5$, $\delta = 0.75$, and $\delta = 1$, respectively

degradation rate δ, as discussed in [40]. Figures 5.12 and 5.13 show consistency in the invasion patterns when we vary the parameters $\mu_2 \in [0.0005, 0.005]$ and $\delta \in [0.5, 1]$. Finally, although not shown here, consistent changes in the invasion patterns have also been observed when the tissue parameter β was perturbed, see [40] for details.

5.5 Concluding Remarks

This chapter offered a multiscale perspective in modelling cancer invasion based on the recent advances in the area proposed in [13, 14, 40, 47]. Having started by presenting two macro-scale modelling approaches concerning the role of cell-adhesion, molecular signalling and matrix degrading enzymes in cancer invasion, we continued the discussion by revisiting some of these important invasion processes from a multiscale moving boundary modelling perspective, which incorporated key aspects of both tissue-scale and cell-scale dynamics as well as the top-down and bottom-up links between the scales.

We began our discussion with the macro-scale non-local modelling described in Sect. 5.2 focused on aspects concerning the effect of cell-adhesion on the growth and development of cancerous tissue. While the approach involving n cancer cell subpopulations was extending previous modelling [18], the invasion results obtained for both one and two cancer cell subpopulations were in line with the infiltrative patterns observed in [27, 33] for esophageal and lung cancer.

Section 5.3 described the development a of a general macroscopic spatio-temporal-structural modelling approach with application to the uPA system in cancer invasion. This allowed us to explore the coupled dynamics of a cancerous tissue consisting of a mixture of tumour cells structured in terms of their enzymatic ability, ECM, and q free molecular species out of which only a subselection of $p < q$ molecular species could bind to the cell surface. After a rigorous derivation of the general spatio-temporal-structural framework, we apply this to the specific case of the uPA system, obtaining this way a structural model that incorporates the binding and unbinding properties of the uPA and PAI-1. Moreover, as expected, an i-state integration of system (5.33) leads to a local non-structural system that is similar in flavour to the one initially proposed by Chaplain and Lolas [9, 10].

Finally, Sect. 5.4 expanded the approach from a multiscale moving boundary perspective. The general multiscale modeling approach that was described here explores in an integrated manner the tissue-scale cell population dynamics and key proteolytic cell-scale molecular mechanics (occurring in a cell-scale neighbourhood of the tumour invasive edge) together with the top-down and the bottom-up link between these two biological scales. This explores the key role that is played in cancer invasion by the matrix-degrading enzymes which are secreted from the outer proliferating rim. The evolution of tissue-scale tumour morphology is expressed here in multiscale manner, by accounting for the invasive edge cell-scale micro-dynamics (induced by the macro-scale), which determines the law for macro-scale

tumour boundary relocation. The computational experiments presented here reveal a pronounced fingering and lobular character in the evolution of the cancer invasion pattern.

Looking forward, all the modelling approaches presented in this chapter could be taken forward by bringing in more details either at the level of cell population, by accounting for instance for tumour cells heterogeneity, or at the level of cell-scale dynamics, by accounting for more complex signalling pathways.

References

1. V. Andasari, A. Gerisch, G. Lolas, A. South, M. Chaplain, Mathematical modeling of cancer cell invasion of tissue: biological insight from mathematical analysis and computational simulation. J. Math. Biol. **63**(1), 141–171 (2011). doi:10.1007/s00285-010-0369-1
2. P.A. Andreasen, R. Egelund, H.H. Petersen, The plasminogen activation system in tumor growth, invasion, and metastasis. Cell Mol. Life Sci. **57**(1), 25–40 (2000). doi:10.1007/s000180050497
3. P.A. Andreasen, L. Kjøller, L. Christensen, M.J. Duffy, The urokinase-type plasminogen activator system in cancer metastasis: a review. Int. J. Cancer **72**(2), 1–22 (1997). doi:10.1002/(SICI)1097-0215(19970703)72:1<1::AID-IJC1>3.0.CO;2-Z
4. N.J. Armstrong, K.J. Painter, J.A. Sherratt, A continuum approach to modelling cell–cell adhesion. J. Theor. Biol. **243**(1), 98–113 (2006). doi:10.1016/j.jtbi.2006.05.030
5. J. Behrens, M.M. Mareel, F.M.V. Roy, W. Birchmeier, Dissecting tumor cell invasion: epithelial cells acquire invasive properties after the loss of uvomorulin-mediated cell-cell adhesion. J. Cell Biol. **108**(6), 2435–2447 (1989). doi:10.1083/jcb.108.6.2435
6. A.L. Berrier, K.M. Yamada, Cell–matrix adhesion. J. Cell Physiol. **213**(3), 565–573 (2007). doi:10.1002/jcp.21237
7. N. Bhagavathula, A.W. Hanosh, K.C. Nerusu, H. Appelman, S. Chakrabarty, J. Varani, Regulation of e-cadherin and β-catenin by Ca^{2+} in colon carcinoma is dependent on calcium-sensing receptor expression and function. Int. J. Cancer **121**, 1455–1462 (2007). doi:10.1002/ijc.22858
8. S.W. Byers, C.L. Sommers, B. Hoxter, A.M. Mercurio, A. Tozeren, Role of e-cadherin in the response of tumor cell aggregates to lymphatic, venous and arterial flow: measurement of cell-cell adhesion strength. J. Cell Sci. **108**(5), 2053–2064 (1995)
9. M.A.J. Chaplain, G. Lolas, Mathematical modelling of cancer cell invasion of tissue: the role of the urokinase plasminogen activation system. Math. Models Methods Appl. Sci. **15**, 1685–1734 (2005). doi:10.1142/S0218202505000947
10. M.A.J. Chaplain, G. Lolas, Mathematical modelling of cancer invasion of tissue: dynamic heterogeneity. Netw. Heterog. Media **1**(3), 399–439 (2006). doi:10.3934/nhm.2006.1.399
11. S.J. Chapman, M.J. Plank, A. James, B. Basse, A nonlinear model of age and size-structured populations with applications to cell cycles. ANZIAM J. **49**, 151–169 (2007). doi:10.1017/S144618110001275X
12. O. Diekmann, H. Heijmans, H. Thieme, On the stability of the cell size distribution. J. Math. Biol. **19**(2), 227–248 (1984). doi:10.1007/BF00277748
13. P. Domschke, D. Trucu, A. Gerisch, M. Chaplain, Mathematical modelling of cancer invasion: implications of cell adhesion variability for tumour infiltrative growth patterns. J. Theor. Biol. **361**, 41–60 (2014)
14. P. Domschke, D. Trucu, A. Gerisch, M.A.J. Chaplain, Structured models of cell migration incorporating molecular binding processes. J. Math. Biol. 1–38 (2016). ArXiv:1607.05353.
15. M.J. Duffy, The urokinase plasminogen activator system: role in malignancy. Curr. Pharm. Des. **10**(1), 39–49 (2004). doi:10.2174/1381612043453559

16. P. Friedl, P.B. Noble, P.A. Walton, D.W. Laird, P.J. Chauvin, R.J. Tabah, M. Black, K.S. Zanker, Migration of coordinated cell clusters in mesenchymal and epithelial cancer explants in vitro. Cancer Res. **55**, 4557–4560 (1995)
17. C.F. Gao, Q. Xie, Y.L. Su, J. Koeman, S.K. Khoo, M. Gustafson, Knudsen, B.S., R. Hay, N. Shinomiya, G.F.V. Woude, Proliferation and invasion: plasticity in tumor cells. Proc. Natl. Acad. Sci. USA **102**(30), 10528–10533 (2005). doi:10.1073/pnas.0504367102
18. A. Gerisch, M. Chaplain, Mathematical modelling of cancer cell invasion of tissue: local and non-local models and the effect of adhesion. J. Theor. Biol. **250**(4), 684–704 (2008). doi:10.1016/j.jtbi.2007.10.026
19. A. Gerisch, K.J. Painter, Mathematical modeling of cell adhesion and its applications to developmental biology and cancer invasion, in *Cell Mechanics: From Single Scale-Based Models to Multiscale Modelling*, ed. by A. Chauvière, L. Preziosi, C. Verdier (CRC, Boca Raton, FL, 2010), pp. 319–350
20. V. Guillemin, A. Pollack, *Differential Topology* (Prentice-Hall, Englewood Cliffs, NJ, 1974)
21. P. Halmos, *Measure Theory* (Springer, New York, 1974)
22. D. Hanahan, R.A. Weinberg, The hallmarks of cancer. Cell **100**, 57–70 (2000)
23. T. Hillen, K. Painter, Global existence for a parabolic chemotaxis model with prevention of overcrowding. Adv. Appl. Math. **26**(4), 280–301 (2001). doi:10.1006/aama.2001.0721
24. C.E. Hills, M.Y.G. Younis, J. Bennett, E. Siamantouras, K.K. Liu, P.E. Squires, Calcium-sensing receptor activation increases cell-cell adhesion and β-cell function. Cell Physiol. Biochem. **30**(3), 575–586 (2012). doi:10.1159/000341439
25. A.M. Hofer, S. Curci, M.A. Doble, E.M. Brown, D.I. Soybel, Intercellular communication mediated by the extracellular calcium-sensing receptor. Nat. Cell Biol. **2**(7), 392–398 (2000). doi:10.1038/35017020
26. W.C. Hung, S.H. Chen, C.D. Paul, K.M. Stroka, Y.C. Lo, J.T. Yang, K. Konstantopoulos, Distinct signaling mechanisms regulate migration in unconfined versus confined spaces. J. Cell Biol. **202**(5), 807–824 (2013). doi:10.1083/jcb.201302132
27. E. Ito, S. Ozawa, H. Kijima, A. Kazuno, T. Nishi, O. Chino, H. Shimada, M. Tanaka, S. Inoue, S. Inokuchi, H. Makuuchi, New invasive patterns as a prognostic factor for superficial esophageal cancer. J. Gastroenterol. **47**, 1279–1289 (2012). doi:10.1007/s00535-012-0587-y
28. R.L. Juliano, Signal transduction by cell adhesion receptors and the cytoskeleton: functions of integrins, cadherins, selectins, and immunoglobulin-superfamily members. Annu. Rev. Pharmacol. **42**(1), 283–323 (2002). doi:10.1146/annurev.pharmtox.42.090401.151133
29. K. Ko, P. Arora, V. Bhide, A. Chen, C. McCulloch, Cell-cell adhesion in human fibroblasts requires calcium signaling. J. Cell Sci. **114**(6), 1155–1167 (2001)
30. J. Kolega, The movement of cell clusters in vitro: Morphology and directionality. J. Cell Sci. **49**, 15–32 (1981)
31. A.F.N.V. Larebeke, M.E. Bracke, M.M. Mareel, Invasive epithelial cells show more fast plasma membrane movements than related or parental non-invasive cells. Cytometry **13**, 9–14 (1992). doi:10.1002/cyto.990130104
32. P.U. Le, T.N. Nguyen, Drolet-P. Savoie, N. Leclerc, I.R. Nabi, Increased β-actin expression in an invasive moloney sarcoma virus-transformed MDCK cell variant concentrates to the tips of multiple pseudopodia. Cancer Res. **58**(8), 1631–1635 (1998)
33. R. Masuda, H. Kijima, N. Imamura, N. Aruga, Y. Nakamura, D. Masuda, H. Takeichi, N. Kato, T. Nakagawa, M. Tanaka, S. Inokuchi, M. Iwazaki, Tumor budding is a significant indicator of a poor prognosis in lung squamous cell carcinoma patients. Mol. Med. Rep. **6**, 937–943 (2012). doi:10.3892/mmr.2012.1048
34. J.A.J. Metz, O. Diekmann, *The Dynamics of Physiologically Structured Populations*. Lecture Notes in Biomathematics, vol. 68 (Springer, Berlin, 1986)
35. C.T. Mierke, B. Frey, M. Fellner, M. Herrmann, B. Fabry, Integrin $\alpha 5\beta 1$ facilitates cancer cell invasion through enhanced contractile forces. J. Cell Sci. **124**, 369–383 (2010). doi:10.1242/jcs.071985

36. K. Moissoglu, M.A. Schwartz, Integrin signalling in directed cell migration. Biol. Cell **98**(9), 547–555 (2006). doi:10.1042/BC20060025
37. A.C. Newby, Matrix metalloproteinases regulate migration, proliferation, and death of vascular smooth muscle cells by degrading matrix and non-matrix substrates. Cardiovasc. Res. **69**(3), 614–624 (2006). doi:10.1016/j.cardiores.2005.08.002
38. S.L. Parsons, S.A. Watson, P.D. Brown, H.M. Collins, R.J. Steele, Matrix metalloproteinases. Br. J. Surg. **84**(2), 160–166 (1997). doi:10.1046/j.1365-2168.1997.02719.x
39. A. Pathak, S. Kumar, Independent regulation of tumor cell migration by matrix stiffness and confinement. Proc. Natl. Acad. Sci. USA **109**(26), 10334–10339 (2012). doi:10.1073/pnas.1118073109
40. L. Peng, D. Trucu, P. Lin, A. Thompson, M.A.J. Chaplain, A multiscale mathematical model of tumour invasive growth (2016). arXiv:1603.07540
41. M.S. Pepper, Role of the matrix metalloproteinase and plasminogen activator-plasmin systems in angiogenesis. Arterioscl. Throm. Vas. **21**(7), 1104–1117 (2001). doi:10.1161/hq0701.093685
42. C.B. Pierce, R. Shikes, L.M. Fink, *Cancer: A Problem of Developmental Biology* (Prentice-Hall, Englewood Cliffs, NJ, 1978)
43. R. Poincloux, O. Collin, LizáF. rraga, M. Romao, M. Debray, M. Piel, P. Chavrier, Contractility of the cell rear drives invasion of breast tumor cells in 3d matrigel. Proc. Natl. Acad. Sci. USA **108**(5), 1943–1948 (2011). doi:10.1073/pnas.1010396108
44. H.W. Smith, C.J. Marshall, Regulation of cell signalling by upar. Nat. Rev. Mol. Cel. Biol. **11**, 23–36 (2010)
45. R. Somerville, S. Oblander, S. Apte, Matrix metalloproteinases: old dogs with new tricks. Genome Biol. **4:216**(6), 11pp. (2003). doi:10.1186/gb-2003-4-6-216
46. M.D. Sternlicht, Z. Werb, How matrix metalloproteinases regulate cell behavior. Annu. Rev. Cell Dev. Biol. **17**(1), 463–516 (2001). doi:10.1146/annurev.cellbio.17.1.463
47. D. Trucu, P. Lin, M.A.J. Chaplain, Y. Wang, A multiscale moving boundary model arising in cancer invasion. Multiscale Model. Simul. **11**(1), 309–335 (2013)
48. S.L. Tucker, S.O. Zimmerman, A nonlinear model of population dynamics containing an arbitrary number of continuous structure variables. SIAM J. Appl. Math. **48**(3), pp. 549–591 (1988). URL http://www.jstor.org/stable/2101595
49. S. Ulisse, E. Baldini, S. Sorrenti, D'M. Armiento, The urokinase plasminogen activator system: a target for anti-cancer therapy. Curr. Cancer Drug Targets **9**(1), 32–71 (2009). doi:10.2174/156800909787314002
50. R. Umbas, J.A. Schalken, T.W. Aalders, e.a.: Expression of the cellular adhesion molecule e-cadherin is reduced or absent in high-grade prostate cancer. Cancer Res. **52**, 5104–5109 (1992)
51. L. Venkatraman, S.M. Chia, B.C. Narmada, J.K. White, S.S. Bhowmick, C.F. Dewey Jr., P.T. So, L. Tucker-Kellogg, H. Yu, Plasmin triggers a switch-like decrease in thrombospondin-dependent activation of tgf-β1. Biophys. J. **103**(5), 1060–1068 (2012)
52. R. Visse, H. Nagase, Matrix metalloproteinases and tissue inhibitors of metalloproteinases: structure function and biochemistry. Circ. Res. **92**, 827–839 (2003). doi:10.1161/01.RES.0000070112.80711.3D
53. G. Webb, Population models structured by age, size, and spatial position, in *Structured Population Models in Biology and Epidemiology*, ed. by P. Magal, S. Ruan. Lecture Notes in Mathematics, vol. 1936 (Springer, Berlin, Heidelberg, 2008), pp. 1–49
54. R.A. Weinberg, *The Biology of Cancer* (Garland Science, New York, 2006)
55. K. Wolf, M. te Lindert, M. Krause, S. Alexander, J. te Riet, A.L. Willis, R.M. Hoffman, C.G. Figdor, S.J. Weiss, P. Friedl, Physical limits of cell migration: control by ECM space and nuclear deformation and tuning by proteolysis and traction force. J. Cell Biol. **201**(7), 1069–1084 (2013). doi:10.1083/jcb.201210152

56. M.H. Zaman, L.M. Trapani, A.L. Sieminski, D. MacKellar, H. Gong, R.D. Kamm, A. Wells, D.A. Lauffenburger, P. Matsudaira, Migration of tumor cells in 3d matrices is governed by matrix stiffness along with cell-matrix adhesion and proteolysis. Proc. Natl. Acad. Sci. USA **103**(29), 10889–10894 (2006). doi:10.1073/pnas.0604460103
57. E. Zamir, B. Geiger, Molecular complexity and dynamics of cell-matrix adhesions. J. Cell Sci. **114**, 3583–3590 (2001)
58. X. Zheng, S. Wise, V. Cristini, Nonlinear simulation of tumour necrosis, neo-vascularization and tissue invasion via an adaptive finite-element/level set method. Bull. Math. Biol. **67**(2), 211–259 (2005)

LECTURE NOTES IN MATHEMATICS Springer

Editors in Chief: J.-M. Morel, B. Teissier;

Editorial Policy

1. Lecture Notes aim to report new developments in all areas of mathematics and their applications – quickly, informally and at a high level. Mathematical texts analysing new developments in modelling and numerical simulation are welcome.

   Manuscripts should be reasonably self-contained and rounded off. Thus they may, and often will, present not only results of the author but also related work by other people. They may be based on specialised lecture courses. Furthermore, the manuscripts should provide sufficient motivation, examples and applications. This clearly distinguishes Lecture Notes from journal articles or technical reports which normally are very concise. Articles intended for a journal but too long to be accepted by most journals, usually do not have this "lecture notes" character. For similar reasons it is unusual for doctoral theses to be accepted for the Lecture Notes series, though habilitation theses may be appropriate.

2. Besides monographs, multi-author manuscripts resulting from SUMMER SCHOOLS or similar INTENSIVE COURSES are welcome, provided their objective was held to present an active mathematical topic to an audience at the beginning or intermediate graduate level (a list of participants should be provided).

   The resulting manuscript should not be just a collection of course notes, but should require advance planning and coordination among the main lecturers. The subject matter should dictate the structure of the book. This structure should be motivated and explained in a scientific introduction, and the notation, references, index and formulation of results should be, if possible, unified by the editors. Each contribution should have an abstract and an introduction referring to the other contributions. In other words, more preparatory work must go into a multi-authored volume than simply assembling a disparate collection of papers, communicated at the event.

3. Manuscripts should be submitted either online at www.editorialmanager.com/lnm to Springer's mathematics editorial in Heidelberg, or electronically to one of the series editors. Authors should be aware that incomplete or insufficiently close-to-final manuscripts almost always result in longer refereeing times and nevertheless unclear referees' recommendations, making further refereeing of a final draft necessary. The strict minimum amount of material that will be considered should include a detailed outline describing the planned contents of each chapter, a bibliography and several sample chapters. Parallel submission of a manuscript to another publisher while under consideration for LNM is not acceptable and can lead to rejection.

4. In general, **monographs** will be sent out to at least 2 external referees for evaluation.

   A final decision to publish can be made only on the basis of the complete manuscript, however a refereeing process leading to a preliminary decision can be based on a pre-final or incomplete manuscript.

   Volume Editors of **multi-author works** are expected to arrange for the refereeing, to the usual scientific standards, of the individual contributions. If the resulting reports can be

forwarded to the LNM Editorial Board, this is very helpful. If no reports are forwarded or if other questions remain unclear in respect of homogeneity etc, the series editors may wish to consult external referees for an overall evaluation of the volume.

5. Manuscripts should in general be submitted in English. Final manuscripts should contain at least 100 pages of mathematical text and should always include
   - a table of contents;
   - an informative introduction, with adequate motivation and perhaps some historical remarks: it should be accessible to a reader not intimately familiar with the topic treated;
   - a subject index: as a rule this is genuinely helpful for the reader.
   - For evaluation purposes, manuscripts should be submitted as pdf files.

6. Careful preparation of the manuscripts will help keep production time short besides ensuring satisfactory appearance of the finished book in print and online. After acceptance of the manuscript authors will be asked to prepare the final LaTeX source files (see LaTeX templates online: https://www.springer.com/gb/authors-editors/book-authors-editors/manuscriptpreparation/5636) plus the corresponding pdf- or zipped ps-file. The LaTeX source files are essential for producing the full-text online version of the book, see http://link.springer.com/bookseries/304 for the existing online volumes of LNM). The technical production of a Lecture Notes volume takes approximately 12 weeks. Additional instructions, if necessary, are available on request from lnm@springer.com.

7. Authors receive a total of 30 free copies of their volume and free access to their book on SpringerLink, but no royalties. They are entitled to a discount of 33.3 % on the price of Springer books purchased for their personal use, if ordering directly from Springer.

8. Commitment to publish is made by a *Publishing Agreement*; contributing authors of multiauthor books are requested to sign a *Consent to Publish form*. Springer-Verlag registers the copyright for each volume. Authors are free to reuse material contained in their LNM volumes in later publications: a brief written (or e-mail) request for formal permission is sufficient.

Addresses:
Professor Jean-Michel Morel, CMLA, École Normale Supérieure de Cachan, France
E-mail: moreljeanmichel@gmail.com

Professor Bernard Teissier, Equipe Géométrie et Dynamique,
Institut de Mathématiques de Jussieu – Paris Rive Gauche, Paris, France
E-mail: bernard.teissier@imj-prg.fr

Springer: Ute McCrory, Mathematics, Heidelberg, Germany,
E-mail: lnm@springer.com